Operando ab initio simulaties van belangrijke chemische transformaties over zeolieten binnen de conversie van methanol naar olefinen

Operando First Principle Simulations of Important Chemical Transformations over Zeolites within the Methanol-to-Olefin Process

Simon Bailleul

Promotor: prof. dr. ir. V. Van Speybroeck
Proefschrift ingediend tot het behalen van de graad van
Doctor in de ingenieurswetenschappen: chemische technologie

UNIVERSITEIT
GENT

Vakgroep Toegepaste Fysica
Voorzitter: prof. dr. ir. C. Leys
Faculteit Ingenieurswetenschappen en Architectuur
Academiejaar 2019 - 2020

ISBN 978-94-6355-320-9
NUR 913, 928
Wettelijk depot: D/2019/10.500/128

Members of the examination committee

Chair

Prof. Dr. Ir. Filip De Turck (Ghent University)

Reading Committee

Prof. Dr. Ir. Joris Thybaut (Ghent University)
Prof. Em. Dr. Michel Waroquier (Ghent University)
Prof. Dr. Ir. Louis Vanduyfhuys (Ghent University)
Prof. Dr. Evgeny Pidko (Delft University of Technology and ITMO University)

Supervisor

Prof. Dr. Ir. Veronique Van Speybroeck (Ghent University)

This research has been conducted at the **Center for Molecular Modeling**, in collaboration with:

- Catalysis Engineering Group, Delft University of Technology, The Netherlands (Prof. Dr. J. Gascon, Prof. Dr. F. Kapteijn, Dr. I. Yarulina)
- KAUST Catalysis Center, King Abdullah University of Science and Technology, Saudi Arabia (Prof. Dr. J. Gascon, Dr. I. Yarulina, Dr. Abhishek Dutta Chowdhury, Dr. Edy Abou-Hamad, Abhay Dokania)

Preface

The more grateful we feel, the happier we become. This is because gratitude helps us realize we are all connected. Nobody feels like an island when feeling grateful. Gratitude awakens us to the truth of our interdependent nature.

With these inspirational words of Haemin Sunim, author of *The Things You Can See Only When You Slow Down*, in mind, I would like to take the time to thank the people which were very important during my Ph.D. and for whom I am grateful.

I would like to start by thanking prof. Veronique Van Speybroeck, my supervisor during both my master's thesis and Ph.D. at the Center of Molecular Modeling (CMM), for the opportunity to perform my Ph.D. under her supervision. She offered me plenty of guidance throughout the years and gave me the opportunity to learn at several workshops, present my research at interesting conferences and publish my results in impressive journals.

Furthermore, prof. Van Speybroeck introduced me into the collaborative project with the experimental partners of the group of prof. Jorge Gascon, who I like to thank for the intensive collaboration and fruitful discussions. From his group, I would especially like to thank Irina Yarulina, Abhishek Dutta Chowdhury, Edy Abou-Hamad and Abhay Dokania for performing the experimental work and guiding me through their results, as such enabling us to draw the right conclusions.

Of course, there are several other people I would like to thank. First of all, prof. em. Michel Waroquier for his guidance through the though revisions we had for some of the articles and the interesting discussions. I would also like to thank Kristof and Julianna to teach me the basics of molecular modeling. Subsequently, I would like to express my gratitude to Ruben for teaching me the enhanced sampling techniques. Similarly, I would like to say thank you to Louis for providing me the tools to properly analyze these enhanced sampling results. I would like to thank Kristof, Julianna, Chiara, Sander and Tobias for being my office mates during the last four years and a half and providing both day to day guidance as well as the necessary distraction. Likewise, I would like the members of the five-a-side football team of the CMM, FC Molmod, to provide the weekly distraction and keeping me in shape. Lastly, I would like to especially thank Sven for helping me organize the CMM/MaChT quiz on a yearly basis, having several drinks with me during the years and watching superhero movies together.

There are several more people who I am grateful for outside of academia. First of all my friends for relaxing together and allowing me to put everything in perspective. Furthermore, I would like to give thanks to my sister for always being there, helping me to settle at the beginning of my Ph.D. and the numerous

bike rides in the summer. I am grateful towards my parents, for giving me all the opportunities that allowed me to get to where I am now and supporting me all the way through.

Lastly, I would like to express my gratitude to my wife, Ellen, for always being there for me and providing me with an environment in which I can express my worries, thoughts and stress, allowing me to relax. I love how you always provide an attentive ear and overwhelm me with your enthusiasm.

With this, I will conclude this preface and I hope you enjoy the further reading.

Simon Bailleul
Ghent, December 2019

Contents

Preface

List of Abbreviations iii

List of Symbols v

Samenvatting vii

Summary xiii

I Operando First Principle Simulations of Important Chemical Transformations over Zeolites within the Methanol-to-Olefin Process 1

1 Introduction 3
- 1.1 Methanol-to-olefin process . . . 3
- 1.2 Zeolite catalysts within the MTO process . . . 5
- 1.3 MTO reaction mechanism . . . 7
  - 1.3.1 Dual cycle mechanism . . . 7
  - 1.3.2 Importance of methylation reactions . . . 8
- 1.4 How to tune catalyst lifetime and product selectivity . . . 10
  - 1.4.1 The nature and strength of the acid site . . . 11
  - 1.4.2 The reaction conditions . . . 13
- 1.5 Molecular modeling in zeolite catalysis . . . 15
- 1.6 Goal and outline . . . 18

2 Operando modeling within zeolite catalysis 21
- 2.1 Density functional theory . . . 22
- 2.2 Periodic zeolite models . . . 25
- 2.3 Molecular simulations . . . 25
  - 2.3.1 Statistical physics . . . 26
  - 2.3.2 Harmonic oscillator approximation . . . 27
  - 2.3.3 *Ab initio* molecular dynamics . . . 29
- 2.4 Enhanced sampling techniques . . . 30
  - 2.4.1 Metadynamics . . . 31

2.4.2 Variationally enhanced sampling . . . 31
2.4.3 Umbrella sampling . . . 33
2.4.4 Thermodynamic integration . . . 34
2.4.5 Comparison of enhanced sampling methods . . . 35
2.5 Collective variables . . . 36
2.5.1 Definition of a collective variable . . . 36
2.5.2 Transformation of collective variables . . . 38
2.5.3 Impact of collective variables on free energy profiles . . . 40
2.6 Thermodynamic quantities and reaction rates . . . 42
2.6.1 Thermodynamic quantities . . . 42
2.6.2 Transition state theory and phenomenological barrier . . . 44
2.6.3 Reaction kinetics for the methylation of ethene . . . 45

3 New insights into the MTO reaction cycles 51
3.1 Nature of active site: Brønsted versus Lewis acidity . . . 52
3.2 The role of water . . . 62
3.3 Effect of topology and Brønsted acid strength . . . 68

4 Conclusions and perspectives 75

II Published papers 83
Paper I: Towards molecular control of elementary reactions in zeolite catalysis by advanced molecular simulations mimicking operating conditions . . . 85
Paper II: Suppression of Aromatic Cycle in Methanol-to-Olefins Reaction over ZSM-5 by post-synthetic modification using Calcium . . . 107
Paper III: Structure–performance descriptors and the role of Lewis acidity in the methanol-to-propylene process . . . 117
Paper IV: Insight into the role of water on the methylation of hexamethylbenzene in H-SAPO-34 from first principle molecular dynamics simulations . . . 129
Paper V: A supramolecular view on the cooperative role of Brønsted and Lewis acid sites in zeolites for methanol conversion . . . 149
Paper VI: Ab initio enhanced sampling kinetic study on MTO ethene methylation reaction . . . 171

A Publication List 261
Publications in international peer-reviewed journals . . . 261
Conference contributions . . . 262

B Weighted histogram analysis method 265

C Acknowledgement 267

Bibliography 269

List of Abbreviations

AFI	Aluminophosphate-five
BAS	Brønsted acid site
BEA	Beta polymorph A
BEC	Born effective charges
Cat	Catalyst model
CHA	Chabazite
CM	Center–of–mass
CMM	Center for Molecular Modeling
CN	Coordination number
CRI	Carbon Recycling International
CV	Collective variable
D3	Third generation of Grimme dispersion corrections
DFPT	Density-functional perturbation theory
DFT	Density functional theory
DI	Distance
DICP	Dalian Institute of Chemical Physics
DME	Dimethyl–ether
EFAl	Extra–framework aluminum
EtL	Emission to Liquids
FES	Free energy surface
FHVA	Full Hessian Vibrational Analysis
GGA	Generalized gradient approximation
HF	Hartree–Fock
HMB	Hexamethylbenzene
HO	Harmonic oscillator
HP	Hydrocarbon pool
IR	Infrared
IZA	International Zeolite Association
LAS	Lewis acid site
LDA	Local density approximation
LFEP	Lowest free energy path
LRT	Linear response theory
MD	Molecular dynamics
MFI	Mordenite Framework Inverted
MM	Molecular mechanics
MOF	Metal-organic framework
MTD	Metadynamics
MTTK	Martyna–Tuckerman–Tobias–Klein

MTO	Methanol–to–olefins
MTP	Methanol–to–propene
NMA	Normal mode analysis
NMR	Nuclear magnetic resonance
NpT	Isothermal–isobaric ensemble
NVE	Microcanonical ensemble
NVT	Canonical ensemble
OCP	Olefin cracking process
ONIOM	Our own n–layered integrated molecular orbital and molecular mechanics
P	Product
PHVA	Partial Hessian Vibrational Analysis
PES	Potential energy surface
QCPMG	quadrupolar Carr–Purcell–Meiboom–Gill
QM	Quantum mechanics
R	Reactant
RCN	Reaction coordinate
RDF	Radial distribution function
RxN	Reaction network
SAPO	Silico–aluminophosphate
SCF	Self–consistent field
SMS	Surface methoxide species
TI	Thermodynamic integration
tICA	time-structure based independent component analysis
TON	Theta-one
TS	Transition state
TST	Transition state theory
US	Umbrella sampling
UV/Vis	Ultraviolet/Visible
VES	Variationally enhanced sampling
WHAM	Weighted histogram analysis method
ZPE	Zero point energy
ZSM-5	Zeolite Socony Mobil–5

List of Symbols

Alphanumeric symbols	
$\ddagger$	Transition state
$\overrightarrow{a_i}$	Acceleration of atom nucleus i
C	General constant
d	Distance
$\Delta E^\ddagger$	Electronic energy barrier
$\Delta F^\ddagger$	Helmholtz free energy barrier
$\Delta G_{ads,ethene}$	Co-adsorption Gibbs free energy for ethene
$\Delta G^\ddagger$	Gibbs free energy barrier
$\Delta H^\ddagger$	Enthalpy barrier
E	Electronic energy
E_{ZPE}	Zero–point vibrational energy
F	Helmholtz free energy
$\overrightarrow{F_i}$	Force acting on nucleus i
$f_i(q)$	Basis functions used in VES
$F_q(q)$	Free energy profile in function of collective variable q
G	Gibbs free energy
H	Enthalpy
$\hat{H}$	Hamiltonian operator
H	Hessian matrix
$H_i(q)$	Histogram of window i in US
h	Planck constant
$h_{t'}$	Amplitude of a Gaussian potential
K	Force constant
k	Reaction rate constant
k_{app}	Apparent reaction rate constant
k_B	Boltzmann constant
k_intnt	Intrinsic reaction rate constant
L	Lagrangian
M	Diagonal mass matrix
M_i	Total number of sample points of window i in US
m_i	Mass of component i
N	Number of particles
N_A	Avogadro constant
N_F	Number of fixed or non-participating atoms
p	Pressure
p_i	Partial pressure of component i

$\vec{\mathbf{p}}^N$	Momentum vector
$p_q(q)$	Probability distribution
$Q(\vec{\mathbf{r}}^N)$, q	Collective variable
R	Gas constant
$\vec{\mathbf{r}}^N$	Position vector
r_{ij}	Interatomic distance between atoms i and j
S	Entropy
T	Temperature
$\hat{T}$	Kinetic energy
t	Time
U	Internal energy
$U(q)$	Bias potential used in enhanced sampling
V	Potential energy or volume
$\hat{V}$	Potential energy
V_0	Molar volume of an ideal gas
w	Width of a Gaussian potential
w_i	Weight assigned to the histogram of window i in US
Z	Partition function
Z_q	Partition function for a fixed value of q

Greek symbols	
α_i	Expansion coefficients used in VES
Δ_i	Deviation of the position components $\mathbf{r}_i$
δ	Dirac delta distribution
θ	Heaviside distribution
ν	Normal modes or eigenfunctions
$\rho(\mathbf{r})$	Electron density
σ^2	Statistical error
Ψ	Many-body electron wave function
ω	Frequencies or eigenvalues
$\Omega\,[U]$	Functional of the bias potential $U(q)$

Samenvatting

Door de uitputting van de oliereserves en de toenemende vraag naar basischemicaliën zoals etheen en propeen is de zoektocht naar processen op basis van alternatieve grondstoffen een actief onderzoeksgebied vanuit zowel industrieel als academisch perspectief. Interessante alternatieve routes zijn die startende van methanol, aangezien methanol geproduceerd kan worden uit elke vergasbare koolstofrijke grondstof. Daarom heeft het proces voor het omzetten van methanol naar koolwaterstoffen (MTH, *methanol-to-hydrocarbons*) veel belangstelling gekregen sinds de toevallige ontdekking bij Mobil eind jaren zeventig. MTH is een overkoepelende term voor alle processen waarbij methanol via een zure zeoliet- of zeotypekatalysator wordt omgezet in waardevolle koolwaterstoffen. Afhankelijk van de gevormde producten kan een onderverdeling worden gemaakt van deze processen zoals het methanol-naar-olefinen (MTO, *methanol-to-olefin*)-proces en het methanol-naar-benzine (MTG, *methanol-to-gasoline*)-proces. Vooral het MTO-proces is van groot belang vanwege zijn hoge selectiviteit voor etheen en propeen. De gebruikte katalysatoren, zeolieten, zijn kristallijne aluminosilicaten die behoren tot de familie van de microporeuze materialen met poriën en holten van moleculaire grootte. Ze kunnen van nature voorkomen als mineralen, maar hun synthetische varianten worden vaak gebruikt als sorbenten, katalysatoren en ionenwisselingsmaterialen. Zeolietkristallen bezitten regelmatige kanalen en holten (ongeveer 3–15 Å), waardoor een labyrint op nanoschaal ontstaat. Vanuit commercieel oogpunt zijn H-SAPO-34 en H-ZSM-5 de meest relevante zeolietkatalysatoren die in het MTO-proces worden gebruikt.

Hoewel er verschillende commerciële MTO-technologieën zijn ontwikkeld en er wereldwijd veel installaties zijn geïnstalleerd, bleek het reactiemechanisme voor de methanolconversie zeer moeilijk te ontrafelen. Intensief onderzoek heeft geleid tot het voorstel dat een MTO-katalysator beschouwd moet worden als een supramoleculaire entiteit bestaande uit het zeolietkanaalsysteem, dat is geactiveerd met Brønsted zure functies, waarin organische verbindingen aanwezig moeten zijn om een actieve katalysator te genereren. Bovendien zou het supramoleculaire systeem met anorganische componenten gemodificeerd kunnen worden om de katalytische functie verder te optimaliseren. Dit leidde tot de algemene aanvaarding dat het *hydrocarbon pool* (HP) mechanisme het MTO-proces regelt. In dit mechanisme werken organische componenten, die vastzitten in de zeolietporiën, als een cokatalysator bij de productie van lichte olefinen. Afhankelijk van de aard van het koolwaterstof kunnen twee met elkaar interagerende reactiecycli worden onderscheiden. Daarom wordt dit mechanisme ook het *dual cycle*-mechanisme genoemd. In een eerste cyclus worden de producten gevormd op basis van alkenen door

middel van alkeengroei en krakingsreacties van de langere olefinen. Binnen de aromatische cyclus leiden methylaties van de zijketen, ringcontracties/expansies en olefineafscheidingsreacties van aromatische tussenproducten tot productvorming. In beide reactiecycli zijn methyleringsreacties sleutelreacties die als gevolg daarvan uitgebreid bestudeerd zijn in het kader van MTO-katalyse. De specifieke werkingscyclus bepaalt in grote mate de productselectiviteit, aangezien aangetoond is dat de productie van etheen en propeen mechanistisch gescheiden is van elkaar. Etheen zou voornamelijk gevormd worden via de aromatische cyclus, terwijl propeen en langere olefinen gevormd worden via de alkeencyclus. Bovendien zijn aromatische tussenproducten geïdentificeerd als cokesprecursoren die de katalysator deactiveren. Als zodanig kunnen experimenteel gemeten productselectiviteiten en de katalysatorlevensduur in verband worden gebracht met deze fundamentele reactiecycli. Door deze redenering verder te zetten, kan men inzien dat onderdrukking van de aromatische cyclus de propeenselectiviteit en de levensduur van de katalysator kan verhogen. Deze eigenschap maakt MTO-conversie vooral interessant als *propene-on-demand*-proces om het toenemende verschil tussen de propeenproductie en de vraag op te lossen. Daarom richt een groot deel van dit proefschrift zich op het effect van post-synthetische zeolietmodificatie met aardalkalimetalen om de propeenselectiviteit en de levensduur van de katalysator te optimaliseren.

Op basis van uitsluitend experimentele gegevens is het zeer uitdagend om op moleculair niveau gedetailleerde inzichten te verzamelen in het reactiemechanisme van een industrieel proces vanwege het grote aantal reacties dat tegelijkertijd plaatsvindt. Deze hindernis kan worden overwonnen door de experimentele informatie aan te vullen met theoretische simulaties. In de laatste decennia is er aanzienlijke vooruitgang geboekt op het gebied van de computationele chemie, waardoor het mogelijk wordt om geavanceerde moleculaire dynamica methoden te introduceren. Deze technieken hebben het potentieel om chemische reacties te modelleren bij operationele condities. Dit inzicht op moleculair niveau kan ons helpen om het ontwerp van heterogene katalysatoren te optimaliseren. Een noodzakelijke voorwaarde voor het verkrijgen van een dergelijk moleculair inzicht is de betrouwbaarheid van de gebruikte berekeningsmethoden en hun vermogen om chemische reacties te simuleren die de experimentele omstandigheden zo goed mogelijk nabootsen. Traditioneel werd gebruikgemaakt van de statische geometrieoptimalisatie bij 0 K van drie stationaire punten, namelijk reactant, transitietoestand en product, om het reactieprofiel en de bijbehorende reactiekinetiek te bepalen. De behoefte om te simuleren bij operationele condities nam toe na het aantonen van de dynamische aard van de actieve site en van de invloed van de flexibiliteit van het katalysatorrooster op de reactiekinetiek. Moleculaire dynamica (MD) simulaties kunnen simuleren bij reactieomstandigheden wat betreft temperatuur en interactie van gastmoleculen in de poriën van het materiaal. Bovendien kunnen ze een groter deel van het potentiële energieoppervlak *samplen*. Deze technieken zijn echter rekentechnisch zeer duur, wat voornamelijk voortkomt uit het feit dat alle punten op het potentiële energie-oppervlak moeten worden beschreven met behulp van computationeel zeer dure *ab initio* elektronische structuurmethoden. Bovendien is een van de belangrijkste nadelen van normale MD-simulaties dat de *sampling* beperkt blijft tot de meest waarschijnlijke toestanden van het systeem, waardoor de *sampling* van geactiveerde toestanden een zeldzaam verschijnsel is. De *sampling*

van deze gebieden met lage waarschijnlijkheid kan worden verbeterd door het toepassen van *enhanced sampling* moleculaire dynamica technieken. In dit proefschrift wordt gekozen voor het gebruik van collectieve variabele (CV) gebaseerde *enhanced sampling* technieken, wat neerkomt op het feit dat de *sampling* verbeterd wordt langs enkele specifieke variabelen die belangrijk zijn voor de te bestuderen reactie. Deze variabelen, aangeduid als collectieve variabelen, zijn een functie van de microscopische coördinaten die de reactiecoördinaten tijdens de *sampling* moeten weergeven. Belangrijke eigenschappen zijn dat ze onderscheid kunnen maken tussen de interessante metastabiele toestanden en transitietoestanden en dat ze de voortgang langs het traject van reactant naar product beschrijven. Deze collectieve variabelen kunnen coördinatiegetallen, afstanden, hoeken of een combinatie van voorgaande variabelen zijn. De keuze van de collectieve variabelen is vaak een niet-triviale taak. De technieken die in dit proefschrift worden gebruikt, zijn metadynamica, *variationally enhanced sampling*, *umbrella sampling* en thermodynamische integratie. Er zal worden aangetoond dat gelijkaardige vrije energiebarrières kunnen verkregen worden met de verschillende technieken op voorwaarde dat de *sampling* voldoende is. Bij aanvang van dit onderzoek was het niet *a priori* duidelijk in hoeverre de verkregen vrije energiebarrières afhankelijk waren van de specifieke keuze van de collectieve variabelen. In het kader van dit proefschrift wordt verder aangetoond dat indien er meerdere collectieve variabelen bestaan die hetzelfde proces beschrijven, de resulterende vrije energieprofielen in elke collectieve variabele ruimte kunnen gereproduceerd worden door toepassing van de juiste transformaties. Als voorbeeld wordt de methylering van etheen in H-ZSM-5 gebruikt. Voor deze reactie kunnen de simulaties die in verschillende collectieve variabele ruimten worden *gesampled* verder gebruikt worden om inzicht te krijgen in de reactiekinetiek van deze reactie, die hier uitgebreid bestudeerd wordt en gebruikt wordt als benchmark. De verkregen apparente reactiesnelheidsconstante, die berekend wordt op basis van een gecombineerde statisch-dynamische methodologie, blijkt op het randje van de kinetische nauwkeurigheidsgrens te liggen ten opzichte van zowel theoretische als experimentele literatuurresultaten.

Vervolgens worden traditionele statische technieken methoden samen met *enhanced sampling* methoden gebruikt om moleculair inzicht te krijgen in het reactiemechanisme van het MTO-proces. De focus ligt op twee onderwerpen, namelijk hoe de reactiviteit in de katalysatorporiën wordt beïnvloed door post-synthetische modificaties met aardalkalimetalen of door de aanwezigheid van water. Binnen het kader van dit proefschrift wordt ook nog meegewerkt aan een aantal andere topics met MTO relevantie, namelijk hoe topologie en zuursterkte de productselectviteit kunnen beïnvloeden.

Een groot deel van dit proefschrift is gewijd aan het effect van postsynthetische modificatie van het zeoliet met aardalkalimetalen op de productselectiviteit en levensduur van de katalysator. Deze studies werden uitgevoerd in nauwe samenwerking met de experimentele groep van Prof. J. Gascon, KAUST, Saudi-Arabië. De verkregen modelleringsresultaten hebben het mogelijk gemaakt om aan te tonen dat de postsynthetische modificaties de dichtheid van de Brønsted zure sites (BASs, *Brønsted acid sites*) verlagen om zo de aromatische cyclus te onderdrukken. Anorganische modificaties van het zeoliet verminderen typisch de Brønsted zure site dichtheid en kunnen zelf katalytische activiteit vertonen, aangezien ze Lewis

zure sites (LASs, *Lewis acid sites*) creëren. Op basis van een uitgebreide theoretische structurele analyse van de actieve site in aardalkalimetaalgemodificeerd ZSM-5 wordt er gevonden dat zowel de mono-, bi- and trinuclaire species kunnen bestaan binnen het rooster van het zeoilet. Hun bestaan wordt verder bevestigd door zowel theoretische als experimentele NMR-spectroscopie. De vorming van deze kationische metaaloxideclusters leidt tot gedeprotoneerde naburige BASs, waardoor hun dichtheid afneemt. Bovendien wordt de Lewis zure aard van deze metaaloxideclusters zowel experimenteel als theoretisch bevestigd, aangezien na de adsorptie van pyridine een karakteristieke piek in het infrarood (IR) spectrum tevoorschijn kwam. Om het effect van deze nieuwe Lewis zure sites op de reactiekinetiek te beoordelen, wordt hun invloed op de stabiliteit en methylering van aromaten en alkenen bestudeerd. De kationische clusters destabiliseren de aromatische tussenproducten en verhogen hun methyleringsbarrières, terwijl ze de alkenen nauwelijks beïnvloeden. Dit bevestigt de onderdrukking van de aromatische cyclus die leidt tot een verhoogde propeenselectiviteit en een langere levensduur van de katalysator. Dankzij de nauwe samenwerking tussen de experimentele groepen en diepgaande moleculaire modellering is in dit deel van de thesis licht geworpen op een gecompliceerd probleem rekening houdend met de complexiteit van de katalysatoromgeving.

Als tweede hoofdthema in dit proefschrift wordt de invloed van water op de dominante paden binnen het MTO-proces onderzocht. Zoals reeds vermeld is de methyleringsreactie van groot belang binnen alle reactiecycli en als zodanig wordt de invloed van water op de methyleringsreacties binnen H-SAPO-34 bij realistische operationele condities onderzocht. Van de methyleringsreacties in het MTO-proces is bekend dat deze via twee mogelijke mechanismen plaatsvinden. In het directe mechanisme wordt de methylgroep van de geadsorbeerde methanolmolecule onmiddellijk overgedragen aan het koolwaterstof. Bij het stapsgewijze mechanisme wordt de methylgroep daarentegen eerst overgebracht naar het zeolietrooster, waarbij een oppervlaktemethoxide intermediair wordt gevormd. De methoxide groep wordt vervolgens naar het koolwaterstof overgebracht. Op basis van experimentele resultaten wordt voorgesteld dat water een vertragend effect heeft op de kinetiek van methoxidevorming. Bovendien kan water de productselectiviteit en de katalysatorstabiliteit veranderen, wat wordt toegeschreven aan het innemen van een groot deel van de zure sites door water. De *ab initio* simulaties van de methylering van hexamethylbenzeen bij verschillende watergehaltes tonen aan dat het directe mechanisme in alle gevallen het geprefereerde mechanisme is. Verder heeft water een positieve invloed op zowel het directe als het stapsgewijze mechanisme, waardoor de reactiebarrières worden verlaagd, wat aantoont dat water niet alleen de reactiviteit kan beïnvloeden door middel van competitieve adsorptie, maar ook door middel van een assisterende werking. Deze resultaten benadrukken het belang van een correcte beschrijving van het dynamische en assisterende gedrag van de protische moleculen binnen de zeolietkatalyse bij operationele condities.

Bovendien hebben de studies die in het kader van dit proefschrift verricht zijn in geringe mate bijgedragen aan andere discussies binnen het MTO-proces. Zoals eerder vermeld, vertonen zeolietkristallen regelmatige kanalen en holten, die variëren afhankelijk van de zeoliet topologie. Aangezien de poriediameters in dezelfde grootteorde liggen als de reagerende moleculen, is vormselectiviteit een

cruciale factor binnen de zeolietkatalyse. Als gevolg hiervan zullen topologische effecten een significante invloed hebben op de selectiviteit en de levensduur van de katalysator. Binnen het kader van deze thesis wordt inderdaad aangetoond dat de hoge selectiviteit voor langere alkenen in TON zeolieten, die kleine poriën bezitten, kan toegeschreven worden aan een onderdrukking van de grote aromatische tussenproducten. Dit als gevolg van sterische belemmeringen. Op dezelfde manier kan de aromatische cyclus ook worden onderdrukt door het verlagen van de zuursterkte of de dichtheid van de zure sites, aangezien geweten is dat een verhoogde zuursterkte niet alleen leidt tot een verhoogde olefineproductie, maar ook tot grotere hoeveelheden aromaten die in de zeolietporiën worden vastgehouden. Om deze hypothese te onderzoeken, worden twee isostructurele AFI zeolieten vergeleken, die een verschillende Brønsted zure sterkte bezitten. Deze studie bevestigt de hogere activiteit van de alkeencyclus in de zwakker zure katalysator.

De resultaten die in dit proefschrift worden gepresenteerd, laten zien hoe geavanceerde moleculaire modelleringssimulaties kunnen helpen om gedetailleerde reactiemechanismen bij operationele omstandigheden te achterhalen. In dit proefschrift is uitgebreid gebruikgemaakt van *enhanced sampling* moleculaire dynamica technieken. Het is pas recent dat deze technieken worden gebruikt binnen de heterogene katalyse. Zulke methoden laten toe om chemische reacties te simuleren onder operationele condities, bijvoorbeeld bij realistische temperaturen, gastmolecule beladingen,... Deze technieken zijn jammer genoeg rekentechnisch erg duur en in die zin kunnen ze zeker niet beschouwd worden als een zelfstandige techniek die gebruikt kan worden voor elke chemische reactie. In plaats daarvan laat dit werk zien hoe inzicht kan worden verkregen door statische en dynamische methoden op een complementaire manier toe te passen. Voor de moleculaire dynamica methoden werd in dit proefschrift verder aangetoond hoe de vrije energiebarrières op een betrouwbare manier kunnen worden verkregen, ongeacht de keuze van de collectieve variabelen. Indien deze methodologieën verder getest en geoptimaliseerd zullen worden, zoals gedaan in deze thesis, kan dit leiden tot een meer algemene aanvaarding van hun veelzijdigheid en hun veelvuldige toepassing. Bovendien toont dit werk aan hoe een nauwe samenwerking met experimentele onderzoekers essentieel is om moleculair inzicht te krijgen in een complex proces zoals de methanolconversie over zeolieten. De samenwerking tussen moleculaire modellering en experimentele spectroscopie werd ook mooi aangetoond. Voor de studie van de aardalkalimetaalgemodificeerde zeolieten was het bijvoorbeeld essentieel om theoretische inzichten op actieve sites te combineren met experimentele IR- en NMR-spectroscopische experimenten. Nauwe samenwerking tussen theoretici en experimentalisten zal cruciaal zijn voor de verdere verduidelijking van de MTH-processen en voor heterogene katalyse in het algemeen.

Summary

Due to depleting oil reserves and the increasing demand for base chemicals such as ethene and propene, the search for processes based on alternative feedstocks is an active research area from both an industrial and academic perspective. Interesting alternative routes are those starting from methanol because it can be produced from any gasifiable carbon-rich feedstock. In this context, the methanol-to-hydrocarbons (MTH) process gained a lot of interest since its accidental discovery at Mobil in the late 1970s. MTH is an overarching term for all processes in which methanol is converted over an acidic zeolite or zeotype catalyst into valuable base chemicals, namely hydrocarbons. Depending on the formed products a subdivision can be made leading to processes such as the methanol-to-olefin (MTO) process and the methanol-to-gasoline (MTG) process. Especially the MTO process is of great interest due to its high selectivity to ethene and propene. The used catalysts, zeolites, are crystalline aluminosilicates belonging to the family of the microporous materials with pores and cavities of molecular size. They can occur naturally as minerals, but the synthetic varieties are widely used as sorbents, catalysts and ion-exchange materials. Zeolite crystals possess regular arrays of channels and cavities (around 3–15 Å), creating a nano-scale labyrinth. From a commercial point of view, H-SAPO-34 and H-ZSM-5 are the most relevant zeolite catalysts used in the MTO process.

Though several commercial MTO technologies have been developed and many plants have been installed worldwide, the reaction mechanism governing the methanol conversion proved to be very difficult to unravel. Intensive research resulted in the proposition that an active MTO catalyst should be regarded as a supramolecular assembly consisting of the zeolite channel system completed with Brønsted acidic functions in which organic compounds need to be present to generate an active catalyst. Furthermore, the supramolecular system could be modified with some inorganic compound to further tune the catalytic function. This led to the general acceptance of the hydrocarbon pool (HP) mechanism governing the MTO process. In this mechanism, organic components, trapped in the zeolite pores act as a co-catalyst in the production of light olefins. Depending on the nature of the hydrocarbon, two interacting reaction cycles could be distinguished. This mechanism is thus also referred to as the dual cycle mechanism. In a first cycle, alkenes govern the product formation via olefin chain growth and cracking reactions. Within the aromatic cycle, side chain methylations, ring contractions/expansions and olefin elimination reactions of aromatic intermediates lead to product formation. In both reaction cycles, methylation reactions are key reactions and as a result have been widely studied in the framework of MTO catalysis. The specific operative cycle

determines to a large extent the product selectivity as the production of ethene and propene was shown to be mechanistically separated from one another. Ethene is supposed to be mainly formed via the aromatic cycle, whereas propene and higher olefins are formed via the alkene cycle. Additionally, aromatic intermediates are identified as coke precursors which deactivate the catalyst. As such, experimentally measured product selectivities and catalyst lifetimes could be associated to these fundamental reaction cycles. By extending this reasoning, one could see that suppression of the aromatic cycle can increase propene selectivity and catalyst lifetime. This characteristic makes MTO conversion especially interesting as propene-on-demand process to solve the increasing disparity between the propene production and demand. Therefore, a major part of this thesis focuses upon the effect of post-synthetic zeolite modification with alkaline earth metals on the propene selectivity and catalyst lifetime to optimize the propene production.

Solely based on experimental data, it is extremely challenging to gather detailed molecular level insights into the reaction mechanism governing an industrial process due to the large number of reactions that take place simultaneously. This hurdle can be overcome by complementing the experimental information with theoretical simulations. In the last decades, significant progress has been made in the field of computational chemistry, making it possible for advanced molecular dynamics methods to enter the scene. These techniques have the potential to model chemical reactions at operating conditions. Such molecular level insight can help us to optimize the design of heterogeneous catalysts. A conditio sine qua non to obtain such molecular level understanding is the reliability of the used computational methods and their potential to simulate chemical reactions which mimic experimental conditions as good as possible. Traditionally, one resorted to the static geometry optimization at 0 K of three stationary points, namely reactant, transition state and product, to determine the reaction profile and its associated kinetics. Due to the proven dynamic nature of the active sites within zeolites and the influence of the flexibility of the catalyst pores on the reaction kinetics, the urge to simulate at operating conditions rose. Molecular dynamics (MD) simulations have the potential to simulate at realistic conditions of temperature and loading of guest molecules in the pores of the material. Moreover they allow one to sample a larger portion of the potential energy surface (PES) at these conditions. However these techniques are computationally very expensive, which mainly originates from the fact that all points on the potential energy surface need to be described using computational very expensive first principle electronic structure methods. Furthermore, one of the main disadvantages of regular MD simulations is that sampling is limited to the most probable states of the system, making the sampling of states high in energy, like transition states, rare events. Sampling of these improbable regions can be improved by applying enhanced sampling molecular dynamics techniques. In this thesis, it is opted to use collective variable (CV) based enhanced sampling techniques, which boils downs to the fact that sampling is improved along some specific variables which are important for the reaction under study. These variables are called collective variables and are a function of the microscopic coordinates which should represent the reaction coordinate during sampling. They should be able to uniquely differentiate between the interesting metastable and transition states, and to unambiguously describe the progress along the trajectory from

reactant to product. These collective variables might be coordination numbers, distances, angles or a combinations of previous variables. The choice of the collective variables is sometimes a non-trivial task. The techniques used in this thesis are metadynamics, variationally enhanced sampling, umbrella sampling and thermodynamic integrations. It will be shown that similar free energy barriers can be obtained with the various techniques on the condition that sampling is sufficient, which is shown to be tedious and computationally expensive. At the onset of this research it was not a priori clear in how far the obtained free energy barriers were dependent on the particular choice of the collective variables. Within the framework of this thesis, we proved that if different collective variables exist which describe the same process, the resulting free energy profiles could be reproduced in each collective variable space by application of the proper transformations. For the example of the methylation of ethene in H-ZSM-5, the simulations sampled in different collective variable spaces could further be used to obtain insight into the proper reaction kinetics of this reaction that is extensively studied and used as benchmark. The apparent reaction rate constant, calculated based on a combined static-dynamic methodology, showed to be on the verge of the kinetic accuracy limit compared to both theoretical and experimental literature results.

Subsequently, both traditional static techniques and the novel enhanced sampling methods are used to obtain molecular insight in the reaction mechanism of the MTO process. The main focus was set on two topics, namely how reactivity in the catalyst pores is affected by post-synthetic modifications or by water. However, also minor contributions to other discussions within the field of MTO chemistry were made within the framework of this thesis. For example, the results obtained in this work could also explain theoretically why topology and acid strength impact the product selectivity.

A major part of this thesis is devoted to the effect of post-synthetic modification of the zeolite with alkaline earth metals on the product selectivity and lifetime of the catalyst. The work was performed in close collaboration with the experimental group of Prof. J. Gascon of KAUST, Saudi Arabia. The obtained modeling results allowed to unveil that the post-synthetic modifications had the ability to alter the acid site density and suppress the aromatic cycle. Inorganic modifications of the zeolite typically reduce the Brønsted acid site (BAS) density and might exhibit catalytic activity themselves, as they create Lewis acid sites (LASs). Indeed, based on an extensive theoretical structural analysis of the active site within alkaline earth metal modified ZSM-5 it is proposed that mono-, bi and trinuclear metal oxide species could exist. Their existence is further confirmed by both theoretical and experimental NMR spectroscopy. The formation of these cationic metal oxide clusters leads to deprotonated neighboring BASs, thus decreasing their density. Furthermore, the Lewis acidic nature of these metal oxide clusters is confirmed both experimentally and theoretically as probing with pyridine revealed the characteristic peak in the infra-red (IR) spectra. To assess the influence of these new Lewis acid sites, their influence on the stability and methylation of aromatic and alkene intermediates is studied. The cationic clusters destabilize the aromatic intermediates and increase their methylation barriers, while barely influencing the alkene species. This confirms the suppression of the aromatic cycle leading to increased propene selectivities and catalyst lifetime. As such, a close

synergy of experimental groups with intensive molecular modeling could shed light on a complex problem in a complicated environment.

As a second main topic within this thesis, the influence of water on the dominating pathways within the MTO process is investigated. As already mentioned the methylation reaction is of key importance within all reaction cycles and as such the influence of water was investigated on the methylation reactions within H-SAPO-34 at realistic operating conditions. The methylation reactions in the MTO process are known to occur through two possible mechanisms. In the concerted mechanism, the methyl group of the adsorbed methanol molecule is immediately transferred to the hydrocarbon. For the stepwise mechanism, on the other hand, the methyl group is first transferred to the framework, forming a surface methoxide species, which can subsequently be transferred to the hydrocarbon. From experiment it is found that water has a retarding effect on the kinetics of methoxide formation. Furthermore, water may alter the product selectivity and catalyst stability, which is attributed to water occupying an important fraction of the acid sites. The ab initio simulations of the methylation of hexamethylbenzene at various water contents show that the concerted mechanism prevails in all cases. More interestingly, water is found to assist in both the concerted and stepwise mechanism, thus lowering the reaction barriers, showing that water might not only influence the reactivity by competitive adsorption, but also via assistance. These results highlight the importance of correctly accounting for the dynamic and assisting behavior of the protic environment within zeolite catalysis at process conditions.

Furthermore, work performed in this thesis contributed to a minor extent to other characteristics of the MTO process. As stated earlier zeolite crystals reveal regular arrays of channels and cavities, which vary depending on the zeolite topology. As these pores are in the same size range as the reacting molecules, shape selectivity is a crucial factor within zeolite catalysis. As a result, topological effects will significantly influence the yield and catalyst lifetime. Indeed, the results show that the high selectivity to higher alkenes in small pore TON zeolites can be ascribed to a suppression of the large aromatic intermediates in these small pores due to steric hindrance. Similarly, the aromatic cycle can also be suppressed by lowering the acid strength or the acid site density, as increased acid strength is known to not only lead to increased olefin production rates, but also to higher amounts of aromatics retained in the zeolite pores. To examine this feature, two isostructural AFI zeolites with different Brønsted acid strengths are compared which confirms the higher activity of the alkene cycle in the weaker acid catalyst.

The results presented in this thesis show how advanced molecular modeling simulations may help to explain detailed reaction mechanisms at operating conditions. Within this thesis extensive use was made of enhanced sampling molecular dynamics techniques. It is only recently that these techniques are being used within heterogeneous catalysis. Such methods allow to simulate chemical reaction at operating conditions, for example at realistic conditions of temperature, guest loadings,... However, these techniques are also computationally very expensive and in this sense, they can certainly not be regarded as a stand-alone technique to be used for any chemical reaction under study. Instead this work shows how insight can be obtained by using static and dynamic methods in a complementary way. With respect to the molecular dynamics methods, it was shown within this thesis

how the free energy barriers could be obtained in a reliable way, irrespective of the choice of the collective variables or sampling technique. Further testing of these methods might lead to a more general acceptance of their versatility and more reliable methodologies. Furthermore this work shows how a close synergistic approach with experimental researchers is essential to obtain molecular insight into a complex process such as the methanol conversion over zeolites. The synergy between molecular modeling and experimental spectroscopy was also nicely shown. For example for the study of the alkaline earth modified zeolites, it was essential to combine theoretical insights on active sites with experimental IR and NMR spectroscopic signals. Close collaboration between theoreticians and experimentalists will be crucial for the further elucidation of the MTH processes and for heterogeneous catalysis in general.

List of Figures

1.1 Flowchart of the Emissions to Liquids (EtL) process by Carbon Recycling International (CRI) with the MTO process representing the carbon neutral cycling proposed in the Methanol economy by George A. Olah. Adapted from ref. [14] with permissions of Springer Nature. 4

1.2 Schematic representation of the zeolite topologies considered within this work, namely MFI, CHA, AFI and TON, with their pore opening indicated as taken from ref. [36] (a) and a schematic representation of a fictitious zeolite showing the three types of shape selectivity distinguished, namely on the reactant, transitions state and product (b). This figure was remade from ref. [40] and ref. [9], with permissions of John Wiley and Sons. 6

1.3 Schematic representation of the stages encountered within methanol conversion over a zeolite catalyst. Adapted from ref. [40] with permissions of John Wiley and Sons. 7

1.4 Schematic representation of the supramolecular view on MTO catalysis proposed by Haw and Marcus [90] where the MTO catalyst can be tailored by tuning the topology, acid function, organic compound or inorganic component. Based on the organic co-catalyst,the dual cycle concept, governing the methanol conversion in zeolite catalysis and consisting of the alkene and aromatic cycle, is proposed. This figure was remade from ref. [91] and [90], with permissions of American Chemical Society and Springer Nature. 9

1.5 Schematic representation of competitive reactions mechanisms proposed for the methylation of hexamethylbenzene, namely the direct or concerted route and the stepwise route. Adapted from ref. [40] with permissions of John Wiley and Sons. 10

1.6 Schematic representation of factors that influence the reactivity within the zeolite pores and are studied in the framework of this dissertation. Adapted from ref. [107] with permissions from The Royal Society of Chemistry. 11

1.7 Snapshots of the frameworks of the two commercially used zeolite catalyst within the MTO process, namely H-ZSM-5 (MFI topology) and H-SAPO-34 (CHA topology). The framework is indicated by thin sticks while the substituted atom necessary to create the Brønsted acid site and the four surrounding T atoms are indicated in ball-and-stick representation. In these snapshots, hydrogen is white, carbon is silver, oxygen is red, aluminum is grey, silicon is beige and phosphorus is orange. 12

1.8 Schematic representation and snapshots of the optimized structures of the isolated extra-framework Ca species in ZSM-5 considered in **Paper II**, **Paper III** and **Paper V**, namely mononuclear (left), binuclear (center) and trinuclear (right) species. For the snapshots, the following color code is used: white is H, red is O, grey is Al, beige is Si and green is Ca. Adapted from ref. [91] with permissions of American Chemical Society. 14

1.9 Schematic representation of the two effects of protic molecules studied via molecular modeling, namely on the one hand, in H-SAPO-34 the assistance of water in the methoxide formation showing the unassisted reaction (a) and the reaction stabilized by the interaction of water (b) [175] and, on the other hand, the change of the local environment of an original BAS (c) when a protonated methanol cluster is formed (d). [41] The following color code is used: white is H, light gray is C, red is O, dark gray is Al and beige is Si. This figure was remade from ref. [175] and [41] with permission of American Chemical Society. 16

1.10 Schematic representation of computational methods commonly used in the framework of heterogeneous catalysis starting from the "ideal" catalyst model towards the realistic operando model. The traffic lights depict how good the model scores in representing the complexity of the catalyst model (Cat), of the reaction coordinate (RCN) and of the reaction network (RxN). Adapted from ref. [187] with permissions of The Royal Society of Chemistry. 17

2.1 Perdew's metaphorical Jacob's ladder of density functional approximations. Each rung corresponds to a more complex model for the unknown exchange-correlation functional on the way to chemical accuracy. Adapted from ref. [226] and [231] with permissions of AIP Publishing and Informa UK Limited, trading as Taylor & Francis Group. 24

2.2 Depiction of the ZSM-5 framework using an extended cluster (46T), where the older 5T cluster is shown in ball-and-stick representation (a) and using a periodic presentation, where the unit cell is shown in ball-and-stick representation and a $2 \times 2 \times 2$ periodic image is shown.In these figures, hydrogen is white, oxygen is red, aluminum is grey and silicon is beige. 26

2.3 Schematic representation of the geometry optimization combined with the harmonic oscillator approximation (left) and of the molecular dynamics simulations (right). 26

2.4 Schematic representation of the enhanced sampling methods considered in this Ph.D. dissertation. For each method, the top graph shows the external bias introduced to enhance the sampling and the bottom figure shows the free energy estimation. The methods to estimate the free energy is also indicated. 32

2.5 Schematic representation of the methylation of ethene with methanol yielding propene. 35

2.6 Free energy profiles and error bars at 350 °C in function of the one-dimensional collective variable obtained with different enhanced sampling methods applied on the methylation reaction of ethene in H-ZSM-5. Furthermore, the minimum-maximum barrier is shown on the graphs for each method. The reactant (R) and product (P) side of the reaction are also indicated. 37

2.7 Graphical representation of a free energy profile $F_{q_1}(q_1)$, which was computed by sampling along q_1 and expressed as a function of q_1, and is transformation to the corresponding free energy profile $F_{q_2}(q_2)$ as a function of q_2. The integral can be interpreted as a weighted average of the Boltzmann probability, with weights given by the conditional probability and indicated through the shading in the middle pane. 39

2.8 Schematic representation of the collective variables used to describe the methylation reaction of ethene with methanol. 40

2.9 Free energy profiles at 350 °C obtained by sampling in the different collective variable spaces (Q_{SAM}), namely Type CN (green), Type DI (blue) and Type 1D-DI (red) and represented (Q_{REP}) in Type CN (left panel) and Type DI (right panel). The profiles for Type CN and Type DI are obtained by sampling in a 2D collective variable space followed by a projection of the free energy surface on a 1D-profile. 41

2.10 Free energy profiles at 350 °C in function of 1D-CVs (Q_{REP}) defined as the difference in coordination numbers ($CN_{CC} - CN_{OC}$, left panel) or in distance ($d_{CM} - d$, right). Left panel: plots belonging to CVs Type 1D-DI and Type DI are obtained after transformation as explained in the text. Right panel: plots belonging to Type CN are obtained after transformation as explained in the text. 43

2.11 Schematic representation of the relation between apparent and intrinsic kinetics. For the calculation of $\Delta G_{ads,ethene}$ various schemes were used, shown by the grey uncertainty in the co-adsorption step of ethene. The value of k_{int} was obtained dynamically in **Paper VI**. 48

3.1 Schematic representation of the structures considered for the relative stability of mono- (left), bi- (center) and trinuclear (right) structures (a) and snapshots of the three considered structures for the Ca case (b). For the snapshots, the following color code is used: white is H, red is O, grey is Al, beige is Si and green is Ca. Adapted from ref. [91] with permissions of American Chemical Society. . . 53

3.2 Experimental ^{43}Ca magic angle spinning (MAS) solid-state hahnecho (blue) and QCPMG (red) NMR spectra of ca. 1.5% Ca-ZSM-5 [900 MHz, 10KHz MAS, recycle delays=1 sec, Number of scans=14k]. On the graph, the theoretical, static NMR peaks are indicated in green, namely mononuclear (light green), binuclear (green) and trinuclear (dark green). Adapted from ref. [91] with permissions of American Chemical Society. 55

3.3 Pyridine adsorption to a mononuclear LAS (a) and a binuclear LAS (b). Also given are the adsorption enthalpies in kJ/mol belonging to the optimized structures at 0 K of pyridine adsorbed in pristine H-ZSM-5 and Mg, Ca, Sr or Ba-ZSM-5. To keep the charge in balance frameworks with only one Al substitution are considered in case of monomers, and with two Al substitutions in case of the binuclear species. In the pristine H-ZSM-5 only one single BAS and thus one Al substitution is taken into account. For the snapshots, the following color code is used: white is H, light grey is C, blue is N, red is O, grey is Al, beige is Si and green is the alkaline earth metal. Adapted from ref. [91] with permissions of American Chemical Society. 57

3.4 FTIR spectra of various zeolitic materials using pyridine as a probe molecule. (a) Theoretical spectrum of pyridine adsorbed on modified ZSM-5 materials with binuclear species, (b) experimental spectrum. Adapted from ref. [91] with permissions of American Chemical Society. 58

3.5 Shifts in the LAS (a and c) and global acidity (b and d) peaks in the IR spectrum with respect to changes in the strength of the incorporated mono- (a and b) or binuclear (c and d) LASs. Adapted from ref. [91] with permissions of American Chemical Society. . . 59

3.6 Summary of the reactivity analysis over alkaline earth metal modified ZSM-5 showing (a) a schematic representation of the three active sites considered for the methylation reactions, namely an isolated BAS, a BAS near a $[M(\mu\text{-}OH)_2M]^{2+}$ moiety and an isolated $[M(\mu\text{-}OH)_2M]^{2+}$ moiety. (b) The change in the overall free energy barrier at 500 °C of the methylation of benzene (red) , propene (green), pseudocumene (orange) and durene (purple) over an BAS near a $[M(\mu\text{-}OH)_2M]^{2}+$ moiety (left and □) and an isolated $[M(\mu\text{-}OH)_2M]^{2+}$ moiety (right and △) relative to the methylation rate over an isolated BAS (black circle) is plotted in function of the pyridine adsorption enthalpy. For the dealuminated species both EFAl/I and EFAl/II variants are considered. Adapted from ref. [91] with permissions of American Chemical Society. 60

3.7 Overview of the results of the calculation of the protonation enthalpy showing the intermediates that are unaffected (green) and affected (red) by the alkaline earth metal modification (upper) and the resulting protonation enthalpies at 500 °C showing this effect (lower) for different cationic clusters considered in the zeolite pore. Adapted from ref. [91] with permissions of American Chemical Society. 61

3.8 Experimental results obtained at 500 °C for the throughput (a), selectivity to ethene (b) and selectivity to propene (c) for the MTO reaction over 1.4 % Mg-ZSM-5 (red), 2.4 % Ca-ZSM-5 (blue) and 5.2 % Sr-ZSM-5 (orange) relative to the parent ZSM-5 (black). Results for 8.2 % Ba-ZSM-5 are not reported, as this sample showed a conversion below 5 %. Adapted from ref. [91] with permissions of American Chemical Society. 62

3.9 Starting structures and schematic representations of the three cases considered to study the concerted and stepwise methylation of HMB in H-SAPO-34, namely an isolated BAS with one HMB and one methanol as base case (Case 1), a more realistic low water content case (Case 2) and high water content case (Case 3). In these snapshots, hydrogen is white, carbon is silver, oxygen is red, aluminum is grey, the silicon substitution is indicated in blue and phosphorus is orange. Adapted from ref. [40] with permissions of John Wiley and Sons. 63

3.10 Radial distribution functions for the pairs formed by (i) all protons present in the catalyst pore and (ii) the oxygens of the methanol molecule(s) in the reactant state for Case 1 (a), Case 2 (b) and Case 3 (c). For Case 1, the statically obtained distances corresponding to the analyzed bonds are added in dotted lines. The encountered peaks are indicated on the schematic representation of the methanol molecule. The first peaks (at distances below about 1.1 Å) are scaled down by a factor of 5 to improve visualization. Adapted from ref. [40] with permissions of John Wiley and Sons. 65

3.11 Free energy profile for the concerted (a) and step 1 (b) and step 2 (c) of the stepwise methylation of HMB at 350 °C in Case 1 using static (full line), metadynamics (short-striped line) and umbrella sampling (long-striped line) simulations. For the static calculations, an extra desorption step of the formed water is taken into account (dotted line). Adapted from ref. [40] with permissions of John Wiley and Sons. 66

3.12 Free energy profile for the concerted (a) and step 1 (b) and step 2 (c) of the stepwise methylation of HMB at 350 °C at higher guest molecule loadings and acid site density, namely Case 2 (full line) and Case 3 (dotted line) obtained with metadynamics. The reference level for the reactants in both cases has been assumed zero, however in Case 2 one water molecule was adsorbed, whereas in Case 3 nine water molecules were adsorbed in the unit cell. The obtained barriers are thus intrinsic energy barriers compared to the state in which all molecules are already adsorbed. Adapted from ref. [40] with permissions of John Wiley and Sons. 67
3.13 Radial distribution function for the pairs formed by (i) all protons and (ii) the oxygens of the methanol molecules from MD runs in the reactant and product state as well as during the MTD simulations for the concerted methylation (top) and methoxide formation (middle) for Case 2 (a) and Case 3 (b), showing the formation of solvation shells at higher water concentrations. Furthermore, the unassisted and assisted transition states are visualized in the snapshots at the bottom. The first peaks of the RDFs (at distances below about 1.1 Å) are scaled down by a factor of 5 to improve visualization. In these snapshots, hydrogen is white, carbon is silver, oxygen is red, aluminum is grey, the silicon substitution is indicated in blue and phosphorus is orange. Adapted from ref. [40] with permissions of John Wiley and Sons. 69
3.14 Radial distribution function for the pairs formed by (i) all protons and (ii) the oxygens of the Brønsted acid sites from MD runs in the reactant and product state as well as during the MTD simulations for the second step of the stepwise mechanism (a) for Case 2 (top) and Case 3 (bottom). Furthermore, a snapshot of the BAS during the transition state is shown to depict the stabilization of the formed deprotonated BAS by the protic molecules present. The first peaks of the RDFs (at distances below about 1.3 Å) are scaled down by a factor of 5 to improve visualization. In these snapshots, hydrogen is white, carbon is silver, oxygen is red, aluminum is grey, the silicon substitution is indicated in blue and phosphorus is orange. Adapted from ref. [40] with permissions of John Wiley and Sons. 70
3.15 Probability of methanol protonation and pre-reactive complex formation for propene (□) and benzene (o) methylation in H-SAPO-5, H-SSZ-24 and H-ZSM-22 at 250 °C (blue) and 350 °C (red). Adapted from ref. [107] with permissions from The Royal Society of Chemistry. 71

Part I

Operando First Principle Simulations of Important Chemical Transformations over Zeolites within the Methanol-to-Olefin Process

1 Introduction

1.1 Methanol-to-olefin process

The depleting oil reserves and growing environmental awareness incites the development of sustainable processes based on biomass valorization for the production of fuels and chemicals. [1–4] As methanol can be produced through syngas (synthesis gas, a mixture of CO, CO_2, H_2 and CO_2) from any gasifiable carbon-rich source, the zeolite catalyzed methanol-to-hydrocarbons (MTH) process is one of the main technologies to bypass the use of crude oil in the production of highly demanded hydrocarbons. [5–10] MTH encompasses several processes in which methanol is converted into valuable base chemicals over an acidic zeolite or zeotype catalyst. Depending on the formed products several types can be distinguished such as the methanol-to-olefin (MTO) process, methanol-to-gasoline (MTG) process,... Especially the MTO process is highly relevant due to its high selectivity to ethene and propene. As such, it perfectly fits in the Methanol economy proposed by George A. Olah which will lead to carbon-neutral cycling and will ultimately relieve us from our dependence on fossil fuels, as depicted in Figure 1.1. [11–14]

The promising process in which methanol is converted to hydrocarbons over zeolite catalysts was accidentally discovered by Mobil scientists in the late 1970s, while trying to produce ethylene oxide and methylate isobutene over H-ZSM-5 with methanol. [15–19] Since then, several commercial technologies have been developed [8, 20] and an extensive amount of research studies have focused upon this process [10, 21–23] trying to understand and improve the two most important characteristics

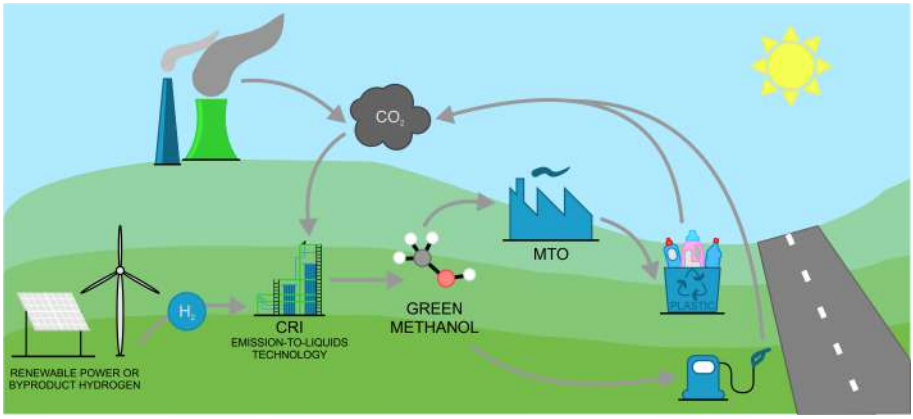

Figure 1.1: Flowchart of the Emissions to Liquids (EtL) process by Carbon Recycling International (CRI) with the MTO process representing the carbon neutral cycling proposed in the Methanol economy by George A. Olah. Adapted from ref. [14] with permissions of Springer Nature.

of this process, namely the catalyst lifetime and product selectivity. Three major commercial MTH technologies are available. Based on H-ZSM-5, Lurgi developed the methanol-to-propene (MTP) process [24] where a methanol/dimethyl-ether (DME) mixture is formed in a first reactor at 260 °C which is sent to the MTP reactors, at atmospheric pressure and 460–480 °C, optimized for high propene yields. The two other technologies use another synthetic catalyst, namely H-SAPO-34. As this catalyst is prone to fast deactivation through coking, this process is operated over a fluidized-bed reactor with a catalyst regenerator at temperatures of 350–550 °C and low pressures around 0.1–0.3 MPa. The ethene and propene yield can subsequently be increased by either sending the C_{4+} stream to the olefin cracking process (OCP) as done by UOP/Norsk Hydro [25] or recycle this C_{4+} stream to the reactor as done at Dalian Institute of Chemical Physics (DICP) in the DMTO process. [26]

This short introduction thus shows that the MTO process is an interesting, but complex process. Numerous parameters can influence the product selectivity and catalyst lifetime and in the coming sections, the scene, necessary to understand the results obtained within this work, will be set. Therefore, Chapter 1 is organized as follows. First of all, several zeolite catalysts can be considered and those considered in this dissertation will be summarized in Section 1.2. Secondly, understanding the reaction mechanism governing the MTO can help explain selectivities and catalyst lifetimes, as will become clear in Section 1.3. Furthermore, the ways to tune the product selectivity and catalyst lifetime studied within this dissertation will be summed up in Section 1.4 and the importance of molecular modeling in zeolite catalysis will be highlighted in Section 1.5 before setting the goal of this work in Section 1.6.

1.2 Zeolite catalysts within the MTO process

Zeolites are porous materials with large-scale applications in the petroleum industry and a significant potential in environmental catalysis. [27–31] Other well-known examples of porous materials are mesoporous silica and metal-organic frameworks (MOFs). [32] Porous materials are divided in classes by IUPAC based on the pore dimensions. As such, they make a distinction between microporous materials, with a pore diameter <2 nm, mesoporous materials with diameters between 2 and 50 nm and macroporous materials with diameters above 50 nm. [33] Zeolites are thus microporous, crystalline aluminosilicates consisting of molecular scale pores and cavities (around 3–15 Å). Their framework is constructed by corner sharing SiO_4 and AlO_4 units and a Si/Al ratio greater that one. Other atoms with tetrahedral coordination such as Ge, B, and Ti can also be introduced into the framework. [32, 34] Zeolites can be found naturally as minerals, but it is rather their synthetic varieties that are widely used as sorbents, catalysts and ion-exchange materials. [35] Over 200 different framework types are currently approved by the structure commission of the international zeolite association (IZA). [36] Several of these topologies are considered within this work, as depicted schematically in Figure 1.2a.

Shape selectivity is a crucial factor within zeolite catalysis due to the similar size range of the reacting molecules and the pores. [8, 9, 37, 38]. Distinction can be made between reactant, transition state and product shape selectivity as shown in 1.2b. Reactant shape selectivity is characterized by diffusion limitation. For example on left of Figure 1.2b the linear alkane chain can easily diffuse into the zeolite, while the branched alkane is to bulky to fit in the window of the zeolite pore. Even though some reactants may diffuse into the zeolite channels, their reactivity might still be suppressed if there is no sufficient space to accommodate the spacious transition state. This is schematically represented in the middle of Figure 1.2b. While the transitions state of the alkanes can easily fit, the methyl transfer between the para-xylene molecules is hampered. Just as for the diffusions of reactants in the zeolite pores, the diffusion of bulky products can be limited. These bulkier molecules thus remain within the zeolite pores. Shape selectivity can even be used to design zeolites. [39] As a result, topological effects will significantly influence the product distribution and catalyst lifetime.

The majority of the research performed within the framework of this thesis has been performed on both commercial catalysts. H-SAPO-34, being a silicoaluminophosphate having the chabazite (CHA) topology, consists of large cages (10.0 x 6.7 x 6.7 $Å^3$), connected by small-pore windows (3.8 x 3.8 $Å^2$). [36] The second commercially used catalyst is H-ZSM-5, characterized by the MFI topology which consists of a 3D network of sinusoidal (5.1 x 5.5 $Å^2$) and straight (5.3 x 5.5 $Å^2$) 10-ring channels. [36] Where the two channels cross, spacious intersections are formed, which offer space to all sorts of guest molecules. [41–44]

Some other topologies will be discussed in this thesis, within the framework of some research that was contributed to during this Ph.D. These are less interesting

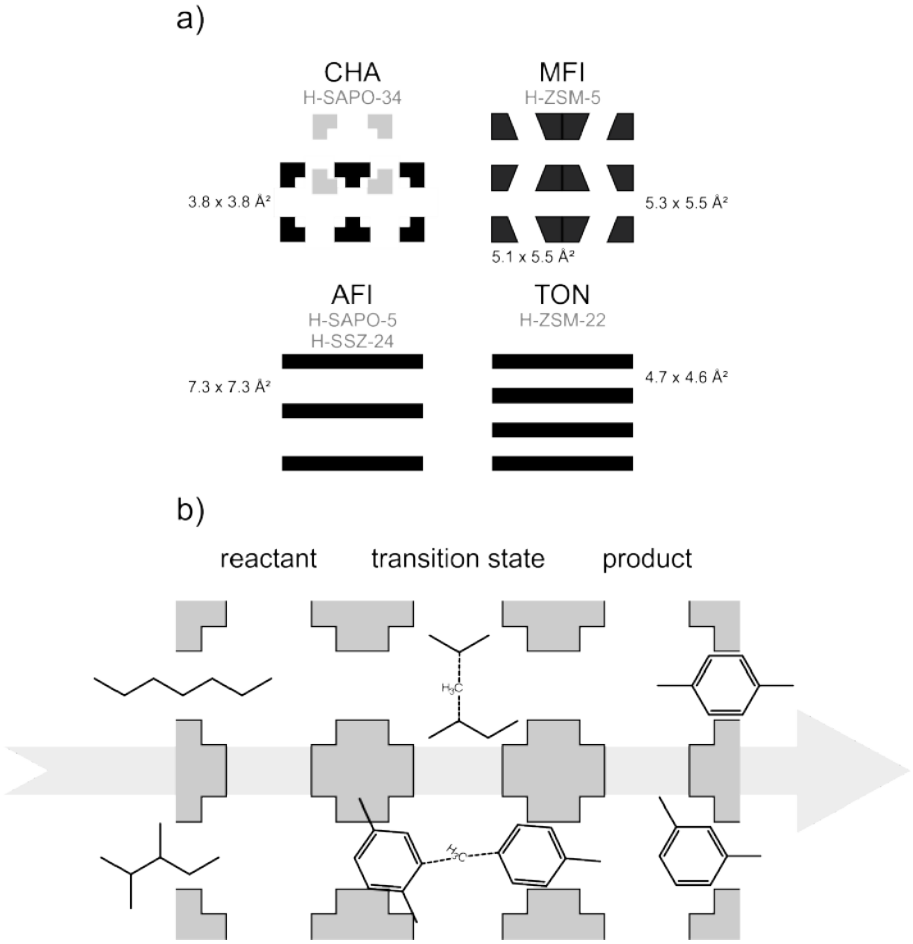

Figure 1.2: Schematic representation of the zeolite topologies considered within this work, namely MFI, CHA, AFI and TON, with their pore opening indicated as taken from ref. [36] (a) and a schematic representation of a fictitious zeolite showing the three types of shape selectivity distinguished, namely on the reactant, transitions state and product (b). This figure was remade from ref. [40] and ref. [9], with permissions of John Wiley and Sons.

for commercial use, but are relevant from academic point of view to study the reaction mechanism. In contrast to the CHA topology, where diffusion in and out of the cages is limited due to the narrow windows, AFI consists of tubular (7.3 x 7.3 Å^2) 12-ring channels. [36] As such, bulky molecules are allowed to diffuse in and out of the pores, making it ideal to monitor the molecules present in the pores during reaction and to perform co-feeding experiments. [45–48] To study the influence of the pore dimensions on the reaction mechanism, the results obtained in the AFI topology is also compared to those obtained in the TON topology, which

is characterized by one-dimensional (4.7 x 4.6 Å^2) 10-rings.

How these topologies might influence the product selectivity and catalyst lifetime, will be further discussed in Section 1.4.

1.3 MTO reaction mechanism

Since its discovery in the 1970s, [15–19] researchers have been eager to elucidate the reaction mechanism governing the MTO process. Haw *et al.* [49] discovered different stages in the methanol conversion process, as depicted in Figure 1.3.

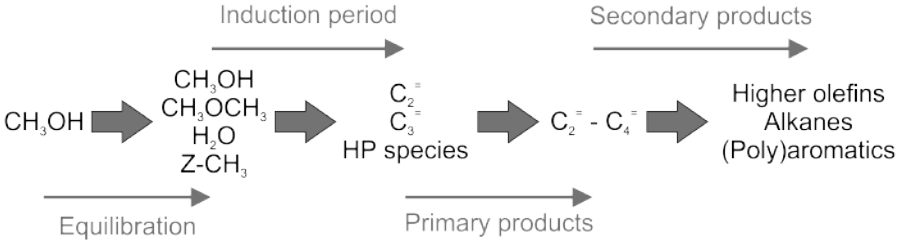

Figure 1.3: Schematic representation of the stages encountered within methanol conversion over a zeolite catalyst. Adapted from ref. [40] with permissions of John Wiley and Sons.

In a first stage, an equilibrium is formed between methanol, dimethyl-ether, water and surface methoxide species (SMS). After this, an induction period is observed in which the first C-C bond is formed. For this reaction, more than 20 reaction mechanism were postulated which can be categorized in the oxonium ylide mechanism, the carbenium mechanism, the carbocationic mechanism and the free radical mechanism. [50] These were first thought to govern the entire MTO reaction mechanism. Nevertheless, most of these mechanisms were shown to be unfeasible based on combined theoretical and experimental work [51, 52] and could not explain the observed induction period and autocatalytic effect. [49, 53] More recently, quite some renewed attention has been devoted to direct carbon-carbon coupling reactions, as they may play an important role in the induction phase. Meticulously tuning and designing the induction phase has also become an active area of research. [54–71] For the primary and secondary products formation on the other hand, the indirect hydrocarbon pool (HP) or dual-cycle mechanism is generally accepted, which will be explained in more detail in the following section.

1.3.1 Dual cycle mechanism

To explain the autocatalytic reactions occurring during the MTO process, an indirect mechanism based olefin chain growth and cracking was first introduced by Dessau *et al.* [72, 73] In the same period, Mole and co-workers [74, 75] found en-

hanced methanol conversion rates when adding aromatics to the reactor feed. Similarly, Langner [76] found improved conversion rates when co-feeding cyclohexanol to methanol. All these findings led to the introduction of the indirect mechanism formulated by Dahl and Kolboe [77–79], in which a hydrocarbon pool, consisting of aromatic or aliphatic molecules, co-catalyzes the reactions leading to olefin production. Depending on the zeolite topology, other molecules were identified as most prominent co-catalysts. As such, polymethylbenzenes are pinpointed as the main "catalytic engine" over H-SAPO-34. [80–83] In contrast, ethene and propene are deemed nonreactive when co-fed with methanol over H-SAPO-34 [77,78], while they are determined to be reactive over H-ZSM-5. [84,85] By combining the alkene cycle suggested in H-ZSM-5 with the aromatic cycle proposed for H-SAPO-34, the dual cycle concept was introduced, as shown in Figure 1.4. [8, 10] ^{13}C labeling experiments performed by Svelle *et al.* [86] showed that ethene is mainly formed by the aromatic cycle, while propene and higher alkenes are linked to the alkene cycle. More recent work by Sun and co-workers [87, 88] shows that instead the aromatic cycle produces both ethene and propene while the alkene cycle is far more selective to propene, which was later confirmed theoretically. [89] They furthermore suggest that suppressing or promoting one of the competing cycles can alter the selectivities in favor of either ethene or propene. [87,88] As such, a supramolecular catalyst concept can be proposed, as done by Haw and Marcus [90], where for main characteristics of the zeolite can be tailored to tune the MTO process, as depicted in Figure 1.4. The proposed tunable parameters are the topology of the catalyst, the acid function, the organic compound present and possible inorganic modifications. This feature of the MTO process was studied in detail in **Paper II**, **Paper III** and **Paper V**, by tuning the zeolite catalyst to improve the propene selectivity by suppressing the aromatic cycle based on combined theoretical and experimental insight.

Promoting one or the other cycle may also have an impact on the catalyst lifetime. In H-SAPO-34, the methylbenzenes are reactive intermediates in the aromatic cycle, but are also coke precursors as they can form polyaromatics, which can block the zeolite pores. [38, 92–97] Although the precise mechanism leading to coke formation is to date not fully unraveled yet. [38, 81, 82, 94, 98, 99] On the other hand, in H-ZSM-5, coke formation is related to growth of large aromatics in the intersections of the channels [100] and formations of graphitic coke at the outer surface of the catalyst. [101] A detailed review of cokes formation in the MTO process is given in ref. [23]. In general one can conclude that suppressing the aromatic cycle might lead to decreased coking and increased catalyst lifetime. This concept was thoroughly tested in **Paper II**, **Paper III** and **Paper V**.

1.3.2 Importance of methylation reactions

From Figure 1.4 it becomes clear that methylation reactions are key reactions in both the alkene and aromatic cycle. Studies show that these reactions are key elementary reaction steps in the conversion of methanol over the zeolite catalyst,

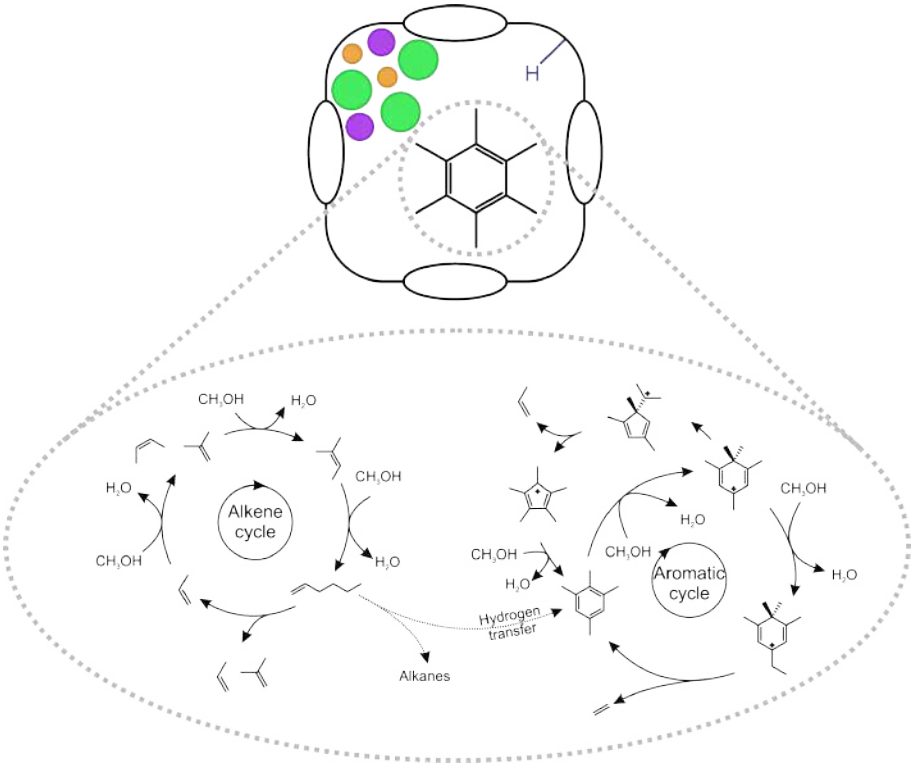

Figure 1.4: Schematic representation of the supramolecular view on MTO catalysis proposed by Haw and Marcus [90] where the MTO catalyst can be tailored by tuning the topology, acid function, organic compound or inorganic component. Based on the organic co-catalyst,the dual cycle concept, governing the methanol conversion in zeolite catalysis and consisting of the alkene and aromatic cycle, is proposed. This figure was remade from ref. [91] and [90], with permissions of American Chemical Society and Springer Nature.

as they are responsible for the growth of the HP species. [84, 85, 102–107] Their importance was already shown by Svelle and co-workers [86, 108–110] via isotope switch experiments from ^{12}C to ^{13}C methanol. The observed incorporation of ^{13}C in the formed products can only satisfactorily be explained by alkene methylations followed by cracking. A joint experimental and theoretical study further emphasized the relevance of this reaction. [97, 106] They found that the band at 400 nm in the in situ UV/Vis microscopy measurements could be assigned to polymethylbenzenes. Furthermore, the activation energies derived from the growth of this characteristic peak correlated well with the theoretical values for the activation energy for the methylation of the benzenic species. [111] Therefore, the methylation reaction is frequently used as model reaction for the MTO process, which is also the case for **Paper I**, **Paper III**, **Paper IV**, **Paper V** and **Paper VI**.

Two different routes are suggested in literature for the methylation reaction. This reaction may occur either via a concerted mechanism in which methanol transfers its methyl group directly towards the aromatic or via a stepwise mechanism, both represented in Figure 1.5 for hexamethylbenzene (HMB). In this stepwise mechanism, methanol first reacts with the catalyst framework, forming a methoxide species, which then transfers its methyl group to the HP species. [44, 107, 110, 112–115] Literature suggests that both mechanisms occur within the zeolite and the prevailing mechanism largely depends on the topology and the operating conditions. [44, 48, 107, 110, 113, 115–119] The studies show that with increasing temperature and decreasing pressure the prevailing mechanism shifts from concerted to stepwise. [119] This effect is attributed to the entropic gain of the intermediate release of water during the stepwise mechanism. [107, 115, 118, 119]

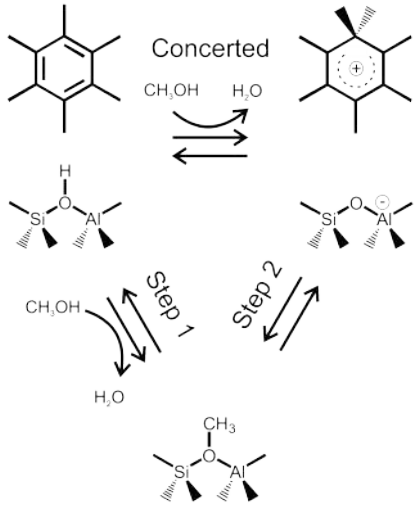

Figure 1.5: Schematic representation of competitive reactions mechanisms proposed for the methylation of hexamethylbenzene, namely the direct or concerted route and the stepwise route. Adapted from ref. [40] with permissions of John Wiley and Sons.

1.4 How to tune catalyst lifetime and product selectivity

In this section, we discuss which factors contribute to the product distribution and catalyst lifetime. Clearly this is a very complex problem and alteration of one parameter for example temperature or acid strength may be intertwined with the effect of another parameter. Obtaining clear correlations between individual parameters and catalyst performance is one of the most challenging problems

within zeolite catalysis. Various factors may affect the catalyst performance as schematically depicted in Figure 1.6. Firstly, the characteristics of the zeolite catalyst are discussed. Subsequently, the process conditions which affect the product yield and catalyst lifetime are summarized. Furthermore also the process conditions such as temperature or addition of water may contribute to the product distribution and catalyst lifetime.

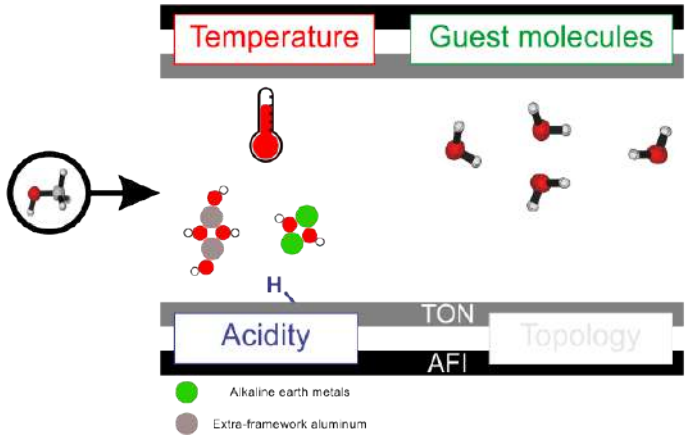

Figure 1.6: Schematic representation of factors that influence the reactivity within the zeolite pores and are studied in the framework of this dissertation. Adapted from ref. [107] with permissions from The Royal Society of Chemistry.

1.4.1 The nature and strength of the acid site

As stated earlier, shape selectivity is a crucial factor within zeolite catalysis due to the similar size range of the reacting and forming molecules and the pores. [8, 9, 37, 38] Apart from the zeolite topology also the composition and the acid strength are of utmost importance for the catalyst performance. For a long time, the nature of the active sites with acidic zeolites was to a large extent solely focused on Brønsted acidic sites (BASs). This type of sites is created by substituting a framework silicon atom by an aluminum atom in a zeolite catalyst or substituting a phosphorus atom by a silicon atom in case of a zeotype material, thus creating an excess negative charge on the framework. This charge can be compensated by a proton, thus creating an Brønsted acid site, as depicted for the two commercial zeolites H-SAPO-34 and H-ZSM-5 in Figure 1.7. [9] More recently, it became clear that active sites within MTO chemistry may be more complex and also the role of Lewis acidity within MTO chemistry was elucidated. [91, 120, 121] This reinforces the supramolecular nature of the MTO catalyst as introduced by Haw *et al.* and depicted in Figure 1.4. [90]

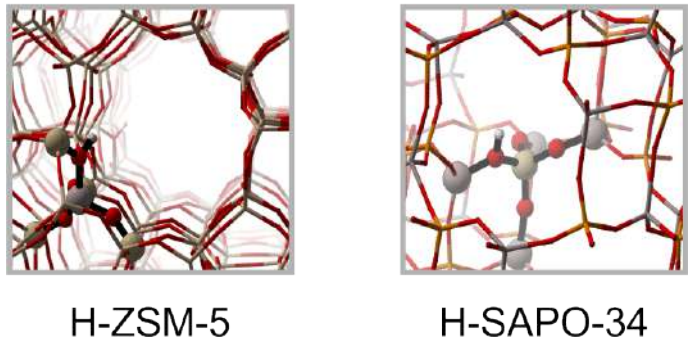

Figure 1.7: Snapshots of the frameworks of the two commercially used zeolite catalyst within the MTO process, namely H-ZSM-5 (MFI topology) and H-SAPO-34 (CHA topology). The framework is indicated by thin sticks while the substituted atom necessary to create the Brønsted acid site and the four surrounding T atoms are indicated in ball-and-stick representation. In these snapshots, hydrogen is white, carbon is silver, oxygen is red, aluminum is grey, silicon is beige and phosphorus is orange.

Topology and Brønsted acid strength

The optimal fit of the reactants in the zeolite pores severely influences the reaction kinetics. [102] As such, the one dimensional pores of H-ZSM-22 are too small to fit aromatic HP species. Methanol conversion over this zeolite is thus governed by the alkene cycle, leading to a high selectivity to branched C_{5+} alkenes as found by Teketel *et al.* [109, 122–124] In contrast, the large cages of H-SAPO-34 can comfortably accommodate the methylated aromatics and the aromatic cycle governs the reactions. [38, 80–83, 106] As this cycle is the main responsible for ethene selectivity [86–89], the insight into the governing reaction mechanism can partly explain the high selectivity to light olefins with high ethene to propene ratios for this catalyst. [25, 109] However, it should be noted that in H-SAPO-34 also diffusion limitations and product shape selectivity are important factors determining the product distribution. [38, 75, 125–129] As both cycles are active in H-ZSM-5, [86, 108] intermediate selectivities are obtained for this topology. [109]

Besides the topology, also the acid site density of the catalyst plays a crucial role for the activity of the HP species. As formation of aromatics typically requires a higher acid density [130], many zeolite modifications, such as dealumination [131–133] and post-synthetic alkaline earth metal modification [91,120,121], create isolated BASs to reduce formation of aromatics and thus increase the importance of the alkene cycle. [134–138] Furthermore, the aromatic cycle can be suppressed by lowering the acid strength of the Brønsted acid sites, as Bleken *et al.* [99] showed that in chabazite structured zeolites increased acid strength not only leads to enhanced production rates of olefins but also to higher aromatics retained in the catalyst. This was confirmed for the AFI structured H-SAPO-5 and H-SSZ-24

materials. Even when co-feeding benzene, the alkene cycle was found to dominate under MTO conditions in the weaker acidic H-SAPO-5 material. [46–48] These experimental findings are studied in detail using advanced molecular modeling methods in **Paper I**.

Brønsted versus Lewis acidity

MTO conversion becomes especially interesting as propene-on-demand process to solve the increasing disparity between the propene production and demand as the product distribution can be tailored. Ethene is mainly produced via the aromatic cycle, whereas propene and higher olefins are characteristic products of the alkene cycle. [139–142] Several methodologies can be followed to suppress the aromatic cycle [91] and one of them is active site engineering by incorporation of extra-framework species in the MTO catalyst. Inorganic modification of the zeolite was explored using phosphorus [143–145], boron [146], transition metals [130, 147–151] and alkaline earth metals. [120, 121, 152–156] These modifications lead to extra-framework species which might be present in the zeolite pores as metal cations or charged metal oxide clusters. [157, 158] Examples are shown in Figure 1.8 for mono-, bi- and trinuclear Ca oxide clusters which could be formed during post-synthetic Ca impregnation, as studied in in **Paper II**, **Paper III** and **Paper V**. Such modifications typically reduce the Brønsted acid site density, which can also be achieved by tuning the Si/Al ratio in the zeolite synthesis stage or by post-synthetic dealumination. [121, 131–133] Additionally, these modifications can exhibit catalytic activity themselves as they are known to create Lewis acid sites (LASs). [50, 120, 121] How the Lewis acidity introduced via post-synthetic modification of the zeolite further influences the product selectivity and catalyst lifetime is studied in detail in **Paper II**, **Paper III** and **Paper V**.

1.4.2 The reaction conditions

In addition to the catalyst, several other process parameters can be optimized to increase selectivities and catalyst lifetime. Typically one can vary the temperature, the pressure, the process feed composition, the recycle stream of undesired products (for example, the C_{4+} stream in the DMTO process of the DICP [26]),... The reaction conditions relevant for this dissertation are discussed in the following sections.

Temperature

A crucial parameter in the MTO process optimization is temperature. Typically, temperature ranges of 350–550 °C are commercially used. [8, 20] Several studies have been performed to elucidate the influence of temperature on the reactivity and product distribution. [87,100,115,159–169] In H-ZSM-5, kinetic measurements and micro-kinetic modeling have shown that the product spectrum can be altered in

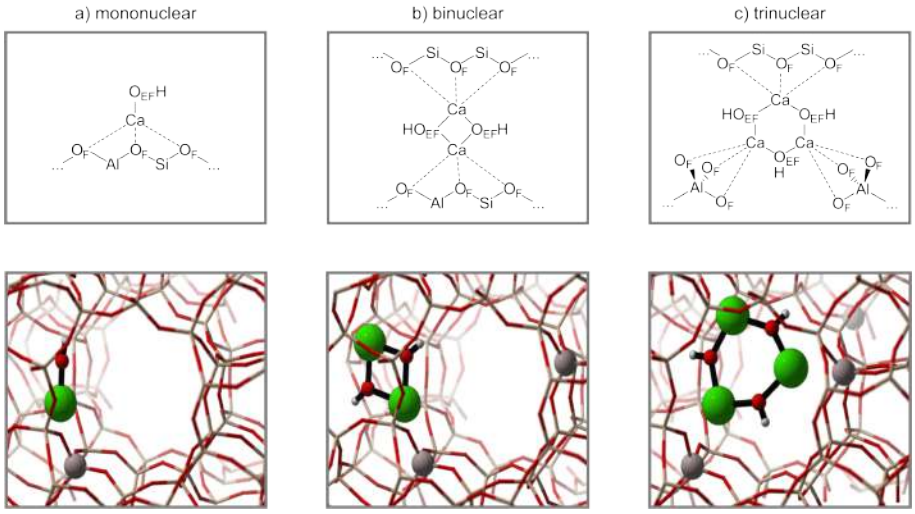

Figure 1.8: Schematic representation and snapshots of the optimized structures of the isolated extra-framework Ca species in ZSM-5 considered in **Paper II**, **Paper III** and **Paper V**, namely mononuclear (left), binuclear (center) and trinuclear (right) species. For the snapshots, the following color code is used: white is H, red is O, grey is Al, beige is Si and green is Ca. Adapted from ref. [91] with permissions of American Chemical Society.

function of the reaction temperature with increasing light olefin selectivity, mainly propene, at higher temperatures. [87,159] On H-SSZ-13 and H-SAPO-34, Borodina *et al.* [160, 161] found that the active HP species are dependent on the reaction temperature, being methylated benzene cations monoenyl carbocations at low temperature and methylated naphthalene carbocations at high temperature. Therefore, lower temperatures are mainly selective to propene, while higher temperatures favor ethene. Also coking rates are influenced by the applied temperatures. As such, high temperatures are found to favor coke formation reactions over olefin production in both H-ZSM-5 and H-SAPO-34, leading to faster deactivations. [162–164] The importance of the reaction temperature was further shown by the group of Iglesia where they promoted the alkene cycle in the large pore zeolite H-BEA, characterized by the aromatic cycle [100, 165–167], by utilization of low temperatures (453–493 K) and high pressures (60–250 kPa). [168, 169] Furthermore, Brogaard *et al.* [115] suggest that in H-ZSM-22, the dominance of the stepwise or concerted methylation mechanism will depend on the temperature. Due to the entropic gain by splitting off water in the intermediate product of the stepwise mechanism, it will prevail at higher temperatures. Therefore, the influence of temperature of the concerted and stepwise methylation reactions is studied in **Paper I** and **Paper IV**.

Guest molecules

Several guest molecules can be present in the pores of the zeolite which can either assist some reactions or suppress some reaction cycles. Those molecules can either take the role of reactants, be a formed (by)product or can be co-fed into the reactor on purpose. Especially the influence of water in the pores of the zeolites is highly relevant. Furthermore, it is an inherent byproduct of the methanol production [170–172] and produced in the equilibration of the MTO process, as depicted schematically in Figure 1.3. [90] Furthermore, early and recent studies also demonstrated an increased olefin selectivity and decreased coking rates upon increasing the water content. These effects were assigned to competitive adsorption of water on the Brønsted acid sites, thus making them unavailable for methanol to react. [173–175] In addition, the theoretical work done by De Wispelaere *et al.* [175] showed that the protic molecules assisted the methoxide formation and thus the first step of the stepwise methylation, as depicted in Figure 1.9a and b. In general, protic molecules may have a significant influence on the reactivity within the catalyst pores. For example, Moors *et al.* [41] found that higher methanol loadings lead to the formation of protonated clusters, depicted in Figure 1.9d compared to the isolated BAS in Figure 1.9c, which increase the methylation barrier as they stabilize the reactant state of the methanol molecule. On the other hand, this protonated cluster is very mobile, so methylation can occur at remote locations relative to the Al substitution, making the exact location of the BAS less influential. As the assistance and competitive adsorptions might significantly influence the methylation kinetics, their effects are studied in detail in **Paper IV**.

1.5 Molecular modeling in zeolite catalysis

From the previous sections it is clear that the MTO is a complicated process with several process parameters influencing the reaction and deactivation rates. How the different parameters influence the process is difficult to unravel experimentally, as several reactions occur simultaneously. Here molecular modeling techniques may offer a great added value, as they allow to study elementary reactions and isolate various parameters. Though it should be mentioned that several intensive experimental studies succeeded to isolate the influence of some parameters from experimental point of view [6, 84, 85, 99, 126], many recent studies are performed in close synergy between theoreticians and experimentalists. Such approach was deemed necessary to unravel the complexity of the MTO process. [48,62,91,120,121,175–178] Nevertheless, simulating chemical reactions in microporous catalysts is very challenging because of the inherent multi-scale nature of the system necessitating sampling of a wide range of time and length scales. To capture the entire scope of levels within a chemical process, theoretical calculations cannot be limited to quantum mechanics (QM), but should be complemented with

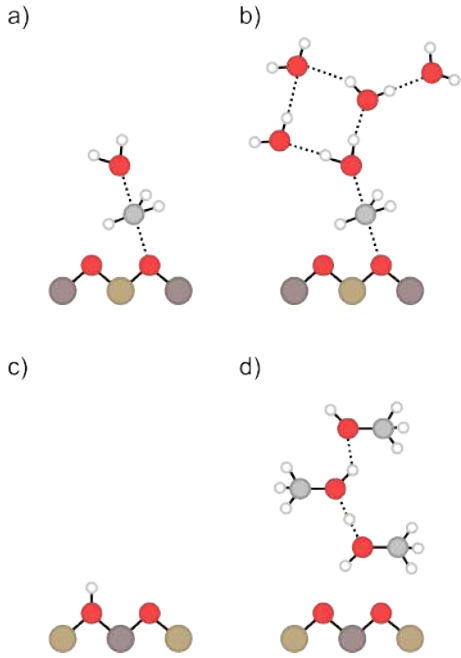

Figure 1.9: Schematic representation of the two effects of protic molecules studied via molecular modeling, namely on the one hand, in H-SAPO-34 the assistance of water in the methoxide formation showing the unassisted reaction (a) and the reaction stabilized by the interaction of water (b) [175] and, on the other hand, the change of the local environment of an original BAS (c) when a protonated methanol cluster is formed (d). [41] The following color code is used: white is H, light gray is C, red is O, dark gray is Al and beige is Si. This figure was remade from ref. [175] and [41] with permission of American Chemical Society.

classic force fields or molecular mechanics (MM), computational fluid dynamics and process or plant simulations. [179–181] The proper combination of such methods is a complex problem needing special attention and is therefore out of the scope of this thesis. [182] As chemical bonds are broken and formed during a chemical transformation, it is necessary to describe the electronic structure problem explicitly using quantum mechanical methods, since classic force fields are unable to describe such events. The use of a reactive force field, like ReaxFF, might be considered, but these still have some limitations. [183, 184]

The standard way to treat chemical reactions is through transition state theory (TST) [185], where only three points on the potential energy surface (PES) are located, namely the reactants, products and transition state. [181, 186] These calculations are inherently done at 0 K and thermal corrections are obtained through the harmonic oscillator approximation. [22, 187] Due to the increased

computational power and introduction of new methodologies, such as enhanced sampling molecular dynamics methods [22, 157], it has become possible to perform calculations at operando conditions. [187] According to Pidko and co-workers [187, 188], these should fulfill three conditions, namely a realistic representation of the catalyst surface, a realistic reaction coordinate and a complex reaction network should be considered. They further suggest that operando modeling cannot be reached by a single computational method that captures the entire complexity of all underlying phenomena. Rather a multi-scale composite methodology should be followed. They propose five methods that are most important to bridge the gap to operando modeling. These are schematically represented in function of the three characteristics in Figure 1.10.

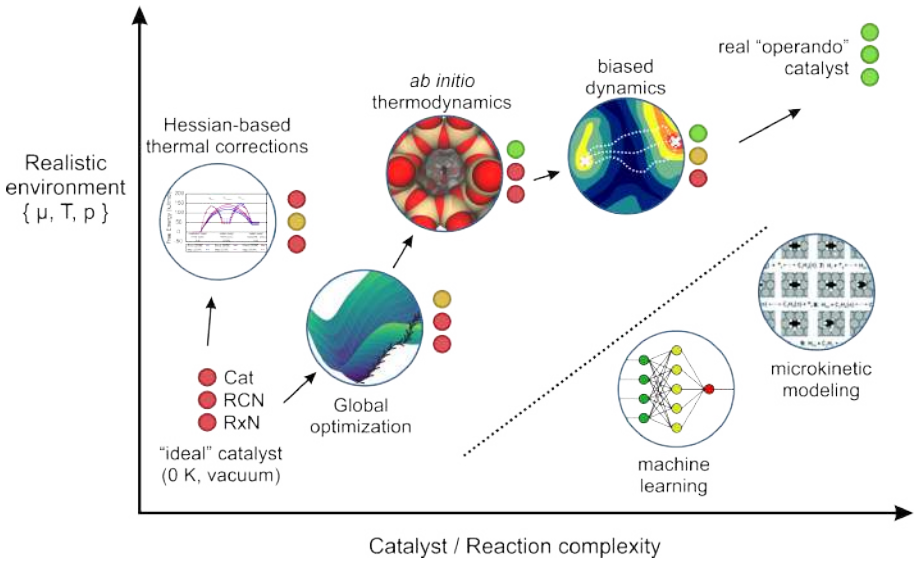

Figure 1.10: Schematic representation of computational methods commonly used in the framework of heterogeneous catalysis starting from the "ideal" catalyst model towards the realistic operando model. The traffic lights depict how good the model scores in representing the complexity of the catalyst model (Cat), of the reaction coordinate (RCN) and of the reaction network (RxN). Adapted from ref. [187] with permissions of The Royal Society of Chemistry.

To simulate at operando-like conditions, molecular dynamics (MD) methods are more and more used, which are intrinsically able to account for dynamic and entropic effects. [175, 186, 189–194] Furthermore, MD techniques have the advantage that the sampling of the potential energy surface is not limited to the static geometry optimization at 0 K of three stationary points, namely reactant, transition state and product, but is extended to a larger part of the PES. [22] Due to the use of quatum mechanical methods, this extensive sampling is computationally expensive. Furthermore, regular MD has the disadvantage that sampling is limited

to the most probable states of the system, thus hindering sampling of states high in energy like transition states. [195, 196] Improved examination of these rare events can be obtained by applying advanced molecular dynamics or enhanced sampling techniques. [195,196] In this thesis, we made use of four main techniques, namely metadynamics (MTD) [197–199], variationally enhanced sampling (VES) [200–202], umbrella sampling (US) [203–205] and thermodynamic integration (TI). [206–212] These are discussed in detail in Chapter 2 of this work, where also an extensive methodological study of the used enhanced sampling methods is presented.

Within this thesis we have used a complementary set of methodologies, going from static to enhanced sampling molecular dynamics methods. As we want to analyze the effect of complex process parameters on the kinetics of heterogeneous catalytic reactions these theoretical techniques are frequently used throughout this dissertation. More in particular methylation reactions in post-synthetic alkaline earth metal modified ZSM-5 zeolites and the role of water in the pores of the zeolite on the kinetics are key study objects in this dissertation to assess the various advanced sampling techniques.

1.6 Goal and outline

The goal of this thesis is to obtain molecular level insight into complex chemical conversions within zeolites at operando conditions. As a case study the methanol-to-olefins process is selected, as it is a prototype example of a zeolite catalyzed process where a lot of factors are influencing the reaction mechanism and consequently the catalyst performance. As theoretical simulations should fully respect the operando-like conditions in which the chemical processes take place, it is crucial to resort to (enhanced sampling) molecular dynamic simulations and a complex description of the catalyst active site and environment. Nevertheless, a methodology to obtain reliable reaction kinetics from dynamic simulations is not straightforward. Therefore, we performed a thorough benchmark study of these methods to obtain reaction kinetics for a frequently used case study reaction, namely the methylation of ethene in H-ZSM-5. As such, their accuracy can be tested before applying this procedure on other reactions governing the MTO process.

One of the main questions to be resolved within the field of the MTO process is how to tune the product selectivity and improve the catalyst lifetime. The reactions and materials studied in this thesis are to a large extent inspired and driven by experimental collaborations. The group of prof. J. Gascon of KAUST (King Abdullah University of Science and Technology) observed that post-synthetic alkaline earth metal modification of ZSM-5 materials leads to increased propene selectivity and longer catalyst lifetimes. To support their results and to elucidate the mechanism behind these findings, we applied a thorough combined experimental and theoretical study to unravel the structure of the active site created by the

alkaline earth metal, their nature and their effect on the kinetics in the catalyst pores.

Similarly, adding water to the process feed is known to alter the product selectivity and stability of the catalyst due to competitive adsorption between water and the MTO reactants on the acidic sites. [173–175] Moreover, water retards the formation of surface methoxide species, formed during the stepwise methylation mechanism. Therefore, we investigated the influence of water on the direct and stepwise methylation of hexamethylbenzene in H-SAPO-34 to unravel its effect on the prevailing mechanism at operando conditions.

To give an overview on the results obtained on the subjects listed above, the remaining chapters are structured as follows:

- In Chapter 2, we first introduce well-known molecular modeling techniques used throughout this work before presenting the more advanced enhanced sampling techniques and applying these concepts on the methylation of ethene in H-ZSM-5 as a case study, as such presenting a thorough methodological study. To this end, first the concept of density functional theory (DFT) and the used zeolite models are introduced. Subsequently, the ways to obtain macroscopic quantities from microscopic simulations are presented, focusing on both static and dynamic approaches. Next, the enhanced sampling techniques considered in this thesis are summarized and applied on the methylation reaction to compare their (dis)advantages. As the applied enhanced sampling techniques make use of collective variables, this concept is introduced and transformation between different possible collective variables are proposed and tested on the case study reaction. Finally, a new protocol has been proposed to determine the rate constants of various complex reactions, which can take place in the pores of nanoporous materials. The protocol makes use of enhanced MD sampling techniques and collective variable(s) to describe the reaction path, but the final kinetic quantity – the reaction rate constant – appears to be independent of the chosen sampling technique and collective variable, and thus model independent. This finding is very important as to date many isolated studied using a variety of enhanced sampling methods have been used but so far it was unclear in how far these methods give the same outcome. In this dissertation the new methodology is first applied to the ethene methylation in H-ZSM-5 and the results compared with experimental and theoretical data available in literature.

- After this thorough methodological introduction and study, the insights obtained via the theoretical studies, supported by experimental data, performed in the framework of this dissertation are discussed. In Chapter 3 we therefore focus on the results of the two main research questions posed in this dissertation, namely the effect of alkaline earth metal modification and of co-feeding water on the MTO process. The insights obtained on these main topics and on some side topics are presented based on the articles published in peer-reviewed journals.

- In Chapter 4, the main conclusions are formulated and some perspectives are formulated on the application of theoretical modeling within heterogeneous catalysis, in particular in the zeolite catalyzed MTO process.

2

Operando modeling within zeolite catalysis

As it is deemed difficult to obtain insight in separate parameters influencing the catalyst lifetime and selectivity due to the high number of reactions occurring simultaneously, experimental studies should be complemented with theoretical simulations. [48,62,91,120,121,175–178] To understand the insights in the MTO cycles discussed in Chapter 3, some background knowledge on molecular modeling is required. Therefore, we will first outline some common and well-known theoretical concepts in this chapter. Some newer methodologies will also be developed and applied to some case study reactions, such as methylation of ethene, to test their efficiency and accuracy. All models used in this dissertation are based on density functional theory (DFT). The basic concepts of DFT will be first introduced after which the focus will lie on more specific models, which have been applied to describe the molecular systems under study. Subsequently, commonly used methodologies to gain macroscopic quantities from molecular simulations are presented. As simulations at operando-like conditions become essential, complex modeling techniques like enhanced sampling are indispensable. [187] Therefore, the theoretical background of the enhanced sampling methods used in this work is outlined. We will make use of these techniques to develop a new protocol to predict reaction rate constants. A set of collective variables can be proposed which may act as reaction coordinate in most of the enhanced sampling methods used in this work. The performance of the new protocol will be tested on the methylation

of ethene over the Brønsted acidic ZSM-5 catalyst, which is considered as one of the prototype reactions within zeolite catalysis for which experimental kinetic data is available, and other advanced theoretical results as well. [84, 85, 213–215] Focus will lie on the free energy profiles which have been derived for the various collective variables and their mutual relationships.

2.1 Density functional theory

To gain molecular level insight into the reaction mechanism of the MTO process, first principle calculations were performed. This means that the electronic structure problem was explicitly solved using quantum mechanical based methods. To this end, one needs to solve the stationary Schrödinger equation: [216]

$$\hat{H} \left|\Psi\right\rangle = E \left|\Psi\right\rangle \tag{2.1}$$

where $\hat{H}$ represents the Hamiltonian, E the energy levels of the system and $\left|\Psi\right\rangle$ the many-body electron wave function. The Hamiltonian can be divided into five contributions:

$$\hat{H} = \hat{T}_N + \hat{V}_{NN} + \hat{T}_e + \hat{V}_{ee} + \hat{V}_{Ne} \tag{2.2}$$

with $\hat{T}_N$ the kinetic energy of the nuclei N, $\hat{T}_e$ the kinetic energy of the electrons e and $\hat{V}$ the potential energy due to charge-interaction between the nucleus-nucleus, electron-electron or nucleus-electron. Unfortunately, an exact solution can only be obtained for the hydrogen atom or the molecular hydrogen ion. Therefore, approximations are made to be able to solve the Schrödinger equation.

A first approximation, known as the Born-Oppenheimer approximation, [217] is made by accounting for the large mass difference between the nuclei and electrons, allowing to decouple their motions. As such, the eigenvalue problem can be solved separately for the electrons and the nuclei. Within the Born-Oppenheimer approximation, one needs to solve the electronic structure problem for fixed positions of the nuclei. This is still a many-body electronic structure problem and therefore various many-body techniques may be used to obtain approximate solutions.

A well known approximation is the Hartree-Fock (HF) method. [218,219] Within this method, the wavefunction is described by a single Slaterdeterminant and any electron correlation is omitted. Furthermore, the electron-electron interaction is replaced by a mean field in which the electrons can move independently. As this mean field depends on the one-particle orbitals, which are the solutions of the HF equations, this is inherently an iterative method. A disadvantage of this method is that it neglects the electron correlation energy resulting in a too high ground state energy as part of the stabilization energy is not accounted for. In post-HF methods, like the Møller-Plesset perturbation theory, [220] part of the correlation energy is included to obtain a better description of the electronic structure problem.

However, these methods are computationally very expensive and intractable to use on extensive zeolite models.

Nowadays, the most common method to solve the electronic structure problem is Density Functional Theory (DFT) where the central quantity is the electron density $\rho(\mathbf{r})$ instead of the wave function Ψ. [221, 222] The first Hohenberg-Kohn theorem proves that a unique relation exists between the electron density and the wave function in the ground state and all properties can thus be derived from the electron density. Furthermore, the second Hohenberg-Kohn theorem provides a variational principle to find the ground state electron density. [223] Density Functional Theory became a practical method in combination with the Kohn-Sham scheme, in which a set of one particle orbitals is introduced in a non-interacting model, which yields the same ground state density as the interacting many-body system. [224, 225] One of the problems within the Kohn-Sham scheme is the introduction of a so-called exchange correlation functional which is unknown and for which approximations have to be proposed. The final accuracy of the method depends on the particular functional chosen. Several functionals have been proposed and are generally divided in classes depending on their complexity and accuracy. This division is generally classified through the Jacob's ladder, as depicted in Figure 2.1. [226, 227] The simplest set of functionals belong to the class of the local density approximation (LDA), thus only using the electron density at one point. A first improvement can be made by including the gradient of the density into the functional. This class is referred to as the generalized gradient approximation (GGA). Including the non-interacting kinetic energy density leads to the next class, called meta-GGA. Using the fact that HF methods correctly implement the exchange energy, hybrid methods combining HF and DFT exchange energy improve the functionals. These functionals including part of the Hartree-Fock exchange are generally referred as hybrid functionals. Even more steps can be taken to improve the quality of the functional, but this is out of the scope of this work. More information can be found in dedicated text books and reviews. [228–232]

A major drawback of the DFT methods is their failure in modeling dispersion interactions. Such dispersion interactions are long-range attractive forces which act between separated molecules even in the absence of charges or permanent electric dipole moments. They originate from many-particle electron-correlation effects that are very difficult to describe accurately, as most applied DFT methods use exchange-correlation terms which are a functional of the local electron density or its gradient. One can overcome this problem in several ways. First of all, the DFT total energy can be corrected in a pragmatic way with an empirical dispersion term. This method, known as DFT-D, was introduced by Grimme [233–236] and includes a semi-empirical correction by using a $-C_6/R^6$ term (where R is the internuclear distance). As the dispersion correction is calculated separately, this is a computationally inexpensive method, but leads to good results. The corrections used in this method are parameterized for different DFT functionals, while a parameter-free method to derive the interatomic coefficients in the dispersion

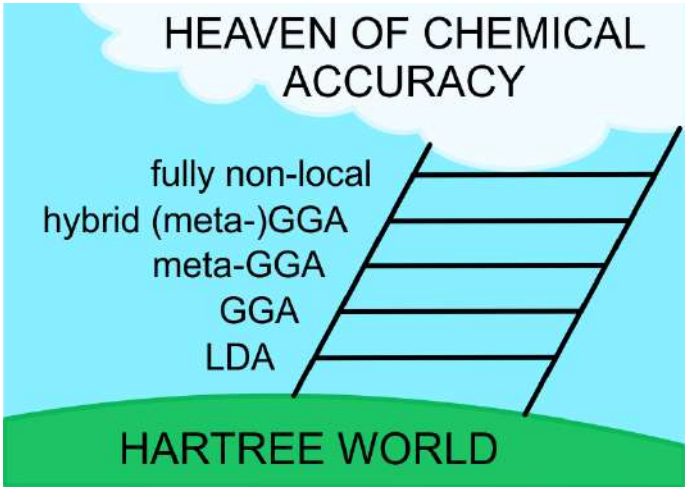

Figure 2.1: Perdew's metaphorical Jacob's ladder of density functional approximations. Each rung corresponds to a more complex model for the unknown exchange-correlation functional on the way to chemical accuracy. Adapted from ref. [226] and [231] with permissions of AIP Publishing and Informa UK Limited, trading as Taylor & Francis Group.

terms was proposed by Tkatchenko and Scheffler. [237] Another possibility is to construct a non-local vdW functional which accounts for long-range electronic correlations [238–240] Furthermore, the functional can be fitted to systems which are governed by dispersion interactions, as such enabling it to model dispersion interactions. A well known example is the Minnesota funcionals series (M05, M06 etc.) developed by the group of Truhlar. [241–245]

Due to the trade-off between accuracy and computational cost, the PBE-D3 or revPBE-D3 functional is applied throughout this work (here D3 denotes the third generation of Grimme corrections, accounting for three-body effects [235]). The latter functional has an improved performance in solid-state calculations compared to the former. [246] Though it should be noted that detailed level of theory studies have shown that the PBE-D method severely underestimates reaction barriers in zeolite catalysis. [22, 213–215, 247] Given the computational expense of enhanced sampling molecular dynamics simulations, it is unfeasible to use more expensive functionals such as hybrid functionals. Furthermore one can go beyond the simple pair-wise dispersion correction terms of the Grimme scheme and introduce many body correction terms. Again these are computationally much more expensive and are not suited to use in combination with enhanced sampling molecular dynamics calculations. Nevertheless, several levels of theory have been compared in **Paper V** and **Paper VI** based on static calculations, showing only minor deviations between PBE-D3, revPBE-D3 and other, some more advanced, methods. [233, 236–238, 248–258] Our methodology thus offers a good balance between computational

cost and accuracy for the problems tackled within this thesis.

2.2 Periodic zeolite models

As described in Chapter 1 the reactions governing the MTO process are catalyzed by acidic sites within the zeolite pores. To accurately describe the kinetics of the reactions under study, a proper model of the zeolite catalyst is needed. As Brønsted acid sites were long thought to be crucial in the reaction mechanism, early molecular modeling studies on zeolite catalyzed reactions focused on these sites to describe the reactions. These type of sites are created by substituting a framework silicon atom by an aluminum atom in a zeolite catalyst or substituting a phosphorus atom by a silicon atom in case of a zeotype material, thus creating an excess negative charge on the framework. This charge can be compensated by a proton, thus creating an Brønsted acid site. [9] In early quantum mechanical studies, the description of the zeolite was consequently limited to a 3T–5T (T = Al, Si or P) cluster around the Al or Si substitution, thus disregarding the influence of the nanoporous environment of the framework. [82, 83, 259–266]

With increasing computational resources, more extended finite clusters or periodically repeated unit cells are employed to capture the influence of topology on the elementary reaction steps, which showed to be of utmost importance in the theoretical analysis of the MTO process. [43,102,267] Both techniques are depicted for H-ZSM-5 in Figure 2.2. As shown, the catalyst is modeled by a fragment that is large enough to capture the topological effects affecting the active site in the extended finite cluster method. Compared to periodic models, these cluster calculations have the advantage that a wider variety of functionals can be used and that techniques for transition state localization are well established. On the other hand, the application of periodic boundary conditions on a complete unit cell is the most suitable solution to capture the true nature of a nanoporous material. [9] Throughout this work, periodic calculations were frequently applied to elucidate not only the role of Brønsted acid sites within the MTO process, but also the influence and nature of possible Lewis acid sites, for example in **Paper II**, **Paper III** and **Paper V**. Cluster calculations, on the other hand, were only used scarcely to generalize or check the conclusions made within the periodic models.

2.3 Molecular simulations

As discussed in Chapter 1, it is near impossible to unravel the reaction mechanism governing the MTO process solely based on experiments, as several reactions will occur simultaneously. Here, molecular simulations come into play, as they are able to gain insight into isolated elementary reaction steps. [9, 22] Nevertheless, to obtain macroscopic observables from our microscopic simulations, the partition function Z needs to be calculated. [22] In the following sections, the partition

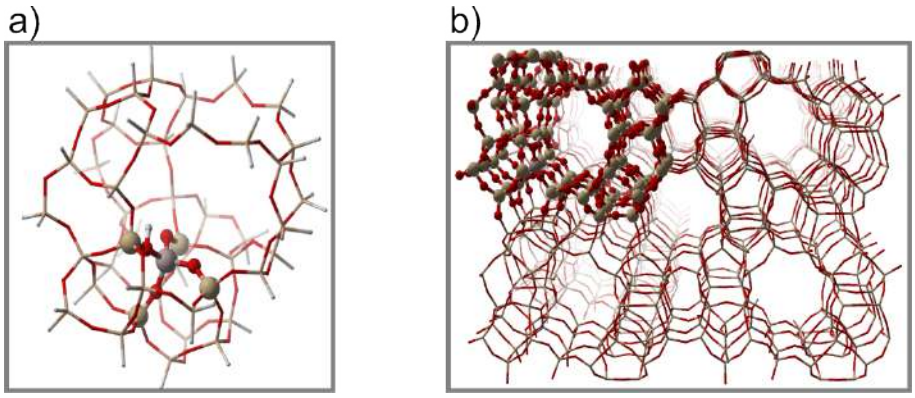

Figure 2.2: Depiction of the ZSM-5 framework using an extended cluster (46T), where the older 5T cluster is shown in ball-and-stick representation (a) and using a periodic presentation, where the unit cell is shown in ball-and-stick representation and a $2 \times 2 \times 2$ periodic image is shown.In these figures, hydrogen is white, oxygen is red, aluminum is grey and silicon is beige.

function is first shortly introduced. It can be constructed in both static and dynamic approximations (Figure 2.3).

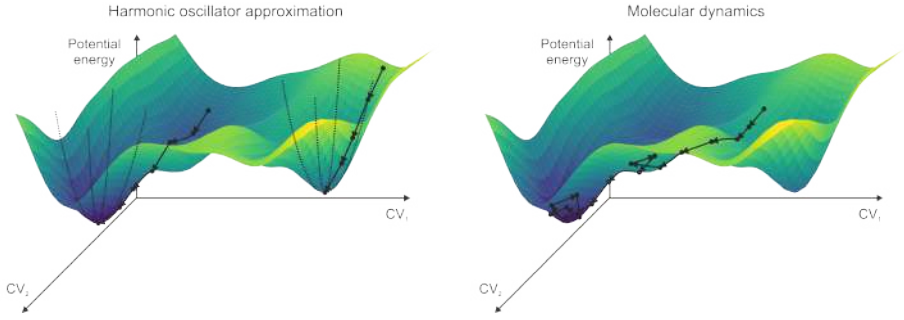

Figure 2.3: Schematic representation of the geometry optimization combined with the harmonic oscillator approximation (left) and of the molecular dynamics simulations (right).

2.3.1 Statistical physics

As it is not our goal to introduce all concepts of statistical physics, only a short introduction of a partition function is given. The interested reader is referred to more elaborate works on statistical physics such as ref. [268]. Here, the concepts are summarized for the canonical ensemble, as it is frequently used throughout this work.

According to classical statistical mechanics, the partition function Z and free energy F in the canonical ensemble of a system described by the Hamiltonian $\hat{H}(\vec{\mathbf{r}}^N, \vec{\mathbf{p}}^N) = \hat{T}(\vec{\mathbf{p}}^N) + \hat{V}(\vec{\mathbf{r}}^N)$ is given by:

$$Z = \frac{1}{h^{3N} N!} \int e^{-\beta \hat{H}(\vec{\mathbf{r}}^N, \vec{\mathbf{p}}^N)} d\vec{\mathbf{r}}^N d\vec{\mathbf{p}}^N \tag{2.3}$$

$$F = -k_B T \ln Z \tag{2.4}$$

Herein, the factor $N!$ only applies if the N particles are indistinguishable. Furthermore, $\beta = \frac{1}{k_B T}$ with k_B the Boltzmann constant. We can now introduce partition functions along a collective variable, i.e. a function of the coordinates describing a collective motion of the particles of the system $q = Q(\vec{\mathbf{r}}^N)$ (see Section 2.5):

$$Z_q(q) = \frac{q_0}{h^{3N} N!} \int \delta(Q(\vec{\mathbf{r}}^N) - q) e^{-\beta \hat{H}(\vec{\mathbf{r}}^N, \vec{\mathbf{p}}^N)} d\vec{\mathbf{r}}^N d\vec{\mathbf{p}}^N \tag{2.5}$$

The factor q_0 was introduced to make $Z_q(q)$ dimensionless. Furthermore, the new partition function satisfies:

$$Z = \frac{1}{q_0} \int_{-\infty}^{+\infty} Z_q(q) dq \tag{2.6}$$

This also allows us to define a probability distribution p_q such that $p_q(q)dq$ represents the probability for the system to be in a state for which $Q(\vec{\mathbf{r}}^N) \in [q, q + dq]$:

$$p_q(q) = (Z_q(q))/(Z q_0) \tag{2.7}$$

Through the relation between the partition function Z and the free energy F, we can relate Z_q to the free energy profile F_q:

$$F_q(q) = -k_B T \ln(Z_q(q)) \tag{2.8}$$

2.3.2 Harmonic oscillator approximation

A first method to obtain the partition function is the harmonic oscillator (HO) approximation. Here only vibrational motions of the molecular system with respect to an equilibrium configuration are considered. To this end, the potential energy surface around the energy minimum $V_0 = V(r_0)$ is expressed in a Taylor expansion:

$$V = V_0 + \sum_{i=1}^{3N} \left. \frac{\partial V}{\partial r_i} \right|_{r=r_0} \Delta_i + \frac{1}{2} \sum_{i,j=1}^{3N} \left. \frac{\partial^2 V}{\partial r_i \partial r_j} \right|_{r=r_0} \Delta_i \Delta_j \tag{2.9}$$

with the deviation $\Delta_i = r_i - r_{i0}$ of the position coordinates with respect to the equilibrium. As the potential energy is defined up to a constant value, V_0 can be set to zero. Furthermore, as the expansion is performed around the minimum

the first derivative will also vanish. Only quadratic terms are left in this HO approximation. Higher order terms determine anharmonic contributions, but they are here neglected.

The potential energy only depends on the internal motions in the molecular system. The $3N$ coordinates r_i are not uncorrelated. There are only $3N-6$ degrees of freedom describing the internal motions represented by the generalized coordinates q_i $(i = 1, 3N-6)$. The equation of motion of these $3N-6$ independent harmonic oscillators is then written in its standard form:

$$m_i \Delta \ddot{q}_i + \sum_{j=1}^{3N-6} \left. \frac{\partial^2 V}{\partial q_i \partial q_j} \right|_{q=q_0} \Delta q_j = 0 \tag{2.10}$$

As solution the following ansatz is suggested: $\Delta q_k = C \nu_k e^{-iwt}$ which leads to the following generalized eigenvalue problem:

$$\sum_{j=1}^{3N-6} \left(-M_{ij}\omega^2 + \mathrm{H}_{ij} \right) \nu_j = 0 \tag{2.11}$$

or in matrix notation:

$$\mathrm{H}\nu = \omega^2 M \nu \tag{2.12}$$

With the Hessian matrix H with elements $\mathrm{H}_{ij} = \left. \frac{\partial^2 V}{\partial q_i \partial q_j} \right|_{q=q_0}$ and the diagonal mass matrix M $(M_{ij} = \delta_{ij} m_i)$. The eigenvector ν corresponding with eigenvalue ω defines the normal mode of the system. Solving this eigenvalue problem – what we call a normal mode analysis (NMA) will give the frequencies ω of the $(3N-6)$ independent harmonic oscillators.

As the approximations made in this section are only valid in the neighborhood of the local minimum, a structural optimization always proceeds an NMA analysis. Furthermore, as the computational cost of an NMA analysis increases with system size, solutions are proposed to suppress costs. A frequently applied approximation is the partial Hessian vibrational analysis (PHVA). [269–271] In these methods, atoms which are far from the reactive site are assumed to not participate in the small amplitude vibrations necessary to describe the reaction at hand. Therefore, their displacements and velocities are set to zero. This can be imposed by assigning an infinite mass to these atoms. In practice, rows and columns corresponding to the coordinates of the fixed atoms in the full (Cartesian) Hessian H and mass matrix M can be disregarded, thus reducing the dimensions of the generalized eigenvalue problem from $3N \times 3N$ to $3(N-N_F) \times 3(N-N_F)$ with N_F the number of fixed or non-participating atoms. Using the PHVA, adsorption entropies could be calculated within an error range of 10–15 J/(mol K) with respect to the computationally more demanding full Hessian vibrational analysis (FHVA). [186,272] Therefore, this methodology is frequently applied throughout this dissertation as implemented in the CMM in-house toolkit TAMkin. [273]

2.3.3 *Ab initio* molecular dynamics

Using the static approach discussed in the previous section, information in the proximity of only one point on the potential energy surface is obtained by calculating the vibrations in the harmonic oscillator approximation. Nevertheless, a large part of the PES is still not sampled. To overcome this limitation a molecular dynamics simulations is able to follow the time-evolution of all atoms in the system. [274–276] Additional information can thus be obtained with *ab initio* MD simulations as these are able to account for dynamical effects as framework flexibility, temperature effect, entropy influence and the influence of surrounding solvent molecules on chemical reactions. [22]

During the MD simulations performed in this work, the Born-Oppenheimer approximation is applied, which decouples the motion of the nuclei and the electrons based on the significant difference in mass. [277, 278] This permits to describe the electrons quantum-mechanically, while the motion of the nuclei can be described classically by Newton's second law:

$$m_i \vec{\mathbf{a}}_i = \vec{\mathbf{F}}_i = -\vec{\boldsymbol{\nabla}}_i V \tag{2.13}$$

where M_i is the mass of the nuclei i, $\vec{\mathbf{a}}_i$ is the acceleration vector of the atom nuclei and $\vec{\mathbf{F}}_i$ is the force acting on the cores. Through the potential energy V, these classical equations still depend on the electronic structure of the system.

One of the aims of MD simulations is to get insight in the average behavior of some observables in many-body systems. When an average is taken over all possible quantum states of a system, this is called an ensemble average. Nevertheless, in experiment and MD simulations, measurements are taken over time and a time average is obtained. In general, both averages are not equal, though most of the time they are assumed to be equal, which is referred to as the ergodic hypothesis. [268] The analysis of time averaged quantities is used frequently throughout this work, more specifically in **Paper I** and **Paper IV**.

Solving the above equations of motion inherently results in quantities described in the microcanonical ensemble (NVE), with constant number of particles N, volume V and total energy E. It is however more convenient to perform simulations in other thermodynamic ensembles such like the NVT ensemble at constant temperature T and volume V or the NpT ensemble with constant T and pressure p. [268] Sampling at constant temperature requires the use of a thermostat, for which a chain of five Nosé-Hoover baths is used throughout this work. [268, 279] A constant pressure can similarly be maintained by using a barostat, for which the MTTK (Martyna-Tuckerman-Tobias-Klein) barostat is chosen in this work. [280]

Unfortunately, MD techniques have one main disadvantage, namely sampling is limited to the most probable states of the system, making the sampling of states high in energy, like transition states, rare events at the macroscale and impossible events at the microscale. [195, 196] These rare events can be visited by applying advanced molecular dynamics or enhanced sampling techniques, which are discussed in more detail in the next section.

2.4 Enhanced sampling techniques

As stated in the previous section, MD techniques have the advantage of sampling broader regions of the potential energy surface compared to the static harmonic oscillator approximation. [22, 107] Nevertheless, the sampling is still limited to regions with high Boltzmann probabilities. [195, 196] This hurdle can be overcome by applying enhanced sampling or advanced molecular dynamics techniques, for which we refer the interested reader to some recent references on the topic. [195, 196, 281, 282] They all emphasize that three components of a free energy calculation should be considered before starting, namely:

i. The choice of a suitable model for the Hamiltonian

ii. The decision on the sampling protocol to explore all relevant parts of the PES

iii. The choice of the estimator to obtain the free energy difference [283]

As stated in Section 2.1, the choice of the model for the Hamiltonian is quite straightforward in this case. Since the chemical reactions under study in this work involve breaking and forming chemical bonds, traditional force fields cannot be used as they are unable to describe such events. The use of a reactive force field, like ReaxFF, might be considered, but these still have some limitations. [183, 184] For example, this method still struggles with describing polarization, charge transfer and stabilizing dispersion interactions, [184] which are important in zeolite catalysis as hydrogen bonding, proton transfer and interactions with the framework occur frequently. [42, 213, 214, 284, 285] Therefore, a quantum-mechanical description of the system is preferred and density functional theory methods have the advantage that they account for the most important electron correlations while being computationally more efficient than wave function methods like Hartree-Fock. [286]

As sampling protocol to explore the PES, MD methods are preferred in this Ph.D. thesis, as discussed in Section 2.3.3, though enhance sampling techniques are necessary to ensure sufficient sampling of the transition region. The selection of the enhanced sampling protocol largely depends on the choice of a collective variable (CV or q in formulas), a function of the microscopic coordinates, that differentiates between the interesting metastable and transition states, thus representing the reaction coordinate, which will be discussed in more detail in Section 2.5. If such variable cannot be selected, one can enhance all degrees of freedom. An example is increasing the temperature as used in replica exchange. [287–289] If, on the other hand, such function is known, the enhancement of the sampling could be limited to this collective variable. [196, 290] As collective variables could be distinguished for the reactions considered in this work, we were able to make use of a whole plethora of enhanced sampling techniques such like metadynamics [197–199], variationally enhanced sampling [200–202], umbrella sampling [203–205] and thermodynamic integration [206–212]. These methods are summarized schematically in Figure 2.4.

The concept in all selected methods is based on the introduction of a bias potential allowing a more steered sampling of the relevant regions of the configuration space. The way such a bias potential is introduced can vary per method and is discussed in the following sections. Lastly, as most sampling methods are correlated with a particular free energy estimator [283], these will be discussed separately for each method in the corresponding section. In Section 2.4.5, all introduced enhanced sampling methods are compared based on a case study reaction, the methylation of ethene in H-ZSM-5. As such, we will benchmark these methods and elucidate the advantages and disadvantages of each technique.

2.4.1 Metadynamics

In this method first introduced by Laio *et al.* [197,198] , the bias potential used to enhance the sampling of all regions of interest is constructed on the fly by gradually adding Gaussian shaped hills. The bias potential $U_G(q,t)$ after a simulation time t then becomes:

$$U_G(q,t) = \sum_{t'=\tau_G,2\tau_G,\ldots}^{t'<t} h_{t'} \exp\left(-\frac{(q-q(t'))^2}{2w^2}\right) \tag{2.14}$$

where $h_{t'}$ is the amplitude and w the width of the Gaussian hills, which are added each time interval τ_G. The amplitude $h_{t'}$ is systematically lowered after recrossing the free energy barrier, to allow accurate and fast convergence. The basic idea of the metadynamics technique is that after a sufficiently long simulation time, the bias potential is related to the free energy $F(q)$ via:

$$\lim_{t\to\infty} U_G(q,t) \sim -F(q) \tag{2.15}$$

As such, the free energy surface of the system can be estimated as the inverse of the time dependent bias potential.

2.4.2 Variationally enhanced sampling

Variationally enhanced sampling is a relatively new advanced molecular dynamics method introduced by Valsson and Parrinello. [201] This technique is based on the introduction of a functional of the bias potential $U(q)$:

$$\Omega[U] = \frac{1}{\beta}\ln\left(\frac{\int \exp(-\beta[F(q)+U(q)])dq}{\int \exp(-\beta F(q))dq}\right) + \int p(q)U(q)dq \tag{2.16}$$

where $\beta = \frac{1}{k_B T}$ and $p(q)$ is the target distribution, a predefined probability distribution which is in principle completely arbitrary. It can be shown that this functional is convex and has a minimum at:

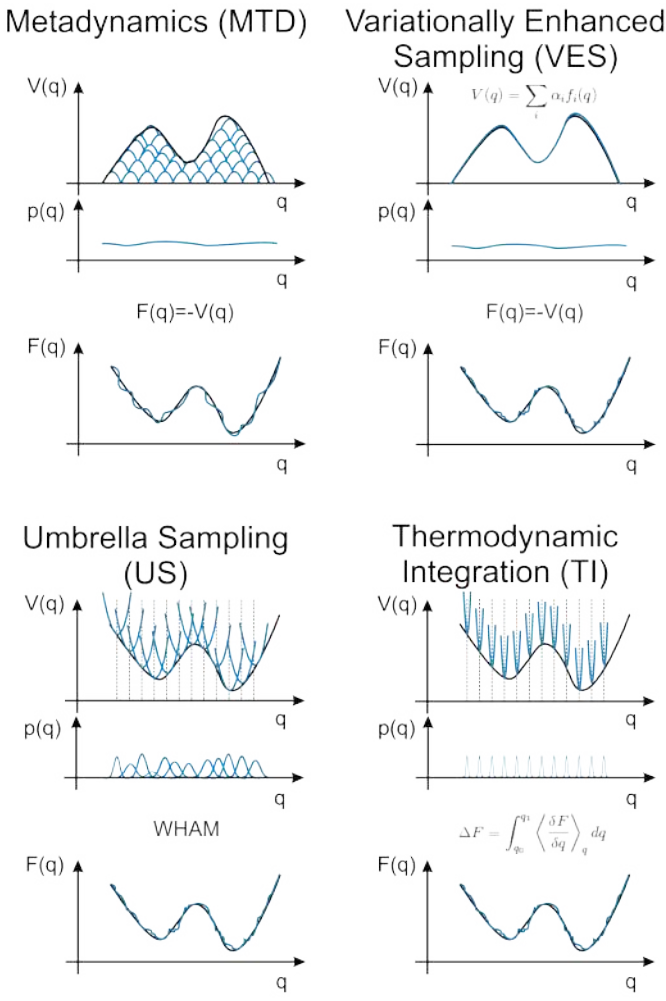

Figure 2.4: Schematic representation of the enhanced sampling methods considered in this Ph.D. dissertation. For each method, the top graph shows the external bias introduced to enhance the sampling and the bottom figure shows the free energy estimation. The methods to estimate the free energy is also indicated.

$$U(q) = -F(q) - \frac{1}{\beta}\ln(p(q)) \tag{2.17}$$

which indicates that the free energy $F(q)$ can be estimated from the target distribution and the bias, once the functional $\Omega[U]$ is minimized. An additional aspect of VES is that this minimization is equivalent to minimizing the Kullback-Leibler divergence between the sampled distribution p_B and the target distribution p:

$$KL\left\langle p|p_B\right\rangle = \int p(q)\ln\left(\frac{p(q)}{p_B(q)}dq\right) \tag{2.18}$$

The minimization can be performed by expanding the bias potential $U(q)$ in some basis functions $f_i(q)$ and applying the variational principle by varying the expansion coefficients α_i until the minimum is reached.

$$U(q) = \sum_i \alpha_i f_i(q) \tag{2.19}$$

The expansion coefficients which minimize the function $\Omega[U]$ can then be obtained via a stochastic gradient descent algorithm: [291]

$$\alpha^{(n+1)} = \alpha^{(n)} - \mu\left[\nabla\Omega\left(\overline{\alpha}^{(n)}\right) + \mathrm{H}\left(\overline{\alpha}^{(n)}\right)\left[\alpha^{(n)} - \overline{\alpha}^{(n)}\right]\right] \tag{2.20}$$

in which μ is the step size, $\overline{\alpha}^{(n)}$ is the running average of $\alpha^{(n)}$ at iteration n. Furthermore, $\nabla\Omega\left(\overline{\alpha}^{(n)}\right)$ and $\mathrm{H}\left(\overline{\alpha}^{(n)}\right)$ are the gradient and Hessian of the function $\Omega[U]$ of the running average at iteration n, respectively.

2.4.3 Umbrella sampling

Beside time-dependent bias potentials, one can also add a fixed external potential (U_b) to the true Hamiltonian ($\hat{H}$) to enhance the sampling in low probability regions. This is used in umbrella sampling, introduced by Torrie and Valleau. [203, 204] The external potential is dependent on the collective variable q and leads to a biased partition function Z_b, a biased free energy F_b, a partitioned partition function $Z_b(q)$ and partitioned probability distribution $p_b(q)$:

$$Z_b = \frac{1}{h^{3N}}\int \exp\left(-\beta(\hat{H}(\vec{\mathbf{r}}^N,\vec{\mathbf{p}}^N) + U_b(Q(\vec{\mathbf{r}}^N,\vec{\mathbf{p}}^N)))\right) d\vec{\mathbf{r}}^N d\vec{\mathbf{p}}^N \tag{2.21}$$

$$F_b = -k_B T\ln Z_b \tag{2.22}$$

$$Z_b(q) = \frac{q_0}{h^{3N}}\int \exp\left(-\beta(\hat{H}(\vec{\mathbf{r}}^N,\vec{\mathbf{p}}^N) + U_b(Q(\vec{\mathbf{r}}^N,\vec{\mathbf{p}}^N)))\right)\delta(Q(\vec{\mathbf{r}}^N,\vec{\mathbf{p}}^N)-q)d\vec{\mathbf{r}}^N d\vec{\mathbf{p}}^N \tag{2.23}$$

$$Z_b(q) = Z(q)\exp(-\beta U_b(q)) \tag{2.24}$$

$$F_b(q) = -k_B T\ln(Z_b(q)) \tag{2.25}$$

$$F_b(q) = -k_B T\ln(p_b(q)) + cte \tag{2.26}$$

Furthermore, the unbiased free energy $F(q)$ can be obtained from the free energy of the biased system $F_b(q)$ as:

$$F_b(q) = -k_B T \ln(Z_b(q)) \tag{2.27}$$

$$F_b(q) = -k_B T \ln(Z(q) \exp(-\beta U_b(q))) \tag{2.28}$$

$$F_b(q) = F(q) + U_b(q) \tag{2.29}$$

As knowledge lack beforehand to select a bias potential that will enhance sampling in all relevant regions, the reaction path is often divided into a number of distinct windows, as indicated in Figure 2.4. In each window, the reaction coordinate is restrained to a target value q_i by applying a bias potential (U_b^i) in each window. Often, a harmonic bias potential with force constant K is used to keep the system close to the target value:

$$U_b^i = \frac{K}{2}(q - q_i)^2 \tag{2.30}$$

For each window, a separate simulation is performed leading to a histogram $H_i(q)$ for each window. From these, we can estimate the biased probability as $p_b^i(q)dq = H_i(q)/M_i$ where $H_i(q)$ is the number of counts in the range $[q, q + dq]$ and M_i is the total number of sample points in window i. Several schemes are proposed to obtain the unbiased probability from the biased histograms, [292, 293] but in this work we will focus on the weighted histogram analysis method (WHAM). [205, 294–296] This method is described in detail in Appendix B.

2.4.4 Thermodynamic integration

This method, introduced by Kirkwood [206], is based on the knowledge that when we want to sample in the vicinity of collective variable q, the system would drift away from this configuration quite rapidly. There is information in the average direction and magnitude drifting, as the 'mean force' $-\langle \partial F/\partial q \rangle_q$ could be a measure for the negative gradient of the free energy. The free energy could then be obtained following a three-step procedure:

i. Sample several points in the collective variable space, for example via constrained molecular dynamics in Blue Moon sampling. [207, 297–299]

ii. Calculate the mean force at that value of q.

iii. Reconstruct the free energy profile by numerically integrating the mean forces:

$$\Delta F(q_0, q_1) = \int_{q_0}^{q_1} \left\langle \frac{\partial F}{\partial q} \right\rangle_q dq \tag{2.31}$$

2.4.5 Comparison of enhanced sampling methods

To gain some more insight into the different available enhanced sampling protocols, these techniques were benchmarked in **Paper VI**. In that work, the methylation of ethene is chosen as a case study, as many experimental and theoretical reference data exist. [84, 85, 213–215] The methylation of ethene, schematically depicted in Figure 2.5, can be described by several collective variables (described in more detail in Section 2.5). To compare the enhanced sampling methods listed in the previous sections, a simple one-dimensional collective variable is selected, namely the difference between the distance between the carbon and oxygen of methanol d and the distance between the carbon of methanol and the center of mass of the carbons of ethene d_{CM}. This collective variable is discussed in detail in Figure 2.8 in Section 2.5.3. The profiles obtained by sampling along this collective variable using the different methods are depicted in Figure 2.6 together with an estimation of the sampling error, which is discussed in more detail in **Paper VI**.

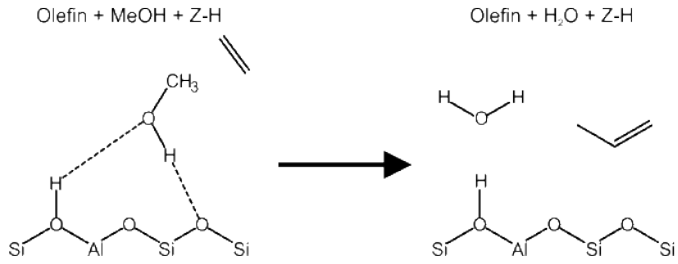

Figure 2.5: Schematic representation of the methylation of ethene with methanol yielding propene.

Figure 2.6 shows that the VES result is distinct from the other sampling techniques by a higher forward barrier, as indicated in the subtitles of Figure 2.6 (120 kJ/mol instead of 100 kJ/mol) and higher error bars. This is not conform the standard performance of VES in other benchmark studies, where free energy profiles are constructed for structural transformations in metal-organic frameworks (MOFs) with the volume of the unit cell as a perfect one-dimensional collective variable. [201, 290] Thus, insufficient sampling could be on the basis of this discrepancy. In addition, the VES protocol requires several barrier recrossings to obtain converged free energy estimates, similar as in metadynamics. For this specific reason, two walls are placed at some specific values of the one-dimensional collective variable ($d_{CM} - d$, depicted in Figure 2.8), as indicated in Figure 2.6, to oppose the diffusion of ethene on the one hand, and to avoid sampling of the product state on the other hand, as several products can be formed, e.g. propene, cyclopropane, propoxide, propanol... These auxiliary tools are not needed in US and TI in this specific application, and therefore US and TI are preferred over MTD and VES. This conclusion is in contrast to other results obtained in the framework of this dissertation. [40] In **Paper IV** discussed in Section 3.2, where MTD was

preferred over US, as for the system under study there, the disadvantage of using walls was outweighed by the fact that less prior knowledge on the reaction path is needed within MTD. [300] As the walls necessary for the system used here are more stringent, the methods which do not use walls are preferential.

When concentrating on the reactant side of the free energy profiles for US and TI, these show large similarities with a forward barrier of about 100 kJ/mol. We did not focus on the product side of the reaction, as several product states are sampled in the US and TI simulations due to the instability of the primary product, protonated propene, giving rise to the discrepancies observed for the two techniques. The lower force constants used in US allow to converge to a more stable product, while the TI runs are stuck in a less stable product. As we were only interested in the forward barrier, no preference could be given to one of both techniques. However, in the execution of the TI method correction factors need to be incorporated in the computation of the sampled mean force when coordination numbers are considered as collective variables. [210, 301] US is free of this cumbersome task and therefore was selected as the most appropriate method. A similar conclusion was made by an earlier benchmark study where force fields were used to compare the efficiency of enhanced sampling techniques in the construction of free energy profiles for breathing metal-organic frameworks. [290] Nevertheless, it should be noted that this discussion shows that this choice largely depends on the system under study. To explain the importance of the transformation between different collective variables, which will be introduced in the next section, US will thus be used as an example.

2.5 Collective variables

The choice of a proper collective variable is crucial to rate the efficiency and accuracy of the enhanced sampling method. Collective variables should obey some strict conditions, which are outlined in the next section. Furthermore, we will show that one cannot directly compare free energy profiles obtained in different collective variable spaces. Therefore, we demonstrate how free energy profiles can be transformed from one space to another. Finally, we will apply these transformations on the case study reaction, the methylation of ethene in H-ZSM-5, as such proving their validity and utility.

2.5.1 Definition of a collective variable

We adopt the definition of a collective variable as introduced by Peters. [302] In this work a distinction is made between:

- a collective variable, which is any function of the phase space coordinates
- an order parameter, which is a collective variable that can differentiate between the reactant and the product

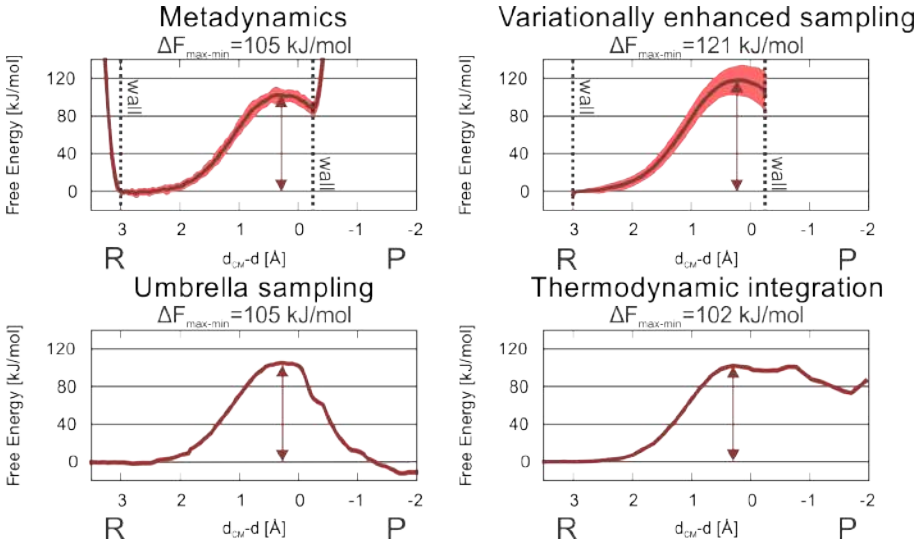

Figure 2.6: Free energy profiles and error bars at 350 °C in function of the one-dimensional collective variable obtained with different enhanced sampling methods applied on the methylation reaction of ethene in H-ZSM-5. Furthermore, the minimum-maximum barrier is shown on the graphs for each method. The reactant (R) and product (P) side of the reaction are also indicated.

- a reaction coordinate, which is an order parameter that can also describe the progress along the trajectory from reactant to product.

Furthermore, the degrees of freedom which are not described by the collective variable are identified as the orthogonal degrees of freedom. Sampling and construction of a free energy profile can be done along any collective variable, though the obtained information will only be relevant if this CV represents a reaction coordinate. The importance of the choice of the CV is already shown in several studies. For example, the dissociation of NaCl in water by Geissler *et al.* [303], the conformational study of alanine dipeptide by Bolhuis *et al.* [304] or the structural transformations in flexible MOFs by Demuynck *et al.* [305] As such, the free energy barrier might be underestimated because it ignores important degrees of freedom or it might be too high as the system gets trapped in local minima. [63, 306–309] The selection of an ideal collective variable is very tedious, but of utmost importance [305–307] and should fulfill three requirements: [306]

- It should only depend on the instantaneous point in configuration space

- It should monotonically increase while moving from the reactant over the transition state to the product

- Projection of the free energy on the CV should result in a one-dimensional free energy profile with reduced dynamics which are consistent with the full phase space

As such, several collective variables can be tested on their ability to act as reaction coordinate. Different sets of collective variables, *e. g.* q_1 and q_2, will lead to different free energy profiles, $F_{q_1}(q_1)$ and $F_{q_2}(q_2)$, respectively. Therefore, their direct comparison is hampered. This hurdle can be overcome by transforming the free energy profile obtained in one collective variable space to another as explained in the following section.

2.5.2 Transformation of collective variables

When using different collective variables, one cannot straightforwardly compare free energies obtained in the various CVs, as explained hereafter. Suppose one introduces two sets of collective variables, q_1 and q_2, which have both the goal of describing the same process or reaction. If one would perform enhanced simulations using both collective variables, it would give rise to two free energy profiles $F_{q_1}(q_1)$ and $F_{q_2}(q_2)$, which can in general not be compared directly since different collective variables give rise to different integrations over microstates. However, if both collective variables indeed describe the same process, they are expected to be correlated and the free energy profiles should be related to each other. [305] In Eqs. 2.7 and 2.8 we have introduced a general expression from statistical physics:

$$F_q(q) = -k_B T \ln(q_0 p_q(q)) \tag{2.32}$$

relating the free energy with the probability $p_q(q)$ that the system is found in conformations defined by the coordinates x giving rise to collective variable q. The probability $p_q(q)$ is normalized: $\int p_q(q)dq = 1$. Although the normalization gives only rise to a shift of the free energy. Instead of the probability function $p_q(q)$ we could also make use of the partition function $Z_q(q)$ which represents the same quantity but with another normalization (Eq. 2.7).

A transformation to another collective variable starting from the knowledge of the probability $p_{q_1}(q_1)$ requires a good estimate of the conditional probability $p_{2|1}(q_2|q_1)$:

$$p_{q_2}(q_2) = \int_{-\infty}^{+\infty} p_{2|1}(q_2|q_1) p_1(q_1) dq_1 \tag{2.33}$$

This brings us to the relation between the two free energy expressions:

$$F_{q_2}(q_2) = -k_B T \ln\left(\frac{q_{20}}{q_{10}} \int_{-\infty}^{+\infty} p_{2|1}(q_2|q_1) e^{-\beta F_{q_1}(q_1)} dq_1\right) \tag{2.34}$$

Note that the constants q_0 in Eq. 2.32 and q_{10} and q_{20} in Eq. 2.34 are introduced to make some quantities dimensionless. They can easily be omitted as they only generate a constant shift of the free energy and thus have no physical

significance. The precision of this transformed free energy profile largely depends on the quality of the sampling of the phase space spanned by the variables q_1 and q_2. A sufficient sampling of q_2 coordinate for each relevant value of q_1 yields a proper conditional probability. The transformation is further illustrated in Figure 2.7 for the 1D case. The expansion to 2D profiles is derived and tested intensively in **Paper VI**.

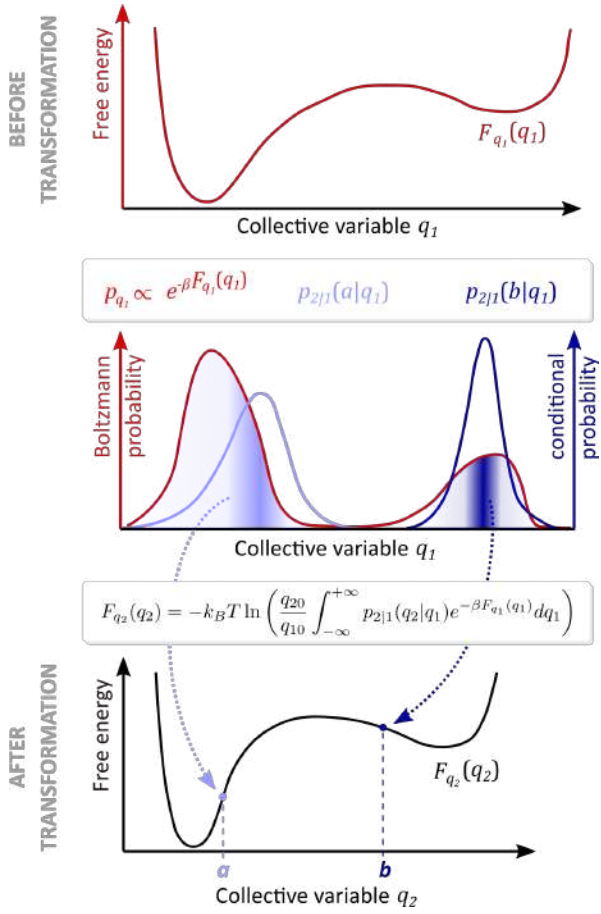

Figure 2.7: Graphical representation of a free energy profile $F_{q_1}(q_1)$, which was computed by sampling along q_1 and expressed as a function of q_1, and is transformation to the corresponding free energy profile $F_{q_2}(q_2)$ as a function of q_2. The integral can be interpreted as a weighted average of the Boltzmann probability, with weights given by the conditional probability and indicated through the shading in the middle pane.

2.5.3 Impact of collective variables on free energy profiles

To show the validity of the transformations introduced in the previous section, we applied them in our case study (**Paper VI**), on the same case study as used in Section 2.4.5, namely the methylation of ethene. Several suggestions of suitable collective variables to describe the methylation of ethene in H-ZSM-5 are proposed in Figure 2.8. We distinguish between two types of collective variables. One type (type CN) consists of coordination numbers (CNs) between two atoms describing the breaking and formation of the C-O and the C-C bond. [22, 41, 44] CN_{ij} represents the coordination number between the atoms i and j defined as:

$$CN_{ij} = \sum_{i,j} \frac{1 - \left(\frac{r_{ij}}{r_0}\right)^{nn}}{1 - \left(\frac{r_{ij}}{r_0}\right)^{nd}} \tag{2.35}$$

with r_{ij} the interatomic distance and r_0 the reference distance, set to 2 Å, which approximately represents the C-C distance in the transition state. Furthermore, the parameters nn and nd where chosen to be 6 and 12, respectively. As such, two collective variables are needed to describe the methylation reaction: CV1 being the coordination number CN_{OC} between the oxygen and carbon of the methanol (green and red in Figure 2.8) and CV2 being the coordination number CN_{CC} between the carbon of methanol and the two carbons of ethene (red and blue in Figure 2.8).

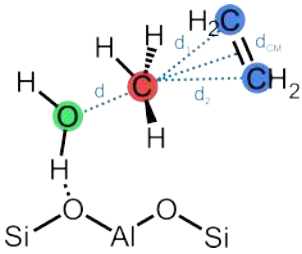

			CV1	CV2
Coordination numbers	Type CN		CN_{OC}	CN_{CC}
Distances	Type DI	DI	d	d_{CM}
		1D-DI	d_{CM}-d	-

Figure 2.8: Schematic representation of the collective variables used to describe the methylation reaction of ethene with methanol.

The second type (type DI) of collective variables is based on distances of the breaking and forming bonds. The first collective variable CV1 is simply the bond distance d between carbon and oxygen of the methanol. For the second collective variable CV2 the two carbon atoms of ethene (blue) need to be taken into account. We account for both by choosing the distance d_{CM} between the C of methanol and the center-of-mass of the ethene molecule. A one-dimensional version of this collective variable (type 1D-DI), namely the difference $d_{CM} - d$ between the two collective variables in variant DI, was already introduced in Section 2.4.5 to compare the different enhanced sampling methods. The option to choose a 1D-CV has the advantage that it seriously speeds up the sampling. [199]

The influence of the collective variable on the free energy profile was analyzed using US, as this technique was selected as the most appropriate method for the envisaged application in **Paper VI**. The collective variables of type CN and DI are two-dimensional, and the free-energy surface should be projected into a 1D-profile which can be done by integration of the 2D probability distribution also defined in **Paper VI**:

$$F_q(q) = -k_B T \ln \left(\frac{q_0}{q_{10} q_{20}} \int_{-\infty}^{+\infty} e^{-\beta F_{12}(q_1,q_2)} \delta \left(f(q_1,q_2) - q \right) dq_1 dq_2 \right) \quad (2.36)$$

More specifically, the 2D profile is projected on the difference between the two collective variables ($f(q_1, q_2) = q_2 - q_1$). This results into the 1D free-energy profiles displayed in Figure 2.9. The plots clearly show that the free energy profiles in terms of the various collective variables have not only different shapes but also different barriers if they are determined by the energy gap between the maximum and the minimum of the profile as done in earlier work. [310] For Type CN a barrier of $\pm$ 127 kJ/mol is observed, while in the type DI collective variables the barrier is systematically lower ($\pm$ 100 kJ/mol).

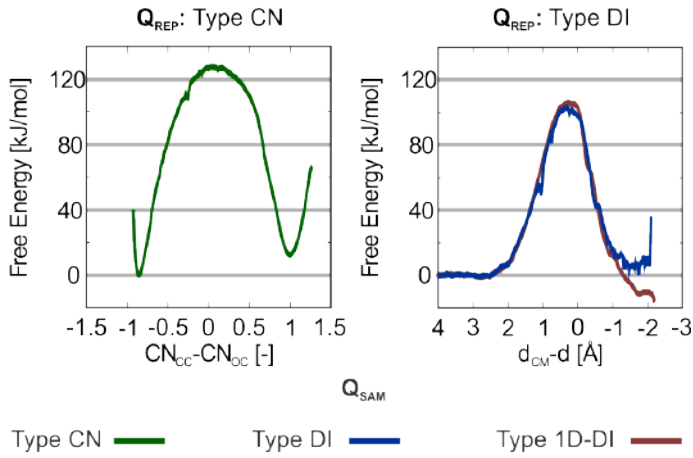

Figure 2.9: Free energy profiles at 350 °C obtained by sampling in the different collective variable spaces (Q_{SAM}), namely Type CN (green), Type DI (blue) and Type 1D-DI (red) and represented (Q_{REP}) in Type CN (left panel) and Type DI (right panel). The profiles for Type CN and Type DI are obtained by sampling in a 2D collective variable space followed by a projection of the free energy surface on a 1D-profile.

To enable direct comparison of the free energy profiles obtained by sampling in different collective variable spaces, the transformations defined in Section 2.5.2 need to be applied. From here on, we will distinguish between the collective variable in which the sampling is performed during the simulation, labeled Q_{SAM},

and the collective variable in which the free energy profile is expressed (Q_{REP}) In Figure 2.10, both the free energy profile in function of the original collective variable (Q_{SAM}), also shown in Figure 2.9, and the transformed profiles are shown. Interestingly, after applying the transformations the region from the reactant valley till the transition state region all coincide quite nicely. The most accurate plot should correspond with the profile expressed in the same CV space, wherein the sampling has been accomplished. The product region does not coincide. However, if the sampling is sufficient, the profiles should nearly coincide after applying the transformation. The discrepancy is inherently related to the rather unstable carbocations formed after the methylation, which transform into various intermediates, such as propene, cyclopropane, propoxide, propanol... As a result, the product region is not equally well sampled in the various simulations. There are some interesting features regarding the shape of the profiles which require some attention. The $F(CN_{CC}-CN_{OC})$ profile shows a thin well for the reactants, predicted by all the types of CVs, while in the $F(d_{CM}-d)$ profiles a broad range of configurations is observed. This can partly be ascribed to the way a coordination number is determined in function of the bond distance, as given in Eq. 2.35 and discussed in more detail in **Paper VI**.

Previous analysis learns that in principle different collective variables may be used. However, to directly compare free energy profiles, proper transformations should be used. If sampling is sufficient, similar profiles should be obtained. In the subsequent section, relevant thermodynamic quantities are introduced, which are afterwards calculated for the methylation of ethene in H-ZSM-5 to obtain collective variable invariant reaction kinetics.

2.6 Thermodynamic quantities and reaction rates

To evaluate the competition between several reactions occurring in the zeolite environment, one can either compare the free energy barrier in between the reactants and the products of interest or compare reaction rates. We will show with the case study reaction that calculating the reaction rate constant or the related phenomenological barrier is crucial to properly describe the studied reactions based on the dynamic free energy.

2.6.1 Thermodynamic quantities

To calculate the free energy F in the NVT ensemble starting from the electronic energy obtained via a static DFT calculation with dispersion correction (E_{DFT-D}), the molecular partition function Z obtained within the harmonic oscillator approximation is used. Introduction of Z links the electronic energy to the internal energy U of the system as follows:

$$U = E_{DFT-D} + k_B T^2 \left\langle \frac{\partial \ln Z}{\partial T} \right\rangle_V \tag{2.37}$$

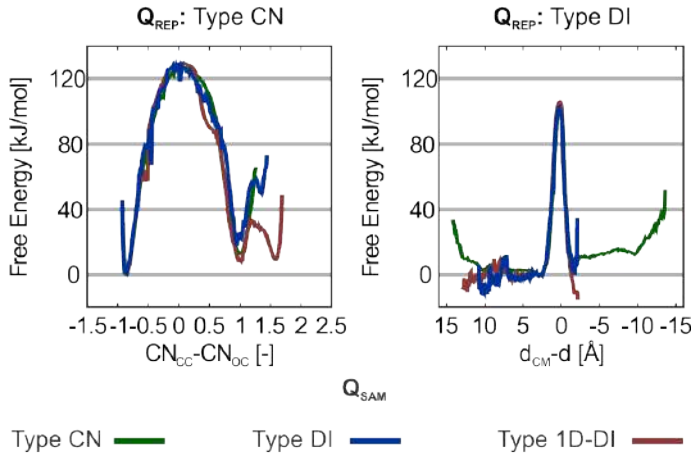

Figure 2.10: Free energy profiles at 350 °C in function of 1D-CVs (Q_{REP}) defined as the difference in coordination numbers ($CN_{CC} - CN_{OC}$, left panel) or in distance ($d_{CM} - d$, right). Left panel: plots belonging to CVs Type 1D-DI and Type DI are obtained after transformation as explained in the text. Right panel: plots belonging to Type CN are obtained after transformation as explained in the text.

with k_B the Boltzmann constant, T the temperature and V the volume. Similarly, the entropy of the system can be obtained from the partition function via:

$$S = R \ln Z + RT \left\langle \frac{\partial \ln Z}{\partial T} \right\rangle_{V,N} \tag{2.38}$$

with R the gas constant. This formula is only useful when an analytic expression for the partition function is available. This is not possible based on the dynamic simulations performed in this thesis. Therefore, this formula is only used within the static simulations. Subsequently, the Helmholtz free energy F can be calculated as:

$$F = -k_B T \ln(Z) = U - TS \tag{2.39}$$

Furthermore, free energy information can be obtained from advanced molecular dynamics simulations, for which the estimators for the free energy are described in Section 2.4.

When adsorption and desorption of reactants and products is taken into account, the pressure in the gas phase needs to be accounted for. In these cases, the internal energy can be related to the enthalpy H of the system by taking the pV work into account:

$$H = U + pV \tag{2.40}$$

where p is the pressure. Lastly, the Gibbs free energy G can be obtained from the enthalpy and entropy as:

$$G = H - TS \tag{2.41}$$

2.6.2 Transition state theory and phenomenological barrier

A second possibility is comparing reaction rates obtained from molecular simulations. To this end, transition state theory (TST), allows to derive an expression for the rate of a reaction $R \rightarrow P$ by defining the transition state as a dividing surface between the reactants (R) and the products (P). [185, 311–314] Furthermore, two key assumptions are postulated:

1. Thermodynamic equilibrium exists for all degrees of freedom throughout the system.

2. If a trajectory crosses the dividing surface, it will not recross it.

The reaction rate k can then be written as: [268, 315]

$$k = \frac{\langle \dot{q}\theta(\dot{q})\delta(q - q^*)\rangle}{\langle \theta(q^* - q)\rangle} \tag{2.42}$$

where q is a function of the molecular configuration (a collective variable as discussed in more detail in Section 2.5) and q^* represents its value at the transition state. Furthermore, $\dot{q}$ is the generalized velocity associated with the coordinate q, and θ and δ represent the Heaviside and Dirac delta distribution, respectively. By subsequently applying a canonical transformation towards mass-weighted coordinates $\vec{x}_i = \sqrt{m_i}\vec{r}_i$ and momenta $\vec{P}_i = m_i^{-1/2}\vec{p}_i$, and perform the integrals over the momenta explicitly, the expression can be rewritten as: [315]

$$k = \sqrt{\frac{1}{2\pi\beta}} \frac{\int \delta(q(\overrightarrow{x}^N) - q^*) \left|\overrightarrow{\nabla}_x q\right| \exp(-\beta U(\overrightarrow{x}^N)) d\overrightarrow{x}^N}{\int_R \exp(-\beta U(\overrightarrow{x}^N)) d\overrightarrow{x}^N} \tag{2.43}$$

Here, the integral in the denominator runs over all reactant states. If the considered system only has one degree of freedom, this formula can be simplified to the well known expression frequently used in static calculations:

$$k = \frac{k_B T}{h} \frac{1}{Z_R} \exp(-\beta \Delta E^{\ddagger}) \tag{2.44}$$

with the partition function of the reactant Z_R and the energy difference between the reactants and transition state $\Delta E^{\ddagger}$. When using enhanced sampling methods, discussed in Section 2.4, the general expression of the reaction rate can be written in function of the free energy profile $F(q)$ as:

$$k = A\frac{\exp(-\beta F(q^*))}{\overline{Z}_R} \tag{2.45}$$

$$A = \frac{1}{\sqrt{2\pi\beta}}\left\langle|\overrightarrow{\nabla}_x q|\right\rangle_{q^*} \tag{2.46}$$

$$\overline{Z}_R = \int_{-\infty}^{q^*}\exp(-\beta F(q))dq \tag{2.47}$$

Herein, A represents a pre-factor which can be obtained from molecular simulations and depends on the gradient of the collective variable, which is related to the rate of change of the collective variable, evaluated at the transition state. It is also a measure for the width of the transition state. The factor $\exp(-\beta F(q^*))$ expresses the maximum at the transition state relative to the minimum in the reactant region. Together with A it represents the stability of the transition state. Lastly, the factor $\overline{Z}_R$ is proportional to the partition function of the reactant region and thus yields information on the stability of the reactant state.

As A is related to the gradient of the collective variable at the transition state value, this suggests that a simulation needs to be performed which is constrained exactly at the transition state q^*. However, this can be estimated using a constant bias potential $U_b(q)$ (for example during Umbrella Sampling discussed in Section 2.4.3):

$$\left\langle|\overrightarrow{\nabla}_x q|\right\rangle_{q^*} = \frac{\left\langle\delta(q-q^*)|\overrightarrow{\nabla}_x q|\right\rangle_{U_b}}{\langle\delta(q-q^*)\rangle_{U_b}} \tag{2.48}$$

This methodology was performed in **Paper VI**. Unfortunately, it is less straightforward to use this formula for other methods, like metadynamics, where the bias potential varies with time. In that case, the prefactor A can be computed in a manner inspired by the procedure proposed by Bučko *et al.* [193] This methodology was applied in **Paper IV**.

By now comparing the formula for the reaction rate (Eq. 2.45) with the Eyring-Polanyi equation [316], a phenomenological free energy barrier ΔF can be introduced, as was done earlier by Bučko et al.: [193]

$$\Delta F = F(q^*) + k_B T\ln\left(\frac{k_B T\overline{Z}_R}{hA}\right) \tag{2.49}$$

This phenomenological barrier is used throughout **Paper IV** and **Paper VI**.

2.6.3 Reaction kinetics for the methylation of ethene

The analysis in Section 2.5.3 suggested that the configurational freedom in the reactant and transition state should be accounted for in order to obtain proper reaction kinetics. This can be done by defining transition rates instead of free energy barriers to get a collective variable independent measure to compare the

Table 2.1: Intrinsic reaction rate k (in 1/s) at 350 °C.

Q_{SAM} \ Q_{REP}	$CN_{CC} - CN_{OC}$	$d_{CM} - d$
Type CN	1.58 10^3	2.83 10^3
Type DI	1.14 10^3	8.82 10^2
Type 1D-DI	9.74 10^2	5.95 10^2

speed of different reactions. We computed the rate constants according to Eq. 2.45 for the methylation reaction and investigated the influence of the choice of the collective variable. Enhanced sampling simulations were performed using various collective variable(s).

Table 2.1 tabulates the predictions of the intrinsic rate constants obtained after different simulations using various CVs (Q_SAM). One-dimensional free energy profiles are in this specific case expressed in ($CN_{CC} - CN_{OC}$) or ($d_{CM} - d$) as Q_{REP}. It is obvious that the non-diagonal rates in the table are obtained using transformations from Q_{SAM} to Q_{REP}. Inspection of all values reported in Table 2.1 learns that all reaction rate constants are differing only less then one order of magnitude, even though the free energy barrier by subtracting the minimum from the maximum itself was dependent on the choice of the collective variable as illustrated in Figure 2.10. Since the rate constant represents a macroscopically measurable quantity, it should indeed be independent of the way we describe it microscopically. Therefore, one cannot simply rely on the free energy barrier to make statements on how fast a reaction will occur. Instead, one needs to compute all contributions to the reaction rate consistently. By calculating the rate expression, we are also accounting for the width and the depth of various parts of the $F(q)$ profile. Finally, if we consider the reaction rates for a single column in Table 2.1, we can investigate the impact of the CV used to perform the enhanced sampling. As can be seen from the table, this influence is also rather limited, indicating that each CV is capable of describing the reaction correctly.

Based on these intrinsic reaction rate constants, a phenomenological barrier [193] can be calculated using Eq. 2.49. The resulting values are tabulated in Table 2.2. They show that similar barriers are obtained before and after the transformation and barriers within chemical accuracy are obtained independent of the collective variable used during sampling (Q_{SAM}). The phenomenological free energy barrier is thus a more correct representation of a free energy difference rather than simply subtracting the free energies of the minimum off the maximum along the profile which yields values largely dependent on the collective variable.

At this moment, it is interesting to compare the here obtained rate constants and free energies with earlier literature data. The particular reaction has been the topic of various comparative studies [213–215] with experimental kinetic data.

Table 2.2: Phenomenological free energy difference obtained via Eq. 2.49 (in kJ/mol) at 350 °C.

Q_{SAM} \ Q_{REP}	$CN_{CC} - CN_{OC}$	$d_{CM} - d$
Type CN	118.3	115.2
Type DI	120.0	121.3
Type 1D-DI	120.8	123.3

[84, 85] Experimentally, one obtains apparent rates, which are in this case referred to the state where methanol is adsorbed on the Brønsted acid site and ethene in the gas phase. Indeed, the reaction was determined to be zeroth order with respect to methanol and first order with respect to ethene [84, 85] and could be described by the following rate equation:

$$r = k_{app} p^0_{methanol} p^1_{ethene} \tag{2.50}$$

with $p_{methanol}$ and p_{ethene} the partial pressures of methanol and ethene, respectively. The reaction rate constants obtained in **Paper VI** with the MD approach correspond to intrinsic kinetics where all reactants, thus methanol and ethene, are adsorbed on the zeolite. These values cannot directly be compared with experiment. However, in ref. [214] also intrinsic rates were reported using at that time a rigid rotor harmonic oscillator model and a finite cluster model consisting of 46 T atoms. At the ONIOM(B3LYP/6-31+g(d):HF/6-31+g(d))-D//ONIOM(B3LYP/6-31+g(d):MNDO) level of theory a value of 5.5 10^3 s^{-1} at 350 °C for k_{int} was obtained, which is in very good agreement with the values tabulated in Table 2.1.

It is however interesting to also compare with the values of Svelle et al. [213] and Piccini et al. [215] Svelle et al. who used a composite scheme to obtain apparent enthalpy barriers with near chemical accuracy, whereas Piccini et al. used anharmonic corrections to get better estimates of the pre-exponential factor. In previous methods, no molecular dynamics simulations were done to sample the configurational space. A direct comparison with the values of Svelle and Piccini is hampered as they did not report intrinsic free energy barriers or intrinsic reaction rates. This makes a direct comparison very difficult, as there are no generally accepted methodologies to extract enthalpic barriers and adsorption enthalpies from ab initio molecular dynamics simulations. To allow a comparison with experimental data and earlier theoretical data, we calculated the co-adsorption free energy for ethene $\Delta G_{ads,ethene}$ from static periodic DFT calculations and determined the apparent rate constant k_{app} based on the equilibrium constant K_1 for the co-adsorption as: [317]

$$k_{app} = K_1 k_{int} \tag{2.51}$$

The equilibrium constant for the co-adsorption of ethene, *i.e.* for the equilibrium between the state [Z-H, CH_3OH(ads), ethene(gas)] and [Z-H, CH_3OH(ads), ethene(ads)] in Figure 2.11, can be calculated based on the co-adsorption free energy as:

$$K_1 = V_0 \exp\left(-\frac{\Delta G_{ads,ethene}}{RT}\right) \tag{2.52}$$

with V_0 the molar volume of an ideal gas which equals 0.0518 m^3/mol at 350 °C and 1 atm and R the gas constant. These formula were derived and discussed in detail in **Paper VI**.

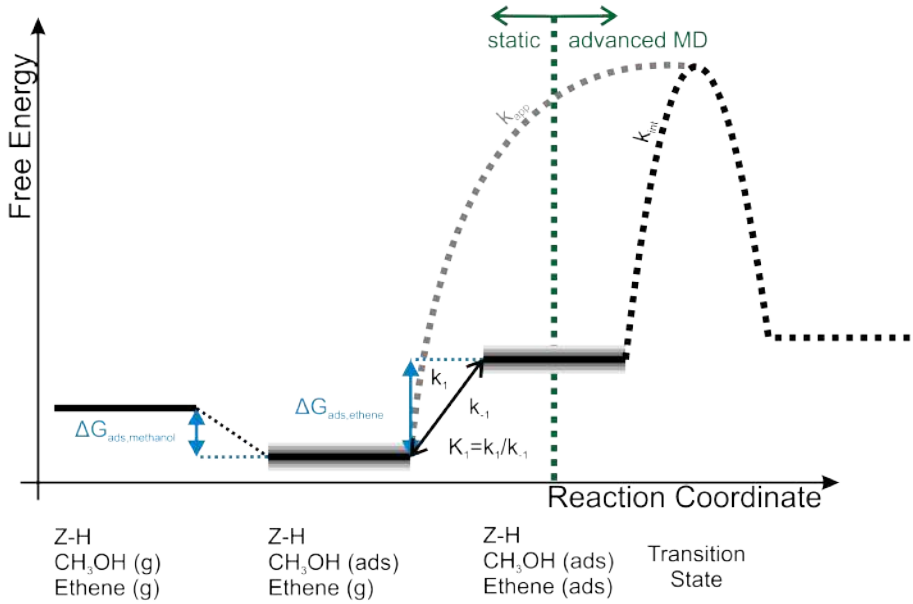

Figure 2.11: Schematic representation of the relation between apparent and intrinsic kinetics. For the calculation of $\Delta G_{ads,ethene}$ various schemes were used, shown by the grey uncertainty in the co-adsorption step of ethene. The value of k_{int} was obtained dynamically in **Paper VI**.

The computation of a co-adsorption energy is always very sensitive to the used level of theory and in particular to the selected dispersion scheme. Large variations are common in this field, and to get a reliable estimate about the spreading of the adsorption energies we performed single point energy calculations with a large set of functionals and dispersion schemes frequently used in literature [318, 319] starting from optimized structures obtained via revPBE-D3. [235,320] As expected, these values show a wide variation of up to 25 kJ/mol. An in-detail discussion can

Table 2.3: Summary of the results for the calculations of k_{app} in **Paper VI**. Only the smallest and the highest values of k_{int} in Table 2.1 are considered. A selection of four co-adsorption energies of ethene is retained from those obtained with various levels of theory (Supporting information of **Paper VI**): the lower limit is predicted by revPBE-dDsC, [253, 254] while the upper limit is delivered by vdW-DF. [238, 255]

	Lower limit	B3LYP-D3	revPBE-D3	Upper limit	Lower limit	B3LYP-D3	revPBE-D3	Upper limit	exp
k_{int} [s^{-1}]	5.95 10^2				2.83 10^3				
$\Delta E_{ads,ethene}$ [kJ/mol]	-11.0	-20.3	-22.7	-36.8	-11.0	-20.3	-22.7	-36.8	-24 – -31 [213, 321]
$\Delta G_{ads,ethene}$ [kJ/mol]	41.7	32.5	30.1	16.0	41.7	32.5	30.1	16.0	
K_1 [m^3/mol]	1.64 10^{-5}	9.75 10^{-5}	1.57 10^{-4}	2.35 10^{-3}	1.64 10^{-5}	9.75 10^{-5}	1.57 10^{-4}	2.35 10^{-3}	
k_{app} [m^3/(mol.s)]	9.76 10^{-3}	5.8 10^{-2}	9.31 10^{-2}	1.40	4.64 10^{-2}	2.76 10^{-1}	4.43 10^{-1}	6.64	
k_{app} [1/(mbar.s)]	1.88 10^{-4}	1.12 10^{-3}	1.80 10^{-3}	2.69 10^{-2}	8.96 10^{-4}	5.33 10^{-3}	8.55 10^{-3}	1.28 10^{-1}	1.95 10^{-4} [84]

be found in **Paper VI**, but the limiting values are summarized in Table 2.3, as well as those corresponding to revPBE-D3 and B3LYP-D3. [257]

These results show that though the variation on the co-adsorption electronic energy is quite wide, namely in the range of -11 to -37 kJ/mol, they do correspond quite well with experimental co-adsorption enthalpies ranging from -24 to -31 kJ/mol. [213, 321] Furthermore, we can see that the experimental value of 1.95 10^{-4} (mbar.s)$^{-1}$ [84] is within the theoretically proposed range of values (see Table 2.3). Looking more closely to the revPBE-D3 results, which are used in both the static as the dynamic simulations, values ranging from 1.8 10^{-3} to 8.55 10^{-3} (mbar.s)$^{-1}$ are attained, on the verge of kinetic accuracy.

The results of **Paper VI** thus show that by combining static and enhanced sampling methodologies one can almost attain kinetic accuracy, although the selection of DFT functional and dispersion scheme remains a crucial factor. As such, further testing and benchmarking of both static and enhanced sampling methodologies for zeolite catalysis remain essential for the development of a generally applicable quantum mechanical methodology.

3

New insights into the MTO reaction cycles

In the previous methodological chapter (Chapter 2) the focus was set on several enhanced sampling techniques as tools to elucidate the influence of the characteristics of the catalyst at real operating conditions from a theoretical point. Their usefulness to understand the reaction mechanism of heterogeneous catalytic reactions has been highlighted in a recent review of Pidko and Nachtigall. [187] In this dissertation we focus on some fundamental reactions governing the MTO process and investigate how modifications of the catalyst may affect the outcome of the reaction.

We first present major results originating from an extended combined theoretical and experimental research effort. We examined how the selectivity and the lifetime of the H-ZSM-5 catalyst are influenced by modifying the nature of the active site which, among others, can be accomplished by incorporating alkaline earth metals in the material. The acid function can thus be altered by introducing Lewis acid sites thus diminishing the number of Brønsted acid sites. Subsequently, the assisting role of water in the methylation reaction of hexamethylbenzene in H-SAPO-34 is elucidated at operando-like conditions. Finally, the effect of the topology of the catalyst on the typical MTO reaction cycles is studied. They form three applications wherein the usefulness of the various diverse methodologies outlined in Chapter 2 has been demonstrated.

3.1 Nature of active site: Brønsted versus Lewis acidity

As Evgeny A. Pidko emphasized on the importance of model accuracy in heterogeneous catalysis [188], it seems interesting to first have a look at the influence of the catalyst on the reactions occurring within the zeolite pores. To this end, the effect of the nature of the acid site is first discussed.

In a pure H-ZSM-5 zeolite the catalytic behavior of the material is entirely monitored by the presence of Brønsted acid sites, whose density can be tuned by adjusting the Si/Al ratio in the zeolite synthesis stage. The production of olefins proceeds through an autocatalytic reaction. Hydrocarbon species, adsorbed in the micropores of the zeolitic catalyst, typically alkenes and arenes, act as "co-catalyst pool species". Both species participate in two competitive pathways, mechanistically described by the dual-cycle concept, as shown by the seminal work of Svelle *et al.* [86] Reaction products may either be formed through an alkene or aromatic-based cycle. Ethene is mainly formed via the aromatic cycle but the aromatic intermediates are known coke precursors [38, 92–97] which deactivate the catalyst, whereas propene and higher olefins are formed via the alkene cycle. Therefore, the MTO conversion is especially interesting as a propene-on-demand process, which can provide a solution for the increasing disparity between the propene production and demand. [139–142] Propene selectivity and resistance to coking and thus catalyst deactivation become the two most important parameters in developing new MTO catalysts. Several strategies have been proposed which may affect the outcome of the MTO process such as feed composition [88], the composition and topology of the catalyst [109, 122–124] and eventually the operating conditions. [168, 169] In this section, focus will mainly lie on the nature of the active site and its influence on the performance of the catalyst in the MTO process, and this in a combined experimental and theoretical effort. It has led to one of the major results of this PhD thesis.

It was demonstrated in literature that Ca-modified ZSM-5 zeolites have a serious influence on the catalytic stability and light olefin selectivity. [153, 154] This behavior has already been reported in 1997 [322] but had not received proper attention, until the latest years wherein the interest on this issue has been renewed explosively. [139–142] Post-synthetic modifications have not only been restricted to Ca, but also phosphorus-modified ZSM-5 zeolites [145, 323, 324] or dealuminated zeolites [121, 131–133] have been investigated intensively. These modifications reduce the Brønsted acid site density and create Lewis acid sites stimulating a cooperative role of both acid sites in zeolites.

In our work we investigate the effect of incorporation of alkaline earth metals (Mg, Ca, Sr and Ba) in the zeolite pores and the effect of extra-framework aluminum (EFAl) species on the MTO process. The results of this combined experimental-theoretical research project are taken up in three high-impact papers (**Paper II**, **Paper III** and **Paper V**).

Depending on the nature of the metal incorporation, the extra-framework species might be present in the zeolite pores as metal cations or charged metal oxide clusters. [157,158] In the first two papers, **Paper II** [120] and **Paper III** [121], these extra-framework species were systematically assumed to be composed of binuclear species bridged by O and OH ligands. In this sense both $[Ca(\mu\text{-}O)(\mu\text{-}OH)Ca]^{+}$ and $[Ca(\mu\text{-}OH)_2Ca]^{2+}$ moieties were proposed as possible modified active sites in Ca-ZSM-5. This suggestion was based on findings in literature that next to alkaline-earth metals, many other metals such as Fe, Ga, Zn, Cu and Al have the tendency to self-organize into multinuclear clusters within the confined space of a zeolite. [133, 158, 325–329] To test the validity of these binuclear species, a structural analysis was performed in **Paper V** starting by calculating the relative stability of mono-, di- and trimeric species, depicted in Figure 1.8. To this end, the structures in Figure 3.1. were introduced respecting full mass balance in order to enable a straightforward energetic comparison.

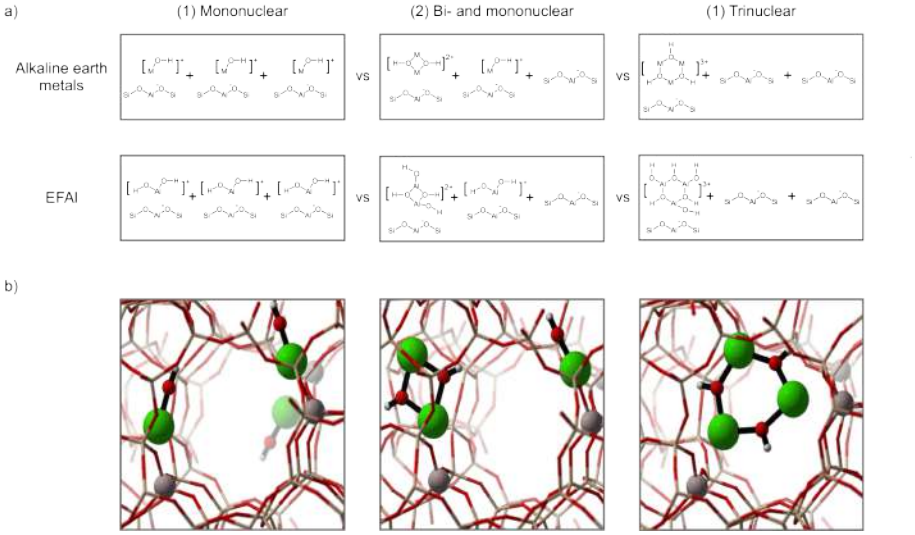

Figure 3.1: Schematic representation of the structures considered for the relative stability of mono- (left), bi- (center) and trinuclear (right) structures (a) and snapshots of the three considered structures for the Ca case (b). For the snapshots, the following color code is used: white is H, red is O, grey is Al, beige is Si and green is Ca. Adapted from ref. [91] with permissions of American Chemical Society.

The free energies and enthalpies resulting from periodic DFT calculations are summarized in Table 3.1 and indicate that the formation of mononuclear alkaline earth metal species is energetically disfavored with respect to binuclear complexes, except for one of the EFAl species which is discussed further. The self-organization of isolated mononuclear cations into binuclear $[M(\mu\text{-}OH)_2M]^{2+}$ is a highly exothermic process. Multinuclear structures are even more stabilized as far as they can

Table 3.1: Free energies (ΔG) and enthalpies (ΔH) relative to the mononuclear case for all structures indicated in Figure 3.1 (in kJ/mol) and calculated at 500 °C.

	(1) Mononuclear		(2) Bi- and mononuclear		(3) Trinuclear	
	ΔH	ΔG	ΔH	ΔG	ΔH	ΔG
EFAl/I	0	0	55	114	5	101
EFAl/II	0	0	-94	-79	20	66
Mg	0	0	-102	-48	-186	-104
Ca	0	0	-153	-120	-237	-194
Sr	0	0	-111	-71	-198	-158
Ba	0	0	-94	-73	-156	-112

be fitted into the pores of the ZSM-5 zeolite. This result follows the general trend that larger clusters better stabilize the system as they are submitted to a higher number of coordination interactions with the zeolite framework. However, due to confinement the size of the cluster is obviously limited and we therefore discarded the possibility that larger clusters than trinuclear alkaline earth metal complexes will be formed in the ZSM-5 channels, which may play an essential role in the methanol conversion.

However, our study shows that the positions of the aluminum substitutions in the framework may have a large effect on the stability of the binuclear EFAl species. They show a deviating behavior with respect to the alkaline earth metal complexes. We refer the interested reader to **Paper V** and the Supporting Information for a detailed description of the EFAl results.

To further structurally characterize the nature of the metal containing clusters, a solid state NMR characterization was performed on Ca-modified ZSM-5 zeolites both from an experimental and theoretical point of view. ^{43}Ca solid state NMR is intrinsically challenging because ^{43}Ca is a quadrupolar nucleus (spin $= 7/2$) with relatively low gyromagnetic ratios as well as with a very low natural abundance (only 0.135 %). The solid-state Hahn Echo NMR spectrum (blue line in Figure 3.2) of ^{43}Ca–enriched ZSM5 displays a relatively broader response (than usual Ca-salts). The peak with the highest intensity centered around 0.6 ppm inevitably advocates for the heterogeneity within the sample. Next, to derive more structural information about the residual Ca-species and enhance the sensitivity, quadrupolar Carr–Purcell–Meiboom–Gill (QCPMG) measurement has been performed (red line in Figure 3.2). Interestingly, the observed non-symmetric nature of the QCPMG spectrum reveals the existence of more than one non-identical Ca-species. To assign the observed peaks, the mono-, bi-, and trinuclear extra-framework Ca species were considered from theoretical point of view. Note that in this case only one isolated mono-, bi- or trinuclear species was considered per unit cell, which is charge

compensated by one, two or three aluminum atoms, as depicted in Figure 1.8. The resulting static NMR chemical shifts of the ^{43}Ca isotope are depicted in green in Figure 3.2. The good agreement between the experimental peaks (gray) and the theoretical peaks (green) give indirect evidence that both mono- and binuclear species may be present in the alkaline-earth metal modified ZSM-5 catalysts, while the trinuclear species are less probable. A more detailed explanation and a dynamic view on these NMR spectra can be found in **Paper V**.

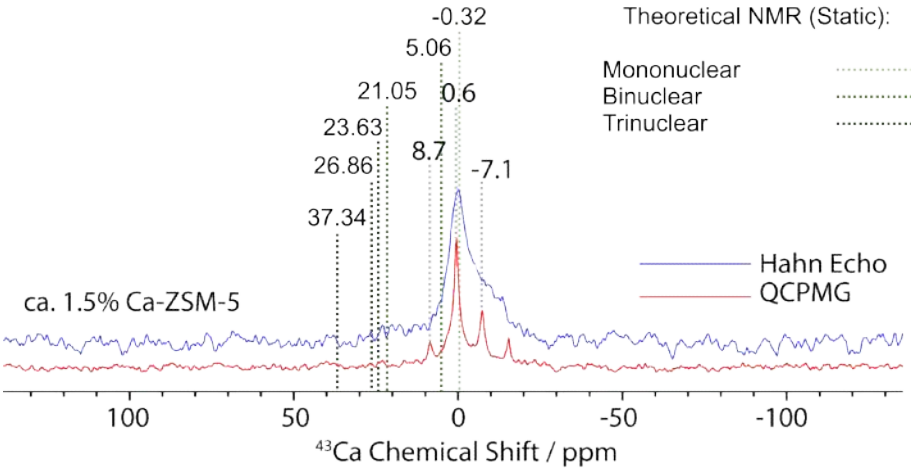

Figure 3.2: Experimental ^{43}Ca magic angle spinning (MAS) solid-state hahnecho (blue) and QCPMG (red) NMR spectra of ca. 1.5% Ca-ZSM-5 [900 MHz, 10KHz MAS, recycle delays=1 sec, Number of scans=14k]. On the graph, the theoretical, static NMR peaks are indicated in green, namely mononuclear (light green), binuclear (green) and trinuclear (dark green). Adapted from ref. [91] with permissions of American Chemical Society.

These structures were subsequently used to characterize the nature of the metal oxide formed in the catalyst pores. As both the alkaline earth metal and EFAl species were suggested to have a Lewis acid nature [120, 121, 330–332], their acidic properties were characterized using IR spectroscopy with pyridine as a probe molecule. Pyridine adsorption is able to discriminate between Brønsted and Lewis acid sites as distinct peaks in the 1400–1700 cm^{-1} range appear in the spectra. Pyridine is protonated upon adsorption on a BAS forming a pyridinium ion and only coordinatively bonds towards a LAS. [178, 333] This difference leads to a characteristic peak in the IR spectrum around 1545 cm^{-1} and 1450 cm^{-1} for a BAS and LAS, respectively. [120, 141, 333–338] Furthermore, the vibrational mode in the region of 1580-1630 cm^{-1} is indicative for the global acidic strength as was shown by Velthoen *et al.* [178]

The static optimization of adsorbed pyridine in the considered unit cells indeed confirmed the distinct adsorption on a BAS and LAS. As depicted in Figure 3.3, pyridine is immediately protonated on a BAS, whereas on the metal complexes –

both mono- and binuclear – pyridine makes a coordination with the alkaline earth metal, confirming the presence of Lewis acid sites.

Based on these optimized structures, theoretical IR spectra could be obtained using density-functional perturbation theory (DFPT) or linear response theory (LRT) calculations to calculate the vibrational intensities from the Born effective charges (BEC). [339–343] The resulting spectra are depicted in Figure 3.4.

Our theoretical and experimental spectra confirm that Lewis acid sites are introduced in the modified catalyst, which goes hand in hand with the elimination of Brønsted acid sites. The correspondence between theoretical and experimental spectra gives strong evidence that the $[M(\mu\text{-}OH)_2M]^{2+}$ representation of the active site on a molecular level is realistic, although the monomeric $[M(\mu\text{-}OH)]^{+}$ alkaline-earth metal complexes yield a similar behavior. Depending on the nature of the metal incorporated cationic cluster, subtle shifts are found in the peak at 1450 cm^{-1} assigned to Lewis acidity. Furthermore blue-shifted vibrational modes in the region (1580–1630 cm^{-1}) are also characteristic for the global acidic strength of the complex as shown in the work of Velthoen *et al.* [178] Therefore, these blue-shifted vibrational modes of the monomeric and dimeric alkaline earth metal oxide clusters are plotted in Figure 3.5 in function of the adsorption enthalpy of pyridine, which is used as a measure for the Lewis acidity of the metal oxide cluster. As can be expected, the results for the alkaline earth metals in Figure 3.3 showed that a more negative adsorption enthalpy leads to a shortened nitrogen-metal distance and thus a stronger Lewis acidity (Mg>Ca>Sr>Ba). More interestingly, for the alkaline earth metals, the adsorption enthalpies can be correlated to the information on the IR peak that is characteristic for the LAS (around 1450 cm^{-1}, Figure 3.5a and c) and peak characteristic for the global acidic strength (1580–1630 cm^{-1}, Figure 3.5b and d), as a stronger adsorption enthalpy yields an increased wavenumber and thus blue shifted peaks. This correlation is close to linear for both peaks and both experimentally and theoretically, as can be seen on the plots depicted in Figure 3.5. This correlation might serve as a very insightful catalyst design guideline, as it directly yields information on the strength of incorporated LASs in zeolites.

Subsequently, the effect of the Lewis acid strength on the reactivity within the zeolite pores was studied. This is achieved by studying the methylation of propene, benzene, pseudocumene and durene over three different active sites at 500 °C. The considered sites are depicted in Figure 3.6a and show an isolated BAS, a BAS near a $[M(\mu\text{-}OH)_2M]^{2+}$ moiety and an isolated $[M(\mu\text{-}OH)_2M]^{2+}$ moiety. Monomeric LASs were also considered in the case of Ca in **Paper V** [91], but they showed to be less reactive compared to the binuclear sites and are therefore omitted from this overview. An in depth discussion of the entire free energy profiles can be found in **Paper V** [91], while here the discussion is limited to the change in the overall free energy barrier relative to the methylation rate over an isolated BAS. The resulting values are depicted in function of their Lewis acid strength (more specifically the adsorption enthalpy of pyridine) in Figure 3.6b.

Following trends can be deduced from the correlation plots. The methylation of all hydrocarbons is found to be more activated over an isolated alkaline earth metal

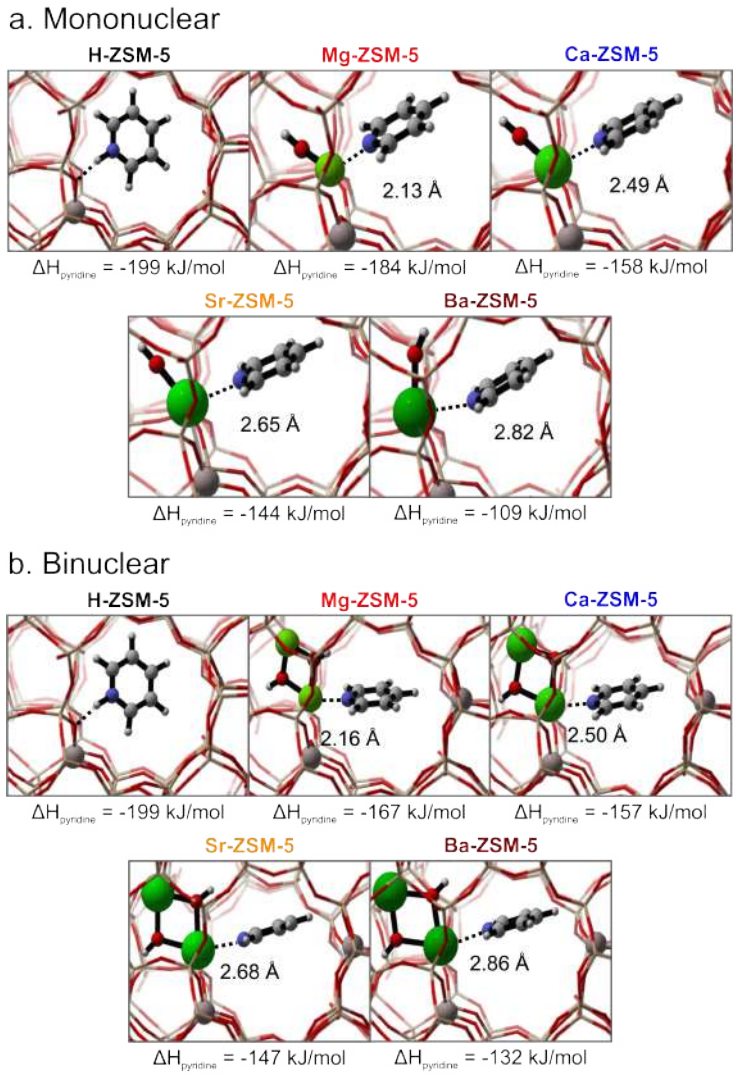

Figure 3.3: Pyridine adsorption to a mononuclear LAS (a) and a binuclear LAS (b). Also given are the adsorption enthalpies in kJ/mol belonging to the optimized structures at 0 K of pyridine adsorbed in pristine H-ZSM-5 and Mg, Ca, Sr or Ba-ZSM-5. To keep the charge in balance frameworks with only one Al substitution are considered in case of monomers, and with two Al substitutions in case of the binuclear species. In the pristine H-ZSM-5 only one single BAS and thus one Al substitution is taken into account. For the snapshots, the following color code is used: white is H, light grey is C, blue is N, red is O, grey is Al, beige is Si and green is the alkaline earth metal. Adapted from ref. [91] with permissions of American Chemical Society.

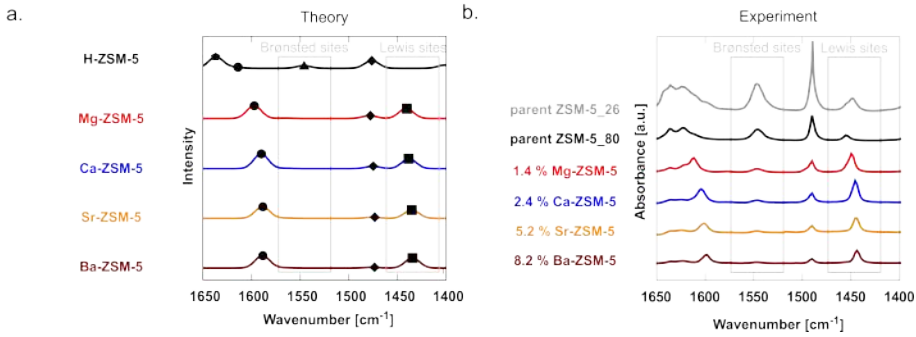

Figure 3.4: FTIR spectra of various zeolitic materials using pyridine as a probe molecule. (a) Theoretical spectrum of pyridine adsorbed on modified ZSM-5 materials with binuclear species, (b) experimental spectrum. Adapted from ref. [91] with permissions of American Chemical Society.

$[M(\mu\text{-}OH)_2M]^{2+}$ moiety, leading to relatively high reaction barriers over isolated cationic alkaline earth metal clusters. An almost linear relation is found between the acidity strength of the LAS and the overall free energy barrier. Most interesting for catalytic purposes is the distinct difference the LAS has on the methylation of benzene compared to propene. LASs clearly slow down methylation reactions of benzene, which is manifestly confirmed by the methylation of the two other HP species: durene and pseudocumene over alkaline earth metals. Translated to the various catalytic cycles operative in the methanol to olefin process, this means that the aromatic cycle would be suppressed in the LAS incorporated zeolites.

Secondly, it is interesting to study the effect on methylation free energy barriers taking place on a BAS but with proximity of a LAS. The effects on the methylation reactions are much less pronounced for a BAS nearby a LAS. Methylation barriers over a BAS near an $[M(\mu\text{-}OH)_2M]^{2+}$ moiety (□) converge to the rate over an isolated BAS with decreased Lewis acid strength of the alkaline earth metaloxide, as the difference in free energy barrier with an isolated BAS becomes smaller than 10–20 kJ/mol, which is the typical accuracy of our DFT simulations. [22, 215] Therefore, these differences are assumed to be insignificant. Only for Mg and Ca a significant increase in the free energy methylation barriers is observed. Furthermore, the increase is more pronounced for methylation of benzene, pseudocumene and durene compared to propene. While benzene and propene methylation rates only exhibit minor differences on an isolated BAS in H-ZSM-5 (overall free energy barriers of 187 kJ/mol and 197 kJ/mol), the results depicted in Figure 3.6b all suggest that LASs induce an increase in the difference between benzene and propene methylation kinetics over the neighboring BAS, again supporting the idea of a suppressed aromatic cycle reactivity due to LAS incorporation.

As some studies suggest that the protonated form of the HP intermediates are the active species, the influence of the metal oxide clusters on the stability of carbocations in the zeolite pores was investigated subsequently. This stability is

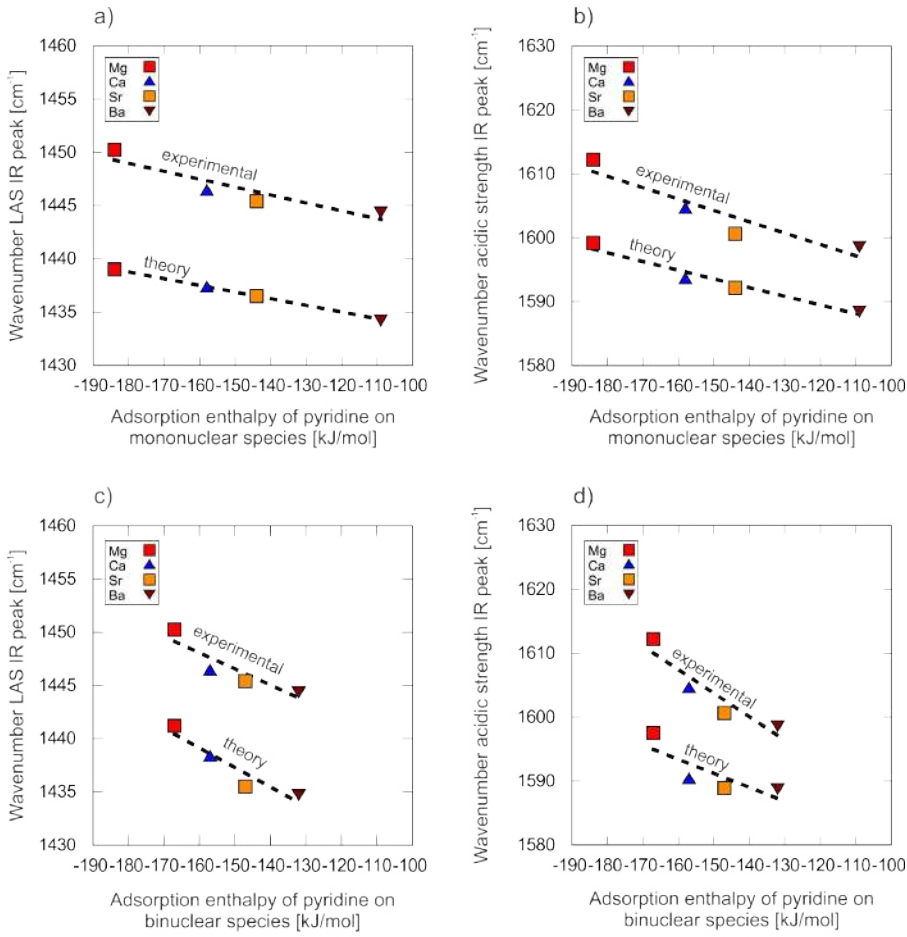

Figure 3.5: Shifts in the LAS (a and c) and global acidity (b and d) peaks in the IR spectrum with respect to changes in the strength of the incorporated mono- (a and b) or binuclear (c and d) LASs. Adapted from ref. [91] with permissions of American Chemical Society.

studied by calculating their protonation enthalpy as:

$$H_{prot} = H(X^{+}_{ads}) - H(X_{ads}) \tag{3.1}$$

where X_{ads} is the neutral form of the HP species adsorbed in the catalyst pore and X^{+}_{ads} is the protonated form of the HP species adsorbed in the catalyst pore. This protonation enthalpy at 500 °C is used as a measure for the stability of the protonated form of the intermediates relative to the neutral species. The more negative this enthalpic value becomes, the more stable the protonated structure becomes. Figure 3.7 shows that the aromatic cycle is characterized by cationic

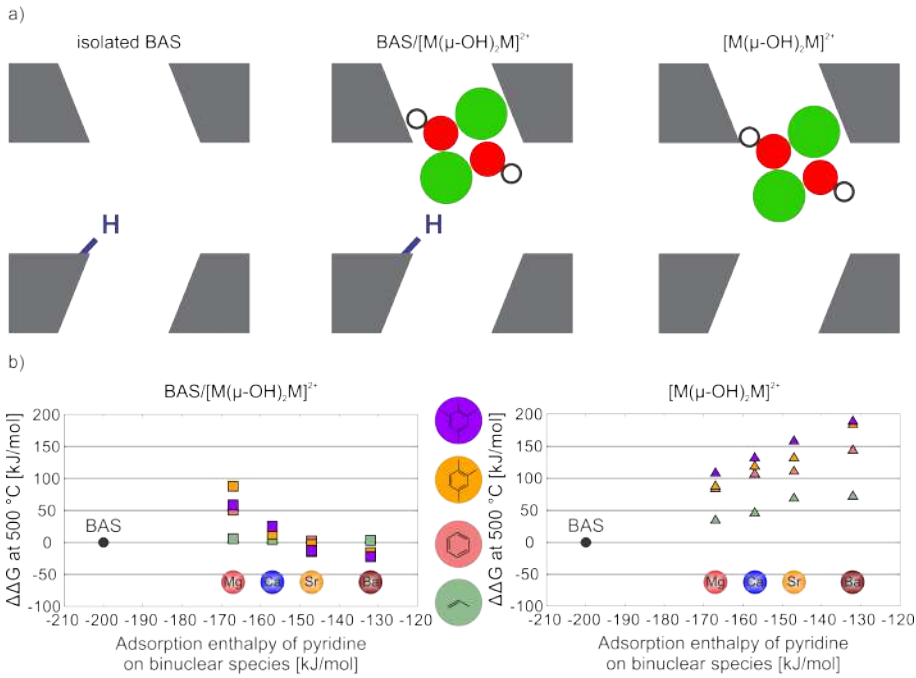

Figure 3.6: Summary of the reactivity analysis over alkaline earth metal modified ZSM-5 showing (a) a schematic representation of the three active sites considered for the methylation reactions, namely an isolated BAS, a BAS near a [M(μ-OH)$_2$M]$^{2+}$ moiety and an isolated [M(μ-OH)$_2$M]$^{2+}$ moiety. (b) The change in the overall free energy barrier at 500 °C of the methylation of benzene (red) , propene (green), pseudocumene (orange) and durene (purple) over an BAS near a [M(μ-OH)$_2$M]$^2+$ moiety (left and □) and an isolated [M(μ-OH)$_2$M]$^{2+}$ moiety (right and △) relative to the methylation rate over an isolated BAS (black circle) is plotted in function of the pyridine adsorption enthalpy. For the dealuminated species both EFAl/I and EFAl/II variants are considered. Adapted from ref. [91] with permissions of American Chemical Society.

six and five ring species, while the alkenes make up the co-catalysts in the alkene cycle. The set of considered HP species for this part of the project is inspired by the work of Fang and co-workers in which the most stable carbenium ions in H-ZSM-5 are theoretically predicted. [344] The set is further extended with aromatic intermediates of both the paring and side-chain mechanism [345] and propene, hexene and isobutene to represent the alkene cycle. The resulting protonation enthalpy, depicted in Figure 3.7, is calculated for each intermediate for both an isolated BAS and on a BAS near a [M(μ-OH)$_2$M]$^{2+}$ moiety of the considered cationic clusters.

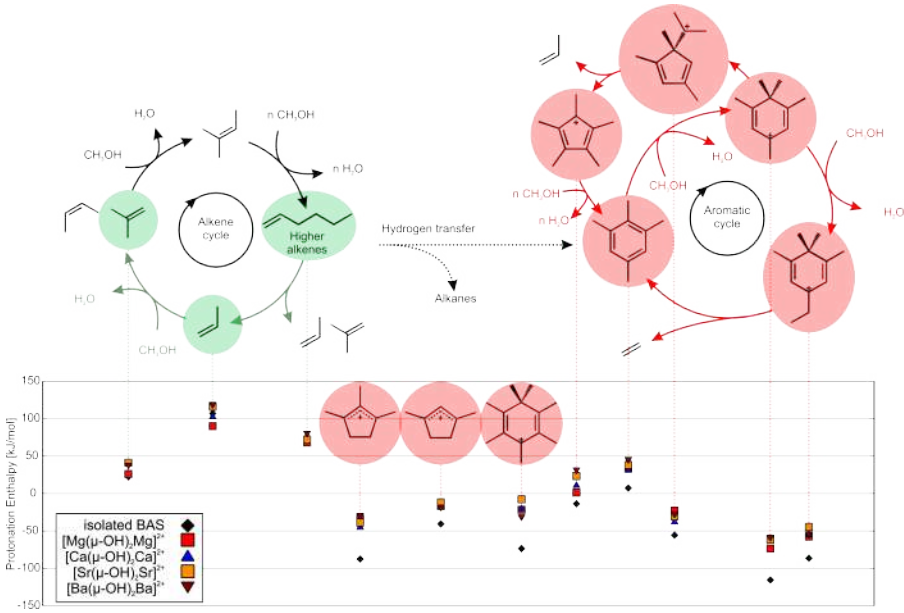

Figure 3.7: Overview of the results of the calculation of the protonation enthalpy showing the intermediates that are unaffected (green) and affected (red) by the alkaline earth metal modification (upper) and the resulting protonation enthalpies at 500 °C showing this effect (lower) for different cationic clusters considered in the zeolite pore. Adapted from ref. [91] with permissions of American Chemical Society.

The results show a different trend for intermediates of the alkene and aromatic cycle. While the alkenes (green in Figure 3.7) seem to be unaffected by the presence of the $[M(\mu\text{-}OH)_2M]^{2+}$ clusters, there seem to be a significant destabilization of the carbenium ions of the aromatic cycle intermediates (red in Figure 3.7). We attributed this to two effects. First, we observed a stabilization of the neutral form, evidenced by clear interactions of the π-electrons of the neutral cyclic intermediates with the $[M(\mu\text{-}OH)_2M]^{2+}$ moieties, as shown in the Supporting Information of **Paper V**. [91] On the other hand, carbocations are also destabilized due to the presence of the positively charged alkaline earth metal cluster. These results thus show that the cyclic HP species are protonated less and thus less reactive. Combined with the more severe impact of Lewis acidity on aromatics methylation compared to alkene methylation, we concluded that introduction of Lewis acidity favors the alkene cycle over the aromatics cycle in the typical MTO HP mechanism.

This suppression of the aromatic cycle was also confirmed experimentally, as shown by the obtained throughput and product selectivity at 500 °C depicted in Figure 3.8. First of all, these graphs show an increased selectivity to propene for alkaline earth metal modified zeolites compared to their parent H-ZSM-5. As Svelle et al. [86] showed that ethene formation is mechanistically separated

from the propene formation, the aromatic cycle is believed to be responsible for ethene formation whereas the alkene cycle yields propene, this is in line with the theoretically found suppression of the aromatic cycle. The LAS modified zeolites also show an increased lifetime with respect to their parent material. To date the mechanisms leading to aromatic growth and coke formation are not fully unraveled yet. Various coke mechanisms might be active during methanol conversion. [23] Our theoretical findings here suggest that cyclic carbocations of the aromatic cycle are less stable. The destabilization of the protonated cyclic intermediates will also decrease their reactivity in further coke formation routes. [97, 121, 346] Also methylated aromatics are considered as coke precursors [347, 348], which are less easily formed on LAS modified zeolites due to the increase in methylation barriers of the aromatics. However, to obtain more mechanistic insight into the increased lifetime a comprehensive study including all possible coke aromatics formation routes would have to be conducted, which was beyond the scope of this work.

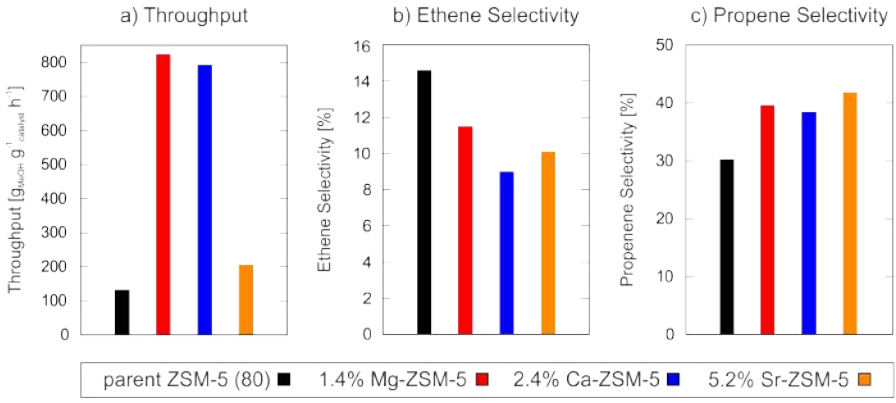

Figure 3.8: Experimental results obtained at 500 °C for the throughput (a), selectivity to ethene (b) and selectivity to propene (c) for the MTO reaction over 1.4 % Mg-ZSM-5 (red), 2.4 % Ca-ZSM-5 (blue) and 5.2 % Sr-ZSM-5 (orange) relative to the parent ZSM-5 (black). Results for 8.2 % Ba-ZSM-5 are not reported, as this sample showed a conversion below 5 %. Adapted from ref. [91] with permissions of American Chemical Society.

3.2 The role of water

The feed composition may greatly influence the catalyst lifetime and product selectivity within the framework of the MTO process. It has already been demonstrated in literature [173–175] that an increase of the water content in the pores leads to an increased olefin selectivity, decreased coke formation and decreased surface methoxide formation. These effects were assigned to the competitive adsorption of water on the Brønsted acid sites, thus making them unavailable for methanol

to react and suppressing the dimerization and cyclization reactions of propene to aromatics. To further elucidate the effect of protic guest molecules on the reactivity in the catalyst pores, in **Paper IV**, the concerted and stepwise methylation of hexamethylbenzene, depicted in Figure 1.5, in H-SAPO-34 is studied at 350 °C using (advanced) molecular dynamics techniques on the three cases shown in Figure 3.9.

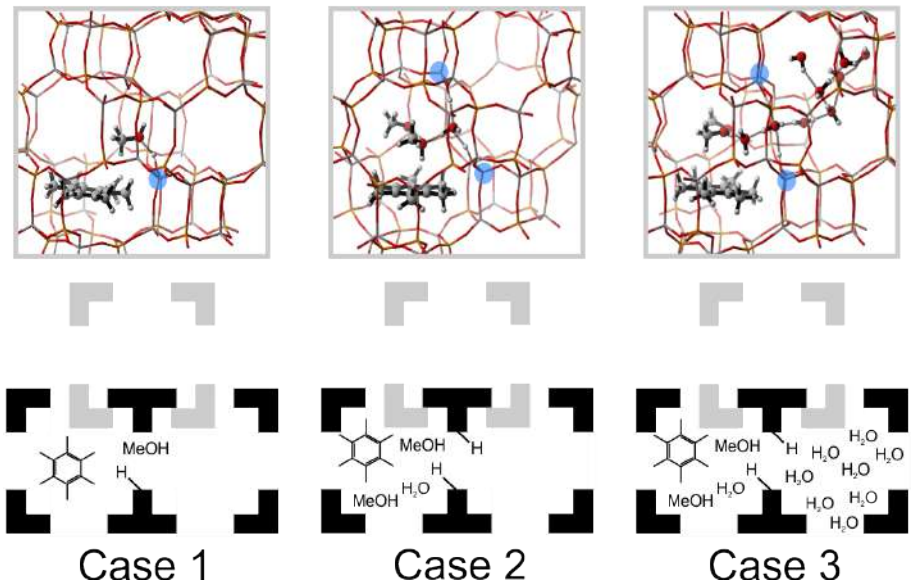

Figure 3.9: Starting structures and schematic representations of the three cases considered to study the concerted and stepwise methylation of HMB in H-SAPO-34, namely an isolated BAS with one HMB and one methanol as base case (Case 1), a more realistic low water content case (Case 2) and high water content case (Case 3). In these snapshots, hydrogen is white, carbon is silver, oxygen is red, aluminum is grey, the silicon substitution is indicated in blue and phosphorus is orange. Adapted from ref. [40] with permissions of John Wiley and Sons.

First, an isolated Brønsted acid site with one hexamethylbenzene molecule and one methanol is considered as the base case (Case 1). This base case will be used here to compare the advanced MD techniques with the static results. Subsequently, we create a more complicated and realistic representation of the catalyst pores. To this end, two adaptations to the system were considered. First of all, one additional methanol molecule and either one or nine adsorbed water molecules were added for Case 2 and Case 3, respectively, as earlier studies show that these protic molecules might interact to form protonated clusters, which decreased the reactivity. [41] This maximum water loading at operating conditions was estimated using an in-house developed thermodynamic model for the adsorption of guest

species in nanoporous materials. [175, 349] Secondly, as there is a high probability to find two silicon atoms in the next nearest neighbor position in SAPO materials, we introduced a second acid site in the unit cell, [350, 351] as was done in earlier work. [106, 189] These adaptations will allow to generalize the conclusions of Case 1 to experimentally more realistic pore environments and the influence of the assisting effect of additional protic molecules on both methylation mechanisms can be assessed.

Note that the schematic representation shown in Figure 3.9 corresponds to starting structures. During the dynamic simulations the system adopts more realistic configurations in the pores of the material. As such, short 50 ps MD simulations already showed that HMB adopts a preferred position oriented along the z-axis (the longest direction of the cage) with the π-clouds oriented to the BAS for Case 1 and Case 2. In Case 3, at a higher water content, the orientation of the π-clouds to the BAS was screened by the additional adsorbed protic molecules, which also deliver new stabilizing interactions for the π-clouds.

Furthermore, higher water loadings led to the formation of solvation shells around methanol which is easily observed in the behavior of the radial distribution function (RDF) belonging to the distance between proton and oxygen of the methanol (Figure 3.10). In Case 2 and 3 corresponding with a more realistic environment, an additional peak arises between 3.1 and 3.5 Å attributed to the formation of a first solvation shell around the methanol. As protonated clusters consisting of protic molecules and the protonated BAS can be formed in this case, the proton donation to the methanol can also occur through another protic molecule instead of directly from the framework. Nevertheless, the protic environment did not significantly influence the pre-reactive complex formation as methanol mostly oriented its methyl group away from the HMB in all cases.

Subsequently, enhanced sampling simulations were performed for both the concerted and stepwise mechanism. We have considered two sampling techniques, which have proven to be very successful in describing this type of reactions in a confined space: metadynamics (MTD) and umbrella sampling (US). Their performance is then compared with the energy profiles resulting from static calculations. This assessment has been performed only in the simplest Case 1. Figure 3.11 displays an overview of all results.

Focusing on the concerted mechanism, the two MD results predict nearly equivalent barriers. The static prediction is somewhat overestimated. However, the most pronounced effect of the dynamic sampling is observed on the stabilization of the products. The free energy is substantially lower when using advanced dynamic methods. This can fully be ascribed to the presence of water, whose configurational freedom is poorly accounted for in the static methods, employing a harmonic oscillator approximation in only one stationary point of the PES. In contrast, in dynamic simulations the product state is stabilized entropically, resulting in lower free energies of the co-adsorbed products. The reaction free energy in the umbrella sampling simulations is slightly lower compared to the MTD simulations, which might be ascribed to the walls imposed in the MTD simulations to enhance

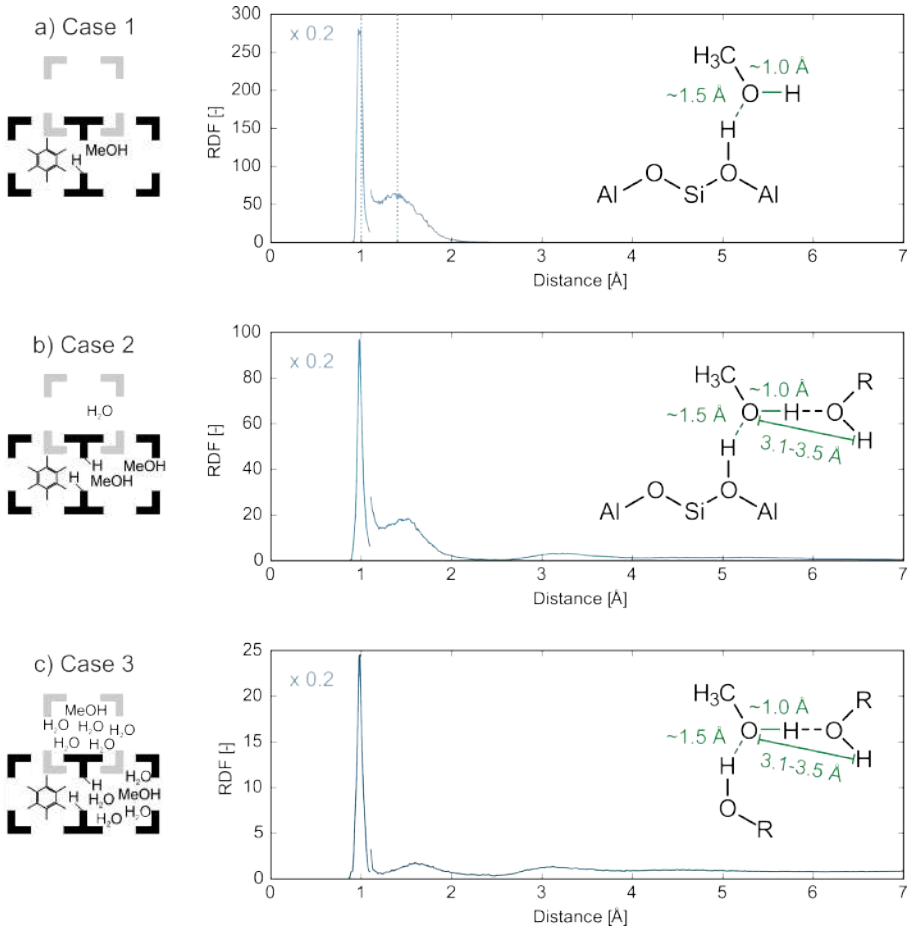

Figure 3.10: Radial distribution functions for the pairs formed by (i) all protons present in the catalyst pore and (ii) the oxygens of the methanol molecule(s) in the reactant state for Case 1 (a), Case 2 (b) and Case 3 (c). For Case 1, the statically obtained distances corresponding to the analyzed bonds are added in dotted lines. The encountered peaks are indicated on the schematic representation of the methanol molecule. The first peaks (at distances below about 1.1 Å) are scaled down by a factor of 5 to improve visualization. Adapted from ref. [40] with permissions of John Wiley and Sons.

recrossing, which affects the regions of the phase space that can be explored.

The same findings can be put forward when analyzing the results in the stepwise mechanism. Qualitatively, we also come to the conclusion that the two reaction mechanisms – the concerted and the stepwise – are competitive at reaction conditions ($T = 350$ °C), though the concerted pathway will prevail due to the high

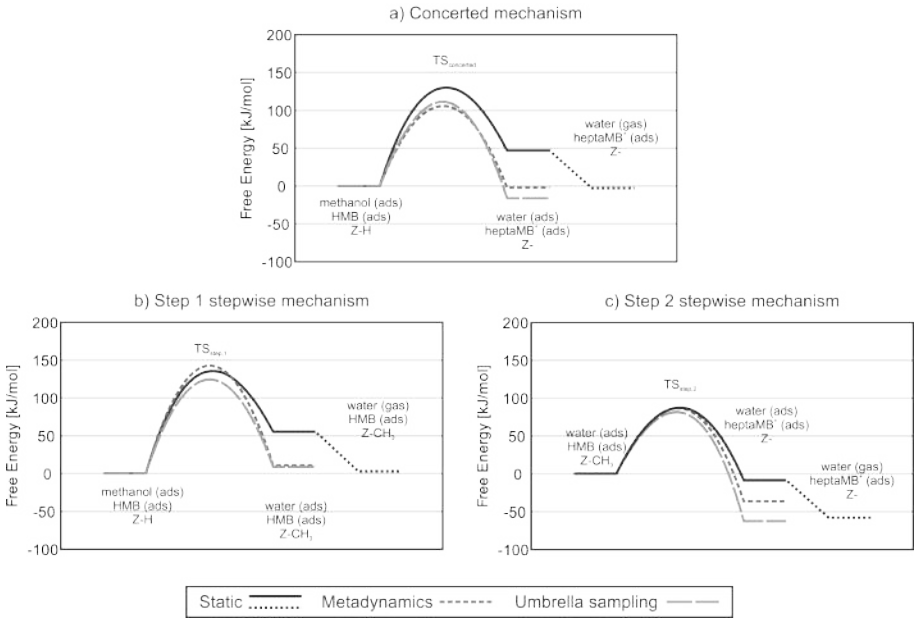

Figure 3.11: Free energy profile for the concerted (a) and step 1 (b) and step 2 (c) of the stepwise methylation of HMB at 350 °C in Case 1 using static (full line), metadynamics (short-striped line) and umbrella sampling (long-striped line) simulations. For the static calculations, an extra desorption step of the formed water is taken into account (dotted line). Adapted from ref. [40] with permissions of John Wiley and Sons.

barrier noticed in the stepwise mechanism for the methoxide formation. Umbrella sampling gives rise to a slightly smaller barrier than MTD. This can be explained by the observation that the US simulations only sample one type of transition state, which is assisted by the presence of the HMB, whereas in MTD broader regions of the phase space were sampled accounting for an assisted and non-assisted transition state. In principle, both methods should be able to sample similar regions of phase space and thus yielding similar predictions of barriers. Unfortunately, we do not succeed in it despite running the simulations sufficiently long. This deficiency is probably due to the choice of the collective variables which does not distinguish between both types of transition states. The broader sampling and the fact that less prior knowledge on the reaction path is needed within metadynamics are the main reasons why we select MTD as the preferred enhanced sampling MD technique in the application on the more complex cases (Case 2 and 3), the more as we lay the main focus on a qualitative description of the effects generated by the presence of water on the methylation of HMB, than a quantitative reproduction of barriers. [300] Results are shown in Figure 3.12.

The free energy profiles at 350 °C show that the concerted mechanism prevails

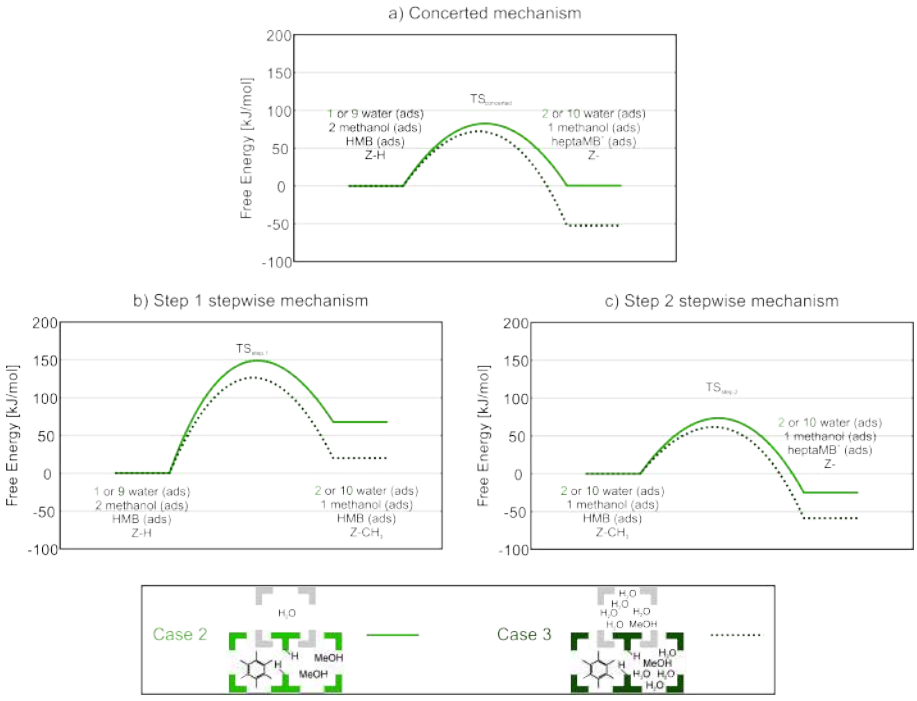

Figure 3.12: Free energy profile for the concerted (a) and step 1 (b) and step 2 (c) of the stepwise methylation of HMB at 350 °C at higher guest molecule loadings and acid site density, namely Case 2 (full line) and Case 3 (dotted line) obtained with metadynamics. The reference level for the reactants in both cases has been assumed zero, however in Case 2 one water molecule was adsorbed, whereas in Case 3 nine water molecules were adsorbed in the unit cell. The obtained barriers are thus intrinsic energy barriers compared to the state in which all molecules are already adsorbed. Adapted from ref. [40] with permissions of John Wiley and Sons.

in all cases. Furthermore, comparison of both profiles shows that the presence of additional protic molecules lowers all barriers and stabilizes the intermediate and product states. The stabilization of the intermediate and product state could be explained by the stabilization of the formed water in the protonated water network. This effect is more pronounced at higher water content.

The decreased barriers for the concerted methylation and methoxide formation due to the assistance of protic molecules, shown in earlier work, [44, 107, 175] is confirmed here and originates from the formation of solvation shells as already mentioned when discussing the MD runs for the reactant valley. The elevated water content in Case 3 leads to an increased solvation shell formation and thus increased assistance compared to Case 2, as depicted in the radial distribution functions for the pairs formed by (i) all protons and (ii) the oxygens of the methanol molecules

depicted in the top and middle panel of Figure 3.13. The peak between 3.1 and 3.5 Å increases for Case 3 relative to Case 2. This peak is attributed to the formation of a first solvation shell around the methanol, as this distance corresponds to the distance between the oxygen of methanol and the hydrogens of a protic molecule – either water or methanol – which is hydrogen bonded to this methanol. For Case 2, the concentration of assisting molecules is too low to always have an efficient assistance and both assisted and unassisted transition states are sampled, shown in the bottom panel of Figure 3.13.

Also for the second step of the stepwise mechanism, a lower free energy barrier is observed when increasing the water content. This can be explained by a stabilization of the BASs with the surrounding protic molecules, though not as direct as for the concerted methylation and methoxide formation. To this end, the RDFs for the pairs formed by (i) all protons and (ii) the oxygens of the BAS are shown for Case 2 and Case 3 in Figure 3.14. For the metadynamics and product state simulations of Case 3, these RDFs reveal an additional peak between 1.8 and 2.25 Å compared to Case 2. As shown in the snapshots in Figure 3.14b, the protic molecules stabilize the unprotonated BAS, which is formed from the methoxide, by a protonated water cluster resembling the Grotthuss mechanism for Case 3. [352] The distances of the hydrogen bonds formed in this chain are within the range of 1.8 and 2.25 Å, thus corresponding to this peak. When considering Case 2, insufficient protic molecules seem to be present to stabilize the unprotonated BAS and thus fail to lower the transition state barrier.

As assistance by the additional water molecules thus explained the decreased barriers and stabilized products between Case 2 and Case 3, this part of the disseration showed that not only competitive adsorption between methanol and water [175] needs to be considered when clarifying the enhanced conversion of methanol in the presence of water. [25, 173] The assisting role of water might have an important effect on the whole reaction profile and a study on its effect on the complete aromatics mechanism might lead to new insights on the problem at hand.

3.3 Effect of topology and Brønsted acid strength

Erichsen *et al.* [46–48] experimentally showed the importance of the strength of the acid site on the reaction cycle governing the methanol conversion, either the alkene or aromatic cycle, for the one dimensional AFI structured H-SAPO-5 and H-SSZ-24 materials. They found that even when co-feeding benzene, the alkene cycle dominated under MTO conditions in the weaker acidic H-SAPO-5 material. Similarly, Teketel *et al.* [109, 122–124] found a high selectivity to branched C_{5+} alkenes over H-ZSM-22 as methanol conversion over this zeolite is governed by the alkene cycle since the one dimensional pores of H-ZSM-22 are too small to fit aromatic HP species. In **Paper I** [107] , simulations have been performed on the competition between the concerted and stepwise methylation of propene, representing the alkene cycle, and benzene, representing the aromatic cycle, over

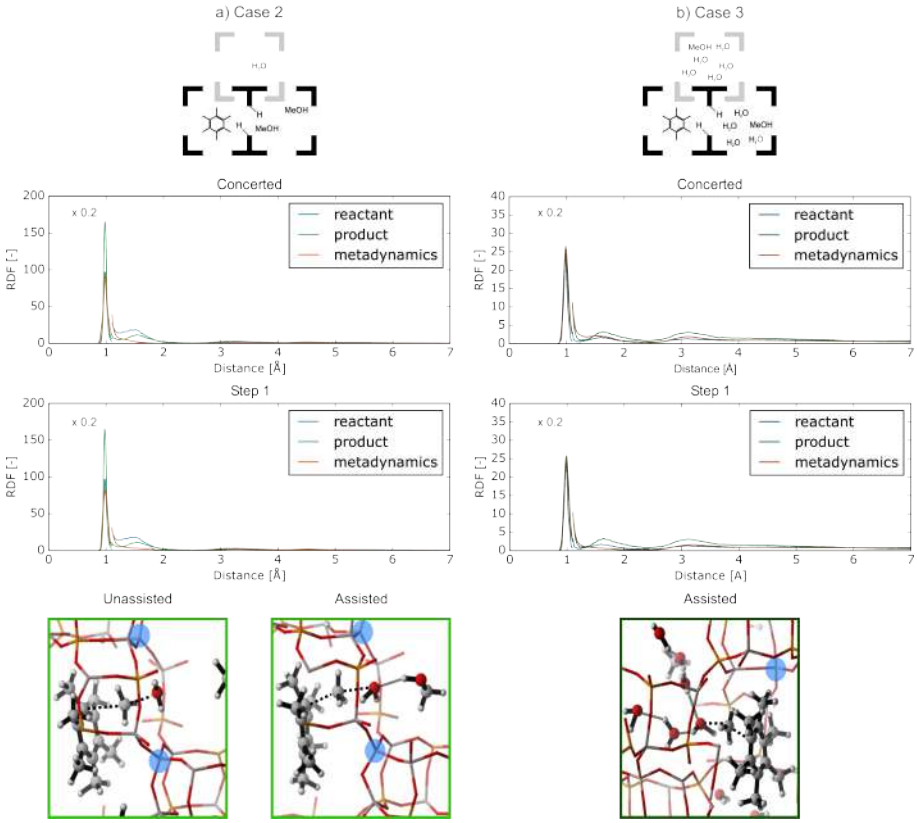

Figure 3.13: Radial distribution function for the pairs formed by (i) all protons and (ii) the oxygens of the methanol molecules from MD runs in the reactant and product state as well as during the MTD simulations for the concerted methylation (top) and methoxide formation (middle) for Case 2 (a) and Case 3 (b), showing the formation of solvation shells at higher water concentrations. Furthermore, the unassisted and assisted transition states are visualized in the snapshots at the bottom. The first peaks of the RDFs (at distances below about 1.1 Å) are scaled down by a factor of 5 to improve visualization. In these snapshots, hydrogen is white, carbon is silver, oxygen is red, aluminum is grey, the silicon substitution is indicated in blue and phosphorus is orange. Adapted from ref. [40] with permissions of John Wiley and Sons.

the AFI-structured H-SSZ-24 and H-SAPO-5 and the TON-structured H-ZSM-22 catalysts. In this way, we tried to elucidate the experimentally found influence of both topology and acid strength from a theoretical point of view.

To gain initial insight on the problem at hand, MD simulations at 250 °C and 350 °C of methanol co-adsorbed with either propene or benzene were performed in

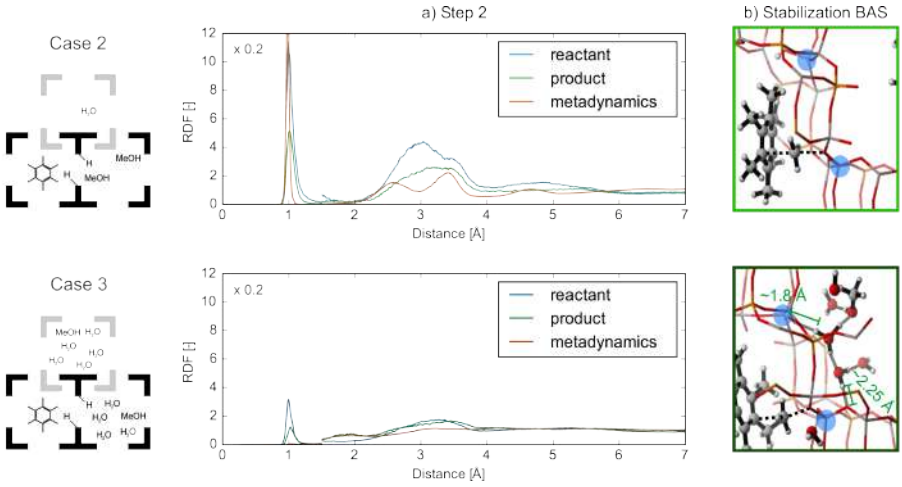

Figure 3.14: Radial distribution function for the pairs formed by (i) all protons and (ii) the oxygens of the Brønsted acid sites from MD runs in the reactant and product state as well as during the MTD simulations for the second step of the stepwise mechanism (a) for Case 2 (top) and Case 3 (bottom). Furthermore, a snapshot of the BAS during the transition state is shown to depict the stabilization of the formed deprotonated BAS by the protic molecules present. The first peaks of the RDFs (at distances below about 1.3 Å) are scaled down by a factor of 5 to improve visualization. In these snapshots, hydrogen is white, carbon is silver, oxygen is red, aluminum is grey, the silicon substitution is indicated in blue and phosphorus is orange. Adapted from ref. [40] with permissions of John Wiley and Sons.

the three considered catalysts. These showed that the tendency to form a more or less reactive configuration between the reactants is significantly influenced by the zeolite framework. To quantify these tendencies, two reactivity indices, introduced in ref. [48], were calculated from the 50 ps MD runs. The indices were defined as the probability that methanol was protonated and the probability that methanol and the hydrocarbon formed a pre-reactive complex for direct methylation according to the concerted pathway. Both indices can be related to reactivity. Indeed, methanol protonation has to occur to activate methanol prior to any reaction [41, 48] and for a concerted methylation step, a favorable orientation of methanol with respect to the hydrocarbon is indispensable for an efficient methyl transfer. The resulting values for the indices are depicted in Figure 3.15.

Clear clustering per material can be observed in Figure 3.15, indicating that acid strength and topology significantly influence these indices and thus the reactivity towards direct methylation. The probability to protonate methanol during the 50 ps MD runs increases in the order H-SAPO-5 $<$ H-SSZ-24 $<$ H-ZSM-22. This quantity is directly related to the acid strength of the studied materials and this

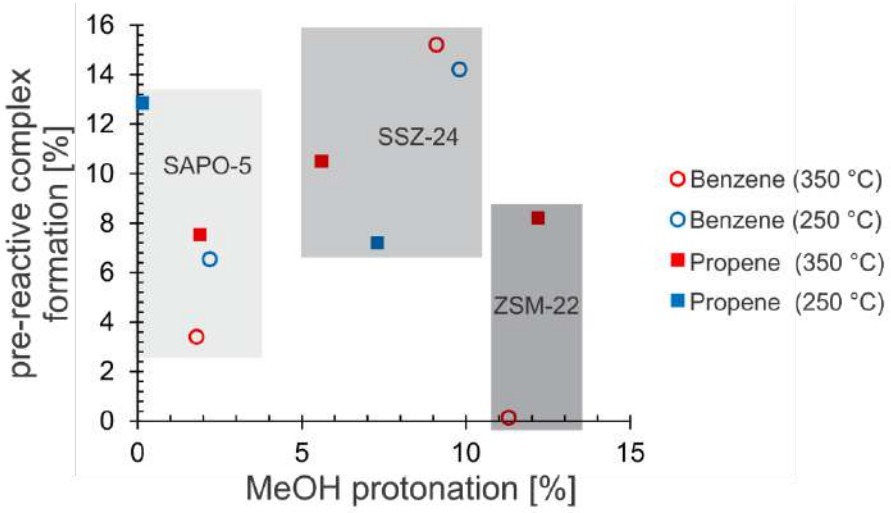

Figure 3.15: Probability of methanol protonation and pre-reactive complex formation for propene (□) and benzene (o) methylation in H-SAPO-5, H-SSZ-24 and H-ZSM-22 at 250 °C (blue) and 350 °C (red). Adapted from ref. [107] with permissions from The Royal Society of Chemistry.

trend follows the order of acid strength. Indeed, an analysis of the acidic hydroxyl groups bond length showed that H-SAPO-5 is the weakest acid, whereas the zeolites H-SSZ-24 and H-ZSM-22 have a similar acid strength as was shown in the Supporting Information of **Paper I**. [107] Due to the smaller pores of H-ZSM-22, protonated methanol can be more efficiently stabilized, which might explain the higher probability for methanol protonation compared to H-SSZ-24. Acid strength also seems to influence the relative reactivity of propene and benzene in the two isostructural AFI materials. Where benzene is more likely to form pre-reactive complexes for methylation in the more acidic H-SSZ-24 material, propene exhibits the highest probability to form favorable co-adsorbed complexes in H-SAPO-5. This is in line with what was earlier reported. [48]

In H-ZSM-22, propene is able to adopt conformations resembling pre-reactive complexes, but for benzene this is not the case as indicated by the nearly zero probability to form pre-reactive complexes. Here, the topological effect is clearly visible. The confined space in the 10-rings of H-ZSM-22 severely limits the mobility of a benzene molecule. Figure 3.15 now reveals that this prohibits the spontaneous formation of favorable co-adsorbed complexes for methylation. The most probable co-adsorption complexes of methanol and benzene or propene revealed that in these most probable configurations, the π-electrons of the hydrocarbons are not easily accessible for reaction with methanol.

To examine the reactivity trends found from the MD simulations, metadynamics simulations were performed subsequently, thus sampling the free energy barrier for

both the concerted and stepwise methylation mechanism of both benzene and propene. The resulting intrinsic free energy barriers and free energies of reaction for the concerted ($\Delta G^{\ddagger}_{concerted}$) and stepwise ($\Delta G^{\ddagger}_{step1}$, $\Delta G_{r,step1}$ and $\Delta G^{\ddagger}_{step2}$) benzene and propene methylations at 350 °C and 250 °C in H-SSZ-24, H-SAPO-5 and H-ZSM-22 are discussed in detail in **Paper I**, while the main conclusions are summarized here.

For benzene and propene methylation in H-SSZ-24 at 350 °C, it was deduced that it is more probable that a concerted methylation instead of methoxide formation occurs as the intrinsic free energy barriers for the concerted pathways are significantly lower than the free energy barrier for methoxide formation. In the weaker acidic H-SAPO-5 catalyst, the concerted pathway also seems to dominate the benzene and propene methylation. It should be noted however that in the case of benzene methylation a concerted methylation and methoxide formation at 350 °C are almost equally high activated, which is not the case for propene. The free energy barrier for the concerted benzene and propene methylations at 350 °C in H-SAPO-5 are respectively around 22 and 5 kJ/mol higher than in H-SSZ-24. Intuitively, one would expect that a lower acid strength results in higher intrinsic free energy barriers; however benzene methylation seems to be much more sensitive to acid strength than propene methylation. A possible explanation has been proposed by Iglesia and co-workers, stating that transition states with more localized charges are less influenced by the Brønsted acid strength than those exhibiting more diffuse charges. [353] Since the charge is more diffuse on benzene due to its conjugated π-system, the increase of the intrinsic barrier is more significant than for propene. The relative increase of the concerted barrier for benzene compared to propene in H-SAPO-5 further shows that the intrinsic reactivity towards methylation of propene is higher than benzene. Returning to the reactivity indices presented in Figure 3.15, this might be related with the fact that propene is more likely to form pre-reactive complexes with methanol for methylation than benzene in H-SAPO-5. These findings are in line with the experimental observation that in H-SAPO-5 the alkene cycles dominates product formation whereas aromatics are the main HP species during methanol conversion in H-SSZ-24. [46–48]

Finally, a similar set of simulations has been performed in the H-ZSM-22 catalyst model. The relative high $\Delta G^{\ddagger}$ values for benzene methylation, despite the high acid strength of H-ZSM-22, can be understood in view of the restricted mobility of benzene in the TON channels, inhibiting the formation of favorable pre-reactive complexes (see Figure 3.15). For propene a high probability to form pre-reactive complexes for a concerted methylation step (Figure 3.15) was found and this is clearly reflected in the relatively low free energy barrier $\Delta G^{\ddagger}_{concerted}$. This increased reactivity towards propene compared to benzene is in line with the experiments of Teketel *et al.* as they claim to suppress the space demanding aromatics based MTO mechanism during methanol conversion in H-ZSM-22. [109, 122–124]

Brogaard *et al.* [115] showed the importance of entropic effects and thus temperature on the concerted versus stepwise methylation mechanism. As the intermediate release of water in the stepswise mechanism led to an entropic gain,

this mechanism prevailed from higher temperatures on. Therefore,the temperature effect on the free energy barriers was also studied by comparing the already discussed results at 350 °C with those at 250 °C. These show that while the $\Delta G^{\ddagger}_{concerted}$ barely alters due to the temperature change (maximum change of 9 kJ/mol), the $\Delta G^{\ddagger}_{step1}$ increases around 20 kJ/mol upon lowering the temperature. This finding is in line with the conclusions made in literature, [115, 118] as indeed the stepswise mechanism only becomes competitive at higher temperatures.

In general, the experimentally observed preference for the alkene cycle due to the lower acidic H-SAPO-5 and due to the shape selectivity in H-ZSM-22 could be supported based on both the reactivity indices and the calculated free energy barriers. Furthermore, the suggested entropic stabilization of the stepwise mechanism at higher temperatures was confirmed.

4

Conclusions and perspectives

Since its discovery in the 1970s, the reaction mechanisms of the methanol-to-olefins process has been the subject of long debate and discussion on both academia and industry. It is now generally accepted that this zeolite catalyzed-process is regulated by a hydrocarbon pool mechanism in which two interacting reaction cycles are active, namely the alkene and aromatic cycle. This mechanism is therefore also known as the dual cycle mechanism. This concept proposes that ethene production, via the aromatic cycle, is mechanistically separated from the propene production, through the alkene cycle. Furthermore, aromatic intermediates are identified as cokes precursors which deactivate the catalyst. Molecular insight in all reactions involved in the dual cycle learns that suppressing the aromatic cycle will benefit the catalyst lifetime and propene selectivity.

The work performed in this thesis, clearly showed how detailed insight into the catalytic function and the governing reaction cycles are ideally obtained by a close synergy between theoreticians and experimentalists. As significant progress has been made in the field of computational zeolite catalysis, new methods such as advanced molecular dynamics simulations, which have the potential to model chemical reaction at operating conditions, have entered the field of heterogeneous catalysis. As these methods are used throughout this dissertation, they were thoroughly tested and benchmarked in **Paper VI**, focusing on two important parameters within these methods, namely the sampling protocol and collective variable as reaction coordinate. In that paper, we studied the methylation of ethene in H-ZSM-5 at 350 °C in the framework of the MTO process with enhanced

sampling MD techniques. This is one of the best characterized reactions from both theoretical and experimental viewpoint in zeolite catalysis as it is one of the rare examples for which experimental kinetic data are available. In the first part of this paper, the forward intrinsic methylation free energy barrier was calculated using four enhanced sampling techniques, namely metadynamics, variationally enhanced sampling, umbrella sampling and thermodynamic integration. The four different methodologies gave similar results, though some had disadvantages compared to others, for example the use of wall to restrict the sampling to the region of interest. The problems encountered within this dissertation showed that advantages and disadvantages are strongly dependent on the specific system under study as some required the introduction of walls, while others need a broader sampling. In the study of the methylation reaction of ethene, MTD and VES techniques required the introduction of walls to restrict sampling in the region of interest, which is not trivial without prior knowledge of the position of the transition state and interesting reactants. TI had the disadvantage that correction factors are needed to go from the sampled mean force to the unbiased ensemble when not using distances as CV. [210, 301] Therefore, umbrella sampling was selected as the most appropriate technique to further study the methylation of ethene. In the second part, several collective variables were proposed which could differentiate between the reactant, transition and product state of the studied methylation reaction, and their influence on the free energy barrier was subsequently examined. Therefore, three types of collective variables were defined, and the resulting free energy profiles were compared. Here, we highlighted the importance of transformation from one collective variable space to another. Nevertheless, the free energy profile still showed a dependence on the collective variable. A collective variable invariant measure is required for enhanced sampling to be competitive with static methodologies. Therefore, reaction rates were introduced which demonstrated the importance of accounting for the configurational freedom in the reactant state when calculating free energy barriers from enhanced sampling simulations. This procedure led to reaction rates and phenomenological free energy barriers which are nearly independent on the particular choice of the collective variable and enhanced sampling technique. Finally, we validated our resulting intrinsic reaction rate constants by comparison with theoretical and experimental data available in literature. Our data correspond very well with the intrinsic reaction rate constant of 5.5 10^3 s^{-1} at 350 °C reported by Van Speybroeck et al. [214] Direct comparison with other theoretical work and experimental work was impeded, as only apparent rates were reported in literature. These apparent kinetics were related with intrinsic kinetics extracted from the advanced MD simulations by the equilibrium constant for the co-adsorption of ethene which can be calculated using static DFT approaches. By taking into account a whole set of functionals and dispersion schemes a range of apparent rate constants was extracted, including the experimental value of 1.95 $(mbar.s)^{-1}$. When consequently using revPBE-D3 in both the static and enhanced sampling simulations, results on the verge of kinetic accuracy were obtained. The results presented in **Paper VI** thus showed that ab initio enhanced sampling techniques

have the potential to extend the insights obtained in computational chemistry when describing chemical reactions in complex environments. Nevertheless, given the computational expense of enhanced sampling molecular dynamics methods, they cannot be used as the default method for any zeolite catalyzed reaction. It is more recommended to use them in combination with static methods and to use enhance samping methods for systems which have complexities that can not be captured by standard static approaches.

The relevance of both static and dynamic approaches is clearly demonstrated. We tried to convince the reader that the combined use of both approaches can assist us in the clarification and understanding of experimental data. We applied this combined procedure in several reaction studies of the PhD thesis. In particular we focused on two main topics within the study of the reaction cycles governing the MTO process: the importance of Lewis acidity, and the influence of water on the reactivity in the catalyst pores. **Paper II**, **Paper III** and **Paper V** concern the first topic and we highlighted the importance of Lewis acidity in the MTO process. In these papers, we investigated the effect of alkaline earth metal modified ZSM-5 on the product selectivity and catalyst lifetime from both an experimental and theoretical point of view. In **Paper III**, it was experimentally observed that the propene selectivity is controlled by the BAS density, as acid site isolation was identified as the key to maximize propene selectivity by preventing the secondary aromatic formation reactions. Furthermore, a typical vulcano plot was obtained for the catalyst lifetime in function of the BAS/LAS ratio. To elucidate these findings, we further investigated the nature of the active site, adsorption and reactivity properties of metal oxide clusters contained in H-ZSM-5 in **Paper V**. The structural analysis of the cationic metal oxide clusters in the zeolite pores showed that introduction of metal oxides enables a reduction of original BASs, since protonation of the bridging free oxygen led to a significant stabilization for all metal oxide species. These extra-framework moieties may be present as mono-, bi- and/or trinuclear metal complexes. From a theoretical point of view, we found that binuclear $[M(\mu\text{-}OH)_2M]^{2+}$ species are more stable than mononuclear species. A structural characterization comprising solid state NMR gave indirect evidence for the presence of both monomeric and binuclear species. The newly proposed active sites were shown to possess well defined Lewis acid sites. This was shown via experimental and theoretical IR spectra for the adsorption of pyridine. An excellent agreement was obtained between theoretical and experimental IR spectra, which gives evidence that our model of the modified active site captures the most important properties and can confidently be used for further kinetic studies. Furthermore, a blue shift in the IR peak characteristic for the LAS was found to correlate linearly with the adsorption enthalpy of pyridine and thus with the Lewis acid strength of the modified active site. This agreement allowed to relate the position of the LAS IR peak to the strength of the Lewis acid site, thus creating an experimental tool to check the Lewis acid strength. For the alkaline earth metal modifications studied following acidity scale was found: Mg>Ca>Sr>Ba. Subsequently, the combined experimental and theoretical analysis of the reactivity

properties of modified active sites confirmed the importance of Brønsted acid site isolation and the suppression of the aromatic cycle by the LAS. All our findings pointed towards a suppression of the aromatic cycle as methylation barriers of aromatic HP species are substantially higher on LAS modified zeolites and typical cyclic carbocations are less well stabilized in the presence of additional LASs. The influence on the alkene cycle was rather limited. An optimal combination of catalyst lifetime and propene selectivity was found for the Mg and Ca modified zeolites. This could be assigned to a subtle interplay between the influence of the LAS on the neighboring BAS and the strength of the LAS itself as for Sr and Ba the weaker LAS is not strong enough to influence the BAS. Our results thus confirm all experimental findings and support the supramolecular concept of the MTO catalyst, which may be tailored at the molecular level. The overall catalyst performance cannot simply be explained using the properties of the BAS but is rather the result of an interplay of the intrinsic zeolite properties, organic compounds and its proximity to additional LASs.

A second main topic within this thesis concerned the influence of water on the reactivity in the catalyst pores, as studied in **Paper IV**. As increased water content was shown to increase olefin selectivity and decreased coking rates, first principle dynamic techniques were used to gain new insights on the influence of protic molecules on the methylation of HMB in H-SAPO-34. To this end, the competitive concerted and stepwise methylation mechanisms were studied for three cases with an increasing amount of protic molecules and an increasing amount of BASs. The simulations were performed using first principle molecular dynamics methods to account for entropic and dynamic effects at elevated temperatures. From the initial MD runs we found that though the water influences the preferred orientation of HMB, the effect on the pre-reactive complex formation was limited due to the contra-productive orientation of methanol for all cases. Subsequently, enhanced sampling simulations were used to calculate the free energy barriers and analyze the competition between both reactions. In general, the results demonstrated that the concerted mechanism prevails at the reaction conditions studied in this work. We concentrated on two aspects which could affect the free energy barriers and reaction free energies. First, the effect of static versus enhanced sampling MD methods was tested for the base case. The main difference between the results obtained from the enhanced sampling techniques and the static methods was observed for the stabilization of the products in which water was formed. In the case of dynamic methods, the water formed in the methylation step becomes rather mobile, which yields an entropic stabilization of the product region. In static methods, this configurational freedom is not properly described as only one point is considered on the free energy surface. Second, by comparing the more complex cases, the effect of additional protic molecules in the catalyst pores could be unraveled. In all cases, decreased barriers and additional stabilization of the products was observed. The decreased barrier for the concerted methylation and methoxide formation and the stabilization of the product could be associated to the solvation shells that are more prominent at higher water content. Furthermore,

a stabilization of the deprotonated BAS formed in the second step of the stepwise mechanism occurred by a Grotthuss type mechanism linking both BASs. This effect leads to a decreased barrier for this second step at higher water concentrations. As such, our results highlight the importance of correctly accounting for the dynamic and assisting behavior of the protic environment within zeolite catalysis at process conditions.

Besides the insights obtained on the two selected main topics within the MTO process, some contributions to other research questions in MTO chemistry were obtained within this thesis. In **Paper I**, for example, advanced MD simulations were applied to study the methylation of benzene and propene in the AFI-structured H-SSZ-24 and H-SAPO-5 and the TON-structured H-ZSM-22 catalysts. In this way, we wanted to confirm the experimental finding that the preference for the alkene cycle could be induced by decreasing the acidity of the framework or limiting the available space. The initial MD runs showed that a vast number of co-adsorbed complexes could be formed for benzene and propene co-adsorbed with methanol, especially in AFI-structured materials. Nonetheless, some co-adsorption hotspots could be identified that correspond to the most probable co-adsorption complex. The location of these hotspots and thus the preferential orientation of benzene and propene in the pores was largely influenced by the catalyst topology and acidity. These were further quantified by two reactivity indices which confirmed the experimental finding that benzene methylation was suppressed due to steric hindrance in H-ZSM-22. This was confirmed by the high benzene methylation barrier obtained via metadynamics. Similarly, the influence of the catalyst acid strength was assessed by comparison of results for two isostructural AFI materials H-SSZ-24 and H-SAPO-5, which have different framework compositions and thus acid strengths. In both materials slightly different co-adsorption complexes were found due to different interactions between the hydrocarbons and the zeolitic walls. In both materials, the concerted methylation dominated benzene and propene methylation. The impact of catalyst acidity on the free energies of activation does not appear to be uniform, but rather depends on the reaction type (concerted or stepwise) and the hydrocarbon undergoing the reaction, *i.e.* benzene or propene. As reported earlier, benzene was more reactive towards methylation in H-SSZ-24, whereas propene was more reactive in H-SAPO-5. This also corresponds with the observation that the alkene mechanism dominates product formation during MTH reactions in H-SAPO-5, whereas aromatics are the most active HP species in H-SSZ-24. These results thus show that we are indeed able to elucidate and confirm experimentally observed effects from a molecular modeling point of view.

In general, the results highlight the importance of theoretical simulations within heterogeneous catalysis as we could confirm and understand some important experimental findings. Nevertheless, there is still room for improvement. Certainly in view of the quest to increased model accuracy and operando simulations put forward by Pidko and co-workers [187, 188], significant improvements are still possible.

For example, the complexity of the catalyst model can still improve. Pidko [188] summarized that going from small clusters to extended clusters to a single site

periodic and even to a multi-site periodic model significantly increased the model accuracy. For the Diels-Alder cycloaddition of dimethylfuran and ethylene [354, 355], they highlighted the importance of the cooperative effect of the numerous cations present in the catalyst pores which align the reactants in a pre-activated state. [356] Similarly, we studied the cooperative role of BAS and LAS sites in **Paper II**, **Paper III** and **Paper V** [91, 120, 121], but also this model could be improved further. One could resort to supercell models to account for even more alkaline earth metal clusters and as such study the cooperative effect between different Lewis acid sites. Furthermore, larger models would allow to also study the effect of the bulky cationic clusters on the diffusive behavior within the catalyst pores. Nevertheless, it should be noted that for now, these calculations are probably too computationally expensive and further improvements in both simulation power and methods are necessary.

Further improvements in the quality of the simulations could be obtained by introducing nuclear quantum effects. [357] As the Born-Oppenheimer approximation is usually used in MD simulations, the atomic nuclei are treated as classical particles, which is a reasonable approximation for heavy atoms at high temperatures, but becomes less realistic when considering lighter atoms. Their importance has already been demonstrated throughout literature for molecular simulations of water [358–361] and the structural properties of metal-organic frameworks. [362] As the influence of water on the MTO process was thoroughly studied in **Paper IV**, the conclusions could be further validated by including these nuclear quantum effects to these simulations, though this would not be trivial due to the necessary computational power.

Similarly, the collective variable describing the reactions under study could be improved. For now, we resorted to intuitively selected distances and coordination numbers based on suggestions in literature. [22, 41, 44] Though it should be kept in mind that these logical collective variables could fail to capture all important degrees of freedom. Peters [306] gives as an example the dissociation of an Na^+Cl^- ion pair in an aqueous solution. An intuitive collective variable to drive this reaction is the distance between both ions. Geissler *et al.* [303] identified the importance of the solvent degrees of freedom, as the rearrangement of the water molecules around the ion pair is equally activated as the separation of the ions. Similar conclusions were made by Bolhuis *et al.* [304] for the isomerization of alanine dipeptide. Systematic protocols exist to identify better collective variables by obtaining the slowest order parameters describing the transformation from reactant to product via time-structure based independent component analysis (tICA). [305, 363, 364] As MD data containing transitions are required to perform this analysis, this became computationally too expensive and out of scope of this work, though it might become possible with increasing computational power. Subsequently, one might improve the collective variable selection even further by applying non-linear dimension reduction methods or even neural networks. [365–368] Another possibility would be to use the path-based collective variables proposed by Branduardi *et al.* [369] They introduce two collective variables based on an initial reaction path,

which can be constructed via linear interpolation of the Cartesian coordinates of the reactant and product state. The first collective variable, denoted s, represents the progress along this path, while the second CV, z, represents the distance from the reference path. As such, each system can be reduced to a two-dimensional problem. This methodology can even be extended further towards path sampling methods which do not require an a priori definition of a set of CVs. [370–372] These methods have not yet been applied on complex heterogeneous catalysis and need proper testing before becoming generally accepted.

A last quality parameter put forward in ref. [187] is the reaction network complexity. To improve this characteristic, one might combine information obtained for single elementary reactions within a microkinetic model, which is able to account for the competitive reactions at operating conditions. Though microkinetic models have already been frequently applied in metal surface catalysis, [373–379] their application in nanoporous catalysts is rather limited due to the complex reaction mechanisms, high computational cost and the necessity for a mean-field approximation. [380–382] This latter assumes a uniform coverage of all active sites, which is difficult to attain in zeolite catalysis. An interesting first principle microkinetic model was presented by De Wispelaere *et al.* [119], where they not only confirm the stepwise methylation mechanism at high temperature and low pressure, but also that the widely accepted rate law, Eq. 2.50, is not generally acceptable and depends on the applied temperature, pressure and feed composition.

Besides accounting for the reaction network via microkinetic modeling, the reactions considered in this work can also be expanded further by not only considering the productive period of the catalyst. Further insight in the MTO process can be obtained by focusing on the new mechanisms for the C-C bond formations which could govern the early stages of the MTO process [54–66] and mechanisms for the subsequent formation of aromatics which could act as active HP species. [383–388] Of course, also the deactivating reactions are of utmost interest, therefore detailed studies of the coking mechanism could further extend our insight and understanding of the MTO process. [23, 347, 348, 389]

Part II

Published papers

Paper I

Towards molecular control of elementary reactions in zeolite catalysis by advanced molecular simulations mimicking operating conditions

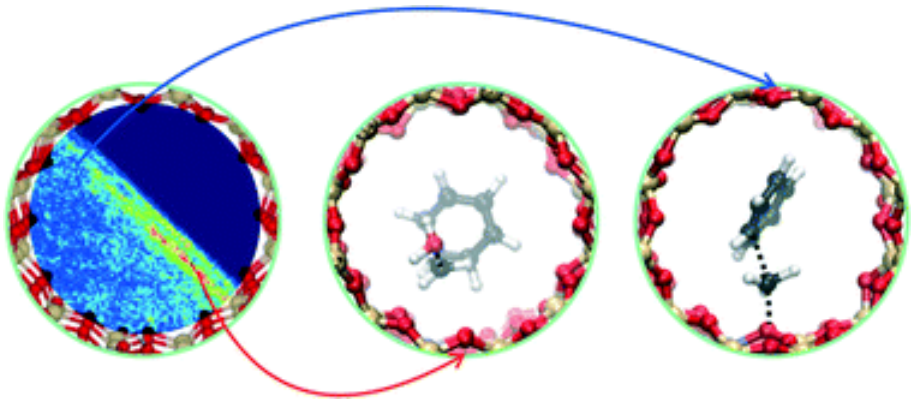

K. De Wispelaere, S. Bailleul, V. Van Speybroeck, *Catalysis Science & Technology*, **6**, 2686–2705 (2016)

S. Bailleul performed some of the computational research and analysis for this paper and was involved during the manuscript preparation.

Catalysis Science & Technology

PAPER

View Article Online
View Journal

Cite this: DOI: 10.1039/c5cy02073e

Towards molecular control of elementary reactions in zeolite catalysis by advanced molecular simulations mimicking operating conditions†

Kristof De Wispelaere, Simon Bailleul and Veronique Van Speybroeck*

Received 30th November 2015,
Accepted 30th January 2016

DOI: 10.1039/c5cy02073e

www.rsc.org/catalysis

Zeolites are the workhorses of today's chemical industry. For decades they have been successfully applied, however many features of zeolite catalysis are only superficially understood and in particular the kinetics and mechanism of individual reaction steps at operating conditions. Herein we use state-of-the-art advanced *ab initio* molecular dynamics techniques to study the influence of catalyst topology and acidity, reaction temperature and the presence of additional guest molecules on elementary reactions. Such advanced modeling techniques provide complementary insight to experimental knowledge as the impact of individual factors on the reaction mechanism and kinetics of zeolite-catalyzed reactions may be unraveled. We study key reaction steps in the conversion of methanol to hydrocarbons, namely benzene and propene methylation. These reactions may occur either in a concerted or stepwise fashion, *i.e.* methanol directly transfers its methyl group to a hydrocarbon or the reaction goes through a framework-bound methoxide intermediate. The DFT-based dynamical approach enables mimicking reaction conditions as close as possible and studying the competition between two methylation mechanisms in an integrated fashion. The reactions are studied in the unidirectional AFI-structured H-SSZ-24, H-SAPO-5 and TON-structured H-ZSM-22 materials. We show that varying the temperature, topology, acidity and number of protic molecules surrounding the active site may tune the reaction mechanism at the molecular level. Obtaining molecular control is crucial in optimizing current zeolite processes and designing emerging new technologies bearing alternative feedstocks.

1. Introduction

Zeolites are prominent and versatile heterogeneous catalysts and chemical conversions in zeolites play an essential role in today's industrial catalysis.[1–3] In view of depleting oil reserves, an increasing demand for base chemicals and the development of more sustainable chemical processes, the industry is shifting towards alternative feedstocks such as natural gas, coal, biomass or waste. To allow conversion of non-conventional feedstocks there is a continuous search for more advanced zeolite structures, with a higher stability and ability to convert heavier feedstocks and molecules containing heteroatoms.[4–7] Although many zeolite-catalyzed processes have successfully been applied for several decades, many features of the materials and reaction mechanisms at the molecular scale are only superficially understood. With the intelligent molecular design of the optimal catalyst for a given process as the ultimate goal, more detailed molecular-level insights are a prerequisite. This is especially important to get track of elementary reactions at operating conditions, which is straightforward neither from experiment[8–10] nor from theory.[11,12]

In modern society, oil derivatives are ubiquitous in daily life. However, during the last decades, petrochemical industry suffers from unstable oil prices due to the waning oil reserves and political instabilities in oil producing countries in the Middle East. Moreover, due to an increasing world population and quality of living, the demand for energy and base chemicals increases exponentially. All these factors initiated the quest for processes to produce hydrocarbons starting from non-conventional feedstocks such as coal, natural gas or biomass, which resulted in a huge interest for the methanol to hydrocarbons (MTH), gasoline (MTG) and olefins (MTO) processes. In the last decades these processes have been commercialized.[13,14] UOP and Norsk Hydro (now INEOS), Total, Lurgi and the Dalian Institute of Chemical Physics (DICP) each developed their own version of the

Center for Molecular Modeling (CMM), Ghent University, Technologiepark 903, B-9052 Zwijnaarde, Belgium. E-mail: veronique.vanspeybroeck@ugent.be

† Electronic supplementary information (ESI) available. See DOI: 10.1039/c5cy02073e

process.[15–18] In view of the large availability of coal in China, many companies have taken up the DICP technology, resulting in a conversion capacity of more than ten million tons of methanol per year.

The MTH process also received a large interest from academia as its reaction mechanism is extremely complex, featuring many often competing reaction cycles at the same time. It has been found that the MTH catalyst has a supramolecular nature, meaning that next to the zeolite framework with its Brønsted acid site, also a hydrocarbon pool (HP) – these are organic molecules occluded in the zeolitic pores – co-catalyzes the reactions as schematically represented in Scheme 1.[13,19–21]

HP species can be subdivided into aromatic and aliphatic compounds and each compound co-catalyzes the MTH chemistry in distinct reaction mechanisms.[11,13,19–21] Aromatics can undergo side-chain growth by methylation in the side-chain mechanism or subsequent ring contraction and expansion reactions in the paring mechanism to form olefins (Scheme 2). In the autocatalytic alkene cycle the olefins undergo methylation and cracking reactions. Both catalytic cycles may exist next to each other, which is called the dual cycle concept.[22–24] Svelle *et al.* found that ethene is the primary product from the aromatic cycle, whereas propene and higher alkenes originate from the alkene driven cycle.[23] The operation of each catalytic cycle during methanol conversion seems to depend on process conditions such as reaction temperature, the nature and composition of the feed and the catalyst topology and acidity.[13,14,19,25,26] Note that each catalytic cycle is initiated by a methylation reaction (highlighted area in Scheme 2). Therefore, the influence of process conditions on methylation reactions is assessed in the current study (*vide infra*).

Given its complexity, studying the MTH process requires the application of a set of advanced experimental and theoretical methods that are able to unravel complex chemical conversions in nanoporous materials. Hence, teams of experimental and theoretical chemists and chemical engineers from all over the globe devote their research projects to unravelling the complex mechanism of the MTH process. Space – and time resolved spectroscopic techniques are nowadays able to image single particles and molecules[9,10,27] and

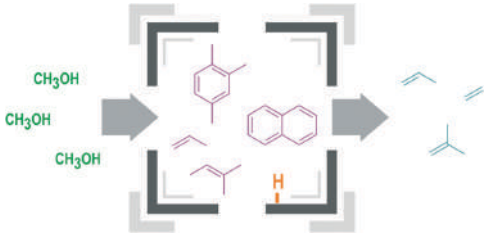

Scheme 1 Schematic representation of the supramolecular nature of the MTH catalyst.[11] Reproduced with permission from The Royal Society of Chemistry.

kinetic measurements can yield information on isolated reaction steps.[28,29] Such kinetic information can at later instance be introduced in a micro-kinetic model to study the steady-state behavior of the process.[30–33] Also from a theoretical perspective many efforts to obtain profound understanding of the chemistry behind the MTH process have been performed and we refer the reader to some interesting reviews on this topic.[11,12]

Molecular modeling in heterogeneous catalysis has matured substantially and received a prominent role as molecular magnifying glass thanks to the development of advanced simulation tools and enormous investments in the ever increasing computer power.[11,12] State-of-the-art molecular modeling techniques are able to compute accurate adsorption enthalpies and rate coefficients of well-defined elementary reaction steps.[34–37] To date many theoretical studies rely on static optimization processes on the potential energy surface (PES), *i.e.* at 0 K, to which corrections can be applied to obtain enthalpic and entropic contributions at the actual reaction temperature.[11,38] The advantage of these techniques is that the most advanced and accurate electronic structure methods may be used to calculate the energy of the system.[11] However, this type of simulations only yields information on a restricted number of points on the PES, *i.e.* the reactant, transition state and product. Another class of simulation techniques consists of methods able to scan larger portions of the PES, hereby enabling to directly account for the dynamical behavior of the catalytic system at the actual reaction conditions. As such, one can account for temperature, pressure, additional guest molecules and the configurational freedom of the system. In this case one also has access to the free energy surface (FES) provided correct techniques are used to calculate the latter.[11,39,40] It should be emphasized that advanced molecular dynamics (MD) techniques to simulate catalytic reactions only recently entered the field of heterogeneous catalysis and their further exploration and application is ongoing.[11,41–54] The introduction of MD based techniques signified an important step towards more realistic models mimicking true reaction conditions. With the forthcoming molecular modeling results on reaction mechanisms, kinetics and thermodynamics it thus eventually becomes possible to impact and rationalize the choice of reaction conditions and the development of next generation MTH catalysts. In this view, MD based techniques are the methods of choice in this study and may give complementary insights.

One of the most investigated reaction steps in the framework of the MTH conversion is the methylation of alkenes and aromatics. These zeolite-catalyzed alkylation reactions are known to be crucial steps in the HP mechanism as they are responsible for carbon incorporation and growth of HP species (see Scheme 2).[55–62] However methylation reactions are also of a more general interest for industrial application to produce for example xylenes.[63] For methylation reactions, two mechanisms are known, being the concerted and stepwise pathway. The concerted mechanism starts from methanol physisorbed at the BAS and simultaneously forms the

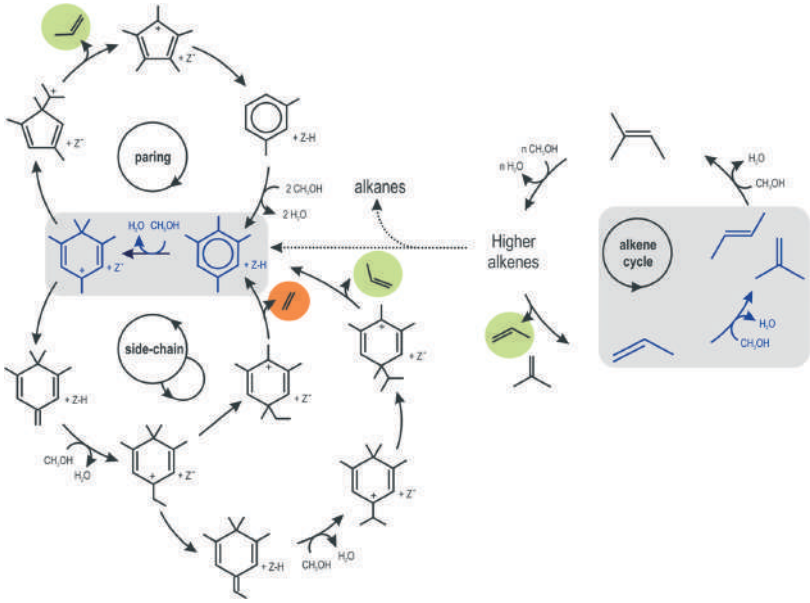

Scheme 2 Overview of aromatic based and alkene based catalytic cycles for olefin formation during MTH conversion.[11] The shaded areas highlight the central role of methylation reactions in each catalytic cycle. Adapted with permission from The Royal Society of Chemistry.

methylation product and a water molecule. In the stepwise mechanism, on the other hand, methanol is dissociated into a framework-bound methoxide and a water molecule prior to the actual methylation. A compilation of the present knowledge on the reaction mechanism of zeolite-catalyzed methylations is given by Svelle *et al.*[29,64] Many theoretical studies available in literature assume the concerted methylation pathway,[28,35,36,56,62,65] however recent studies also account for the stepwise pathway.[21,59,66–70] Experimentalists, on the other hand, encounter major challenges to distinguish the concerted and stepwise methylation pathways.[29] Experimentally defined rate laws for methylation reactions typically exhibit a zeroth order methylation rate dependence on methanol partial pressure, irrespective of the reaction path.[60,61,71] Infrared and NMR measurements have demonstrated that surface-bound methoxides can be present during methylation reactions, indicating methylation might occur through the stepwise mechanism.[29] However, measurements at steady-state conditions indicate that the concerted pathway might prevail.[29] The mechanisms for benzene and propene methylation are shown in Scheme 3 and will be thoroughly investigated in this study.

Herein, some key aspects that have a distinct influence on the MTH conversion have been isolated and thoroughly investigated. Thereby we focused on two classes of influence factors, being (1) the influence of catalyst topology and acid strength and (2) process related factors being reaction temperature and the presence of additional guest molecules in

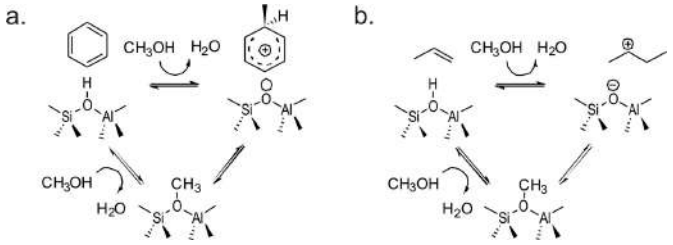

Scheme 3 Concerted and stepwise pathways for the zeolite-catalyzed benzene (a) and propene (b) methylation reaction.

the reaction environment. An overview of the investigated influence factors is shown in Scheme 4. We selected benzene and propene methylation as case study since these are model compounds for the typical hydrocarbon pool species acting as co-catalysts during methanol conversion. This study more specifically aims at understanding how some operating conditions may tune the competition between a concerted and stepwise methylation reaction as schematically drawn in Scheme 4.

In this study, we consider two zeolite topologies characterized by one-dimensional pores of different sizes, namely the AFI and TON topology (Scheme 5). The similar shape and differing size enables to straightforwardly study the influence of confinement. For the AFI topology, we consider H-SSZ-24 and H-SAPO-5. Because of their different chemical composition, both frameworks exhibit different acid strength. Further, we study the influence of an additional methanol molecule surrounding the Brønsted acid site (BAS) to mimic different guest molecule loadings in the pores. Also the influence of temperature on the different reaction steps was studied.

The catalyst topology is an important factor during the methanol conversion process as it determines which HP species are active for olefin formation and thus the product selectivity as depicted in Scheme 5. In the one-dimensional pores of H-ZSM-22 only alkenes were found to be active HP species resulting in the production of branched C_{5+} alkenes,[72–78] whereas aromatics were found to be dominating HP species in H-SAPO-34 and large pore zeolites H-beta and H-SSZ-24.[22,24,79–82] A high activity of aromatics is mostly coupled with a high selectivity towards ethene and propene. The role of catalyst topology has also extensively been studied for methylation reactions of alkenes and aromatics.[28,35,36,65] An optimal fit of the guest molecules in the zeolite pores seemed to be a determining factor for the reaction kinetics.[56] Next to reactivity, the catalyst topology and acidity were also found to impact diffusion rates of reaction products.[50,83,84]

Next to the catalyst's topology, also its acid strength plays a determining role for the activity of HP species. Studies with isostructural catalysts with different framework compositions and thus different acid strength show distinct behavior in terms of product selectivity and deactivation rate during methanol conversion.[53,82,86,87] Recently it has been

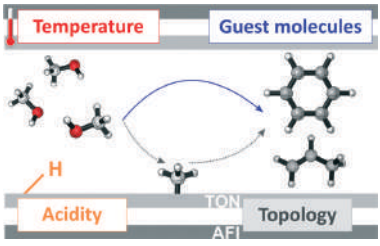

Scheme 4 Overview of the influence factors on benzene and propene methylation investigated in this study.

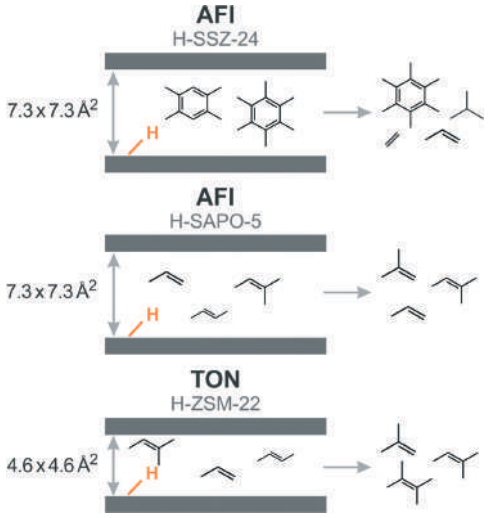

Scheme 5 Schematic representation of the AFI-structured H-SAPO-5 and H-SSZ-24 catalysts and the TON-structured H-ZSM-22 zeolite, with indication of an acid site, the size of the pore opening (taken from the IZA database[85]) and the dominant hydrocarbon pool species and reaction products during methanol conversion.

demonstrated that the relative importance of the alkene and arene cycles can be tuned with acid strength in AFI materials.[53,82] While in the weaker acidic H-SAPO-5 the alkene cycle operates, aromatics are more important in the stronger acidic H-SSZ2-24. As a result, C_{4+} alkenes are primary products in H-SAPO-5, whereas H-SSZ-24 mainly produces C_{2-3} alkenes, aromatics and alkanes as depicted in Scheme 5.

On the side of process conditions, reaction temperature is a crucial parameter. Kinetic measurements and single event micro-kinetic modeling in H-ZSM-5 have demonstrated that the MTH product spectrum can be tuned by varying the reaction temperature.[30,88] Moreover, for methanol conversion in chabazite a combined operando UV-vis spectroscopy and online gas chromatography underlined the influence of temperature on the nature of active and deactivating species.[89] Methanol conversion over large-pore zeolites proceeds mainly *via* the arene cycle[22,24,80,81] but Iglesia and co-workers succeeded to promote the alkene cycle in large-pore materials by applying low temperatures and high pressures.[90,91] Also at the level of individual reaction steps, temperature has a major impact. The adsorption strength,[45,46] reaction kinetics and even the reaction mechanism depend on temperature. Recently Brogaard *et al.* applied a combined theoretical and experimental approach to study the various methylation pathways in ZSM-22,[32] revealing that alkene methylation proceeds *via* the stepwise mechanism (see Scheme 3) at typical MTH temperatures. A similar conclusion was recently drawn by Jones and Iglesia in a kinetic, spectroscopic and theoretical study,[92] showing that methoxy-mediated dissociative routes

become prevalent at higher temperatures and lower pressures due to a delicate balance between entropic and enthalpic effects. Van der Mynsbrugge *et al.* demonstrated after separating enthalpic and entropic barriers contributions to the free energy, that methoxide formation indeed involves a lower entropic barrier, compared to the direct methylation step.[12,52] This further gives evidence that the stepwise mechanism would be preferred at higher temperatures, due to favorable entropic effects. It thus becomes clear that disclosure of various competitive pathways may certainly not solely be based on potential energy profiles at 0 K. We refer the reader to the work of Gounder and Iglesia for a more in-depth discussion on the interplay between enthalpic and entropic effects.[93]

Finally, it should be noted that many theoretical studies assume the adsorption of a single methanol molecule per active site. This may hold under the conditions applied in experimental kinetic studies, which are typically performed at ambient pressure using dilute reagent streams at high feed rates to inhibit secondary reactions. However, under industrial MTH conditions, the conversion may occur at elevated pressures and temperatures.[94,95] Consequently, it might be important to take into account the presence of additional methanol molecules at the active site. It has been demonstrated earlier that the number of methanol molecules present at the BAS can influence the mechanism and kinetics of benzene methylation and methoxide formation in H-ZSM-5.[51,52]

Altogether, the zeolite-catalyzed MTH process is complex yet extremely versatile and by tuning some crucial process parameters, the process is able to meet the fluctuating market demands of ethene and propene. To obtain molecular control over the process, dedicated studies are indispensable to assess the influence of process conditions at the molecular level. Herein we show that state-of-the-art advanced MD techniques are able to describe the influence of catalyst and process related parameters on the mechanism and kinetics of methylation reactions. More specifically, we perform molecular dynamics and metadynamics simulations to assess the influence of catalyst's topology and acid strength, reaction temperature and the presence of additional methanol molecules at the active site on the reaction mechanism and kinetics of benzene and propene metylation reactions.

2. Materials and methods

2.1 Materials

Our simulations have been performed in the AFI-structured H-SSZ-24 and H-SAPO-5 and the TON- structured H-ZSM-22 catalysts. AFI catalysts are large pore materials characterized by one-dimensional 12 ring channels, whereas TON materials have smaller one-dimensional medium pores consisting of 10 rings as schematically represented in Scheme 5. For the AFI materials we considered both the aluminosilicate and silicoaluminophosphate version. The catalyst frameworks were represented by periodic models. For the AFI materials a 1 × 1 × 2 super cell consisting of 48 T atoms has been used, whereas for the TON material a 1 × 1 × 3 super cell consisting of 72 T atoms has been applied (see ESI† Fig. S1). Each catalyst model contains one BAS consisting of a substitutional defect (at the T1 position in the AFI topology and the T3 position in the TON topology) and a charge compensating proton. This corresponds with Si/Al ratios of 47 and 71 for H-SSZ-24 and H-ZSM22 and a (Al + P)/Si ratio of 47 for H-SAPO-5. The closest distances between two acid sites in the same channel were approximately 17 Å and 15 Å in the AFI and TON topologies and 14 Å between two acid sites in adjacent channels for both topologies. As such we can conclude that we modeled isolated acid sites. It has previously been reported that the rate per acid site of propene oligomerization over MFI type materials was affected by the acid site density up to Si/Al ratios of 40, but a further increase did not significantly affect the rate.[96] As the MD runs have been performed in the NPT ensemble (*vide infra*) the unit cell volume and parameters were variables during the simulations. Average cell volumes and parameters are listed in Table S1 of the ESI.†

2.2 *Ab initio* molecular dynamics

The behavior of guest molecules in the different catalysts is analyzed by density functional theory (DFT) based *ab initio* MD simulations. All DFT simulations have been performed with the CP2K software package[97,98] by using the combined Gaussian and Plane Wave (GPW) basis sets approach.[99,100] The revPBE functional was chosen for its improved performance for solid-state calculations relative to the commonly used PBE functional.[101] The DZVP-GTH basis set and pseudopotentials[102] were used, and Grimme D3 dispersion corrections[103] were added. To fully take the flexibility of the host frameworks and the dynamics of the guest molecules into account, simulations were carried out in the NPT ensemble at 250 °C or 350 °C and around 1 bar. During the *ab initio* MD simulations, the temperature was controlled by a chain of five Nosé–Hoover thermostats[104] and the pressure by an MTK barostat.[105] The time step for integration of the equations of motion was set to 0.5 fs. All systems were first equilibrated for 5 ps, followed by a production run of 50 ps. With our *ab initio* MD approach we only have access to relatively short time scales; however, these simulation times were sufficient to obtain convergence of the reported data (*vide infra*).

2.3 Metadynamics

Subsequently, metadynamics (MTD) simulations were performed in the NVT ensemble at 250 °C and 350 °C starting from equilibrated structures from the MD simulations. During the MTD simulations, the temperature is again controlled by a chain of five Nosé–Hoover thermostats. Furthermore, time-averaged cell parameters obtained from the NPT runs are used as constant values. These time-averaged cell parameters are summarized in Table S1.† The idea behind metadynamics calculations is that free energy wells are filled with Gaussian hills along a set of collective variables

(CV), here defined by coordination numbers (CN):

$$CN = \sum_{i,j} \frac{1-\left(r_{ij}/r_0\right)^{nn}}{1-\left(r_{ij}/r_0\right)^{nd}} \quad (1)$$

where the sum runs over two sets of atoms i and j, r_{ij} is the distance between atoms i and j and r_0 represents the reference distance.[106] For all coordination numbers used in this study, a reference distance r_0 of 2.0 Å was chosen, because this value lies in the range of typical transition state distances of the bonds that have to be broken and formed during a methylation or methoxide formation. The parameters *nn* and *nd* are set to 6 and 12, respectively, ensuring a value of 0.5 for each CN term at the reference distance and fast decaying value at larger distances. Quadratic walls were used to restrict the simulations to an area of interest on the free energy surface (FES) (details are given in Fig. S2†). The reacting methanol molecule is kept close to the acidic proton and the free energy valley corresponding with the methylation product is not entirely sampled to prevent the formation of more stable cations and as such enhance barrier recrossings. The initial hills were 5 kJ mol^{-1} high and after each barrier recrossing, the height of the added Gaussian hills is adequately halved to enhance the FES convergence until hills of 0.625 kJ mol^{-1} are added. A new hill was spawned every 50 time steps. The width of all Gaussians was set to 0.02. The integration time step was set to 0.5 fs for all MTD simulations. Two sets of MTD simulations have been carried out and an overview of the studied reaction steps and applied CVs is given in Scheme 6. Initially, MTD simulations with three CVs starting from the co-adsorbed complexes were performed to directly sample the competition between the concerted and stepwise methylation mechanism. As such, the two sets of three reaction steps displayed in Scheme 3a and b were each sampled in one simulation, hereby using CN1, CN2 and CN3 (Scheme 6) to break methanol's C–O bond, form a new C–C bond or form a new C–O bond with the framework. As these simulations typically require very long simulation times to obtain converged free energy barriers, the 3D simulations were only used to extract information on which barrier was crossed first and thus which reaction exhibits the lowest free energy barrier. Next, for each system three MTD simulations applying two CVs were performed to determine accurate free energy barriers for the concerted and stepwise methylation steps. For the concerted methylation CN1 and CN2 as shown in Scheme 6 were applied. For the first and second step of the stepwise methylation, (CN1, CN3) and (CN3, CN2) were used as CVs, respectively. While simulating the formation of methoxides in these 2D simulations, the hydrocarbon molecule was assumed not to be co-adsorbed yet. Furthermore, the water molecule formed upon methoxide formation was assumed to be desorbed when sampling the methylation by a framework-bound methoxide.

Scheme 6 Schematic of the applied collective variables for the MTD simulations of benzene and propene methylation.

The MTD simulations with 2 CVs yield two-dimensional FESs. Consequently, a free energy barrier $\Delta G^{\ddagger}$ can be computed after projection of the 2D FES onto a 1D surface, taking the difference (CV2–CV1) as the reaction coordinate:

$$G(CV2-CV1) = -\frac{1}{\beta}\ln\left(\int_{-\infty}^{+\infty} d_{CV1}\exp\left[-\beta G(CV2-CV1,CV1)\right]\right) \quad (2)$$

Subsequently, the $\Delta G^{\ddagger}$ values can be calculated as the difference between the free energy of the transition state ensemble and the free energy of the reactant region on the obtained 1D FES:

$$\Delta G^{\ddagger} = -\frac{1}{\beta}\ln\frac{\exp\left[-\beta G(TS)\right]}{\int_{-1}^{+1}\exp\left(-\beta G(s)\right)ds} \quad (3)$$

where $\beta = \frac{1}{k_B T}$ with k_B the Boltzmann constant and TS is the position at the top of the barrier along the normalized reaction coordinate s. Analogously, the free energy of reaction ΔG_r can be calculated by comparing the free energy in the product valley and reactant valley according to

$$\Delta G_r = -\frac{1}{\beta}\ln\frac{\int_{+1}^{+\infty}\exp\left(-\beta G(s)\right)ds}{\int_{-1}^{+1}\exp\left(-\beta G(s)\right)ds} \quad (4)$$

In practice, the boundaries of the integrals in eqn (3) and (4) are not infinite, but −1 and +1 due to the definition of the 1D coordinate.

The reported free energies were calculated as the mean free energy over the part of the simulation where the barrier height starts to fluctuate around a mean value and the dynamics along the reaction coordinate become diffusive. The statistical errors were computed as the standard deviation of the mean after removal of correlated data values. The MTD simulations were continued until a statistical error lower than 5 kJ mol^{-1} on the barrier height was obtained. This resulted in total simulation times varying between 50 and 140 ps. Note that due to the accelerating effect of the bias potential on the dynamics of the system, these simulation times do not have a physical meaning. Recently schemes have been developed to translate metadynamics back to regular

dynamics to calculate transition rates.[107] As we do not aim at calculating the most accurate free energy barriers and reactions free energies, our DFT-D approach gives enough insights to understand the observed trends. Moreover, the high computational cost of our dynamical approach hampers the application of higher level DFT methods[11,108] such as hybrid functionals (*e.g.* B3LYP or PBE0) or functionals including parametrization for dispersion interactions such as M06-2X developed by Truhlar,[109–112] ωB97X-D developed by Head-Gordon[113] or BEEF-vdw developed by Nørskov.[114]

Further, it is worth mentioning that in total 14 MD simulations, 14 MTD simulations with 3 CVs and 29 MTD simulations with 2 CVs have been performed. The total estimated calculation time on single 2 × 8 core Intel E5-2670 (Sandy Bridge) nodes was approximately 1350 nodedays.

2.4. Geometrical analysis

From the MD and MTD simulations, we extracted the orientation of the hydrocarbons in the channels throughout the simulations. Therefore, two angles – denoted as α and β in the remainder of this article – were defined to uniquely define the orientation of benzene and propene in the AFI and TON channels. α was defined as the angle between the channel axis and the plane spanned by the six carbons atoms of benzene (Scheme 7a) or the plane spanned by the three carbon atoms of propene (Scheme 7b). β was defined as the angle between a vector in a cross section of the channels, perpendicular to the O–H bond of the BAS, and the planes spanned by the carbon atoms of benzene or propene (Scheme 7c and d). Due to the definition of both angles and for symmetry reasons, α and β can vary between 0° and 90°. The accessible (α, β) range is furthermore restricted by the boundary condition that $\alpha + \beta = 90°$, which also originates from the definition of both angles. The orientations of benzene and propene corresponding with the boundaries are shown in Scheme 8. It can be expected that a higher likelihood to adopt a configuration close to (90°, 0°) (Scheme 8c and f), the more accessible the hydrocarbon's π-electrons are for reaction with methanol (*vide infra*). When methoxides are present on the BAS, on the other hand, it can be anticipated that orientations close to (α, β) values of (0°, 0°) (Scheme 8a and d) will be susceptible to reaction with a framework-bound methoxide.

From the MD simulations, also two reactivity indices were calculated which relate to the relative position of the methylating agent and the hydrocarbon with respect to each other and the position of methanol with respect to the BAS. A similar approach was followed in ref. 53. The probability of methanol protonation was calculated as the probability that the O–H interaction distance between methanol's oxygen atom and the proton of the BAS is smaller than 1.2 Å. This index merely represents the intrinsic reactivity of the methanol molecule as it needs to get protonated in any reactive event. To calculate the probability to form a pre-reactive complex between methanol and benzene or propene, three criteria were tested. First, the orientation of methanol and the hydrocarbon with respect to each other has to be favorable, meaning that the methyl group has to point towards the hydrocarbon to enable the methyl transfer. This was expressed by a distance and angle criterion. The distance difference Δ (Scheme 7g and h) between the shortest O–C distance between methanol and the hydrocarbon (d_2) and the shortest C–C-distance between methanol and the hydrocarbon (d_1) had to exceed 0.5 Å. Additionally, an angle γ was introduced to trace the angle between the methanol C–O bond and the plane spanned by the hydrocarbon's carbon atoms (Scheme 7e and f). The angle γ can range from 0° to 90° and both boundaries are presented in Scheme 8g–j for co-adsorbed benzene and propene. The C–O bond was considered to adopt a favorable orientation with respect to the hydrocarbon when γ exceeded the cut-off value of 30°. Finally, also the orientation of the hydrocarbon within the channel has to be favorable to enable the methylation reaction. Indeed, methyl transfer can only take place when the π-electrons of the double bond(s) to which it will attach are accessible for the methyl group. From Schemes 7 and 8 it can be seen that this is the case when α is not too close to zero. Therefore we selected a cut-off value for α of 30°. The full criterion for pre-reactive complex formation was then $\Delta > 0.5$ Å, $\alpha > 30°$ and $\gamma > 30°$.

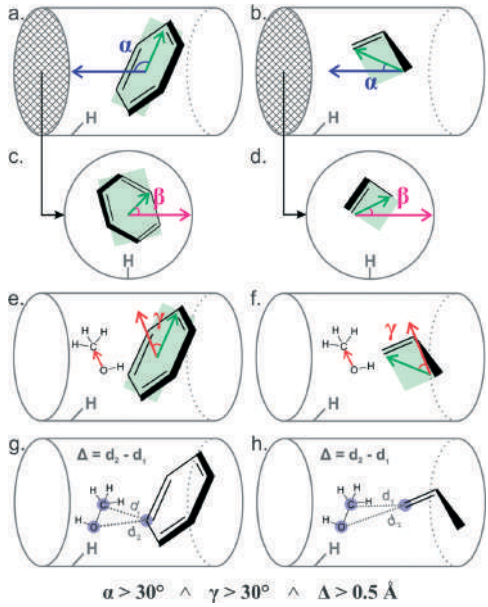

Scheme 7 Schematic representation of the calculated angles between the plane spanned by the carbon atoms of benzene or propene and (a,b) the channel axis (α), (c,d) the channel cross-section (β) and (e,f) the methanol C–O bond (γ) during the set of MD simulations. (g–h) Difference Δ of distances d_2 and d_1 between methanol and benzene or propene.

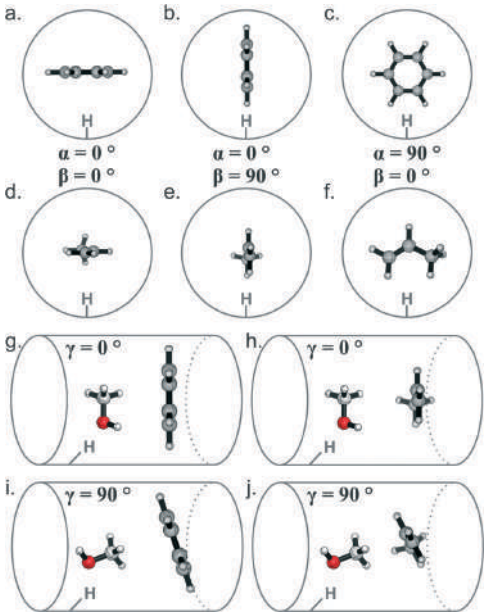

Scheme 8 Orientations of benzene (a–c) and propene (d–f) corresponding with the boundaries of the accessible (α, β) range in a one-dimensional zeolitic channel with indication of the α and β values; orientations in which methanol and benzene (g) or propene (h) are not pointing towards each other (γ = 0°) and orientation in which methanol and benzene (i) or propene (j) do point towards each other (γ = 90°).

3. Results and discussion

By performing advanced MD simulations we aim at obtaining insights into the impact of catalyst topology and acidity, reaction temperature and the presence of additional protic guest in the reaction environment on methylation reactions of benzene and propene under MTH conditions. Therefore, the first goal of this study was to investigate the dynamic behavior and mobility of the reactants for benzene and propene methylation by a detailed MD study. For this purpose, we determined the most probable co-adsorption complexes of methanol with benzene or propene in a detailed MD study and attempted to link these observations with the actual reactivity for the concerted and stepwise methylation reactions.

3.1 Co-adsorption of reactants for benzene and propene methylation

A first set of MD runs comprises simulations of methanol with co-adsorbed benzene or propene in H-SSZ-24, H-SAPO-5 and H-ZSM-22 at 250 °C and 350 °C and around ambient pressure. A first analysis of these runs consists of a thorough assessment of the orientation of the hydrocarbons in the one-dimensional zeolitic pores using the angles α and β as defined in Schemes 7 and 8. For each state sampled during the MD runs, the values for α and β have been calculated. The resulting normalized 2D histograms are shown in Fig. 1 and snapshots corresponding with the (0°, 0°), (0°, 90°) and (90°, 0°) boundaries are displayed in Fig. 2.

From Fig. 1a it seems that benzene is relatively mobile in the AFI channels of H-SSZ-24 at 350 °C as almost the entire accessible (α, β) area has been sampled during a 50 ps simulation. It can also be observed that benzene preferentially adopt an orientation with its plane facing the pore aperture, *i.e.* a structure resembling snapshot 3 in Fig. 2a with (α, β) = (90°, 0°) as suggested by the hotspot indicated by the white arrow in the bottom-right part of Fig. 1a. The snapshot corresponding with this hotspot as displayed in Fig. 3a suggests that with such orientation, the π-electrons of the benzene ring are optimally accessible for methyl transfer from methanol during a methylation reaction. When the temperature for the same system is decreased to 250 °C, benzene becomes slightly less mobile and the preference for favorable structures for methylation in the bottom-right part of the (α, β) plane becomes more pronounced as seen in Fig. 1c. A similar analysis was performed for co-adsorbed propene and it was found that propene is slightly more mobile than benzene in H-SSZ-24 (Fig. 1b and d). The preferential orientation of propene is similar to the one of benzene (Fig. 3b) meaning that also propene's π-electrons of the double bond are likely to be accessible for methyl transfer from methanol during a methylation reaction in H-SSZ-24.

When looking at the results for the AFI-structured H-SAPO-5 material at 350 °C (Fig. 1e and f), one can observe that an even larger range of (α, β) combination has been sampled compared to H-SSZ-24. This might be related with the slightly larger pore size. Indeed, Table S1† shows that the time-averaged super cell volume of H-SAPO-5 is approximately 3% higher than for H-SSZ-24. Consequently, more configurations resembling snapshots 1 and 2 in Fig. 2a and b have been visited compared to H-SSZ-24. Fig. 1e and f display some hotspots indicated by the white arrows for the co-adsorbed complexes, but the normalization of the histograms reveals that in H-SAPO-5 there is a less pronounced preferential orientation of benzene and propene molecules in this less acidic AFI material. This suggests that the slightly larger pore diameter and lower acid strength induce weaker interactions between benzene or propene and the channel walls. This has been confirmed by calculated energies of interaction listed in Table S2.† That benzene interacts stronger with the SSZ-24 framework than with $AlPO_4$–5 was previously reported in an experimental and theoretical adsorption study of McCullen *et al.*[115] Fig. 3c and d displays snapshots corresponding with the co-adsorption hotspots for benzene and propene.

Just as in H-SSZ-24, the hotspots in the orientation histograms become more pronounced for benzene and propene in H-SAPO-5 at 250 °C (Fig. S3†). The multitude of sampled co-adsorbed complexes in the AFI materials gives a first

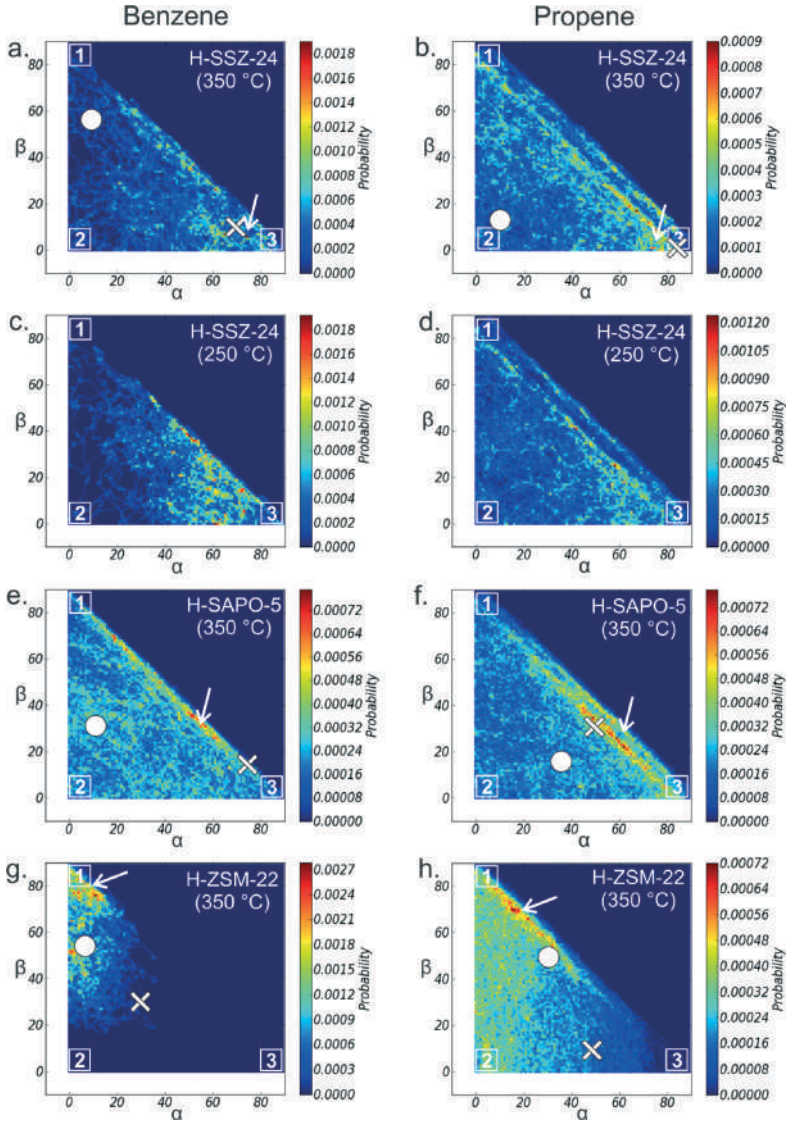

Fig. 1 Two-dimensional normalized histograms displaying the orientation of co-adsorbed benzene and propene in H-SSZ-24 (a–d), H-SAPO-5 (e,f) and H-ZSM-22 (g,h) at 250 °C and 350 °C during a 50 ps MD simulation around ambient pressure and with one methanol molecule. The white arrows indicate the hotspots displayed in Fig. 3, the cross and circle the transition points for methylation by methanol and a methoxide as shown in Fig. 5.

indication of the complexity of the underlying potential and free energy surfaces for further methylation reactions.

Finally, the influence of the channel size was assessed by considering the TON-structured H-ZSM-22 catalyst. Fig. 1g clearly shows that benzene's mobility is severely hampered in this 10-ring channel and that benzene now preferentially co-adsorbs with its plane aligned with the channel axis as shown by the high probability to find benzene in a

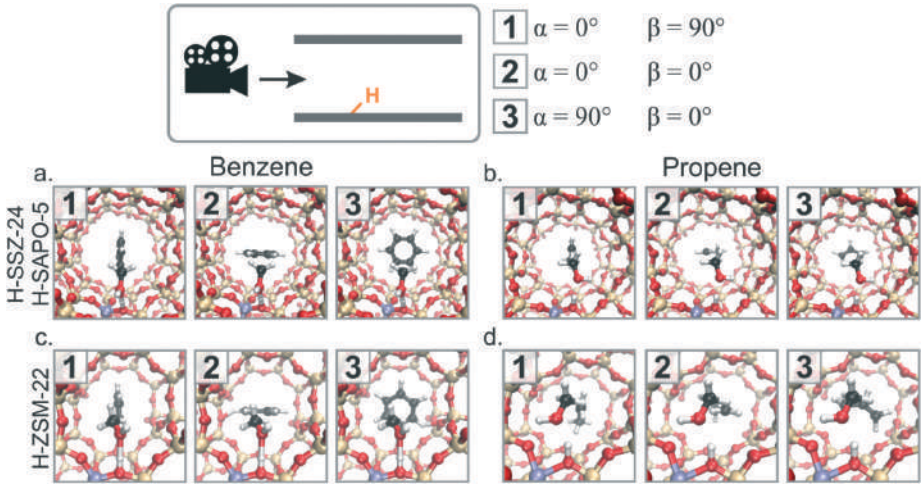

Fig. 2 Snapshots at the boundaries of the accessible (α, β) area for co-adsorbed benzene and propene in the isostructural H-SSZ-24 and H-SAPO-5 materials (a,b) and the TON-structured H-ZSM-22 material (c,d) from MD simulations with one methanol molecule at 350 °C and around ambient pressure.

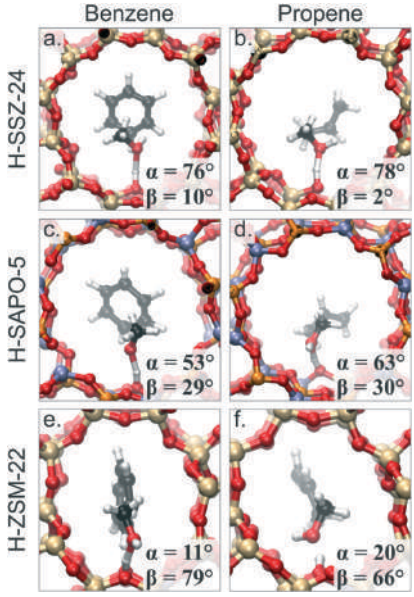

Fig. 3 Snapshots of the most probable co-adsorption complexes of benzene and propene in H-SSZ-24 (a,b), H-SAPO-5 (c,d) and H-ZSM-22 (e,f) from MD simulations at 350 °C and around ambient pressure. The values of α and β are indicated.

configuration with (α, β) = (0°, 0°) (cfr. snapshot 1 in Fig. 2c). In this case, benzene's π-electrons are less accessible for further reaction as also seen in Fig. 3e. Propene, on the other hand, exhibits a much higher mobility in H-ZSM-22 (Fig. 1h) and is thus expected to be more reactive towards methylation than benzene.

Furthermore, Fig. 1 displays the orientations of benzene and propene adopted during the first barrier crossing of the concerted methylation (indicated by the cross) and stepwise methylation (indicated by the circle) as sampled during the MTD simulations at 350 °C (see section 3.3). The proximity of the co-adsorption hotspots indicated by the white arrows and orientation for the concerted methylation for benzene and propene in H-SSZ-24 and propene in H-SAPO-5 makes us expect a high reactivity towards these reaction steps. In H-ZSM-22, on the other hand, it can be anticipated that methylation by a methoxide will be more reactive than by methanol.

To assess the influence of an additional methanol molecule on the co-adsorption behavior prior to methylation we also performed simulations of benzene and propene with 2 methanol molecules in H-SSZ-24 and H-SAPO-5 at 350 °C. We observed that an additional methanol molecule did not significantly alter the preferential orientation of the co-adsorbed hydrocarbons as seen in Fig. S4.†

From a detailed analysis of the orientation of benzene and propene co-adsorbed with methanol it can be concluded that catalyst topology, acid strength and reaction temperature substantially influence the mobility and preferential orientation of co-adsorption complexes for benzene and propene

methylation. The presence of an additional methanol molecule only has a minor influence. The snapshots depicted in Fig. 3 correspond to the hotspot regions in Fig. 1 and thus represent the most probable co-adsorbed complexes. Between H-SSZ-24 and H-SAPO-5, some differences can be noted between the orientations of benzene and propene in these most probable co-adsorbed complexes, which are originating from weaker interactions between the hydrocarbon guest molecules and the H-SAPO-5 framework. In H-ZSM-22, on the other hand, significantly different orientations were adopted compared to the AFI catalysts due to severe confinement effects. This effect is more pronounced for benzene than for propene. The medium-pore zeolite H-ZSM-22 severely restricts the mobility of guest molecules like benzene and propene compared to the large-pore AFI materials, which is expected to have implications on the kinetics and mechanism of methylation reactions.

3.2 Reactivity indices from MD

The preceding discussion pointed towards some more or less reactive configuration of the reactants for methylation in the (α, β) space. In this section, we explicitly study some reactivity indices computed from the MD trajectories as introduced in section 2.4. These indices correspond to favorable orientations of methanol and benzene or propene with respect to each other for methylation reactions. The indices were defined as the probability that methanol is protonated and the probability that methanol and the hydrocarbon form a pre-reactive complex for direct methylation according to the concerted pathway. Fig. 4 displays these two indices for propene and benzene co-adsorbed with one methanol molecule in H-SSZ-24, H-SAPO-5 and H-ZSM-22 at 250 and 350 °C.

In Fig. 4 the impact of three factors as presented in Scheme 3 becomes clear, *i.e.* catalyst acidity, topology and reaction temperature. The results show a clear clustering per material, indicating that acid strength and topology significantly influence these indices and thus the reactivity towards direct methylation. The probability to protonate methanol during the 50 ps MD runs increases in the order H-SAPO-5 < H-SSZ-24 < H-ZSM-22. This quantity is directly related to the acid strength of the studied materials and this trend follows the order of acid strength. Indeed, an analysis of the acidic hydroxyl group's bond length shows that H-SAPO-5 is the weakest acid, whereas the zeolites H-SSZ-24 and H-ZSM-22 have a similar acid strength (Fig. S5†). Due to the smaller pores of H-ZSM-22, protonated methanol can be more efficiently stabilized, which might explain the higher probability for methanol protonation compared to H-SSZ-24. Note that many measures for acidity of solid acids are available based on *e.g.* IR spectra and adsorption enthalpies.[116,117] Acid strength also seems to influence the relative reactivity of propene and benzene in the two isostructural AFI materials. Where benzene is more likely to form pre-reactive complexes for methylation in the more acidic H-SSZ-24 material, propene exhibits the highest probability to form favorable co-adsorbed complexes in H-SAPO-5. This is in line with what was earlier reported.[53]

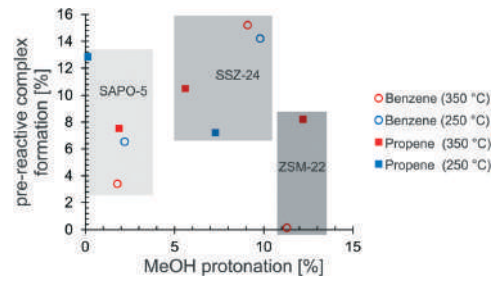

Fig. 4 Probability of methanol protonation and formation of a pre-reactive complex for benzene and propene methylation with one methanol molecule in H-SAPO-5, H-SSZ-24 and H-ZSM-22 at 250 °C (blue symbols) and 350 °C (red symbols).

In H-ZSM-22, propene is able to adopt conformations resembling pre-reactive complexes, but for benzene this is not the case as indicated by the nearly zero probability to form pre-reactive complexes for benzene. Here, the topological effect is clearly visible. According to Fig. 1g, the confined space in the 10-rings of H-ZSM-22 severely limits the mobility of a benzene molecule. Fig. 4 now reveals that this prohibits the spontaneous formation of favorable co-adsorbed complexes for methylation. The most probable co-adsorption complexes of methanol and benzene or propene shown in Fig. 3e and f already revealed that in these most probable configurations, the π-electrons of the hydrocarbons are not easily accessible for reaction with methanol.

The reaction temperature mainly impacts the vertical axis in Fig. 4. In H-SAPO-5, an increased temperature induces a lower probability to find a favorable co-adsorbed complex, whereas the reverse was found in H-SSZ-24. This can be attributed to a different temperature dependence of geometrical parameter Δ (Scheme 7g and h) in both AFI materials. While the probability that α and γ are larger than 30° only slightly decreases with increasing temperature, the probability that Δ is larger than 0.5 Å increases in H-SSZ-24 and decreases in H-SAPO-5 (Fig. S6 and Table S3†). As this different temperature behavior is not straightforwardly reflected in the calculated free energy barriers (*vide infra*), it is hypothesized that our reactivity indices are not robust enough to properly distinguish between the two applied temperatures.

A similar analysis has been performed for the simulations of benzene with an additional methanol molecule. Addition of a methanol molecule to the co-adsorbed methanol–benzene system results in the formation of (protonated) hydrogen bonded clusters of the protic molecules which was found to mainly affect the reactivity index concerning methanol protonation. In H-SSZ-24 we found a 82% chance to find a methanol dimer, whereas this probability was only 27% in H-SAPO-5. For co-adsorbed benzene in H-SSZ-24 at 350 °C, the probability for methanol protonation increased from 9% for

a single methanol molecule at the BAS to 47% for two methanol molecules. Under the same conditions in H-SAPO-5, these probabilities were 2% and 10%. These results show that two methanol molecules more likely deprotonate the BAS prior to reaction than a single methanol molecule. These results correspond with earlier findings from theoretical studies applying static and dynamical approaches, stating that two methanol molecules are able to deprotonate the BAS in zeolitic catalysts.[49,118–122] Even if an additional methanol molecule is present, the lower acid strength of H-SAPO-5 as compared to H-SSZ-24 is still reflected in the relatively low probabilities to protonate methanol.

A convergence check of the calculated probabilities confirmed that the 50 ps MD simulations give sufficient sampling to obtain reliable results concerning co-adsorption behavior (see Fig. S7 of the ESI†).

Our simulations show that catalyst topology, acidity, reaction temperature and presence of an additional protic molecule have an important influence on the tendency to form protonated methanol and the probability to form a co-adsorbed complex for direct methylation in which the methyl group points towards the hydrocarbon and thus interacts with the π-electrons of its double bond(s). Based on these indices, it is expected that benzene and propene in H-SSZ-24, propene in H-SAPO-5 and propene in H-ZSM-22 will exhibit a high reactivity for the concerted methylation at 350 °C. In the next section these insights based on the dynamic co-adsorption behavior and mobility of guest molecules in the zeolite pores will be coupled to intrinsic free energy barriers for methylation.

3.3 Influence of reaction conditions on the free energy barriers for methylation

3.3.1 Catalyst topology, acidity and reaction temperature. After the MD simulations, metadynamics simulations were carried out to explicitly sample the reactive events. This allows to directly assess the impact of the factors listed in Scheme 4, *i.e.* zeolite topology and acidity, reaction temperature and presence of an additional guest molecule on the mechanism and free energy barriers for benzene and propene methylation. Hereby, we aimed at correlating the intrinsic reactivity from the MTD simulations with the in depth analysis of co-adsorbed complexes from the MD simulations and in particular the preferred orientation of co-adsorbed complexes or so-called hotspots (Fig. 1 and 3). As mentioned before, it is known that methylation reactions occur either in a concerted or stepwise fashion (see Scheme 3) and the MTD study specifically focused on the governing reaction mechanism.

We started the MTD simulations from equilibrated structures of the MD simulations of benzene or propene co-adsorbed with a single methanol molecule. Initially, explorative MTD simulations employing three collective variables were performed as sketched in Scheme 6 to obtain insights into the competition of the concerted and stepwise pathways when all molecules are adsorbed. The advantage of such MTD simulation is that it enables simulating competitive pathways in one run under the same conditions. As the MTD algorithm in principle first crosses the lowest free energy barrier, we can as such obtain information on the lowest activated mechanism by inspecting which barrier has been crossed first. For all simulations with one methanol molecule, it seemed that the concerted reaction step is the lowest activated step when all molecules are adsorbed in the system. At 350 °C methoxide formation has been sampled later in the simulation for all systems, whereas methoxide formation was never sampled at 250 °C during the 3D MTD simulations. This already indicates that the stepwise mechanism becomes a viable pathway at relatively high temperatures, which has been related with an entropic effect in earlier studies.[32,92]

To calculate free energy barriers, a set of 2D simulations was carried out for all systems. The resulting intrinsic free energy barriers and free energies of reaction for the concerted ($\Delta G^{\ddagger}_{\text{concerted}}$) and stepwise ($\Delta G^{\ddagger}_{\text{step1}}$, $\Delta G_{\text{r,step1}}$ and $\Delta G^{\ddagger}_{\text{step2}}$) benzene and propene methylations with one methanol molecule at 350 °C and 250 °C in H-SSZ-24, H-SAPO-5 and H-ZSM-22 are listed in Table 1, the corresponding FESs are displayed in Fig. S8–S11.† It was assumed that methoxide formation is not influenced by the hydrocarbon guest molecule and as such, only one set of $\Delta G^{\ddagger}$ and ΔG_{r} values is reported for methoxide formation per material and per temperature. Note that the aim was not to calculate the most accurate free energy barriers; instead we wanted to observe important trends related to the process conditions we are investigating in this study. To obtain barriers near chemical accuracy, other techniques need to be applied which are computationally extremely demanding. Such methods may be used for benchmark purposes on a selected set of reactions as was done in the work of Svelle and co-workers[35] and Göltl and co-workers.[45,123] Furthermore for AFI type materials under study here, it was shown by the present authors that not one single transition state exists, but rather a transition state ensemble which may be quite broad.[49] For ZSM-22, Brogaard found better defined transition states and in this case static methods might be employed as well.[32]

From the results for benzene and propene methylation in H-SSZ-24 at 350 °C it is clear that a concerted methylation is preferred over a methoxide formation, which is consistent with what was seen during the explorative 3D metadynamics simulations (*vide supra*). Indeed, the intrinsic free energy barriers for the concerted pathways (134 ± 3 and 123 ± 2 kJ mol^{-1} for benzene and propene, respectively) are significantly lower than the free energy barrier for methoxide formation (160 ± 3 kJ mol^{-1}). Moors *et al.* calculated that the concerted benzene methylation in H-ZSM-5 at 400 °C exhibits a free energy barrier of only 118 ± 5 kJ mol^{-1}.[51] The higher value of 134 ± 3 kJ mol^{-1} obtained here for H-SSZ-24 at 350 °C can be attributed to a more optimal fit of the reacting molecules in the MFI channel intersections than in the large AFI pores.[56] Methylations by methoxides under these conditions seem to be only slightly higher activated (137 ± 2 and 132 ± 1 kJ mol^{-1} for benzene and propene, respectively) compared to the

Table 1 Free energy barriers and reaction energies in kJ mol^{-1} for the concerted ($\Delta G^{\ddagger}_{concerted}$) and stepwise methylation ($\Delta G^{\ddagger}_{step1}$, $\Delta G_{r,step1}$, $\Delta G^{\ddagger}_{step2}$) for benzene and propene with 1 methanol molecule at 250 °C and 350 °C in H-SSZ-24, H-SAPO-5 and H-ZSM-22. Values for propene methylation in H-ZSM-22 at 400 °C between parenthesis were taken from Brogaard et al[32]

			Concerted	Stepwise		
			$\Delta G^{\ddagger}_{concerted}$ (kJ mol^{-1})	$\Delta G^{\ddagger}_{step1}$ (kJ mol^{-1})	$\Delta G_{r,step1}$ (kJ mol^{-1})	$\Delta G^{\ddagger}_{step2}$ (kJ mol^{-1})
H-SSZ-24	Benzene	350 °C	134 ± 3	160 ± 3	46 ± 4	137 ± 2
		250 °C	136 ± 1	179 ± 3	48 ± 4	127 ± 1
	Propene	350 °C	123 ± 2	160 ± 3	46 ± 4	132 ± 1
		250 °C	118 ± 1	179 ± 3	48 ± 4	152 ± 3
H-SAPO-5	Benzene	350 °C	156 ± 1	162 ± 3	3 ± 1	130 ± 1
		250 °C	165 ± 4	180 ± 5	18 ± 5	[a]
	Propene	350 °C	128 ± 5	162 ± 3	3 ± 1	127 ± 1
		250 °C	131 ± 1	180 ± 5	18 ± 5	152 ± 2
H-ZSM-22	Benzene	350 °C	151 ± 2	148 ± 3	31 ± 2	124 ± 3
	Propene	350 °C	115 ± 1 (122)	148 ± 3 (158)	31 ± 2 (1)	101 ± 1 (65)

[a] No converged value could be obtained.

concerted reaction with methanol. A similar intrinsic reactivity of methanol and methoxides was also reported by Van der Mynsbrugge *et al.* and Brogaard *et al.* for alkene methylation in H-ZSM-5 and H-ZSM-22 with a static DFT approach.[32,52]

When comparing the intrinsic free energy barriers for benzene and propene at 350 °C, it seems that propene methylation is lower activated than benzene methylation by approximately 11 kJ mol^{-1}. Experimentally measured rates however show that benzene methylation occurs faster than propene methylation in H-SSZ-24 at 350 °C.[53] However, experimentally one measures the apparent kinetics, hence direct comparison with our intrinsic reactivity study is not possible. Moreover, Brogaard and co-workers stressed that it is in general not possible to compare calculated apparent activation energies of methylation reactions with values obtained from steady-state kinetic experiments.[32] Calculation of apparent free energy barriers and kinetics requires the determination of the reaction order for each reactant to construct a rate expression and subsequently the accurate determination of adsorption and co-adsorption free energies. This is however beyond the scope of this work.

When the temperature is lowered to 250 °C, the differences between the free energy barriers for the concerted and stepwise methylations in H-SSZ-24 become more pronounced. The free energy barriers for the concerted benzene and propene methylations are not very sensitive to the applied temperature change as differences lie within the 5 kJ mol^{-1} error margin of barriers calculated with DFT methods. This indicates that no major entropic effects are at play for this reaction mechanism. The free energy barrier for methoxide formation instead increased substantially (17 kJ mol^{-1}) with decreasing temperature, suggesting this reaction exhibits a considerable entropic barrier. This effect has in earlier studies been attributed to the intermediate release of a water molecule and attachment of the methyl group to the framework during methoxide formation.[32,92] Brogaard and co-workers pointed out that the stepwise mechanism for propene methylation in H-ZSM-22 becomes important at temperatures above 327 °C based on a combined study comprising TAP kinetic experiments, DFT calculation and micro-kinetic modeling.[32]

In the weaker acidic H-SAPO-5 catalyst, the concerted pathway also seems to dominate the benzene and propene methylation. Note however that in the case of benzene methylation a concerted methylation (156 ± 1 kJ mol^{-1}) and methoxide formation (162 ± 3 kJ mol^{-1}) at 350 °C are almost equally high activated, which is not the case for propene (128 + 5 kJ mol^{-1} *versus* 162 ± 3 kJ mol^{-1}). The free energy barrier for the concerted benzene and propene methylations at 350 °C in H-SAPO-5 are respectively around 22 and 5 kJ mol^{-1} higher than in H-SSZ-24. Intuitively, one would expect that a lower acid strength results in higher intrinsic free energy barriers; however benzene methylation seems to be much more sensitive to acid strength than propene methylation. A possible explanation has been proposed by Iglesia and co-workers, stating that transition states with localized charges are less sensitive to acid strength than those with diffuse charges.[124] It can indeed be expected that the positive charge on the transition state for propene methylation is more localized than for benzene, due to the conjugated π-system of the latter. The difference of 22 kJ mol^{-1} between the $\Delta G^{\ddagger}_{concerted}$ values for benzene and propene methylation at 350 °C in H-SAPO-5 further show that the intrinsic reactivity towards methylation of propene is higher than benzene. Returning to the reactivity indices presented in Fig. 4, this might be related with the fact that propene is more likely to form pre-reactive complexes with methanol for methylation than benzene in H-SAPO-5.

In the context of the MTH process, these findings are in line with the experimental observation that in H-SAPO-5 the alkene cycle dominates product formation whereas aromatics are the main HP species during methanol conversion in H-SSZ-24.[53,82,87] To the best of our knowledge no direct experimentally derived kinetics are available for methylation reactions in the AFI topology. It should however be noted that the two reactivity indices extracted from MD, being methanol protonation and pre-reactive complex formation for methylation, were found to correlate well with experimentally

measured reaction rates for methylation at 350 °C. Benzene methylation was found to be much faster than propene methylation in H-SSZ-24, whereas both reactions occurred at similar rates in H-SAPO-5. So far, no experimentally defined free energies of activation have been reported.[53]

Methoxide formation does not exhibit a significant influence of acid strength, which can again be related with the rather localized positive charge on the methyl cation in the transition state (see ESI† section 10 for a further discussion). Furthermore, it seems that methoxides in H-SAPO-5 at 350 °C are much more stable with respect to the reactants than in H-SSZ-24 as can be seen from the largely differing $\Delta G_{\text{rsstep1}}$ values in both materials, which can be related with the lower acid strength of the H-SAPO-5 framework. At 350 °C methoxides appear to be very reactive towards methylation in H-SAPO-5. When comparing the $\Delta G^{\ddagger}_{\text{step2}}$ values for benzene and propene H-SAPO-5 (130 ± 1 and 127 ± 1 kJ mol^{-1}) and H-SSZ-24 (137 ± 2 and 122 ± 1 kJ mol^{-1}) it can also be observed that methylation by a methoxide are not very sensitive to acid strength. In H-SAPO-5, the influence of lowering the temperature by 100 °C is similar as in H-SSZ-24.

Finally, a similar set of simulations has been performed in the H-ZSM-22 catalyst model. From the free energy barriers for benzene methylation at 350 °C is seems that the concerted pathway (151 ± 2 kJ mol^{-1}) and the first step of the stepwise pathway (148 ± 3 kJ mol^{-1}) are equally high activated, suggesting both mechanisms might be active at 350 °C in this material. That methylation of benzene with methanol in H-ZSM-22 exhibits relatively high $\Delta G^{\ddagger}$ values, despite the high acid strength, can be understood in view of the restricted mobility of benzene in the TON channels, inhibiting the formation of favorable pre-reactive complexes (see Fig. 1g and 4). For propene a high probability to form pre-reactive complexes for a concerted methylation step (Fig. 4) was found and this is clearly reflected in the relatively low free energy barrier $\Delta G^{\ddagger}_{\text{concerted}}$ (115 ± 1 kJ mol^{-1}). In Table 1 values in parentheses for propene methylation in H-ZSM-22 at 400 °C were taken from the work of Brogaard *et al.*, in which a static periodic BEEF-vdw approach was applied. There is a relatively good agreement between those results and our dynamical revPBE-D3 free energy barriers for concerted methylation and methoxide formation at 350 °C. Our calculations show that methoxides are less stable with respect to physisorbed methanol and also less reactive towards methylation of propene, compared to the results of Brogaard *et al.* For ZSM-22 transition state valleys are less broad and a relatively good correspondence between static and dynamic approaches may be expected, as observed here. Indeed, in terms of hydrocarbon orientation, the ensemble of transition states sampled with metadynamics in H-ZSM-22 is less broad than in the AFI materials (Fig. S14,† *vide infra*). This conclusion is also supported by the well-defined co-adsorption complexes of methanol and benzene or propene as displayed by the relatively small accessible (α, β) area in Fig. 1g and h as compared to what was found for the AFI materials.

It can further be observed from Table 1 that propene is much more reactive towards methylation than benzene in H-ZSM-22, which is in line with what the MD based reactivity indices in Fig. 4 suggested and the experimental observation that the alkene cycle dominates in H-ZSM-22. Several experimental studies clearly pointed out that methanol conversion in H-ZSM-22 occurs through the alkene cycle and that aromatic HP species are not active.[73–75,77,78,125] Cui *et al.* reported that olefin growth occurs by subsequent methylation reactions and confirmed that growth of aromatic molecules was inhibited in the medium-sized pores of ZSM-22.[73] These findings are also clearly reflected in the free energy barriers for benzene and propene methylation reported in Table 1. Indeed, despite the relatively easy proton transfer reflected in the high probability to protonate methanol, the formation of favorable pre-reactive complexes for benzene methylation is hindered by spatial restrictions. In this respect, the results reported by Teketel *et al.* are worth mentioning as they claim to suppress the space demanding aromatics based MTO mechanism during methanol conversion in H-ZSM-22.[76–78] Analysis of the retained coke species after their MTO experiments showed that benzene derivatives are deactivating molecules during the reaction. Based on a single-event micro-kinetic modeling study, Kumar *et al.* also concluded that the alkene cycle dominates during methanol conversion in H-ZSM-23, which has a similar topology as H-ZSM-22.[31] Furthermore, the results for H-ZSM-22 in Table 1 show that methoxides are more reactive towards methylation than methanol, which can be understood in view of the less space demanding transition states during methylation by a methoxide as compared to physisorbed methanol (see Fig. 5).

Fig. 5 displays snapshots from the MTD simulations at 350 °C of benzene and propene methylation by methanol or a methoxide (a more extensive overview is given in Fig. S12†). For each snapshot, the values for α and β at the top of the barrier are displayed and these values were indicated with a cross and circle in the histograms of Fig. 1 for a concerted and stepwise methylation step respectively. The entire evolution of the geometrical parameters α, β, γ and Δ as defined in Scheme 7 during reaction are displayed in Fig. S13.† We observed important reorientations of the guest molecules inside the one-dimensional pores during the barrier crossings (see videos in ESI†). In the AFI topology high α values and low β values are adopted during the concerted methylation by methanol, whereas low α values and high β values are required for methylation by a methoxide. It can be concluded that if a co-adsorption hotspot (white arrow in Fig. 1) occurs in the same (α, β) value range as a required orientation for methylation by methanol (cross in Fig. 1) or a methoxide (circle in in Fig. 1), the system is very reactive towards a methylation. This is particularly the case for benzene and propene in H-SSZ-24 and propene in H-SAPO-5 (Fig. 1), which indeed all exhibit relatively low intrinsic free energy barriers in the range of 123–134 kJ mol^{-1}. This also fits the hypothesis based on the reactivity indices discussed in section 3.2. In the TON-structured H-ZSM-22 catalyst, the guest molecule orientations

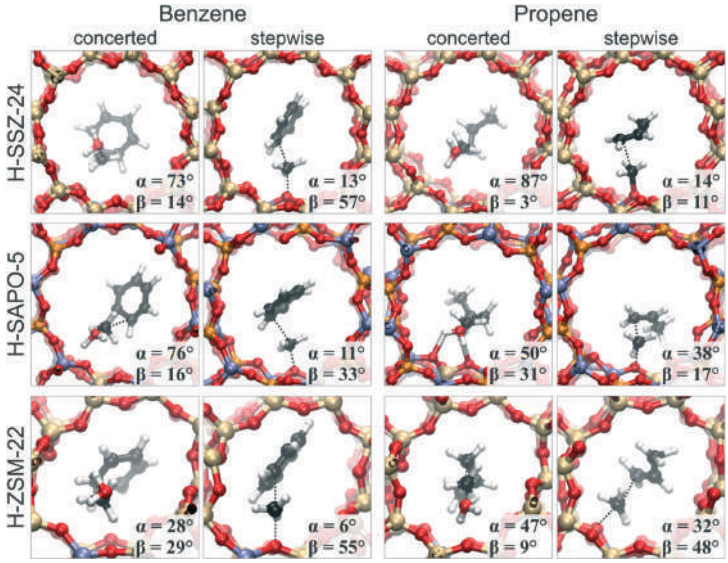

Fig. 5 Snapshots of barrier crossings during MTD simulations of benzene methylation by methanol (concerted) or a methoxide (stepwise) at 350 °C in H-SSZ-24, H-SAPO-5 and H-ZSM-22 with indication of the α and β value.

are much more confined and co-adsorption hotspots in Fig. 1g and h do not correspond to favorable orientations for methylation. In particular for the concerted benzene methylation in H-ZSM-22, an orientation has to be adopted that lies in a low probability region in Fig. 1g. It can thus be expected that in such case the reorientation of the hydrocarbons is an activated process and thus contributes to the relatively high free energy barrier for direct benzene methylation (151 ± 2 kJ mol^{-1}). The range in which the angles α and β varied along the reaction paths sampled with the MTD simulations are presented in Fig. S14.†

A close inspection of the hydrocarbon orientation during simulation of concerted and stepwise methylation reactions revealed a correlation between co-adsorption hotspots prior to reaction, orientations at the top of the barrier and free energy barriers. Catalyst topology, acidity and reaction temperature each have a distinct impact on the reaction mechanism and kinetics and it seemed that this impact is not uniform for all reactions and differs for benzene and propene methylation.

3.3.2 Additional guest molecules. An additional set of MTD simulations of benzene methylation at 350 °C has been carried out, in which an additional methanol molecule was present around the BAS. Such additional protic molecule might play an active role during reactions in which proton transfer occurs, in this case the concerted methylation step and methoxide formation. The 2D FESs are displayed in Fig. S15.† The resulting free energy barriers and free energies of reaction are listed in Table 2.

Comparison between the results for one or two methanol molecules listed in Table 2 shows that the free energy barriers for the concerted methylation are all lowered by the presence of an additional protic molecule and the effect on the free energy barriers is more pronounced in H-SAPO-5 than in H-SSZ-24. In H-SSZ-24, methoxide formation is also facilitated by methanol; the assistance lowers the $\Delta G^{\ddagger}_{\text{step1}}$ values by 9 kJ mol^{-1}. This is however not the case in H-SAPO-5, in which methanol presence increases the free energy barrier for methoxide formation by 17 kJ mol^{-1}. This observation could be attributed to the low probability for methanol–methanol interactions in H-SAPO-5 in the absence of a hydrocarbon in the reactant state. Prior to reaction, the probability that the two methanol molecules interact *via* a hydrogen bond in H-SAPO-5 was less than 10%, whereas this was around 60% in H-SSZ-24. In H-SAPO-5 the assisting methanol

Table 2 Free energy barriers and reaction energies in kJ mol^{-1} for the concerted methylation of benzene ($\Delta G^{\ddagger}_{\text{concerted}}$) and methoxide formation ($\Delta G^{\ddagger}_{\text{step1}}$ and $\Delta G_{\text{r,step1}}$) by methanol assisted by an additional methanol molecule at 350 °C in H-SSZ-24 and H-SAPO-5. Reference values with 1 methanol molecule are given (cfr. Table 1)

		Concerted	Stepwise	
	350 °C benzene	$\Delta G^{\ddagger}_{\text{concerted}}$ (kJ mol^{-1})	$\Delta G^{\ddagger}_{\text{step1}}$ (kJ mol^{-1})	$\Delta G_{\text{r,step1}}$ (kJ mol^{-1})
H-SSZ-24	1 MeOH	134 ± 3	160 ± 3	46 ± 4
	2 MeOH	129 ± 5	151 ± 1	38 ± 1
H-SAPO-5	1 MeOH	156 ± 1	162 ± 3	3 ± 1
	2 MeOH	142 ± 5	179 ± 1	43 ± 2

molecule mainly gets involved in the reaction once the reacting molecule is fully protonated, meaning that the enthalpic gain of the assistance is probably not high enough to compensate the associated entropic penalty.

The snapshots shown in Fig. 6 clearly show how 2 methanol molecules pair up to form a protonated hydrogen bonded cluster prior to reaction. However, we also observed reaction paths in which the additional methanol molecule did not play an active role (Fig. S16 and S17†). For the given conditions, it is thus not straightforward how such additional methanol molecule affects the kinetics and mechanism of benzene methylation. It can be expected that participation of an additional protic molecule introduces an additional entropic barrier; however an extended study is beyond the scope of this work.

4. Conclusions

In this study state-of-the-art advanced *ab initio* molecular dynamics (MD) techniques were used to assess the impact of reaction conditions and catalyst material on some crucial reaction steps of the zeolite-catalyzed methanol conversion process. In particular, the influence of catalyst topology and Brønsted acidity, reaction temperature and presence of an additional methanol molecule on the adsorption behavior and reaction mechanism and kinetics was investigated. The methylation of benzene and propene were selected as case studies as these are crucial reaction steps in the MTH chemistry. It is known that these reactions can occur either in a concerted or stepwise fashion, *i.e.* methanol directly transfers its methyl group to a hydrocarbon or the reaction goes through a framework-bound methoxide intermediate. The dynamical approach enables mimicking true reactions conditions as close as possible and studying the competition between two competing methylation mechanisms in an integrated fashion. The selectivity for one or the other mechanism has earlier been suggested to be entropy driven. A set of DFT-based MD and MTD simulations, which fully account for the mobility of the reacting species, has been performed on benzene and propene methylation in the AFI-structured H-SSZ-24 and H-SAPO-5 and the TON-structured H-ZSM-22 catalysts at 250 and 350 °C.

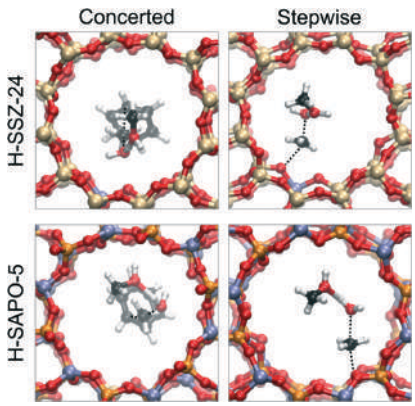

Fig. 6 Snapshots of barrier crossings during MTD simulations of the concerted benzene methylation and first step of the stepwise pathway (methoxide formation) in H-SSZ-24 and H-SAPO-5 at 350 °C assisted by an additional methanol molecule.

Our MD simulations point out that a vast number of co-adsorbed complexes can be formed for benzene and propene co-adsorbed with methanol, especially in AFI-structured materials. Nonetheless, some co-adsorption hotspots could be identified that correspond to the most probable co-adsorption complex. The location of these hotspots and thus the preferential orientation of benzene and propene in the pores were largely influenced by the catalyst topology and acidity, while temperature and presence of an additional methanol molecule only had a minor impact.

Additional insights on the reactivity towards methylation of these co-adsorption complexes were obtained by calculating the probability to protonate methanol and the probability to form favorable pre-reactive complexes for methylation. These indices and the insights based on the co-adsorption hotspots showed a clear correlation with the reactivity as calculated from the metadynamics simulations.

Next to the dynamical co-adsorption behavior and mobility of the guest molecules, the investigated process parameters also influenced the competition between a concerted and stepwise methylation mechanism. This competition was simulated by a large number of metadynamics simulations to obtain free energy barriers for every reaction step. At higher temperatures the stepwise pathway might become competitive with the concerted methylation, which indeed confirms the distinct entropic effects for both mechanisms. However, the competition between the two pathways is largely influenced by the specific material and hydrocarbon species. We observed in particular that for benzene methylation in H-SAPO-5 and H-ZSM-22 that a concerted methylation step and methoxide formation are nearly equally high activated. For a further assessment of this competition, the use of microkinetic models could be beneficial.

The influence of the catalyst's acid strength was assessed by comparison of results for two isostructural AFI materials H-SSZ-24 and H-SAPO-5, which have different framework compositions and thus acid strengths. In both materials slightly different co-adsorption complexes were found due to different interactions between the hydrocarbons and the zeolitic walls. In both materials, the concerted methylation dominates benzene and propene methylation, even at 350 °C. The impact of catalyst acidity on the free energies of activation does not seem to be uniform, but rather depends on the reaction type (concerted or stepwise) and the hydrocarbon undergoing the reaction, *i.e.* benzene or propene. As reported earlier in a combined experimental and theoretical study, benzene is more reactive towards methylation in H-SSZ-24,

whereas propene is more reactive in H-SAPO-5. This also corresponds with the experimental observation that the alkene mechanism dominates product formation during MTH reactions in H-SAPO-5, whereas aromatics are the most active HP species in H-SSZ-24.

Next, we also compared results for the AFI materials and TON catalyst to demonstrate the role of confinement on the methylation mechanism. Due to restricted mobility in the 10-ring channels, benzene exhibits a low reactivity towards methylation which can be related with its role as deactivating HP compound during methanol conversion. Once methoxides are formed, it is more probable that benzene gets methylated by a framework-bound methoxide due to a less space demanding transition state. Propene, which is assumed to be the dominant HP species in H-ZSM-22, indeed exhibits relatively low barriers for methylation from methanol and a methoxide. The higher reactivity of propene and low reactivity of benzene towards methylation are in line with experimental studies reporting that the medium-sized TON channels suppress the aromatics based reaction cycle and promote the alkene cycle during methanol conversion.

Finally, we addressed the impact of an additional methanol molecule on the kinetics of benzene methylation. The presence of such additional protic guest molecule mainly influences the ease of methanol protonation prior to reaction. We observed two types of reaction paths: paths in which the additional methanol actively participates and paths in which it doesn't. It seemed that the influence of such assistance on the free energy barriers of benzene methylation is not straightforward. Further dedicated studies on the impact of guest molecule loading and in particular the feed composition on the reaction mechanism are recommended from both an experimental and theoretical viewpoint.

Catalyst topology and acidity, reaction temperature and the presence of additional guest molecules, as included in this study each have a distinct impact on the reactivity of benzene and propene towards concerted or stepwise methylation. Our study clearly shows that obtaining profound insights into each of these factors is a complex task. However, by ingeniously selecting or varying each of the four factors, one is able to tune the reaction mechanism of an elementary zeolite-catalyzed reaction step. As we set focus on the complex dynamical behavior of the guest molecules in the pores, MD based techniques were the methods of choice in this study. As put forward in our recent review paper, theoretical models have matured substantially in the last decades. Chemical accuracy for barriers and kinetics was achieved for some particular case studies where the active site and mechanism was known, by using static yet very accurate theoretical methods. To deal with complexity at operating conditions complementary methods are needed as was shown in this paper. Future treatment of zeolite catalyzed reactions at operating conditions will need a close integration of different modeling tools at various length and time scales as was pointed out in ref. 12.

Acknowledgements

We thank the Foundation of Scientific Research – Flanders (FWO), the Research Board of Ghent University, BELSPO (IAP P7/05) and the European Union's Horizon 2020 research and innovation programme (consolidator ERC grant agreement no 647755 – DYNPOR (2015-2020)). Computational resources and services were provided by the Stevin Supercomputer Infrastructure of Ghent University and by the Flemish Supercomputer Center (VSC), funded by the Hercules Foundation and the Flemish Government – department EWI.

References

1 M. Guisnet and J. P. Gilson, *Zeolites for Cleaner Technologies*, Imperial College Press, London, 2002.
2 W. Vermeiren and J. P. Gilson, *Top. Catal.*, 2009, **52**, 1131–1161.
3 B. Yilmaz and U. Muller, *Top. Catal.*, 2009, **52**, 888–895.
4 J. Čejka, G. Centi, J. Perez-Pariente and W. J. Roth, *Catal. Today*, 2012, **179**, 2–15.
5 R. Chal, C. Gerardin, M. Bulut and S. van Donk, *ChemCatChem*, 2011, **3**, 67–81.
6 P. A. Jacobs, M. Dusselier and B. F. Sels, *Angew. Chem., Int. Ed.*, 2014, **53**, 8621–8626.
7 W. J. Roth, P. Nachtigall, R. E. Morris and J. Čejka, *Chem. Rev.*, 2014, **114**, 4807–4837.
8 M. B. J. Roeffaers, G. De Cremer, J. Libeert, R. Ameloot, P. Dedecker, A. J. Bons, M. Buckins, J. A. Martens, B. F. Sels, D. E. De Vos and J. Hofkens, *Angew. Chem., Int. Ed.*, 2009, **48**, 9285–9289.
9 B. M. Weckhuysen, *Angew. Chem., Int. Ed.*, 2009, **48**, 4910–4943.
10 I. L. C. Buurmans and B. M. Weckhuysen, *Nat. Chem.*, 2012, **4**, 873–886.
11 V. Van Speybroeck, K. De Wispelaere, J. Van der Mynsbrugge, M. Vandichel, K. Hemelsoet and M. Waroquier, *Chem. Soc. Rev.*, 2014, **43**, 7326–7357.
12 V. Van Speybroeck, K. Hemelsoet, L. Joos, M. Waroquier, R. G. Bell and C. R. A. Catlow, *Chem. Soc. Rev.*, 2015, **44**, 7044–7111.
13 U. Olsbye, S. Svelle, M. Bjørgen, P. Beato, T. V. W. Janssens, F. Joensen, S. Bordiga and K. P. Lillerud, *Angew. Chem., Int. Ed.*, 2012, **51**, 5810–5831.
14 J. Lefevere, S. Mullens, V. Meynen and J. Van Noyen, *Chem. Pap.*, 2014, **68**, 1143–1153.
15 B. V. Vora, T. L. Marker, P. T. Barger, H. R. Nilsen, S. Kvisle and T. Fuglerud, in *Studies in Surface Science and Catalysis*, ed. M. de Pontes, R. L. Espinoza, C. P. Nicolaides, J. H. Scholtz and M. S. Scurrell, Elsevier, 1997, vol. 107, pp. 87–98.
16 J. Q. Chen, A. Bozzano, B. Glover, T. Fuglerud and S. Kvisle, *Catal. Today*, 2005, **106**, 103–107.
17 H. Koempel and W. Liebner, in *Studies in Surface Science and Catalysis*, ed. F. B. Noronha, M. Schmal, E. Falabella and Sousa-Aguiar, Elsevier, 2007, vol. 167, pp. 261–267.

18 P. Tian, Y. Wei, M. Ye and Z. Liu, *ACS Catal.*, 2015, **5**, 1922–1938.
19 K. Hemelsoet, J. Van der Mynsbrugge, K. De Wispelaere, M. Waroquier and V. Van Speybroeck, *ChemPhysChem*, 2013, **14**, 1526–1545.
20 M. Stöcker, *Microporous Mesoporous Mater.*, 1999, **29**, 3–48.
21 S. Ilias and A. Bhan, *ACS Catal.*, 2013, **3**, 18–31.
22 S. Svelle, U. Olsbye, F. Joensen and M. Bjørgen, *J. Phys. Chem. C*, 2007, **111**, 17981–17984.
23 S. Svelle, F. Joensen, J. Nerlov, U. Olsbye, K. P. Lillerud, S. Kolboe and M. Bjørgen, *J. Am. Chem. Soc.*, 2006, **128**, 14770–14771.
24 M. Bjørgen, F. Joensen, K. P. Lillerud, U. Olsbye and S. Svelle, *Catal. Today*, 2009, **142**, 90–97.
25 D. Chen, K. Moljord and A. Holmen, *Microporous Mesoporous Mater.*, 2012, **164**, 239–250.
26 U. Olsbye, S. Svelle, K. P. Lillerud, Z. H. Wei, Y. Y. Chen, J. F. Li, J. G. Wang and W. B. Fan, *Chem. Soc. Rev.*, 2015, **44**, 7155–7176.
27 K. P. F. Janssen, G. De Cremer, R. K. Neely, A. V. Kubarev, J. Van Loon, J. A. Martens, D. E. De Vos, M. B. J. Roeffaers and J. Hofkens, *Chem. Soc. Rev.*, 2014, **43**, 990–1006.
28 J. Van der Mynsbrugge, M. Visur, U. Olsbye, P. Beato, M. Bjørgen, V. Van Speybroeck and S. Svelle, *J. Catal.*, 2012, **292**, 201–212.
29 S. Svelle, M. Visur, U. Olsbye, Saepurahman and M. Bjørgen, *Top. Catal.*, 2011, **54**, 897–906.
30 P. Kumar, J. W. Thybaut, S. Svelle, U. Olsbye and G. B. Marin, *Ind. Eng. Chem. Res.*, 2013, **52**, 1491–1507.
31 P. Kumar, J. W. Thybaut, S. Teketel, S. Svelle, P. Beato, U. Olsbye and G. B. Marin, *Catal. Today*, 2013, **215**, 224–232.
32 R. Y. Brogaard, R. Henry, Y. Schuurman, A. J. Medford, P. G. Moses, P. Beato, S. Svelle, J. K. Nørskov and U. Olsbye, *J. Catal.*, 2014, **314**, 159–169.
33 S. M. Alwahabi and G. F. Froment, *Ind. Eng. Chem. Res.*, 2004, **43**, 5098–5111.
34 J. Van der Mynsbrugge, K. Hemelsoet, M. Vandichel, M. Waroquier and V. Van Speybroeck, *J. Phys. Chem. C*, 2012, **116**, 5499–5508.
35 S. Svelle, C. Tuma, X. Rozanska, T. Kerber and J. Sauer, *J. Am. Chem. Soc.*, 2009, **131**, 816–825.
36 V. Van Speybroeck, J. Van der Mynsbrugge, M. Vandichel, K. Hemelsoet, D. Lesthaeghe, A. Ghysels, G. B. Marin and M. Waroquier, *J. Am. Chem. Soc.*, 2011, **133**, 888–899.
37 G. Piccini, M. Alessio, J. Sauer, Y. C. Zhi, Y. Liu, R. Kolvenbach, A. Jentys and J. A. Lercher, *J. Phys. Chem. C*, 2015, **119**, 6128–6137.
38 G. Piccini and J. Sauer, *J. Chem. Theory Comput.*, 2013, **9**, 5038–5045.
39 T. Bučko, *J. Phys.: Condens. Matter*, 2008, **20**, 9.
40 B. Ensing, A. Laio, M. Parrinello and M. L. Klein, *J. Phys. Chem. B*, 2005, **109**, 6676–6687.
41 L. Benco, T. Bučko and J. Hafner, *J. Catal.*, 2011, **277**, 104–116.
42 T. Bučko, L. Benco, O. Dubay, C. Dellago and J. Hafner, *J. Chem. Phys.*, 2009, **131**, 11.
43 T. Bučko, L. Benco, J. Hafner and J. G. Angyan, *J. Catal.*, 2011, **279**, 220–228.
44 T. Bučko and J. Hafner, *J. Catal.*, 2015, **329**, 32–48.
45 F. Göltl and J. Hafner, *Microporous Mesoporous Mater.*, 2013, **166**, 176–184.
46 T. Jiang, F. Göltl, R. E. Bulo and P. Sautet, *ACS Catal.*, 2014, **4**, 2351–2358.
47 J. Gomes, M. Head-Gordon and A. T. Bell, *J. Phys. Chem. C*, 2014, **118**, 21409–21419.
48 P. M. Zimmerman, D. C. Tranca, J. Gomes, D. S. Lambrecht, M. Head-Gordon and A. T. Bell, *J. Am. Chem. Soc.*, 2012, **134**, 19468–19476.
49 K. De Wispelaere, B. Ensing, A. Ghysels, E. J. Meijer and V. Van Speybroeck, *Chem. – Eur. J.*, 2015, **21**, 9385–9396.
50 A. Ghysels, S. L. C. Moors, K. Hemelsoet, K. De Wispelaere, M. Waroquier, G. Sastre and V. Van Speybroeck, *J. Phys. Chem. C*, 2015, **119**, 23721–23734.
51 S. L. C. Moors, K. De Wispelaere, J. Van der Mynsbrugge, M. Waroquier and V. Van Speybroeck, *ACS Catal.*, 2013, **3**, 2556–2567.
52 J. Van der Mynsbrugge, S. L. C. Moors, K. De Wispelaere and V. Van Speybroeck, *ChemCatChem*, 2014, **6**, 1906–1918.
53 M. Westgård Erichsen, K. De Wispelaere, K. Hemelsoet, S. L. C. Moors, T. Deconinck, M. Waroquier, S. Svelle, V. Van Speybroeck and U. Olsbye, *J. Catal.*, 2015, **328**, 186–196.
54 S. H. Zheng and J. Pfaendtner, *Mol. Simul.*, 2015, **41**, 55–72.
55 K. De Wispelaere, K. Hemelsoet, M. Waroquier and V. Van Speybroeck, *J. Catal.*, 2013, **305**, 76–80.
56 D. Lesthaeghe, B. De Sterck, V. Van Speybroeck, G. B. Marin and M. Waroquier, *Angew. Chem., Int. Ed.*, 2007, **46**, 1311–1314.
57 D. M. McCann, D. Lesthaeghe, P. W. Kletnieks, D. R. Guenther, M. J. Hayman, V. Van Speybroeck, M. Waroquier and J. F. Haw, *Angew. Chem., Int. Ed.*, 2008, **47**, 5179–5182.
58 C. M. Wang, Y. D. Wang, Z. K. Xie and Z. P. Liu, *J. Phys. Chem. C*, 2009, **113**, 4584–4591.
59 I. M. Hill, S. Al Hashimi and A. Bhan, *J. Catal.*, 2012, **285**, 115–123.
60 S. Svelle, P. A. Ronning and S. Kolboe, *J. Catal.*, 2004, **224**, 115–123.
61 S. Svelle, P. O. Ronning, U. Olsbye and S. Kolboe, *J. Catal.*, 2005, **234**, 385–400.
62 V. Van Speybroeck, K. Hemelsoet, K. De Wispelaere, Q. Qian, J. Van der Mynsbrugge, B. De Sterck, B. M. Weckhuysen and M. Waroquier, *ChemCatChem*, 2013, **5**, 173–184.
63 S. Al-Khattaf, S. A. Ali, A. M. Aitani, N. Zilkova, D. Kubicka and J. Čejka, *Catal. Rev.: Sci. Eng.*, 2014, **56**, 333–402.
64 S. Svelle and M. Bjørgen, *J. Phys. Chem. A*, 2010, **114**, 12548–12554.
65 J. Van der Mynsbrugge, J. De Ridder, K. Hemelsoet, M. Waroquier and V. Van Speybroeck, *Chem. – Eur. J.*, 2013, **19**, 11568–11576.
66 T. Maihom, B. Boekfa, J. Sirijaraensre, T. Nanok, M. Probst and J. Limtrakul, *J. Phys. Chem. C*, 2009, **113**, 6654–6662.

67 H. Yamazaki, H. Shima, H. Imai, T. Yokoi, T. Tatsumi and J. N. Kondo, *Angew. Chem., Int. Ed.*, 2011, **50**, 1853–1856.
68 I. M. Hill, Y. S. Ng and A. Bhan, *ACS Catal.*, 2012, **2**, 1742–1748.
69 I. Hill, A. Malek and A. Bhan, *ACS Catal.*, 2013, **3**, 1992–2001.
70 S. Ilias and A. Bhan, *J. Catal.*, 2012, **290**, 186–192.
71 S. Svelle, S. Kolboe, O. Swang and U. Olsbye, *J. Phys. Chem. B*, 2005, **109**, 12874–12878.
72 Y. Y. Chu, X. Y. Sun, X. F. Yi, L. H. Ding, A. M. Zheng and F. Deng, *Catal. Sci. Technol.*, 2015, **5**, 3507–3517.
73 Z. M. Cui, Q. Liu, Z. Ma, S. W. Bian and W. G. Song, *J. Catal.*, 2008, **258**, 83–86.
74 J. Z. Li, Y. X. Wei, G. Y. Liu, Y. Qi, P. Tian, B. Li, Y. L. He and Z. M. Liu, *Catal. Today*, 2011, **171**, 221–228.
75 J. Z. Li, Y. X. Wei, Y. Qi, P. Tian, B. Li, Y. L. He, F. X. Chang, X. D. Sun and Z. M. Liu, *Catal. Today*, 2011, **164**, 288–292.
76 S. Teketel, U. Olsbye, K. P. Lillerud, P. Beato and S. Svelle, *Microporous Mesoporous Mater.*, 2010, **136**, 33–41.
77 S. Teketel, W. Skistad, S. Benard, U. Olsbye, K. P. Lillerud, P. Beato and S. Svelle, *ACS Catal.*, 2012, **2**, 26–37.
78 S. Teketel, S. Svelle, K. P. Lillerud and U. Olsbye, *ChemCatChem*, 2009, **1**, 78–81.
79 B. P. C. Hereijgers, F. Bleken, M. H. Nilsen, S. Svelle, K. P. Lillerud, M. Bjørgen, B. M. Weckhuysen and U. Olsbye, *J. Catal.*, 2009, **264**, 77–87.
80 M. Bjørgen, S. Akyalcin, U. Olsbye, S. Benard, S. Kolboe and S. Svelle, *J. Catal.*, 2010, **275**, 170–180.
81 M. Bjørgen, U. Olsbye, D. Petersen and S. Kolboe, *J. Catal.*, 2004, **221**, 1–10.
82 M. Westgård Erichsen, S. Svelle and U. Olsbye, *Catal. Today*, 2013, **215**, 216–223.
83 C. Wang, B. Li, Y. Wang and Z. Xie, *J. Energy Chem.*, 2013, **22**, 914–918.
84 A. F. Combariza, G. Sastre and A. Corma, *J. Phys. Chem. C*, 2011, **115**, 875–884.
85 Database of zeolite structures, http://www.iza-structure.org/databases/.
86 F. Bleken, M. Bjørgen, L. Palumbo, S. Bordiga, S. Svelle, K. P. Lillerud and U. Olsbye, *Top. Catal.*, 2009, **52**, 218–228.
87 M. Westgård Erichsen, S. Svelle and U. Olsbye, *J. Catal.*, 2013, **298**, 94–101.
88 X. Y. Sun, S. Mueller, Y. Liu, H. Shi, G. L. Haller, M. Sanchez-Sanchez, A. C. van Veen and J. A. Lercher, *J. Catal.*, 2014, **317**, 185–197.
89 E. Borodina, F. Meirer, I. Lezcano-González, M. Mokhtar, A. M. Asiri, S. A. Al-Thabaiti, S. N. Basahel, J. Ruiz-Martínez and B. M. Weckhuysen, *ACS Catal.*, 2015, **5**, 992–1003.
90 J. H. Ahn, B. Temel and E. Iglesia, *Angew. Chem., Int. Ed.*, 2009, **48**, 3814–3816.
91 D. A. Simonetti, J. H. Ahn and E. Iglesia, *J. Catal.*, 2011, **277**, 173–195.
92 A. J. Jones and E. Iglesia, *Angew. Chem., Int. Ed.*, 2014, **53**, 12177–12181.
93 R. Gounder and E. Iglesia, *Acc. Chem. Res.*, 2012, **45**, 229–238.
94 J. A. Brennan, S. J. Lucki and H. J. Schoennagel, Catalysts for the conversion of methanol to ethylene plus gasoline, *US Pat.*, 4480145, 1984.
95 W. W. Kaeding and S. A. Butter, Conversion of methanol and dimethyl ether, *US Pat.*, 3911041, 1975.
96 A. N. Mlinar, P. M. Zimmerman, F. E. Celik, M. Head-Gordon and A. T. Bell, *J. Catal.*, 2012, **288**, 65–73.
97 J. Hutter, M. Iannuzzi, F. Schiffmann and J. VandeVondele, *Wiley Interdiscip. Rev.: Comput. Mol. Sci.*, 2014, **4**, 15–25.
98 J. VandeVondele, M. Krack, F. Mohamed, M. Parrinello, T. Chassaing and J. Hutter, *Comput. Phys. Commun.*, 2005, **167**, 103–128.
99 G. Lippert, J. Hutter and M. Parrinello, *Theor. Chem. Acc.*, 1999, **103**, 124–140.
100 G. Lippert, J. Hutter and M. Parrinello, *Mol. Phys.*, 1997, **92**, 477–487.
101 K. Yang, J. J. Zheng, Y. Zhao and D. G. Truhlar, *J. Chem. Phys.*, 2010, **132**, 10.
102 S. Goedecker, M. Teter and J. Hutter, *Phys. Rev. B: Condens. Matter Mater. Phys.*, 1996, **54**, 1703–1710.
103 S. Grimme, J. Antony, S. Ehrlich and H. Krieg, *J. Chem. Phys.*, 2010, **132**, 19.
104 D. Frenkel and B. Smit, *Understanding Molecular Simulations*, Academic press, Elsevier, 2nd edn, 2002.
105 G. J. Martyna, D. J. Tobias and M. L. Klein, *J. Chem. Phys.*, 1994, **101**, 4177–4189.
106 A. Laio and F. L. Gervasio, *Rep. Prog. Phys.*, 2008, **71**, 22.
107 P. Tiwary and M. Parrinello, *Phys. Rev. Lett.*, 2013, **111**, 5.
108 L. Goerigk and S. Grimme, *Phys. Chem. Chem. Phys.*, 2011, **13**, 6670–6688.
109 Y. Zhao and D. G. Truhlar, *J. Phys. Chem. C*, 2008, **112**, 6860–6868.
110 Y. Zhao and D. G. Truhlar, *Theor. Chem. Acc.*, 2008, **120**, 215–241.
111 Y. Zhao and D. G. Truhlar, *J. Chem. Theory Comput.*, 2008, **4**, 1849–1868.
112 Y. Zhao and D. G. Truhlar, *Acc. Chem. Res.*, 2008, **41**, 157–167.
113 J. D. Chai and M. Head-Gordon, *Phys. Chem. Chem. Phys.*, 2008, **10**, 6615–6620.
114 J. Wellendorff, K. T. Lundgaard, A. Møgelhøj, V. Petzold, D. D. Landis, J. K. Nørskov, T. Bligaard and K. W. Jacobsen, *Phys. Rev. B: Condens. Matter Mater. Phys.*, 2012, **85**, 235149.
115 S. B. McCullen, P. T. Reischman and D. H. Olson, *Zeolites*, 1993, **13**, 640–644.
116 C. O. Arean, M. R. Delgado, P. Nachtigall, H. V. Thang, M. Rubes, R. Bulanek and P. Chlubna-Eliasova, *Phys. Chem. Chem. Phys.*, 2014, **16**, 10129–10141.
117 E. G. Derouane, J. C. Vedrine, R. R. Pinto, P. M. Borges, L. Costa, M. Lemos, F. Lemos and F. R. Ribeiro, *Catal. Rev.: Sci. Eng.*, 2013, **55**, 454–515.
118 C. Lo, C. A. Giurumescu, R. Radhakrishnan and B. L. Trout, *Mol. Phys.*, 2004, **102**, 281–288.
119 J. Sauer, M. Sierka and F. Haase, in *Transitions State Modeling for Catalysis*, ed. K. Morokuma and D. G. Truhlar, American Chemical Society, Washington DC, 1999, pp. 358–367.

120 F. Haase, J. Sauer and J. Hutter, *Chem. Phys. Lett.*, 1997, **266**, 397–402.

121 J. D. Gale, R. Shah, M. C. Payne, I. Stich and K. Terakura, *Catal. Today*, 1999, **50**, 525–532.

122 I. Stich, J. D. Gale, K. Terakura and M. C. Payne, *J. Am. Chem. Soc.*, 1999, **121**, 3292–3302.

123 F. Göltl, A. Gruneis, T. Bučko and J. Hafner, *J. Chem. Phys.*, 2012, **137**, 17.

124 J. Macht, R. T. Carr and E. Iglesia, *J. Am. Chem. Soc.*, 2009, **131**, 6554–6565.

125 Q. Wang, Z. M. Cui, C. Y. Cao and W. G. Song, *J. Phys. Chem. C*, 2011, **115**, 24987–24992.

Paper II

Suppression of Aromatic Cycle in Methanol-to-Olefins Reaction over ZSM-5 by post-synthetic modification using Calcium

I. Yarulina, S. Bailleul, A. Pustovarenko, J. Ruiz-Martinez, K. De Wispelaere, J. Hajek, B.M. Weckhuysen, K. Houben, M. Baldus, V. Van Speybroeck, F. Kapteijn, J. Gascon, *ChemCatChem*, **8**, 3057–3063 (2016)

S. Bailleul performed the computational research and analysis for this paper together with K. De Wispelaere and J. Hajek and was involved during the manuscript preparation.

ChemPubSoc Europe

DOI: 10.1002/cctc.201600650

CHEMCATCHEM Full Papers

Suppression of the Aromatic Cycle in Methanol-to-Olefins Reaction over ZSM-5 by Post-Synthetic Modification Using Calcium

Irina Yarulina,[a] Simon Bailleul,[b] Alexey Pustovarenko,[a] Javier Ruiz Martinez,[c] Kristof De Wispelaere,[b] Julianna Hajek,[b] Bert M. Weckhuysen,[c] Klaartje Houben,[d] Marc Baldus,[d] Veronique Van Speybroeck,[b] Freek Kapteijn,[a] and Jorge Gascon*[a]

Incorporation of Ca in ZSM-5 results in a twofold increase of propylene selectivity (53%), a total light-olefin selectivity of 90%, and a nine times longer catalyst lifetime (throughput 792 $g_{MeOH}\,g_{catalyst}^{-1}$) in the methanol-to-olefins (MTO) reaction. Analysis of the product distribution and theoretical calculations reveal that post-synthetic modification with Ca^{2+} leads to the formation of $CaOCaOH^{+}$ that strongly weaken the acid strength of the zeolite. As a result, the rate of hydride transfer and oligomerization reactions on these sites is greatly reduced, resulting in the suppression of the aromatic cycle. Our results further highlight the importance of acid strength on product selectivity and zeolite lifetime in MTO chemistry.

Introduction

The discovery of the methanol-to-gasoline (MTG) process over ZSM-5 catalysts by Mobil Corporation in 1977[1] opened an oil-free route for the synthesis of hydrocarbons. Since then, a great deal of effort has been devoted to mechanistic studies that led to a better understanding of this catalytic process.

The evolution in mechanism comprehension started from understanding the first C–C bond formation (which is still under the debate)[2] and slowly developed to the currently accepted dual-cycle concept.[3] An important milestone in methanol-to-olefins (MTO) history was the introduction of the "hydrocarbon pool" concept by Dahl and Kolboe, who proposed the existence of intermediates of coke deposits responsible for olefin formation.[4] These intermediates were later clarified to be methylbenzenes and/or their protonated versions.[5] Transient $^{12}C/^{13}C$ experiments, however, revealed that whereas ethylene is predominantly formed through the abovementioned aromatic species, propylene and higher alkenes are formed from olefin methylation and cracking reactions.[3b,5] These observations led to the acceptance of the dual-cycle mechanism, involving the presence of two cycles, namely, a methylation/cracking cycle, in which mostly propylene is produced, and an aromatic cycle, responsible for ethylene and aromatics formation and catalyst deactivation.

Sun et al. have shown that one cycle can be promoted over the other by co-feeding species participating in these cycles, that is, co-feeding of propylene led to the increased selectivity of olefinic species, whereas co-feeding of aromatics promoted the formation of methane, ethylene and aromatic species.[3c,6]

An approach to suppress the aromatic cycle is currently of utmost interest as it is the key to prolong catalyst lifetime and to increase the selectivity to propylene. Teketel et al. have shown, using ZSM-22, that by choosing the appropriate zeolite topology the methylation/cracking cycle can be promoted over the aromatic one.[7,8]

Considering that aromatic species are formed from higher alkenes, another approach to suppress the aromatic cycle would involve tuning the acidity of the catalyst, since less acidic catalysts are known to promote the alkene cycle.[9] In this way, it would be possible to produce olefins via the methylation/cracking cycle but their further conversion to aromatics would be restricted.

Some studies, mainly performed in the early 1990s, showed that modification of ZSM-5 with elements such as Ca,[10] B[11] or

[a] I. Yarulina, A. Pustovarenko, Prof. Dr. F. Kapteijn, Prof. Dr. J. Gascon
Catalysis Engineering Group, Department of Chemical Engineering, Faculty of Applied Sciences
Delft University of Technology
Julianalaan 136
2628 BL Delft (The Netherlands)
E-mail: j.gascon@tudelft.nl

[b] S. Bailleul, Dr. K. D. Wispelaere, J. Hajek, Prof. Dr. V. V. Speybroeck
Center for Molecular Modeling
Ghent University
Technologiepark 903
9052 Zwijnaarde (Belgium)

[c] Dr. J. R. Martinez, Prof. Dr. B. M. Weckhuysen
Inorganic Chemistry and Catalysis Group, Debye Institute for Nanomaterials Science
Utrecht University
Universiteitsweg 99
3584 CG Utrecht (The Netherlands)

[d] Dr. K. Houben, Prof. Dr. M. Baldus
NMR Research Group, Debye Institute for Nanomaterials Science
Utrecht University
Universiteitsweg 99
3584 CG Utrecht (The Netherlands)

Supporting information and the ORCID identification number(s) for the author(s) of this article can be found under http://dx.doi.org/10.1002/cctc.201600650.

P[12] leads to the increased formation of olefins. Many of these results were very promising but did not receive the worthwhile attention as "the most valuable ethylene was formed very little".[13] Nowadays, the industrial focus has shifted towards propylene. The observed high selectivities to propylene and butenes and low selectivities to ethylene are already indicative that this modification might result in the promotion of the olefinic cycle over the aromatic cycle.

Results and Discussion

In this work, we modified the ZSM-5 acidity by Ca incorporation and investigated, using a combined experimental and theoretical approach, how this modification changes the nature of the acid sites, which in turn leads to the suppression of the aromatic cycle in favour of the olefinic cycle, leading to enhanced propylene formation.

The parent ZSM-5 zeolite used for the preparation of the Ca containing catalysts was purchased from Zeolyst (Si/Al = 40, CBV8014). Depending on the method of preparation, the obtained catalysts are denoted as Ca-ZSM5-IE, 6Ca-ZSM-5-SSIE, 6Ca-ZSM5-IWI, 6Ca-ZSM5-EW, where IE, SSIE, IWI and EW stand for ion-exchange, solid state ion-exchange, incipient wetness impregnation and wet impregnation, respectively. All catalysts were prepared aiming at a 6 wt. % Ca loading. Another set of catalysts was prepared by incipient wetness impregnation by varying Ca loading from 1 to 6 wt. % respectively. Details about catalyst preparation can be found in the Experimental Section. XRD results show (Figure S1, Supporting Information) that the original MFI topology is preserved in all samples.[12a]

Textural properties displayed in Table 1 demonstrate that Ca incorporation produces a small decrease in micropore volume, whereas no additional mesopores are created. NH_3 temperature-programmed desorption (TPD) results (Table 1 and Figure 1a) show that the concentration of acid sites for all catalysts except 6Ca-ZSM5-SSIE is similar to that of the parent ZSM-5, whereas the desorption maximum shifts from 435 °C to 290 °C for 6Ca-ZSM5-EW and 6Ca-ZSM5-IWI, already indicating a qualitative weakening in the strength of these acid sites upon Ca incorporation. As NH_3 TPD is not an adequate tool to quantify the nature and strength of acid sites,[14] the catalysts under study were additionally characterized by FTIR spectroscopy using pyridine as a probe molecule (Figure 1b). Parent ZSM-5 shows two IR bands at 1546 cm^{-1} and 1455 cm^{-1} representing adsorption of pyridine on Brønsted and Lewis acid sites, respectively. The Lewis acidity in the parent zeolite is ascribed to extra-framework Al species[15] but can be the result of both extra-framework and perturbed framework Al.[16] Incorporation of Ca into the zeolite caused a significant decrease of Brønsted acidity for all samples, especially for 6Ca-ZSM5-EW and 6Ca-ZSM5-IWI, for which the vibration at 1545 cm^{-1} almost completely disappeared. Direct observation of the zeolite IR spectrum in Figure 1c shows a similar disappearance of the 3600 cm^{-1} band characteristic for the Brønsted hydroxyl stretching. Along with the disappearance of Brønsted acidity, a new pyridine band at 1446 cm^{-1}, assigned to acid sites of Lewis nature, arises for Ca-containing catalysts, indicating transformation of strong Brønsted acid sites to Lewis acid ones. Interestingly, Ca-ZSM5-IE displays both IR bands at 1455 and 1446 cm^{-1} and can be considered as in between ZSM-5 and 6Ca-ZSM5-IWI, having intermediate acidic properties. FTIR spectroscopy using CO as a probe molecule (Figure S2) further confirms the transformation of Brønsted into Lewis acid sites and suggests the existence of Ca sites of different nature.

To obtain a full picture of the acidic properties of these catalysts, we performed additional characterization by solid-state NMR spectrometry using trimethylphosphine oxide (TMPO) as a probe molecule (Figure 1d). Several ^{31}P resonance peaks at 99, 75, 67, 63, 47, 43, 36 and 30 ppm are observed. The resonance peak at 30 ppm is ascribed to "mobile" TMPO, and peaks at 47, 43 and 36 ppm are characteristic for physisorbed TMPO.[17] Peaks in the range between 60 and 90 ppm are arising from $TMPOH^+$ complexes on Brønsted acid sites.[18] The peak at 99 ppm can be attributed to very strong Lewis acid sites.[19] Adsorption of TMPO on Ca-ZSM5-IE resulted in the appearance of similar peaks, however, a significant decrease of the resonance at 67 ppm suggests that, during ion exchange, Ca preferentially occupies certain Brønsted acid sites. In contrast, in the spectra of 6Ca-ZSM5-IWI the peaks in the 60–90 ppm range are absent. In summary, the extensive acidity characterization performed demonstrates the transformation of Brønsted into Lewis acidity.

The as-prepared catalysts were tested at 500 °C in the MTO reaction. Such a relatively high reaction temperature was

Table 1. Textural and catalytic properties of the ZSM-5 catalyst materials under study.

Entry	Catalyst	V_{total}[a] [$cm^3\,g^{-1}$]	V_{micro}[a] [$cm^3\,g^{-1}$]	S_{BET}[a] [$m^2\,g^{-1}$]	S_{micro}[a] [$m^2\,g^{-1}$]	c_{AS}[b] [$\mu mol\,g^{-1}$]	c_{BAS}[c] [$\mu mol\,g^{-1}$]	c_{LAS}[c] [$\mu mol\,g^{-1}$]	Throughput[d] [$g_{MeOH}\,g_{catalyst}^{-1}$]	$S(C_{3=})$ [C mol%]
1	ZSM-5	0.256	0.152	448	363	387	232	35	88	25
2	Ca-ZSM5-IE	0.273	0.145	429	344	402	138	108	264	39
3	6Ca-ZSM5-SSIE	0.212	0.111	323	267	171	128	0	136	39
4	6Ca-ZSM5-EW	0.199	0.110	336	276	374	38	208	304	43
5	6Ca-ZSM5-IWI	0.226	0.124	385	310	384	29	240	504	53
6	4Ca-ZSM5-IWI	0.223	0.126	387	313	381	27	240	480	45
7	2Ca-ZSM5-IWI	0.238	0.128	392	315	332	40	228	792	39
8	1Ca-ZSM5-IWI	0.246	0.138	418	334	347	66	198	272	46

[a] From N_2 adsorption. [b] Concentration of acid sites (AS) derived from NH_3 TPD. [c] Concentration of Brønsted (BAS) and Lewis (LAS) acid sites derived from pyridine IR spectroscopy. [d] Amount of methanol (g) converted per gram of zeolite before conversion decreases below 80%.

ChemPubSoc Europe

CHEMCATCHEM Full Papers

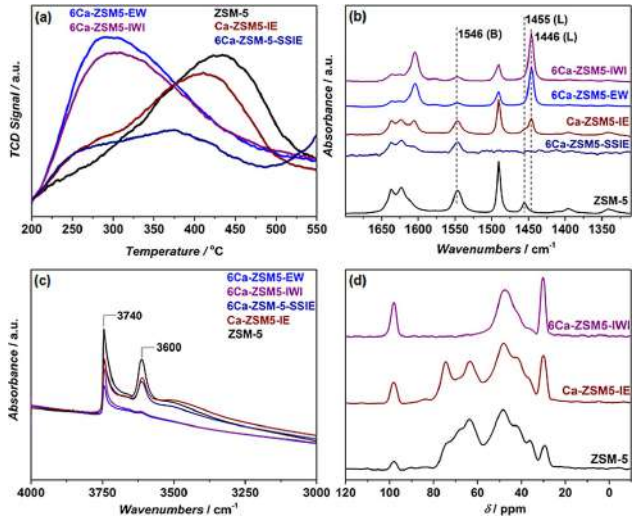

Figure 1. Acidity characterization of Ca-containing ZSM-5 catalysts and parent ZSM-5. (a) NH_3 TPD profiles, (b) FTIR spectra of adsorbed pyridine, (c) FTIR spectra in the OH stretching region, (d) ^{1}H-^{31}P CP MAS NMR spectra for TMPO adsorbed on 6Ca-ZSM5-IWI, Ca-ZSM5-IE and ZSM-5.

chosen because higher temperatures favour the formation of short chain olefins.[20] Furthermore, owing to their lower acidity, some of the catalysts were not catalytically active below 475 °C. The conversion results in Figure 2a demonstrate that incorporation of Ca into ZSM-5 prolong catalyst lifetime. Herein, the method of catalyst preparation is crucial to obtain the longest lifetime and selectivity to propylene, and the best results were obtained by using the catalyst prepared by IWI (504 vs. 88 g MeOH converted per gram of catalyst). As shown above, other preparation methods are less effective in weakening zeolite acidity and led to shorter catalyst lifetimes. Remarkably, Ca incorporation caused significant changes in product distribution (Figure 2b), the most important of which are the decrease in the formation of paraffins and ethylene. For 6Ca-ZSM5-IWI and 6Ca-ZSM5-EW, the selectivity to paraffins drops from 27 down to 3%, and the selectivity to ethylene from 16% down to 8 and 6%, respectively, compared with the performance of parent ZSM-5. Moreover, 6Ca-ZSM5-IWI showed only negligible formation of aromatics in comparison to parent ZSM-5 (compare $S_{C6-8} = 0.5\%$ and 9% respectively, Figure 2). Both, the much lower selectivity to aromatics along with smaller ethylene productivity indicate—to a large extent—the suppression of the aromatic cycle. Indeed, ethylene is considered to be the main product of this cycle.[3b,5,21] On the other hand, the lower paraffin selectivity indicates the partial suppression of intermolecular hydride transfer reactions responsible for the conversion of olefins to paraffins and aromatics.[21a] The latter is considered to be the bridging step between the olefinic and aromatic cycles. We thus conclude that the observed suppres-

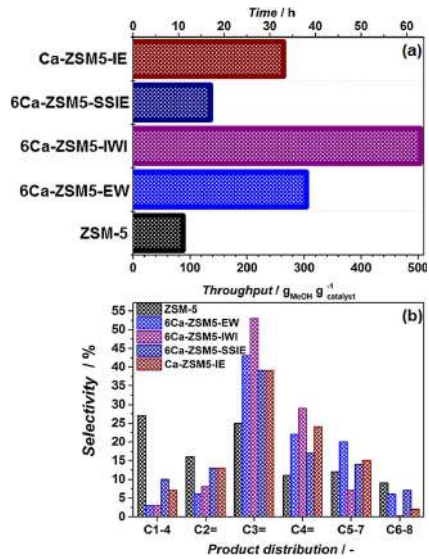

Figure 2. Methanol conversion over Ca-modified ZSM-5 prepared by different methods tested at 500 °C in MTO. (a) Catalyst lifetime, (b) product distribution. $m_{cat} = 0.5$ g, WHSV = 8 $g_{MeOH}\,g_{catalyst}^{-1}\,h^{-1}$, $MeOH/N_2 = 1{:}1$.

ChemPubSoc Europe

CHEMCATCHEM Full Papers

sion of the aromatic cycle is achieved by reducing the rate of hydride transfer and oligomerisation reactions on significantly weaker acid sites.[22]

As catalyst 6 Ca-ZSM5-IWI prepared by IWI showed the highest selectivity to propylene (53%) and butenes (29%) and the longest lifetime, this method was used to further to optimize the Ca content. NH_3 TPD and pyridine FTIR spectrometry (Figures S3 and S4) reveal that all samples possess a similar concentration of acid sites and modification with Ca caused almost complete disappearance of Brønsted acidity as was observed for 6 Ca-ZSM5-IWI.

Catalytic experiments (Figure 3) showed that by employing a Ca loading of 2 wt.% with a molar ratio of Ca to Al 2:1

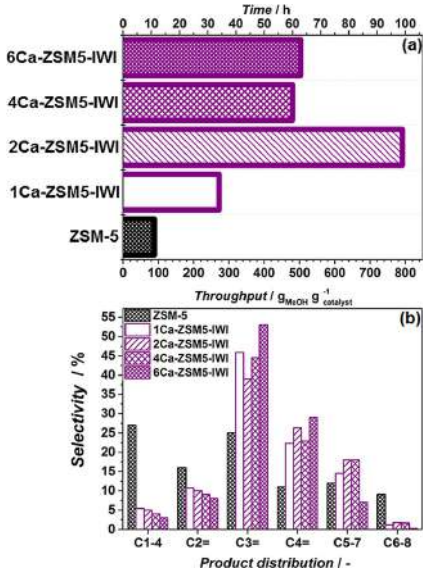

Figure 3. Methanol conversion over Ca-modified ZSM-5 prepared by the IWI method with different Ca loading tested at 500 °C in MTO. (a) Catalyst lifetime, (b) product distribution. $m_{cat} = 0.5$ g, WHSV = 8 $g_{MeOH}\,g_{catalyst}^{-1}\,h^{-1}$, $MeOH/N_2 = 1:1$.

(Table S1), catalyst lifetime was further prolonged up to 99 h, corresponding to 792 g of MeOH converted per gram of catalyst before the catalyst became fully deactivated, which is nine times longer than for the commercial ZSM-5. The selectivities to propylene (39%) and butenes (26%) were slightly lower than for 6 Ca-ZSM5-IWI. Observed differences in selectivities caused by different Ca loadings are tentatively attributed to additional spatial restrictions caused by Ca deposition inside the micropores, that is, reducing micropore volume (see Table 1), resulting in less aromatics formation, thus enhancing formation of propylene and decreasing formation of ethylene (Figure 3b). However, based on toluene adsorption isotherms (Figure S5), shape selective effects can be ruled out. Whether bulkier aromatic molecules,[12b,21a] as suggested by Abubakar et al.[23] on P-modified ZSM-5, can be formed inside of the pores of the Ca modified ZSM-5 catalyst is still not clear.

As mentioned in the introduction, a great deal of effort has been dedicated in the open literature to the modification of acid sites and its consequences in MTO performance,[24] including Ca modification.[10a,b,25] For example, Zhang et al. modified ZSM-5 with $Ca(NO_3)_2$ to achieve a propylene selectivity up to 50% with catalyst lifetime increasing from 13 to 75 h at WHSV = 4.2 h^{-1}.[10b] Observed differences were attributed to the acid site weakening through the formation of acid-base centres but without spectroscopic evidence to support this hypothesis. Nonetheless, the observed large decrease in paraffin and ethylene selectivities was not discussed either by these authors. High selectivity towards propylene is generally demonstrated for mesoporous ZSM-5.[26] It is claimed that this is a result of both improved diffusion properties and acid site strength modification. However, according to Olsbye et al.[27] the observed differences are not yet satisfactorily described and explained. By creating mesopores in ZSM-5, Mei et al. reached a selectivity to propylene of approximately 42% together with a considerable drop in the production of paraffins (from 20.5 down to 5.7%) and ethylene (from 15.3 down to 4.2%).[26a] These results were rationalized on the basis of a different contribution of the aromatic and olefinic route, that is, by partial suppression of the aromatic cycle.

On the other hand, the modification of the acidity might simply lead to a decreased amount of working acid sites, i.e. partial poisoning. Thus, application of ZSM-5 with a high SiO_2/Al_2O_3 ratio, and therefore a much lower density of acid sites, has been widely reported with light olefin selectivity increasing upon decreasing Al content.[28] Although very effective in terms of selectivity, these zeolites with low Al content usually deactivate faster[12a] owing to selective coke deposition on the few active sites. We tentatively suggest that the promotional effect of acid site modification is mainly related to the decreasing the strength of acid sites rather than their amount. Thus, the biggest difference between decreasing Al content and "poisoning" (or "modifying") acid sites with Ca is that in the former case the amount of acid sites has been lowered whereas in the latter their strength has been weakened through changing their nature but preserving their amount.

To obtain molecular level insight into the nature of the active site of the pristine and Ca-modified catalysts, a set of periodic DFT calculations were performed using the Vienna Ab Initio Simulation Package (VASP).[29] Simulation details are provided in the Supporting Information.[30] Inspired by earlier literature reports[10a,31] and the experimentally defined optimal Ca:Al ratio of 2, we calculated the electronic energies for a systematic set of $CaOCaOH^+$ structures coordinated to framework oxygen atoms near the Al substitution and with different orientations in the channel intersections (Figures S10 and S11). An overview of all considered structures is given in the Supporting Information. We assumed isolated Brønsted acid sites in the pristine H-ZSM-5 material, which is a realistic representa-

ChemPubSoc Europe

CHEMCATCHEM Full Papers

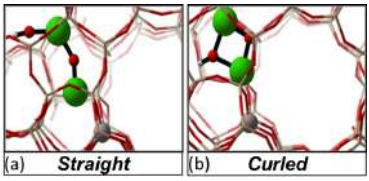

Figure 4. Representation of suggested active sites in Ca-ZSM-5 with (a) straight and (b) curled configuration. Color code: H white, O red, Al grey, Si cream and Ca green.

tion since the experimentally used Si/Al ratio amounts to 40. We observed two stable configurations of Ca species as displayed in Figure 4: the $CaOCaOH^+$ tail may adopt either a straight (Figure 4a) or curled (Figure 4b) configuration. The latter is electronically more stable. A detailed comparison of the vibrational frequencies of the modified Ca-ZSM-5 and pristine ZSM-5 yields some distinct differences for the Ca-modified ZSM-5 catalyst. The calculated OH stretch frequency of the H-ZSM-5 catalyst at 3684 cm^{-1} shifts upwards to 3848 cm^{-1} and 3796 cm^{-1} for the straight and curled Ca chains in the Ca-ZSM-5 catalyst, respectively, located in the range of less acidic silanol groups (3740 cm^{-1}), which corresponds to the spectra shown in Figure 1c.[32] These calculations suggest that the active site in Ca-ZSM-5 catalysts is a combination of multiple $CaOCaOH^+$ structures, and the shift of the OH stretch frequencies points towards a lower Brønsted acidity of the calcium-modified catalyst.

Conclusions

The post-synthetic incorporation of Ca into ZSM-5 leads to the formation of $CaOCaOH^+$ species that strongly weaken the acid strength of the parent zeolite. As a result, the rates of hydride transfer and oligomerisation reactions on these sites are greatly reduced, resulting in the suppression of the aromatic cycle and to increased total light olefin selectivity in the range of 90%. These results further demonstrate the importance of acid strength on product selectivity and zeolite lifetime in MTO chemistry.

Experimental Section

Synthesis of catalysts

Ca-modified ZSM-5 catalysts were prepared from commercial ZSM-5 (Zeolyst, CBV 8014). Ca-ZSM5-IE was prepared by ion- exchange with 1 M $Ca(NO_3)_2{\cdot}4H_2O$ solution at 80 °C for 2 h repeated three times with filtration step in between and followed by calcination at 550 °C. 6Ca-ZSM5-SSIE was prepared by solid-state ion-exchange with $Ca(CH_3COO)_2$. SSIE was achieved by grinding required amount of calcium acetate with commercial ZSM-5 for 30 min in a mortar followed by calcination at 550 °C. 6Ca-ZSM5-EW was prepared by wet impregnation. In a typical procedure the required amount of $Ca(NO_3)_2{\cdot}4H_2O$ was dissolved in water (5 mL). Zeolite (4 g) was added to this solution and left overnight under stirring at RT. Subsequently, the catalyst was dried for 12 h at 80 °C and calcined at 550 °C. 6Ca-ZSM5-IWI, 4Ca-ZSM5-IWI, 2Ca-ZSM5-IWI and 1Ca-ZSM5-IWI were prepared by incipient wetness impregnation (IWI). Parent zeolite (4 g) was impregnated with $Ca(NO_3)_2{\cdot}4H_2O$ solution (1.06 g) corresponding to the total pore volume of the zeolite. After impregnation, the catalysts were kept overnight in a desiccator followed by drying for 12 h at 80 °C and calcination at 550 °C. A heating rate of 2 °C min^{-1} and static air conditions were applied in all cases for calcination.

Characterization of catalysts

N_2 adsorption at 77 K was performed by using the Tristar II 3020 analyzer (Micromeritics). Prior to the experiment, samples were outgassed at 350 °C for 16 h. Toluene adsorption measurements were performed at 25 °C using Micromeritics 3Flex equipped with a 15 mL stainless steel vapor vessel.

Images were recorded by using a JEOL JSM-6010LA with a standard beam potential of 10 kV and an Everhart–Thornley detector. X-ray microanalysis (SEM/EDX) confirmed the elemental composition in the sample by scanning microscopy (SEM) coupled with a dispersive X-ray microanalysis system (EDX) with a Silicon-drift detector.

The XRD patterns of the powders are recorded in Bragg–Brentano geometry with a Bruker D8 Advance X-ray diffractometer equipped with a LynxEye position-sensitive detector. Measurements were performed at RT by using monochromatic $Co_{K\alpha}$ ($\lambda = 1.788970$ Å) radiation between $2\theta = 5^\circ$ and 50°. Elemental analysis was performed with a PerkinElmer Optima 4300 DV instrument. The samples were first digested in an aqueous mixture of 1% HF and 1.25% H_2SO_4. After dilution, analysis was done by inductively coupled plasma optical emission spectrometry (ICP-OES).

Temperature-programmed NH_3 desorption (NH_3-TPD) was performed with an AutoChem II chemisorption analyzer (Micromeritics). Approximately 0.2 g of the material was first degassed under He flow at 400 °C and then saturated with NH_3 at 200 °C during 1 h using a flow of 1.65% NH_3 in He. The gas mixture was then switched back to He and the sample was purged at 200 °C for about 1 h to remove weakly adsorbed NH_3 molecules. TPD was subsequently recorded under He flow, from 200 °C to 800 °C. All flow rates were adjusted to 25 mL min^{-1}, and the heating rate was 10 °C min^{-1} during the different stages of the experiment.

Transmission FTIR spectroscopy using CO as a probe molecule was performed by using a Nicolet Nexus spectrometer at 4 cm^{-1} resolution equipped with an extended KBr beam splitting and a mercury cadmium telluride (MCT) cryo-detector. The pellets were placed in an IR quartz cell equipped with CaF_2 windows. A movable sample holder allows the sample to be placed in the infrared beam for the measurements or into the furnace for thermal treatments. The cell was connected to a vacuum line for pretreatment. The specimen was activated in vacuum at 400 °C for 16 h to remove adsorbed species. After this step, the samples were cooled down to −130 °C and CO was dosed up to 30 mbar.

Transmission FTIR spectroscopy using pyridine as a probe molecule was performed by using a Nicolet 6700 spectrometer equipped with MCT/B detector. The specimen was activated in vacuum at 400 °C for 16 h to remove adsorbed species. After activation, pellets were saturated with pyridine vapor and further evacuated at 160 °C for 2 h. Spectra were recorded in 1000–4000 cm^{-1} range at 4 cm^{-1} resolution and co-addition of 128 scans. The amount of Brønsted (BAS) and Lewis (LAS) acid sites was derived from the bands at 1545 and 1456 cm^{-1} as described elsewhere using extinc-

ChemPubSoc Europe

CHEMCATCHEM Full Papers

tion coefficients of 1.67 and 2.22 respectively.[15,33] Assuming that one molecule of pyridine is adsorbed on one acid site, the following expressions were used to calculate C_{BAS} and C_{LAS}.[33]

$$C_{BAS} = 1.88 \times IA(B) \times R^2/W \quad (1)$$

$$C_{LAS} = 1.42 \times IA(L) \times R^2/W \quad (2)$$

where *IA* (BAS, LAS) is the integrated absorbance of BAS or LAS band (cm^{-1}), *R* is the radius of catalyst disk (cm), and *W* is the mass of catalyst (mg).

For solid-state NMR measurements using trimethoxyphosphine oxide (TMPO) as a probe molecule, the preparation procedure was adapted from Wiper et al.[34] TMPO (50 mg) was dissolved in anhydrous CH_2Cl_2 (15 mL) in an Ar glove box. A 15 mL volume of this solution was added to the dehydrated at 400 °C for 16 h zeolite and left under stirring for 1 h. Subsequently, materials were heated at 150 °C for 1 h under vacuum to allow homogeneous distribution of TMPO. Finally, cooled down samples were transferred into a zirconia MAS rotor (3.2 mm). Solid-state ^{31}P NMR spectra were recorded on a Bruker spectrometer operating at a ^1H Larmor frequency of 500 MHz equipped with a triple resonance 3.2 mm Magic Angle Spinning (MAS) probe, using an MAS frequency of 19 kHz. After a ^1H 90 pulse, ^1H-^{31}P cross-polarization (CP) was achieved by applying simultaneously a 46 kHz ^{31}P and a 94 kHz ^1H RF field (ramp 70–100%) with a contact time of 4.2 ms. During acquisition 83 kHz SPINAL64 proton decoupling[35] was applied. For each experiment, 256 scans were used with a recycle delay of 4 s.

Methanol-to-olefins testing

Catalytic experiments were performed in a Microactivity Reference unit (PID Eng&Tech) at 500 °C and ambient pressure. The catalyst (pressed, crushed and sieved to particle sizes 250–420 μm) was placed in a fixed-bed reactor with internal diameter 9 mm for standard experiments. An HPLC pump (307 5-SC-type piston pump, Gilson) was used to feed methanol to the reactor system. A weight-hourly space velocity (WHSV) of 8 $g_{MeOH}\,g_{cat}^{-1}\,h^{-1}$, a 1:1 molar feed composition of N_2 and MeOH and atmospheric pressure were utilized. The product mixture was analyzed online with an Interscience CompactGC equipped with a 15 m capillary RTX-1 (1% diphenyl-, 99% dimethylpolysiloxane) column and a flame ionization detector. Conversion, selectivities and yields were calculated on a molar carbon basis. Thus, conversion was defined as the carbon based fraction of light oxygenates (methanol and dimethyl ether) consumed during the reaction:

$$X = \frac{n_{C,MeOH_{in}} - n_{C,MeOH_{out}} - 2 \times n_{C,DME_{out}}}{n_{C,MeOH_{in}}} \times 100\% \quad (3)$$

The selectivity towards ethylene (2) and propylene (3) was calculated based on the carbon number as follows:

$$S_{ethylene} = \frac{2 \times n_{C_2H_4}}{n_{C,MeOH_{in}} - n_{C,oxy_{out}}} \times 100\% \quad (4)$$

$$S_{propylene} = \frac{3 \times n_{C_3H_6}}{n_{C,MeOH_{in}} - n_{C,oxy_{out}}} \times 100\% \quad (5)$$

and the yield of a component *i* was defined from its selectivity and methanol conversion:

$$Y_i = \frac{S_i \times X}{100} \quad (6)$$

The performance results were presented in graphs as a function of the methanol throughput per amount of catalyst used ($g_{MeOH}\,g_{cat}^{-1}$) and defined as overall MeOH throughput fed through the catalytic bed before the conversion of oxygenates drops to 80%. Selectivities were taken after testing catalysts for 1.5 h. Remarkably, for Ca-modified samples the steady state was achieved after approximately 40 min on stream and product distribution did not change significantly (Figure S6) after that time. For ZSM-5, no steady state was achieved, and the early stages were characterized by the high selectivity towards paraffins decreasing with time on stream in favor of olefins.

Acknowledgements

This research received funding from the Netherlands Organisation for Scientific Research (NWO) in the framework of the TASC Technology Area "Syngas, a Switch to Flexible New Feedstock for the Chemical Industry (TA-Syngas)". K.D.W., S.B., J.H. and V.V.S. acknowledge the Foundation of Scientific Research, Flanders (FWO), the Research Board of Ghent University, and the European Union's Horizon 2020 research and innovation programme (consolidator ERC grant agreement No. 647755—DYNPOR (2015–2020)). Computational resources and services were provided by the Stevin Supercomputer Infrastructure of Ghent University and by the Flemish Supercomputer Center (VSC), funded by the Hercules Foundation and the Flemish Government—department EWI.

Keywords: acidity · alkenes · calcium · density functional calculations · zeolites

[1] C. D. Chang, C. T. W. Chu, Mobil Oil Corp, **1977**.
[2] a) A. Comas-Vives, M. Valla, C. Copéret, P. Sautet, *ACS Cent. Sci.* **2015**, *1*, 313–319; b) D. Lesthaeghe, V. Van Speybroeck, G. B. Marin, M. Waroquier, *Angew. Chem. Int. Ed.* **2006**, *45*, 1714–1719; *Angew. Chem.* **2006**, *118*, 1746–1751.
[3] a) K. Hemelsoet, J. Van der Mynsbrugge, K. De Wispelaere, M. Waroquier, V. Van Speybroeck, *ChemPhysChem* **2013**, *14*, 1526–1545; b) U. Olsbye, S. Svelle, M. Bjorgen, P. Beato, T. V. W. Janssens, F. Joensen, S. Bordiga, K. P. Lillerud, *Angew. Chem. Int. Ed.* **2012**, *51*, 5810–5831; *Angew. Chem.* **2012**, *124*, 5910–5933; c) X. Sun, S. Mueller, Y. Liu, H. Shi, G. L. Haller, M. Sanchez-Sanchez, A. C. van Veen, J. A. Lercher, *J. Catal.* **2014**, *317*, 185–197.
[4] I. M. Dahl, S. Kolboe, *Catal. Lett.* **1993**, *20*, 329–336.
[5] M. Bjorgen, S. Svelle, F. Joensen, J. Nerlov, S. Kolboe, F. Bonino, L. Palumbo, S. Bordiga, U. Olsbye, *J. Catal.* **2007**, *249*, 195–207.
[6] X. Sun, S. Mueller, H. Shi, G. L. Haller, M. Sanchez-Sanchez, A. C. van Veen, J. A. Lercher, *J. Catal.* **2014**, *314*, 21–31.
[7] S. Teketel, W. Skistad, S. Benard, U. Olsbye, K. P. Lillerud, P. Beato, S. Svelle, *ACS Catal.* **2012**, *2*, 26–37.
[8] S. Teketel, L. F. Lundegaard, W. Skistad, S. M. Chavan, U. Olsbye, K. P. Lillerud, P. Beato, S. Svelle, *J. Catal.* **2015**, *327*, 22–32.
[9] M. W. Erichsen, K. De Wispelaere, K. Hemelsoet, S. L. C. Moors, T. Deconinck, M. Waroquier, S. Svelle, V. Van Speybroeck, U. Olsbye, *J. Catal.* **2015**, *328*, 186–196.
[10] a) S. Zhang, B. Zhang, Z. Gao, Y. Han, *Ind. Eng. Chem. Res.* **2010**, *49*, 2103–2106; b) S. Zhang, B. Zhang, Z. Gao, Y. Han, *React. Kinet. Mech. Catal.* **2010**, *99*, 447–453; c) A. M. Al-Jarallah, U. A. El-Nafaty, M. M. Abdillahi, *Appl. Catal. A* **1997**, *154*, 117–127.

ChemPubSoc Europe

CHEMCATCHEM Full Papers

[11] N. V. Klyueva, N. D. Tien, K. G. Ione, *React. Kinet. Catal. Lett.* **1985**, *29*, 427 – 432.
[12] a) J. Liu, C. Zhang, Z. Shen, W. Hua, Y. Tang, W. Shen, Y. Yue, H. Xu, *Catal. Commun.* **2009**, *10*, 1506 – 1509; b) H. E. van der Bij, B. M. Weckhuysen, *Chem. Soc. Rev.* **2015**, *44*, 7406 – 7428; c) J. C. Vedrine, A. Auroux, P. Dejaifve, V. Ducarme, H. Hoser, S. Zhou, *J. Catal.* **1982**, *73*, 147 – 160.
[13] M. Stöcker, *Microporous Mesoporous Mater.* **1999**, *29*, 3 – 48.
[14] L. Rodríguez-González, U. Simon, *Meas. Sci. Technol.* **2010**, *21*, 027003.
[15] S. Sartipi, K. Parashar, M. J. Valero-Romero, V. P. Santos, B. van der Linden, M. Makkee, F. Kapteijn, J. Gascon, *J. Catal.* **2013**, *305*, 179 – 190.
[16] J. Brus, L. Kobera, W. Schoefberger, M. Urbanova, P. Klein, P. Sazama, E. Tabor, S. Sklenak, A. V. Fishchuk, J. Dedecek, *Angew. Chem. Int. Ed.* **2015**, *54*, 541 – 545; *Angew. Chem.* **2015**, *127*, 551 – 555.
[17] a) Q. Zhao, W. H. Chen, S. J. Huang, Y. C. Wu, H. K. Lee, S. B. Liu, *J. Phys. Chem. B* **2002**, *106*, 4462 – 4469; b) A. Zheng, S.-J. Huang, W.-H. Chen, P.-H. Wu, H. Zhang, H.-K. Lee, L.-C. de Menorval, F. Deng, S.-B. Liu, *J. Phys. Chem. A* **2008**, *112*, 7349 – 7356.
[18] S. Hayashi, K. Jimura, N. Kojima, *Microporous Mesoporous Mater.* **2014**, *186*, 101 – 105.
[19] W.-H. Chen, H.-H. Ko, A. Sakthivel, S.-J. Huang, S.-H. Liu, A.-Y. Lo, T.-C. Tsai, S.-B. Liu, *Catal. Today* **2006**, *116*, 111 – 120.
[20] N.-L. Michels, S. Mitchell, J. Perez-Ramirez, *ACS Catal.* **2014**, *4*, 2409 – 2417.
[21] a) J. F. Haw, W. G. Song, D. M. Marcus, J. B. Nicholas, *Acc. Chem. Res.* **2003**, *36*, 317 – 326; b) R. Khare, D. Millar, A. Bhan, *J. Catal.* **2015**, *321*, 23 – 31.
[22] L. R. Aramburo, E. de Smit, B. Arstad, M. M. van Schooneveld, L. Sommer, A. Juhin, T. Yokosawa, H. W. Zandbergen, U. Olsbye, F. M. F. de Groot, B. M. Weckhuysen, *Angew. Chem. Int. Ed.* **2012**, *51*, 3616 – 3619; *Angew. Chem.* **2012**, *124*, 3676 – 3679.
[23] S. M. Abubakar, D. M. Marcus, J. C. Lee, J. O. Ehresmann, C. Y. Chen, P. W. Kletnieks, D. R. Guenther, M. J. Hayman, M. Pavlova, J. B. Nicholas, J. F. Haw, *Langmuir* **2006**, *22*, 4846 – 4852.
[24] a) M. Khanmohammadi, S. Amani, A. B. Garmarudi, A. Niaei, *Chin. J. Catal.* **2016**, *37*, 325 – 339; b) F. L. Bleken, S. Chavan, U. Olsbye, M. Boltz, F. Ocampo, B. Louis, *Appl. Catal. A* **2012**, *447*, 178 – 185.
[25] a) K. Omata, Y. Yamazaki, Y. Watanabe, K. Kodama, M. Yamada, *Ind. Eng. Chem. Res.* **2009**, *48*, 6256 – 6261; b) J. Li, S. Liu, H. Zhang, E. Lu, P. Ren, J. Ren, *Chin. J. Catal.* **2016**, *37*, 308 – 315.
[26] a) C. Mei, P. Wen, Z. Liu, H. Liu, Y. Wang, W. Yang, Z. Xie, W. Hua, Z. Gao, *J. Catal.* **2008**, *258*, 243 – 249; b) F. L. Bleken, K. Barbera, F. Bonino, U. Olsbye, K. P. Lillerud, S. Bordiga, P. Beato, T. V. W. Janssens, S. Svelle, *J. Catal.* **2013**, *307*, 62 – 73; c) J. Ahmadpour, M. Taghizadeh, *J. Nat. Gas Sci. Eng.* **2015**, *23*, 184 – 194.
[27] U. Olsbye, S. Svelle, K. P. Lillerud, Z. H. Wei, Y. Y. Chen, J. F. Li, J. G. Wang, W. B. Fan, *Chem. Soc. Rev.* **2015**, *44*, 7155 – 7176.
[28] a) C. D. Chang, C. T. W. Chu, R. F. Socha, *J. Catal.* **1984**, *86*, 289 – 296; b) C. T. W. Chu, C. D. Chang, *J. Catal.* **1984**, *86*, 297 – 300.
[29] J. Hafner, *J. Comput. Chem.* **2008**, *29*, 2044 – 2078.
[30] a) V. Van Speybroeck, K. De Wispelaere, J. Van der Mynsbrugge, M. Vandichel, K. Hemelsoet, M. Waroquier, *Chem. Soc. Rev.* **2014**, *43*, 7326 – 7357; b) V. Van Speybroeck, K. Hemelsoet, L. Joos, M. Waroquier, R. G. Bell, C. R. A. Catlow, *Chem. Soc. Rev.* **2015**, *44*, 7044 – 7111.
[31] a) A. V. Larin, G. M. Zhidomirov, D. N. Trubnikov, D. P. Vercauteren, *J. Comput. Chem.* **2010**, *31*, 421 – 430; b) G. Li, E. A. Pidko, R. A. van Santen, Z. Feng, C. Li, E. J. M. Hensen, *J. Catal.* **2011**, *284*, 194 – 206; c) G. Li, E. A. Pidko, R. A. van Santen, C. Li, E. J. M. Hensen, *J. Phys. Chem. C* **2013**, *117*, 413 – 426; d) G. Yang, Y. Wang, D. H. Zhou, X. C. Liu, X. W. Han, X. H. Bao, *J. Mol. Catal. A* **2005**, *237*, 36 – 44; e) G. M. Zhidomirov, A. V. Larin, D. N. Trubnikov, D. P. Vercauteren, *J. Phys. Chem. C* **2009**, *113*, 8258 – 8265.
[32] a) T. Armaroli, L. J. Simon, M. Digne, T. Montanari, M. Bevilacqua, V. Valtchev, J. Patarin, G. Busca, *Appl. Catal. A* **2006**, *306*, 78 – 84; b) C. Carteret, *J. Phys. Chem. C* **2009**, *113*, 13300 – 13308.
[33] C. A. Emeis, *J. Catal.* **1993**, *141*, 347 – 354.
[34] P. V. Wiper, J. Amelse, L. Mafra, *J. Catal.* **2014**, *316*, 240 – 250.
[35] B. M. Fung, A. K. Khitrin, K. Ermolaev, *J. Magn. Reson.* **2000**, *142*, 97 – 101.

Received: May 30, 2016
Published online on July 28, 2016

Paper III

Structure–performance descriptors and the role of Lewis acidity in the methanol-to-propylene process

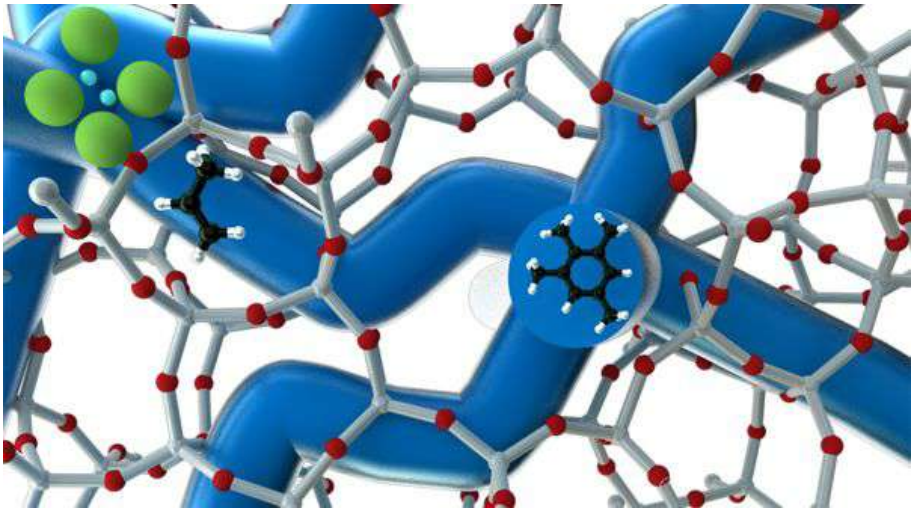

I. Yarulina, K. De Wispelaere, S. Bailleul, J. Goetze, M. Radersma, E. Abou-Hamad, I. Vollmer, M. Goesten, B. Mezari, E.J.M. Hensen, J. S. Martínez-Espín, M. Morten, S. Mitchell, J. Perez-Ramirez, U. Olsbye, B.M. Weckhuysen, V. Van Speybroeck, F. Kapteijn, J. Gascon, *Nature Chemistry*, **10**, 804–812 (2018)

S. Bailleul performed the computational research and analysis for this paper together with K. De Wispelaere and was involved during the manuscript preparation.

ARTICLES
https://doi.org/10.1038/s41557-018-0081-0

nature chemistry

Corrected: Publisher Correction

Structure–performance descriptors and the role of Lewis acidity in the methanol-to-propylene process

Irina Yarulina[1,2], Kristof De Wispelaere[3], Simon Bailleul[3], Joris Goetze[4], Mike Radersma[1], Edy Abou-Hamad[5], Ina Vollmer[1], Maarten Goesten[6], Brahim Mezari[6], Emiel J. M. Hensen[6], Juan S. Martínez-Espín[7], Magnus Morten[7], Sharon Mitchell[8], Javier Perez-Ramirez[8], Unni Olsbye[7], Bert M. Weckhuysen[4], Veronique Van Speybroeck[3], Freek Kapteijn[1] and Jorge Gascon[1,2]*

The combination of well-defined acid sites, shape-selective properties and outstanding stability places zeolites among the most practically relevant heterogeneous catalysts. The development of structure–performance descriptors for processes that they catalyse has been a matter of intense debate, both in industry and academia, and the direct conversion of methanol to olefins is a prototypical system in which various catalytic functions contribute to the overall performance. Propylene selectivity and resistance to coking are the two most important parameters in developing new methanol-to-olefin catalysts. Here, we present a systematic investigation on the effect of acidity on the performance of the zeolite 'ZSM-5' for the production of propylene. Our results demonstrate that the isolation of Brønsted acid sites is key to the selective formation of propylene. Also, the introduction of Lewis acid sites prevents the formation of coke, hence drastically increasing catalyst lifetime.

The methanol-to-olefins (MTO) process is a prototypical case study of zeolite catalysis with the potential to alleviate the progressively growing demand for olefins[1]. Zeolites containing Brønsted acidity are the catalysts of choice[2], with ZSM-5 and SAPO-34 being the two materials applied industrially[3]. Zeolite topology is an important parameter[4], however, it is not the only one that defines MTO catalyst performance[5]. Accessibility[6], strength, distribution[7], amount[8] and the nature[9] of acid sites are also of high importance.

Brønsted acid sites (BAS) are believed to be the active sites for olefin production[5,10], however there is currently a consensus that the production of olefins proceeds through an autocatalytic reaction. Accordingly, adsorbed hydrocarbon species in the micropores of a zeolitic catalyst, typically alkenes and arenes, act as 'co-catalyst pool species' (Fig. 1a). Both species participate in two competitive reaction pathways, mechanistically described by the dual-cycle concept: reaction products may either be formed through an alkene- or aromatic-based cycle via methylation/cracking reactions, depending on the nature of the hydrocarbon pool (HP) species[5,11,12].

Optimization of the active site has primarily focused on the nature of the BAS and the HP species. Herein, we show that the active site has an even higher degree of complexity: the combined presence of BAS and Lewis acid sites (LAS) may drastically improve the overall performance of the catalyst. Olefin selectivity and resistance to coking are the two most important parameters in developing new catalysts for this process. In the past few decades, modification of ZSM-5 zeolites with different elements like phosphorus, boron or alkaline-earth metals[13] has been shown to strongly improve the selectivity to propylene and, simultaneously, improve catalyst lifetime. This sets up the grounds for the methanol-to-propylene (MTP) process: carried out over mildly Brønsted acidic ZSM-5 catalysts at slightly higher temperatures than classical MTO chemistry ($T \geq 500\,°C$). The improved propylene yields have been rationalized on the basis of the lower density of BAS and, in some cases, spatial constrains due to post-synthetic modifications[14], however no clear structure–performance descriptors have been developed.

Here we present a systematic investigation on the effect of acid-site isolation and Brønsted and Lewis acidity on the performance of ZSM-5 zeolites in the MTO process. By establishing a correlation between the type and concentration of acid sites with lifetime and selectivity to ethylene and propylene, we decouple the effect of Brønsted acidity from the effect of Lewis acidity, further determining the respective contributions of BAS and LAS. Next, by combining theory with operando UV–vis and ^{1}H NMR we are able to understand the role of Lewis acidity and to demonstrate that these sites are not spectators. Indeed, LAS become an integral part of the active site and influence the reactivity of intermediates in the HP cycle. The established structure–performance relationships may be applied to other high-temperature zeolite-catalysed reactions.

Results

Assessing textural and acidic properties of the catalysts. We prepared three series of ZSM-5 zeolites with different amounts and

[1]Catalysis Engineering, Chemical Engineering Department, Delft University of Technology, Delft, the Netherlands. [2]King Abdullah University of Science and Technology, KAUST Catalysis Center, Advanced Catalytic Materials, Thuwal, Saudi Arabia. [3]Center for Molecular Modeling, Ghent University, Zwijnaarde, Belgium. [4]Inorganic Chemistry and Catalysis, Debye Institute for Nanomaterials Science, Utrecht University, Utrecht, the Netherlands. [5]King Abdullah University of Science and Technology (KAUST), Core Labs, Thuwal, Saudi Arabia. [6]Schuit Institute of Catalysis, Laboratory of Inorganic Materials Chemistry, Eindhoven University of Technology, Eindhoven, the Netherlands. [7]Centre for Materials Science and Nanotechnology, Department of Chemistry, University of Oslo, Oslo, Norway. [8]Institute for Chemical and Bioengineering, Department of Chemistry and Applied Biosciences, ETH Zurich, Zurich, Switzerland. *e-mail: jorge.gascon@kaust.edu.sa

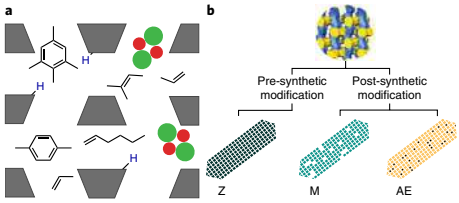

Fig. 1 | Schematic illustrations of the HP concept for the MTO reaction and the synthesis of pre- and post-synthetically modified zeolites. **a**, Representation of a ZSM-5 catalyst with Brønsted acid sites (blue) located at the intersection of straight and sinusoidal channels and Lewis acid sites appearing due to the incorporation of extraframework species (green and red). During MTO reaction, ZSM-5 channels are 'inhabited' by olefins and aromatics, which act as 'co-catalysts pool species'. **b**, Series Z was prepared by varying the Si/Al ratio and/or SDA during the ZSM-5 zeolite synthesis, series M was prepared by post-synthetic demetallation of microporous ZSM-5 zeolite, whereas series AE was prepared by post-synthetic incorporation of alkaline-earth metals into microporous ZSM-5 zeolite.

types of acid sites. We followed two main approaches: (i) controlling the amount of acid sites and their location during zeolite synthesis, and (ii) modifying the acidity of pre-synthesized zeolites (Fig. 1b). The first series of pre-synthetically modified zeolites (**Z**) was prepared by varying the amount of Al in the synthesis gel and/or utilizing different structure-directing agents (SDA). Another two series of catalysts were obtained following different protocols of post-synthetic modification using commercial Z1 as the starting material. The **M**-series was obtained by Z1 demetallation with various desilicating and dealuminating agents, whereas the **AE**-series was prepared by incorporation of different amounts and types of alkaline-earth metal (AE1–AE5 are Ca-modified, AE6 is Sr-modified and AE7 is Mg-modified).

All synthesized zeolites from the Z-series have the expected MFI topology, comparable morphology and crystal size (Supplementary Figs. 1, 2). Variation of Al during the synthesis resulted in zeolites with different Si/Al ratios (260 and 1,280 for Z2 and Z3, respectively), whereas variation in SDA affected textural properties. N_2 adsorption reveals the existence of a hysteresis loop in the pre-capillary condensation region of microporous Z2 and Z3 (Supplementary Figs. 3, 4) attributed to the phase transition from a disordered phase to a lattice-like fluid phase[15]. This becomes less evident with increasing Al content and completely disappears for Z1 with Si/Al = 40. Z4, synthesized using a di-quaternary ammonium-type surfactant as described previously[16], additionally exhibits a hysteresis loop at high relative pressures, indicative of mesoporosity between stacked sheets[17].

FT-IR spectroscopy of pyridine adsorbed (Supplementary Fig. 5) indicates a decrease in Brønsted acidity[18] (absorbance at 1,546 cm^{-1}) in the Z1–Z4 series, in line with the increasing Si/Al ratio. For the M-series, treatment with various demetallating agents caused a decrease of BAS in comparison to Z1 (Table 1) and resulted in an increased amount of LAS. Lewis acidity is due to the presence of extraframework Al and/or perturbed Al species[19]. Another side-effect of this post-synthetic modification was the generation of mesopores, which are generally held responsible for lifetime improvement in methanol conversion[20,21]. For all samples except M4, demetallation caused a significant increase in the mesoporous surface area (Table 1). Contrastingly, incorporation of alkaline-earth metals resulted in a significant decrease of both surface area (S_{BET}) and pore-volume (V_p), both gradually reduced with an increase of alkaline-earth loading (Supplementary Fig. 3). Besides, the modification also caused almost a tenfold decrease in BAS concentration (from 232 μmol g^{-1} to 27 μmol g^{-1} for Z1 and AE4). Another clear difference between the Z1 sample and the AE series is the appearance of a significantly higher concentration of LAS (Supplementary Fig. 5).

Comparison of the acidic properties of the studied catalysts reveals that Z3 possesses the same concentration of BAS as AE4 and AE5. The only difference between these samples is the presence of a notable amount of LAS resulting from Ca incorporation. To gain insight into the proximity between these two acid functionalities, two-dimensional ^{1}H–^{1}H DQ (double-quantum) and ^{1}H–^{1}H RFDR (radio-frequency-driven recoupling) MAS NMR was carried out (Fig. 2). These two methods are particularly powerful when combined: RFDR gives a self-correlation peak, whereas DQ does not[22]. The cross-peaks in the horizontal frequency span of 1–2 ppm belong to both terminal Si-OH protons and bridging Ca-OH protons (Fig. 2)[22,23]. When AE3 is fully dehydrated at 450 °C (Supplementary Fig. 6), the DQ correlation vanishes, but the RFDR correlation does not. This indicates that, under reaction conditions, the acidic protons behave as isolated entities.

Effect of pre-synthetic and post-synthetic modification. The impact of acidic properties was evaluated under conditions relevant for the MTO process. Z1 exhibits the shortest lifetime in comparison to the other samples, it deactivates after 16.5 h on stream, which corresponds to an integral throughput of 132 $g_{MeOH}\,g_{catalyst}^{-1}$ (Fig. 3a,b). The lower concentration of Brønsted acidity in Z3 extends the catalyst lifetime up to 28 h (Fig. 3b, Supplementary Fig. 7)[24]. According to a previous study[24], the lower the Si/Al, the faster the formation rate of methylated aromatic species, in turn leading to faster coking rates. Z3 is characterized by steady formation of all products, propylene being the dominant one (up to 48%) (Supplementary Fig. 7). Another striking difference is the much lower fraction of paraffins, ethylene and aromatics in comparison with Z1 (Supplementary Fig. 10). It has been previously demonstrated[11] that the formation of ethylene is mechanistically separated from other olefins, being mostly formed via xylenes and/or trimethylbenzenes, whereas propylene is selectively formed via methylation and cracking reactions within the alkene cycle (Fig. 4b). The formation of paraffins is a result of hydrogen transfer to olefins, where methanol can act as hydrogen donor. Proton transfer occurs on both BAS[25] and extraframework aluminium species[26]. The sharp decrease in formation of ethylene and aromatics in sample Z3 suggests almost full suppression of the aromatic cycle[3,20,26]. As hypothesized previously[27], the aromatic cycle dominates when zeolites with high acid site densities are used. In this line, isolation of BAS by decreasing the Al content leads to higher propylene yields[1]. Further comparison of Z3 with AE5 confirms that the concentration of BAS is indeed the main descriptor for the observed selectivity (Supplementary Fig. 8). These two catalysts, having very similar concentrations of acid sites, exhibit almost identical selectivity to paraffins, ethylene and propylene. In contrast, AE5, prepared by post-synthetic modification with Ca, displays a two times longer lifetime (Fig. 3b). The only obvious difference between these two catalysts is the presence of Lewis acidity in AE5 arising from Ca incorporation.

Demetallated mesoporous M1–M4 show longer lifetimes and higher selectivities to propylene in comparison with the parent Z1 (Supplementary Fig. 9). The improved stability towards deactivation of mesoporous zeolites is generally explained by a facilitated molecular transport[28], along with a higher external surface area that provides more space for coke deposition[29,30]. On the other hand an increased selectivity to propylene can be explained by the decreased concentration of acid sites, the latter being also responsible for the

Table 1 | Textural and acidic properties of the ZSM-5 zeolites under study.

Catalyst	Si/Al[a] (mol mol^{-1})	Cation[b] (%)	V_{total}[c] (cm^3 g^{-1})	V_{micro}[c] (cm^3 g^{-1})	S_{BET}[d] (m^2 g^{-1})	S_{meso}[b] (m^2 g^{-1})	S_{micro}[e] (m^2 g^{-1})	n_{BAS}[f] (μmol g^{-1})	n_{LAS}[f] (μmol g^{-1})
Z1	39	-	0.26	0.15	448	85	363	232	35
Z2	260	-	0.22	0.15	425	85	340	50	12
Z3	1,280	-	0.21	0.17	429	74	355	28	11
Z4	61	-	0.67	0.09	535	328	207	96	74
M1	65	-	1.20	0.12	575	314	261	149	77
M2	36	-	0.35	0.14	456	142	314	188	53
M3	31	-	0.43	0.14	584	276	308	154	108
M4	41	-	0.28	0.11	347	127	220	49	50
AE1	42	Ca (6.1)	0.21	0.11	323	56	267	128	1
AE2	45	Ca (0.2)	0.27	0.15	429	85	344	138	108
AE3	47	Ca (2.4)	0.24	0.13	392	77	315	40	228
AE4	46	Ca (3.8)	0.22	0.13	387	74	313	27	240
AE5	46	Ca (4.6)	0.23	0.12	385	75	310	29	240
AE6	45	Sr (5.2)	0.20	0.13	379	106	273	85	108
AE7	44	Mg (1.4)	0.22	0.14	417	95	322	76	217

[a]Molar ratio determined by ICP-OES. [b]**AE1** was prepared by solid-state ion-exchange with $Ca(CH_3COO)_2$. **AE2** was prepared by ion-exchange with 1 M $Ca(NO_3)_2{\cdot}4H_2O$. **AE3–AE5** were prepared by incipient wetness impregnation with aqueous solutions of $Ca(NO_3)_2{\cdot}4H_2O$ of different concentrations. **AE6** and **AE7** were prepared by incipient wetness impregnation with $Sr(NO_3)_2$ and $Mg(NO_3)_2{\cdot}6H_2O$, respectively. Further details are provided in the Methods section. [c]From N_2 adsorption isotherm using the *t*-plot method. [d]From N_2 adsorption isotherm using the BET method. [e]From N_2 adsorption isotherm. $S_{micro} = S_{BET} - S_{meso}$. [f]Concentrations of BAS and LAS derived from FT-IR spectroscopy with pyridine as a probe molecule.

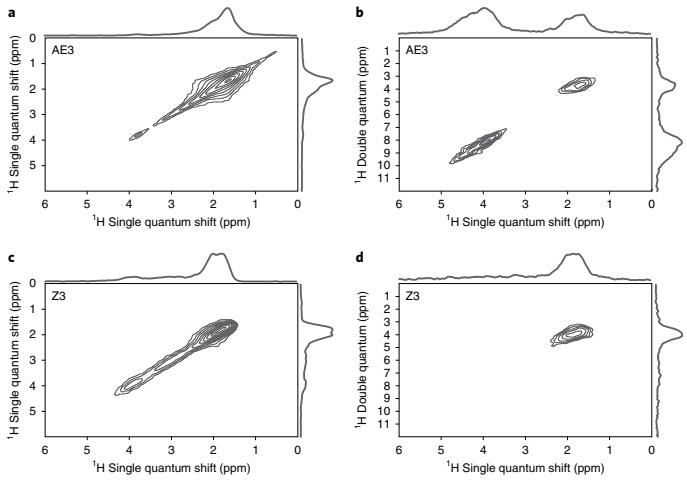

Fig. 2 | Evaluation of Brønsted and Lewis acid site interactions. a–d, ^{1}H–^{1}H RFDR (**a**,**c**) and ^{1}H–^{1}H DQ (**b**,**d**) MAS NMR spectra of AE3 modified with Ca (**a**,**b**) and Z3 with the same amount of BAS (**c**,**d**). Both samples were dehydrated at 200 °C (1 °C min^{-1}).

improved lifetimes[20,30]. Further examination of the textural and catalytic properties reveals a linear correlation between mesopore surface area and catalyst lifetime (Supplementary Fig. 11). Analysis of the spent catalyst indicates a significantly higher amount of coke deposited in micro- and mesopores for the M-series of zeolites in comparison with Z1. Another striking observation is the significantly longer lifetime of M4, having the lowest surface area in comparison with other samples from the M-series. In the same manner, Z2 and M4 are rather similar both in porosity and concentration of BAS, but differ in concentration of LAS.

Establishing acidity–performance relationship. The integral propylene selectivity was related to changes in BAS concentration. To account for changes in textural properties, we normalized the concentration of BAS (n_{BAS}) by the BET area (S_{BET}) to yield an acid site surface density (c_{BAS}). During the normalization procedure, we

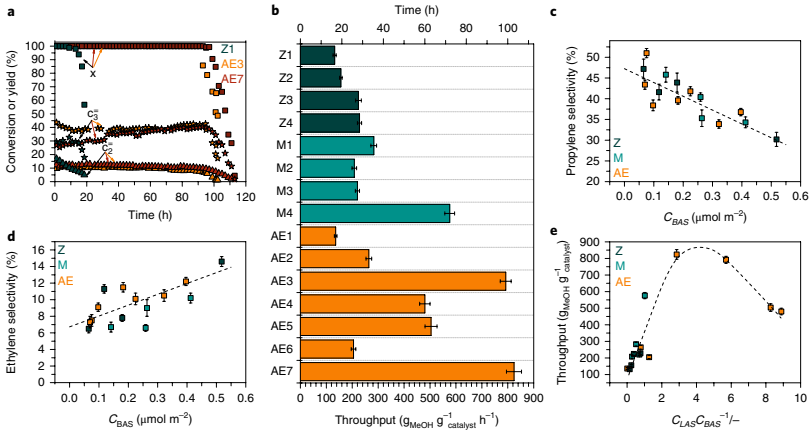

Fig. 3 | Catalytic behaviour of pre- and post-synthetically modified catalysts. a, The modification with Ca (AE3) and Mg (AE7) leads to significant prolongation of catalyst lifetime (black squares), increases yield of propylene (black stars) and decreases yield of ethylene (black triangles). **b**, Methanol throughput and lifetimes of catalysts under study. Reaction conditions: $T = 500$ °C, WHSV = 8 g_{MeOH} $g_{catalyst}^{-1}$ h^{-1}. **c**–**e**, Descriptors of ZSM-5 acidity in MTO. Z (black), pre-synthetically modified ZSM-5 with different Si/Al ratio; M (green), post-synthetically demetallated ZSM-5; AE (orange), zeolites modified by post-synthetic incorporation of alkaline-earth metals. The acidity–performance relationship clearly shows that the density of BAS (C_{BAS}) determines propylene (**c**) and ethylene (**d**) selectivity, whereas the ratio of LAS and BAS (C_{BAS}/C_{LAS}) governs catalyst lifetime (**e**). Error bars represent standard deviation of the catalytic performance results performed at least two times for each sample. Dashed lines in **c** and **d** represent linear fit to the provided data, whereas the dashed line in **e** is to guide the eye.

assumed an even distribution of Al within the zeolite framework. This assumption was later validated by UV–vis spectroscopy (vide infra) and ^{27}Al NMR experiments (Supplementary Figs. 12–14).

Figure 3c,d shows the integral propylene and ethylene selectivity as a function of BAS density. These figures clearly demonstrate a linear correlation between C_{BAS} and selectivity to propylene and ethylene for all samples. At high BAS densities, acid sites are in closer proximity. As a consequence, successive reactions can occur at these sites along the diffusion pathway, promoting the aromatic cycle[27]. Low BAS densities prevent consecutive reactions leading to aromatization and coking, thus favouring methylation and cracking reactions. Altogether, these results confirm that BAS isolation is instrumental to attain a high propylene selectivity. Opposite trends obtained for ethylene and propylene also confirm that these two products are formed through two competitive routes. To decrease the impact of the 'secondary reactions' we also plotted ethylene and propylene selectivity taken at 98% oxygenate conversion (Supplementary Fig. 15), that is, when almost the entire catalytic bed is deactivated and only the lower part participates in MTO. As it can be observed, similar correlations are obtained.

The relationship between C_{BAS} and methanol throughput is more complex. Although high BAS densities result in faster deactivation due to faster coking rates, not only BAS density but also distribution play an important role. It has been shown previously[7] that the same concentration of BAS can still lead to different lifetimes due to an uneven Al distribution and formation of Al pairs. Analysis of Al distribution by UV–vis of Co-exchanged zeolites shows that this distribution within α-, β- and γ-sites is rather similar (Supplementary Fig. 12), excluding the effect of Al location. Therefore, the different resistance to deactivation of AE5 and Z3 with similar C_{BAS} is a strong argument to claim that C_{BAS} is not the only descriptor for catalyst lifetime. The same discussion holds for Z2 and M4, the latter being stable for at least three times longer. Considering that demetallation of M4 did not result in significant development of the external surface area, the potential effect of mesopores on catalyst lifetime can be ruled out. Preparation of M4 involved extraction of framework Al by steaming, leading to the formation of 'inefficient' occluded mesopores barely impacting intracrystalline diffusion[31–33]. It has been shown[6] that interconnectivity of mesopores in hierarchical ZSM-5 has the largest impact on lifetime. This catalyst however showed the longest lifetime among the M-series. As the only obvious difference between these catalysts (AE5 versus Z3 and M4 versus Z3) is the presence of LAS, it seems logical to study the effect of C_{LAS}. Figure 3e shows the methanol throughput plotted as a ratio of LAS and BAS. The obtained 'volcano' plot yields an optimum LAS/BAS ratio between 2 and 6. Interestingly, the two optimal catalysts are AE3 and AE7, samples prepared by Ca and Mg incorporation, respectively, both with an AE/Al molar ratio of 1.8.

On the role of Lewis acidity. The impact of Lewis acidity on MTO is not yet fully understood. There are only a few works dealing with this topic and often reporting a rather negative influence on performance[26]. The majority of those works focus on the presence of extraframework Al (EFAl). Here, we investigate the beneficial effect of alkaline-earth metal modification at the molecular level by performing a series of density functional theory (DFT) based simulations. Earlier, we proposed $[Ca(\mu\text{-}O)(\mu\text{-}OH)Ca]^+$ moieties as possible active sites in the Ca-modified ZSM-5 catalyst[34], inspired by the experimentally defined optimal Ca:Al ratio of 2 and the literature reports that divalent extraframework cations tend to self-organize into binuclear complexes in zeolites[35]. We studied the stability of various Ca binuclear complexes when incorporated in a ZSM-5 structure containing two BAS per unit cell. The $[Ca(\mu\text{-}O)_2Ca]$ has a very high basicity and quickly deprotonates the vicinal BAS.

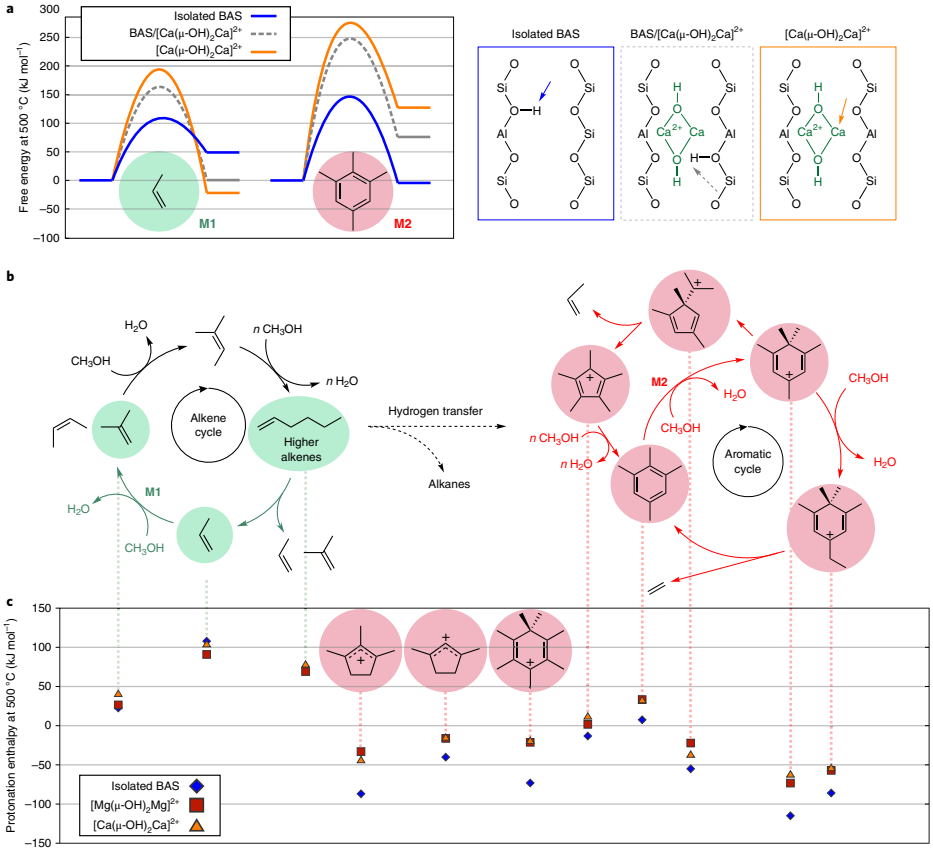

Fig. 4 | Modified zeolites decrease the stability and growth rate of aromatic MTO intermediates. a, Free energy profiles at 500 °C (kJ mol^{-1}) for propene and 1,2,3,5-tetramethylbenzene methylation by methanol catalysed by an isolated BAS, a BAS near a $[Ca(\mu\text{-}OH)_2Ca]^{2+}$ moiety and an LAS formed by the $[Ca(\mu\text{-}OH)_2Ca]^{2+}$ site. **b**, The dual cycle mechanism for the MTO process with indication of intermediates that are unaffected by the alkaline-earth modification (green) and destabilized by the modification (red). **c**, Calculated protonation enthalpies at 500 °C (kJ mol^{-1}) for the various MTO intermediates at an isolated BAS (blue diamonds) in the presence of a $[Mg(\mu\text{-}OH)_2Mg]^{2+}$ (red squares) or a $[Ca(\mu\text{-}OH)_2Ca]^{2+}$ (orange triangles) moiety.

An alternative stabilizing interaction for the singly protonated $[Ca(\mu\text{-}O)(\mu\text{-}OH)Ca]^{+}$ is to bind to the zeolite framework, but this is by far less stabilizing than the formation of $[Ca(\mu\text{-}OH)_2Ca]^{2+}$ (Fig. 5). This analysis clearly shows the capacity of alkaline earth modification to reduce the number of BAS sites in the catalyst.

Further, we investigated the reactivity and stability of some key HP species at LAS and BAS. Figure 4a shows that the free energies of activation for the methylation reactions of propene and 1,2,3,5-tetramethylbenzene (tetraMB) significantly increase upon Ca incorporation. The obtained transition states are shown in Supplementary Figs. 26 and 27. These two reactions are crucial for the alkene and aromatics catalytic cycles[36–38]. When the reaction is catalysed by a BAS near a Ca moiety (BAS/$[Ca(\mu\text{-}OH)_2Ca]^{2+}$) or by a LAS formed by the $[Ca(\mu\text{-}OH)_2Ca]^{2+}$ moiety, the free energy barriers increase by 54–67 kJ mol^{-1} for propene and 101–129 kJ mol^{-1} for tetraMB compared to the reactions catalysed by an isolated BAS. Thus, alkene and aromatics methylation are slowed down to a different extent in Ca-ZSM-5. These results show that the growth of aromatics by methylation, and thus the propagation of the aromatics-based HP cycle, is strongly suppressed by Ca incorporation while alkene methylation and the propagation of the autocatalytic cycle can still take place. These calculations were experimentally verified by co-feeding benzene with DME over samples Z3 and AE5. The apparent activation energy of benzene methylation increased from 64 kJ mol^{-1} over Z3 to 85 kJ mol^{-1} over AE5 (Supplementary Fig. 21). In line with this observation, higher selectivity to secondary products was observed over Z3 than over AE5 (Supplementary Fig. 20). At 500 °C, alkaline earth modification was found to decrease the

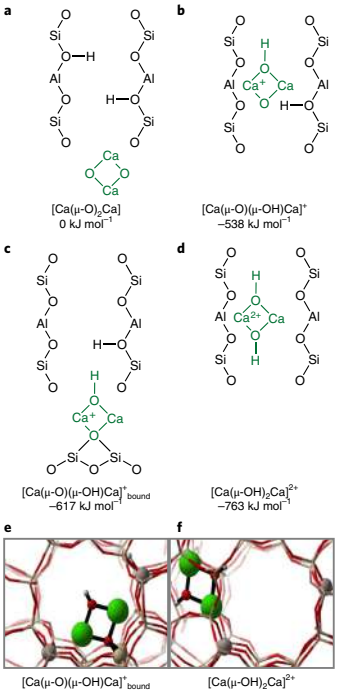

Fig. 5 | DFT-based enthalpy calculations at 500 °C reveal the most stable structure of binuclear Ca species in ZSM-5. a–**f**, Reference state (**a**), [Ca(μ-O)(μ-OH)Ca]$^+$ compound in ZSM-5 (**b**), [Ca(μ-O)(μ-OH)Ca] bound to the framework (**c**), [Ca(μ-OH)$_2$Ca]$^{2+}$ in ZSM-5 (**d**), snapshot of [Ca(μ-O)(μ-OH)Ca] bound to the framework (**e**) and snapshot of [Ca(μ-OH)$_2$Ca]$^{2+}$ in ZSM-5 (**f**).

rate of benzene conversion by a factor of 4.1. Similar co-feeding experiments with isobutene also indicate a decrease of the rate of isobutene conversion by a factor of 2.4 at 500 °C, which is smaller than for benzene conversion. We further investigated the stability of carbocations, which are known to be key intermediates in the aromatic cycle[39]. Proton enthalpies for a series of MTO intermediates were studied in ZSM-5 samples with an isolated BAS and samples with a BAS nearby a [Ca(μ-OH)$_2$Ca]$^{2+}$ or [Mg(μ-OH)$_2$Mg]$^{2+}$ site. The selection of HP species is inspired by the proposed intermediates in the alkene and aromatic-based cycle[40]. We found that the stability of carbenium ions is largely reduced in LAS-modified zeolites, for example the protonation enthalpy of 1,2,2,3,5-pentamethylbenzenium ion reduces from −120 kJ mol^{-1} to −75 and −65 in Mg- and Ca-modified zeolites (Fig. 4c). The difference in protonation enthalpies may be ascribed to the stabilizing interaction of the double bonds of the neutral cyclic species with the [Ca(μ-OH)$_2$Ca]$^{2+}$ sites. Our findings show that cyclic HP intermediates formed in LAS-modified zeolites would be much less reactive in the aromatic based cycles. The influence on alkenes is far less pronounced, which is an indication that this cycle is less affected by incorporating LAS. These conclusions are fully in line with the free energy profiles for methylation of propene and tetraMB shown in Fig. 4a. We also investigated the lifetimes of neutral species at a realistic working condition of 500 °C (Supplementary Fig. 41). We performed molecular dynamics simulations on the neutral species and investigated the tendency of the zeolite framework to protonate the HP compounds. In accordance with our static simulations, systematically longer lifetimes are found for the neutral species in LAS -modified zeolites. We observe similar features for EFAl species with a [HOAl(μ-OH)$_2$AlOH]$^{2+}$ structure, indicating similarities between EFAls and Ca species (see Supplementary Figs. 34–38).

Operando UV–vis diffuse reflectance spectroscopy (UV–vis DRS) is an insightful technique to follow the evolution of HP formed in a zeolitic microenvironment[41–43], able to distinguish between different neutral and protonated species. To identify experimentally whether the presence of Lewis acidity affects the nature of HP species, we monitored the formation of hydrocarbons produced during MTO via UV–vis DRS for Ca-containing AE3 and compared the obtained spectra with Z1 and Z2. The spectra of Z1 and Z2 taken during the first minutes of MTO are characterized by similar absorption bands but different intensities (Fig. 6 and Supplementary Fig. 16). This points to the fact that hydrocarbon species are of the same nature but form in different amounts, the nature of hydrocarbon species is independent from the amount of BAS. In UV–vis, the region above 35,000 cm^{-1} corresponds to neutral aromatic species, while protonated aromatics and neutral polyaromatics absorb light at lower wavenumbers. For samples Z1 and Z2, the first minutes of MTO are characterized by the appearance of a band around 35,000 cm^{-1} corresponding to neutral benzene and a broad component composed by a combination of bands around 23,600, 20,600 and 17,000 cm^{-1} (Supplementary Fig. 16), corresponding to methyl-substituted benzenium cations[41,42]. With time-on-stream, the appearance of the absorption band below 15,000 cm^{-1} (Supplementary Fig. 16) indicates an accumulation of polyaromatic species in Z1 and Z2. The early appearance of this band indicates that formation of polyaromatics starts at the beginning of the reaction (Supplementary Fig. 16). In sharp contrast, the UV–vis DRS of AE3 reveal neither neutral nor charged aromatic species. The spectra are characterized by a wide band around 30,000 cm^{-1} becoming much broader with increasing time-on-stream. Attribution of this region is rather controversial in literature but it is generally agreed that these bands are indicative for monoenylic and dienylic cations[44]. After 5 h on stream, the absorption bands below 15,000 cm^{-1} display the highest intensity for samples Z1 and Z2 pointing at the prevalence of naphthalene and its homologues; they are still not observable for AE3. These observations support the theoretical calculations (vide supra) and suggest that indeed LAS prevent further reactions involving aromatic moieties.

Finally, ^{1}H and ^{1}H–^{1}H DQ MAS NMR experiments at very high spinning speed were performed to validate the nature of trapped species in fully deactivated AE5, Z1 and Z3. The ^{1}H (MAS) NMR spectra of the analysed samples clearly show a difference, especially for the resonance at 7 ppm (Fig. 6b). The signals at 7.8 and 7.1 ppm with a strong autocorrelation in DQ experiments (Fig. 6c,d) are assigned to aromatic hydrogen. In line with UV–vis, MAS NMR also demonstrates that aromatic species do not accumulate in Ca-containing zeolites and play a minor role in catalyst deactivation. The trapped species in Ca-containing AE5 are mainly of aliphatic nature, as confirmed by the resonances appearing in the range between 4.3–0 ppm (ref. [45]).

Discussion

In pursuit of a long-living MTP catalyst, a great number of zeolite-based catalysts with ZSM-5 topology have been engineered[13]. Herein, we identified the main descriptors governing selectivity and lifetime by rationalizing catalytic results of samples prepared

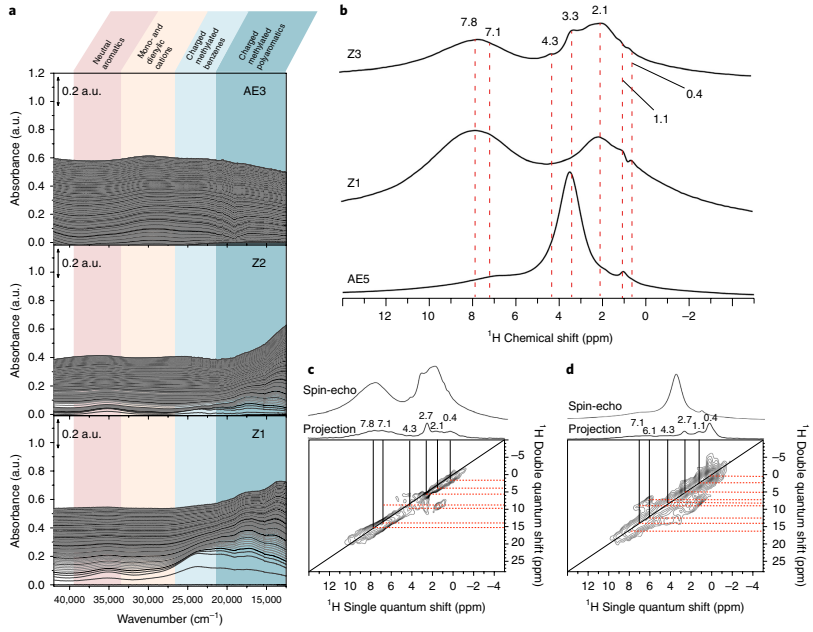

Fig. 6 | Visualization of the trapped hydrocarbon species in Z- and AE-series. a, Operando UV–vis diffuse reflectance spectra collected during methanol conversion over Z1 and Z2 zeolites with different Si/Al ratios and Ca-modified AE3 at 500 °C indicates that aromatic species do not accumulate in Ca-modified samples. For Z1 and Z2 zeolites, formation of polyaromatic species (naphthalene and homologues) is observed during the first seconds of MTO, indicating that catalyst deactivation starts at the beginning of the reaction. UV–vis diffuse reflectance spectra were taken every 20 s. **b**, Analysis of the spent catalyst by ^{1}H NMR indicates further that aromatic species are the minor components in completely deactivated Ca-modified catalysts, which is characterized by the predominant presence of aliphatic protons. **c**, ^{1}H–^{1}H DQ MAS NMR spectra of Z3 shows that aliphatic protons are correlating with aromatic protons, suggesting that trapped species are mainly represented by alkylated aromatics. **d**, In AE5, aliphatic protons are mainly autocorrelated. Black lines indicate peaks in single quantum space, whereas red dashed lines show the (auto-)correlation in DQ space.

by different synthetic protocols. Normalization of acidity by surface area helped elucidate catalytic behaviour not only of microporous but also of mesoporous zeolites, which are generally more stable towards deactivation due to the combination of improved mass-transfer properties and ability to hold more coke. We have demonstrated that BAS isolation and Lewis acidity are the most important parameters in defining catalyst selectivity and lifetime.

We have confirmed that propylene selectivity is controlled by BAS density (C_{BAS}). Acid site isolation is the key to maximize propylene selectivity by preventing secondary reactions leading to the formation of aromatics. Thus, BAS is the first descriptor of catalytic performance, and its influence on product distribution is generally confirmed in the literature[1]. BAS isolation may be achieved using various approaches. Herein, we showed that, apart from decreasing Al content, incorporation of alkaline-earth metals also results in generation of isolated BAS. Taking Ca species as an example, we showed that alkaline-earth metals tend to deprotonate BAS thus neutralizing inherent zeolite acidity, forming $[Ca(\mu\text{-}OH)_2Ca]^{2+}$ species of Lewis acidic nature and isolated BAS, as demonstrated by ^{1}H–^{1}H DQ and ^{1}H–^{1}H RFDR MAS NMR. The generation of a new type of LAS turned out to be critical to obtain long-living catalysts. Catalyst lifetime may be optimized by tuning the LAS/BAS ratio according to a typical volcano plot. We found that $[Ca(\mu\text{-}OH)_2Ca]^{2+}$ LAS species have the tendency to suppress aromatics growth by methylation and destabilize crucial carbenium ions for the aromatic cycle, thereby blocking this reaction pathway. Hand in glove, UV–vis DRS showed that 'LAS-containing' catalysts do not form polyaromatic species—notorious for catalyst deactivation—in contrast to 'LAS-free' catalysts. For the latter, the formation and evolution of aromatic species was witnessed during the first minutes of MTO independently on the amount of BAS. Finally, the destabilizing effect of LAS presence on aromatic cycle was confirmed by ^{1}H MAS NMR performed on fully deactivated catalysts. The trapped hydrocarbons in the case of Ca-containing samples were mainly aliphatic of nature, while non-modified catalyst materials had a large amount of aromatic species.

With this information in hand, we can now formulate clear design rules to achieve ideal MTO catalysts maximizing propylene selectivity and lifetime. The presented case shows that a subtle interplay between various functions in the catalyst—in this case incorporation of LAS and BAS sites—may be used to obtain an optimally performing catalyst. Given the fact that zeolite catalysis often encounters similar reaction intermediates, we expect that the trends discovered here will also be of high relevance for many other zeolite

catalysed processes, such as catalytic cracking or isomerization. We conceptually showed the potential for tuning active sites in zeolite acid-catalysed reactions to a greater degree of complexity.

Methods

Synthesis of the Z-series catalysts. **Z1** is commercially available ZSM-5 zeolite calcined at 550 °C (CBV 8014, Zeolyst International). **Z2** and **Z3** were hydrothermally synthesized following the procedure described previously[46]. **Z4** was synthesized according to a previous protocol[47]. As-synthesized **Z2**, **Z3** and **Z4** were calcined in air at 550 °C to remove the template, and ion-exchanged with NH_4NO_3 (1 M, 80 °C, 2 h) followed by calcination in air at 500 °C for 5 h.

Synthesis of the M-series catalysts. **M1** was obtained from **Z1** by desilication and acid leaching. Desilication was carried out in 1 M NaOH at 70 °C for 1 h. **M2** and **M3** were obtained by treatment of **Z1** in 0.1 and 0.2 M NaOH at 65 °C for 30 min. In the preparation of **M3**, the treatment solution also contained 0.2 M tetrapropylammonium bromide. Both samples were converted into protonic form by ion exchange in NH_4NO_3 solution (0.1 M, 25 °C, 8 h) and calcined at 550 °C for 5 h. **M4** was obtained from microporous **Z1** by in situ dealumination in two consecutive MTO runs.

Synthesis of the AE-series catalysts. **AE1** was prepared by solid-state ion-exchange with $Ca(CH_3COO)_2$. **AE2** was prepared by triple ion-exchange with 1 M $Ca(NO_3)_2{\cdot}4H_2O$ at 80 °C. **AE3**, **AE4** and **AE5** were prepared by incipient wetness impregnation (IWI) with an aqueous solution of $Ca(NO_3)_2{\cdot}4H_2O$ (2.4 M, 4.0 M and 6.0 M, respectively). **AE6** and **AE7** were prepared by IWI with 2.4 M $Sr(NO_3)_2$ and 2.4 M $Mg(NO_3)_2{\cdot}6H_2O$. After the modification, all AE samples were calcined at 550 °C. Detailed information is further provided in Supplementary Experimental Section.

Characterization. N_2 adsorption at −196 °C was carried out using a Tristar II 3020 analyser (Micromeritics). Microscopy images were recorded using a JEOL JSM-6010LA with a standard beam potential of 10 kV and an Everhart–Thornley detector. The XRD patterns of the powders were recorded with a Bruker D8 Advance X-ray diffractometer equipped with a LynxEye position-sensitive detector and monochromatic CoKα ($\lambda = 1.788970$ Å). Transmission FT-IR spectroscopy using pyridine as a probe molecule was performed using a Nicolet 6700 spectrometer with a MCT/B detector. For the wafer preparation, 50 mg of catalyst was used without any dilution. The amount of Brønsted (BAS) and Lewis (LAS) acid sites was derived from the bands at 1,545 and 1,456 cm^{-1} using extinction coefficients of 1.67 and 2.22, respectively[19]. ^{1}H MAS NMR (magic angle spinning nuclear magnetic resonance) measurements were performed on a 11.7 Tesla Bruker DMX500 NMR spectrometer operating at a ^{1}H Larmor frequency of 500 MHz. A Bruker triple resonance 4 mm MAS probe head with a sample rotation rate of 10 kHz was used. ^{1}H NMR spectra were recorded with a 90° pulse of 5 µs duration and 3 s interscan delay. DQ experiments were performed using the back-to-back (BABA) recoupling sequence for excitation and reconversion of the DQ coherences with a 100 µs duration. The 2D RFDR (radio frequency-driven recoupling) experiments were implemented via the application of rotor-synchronized 180-degree pulses (one inversion pulse per rotor period) for homonuclear dipolar recoupling. A total mixing time duration of 1.6 ms was used. Deactivated zeolite materials were analysed by one-dimensional ^{1}H MAS SS NMR and ^{1}H−^{1}H multiple-quantum spectroscopy. One-dimensional ^{1}H MAS SS NMR spectra were recorded on Bruker AVANCE III spectrometers operating at 600 MHz resonance frequencies for ^{1}H. The sample spinning frequency was 30 kHz for ^{1}H. Two-dimensional DQ experiments were recorded on a Bruker AVANCE III spectrometer operating at 600 MHz with a conventional double-resonance 2.5 mm CP/MAS probe. The ultraviolet–visible diffuse reflectance spectra (UV–vis DRS) were collected on a Perkin–Elmer Lambda 900 spectrophotometer equipped with an integrating sphere (Labsphere) in the 200–800 nm range. The absorption intensity was expressed by the Schuster–Kubelka–Munk equation. Quantification of Al_{pairs} and determination of their location has been reported previously[48]. Operando UV–vis diffuse reflectance spectra were obtained using an AvaSpec 2048L spectrometer connected to a high temperature UV–vis optical fibre probe. The measurements were performed in the wavenumber range 11,000–50,000 cm^{-1}.

Catalyst testing. Catalytic experiments were carried out in a Microactivity Reference unit (PID Eng&Tech) at 500 °C and ambient pressure. The catalyst (pressed, crushed and sieved to particle sizes 250–420 µm) was mixed with SiC (6:1 wt%) and placed in a fixed-bed with an internal diameter of 9 mm for standard experiments. An ISCO pump was used to feed methanol to the reactor system. A weight-hourly space velocity (WHSV) of 8 $g_{MeOH}\,g_{cat}^{-1}\,h^{-1}$, an N_2:MeOH = 1:1 molar feed composition and atmospheric pressure were utilized. Conversion, selectivities and yields were calculated on a molar carbon basis. The performance results are presented in graphs as a function of the methanol mass throughput per amount of catalyst used ($g_{MeOH}\,g_{cat}^{-1}$) and defined as the overall amount MeOH fed through the catalytic bed before the conversion of oxygenates drops below 80%. Presented selectivities are integral values. In each case, the catalyst was operated in a fixed bed reactor until methanol conversion dropped below 50%.

Static calculations. Periodic DFT calculations are performed using the Vienna Ab Initio Simulation Package (VASP 5.3) with the PBE functional and using Grimme D3 dispersion corrections[49–52]. During the calculations, the projector augmented wave method is used. Furthermore, a plane-wave cutoff of 600 eV is used during the calculations and the self-consistent field convergence criterion is set to 10^{-5} eV. The sampling of the Brillouin zone is restricted to the Γ-point. The static calculations are performed in a ZSM-5 unit cell consisting of 96 T atoms. More information on the introduction of Al substitutions and unit cell parameters can be found in the Supplementary Computational Section. For a comprehensive overview of the state-of-the-art in modelling zeolite catalysis refer to ref. [38].

Dynamic calculations. The ab initio MD simulations are performed using the CP2K software package[53,54]. To account for the flexibility of the catalyst framework at realistic reaction conditions the NPT ensemble at 673 K and 773 K and 1 bar is used. During the ab initio MD simulations, the temperature is controlled by a chain of five Nosé–Hoover thermostats and the pressure by an MTK barostat. To represent the ZSM-5 zeolite, the same unit cell is used as during the static calculations, so extra information can be found in the Supporting Computational Section.

Code availability. The applied DFT codes (VASP and CP2K) are commercially available. Analysis of static calculations was performed with the TAMkin toolkit, which is freely available from https://molmod.ugent.be/software. Molecular dynamics runs were analysed using the freely available VMD software (http://www.ks.uiuc.edu/Research/vmd/).

Data availability. Data supporting the findings of this study are available within this paper and its Supplementary Information, and are available from the corresponding author upon reasonable request.

Received: 7 September 2017; Accepted: 14 May 2018;
Published online: 25 June 2018

References

1. Bleken, F. L. et al. Conversion of methanol into light olefins over ZSM-5 zeolite: strategy to enhance propene selectivity. *Appl. Catal. A* **447**, 178–185 (2012).
2. Keil, F. J. Methanol-to-hydrocarbons: process technology. *Microporous Mesoporous Mater.* **29**, 49–66 (1999).
3. Sun, X. Y. et al. On reaction pathways in the conversion of methanol to hydrocarbons on HZSM-5. *J. Catal.* **317**, 185–197 (2014).
4. Teketel, S. et al. Morphology-induced shape selectivity in zeolite catalysis. *J. Catal.* **327**, 22–32 (2015).
5. Olsbye, U. et al. Conversion of methanol to hydrocarbons: how zeolite cavity and pore size controls product selectivity. *Angew. Chem. Int. Ed.* **51**, 5810–5831 (2012).
6. Milina, M., Mitchell, S., Crivelli, P., Cooke, D., & Perez-Ramirez, J. Mesopore quality determines the lifetime of hierarchically structured zeolite catalysts. *Nat. Commun.* **5**, 3922 (2014).
7. Liang, T. et al. Conversion of methanol to olefins over H-ZSM-5 zeolite: reaction pathway is related to the framework aluminum siting. *ACS Catal.* **6**, 7311–7325 (2016).
8. Yarulina, I. et al. Methanol-to-olefins process over zeolite catalysts with DDR topology: effect of composition and structural defects on catalytic performance. *Catal. Sci. Technol.* **6**, 2663–2678 (2016).
9. Deimund, M. A. et al. Effect of heteroatom concentration in SSZ-13 on the methanol-to-olefins reaction. *ACS Catal.* **6**, 542–550 (2016).
10. Hemelsoet, K., Van der Mynsbrugge, J., De Wispelaere, K., Waroquier, M. & Van Speybroeck, V. Unraveling the reaction mechanisms governing methanol-to-olefins catalysis by theory and experiment. *ChemPhysChem* **14**, 1526–1545 (2013).
11. Svelle, S. et al. Conversion of methanol into hydrocarbons over zeolite H-ZSM-5: ethene formation is mechanistically separated from the formation of higher alkenes. *J. Am. Chem. Soc.* **128**, 14770–14771 (2006).
12. Haw, J. F., Song, W. G., Marcus, D. M. & Nicholas, J. B. The mechanism of methanol to hydrocarbon catalysis. *Acc. Chem. Res.* **36**, 317–326 (2003).
13. Stöcker, M. Methanol-to-hydrocarbons: catalytic materials and their behavior. *Microporous Mesoporous Mater.* **29**, 3–48 (1999).
14. Janardhan, H. L., Shanbhag, G. V. & Halgeri, A. B. Shape-selective catalysis by phosphate modified ZSM-5: Generation of new acid sites with pore narrowing. *Appl. Catal. A* **471**, 12–18 (2014).
15. Llewellyn, P. L. et al. Adsorption by MFI-type zeolites examined by isothermal microcalorimetry and neutron-diffraction. 2. Nitrogen and carbon-monooxide. *Langmuir* **9**, 1852–1856 (1993).

16. Choi, M. et al. Stable single-unit-cell nanosheets of zeolite MFI as active and long-lived catalysts. *Nature* **461**, 246–249 (2009).
17. Cychosz, K. A., Guillet-Nicolas, R., Garcia-Martinez, J. & Thommes, M. Recent advances in the textural characterization of hierarchically structured nanoporous materials. *Chem. Soc. Rev.* **46**, 389–414 (2017).
18. Emeis, C. A. Determination of integrated molar extinction coefficients for infrared-absorption bands of pyridine adsorbed on solid acid catalysts. *J. Catal.* **141**, 347–354 (1993).
19. Brus, J. et al. Structure of framework aluminum Lewis sites and perturbed aluminum atoms in zeolites as determined by Al-27{H-1} REDOR (3Q) MAS NMR spectroscopy and DFT/Molecular mechanics. *Angew. Chem. Int. Ed.* **54**, 541–545 (2015).
20. Mei, C. S. et al. Selective production of propylene from methanol: mesoporosity development in high silica HZSM-5. *J. Catal.* **258**, 243–249 (2008).
21. Milina, M., Mitchell, S., Michels, N. L., Kenvin, J. & Perez-Ramirez, J. Interdependence between porosity, acidity, and catalytic performance in hierarchical ZSM-5 zeolites prepared by post-synthetic modification. *J. Catal.* **308**, 398–407 (2013).
22. Volkringer, C. et al. The Kagome topology of the gallium and indium metal-organic framework types with a MIL-68 tructure: synthesis, XRD, solid-state NMR characterizations, and hydrogen adsorption. *Inorg. Chem.* **47**, 11892–11901 (2008).
23. Ruspic, C. et al. A well-defined hydrocarbon-soluble calcium hydroxide: synthesis, structure, and reactivity. *J. Am. Chem. Soc.* **128**, 15000–15004 (2006).
24. Mores, D., Kornatowski, J., Olsbye, U. & Weckhuysen, B. M. Coke formation during the methanol-to-olefin conversion: in situ microspectroscopy on individual H-ZSM-5 crystals with different Bronsted acidity. *Chem. Eur. J.* **17**, 2874–2884 (2011).
25. Martínez-Espín, J. S. et al. Hydrogen transfer versus methylation: on the genesis of aromatics formation in the methanol-to-hydrocarbons reaction over H-ZSM-5. *ACS Catal.* **7**, 5773–5780 (2017).
26. Müller, S. et al. Hydrogen transfer pathways during zeolite catalyzed methanol conversion to hydrocarbons. *J. Am. Chem. Soc.* **138**, 15994–16003 (2016).
27. Guisnet, M., Costa, L. & Ribeiro, F. R. Prevention of zeolite deactivation by coking. *J. Mol. Catal. A Chem.* **305**, 69–83 (2009).
28. Mitchell, S. et al. Structural analysis of hierarchically organized zeolites. *Nat. Commun.* **6**, 8633 (2015).
29. Schmidt, F. et al. Coke location in microporous and hierarchical ZSM-5 and the impact on the MTH reaction. *J. Catal.* **307**, 238–245 (2013).
30. Bleken, F. L. et al. Catalyst deactivation by coke formation in microporous and desilicated zeolite H-ZSM-5 during the conversion of methanol to hydrocarbons. *J. Catal.* **307**, 62–73 (2013).
31. Kortunov, P. et al. The role of mesopores in intracrystalline transport in USY zeolite: PFG NMR diffusion study on various length scales. *J. Am. Chem. Soc.* **127**, 13055–13059 (2005).
32. Karger, J. & Valiullin, R. Mass transfer in mesoporous materials: the benefit of microscopic diffusion measurement. *Chem. Soc. Rev.* **42**, 4172–4197 (2013).
33. Karger, J. Transport phenomena in nanoporous materials. *ChemPhysChem* **16**, 24–51 (2015).
34. Yarulina, I. et al. Suppression of the aromatic cycle in methanol-to-olefins reaction over ZSM-5 by post-synthetic modification using calcium. *ChemCatChem* **8**, 3057–3063 (2016).
35. Pidko, E. A., Hensen, E. J. M. & van Santen, R. A. Self-organization of extraframework cations in zeolites. *Proc. R. Soc. A* **468**, 2070–2086 (2012).
36. De Wispelaere, K., Bailleul, S. & Van Speybroeck, V. Towards molecular control of elementary reactions in zeolite catalysis by advanced molecular simulations mimicking operating conditions. *Catal. Sci. Technol.* **6**, 2686–2705 (2016).
37. Van Speybroeck, V. et al. First principle kinetic studies of zeolite-catalyzed methylation reactions. *J. Am. Chem. Soc.* **133**, 888–899 (2011).
38. Van Speybroeck, V. et al. Advances in theory and their application within the field of zeolite chemistry. *Chem. Soc. Rev.* **44**, 7044–7111 (2015).
39. Nicholas, J. B. & Haw, J. F. The prediction of persistent carbenium ions in zeolites. *J. Am. Chem. Soc.* **120**, 11804–11805 (1998).
40. Fang, H. et al. Theoretical investigation of the effects of the zeolite framework on the stability of carbenium ions. *J. Phys. Chem. C.* **115**, 7429–7439 (2011).
41. Goetze, J. et al. Insights into the activity and deactivation of the methanol-to-olefins process over different small-pore zeolites as studied with operando UV–vis spectroscopy. *ACS Catal.* **7**, 4033–4046 (2017).
42. Hemelsoet, K. et al. Identification of intermediates in zeolite-catalyzed reactions by in situ UV/Vis microspectroscopy and a complementary set of molecular simulations. *Chem. Eur. J.* **19**, 16595–16606 (2013).
43. Goetze, J., Yarulina, I., Gascon, J., Kapteijn, F. & Weckhuysen, B. M. Revealing lattice expansion of small-pore zeolite catalysts during the methanol-to-olefins process using combined operando X-ray diffraction and UV–vis spectroscopy. *ACS Catal.* **8**, 2060–2070 (2018).
44. Wulfers, M. J. & Jentoft, F. C. The role of cyclopentadienium ions in methanol-to-hydrocarbons chemistry. *ACS Catal.* **4**, 3521–3532 (2014).
45. Behera, B., Ray, S. S. & Singh, I. D. NMR Studies of FCC feeds, catalysts and coke. *Fluid Catal. Crack. VII Mater. Methods Process Innov.* **166**, 163–200 (2007).
46. Hong, Y. et al. Platinum nanoparticles supported on Ca(Mg)-zeolites for efficient room-temperature alcohol oxidation under aqueous conditions. *Chem. Commun.* **50**, 9679–9682 (2014).
47. Na, K. et al. Pillared MFI zeolite nanosheets of a single-unit-cell thickness. *J. Am. Chem. Soc.* **132**, 4169–4177 (2010).
48. Dedecek, J., Balgová, V., Pashkova, V., Klein, P. & Wichterlová, B. Synthesis of ZSM-5 zeolites with defined distribution of Al atoms in the framework and multinuclear MAS NMR analysis of the control of Al distribution. *Chem. Mater.* **24**, 3231–3239 (2012).
49. Kresse, G. & Hafner, J. Ab initio. *Phys. Rev. B* **47**, 558–561 (1993).
50. Kresse, G. & Hafner, J. Ab initio. *Phys. Rev. B* **49**, 14251–14269 (1994).
51. Kresse, G. & Furthmüller, J. Efficient iterative schemes for ab initio total-energy calculations using a plane-wave basis set. *Phys. Rev. B* **54**, 11169–11186 (1996).
52. Kresse, G. & Furthmüller, J. Efficiency of ab-initio total energy calculations for metals and semiconductors using a plane-wave basis set. *Comput. Mater. Sci.* **6**, 15–50 (1996).
53. Hutter, J., Iannuzzi, M., Schiffmann, F. & VandeVondele, J. CP2K: atomistic simulations of condensed matter systems. *Wiley Interdiscip. Rev. Comput. Mol. Sci.* **4**, 15–25 (2014).
54. VandeVondele, J. et al. Quickstep: Fast and accurate density functional calculations using a mixed Gaussian and plane waves approach. *Comput. Phys. Commun.* **167**, 103–128 (2005).

Acknowledgements

This research received funding from the Netherlands Organization for Scientific Research (NWO) in the framework of the TASC Technology Area 'Syngas, a Switch to Flexible New Feedstock for the Chemical Industry (TA-Syngas). S.B., K.D.W. and V.V.S. acknowledge the Fund for Scientific Research: Flanders (FWO), the Belgian American Educational Foundation, the Research Board of Ghent University (BOF), BELSPO in the frame of IAP/7/05 and funding from the European Union's Horizon 2020 research and innovation programme (consolidator ERC grant agreement no. 647755—DYNPOR (2015–2020)). The computational resources and services used were provided by Ghent University (Stevin Supercomputer Infrastructure) and the VSC (Flemish Supercomputer Center), funded by the Research Foundation: Flanders (FWO).

Author contributions

I.Y. and J.Ga. conceived, coordinated the research and designed the experiments in close collaboration with V.V.S. I.Y. synthesized and characterized most catalysts and performed all catalytic tests with support from M.R. and I.V.S.M. and J.P.R. provided several demetallated zeolite catalysts and J.S.M.E. and M.M. provided the ZSM-5 nanosheets and performed the methylation reactions. S.B., K.D.W. and V.V.S. performed the DFT and ab initio MD calculations. B.M. and E.A.H. performed NMR characterization and J.Go. performed the in situ UV–vis analysis. All authors contributed to analysis and discussion of the data. The manuscript was primarily written by I.Y., K.D.W., V.V.S. and J.Ga. with input from all authors.

Competing interests

The authors declare no competing interests.

Additional information

Supplementary information is available for this paper at https://doi.org/10.1038/s41557-018-0081-0.

Reprints and permissions information is available at www.nature.com/reprints.

Correspondence and requests for materials should be addressed to J.G.

Publisher's note: Springer Nature remains neutral with regard to jurisdictional claims in published maps and institutional affiliations.

Paper IV

Insight into the role of water on the methylation of hexamethylbenzene in H-SAPO-34 from first principle molecular dynamics simulations

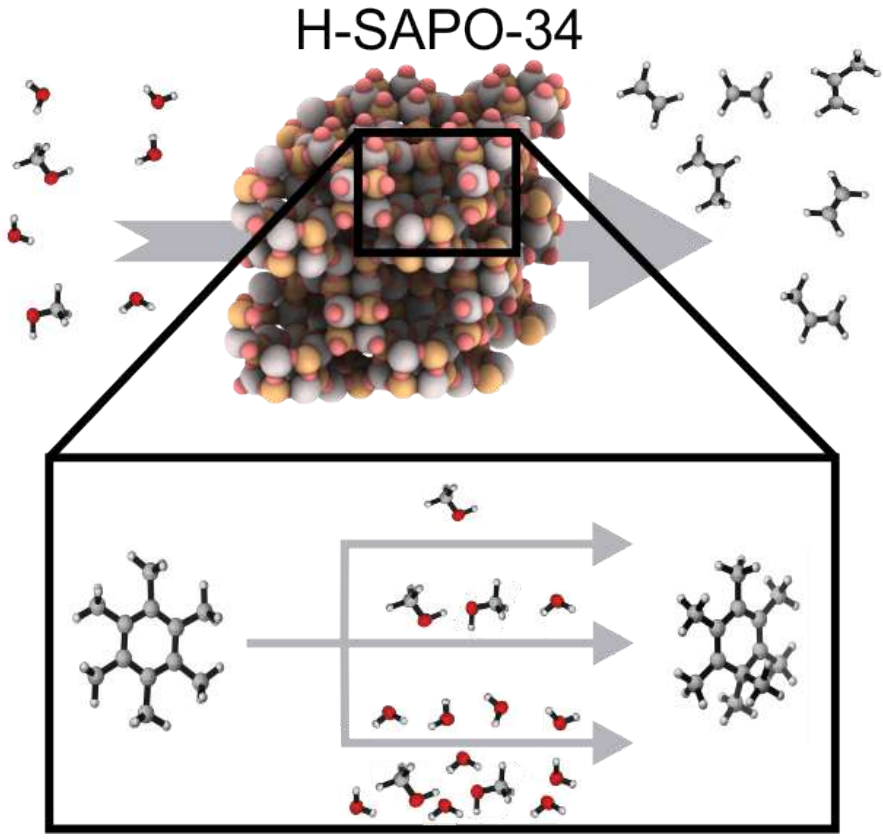

S. Bailleul, S.M.J. Rogge, L. Vanduyfhuys, V. Van Speybroeck, *ChemCatChem*, **11**, 3993–4010 (2019)

S. Bailleul performed all calculations and prepared the manuscript.

ChemPubSoc Europe

DOI: 10.1002/cctc.201900618

CHEMCATCHEM Full Papers

Insight into the Role of Water on the Methylation of Hexamethylbenzene in H-SAPO-34 from First Principle Molecular Dynamics Simulations

Simon Bailleul,[a] Sven M. J. Rogge,[a] Louis Vanduyfhuys,[a] and Veronique Van Speybroeck*[a]

The methylation of hexamethylbenzene with methanol is one of the key reactions in the methanol-to-olefins hydrocarbon pool reaction cycle taking place over the industrially relevant H-SAPO-34 zeolite. This methylation reaction can occur either via a concerted or via a stepwise mechanism, the latter being the preferred pathway at higher temperatures. Herein, we systematically investigate how a complex reaction environment with additional water molecules and higher concentrations of Brønsted acid sites in the zeolite impacts the reaction mechanism. To this end, first principle molecular dynamics simulations are performed using enhanced sampling methods to characterize the reactants and products in the catalyst pores and to construct the free energy profiles. The most prominent effect of the dynamic sampling of the reaction path is the stabilization of the product region where water is formed, which can either move freely in the pores of the zeolite or be stabilized through hydrogen bonding with the other protic molecules. These protic molecules also stabilize the deprotonated Brønsted acid site, created due to the formation of the heptamethylbenzenium cation, via a Grotthuss-type mechanism. Our results provide fundamental insight in the experimental parameters that impact the methylation of hexamethylbenzene in H-SAPO-34, especially highlighting and rationalizing the crucial role of water in one of the main reactions of the aromatics-based reaction cycle.

1. Introduction

The depleting oil reserves and growing environmental awareness incites the development of sustainable processes based on biomass valorization for the production of fuels and chemicals.[1–4] As methanol can be produced from any gasifiable carbon-rich source, the methanol-to-olefins (MTO) process is one of the main technologies to bypass the use of crude oil in the production of highly demanded ethene and propene.[5–10] In particular the chabazite structured H-SAPO-34 is of industrial interest due to its high selectivity to light olefins.[11–13] Decreasing the particle size,[14–17] creating mesopores[18] or adding water[13,19–23] all improve the stability of the catalyst. Especially the influence of water on the process is highly relevant, as it is an inherent byproduct of the methanol production[24–26] and produced in the equilibration of the MTO process, as depicted schematically in Figure 1a.[27] Furthermore, early and recent studies also demonstrated an increased olefin selectivity and decreased coking rates upon increasing the water content, effects which were assigned to competitive adsorption of water

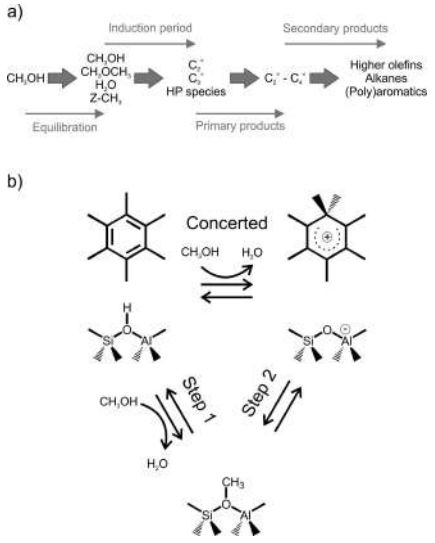

Figure 1. Schematic representation of the different stages encountered during the methanol-to-olefins (MTO) process (a) and of the mechanisms suggested for the zeolite-catalyzed hexamethylbenzene (HMB) methylation reaction, namely the direct and stepwise mechanism (b). Figure 1b was adapted from ref. [44] with permission from The Royal Society of Chemistry.[27,44]

[a] S. Bailleul, Dr. S. M. J. Rogge, Dr. L. Vanduyfhuys, Prof. V. Van Speybroeck
Center for Molecular Modeling (CMM)
Ghent University
Technologiepark 46
Zwijnaarde B-9052 (Belgium)
E-mail: veronique.vanspeybroeck@ugent.be

Supporting information for this article is available on the WWW under https://doi.org/10.1002/cctc.201900618

This manuscript is part of the Special Issue dedicated to the Women of Catalysis.

ChemPubSoc Europe

CHEMCATCHEM Full Papers

on the Brønsted acid sites (BAS), thus making them unavailable for methanol to react.[13,19,20]

Despite being commercialized, the MTO process still draws a lot of attention from both academia and industry due to its complex reaction mechanism.[8–10,28,29] Intensive research performed in the last decades to elucidate the complex MTO reaction mechanism led to the general acceptance of the hydrocarbon pool (HP) mechanism. In this mechanism, an organic compound that is trapped in the catalyst pores acts as a co-catalyst.[27,30–33] Different organic compounds are suggested as co-catalysts in literature, from which the polymethylbenzenes are identified as the dominant HP species in H-SAPO-34.[14] Especially the methylation reactions of these polymethylbenzenes are determined to be important reaction steps in the HP reaction mechanism.[34,35] A joint experimental and theoretical study has emphasized the relevance of this reaction.[36,37] They found that the band at 400 nm of the in situ UV/Vis microscopy measurements could be assigned to polymethylbenzenes. Furthermore, the activation energies derived from the growth of this characteristic peak correlated well with the activation energy for methylation of the benzenic species.

Two different routes are suggested in literature for the methylation reaction. This reaction may occur either via a concerted mechanism in which methanol transfers its methyl group directly towards the aromatic or via a stepwise mechanism, both represented in Figure 1b. In this stepwise mechanism, methanol first reacts with the catalyst framework, forming a methoxide species, which then transfers its methyl group to the HP species.[38–44] Literature suggests that both mechanisms occur within the zeolite and the prevailing mechanism largely depends on the topology and the operating conditions.[40–49] The studies show that with increasing temperature and decreasing pressure the prevailing mechanism shifts from concerted to stepwise.[45] This effect is attributed to the entropic gain of the intermediate release of water during the stepwise mechanism.[43,44,47]

The temperature and entropic effects make this reaction especially interesting to demonstrate the importance of a good description of the reaction conditions and entropic contributions using dynamic methods instead of static modeling techniques. Recent theoretical modeling work is more and more focused on the use of molecular dynamic (MD) techniques.[13,28,50–55] Nevertheless, regular MD simulations have the disadvantage of mainly sampling the most probable regions of the phase space making the elementary reactions that are interesting in most reaction mechanism rare events and thus difficult to examine. This hurdle can be overcome via enhanced sampling methods that steer the system to cross the reaction barrier.[56] Several of these free energy methods are already reviewed in literature.[56–60] In this paper, metadynamics (MTD)[61–63] and umbrella sampling (US)[64–66] are used to study the reaction under consideration. Both free energy methods, also referred to as non-Boltzmann sampling methods, use controlled bias potentials to enhance the sampling of the configurational space.[56] The main difference between both techniques is that, while the bias potentials used in umbrella sampling need to be chosen and constructed at the beginning of the simulations, metadynamics has the advantage of building a bias potential on-the-fly during an MD simulation.

In this work, we want to obtain insight into one of the main steps – the methylation reaction – of the operative cycle in H-SAPO-34 and the influence of water on it, as the intermediate removal of the water molecule is suggested to be of great importance[43,44] and co-feeding of water showed significant influence on the product selectivity and catalyst lifetime.[13,19,20] To mimic as closely as possible realistic operating conditions during the MTO process, three cases are investigated in this work, depicted in Figure 2. Firstly, an isolated Brønsted acid site (BAS) with one hexamethylbenzene (HMB) molecule and one methanol is considered as the base case (Case 1). This base case will be used to compare the advanced MD techniques with the static results, which will allow us to study the influence of the computational methodology and to highlight the importance of a good description of the diffusional freedom of water. Subsequently, we create a more complicated and realistic representation of the catalyst pores. To this end, two adaptations to the system are considered. First of all, one additional methanol molecule and either one or nine adsorbed water molecules were added for Case 2 and Case 3, respectively, as earlier studies show that these protic molecules might interact to form protonated clusters, which decreased the reactivity.[67] This maximum water loading at operating conditions was estimated using an in-house developed thermodynamic model for the adsorption of guest species in nanoporous materials.[13,68] Furthermore, there is quite some experimental work available on how the water loadings depend on the acid site density, water vapor pressure and temperature in H-ZSM-5 and for which some interesting analogies can be found with our work.[69–73] Secondly, as there is a high probability to find two silicon atoms in the next nearest neighbor position in SAPO materials, we introduced a second acid site in the unit cell,[74,75] as was done in our earlier work.[36,52] Note that the schematic representation shown in Figure 2 corresponds to starting structures. During the simulations the system adopts more realistic configurations in the pores of the material (*vide infra*). Thanks to these adaptations, the conclusions of Case 1 can be generalized to experimentally more realistic pore environments and the influence of the assisting effect of additional protic molecules on both methylation mechanisms can be assessed.[13,41,44] For the system under study, molecular dynamics methods are of utmost importance to properly account for the dynamic interplay between the methylating agent, hexamethylbenzene and water.

2. Computational Methodology

2.1. Catalyst Model and Water Loading

Due to its commercial importance for the MTO reaction,[11] this study focuses on the H-SAPO-34 framework. This zeotype catalyst exhibits the CHA topology, which consists of large cages (10.0×6.7 Å^2) connected via small windows (3.8×

ChemPubSoc Europe

CHEMCATCHEM Full Papers

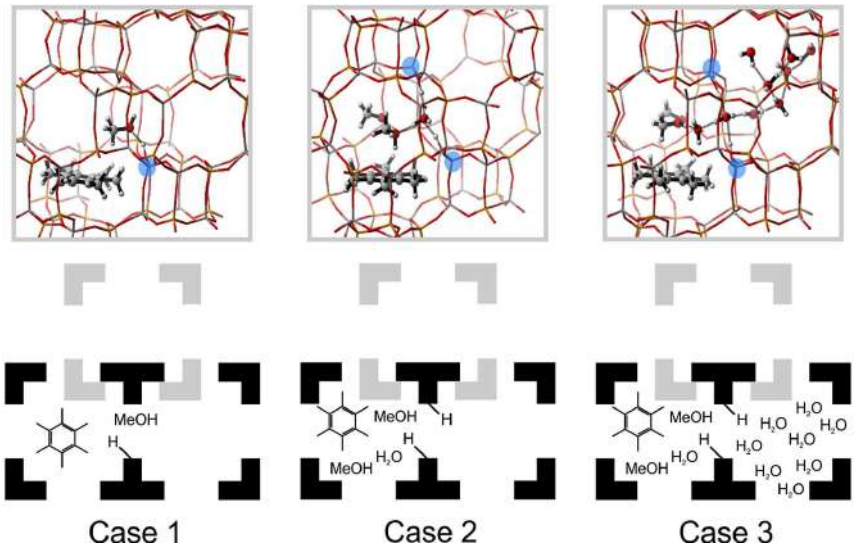

Figure 2. Starting structures and schematic representations of the three cases considered to study the concerted and stepwise methylation of HMB, namely an isolated BAS with one HMB and one methanol as base case (Case 1), a more realistic low water content case (Case 2) and high water content case (Case 3). In these snapshots, hydrogen is white, carbon is silver, oxygen is red, aluminum is grey, the silicon substitution is indicated in blue and phosphorus is orange.

3.8 Å^2).[76] In contrast to the finite cluster models which are used in some earlier studies,[12] density functional theory (DFT) calculations are applied on periodic catalyst models in this work. Therefore, a unit cell of 36T atoms (see Figure S1 in ESI) that contains one Brønsted acid site (BAS) on the O(2) position to make the catalyst active for reaction is used to represent the catalyst framework for the base case (Case 1).[77] This unit cell is shown in detail in Figure S1c. Furthermore, as there is a high probability to find two silicon atoms in the next nearest neighbor position in SAPO materials, we introduced a second acid site in the unit cell for Cases 2 and 3,[74,75] as shown in Figure S1d.[36,52]

As described in the introduction, additional water molecules were added in Case 2 and 3 respectively. To rationalize the proposed water loading in the various cases investigated in this work, we estimated the water loading using an in-house developed thermodynamic model for the adsorption of guest species in nanoporous materials.[13,68] This model allows one to estimate the number of adsorbed water molecules inside the zeolite as a function of the chemical potential of water given the adsorption energy of water, the accessible pore volume of the framework and the van der Waals parameters of water. More details on this thermodynamic model can be found in Section 1.2 of the ESI. The adsorption enthalpy was taken from literature as −42 kJ/mol.[69,78] Olson et al.[69] found that the isosteric heats of adsorption are dependent on the water content, but varies from a high value of −105 kJ/mol at low water loading to −42 kJ/mol a higher water loading. Furthermore, from earlier theoretical calculations, an adsorption enthalpy of −75 kJ/mol was found.[13] The previous values may be prone to some uncertainties both from theoretical and experimental point of view, but the adsorption enthalpy taken as input for our thermodynamic analysis is the lower limit of −42 kJ/mol. The pore volume was calculated using Zeo++ to be 1250 Å^3.[79] To account for the space occupied by hexamethylbenzene and the two methanol molecules already present in the pores, we subtracted from the total pore volume the van der Waals volume of these molecules (i.e. its van der Waals *b* parameter). For methanol, this value was taken directly from ref. [80] (b_{CH3OH} = 109 Å^3), while for HMB this value was extrapolated from the benzene, toluene, xylene, trimethylbenzene and tetramethylbenzene values also taken from ref. [80] (b_{HMB} = 493 Å^3). As such, we arrive at an accessible pore volume of 538 Å^3. Finally, the van der Waals parameters of water (a_{H2O} = 919 kJ/(mol.Å^3) and b_{H2O} = 50.6 Å^3) were taken from ref. [80] After applying the model for a temperature of 623 K and a water partial pressure of 0.8 atm[19,23] we finally arrive at an equilibrium loading of 8.6 water molecules per unit cell at these thermodynamic conditions. As each unit cell consists of three cages (schematically depicted in Figure 2), where one cage contains the HMB, the additional water molecules can be accommodated in the other two cages. To further test the

ChemPubSoc Europe

CHEMCATCHEM Full Papers

dependency of this water loading content, we tested in how far the water loading depends on the adsorption energy and vapor pressure. Only for very low vapor pressures (below 0.06 atm) or very low adsorption energies (lower than −25 kJ/mol), the loading would drop drastically. More information is given in section 1.2 of the ESI. Previous consideration and analysis shows that the assumed water content is a reasonable estimate, however the true water content may be dependent on the pore volume and other process condition factors. In this sense the assumed loading here should merely be interpreted as a rough but realistic estimate and a limiting case. More advanced models, for instance relying on grand canonical Monte Carlo simulations to estimate the adsorption isotherms at operating conditions, are out of the scope of this study.[81,82]

The unit cell parameters used to describe the H-SAPO-34 framework depend on the calculation method and guest loading, as statically the unit cell parameters are calibrated for the empty-host structure at 0 K, while the unit cell parameters for the enhanced sampling simulations are obtained at 623 K and with realistic guest loadings. The equilibration procedures are described in Section 1.1.2 of the ESI and the resulting unit cell parameters are summarized in Table S1 (ESI).

2.2. Static Calculations

The static periodic DFT calculations are performed using the Vienna Ab Initio Simulation Package (VASP 5.3)[83–86] using a methodology frequently applied in literature.[87–90] We here opted to use the revPBE functional due to its improved performance for solid-state calculations compared to the commonly used PBE functional.[91] However, for this particular reaction the differences in reaction barriers and energies are relatively small at the temperature of interest. A comparative table for the reactions of interest is taken up in Table S1, Table S7 and Table S8 of the SI. During the calculations, the projector augmented wave (PAW) method is used.[92,93] Furthermore, a plane-wave cutoff of 600 eV is used during the calculations, the self-consistent field (SCF) convergence criterion is set to 10^{-5} eV, and the Brillouin zone is restricted to the Γ-point. Lastly, Grimme D3 dispersion corrections are used to account for attractive London dispersion interactions.[94] The electronic level of theory adopted in this study is commonly used in zeolite catalysis due to its computational efficiency. Detailed level of theory studies have been performed on various zeolite catalyzed reactions, which show that barriers may be severely underestimated using the PBE-D method.[28,95–98] Seminal work was done by Sauer and co-workers to compare the accuracy of commonly used DFT methods in combination with various schemes to include the dispersion interactions. They also considered more accurate but also computationally more demanding methods which include contributions from the Møller-Plesset perturbation theory (MP2) or methods where the exact exchange is combined with correlation treated in the random phase approximation.[99–101] In addition, also hybrid functionals may be an interesting alternative.[102–105] However, as it is the intention to compare static with molecular dynamics results the usage of these computationally more expensive levels of theory is beyond current computational feasibilities.

Transition states are initially optimized with the improved dimer method of Heyden et al.[106] and then refined with a quasi-Newton algorithm as implemented in VASP.[107] Geometries are slightly displaced along the normal mode corresponding to the motion that leads the system over the barrier to generate starting geometries for the optimization of reactant and product states. For these calculations, a conjugate gradient algorithm is applied.[108]

As earlier work showed that a partial Hessian vibrational analysis (PHVA) is able to predict adsorption entropies within a 10–15 J/(mol K) error of computationally more demanding full Hessian calculations (FHVA) and experimental data,[109,110] it has become a frequently applied and attractive methodology.[87–90] For this reason, it is also used for the normal mode analysis (NMA) in this work using TAMkin.[109,111] In a PHVA calculation, not the entire system, but only a part, namely the guest molecules and the 8T cluster of the framework around the active site indicated in Figure S1c of the ESI, are accounted for during the NMA.

2.3. Ab Initio Molecular Dynamics

The ab initio MD simulations are performed using the CP2K software package.[112,113] To account for the flexibility of the catalyst framework at realistic reaction conditions, we sample in the NPT ensemble at 623 K and 1 atm. During the ab initio MD simulations, the temperature is controlled by a Nosé-Hoover chain consisting of five beads[59] and the pressure by an MTK barostat.[114] Also for these simulations, the revPBE functional is chosen because of its improved performance for solid-state calculations compared to the commonly used PBE functional.[91] Furthermore, the combined Gaussian and Plane Wave (GPW) basis sets approach is used.[115,116] The DZVP-GTH basis set and pseudopotentials[117] are used, and Grimme D3 dispersion corrections[94] are added. The time step for integration of the equations of motion is set to 0.5 fs. All systems are first equilibrated for 5 ps, followed by a production run of 50 ps. These simulation times are relatively short, due to the high computational demand for ab initio MD simulations on these periodic systems.

These first principle molecular dynamics simulations are used to study the influence of dynamically sampling the phase space on the reactant configurations visited compared to the statically obtained configurations. To compare both methodologies, the geometric analysis[44,46] described in Section 1.3 of the ESI is performed on the static and MD simulations for Case 1 and on the MD simulations of Case 2 and Case 3.

To systematically analyze the interactions between the molecules inside the catalyst pores for all three cases considered here, radial distribution functions (RDFs) for pairs formed by key atoms of the adsorbed molecules and/or the BAS(s) of the catalyst are constructed. For all RDFs considered here, only interactions at distances below 7 Å are probed, which do not

ChemPubSoc Europe

CHEMCATCHEM Full Papers

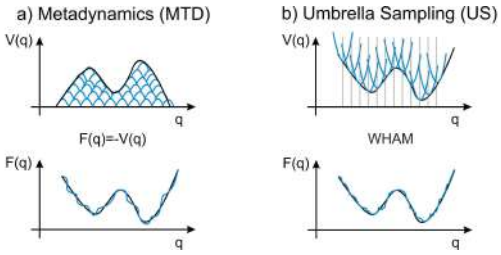

Figure 3. Schematic representation of the used enhanced sampling techniques: metadynamics (a) and umbrella sampling (b). More information on these techniques can be found in paragraph 2.4.

exceed halve of the smallest cell dimension to avoid spurious interactions with periodic images when using the minimum image convention.[59] The RDF analysis is carried out with YAFF starting from the MD trajectories using a resolution of 0.01 Å.[118] Besides the RDFs for the equilibrium NPT simulations in the reactant and product state, we additionally report RDFs as obtained from the non-equilibrium MTD simulations (*vide infra*). While these non-equilibrium RDFs no longer retain the property that they reveal the equilibrium distribution of the considered pairs of key atoms, they do provide information on (i) how the MTD simulation steers the reaction from the reactant to the product state and (ii) the influence of the walls used during the MTD simulations on the RDFs, which should remain negligible in all cases so not to interfere with the dynamics of the system.

2.4. Enhanced Sampling Methods

Subsequently, the influence of the reaction temperature and the water loading on the reaction profile of the direct and stepwise methylation of HMB is assessed by using metadynamics and umbrella sampling simulations, both shown schematically in Figure 3.

2.4.1. Metadynamics

In metadynamics, the system is driven over the reaction barrier by a time-dependent bias potential $V_G(q,t)$. Typically, this bias consists of a superposition of Gaussian shaped hills [Eq. (1)]:[57]

$$V_G(q,t) = w \sum_{t'=\tau_G,2\tau_G,t'<t} \exp\left(-\frac{(q-q(t'))^2}{2\delta s^2}\right) \quad (1)$$

where w, δs and τ_G are the height of, the width of and the time interval between two spawn Gaussian hills, respectively. The basic assumption of MTD is that in the limit of a sufficiently long simulation time, the bias potential is related to the free energy via Equation (2):[57,61,62]

$$\lim_{t\to\infty} V_G(q,t) = -F(q) \quad (2)$$

Therefore, the free energy surface (FES) of the system can be reconstructed based on the inversion of the time dependent bias potential as represented schematically in Figure 3a.

The Gaussian hills are spawned along a collective variable (q). In this work, coordination numbers (*CN*) are used as the collective variables, similar to earlier work [Eq. (3)]:[44,67]

$$CN = \sum_{i,j} \frac{1-(r_{ij}/r_0)^{nn}}{1-(r_{ij}/r_0)^{nd}} \quad (3)$$

In this expression, the sum runs over two sets of atoms i and j, r_{ij} is the distance between atoms i and j, and r_0 represents the reference distance.[28] For all coordination numbers used in this study, a reference distance r_0 of 2.0 Å was chosen, because this value lies in the range of typical transition state distances of the bonds that have to be broken and formed during a methylation or methoxide formation. The parameters *nn* and *nd* are set to 6 and 12, respectively, ensuring a value of 0.5 for each CN term at the reference distance and a fast decaying value at larger distances. Quadratic walls were used to restrict the simulations to the area of interest on the FES (Section 1.4 of ESI).[44] In this way, the reacting methanol molecule is kept close to the acidic proton and the diffusion of the formed water is limited to enhance barrier recrossings. The initial height of the Gaussian potentials is set to 5 kJ/mol and after each recrossing of the transition point, the height of the added Gaussian hill is halved to enhance the FES convergence, until a value of 0.625 kJ/mol is obtained. A new hill is spawned every 50 time steps. The width of all Gaussians is set to 0.02. The integration time step is set to 0.5 fs for all MTD simulations.

As displayed in Figure 1, three reaction steps need to be simulated to analyze both possible pathways of the methylation reaction. These reactions can all be described using the three CVs given in Figure 4.[44] The concerted methylation is characterized by the breaking of the C–O bond in methanol (CV1) and the formation of a bond between the carbon of the methyl group and one of the carbons of the aromatic ring of HMB (CV2). In the first step of the stepwise pathway, again the

ChemPubSoc Europe
CHEMCATCHEM Full Papers

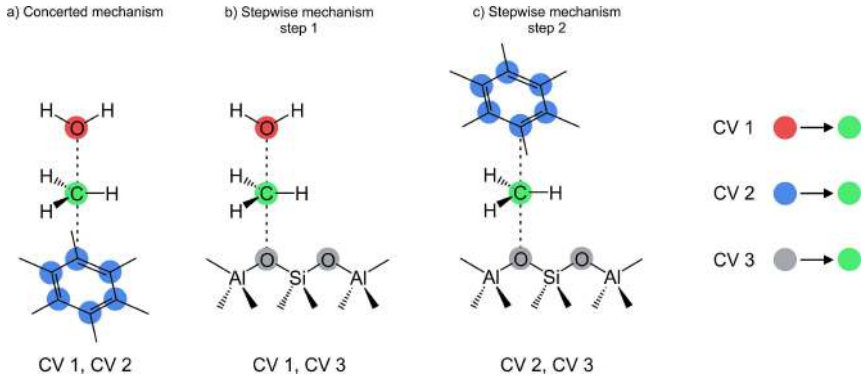

Figure 4. Schematic representation of the collective variables applied in the metadynamics and umbrella sampling simulations of the HMB methylation. [44]

methanol C–O bond is broken (CV1), but now a bond is formed between the carbon of the methyl group and one of the oxygens next to the silicon substitution of the framework BAS(s) (CV3). In the second step, the formed methoxide C–O bond is broken (CV3), while the bond between the carbon of the methyl group and one of the carbons of the aromatic ring of HMB is formed (CV2).

So, each reaction can be simulated separately by combining two of the three collective variables. In principle, it is also possible to sample both mechanisms simultaneously by using the three collective variables during one metadynamics simulation,[52] but this is omitted in this work as this is computationally too expensive. It is known that the efficiency of metadynamics scales exponentially with the number of collective variables.[63] Furthermore, further work by De Wispelaere et al.[44] showed that no reaction free energies could be obtained from the 3D MTD simulations, as the product region was insufficiently sampled within feasible simulation times. One could also directly compute the 1D profiles using a single CV. However, that requires a priori knowledge on which mathematical function of the two relevant CVs represents an efficient direction to steer the reaction. Since such knowledge is not always available, metadynamics simulations are performed using two CVs, and 2D FESs are obtained. From these FESs, a free energy barrier ΔF can be computed after projection of the 2D FES onto a 1D surface, taking the difference $q = q_2 - q_1$ as the reaction coordinate [Eq. (4)]:

$$F(q) = -\frac{1}{\beta}\ln\left\{C\int_{-\infty}^{+\infty}\exp[-\beta F(q_1, q_1+q)]dq_1\right\} \quad (4)$$

where $\beta = \frac{1}{k_B T}$ with k_B the Boltzmann constant and q^* is the position at the top of the barrier along the reaction coordinate. The factor C was introduced to ensure consistent dimensions in the definition of $F(q)$ and $F(q_1, q_1+q)$ and as a result also makes sure that the argument of the logarithm is dimensionless (see Section 3.1 of the ESI for more details). However, it only results in a global shift of the free energy profile and hence does not influence free energy barriers and differences. Therefore, it is set to unity in this work.

Finally, based on the reaction rate derived from transition state theory, we can define phenomenological free energy barriers ΔF [Eq. (5)]:

$$\Delta F = F(q^*) + k_B T \ln\left(\frac{k_B T \bar{Z}_R}{hA}\right) \quad (5)$$

with k_B Boltzmann's constant, h Planck's constant and T the temperature. Furthermore, $F(q^*)$ represents the free energy of the transition state q^* (relative to the minimum in the reactant valley), $\bar{Z}_R$ is proportional to the partition function of the reactant valley and hence accounts for the broadness of the reactant valley, while the factor $A = \frac{1}{2}\langle|\dot{q}|\rangle_{q^*}$ is related to the rate of change of the collective variable in the transition state and was computed by the procedure proposed by Bučko et al.[54] More details can be found in Section 3.2 of the ESI.

The metadynamics simulations are performed using the CP2K software package.[112,113] As the change in cell parameters was found to be negligible during the methylation reaction for each of the three cases (see Table S1 (ESI)), these simulations were performed in the NVT ensemble at 623 K for computational efficiency as explained in Section 1.1.2 of the ESI. During these simulations, the temperature is again controlled by a Nosé-Hoover chain of five thermostat beads.[59] Furthermore, time-averaged cell parameters obtained from the NPT runs for each of the three cases are used as constant values. These time-averaged cell parameters are summarized in Table S1 (ESI). The remainder of the settings are kept the same as for the MD simulations described in paragraph 2.3.

ChemPubSoc Europe

CHEMCATCHEM Full Papers

2.4.2. Umbrella Sampling

During umbrella sampling, the reaction path is separated into distinct windows, as shown in Figure 3b. In each window, the reaction coordinate is restrained to a target value q_i^{ref} by applying a bias potential in each window. Often, a harmonic bias potential with strength K is used to keep the system close to the target value [Eq. (6)]:

$$w_i(q) = \frac{K}{2}(q - q_i^{ref})^2 \quad (6)$$

In each window, the system mainly samples perpendicular to the reaction coordinate. After the simulations are completed, the probability distribution of all windows is combined to a total distribution function using the weighted histogram analysis method (WHAM) to obtain the free energy surface of the unbiased system.[119,120]

The umbrella sampling simulations are performed using the CP2K software package[112,113] which is interfaced with the advanced simulations library PLUMED.[121] To keep the simulations as similar as possible to the metadynamics simulations, the settings are kept the same. The simulations are therefore performed in the NVT ensemble at 623 K. The temperature is again controlled by a Nosé-Hoover chain of five thermostat beads.[59] Again, time-averaged cell parameters obtained from the NPT runs are used as constant values as summarized in Table S1 (ESI). The remainder of the settings are kept the same as for the MD simulations described in paragraph 2.3.

The collective variables that are used to describe the analyzed reactions are the same as discussed in paragraph 2.4.1. To create the snapshots used as a starting point for each window, a moving restrained MD simulation is used in which a bias potential is moved from one minimum to the other. Along this 2000 step reaction path, a snapshot is taken every 80 steps, leading to 26 umbrellas for each reaction. Subsequently, a restrained ab initio MD simulation of 50 ps is run for each umbrella. If insufficient overlap between the different umbrellas occurred, extra umbrellas were added in the poorly sampled regions. This methodology led to the umbrellas summarized in Table S2 and Table S3 (ESI) where the location for each window is summarized. The force constant is always set to 1500 kJ/mol.

3. Results and Discussion

The concerted and stepwise methylation mechanisms are studied using both static and dynamic simulation methods.[38–42] Earlier studies have emphasized on the importance of the water released during the stepwise mechanism.[43,44] This makes this reaction especially interesting to demonstrate the importance of a good description of the entropic contributions by release of water using dynamic methods instead of static techniques. At first instance, a structural analysis of all reaction components within a realistic representation of the catalyst pores will be discussed. In the second part, the influence of the dynamic analysis and the realistic pore environment on the reaction barriers for both the concerted and the stepwise mechanisms will be discussed. We use a variety of analysis tools which will first be introduced for the simplest case, namely Case 1. Afterwards, the conclusions will be generalized to experimentally more realistic systems by expanding the analysis to Case 2 and Case 3.

3.1. Dynamic Reactant and Product Behavior

To obtain insight in the effect of the dynamic behavior and mobility of the reactants on the co-adsorption of the HP species, a geometric analysis is performed on the results of the MD simulations at 623 K. Firstly, the mobility of the HMB will be analyzed. Subsequently, the diffusive and protic behavior of methanol in the reactant state is studied. Lastly, the relative orientation of HMB and methanol will be investigated to unveil their tendency to form pre-reactive complexes.

3.1.1. Preferential Orientation of Polymethylbenzene

To analyze the mobility and orientation of the organic co-catalyst in the H-SAPO-34 framework, two angles α and β, defined in Figure S7 of the ESI, are monitored during a regular MD simulation in the reactant valley. The angle α describes the orientation of HMB along the longest axis of the cage (z-direction), where an angle close to 0° indicates that HMB is oriented parallel to the length of the cage and an angle close to 90° indicates a perpendicular orientation. The angle β is defined as the angle between the HMB and the normal of the 8T-ring of the catalyst in which the BAS(s) are found. Here, an angle close to 90° means parallel to this window and thus a favorable orientation of the π-clouds to the BAS, while an angle close to 0° means perpendicular, as visualized in Figure S8 of the ESI. The time-dependent values for these angles are calculated over the trajectory of a 50 ps MD simulation for the reactant state of all three cases and the resulting normalized histograms are depicted in Figure 5a and b. For Case 1, the static result is also included as a dotted line. Snapshots of the most probable configurations for all three cases are depicted in Figure 5c. The histograms show that in all three cases, the most probable structures obtained dynamically correspond to configurations in which α is in the range of 0°–30°. Thus, HMB orients itself more or less parallel to the length of the cage irrespective of the starting configuration. For Case 1, also the statically obtained configuration agrees well with the dynamically obtained most probable configuration, although it neglects the width of the dynamic distribution. The angle β adopts values in the range of 70°–90° in Case 1, as in this orientation the π-clouds orient themselves towards the BAS. Also for Case 2, the largest contribution of β is found in the same range, although the histograms show a slightly higher contribution at other values. These residual contributions at other values originate from the chosen input structures as depicted in Figure 2. The HMB reorients itself towards the most favorable configuration during the course of the MD run. However, due to the presence

ChemPubSoc Europe

CHEMCATCHEM Full Papers

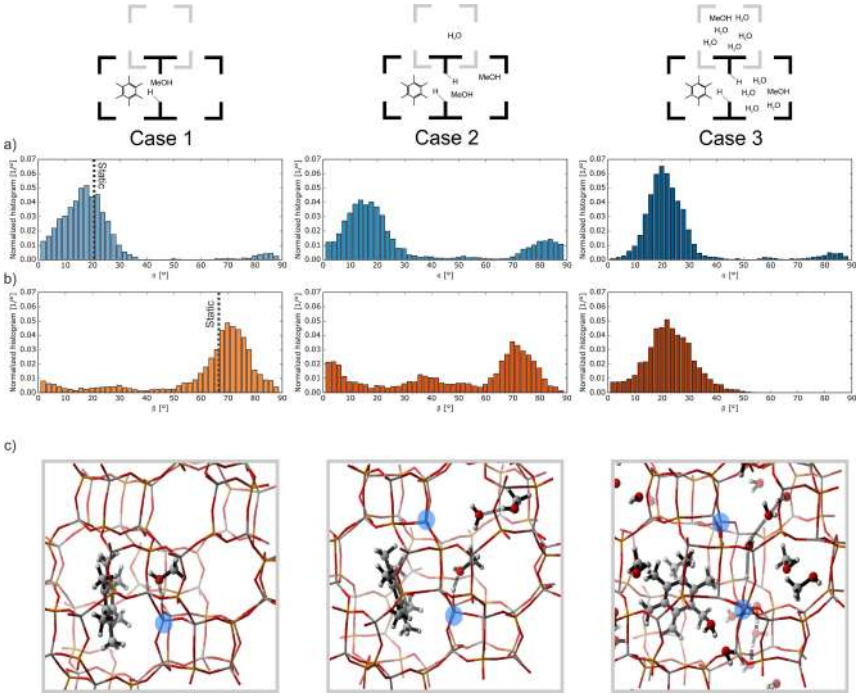

Figure 5. Summary of the geometric analysis for a 50 ps MD simulation of the reactant state of Case 1 (left), Case 2 (middle) and Case 3 (right) showing the normalized histogram for the angle α (a) and the angle β (b) defined in Section 1.3 of the ESI and snapshots showing the most probable orientation adapted by the HMB (c). The dotted line depicts the corresponding reactant structure obtained via static simulations of Case 1.

of more guest molecules this goes slightly slower in Case 2 compared to 1. In Case 3 the most probable configuration of HMB corresponds to β values in the range of 15°–30°, while the HMB molecule still orients itself along the z-axis for Case 3 (α ≈20°). In this case the preferential orientation of the π-clouds towards the BASs is lost. This can be understood since the additional protic molecules in Case 3 both screen the BAS and offer new stabilizing interactions for the π-clouds through the other 8-ring windows, such that the HMB no longer needs to orient its π-clouds towards the 8-ring containing the BASs.

3.1.2. Diffusive and Protic Behavior of Methanol and Water

Further insight in the early stages of the methylation process can be obtained by analyzing the mobility and orientation of the methanol. Since it is well known that methanol needs to be protonated to be active for the methylation reaction, the interaction of methanol with the protons present in the catalyst pores is studied.[67] To this end, the RDFs for the pairs formed by (i) the oxygen of methanol and (ii) all protons present, depicted in Figure 6, are discussed. The RDF of Case 1 shows two interesting peaks, which correspond to the O–H covalent bond of methanol itself (around 1.0 Å) and the O–H hydrogen bond with the proton of the Brønsted acid site, as schematically indicated in Figure 6. The presence of this hydrogen bond peak indicates that methanol adsorbs quite localized on the BAS in Case 1. These two peaks correspond very well with the corresponding distances obtained from the statically optimized reactant state, indicated by the dotted lines in the top RDF. These peaks and bond types remain present in the more complicated Case 2 and Case 3. However, an additional peak between 3.1 and 3.5 Å arises at this more complex reaction environment. This peak is attributed to the formation of a first solvation shell around the methanol, as this distance corresponds to the distance between the oxygen of methanol and the hydrogens of a protic molecule – either water or methanol – which is hydrogen bonded to this methanol, as indicated in

ChemPubSoc Europe
CHEMCATCHEM Full Papers

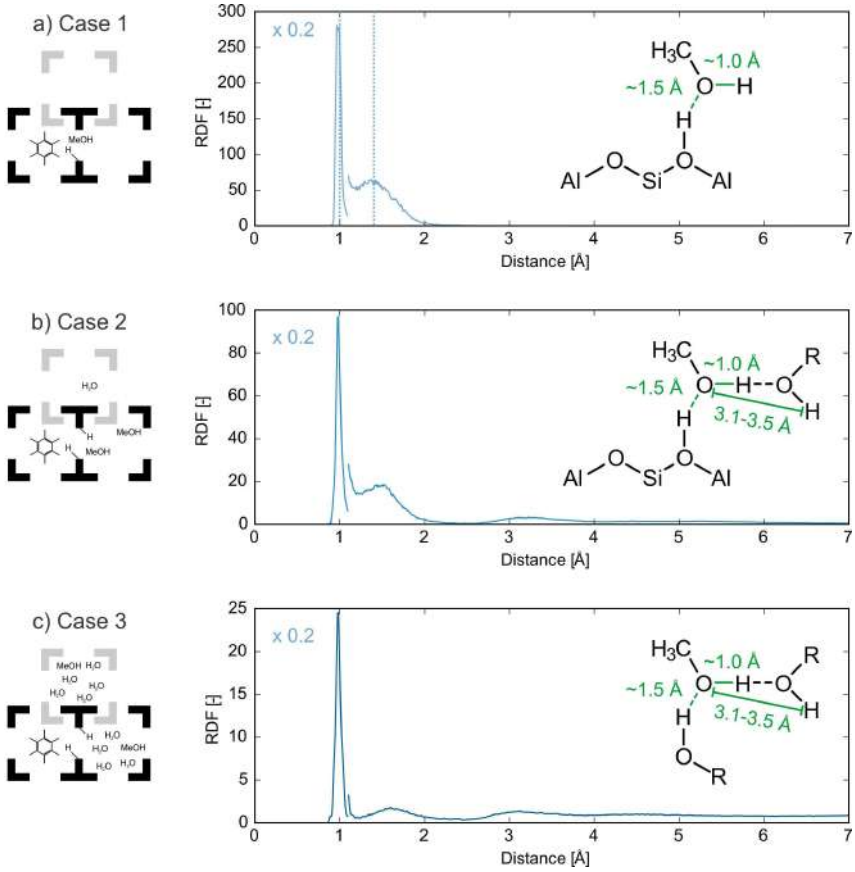

Figure 6. Radial distribution functions for the pairs formed by (i) all protons present in the catalyst pore and (ii) the oxygens of the methanol molecule(s) in the reactant state for Case 1 (a), Case 2 (b) and Case 3 (c). For Case 1, the statically obtained distances corresponding to the analyzed bonds are added in dotted lines. The encountered peaks are indicated on the schematic representation of the methanol molecule. The first peaks (at distances below about 1.1 Å) are scaled down by a factor of 5 to improve visualization.

the middle and bottom panel of Figure 6. In Case 3, this solvation effect becomes even more prominent, since the relative intensity of this peak increases. As protonated clusters consisting of protic molecules and the protonated BAS can be formed in this case, the proton donation to the methanol can also occur through another protic molecule instead of directly from the framework. Similar results were found for the solvation shells around water as discussed in Figure S24 of the ESI.

3.1.3. Pre-Reactive Complexes

To have a favorable reactive environment for the methylation reaction, not only the separate orientation and movement of both adsorbed molecules with respect to the catalyst pore is important, but also a favorable position and orientation between methanol and HMB is necessary for the methylation to take place. To this end, the RDF for the pairs formed by (i) the carbon of methanol and (ii) the carbons of the aromatic ring of HMB are calculated, as depicted in Figure 7a. To form a pre-reactive complex, the methyl group of the methanol molecule

ChemPubSoc Europe
CHEMCATCHEM Full Papers

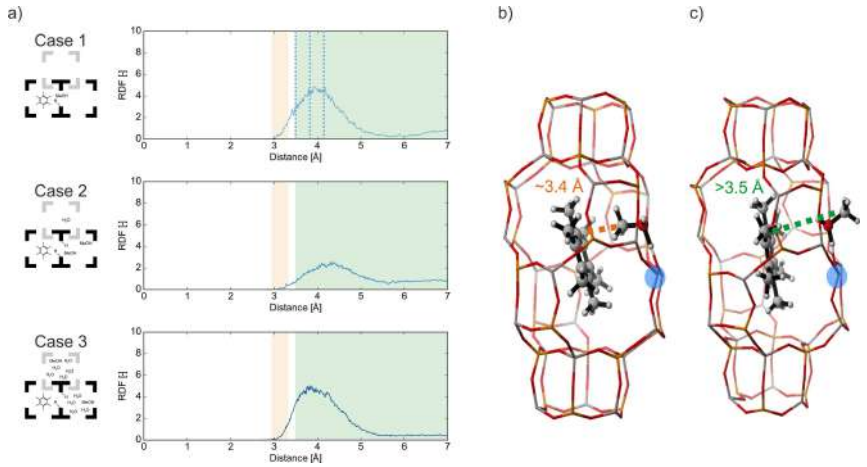

Figure 7. Radial distribution functions for the pairs formed by (i) the methyl group of the methanol molecule(s) and (ii) the carbon atoms of the benzene ring of the hexamethylbenzene molecule in the reactant state for the three cases (a). These RDFs show that the formation of a pre-reactive complex for the concerted methylation (b and orange zone in a) with a C–C distance of around 3.4 Å is rather unlikely. Instead, configurations where the methyl group of methanol is not oriented towards the aromatic ring (c and green zone in a), with distances ranging from 3.5 Å and higher, are sampled. The snapshots are obtained by static optimizations. In these snapshots, hydrogen is white, carbon is silver, oxygen is red, aluminum is grey, the silicon substitution is indicated in blue and phosphorus is orange.

should orient itself towards the HMB molecule. For Case 1, the RDF shows a broad peak around 4.0 Å. However, typical distances occurring within a pre-reactive complex optimized statically amount to only around 3.4 Å, as shown in Figure 7b. Hence, rather high methyl-HMB distances are sampled, corresponding with methanol pointing away from the aromatic ring as for the snapshot in Figure 7c. As the most stable statically obtained structure also resembles the structure in Figure 7c, good correspondence is obtained between the static distances and the RDF obtained dynamically for Case 1. Case 2 and 3 provide in general terms a rather similar picture, although some subtle differences are noted. The RDF peak for Case 3 is shifted to slightly lower values compared to Case 2, which is due to the additional guest molecules present rather than an enhanced probability to form a pre-reactive complex. The increased filling of the cages with water pushes the methanol closer to HMB.

By combining all observations from this section, we can conclude that although the HMB is oriented favorably towards the BAS and methanol can frequently interact with a second proton, the unfavorable orientation of methanol with respect to the aromatic ring limits the reactivity for the methylation reaction. To increase the likelihood of HMB methylation, it is therefore a prerequisite to use enhanced sampling techniques. Further insight into the effect of water on the reactivity for methylation will thus be obtained by calculating the methylation barriers using different methodologies in the next section.

3.2. Influence of Water on the Reaction Free Energy Profile

To unravel the full reaction mechanism, not only insight into the dynamic behavior of the reactant state is necessary, but also information on the free energy barrier and reaction free energy is indispensable. Therefore, this section will describe the influence of a dynamic description of the pore environment and the realistic filling of the catalyst pores on this barrier obtained for both the concerted and stepwise methylation mechanisms. A summary of all obtained barriers can be found in Table 1. In addition, we also performed an error analysis according to a procedure described in Section 1.6 of the SI. The error bars are also reported in Table S4 and Table S5. Before discussing in depth the numerical results, it is important to acknowledge that obtaining accurate free energies from enhanced sampling molecular dynamics simulations is extremely challenging, certainly when the sampling has been performed based on first principle simulations which poses limits on the number of simulations and the length of the simulations that may be performed within a feasible computational time.[55] For the interested reader an estimate of the computational time used for the reactions under study has been given in Table S6 of the ESI. As reviewed earlier, the accuracy of the final results depends on the level of theory used to describe the system, the sampling protocol, and the estimator to obtain the free energy differences.[60,122–124] For DFT based reactions in zeolites only a few works are available which

ChemPubSoc Europe

CHEMCATCHEM Full Papers

Table 1. - Free energy at 623 K for the concerted and stepwise methylation of HMB obtained with different methodologies, namely statically, via metadynamics (MTD) or umbrella sampling (US) (in kJ/mol). $\Delta F^{\neq}$ is used for the free energy barrier, while ΔF_r shows the reaction free energy and $\Delta G_{r,des}$ for the reaction free enthalpy after desorption of the formed water.

		Concerted			Step 1			Step 2		
		$\Delta F^{\neq}$	ΔF_r	$\Delta G_{r,des}$	$\Delta F^{\neq}$	ΔF_r	$\Delta G_{r,des}$	$\Delta F^{\neq}$	ΔF_r	$\Delta G_{r,des}$
Case 1	**Static**	129.9	46.8	−2.8[a]	135.2	55.3	3.1[a]	87.2	−8.5	−58.0[a]
	US	111.4	−16.1	–	124.3	8.9	–	81.1	−62.5	–
	MTD	105.8	−2.1	–	142.6	10.9	–	86.4	−36.4	–
Case 2	**MTD**	82.4	0.4	–	148.0	67.5	–	73.4	−24.9	–
Case 3	**MTD**	71.5	−52.4	–	126.1	19.7	–	61.0	−58.8	–

[a] It should be noted that as long as the water is adsorbed within the zeolite pore, Helmholtz free energies are obtained, as the volume of the unit cell is kept constant (see Section 1.1 of the ESI), thus omitting the pV term. If the desorption of water is considered, a Gibbs free energy value is obtained as the gas phase accessible volume should be accounted for at the correct pressure.

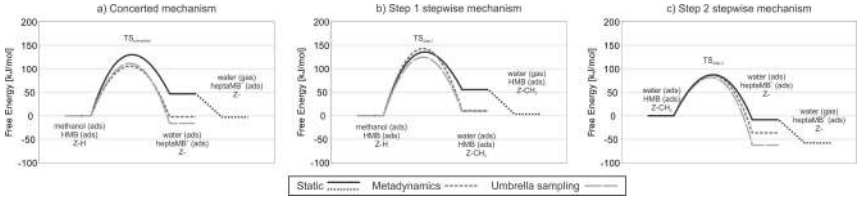

Figure 8. Free energy profile for the concerted (a) and step 1 (b) and step 2 (c) of the stepwise methylation of HMB at 623 K in Case 1 using static (full line), metadynamics (short-striped line) and umbrella sampling (long-striped line) simulations. For the static calculations, an extra desorption step of the formed water is taken into account (dotted line).

assess each of the components on the finally obtained free energies.[51,54,55]

3.2.1. Dynamic Versus Static Methods for Case 1 without Additional Water Molecules

To assess the influence of the dynamic approach on the direct and stepwise methylation routes, the simplest case (Case 1) where no additional water molecules are present is first discussed. The free energy results for Case 1 obtained via static, metadynamics, and umbrella sampling simulations are summarized in Figure 8 and Table 1. All results refer to the state where all species are adsorbed on the catalyst and thus intrinsic barriers are reported. As a result of the reaction, the heptamethylbenzenium cation and water are formed, which are both adsorbed in the cages of the zeolite. When water desorbs and is brought to the gas phase, entropy is gained. This state, which was evaluated based on the static results, is also shown on the figure. For the stepwise mechanism, the free energies are the result of two subsequent umbrella/metadynamics simulations and thus one must be careful in connecting the product state of the first step with the reactant of the next step. More information on this aspect is given further in this section.

The static free energy barriers together with a more detailed analysis of the influence of temperature on all static results and comparison of the static results with literature data can be found in Section 2 of the ESI. In general, our static calculations suggest that the stepwise mechanism becomes more important at higher temperatures, though the temperature range differs with the work of Brogaard and co-workers,[43] and suggest higher temperature ranges similarly to the results found in ref. [44].

At first instance, it is interesting to compare the static and the dynamic results for the concerted methylation step. The most pronounced effect of the dynamic sampling is observed on the stabilization of the products, where water is still co-adsorbed, which are substantially lower in free energy when using advanced dynamic methods. This can be ascribed to the different description of the mobility of the formed water, as revealed by the RDFs for the pairs formed by (i) the carbon and (ii) oxygen of methanol, shown in Figure 9. These RDFs indicate that the water molecules in the product state exhibit a substantial configurational freedom, shown by the broadly smeared probability. This is confirmed by the RDFs for the pairs formed by (i) the oxygens of the BAS and (ii) all protons, depicted in Figure S26 and Figure S27 in the ESI. This configurational freedom is poorly accounted for by the static methods, employing a harmonic oscillator approximation in only one static point, indicated by the green dotted lines in Figure 9. By accounting for this configurational freedom using dynamic simulations, the product state is stabilized entropically in line with the lower free energies of the co-adsorbed products in Figure 8. The reaction free energy in the umbrella sampling simulations is slightly lower compared to the MTD simulations, which might be ascribed to the walls imposed in the

ChemPubSoc Europe

CHEMCATCHEM Full Papers

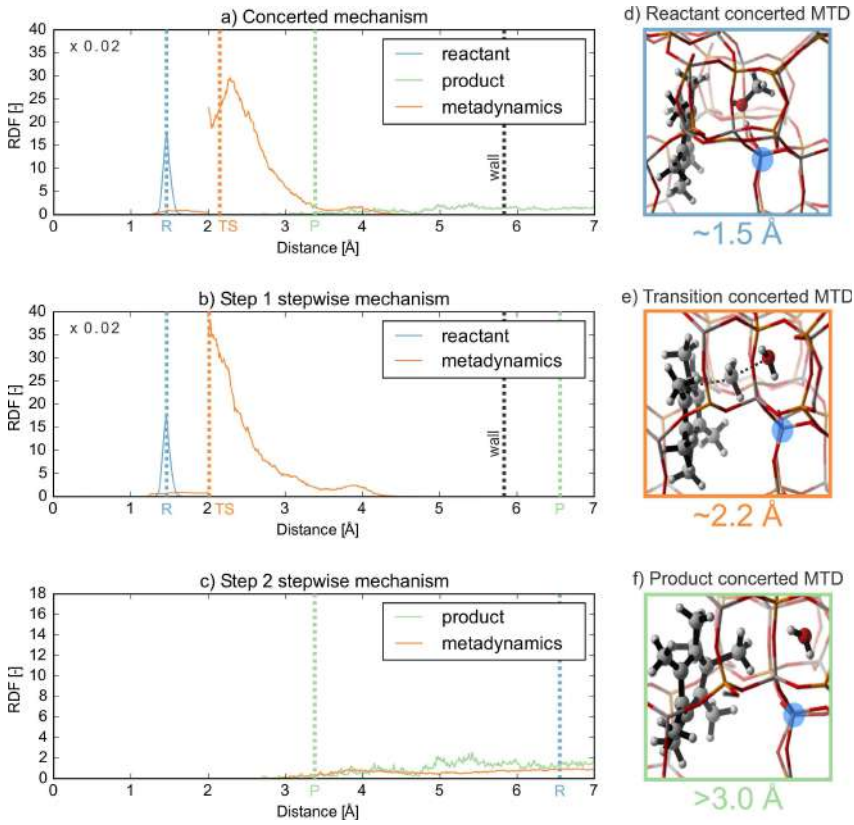

Figure 9. Radial distribution functions for the pairs formed by (i) the methyl group and (ii) the oxygen of the methanol molecule from MD runs in the reactant (blue) and product (green) state as well as for the MTD simulation (orange) for Case 1. These RDFs are calculated for the concerted methylation (a) and both step 1 (b) and step 2 (c) of the stepwise mechanism. Furthermore, the measured distances in the reactant (R), product (P) and different transition states (TS) calculated statically are added as dotted lines. The static value for the transition state of step 2 of the stepwise mechanism could not be added, as it attained a value of 8.7 Å, thus higher than the maximum used in the RDFs. Lastly, the position of the wall limiting the diffusion of the formed water to enhance recrossing in the MTD simulation is added. The first peak (at distances below 2 Å) is scaled down by a factor of 50 to improve visualization. Three snapshots of the reactant (d), transition (e) and product (f) states sampled in the metadynamics simulations of the concerted mechanism are added, with typical distances between the methyl group and the oxygen of the methanol indicated. In these snapshots, hydrogen is white, carbon is silver, oxygen is red, aluminum is grey, the silicon substitution is indicated in blue and phosphorus is orange.

metadynamics simulations to enhance recrossing as described in Section 2.4.1 and Section 1.4 of the ESI. While this wall does affect the regions of the phase space that can be explored, its location was chosen so to minimally affect the metadynamics simulation. As can be observed from Figure 9, the wall is indeed located far inside the product region, at a point where the RDF determined from metadynamics for the pairs formed by (i) the methyl group and (ii) the oxygen of the methanol molecule is vanishingly small. In general, it is rather challenging to sample the product state where water diffuses quickly away from the active site into the pores of the zeolites. In this sense the product state is less well defined compared to the reactant state which is quite similar for all methods, as the discussion of Figure 6 demonstrated that methanol is fixed on the BAS in all cases (see Figure 9d). Irrespective of the errors induced by the sampling procedure (see Section 1.6 of the ESI for more information), the geometrical analysis and the obtained free energies clearly show that the mobility of the co-adsorbed

ChemPubSoc Europe

CHEMCATCHEM Full Papers

water is insufficiently described by the static methods, which only consider one point on the free energy surface.

In a next step, it is interesting to study in how far similar effects are observed for the stepwise mechanism. Note that water is released after the first step in the stepwise mechanism. In our dynamic simulations, we opted to keep the water in the pores of the material. However, it was observed that water diffuses quickly to a neighboring cage. For the static simulations we investigated in how far the barriers of the second step are affected by removing water after step 1. As discussed in Section 2.2 of the ESI, the effect on the barrier is minimal. The dynamic results of the stepwise mechanism are the result of two enhanced sampling MD simulations where in the first set of simulations CV1 and CV3 are used and in the second step CV2 and CV3 are used, as schematically shown in Figure 4. To directly investigate the competition between the direct and stepwise mechanism from MD simulations, it is necessary to perform MTD or US simulations with a fixed set of the three collective variables, as this would allow to sample all possible steps, namely the methoxide formation (CV3), the carbon-carbon bond formation (CV2) and the carbon-oxygen breakage (CV1) all in the same run. Such study was performed in reference [52]. However, as the simulation time scales exponentially with the number of collective variables,[63] it was impossible to perform these simulations within this work. Furthermore, it was pointed out by De Wispelaere et al.[44,52] that no reaction free energies could be obtained from the 3D MTD simulations, as the product region was insufficiently sampled.

When comparing the static versus the dynamic results for the first step, a similar stabilization of the formed products, i.e. the methoxide formation and the co-adsorbed water, are observed compared to the static results. Also for step 2 the products before desorption of water are substantially stabilized in the dynamic simulations compared to the static results. It was statically observed that for the product state of step 2, the water molecule is stabilized through a hydrogen bond with the negatively charged framework, thereby losing a large portion of its entropy in this step, as depicted in Figure S10 of the ESI. In the dynamic simulations, water remains diffusive. Finally, it is important to note that one cannot connect the product of step 1 and reactant of step 2 directly as the two states have been obtained from biased MD simulations with different collective variables. More information is given in the ESI, Section 4.

The overall free energy barriers obtained with all methods show similar trends given the numerical inaccuracies and sampling errors. A more detailed explanation regarding the errors on the various methods is given in Section 1.6 of the ESI. Rather large differences are obtained for the free energy barrier of the methoxide formation obtained with the MTD and US methods. Our error analysis shows that the sampling error on the US simulations is larger for the here conducted results. Further analysis demonstrates that the US simulations only sample one type of transition state, which is assisted by the presence of the HMB, whereas in MTD broader regions of the phase space were sampled accounting for an assisted and non-assisted transition state. If the sampling were to be sufficient, both methods should sample similar regions of phase space. However, even after an excessive number of simulations, our simulations show that it is very challenging to obtain similar barriers. More information can be found in Section 1.5 and 1.6 of the ESI. For the current study focus is not to calculate the most accurate free energy barriers, instead we wanted to obtain important trends regarding the role of water on the methylation of HMB.

Qualitatively, the dynamic results of Case 1 lead to a similar conclusion as the static methodology discussed in Section 2 of the ESI, namely that the concerted and stepwise mechanisms are competitive at 623 K, though the concerted will prevail due to the high barrier for methoxide formation. Furthermore, the dynamic results highlight the importance of the release of water in this process.

For the more complicated cases (Case 2 and 3), where more guest molecules are present in the pores of the material, only enhanced sampling MD techniques are used. Based on previous findings and the fact that less prior knowledge on the reaction path is needed within metadynamics, we opted to further use metadynamics in Case 2 and 3.[125]

3.2.2. Influence of the Protic Environment in Case 2 and 3

In a next step, we want to elucidate the role of additional protic molecules present in the catalyst by comparing the methylation free energies in Case 2 and 3. The free energy profiles obtained using metadynamics, which are also listed in Table 1, are presented in Figure 10.

The profiles show that the concerted mechanism prevails in all cases. Furthermore, comparison of both profiles shows that the presence of additional protic molecules lowers all barriers and stabilizes the intermediate and product states. The stabilization of the intermediate and product state can be explained by the stabilization of the formed water in the protonated water network. This effect is more pronounced at higher water content.

The decreased barriers for the concerted methylation and methoxide formation due to the assistance of protic molecules, shown in earlier work,[13,41,44] is confirmed here and originates from the formation of solvation shells as already introduced earlier for the reactant valley in Figure 6. Recalculating these RDFs for the metadynamics of these two reactions runs confirms the existence of these shells as shown in Figure 11a and b. As the intensity of the peak between 3.1 Å and 3.5 Å increases when going from Case 2 to Case 3, the elevated water content in the latter case leads to an increased solvation shell formation and thus increased assistance compared to Case 2. Furthermore, a detailed visual analysis of the transition states shows that for Case 3 the transition state is efficiently stabilized by the surrounding molecules. For Case 2 on the other hand, the concentration of assisting molecules is too low and both assisted and unassisted transition states are sampled, as depicted in the snapshots for Figure 11a. Similar snapshots for the methoxide formation are provided in Figure S15 of the ESI. The decreased assistance leads to higher barriers in Case 2, which is in line with earlier work.[13]

ChemPubSoc Europe

CHEMCATCHEM Full Papers

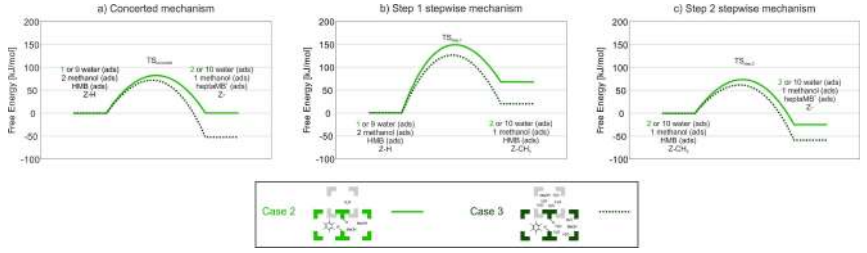

Figure 10. Free energy profile for the concerted (a) and step 1 (b) and step 2 (c) of the stepwise methylation of HMB at 623 K at higher guest molecule loadings and acid site density, namely Case 2 (full line) and Case 3 (dotted line) obtained with metadynamics. The reference level for the reactants in both cases has been assumed zero, however in Case 2 one water molecule was adsorbed, whereas in Case 3 nine water molecules were adsorbed in the unit cell. The obtained barriers are thus intrinsic energy barriers compared to the state in which all molecules are already adsorbed.

Also for the second step of the stepwise mechanism, a lower free energy barrier is observed when increasing the water content. This can be explained by a stabilization of the BASs with the surrounding protic molecules, though not as straightforwardly as for the concerted methylation and methoxide formation. To this end, the RDFs for the pairs formed by (i) all protons and (ii) the oxygens of the BAS are shown for Case 2 and Case 3 in Figure 12. For the metadynamics and product state simulations of Case 3, these RDFs reveal an additional peak between 1.8 and 2.25 Å compared to Case 2. As shown in the snapshots in Figure 12b, the protic molecules stabilize the unprotonated BAS, which is formed from the methoxide, by a protonated water cluster resembling the Grotthuss mechanism for Case 3.[126] The distances of the hydrogen bonds formed in this chain are within the range of 1.8 and 2.25 Å, thus corresponding to this peak. When considering Case 2, insufficient protic molecules seem to be present to stabilize the unprotonated BAS and thus fail to lower the transition state barrier.

As assistance by the additional water molecules thus explains the decreased barriers and stabilized products between Case 2 and Case 3, this study shows that not only competitive adsorption between methanol and water[13] needs to be considered when clarifying the enhanced conversion of methanol in the presence of water.[11,19,127,128] The assisting role of water might have an important effect on the whole reaction profile and a study on its effect on the complete aromatics mechanism might lead to new insights on the problem at hand.

4. Conclusions

In this work, new insights on the influence of protic molecules on the methylation of hexamethylbenzene (HMB) in H-SAPO-34 were obtained using dynamic first principle techniques. To this end, the competitive concerted and stepwise methylation mechanisms were studied for three cases with an increasing amount of protic molecules and an increasing amount of BASs. The simulations are performed using first principle molecular dynamics methods to account for entropic and dynamic effects at elevated temperatures.

First, the influence of the protic environment on the adsorption of the reactants in the catalyst pores was investigated. It was observed that HMB adopts a preferred position oriented along the z-axis (the longest direction of the cage) with the π-clouds oriented to the BAS for Case 1 and Case 2. In Case 3, at a higher water content, the orientation of the π-clouds to the BAS was screened by the adsorbed protic molecules, which also offered new stabilizing interactions for the π-clouds. Furthermore, higher water loadings lead to the formation of solvation shells around methanol in Case 3, thus allowing for the proton donation from the BAS to methanol to occur by another protic molecule. Nevertheless, the protic environment did not significantly influence the pre-reactive complex formation as methanol mostly oriented its methyl group away from the HMB in all cases.

Subsequently, the competition between the concerted and stepwise mechanisms was analyzed by calculating the free energy barriers for all elementary reaction steps. In general, the results demonstrated that the concerted mechanism prevails at the reaction conditions studied in this work. Furthermore, two main influences on the free energy barriers and the reaction free energies could be distinguished.

First, the effect of static versus enhanced sampling MD methods was tested for Case 1. The main difference between the results obtained from the enhanced sampling methods and the static simulation methods was observed for the stabilization of the products in which water was formed. In the case of dynamic methods, the water formed in the methylation step becomes rather mobile, which yields an entropic stabilization of the product region. In static methods, this configurational freedom is not properly described as only one point is considered on the free energy surface. The radial distribution function between the carbon and oxygen of methanol showed a substantial diffusional freedom of water in the product state, which cannot be captured statically. Apart from these qualitative observations, our results also show that obtaining accurate free energy barriers and reaction free energies from biased

ChemPubSoc Europe

CHEMCATCHEM Full Papers

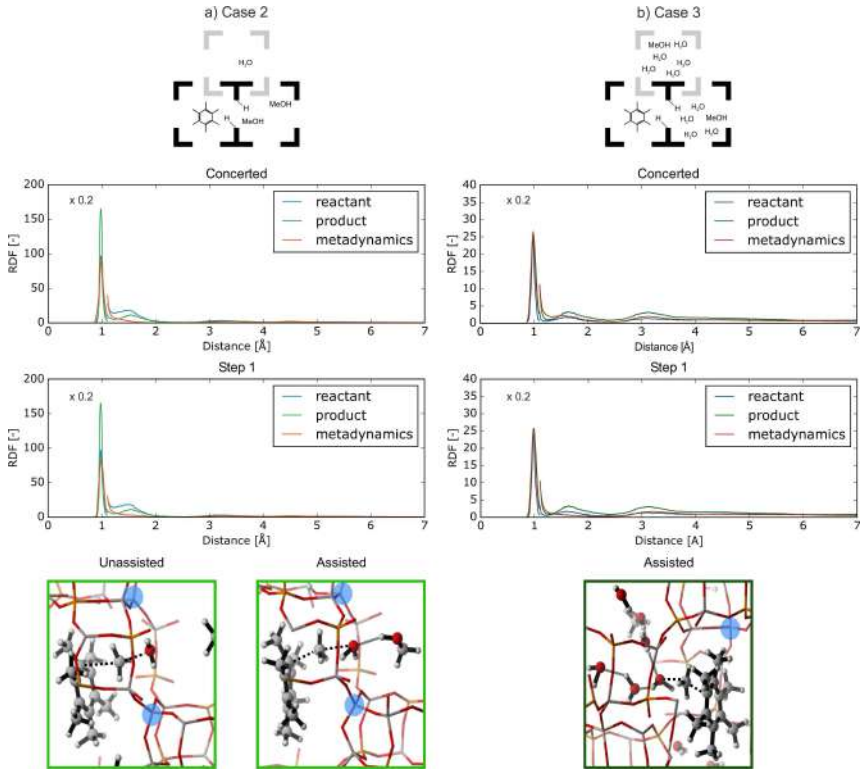

Figure 11. Radial distribution function for the pairs formed by (i) all protons and (ii) the oxygens of the methanol molecules from MD runs in the reactant and product state as well as during the MTD simulations for the concerted methylation (top) and methoxide formation (middle) for Case 2 (a) and Case 3 (b). Furthermore, the unassisted and assisted transition states are visualized in the snapshots at the bottom. The first peaks of the RDFs (at distances below about 1.1 Å) are scaled down by a factor of 5 to improve visualization. In these snapshots, hydrogen is white, carbon is silver, oxygen is red, aluminum is grey, the silicon substitution is indicated in blue and phosphorus is orange.

molecular dynamics simulation methods remains very challenging. An exhaustive number of simulations are necessary to obtain converged free energies along the reaction coordinate. A detailed comparison of various enhanced sampling methods and the impact of collective variables on the results would be interesting for future studies.

Second, by comparing the more complex Case 2 and Case 3, the effect of additional protic molecules in the catalyst pores could be unraveled. In all cases, decreased barriers and additional stabilization of the products was observed. The decreased barrier for the concerted methylation and methoxide formation and the stabilization of the product could be associated to the solvation shells that are more prominent in Case 3. Furthermore, a stabilization of the deprotonated BAS formed in the second step of the stepwise mechanism occurred by a Grotthuss-type mechanism linking both BASs. This effect leads to a decreased barrier for this second step in Case 3.

In conclusion, our results highlight the importance of correctly accounting for the dynamic and assisting behavior of the protic environment within zeolite catalysis at process conditions. Therefore, the use of advanced molecular dynamics to further unravel the reaction mechanism governing the MTO process is indispensable.

Acknowledgements

V.V.S. and S.B. acknowledge funding from the European Union's Horizon 2020 research and innovation program (consolidator ERC grant agreement No. 647755 – DYNPOR (2015-2020)). S.M.J.R and

ChemPubSoc Europe

CHEMCATCHEM Full Papers

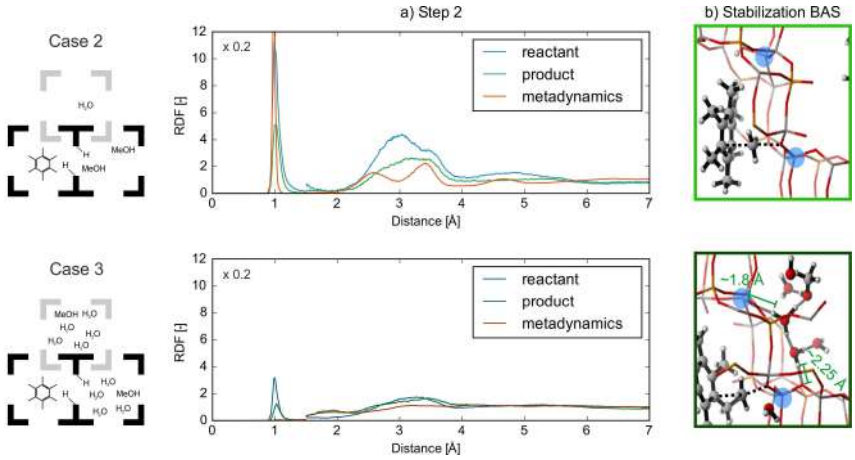

Figure 12. Radial distribution function for the pairs formed by (i) all protons and (ii) the oxygens of the Brønsted acid sites from MD runs in the reactant and product state as well as during the MTD simulations for the second step of the stepwise mechanism (a) for Case 2 (top) and Case 3 (bottom). Furthermore, a snapshot of the BAS during the transition state is shown to depict the stabilization of the formed deprotonated BAS by the protic molecules present (b). The first peaks of the RDFs (at distances below about 1.3 Å) are scaled down by a factor of 5 to improve visualization. In these snapshots, hydrogen is white, carbon is silver, oxygen is red, aluminum is grey, the silicon substitution is indicated in blue and phosphorus is orange.

L.V. acknowledge the Fund for Scientific Research Flanders (FWO) for their postdoctoral fellowships. V.V.S. acknowledges the Research Board of the Ghent University (BOF). The computational resources and services used were provided by Ghent University (Stevin Supercomputer Infrastructure), the VSC (Flemish Supercomputer Center), funded by the Research Foundation – Flanders (FWO).

Conflict of Interest

The authors declare no conflict of interest.

Keywords: density functional theory · enhanced sampling · H-SAPO-34 · methylation · water

[1] R. W. Bentley, *Energy Policy* **2002**, *30*, 189–205.
[2] A. Corma, S. Iborra, A. Velty, *Chem. Rev.* **2007**, *107*, 2411–2502.
[3] C. Briens, J. Piskorz, F. Berruti, *Int. J. Chem. React. Eng.* **2008**, *6*, R2.
[4] P. Sudarsanam, R. Zhong, S. V. den Bosch, S. M. Coman, V. I. Parvulescu, B. F. Sels, *Chem. Soc. Rev.* **2018**, *47*, 8349–8402.
[5] P. L. Spath, D. C. Dayton, **2003**, DOI: 10.2172/15006100.
[6] F. L. Bleken, S. Chavan, U. Olsbye, M. Boltz, F. Ocampo, B. Louis, *Appl. Catal. A* **2012**, *447–448*, 178–185.
[7] S. Abrol, C. M. Hilton, *Comput. Chem. Eng.* **2012**, *40*, 117–131.
[8] U. Olsbye, S. Svelle, M. Bjørgen, P. Beato, T. V. W. Janssens, F. Joensen, S. Bordiga, K. P. Lillerud, *Angew. Chem. Int. Ed.* **2012**, *51*, 5810–5831.
[9] K. Hemelsoet, J. Van der Mynsbrugge, K. De Wispelaere, M. Waroquier, V. Van Speybroeck, *ChemPhysChem* **2013**, *14*, 1526–1545.
[10] I. Yarulina, A. D. Chowdhury, F. Meirer, B. M. Weckhuysen, J. Gascon, *Nat. Catal.* **2018**, *1*, 398–411.
[11] J. Q. Chen, A. Bozzano, B. Glover, T. Fuglerud, S. Kvisle, *Catal. Today* **2005**, *106*, 103–107.
[12] K. De Wispelaere, K. Hemelsoet, M. Waroquier, V. Van Speybroeck, *J. Catal.* **2013**, *305*, 76–80.
[13] K. De Wispelaere, C. S. Wondergem, B. Ensing, K. Hemelsoet, E. J. Meijer, B. M. Weckhuysen, V. Van Speybroeck, J. Ruiz-Martínez, *ACS Catal.* **2016**, 1991–2002.
[14] B. P. C. Hereijgers, F. Bleken, M. H. Nilsen, S. Svelle, K.-P. Lillerud, M. Bjørgen, B. M. Weckhuysen, U. Olsbye, *J. Catal.* **2009**, *264*, 77–87.
[15] M. Yang, P. Tian, C. Wang, Y. Yuan, Y. Yang, S. Xu, Y. He, Z. Liu, *Chem. Commun.* **2014**, *50*, 1845–1847.
[16] T. Álvaro-Muñoz, C. Márquez-Álvarez, E. Sastre, *Catal. Today* **2012**, *179*, 27–34.
[17] T. Álvaro-Muñoz, C. Márquez-Álvarez, E. Sastre, *Appl. Catal. A* **2014**, *472*, 72–79.
[18] L. Wu, E. J. M. Hensen, *Catal. Today* **2014**, *235*, 160–168.
[19] A. J. Marchi, G. F. Froment, *Appl. Catal.* **1991**, *71*, 139–152.
[20] X. Wu, R. G. Anthony, *Appl. Catal. A* **2001**, *218*, 241–250.
[21] W. Song, H. Fu, J. F. Haw, *J. Am. Chem. Soc.* **2001**, *123*, 4749–4754.
[22] M. Shahda, Y. Dengchao, W. Huixin, *Pet. Sci. Technol.* **2008**, *26*, 1893–1903.
[23] A. Taheri Najafabadi, S. Fatemi, M. Sohrabi, M. Salmasi, *J. Ind. Eng. Chem.* **2012**, *18*, 29–37.
[24] S. Tjandra, R. G. Anthony, A. Akgerman, *Ind. Eng. Chem. Res.* **1993**, *32*, 2602–2607.
[25] X. Yin, D. Y. C. Leung, J. Chang, J. Wang, Y. Fu, C. Wu, *Energy Fuels* **2005**, *19*, 305–310.
[26] A. Demirbas, *Prog. Energy Combust. Sci.* **2007**, *33*, 1–18.
[27] J. F. Haw, D. M. Marcus, *Top. Catal.* **2005**, *34*, 41–48.
[28] V. Van Speybroeck, K. De Wispelaere, J. Van der Mynsbrugge, M. Vandichel, K. Hemelsoet, M. Waroquier, *Chem. Soc. Rev.* **2014**, *43*, 7326–7357.
[29] A. D. Chowdhury, A. L. Paioni, K. Houben, G. T. Whiting, M. Baldus, B. M. Weckhuysen, *Angew. Chem. Int. Ed.* **2018**, *57*, 8095–8099.
[30] J. F. Haw, W. Song, D. M. Marcus, J. B. Nicholas, *Acc. Chem. Res.* **2003**, *36*, 317–326.
[31] I. M. Dahl, S. Kolboe, *Catal. Lett.* **1993**, *20*, 329–336.
[32] I. M. Dahl, S. Kolboe, *J. Catal.* **1994**, *149*, 458–464.
[33] I. M. Dahl, S. Kolboe, *J. Catal.* **1996**, *161*, 304–309.

ChemPubSoc Europe

CHEMCATCHEM Full Papers

[34] J. Van der Mynsbrugge, M. Visur, U. Olsbye, P. Beato, M. Bjørgen, V. Van Speybroeck, S. Svelle, *J. Catal.* **2012**, *292*, 201–212.
[35] D. Lesthaeghe, B. De Sterck, V. Van Speybroeck, G. B. Marin, M. Waroquier, *Angew. Chem. Int. Ed.* **2007**, *46*, 1311–1314.
[36] V. Van Speybroeck, K. Hemelsoet, K. De Wispelaere, Q. Qian, J. Van der Mynsbrugge, B. De Sterck, B. M. Weckhuysen, M. Waroquier, *ChemCatChem* **2013**, *5*, 173–184.
[37] K. Hemelsoet, Q. Qian, T. De Meyer, K. De Wispelaere, B. De Sterck, B. M. Weckhuysen, M. Waroquier, V. Van Speybroeck, *Chem. Eur. J.* **2013**, *19*, 16595–16606.
[38] I. I. Ivanova, A. Corma, *J. Phys. Chem. B* **1997**, *101*, 547–551.
[39] S. Svelle, S. Kolboe, U. Olsbye, O. Swang, *J. Phys. Chem. B* **2003**, *107*, 5251–5260.
[40] S. Svelle, M. Visur, U. Olsbye, Saepurahman, M. Bjørgen, *Top. Catal.* **2011**, *54*, 897–906.
[41] J. Van der Mynsbrugge, S. L. C. Moors, K. De Wispelaere, V. Van Speybroeck, *ChemCatChem* **2014**, *6*, 1906–1918.
[42] A. M. Vos, K. H. L. Nulens, F. De Proft, R. A. Schoonheydt, P. Geerlings, *J. Phys. Chem. B* **2002**, *106*, 2026–2034.
[43] R. Y. Brogaard, R. Henry, Y. Schuurman, A. J. Medford, P. G. Moses, P. Beato, S. Svelle, J. K. Nørskov, U. Olsbye, *J. Catal.* **2014**, *314*, 159–169.
[44] K. De Wispelaere, S. Bailleul, V. Van Speybroeck, *Catal. Sci. Technol.* **2016**, *6*, 2686–2705.
[45] K. De Wispelaere, J. S. Martínez-Espín, M. J. Hoffmann, S. Svelle, U. Olsbye, T. Bligaard, *Catal. Today* **2018**, *312*, 35–43.
[46] M. Westgård Erichsen, K. De Wispelaere, K. Hemelsoet, S. L. C. Moors, T. Deconinck, M. Waroquier, S. Svelle, V. Van Speybroeck, U. Olsbye, *J. Catal.* **2015**, *328*, 186–196.
[47] A. J. Jones, E. Iglesia, *Angew. Chem. Int. Ed.* **2014**, *53*, 12177–12181.
[48] T. Maihom, B. Boekfa, J. Sirijaraensre, T. Nanok, M. Probst, J. Limtrakul, *J. Phys. Chem. C* **2009**, *113*, 6654–6662.
[49] M. N. Mazar, S. Al-Hashimi, A. Bhan, M. Cococcioni, *J. Phys. Chem. C* **2012**, *116*, 19385–19395.
[50] L. Benco, T. Bučko, J. Hafner, *J. Catal.* **2011**, *277*, 104–116.
[51] T. Bučko, L. Benco, J. Hafner, J. G. Ángyán, *J. Catal.* **2011**, *279*, 220–228.
[52] K. De Wispelaere, B. Ensing, A. Ghysels, E. J. Meijer, V. Van Speybroeck, *Chem. Eur. J.* **2015**, *21*, 9385–9396.
[53] T. Bučko, J. Hafner, *J. Catal.* **2015**, *329*, 32–48.
[54] T. Bučko, S. Chibani, J.-F. Paul, L. Cantrel, M. Badawi, *Phys. Chem. Chem. Phys.* **2017**, *19*, 27530–27543.
[55] J. Rey, A. Gomez, P. Raybaud, C. Chizallet, T. Bučko, *J. Catal.* **2019**, *373*, 361–373.
[56] C. Abrams, G. Bussi, *Entropy* **2013**, *16*, 163–199.
[57] T. Bučko, *J. Phys. Condens. Matter* **2008**, *20*, 064211.
[58] D. Trzesniak, A.-P. E. Kunz, W. F. van Gunsteren, *ChemPhysChem* **2007**, *8*, 162–169.
[59] D. Frenkel, B. Smit, *Understanding Molecular Simulation: From Algorithms to Applications*, Academic Press, **2001**.
[60] C. D. Christ, A. E. Mark, W. F. van Gunsteren, *J. Comput. Chem.* **2010**, *31*, 1569–1582.
[61] A. Laio, M. Parrinello, *Proc. Mont. Acad. Sci.* **2002**, *99*, 12562–12566.
[62] M. Iannuzzi, A. Laio, M. Parrinello, *Phys. Rev. Lett.* **2003**, *90*, 238302.
[63] A. Laio, F. L. Gervasio, *Rep. Prog. Phys.* **2008**, *71*, 126601.
[64] G. M. Torrie, J. P. Valleau, *Chem. Phys. Lett.* **1974**, *28*, 578–581.
[65] G. M. Torrie, J. P. Valleau, *J. Comput. Phys.* **1977**, *23*, 187–199.
[66] J. Kästner, *Wiley Interdiscip. Rev.: Comput. Mol. Sci.* **2011**, *1*, 932–942.
[67] S. L. C. Moors, K. De Wispelaere, J. Van der Mynsbrugge, M. Waroquier, V. Van Speybroeck, *ACS Catal.* **2013**, *3*, 2556–2567.
[68] L. Vanduyfhuys, A. Ghysels, S. M. J. Rogge, R. Demuynck, V. Van Speybroeck, *Mol. Simul.* **2015**, *41*, 1311–1328.
[69] D. H. Olson, W. O. Haag, W. S. Borghard, *Microporous Mesoporous Mater.* **2000**, *35–36*, 435–446.
[70] D. H. Olson, W. O. Haag, R. M. Lago, *J. Catal.* **1980**, *61*, 390–396.
[71] H. Nakamoto, H. Takahashi, *Zeolites* **1982**, *2*, 67–68.
[72] T. Sano, T. Kasuno, K. Takeda, S. Arazaki, Y. Kawakami, in *Stud. Surf. Sci. Catal.* (Eds.: H. Chon, S.-K. Ihm, Y. S. Uh), Elsevier, **1997**, pp. 1771–1778.
[73] S. Eckstein, P. H. Hintermeier, R. Zhao, E. Baráth, H. Shi, Y. Liu, J. A. Lercher, *Angew. Chem. Int. Ed.* **2019**, *58*, 3450–3455.
[74] V. Termath, F. Haase, J. Sauer, J. Hutter, M. Parrinello, *J. Am. Chem. Soc.* **1998**, *120*, 8512–8516.
[75] G. Sastre, D. W. Lewis, C. R. A. Catlow, *J. Phys. Chem.* **1996**, *100*, 6722–6730.
[76] "Database of Zeolite Structures," can be found under http://www.iza-structure.org/databases/.
[77] C.-M. Wang, Y.-D. Wang, Y.-J. Du, G. Yang, Z.-K. Xie, *Catal. Sci. Technol.* **2015**, *5*, 4354–4364.
[78] M. Nielsen, R. Y. Brogaard, H. Falsig, P. Beato, O. Swang, S. Svelle, *ACS Catal.* **2015**, *5*, 7131–7139.
[79] T. F. Willems, C. H. Rycroft, M. Kazi, J. C. Meza, M. Haranczyk, *Microporous Mesoporous Mater.* **2012**, *149*, 134–141.
[80] D. W. H. Rankin, *Crystallogr. Rev.* **2009**, *15*, 223–224.
[81] J. Kuhn, J. M. Castillo-Sanchez, J. Gascon, S. Calero, D. Dubbeldam, T. J. H. Vlugt, F. Kapteijn, J. Gross, *J. Phys. Chem. C* **2009**, *113*, 14290–14301.
[82] S. M. J. Rogge, R. Goeminne, R. Demuynck, J. J. Gutiérrez-Sevillano, S. Vandenbrande, L. Vanduyfhuys, M. Waroquier, T. Verstraelen, V. Van Speybroeck, *Adv. Theory Simul.* **2019**, *2*, 1800177.
[83] G. Kresse, J. Hafner, *Phys. Rev. B* **1993**, *47*, 558–561.
[84] G. Kresse, J. Hafner, *Phys. Rev. B* **1994**, *49*, 14251–14269.
[85] G. Kresse, J. Furthmüller, *Comput. Mater. Sci.* **1996**, *6*, 15–50.
[86] G. Kresse, J. Furthmüller, *Phys. Rev. B* **1996**, *54*, 11169–11186.
[87] J. Hajek, J. Van der Mynsbrugge, K. De Wispelaere, P. Cnudde, L. Vanduyfhuys, M. Waroquier, V. Van Speybroeck, *J. Catal.* **2016**, *340*, 227–235.
[88] J. Hajek, B. Bueken, M. Waroquier, D. De Vos, V. Van Speybroeck, *ChemCatChem* **2017**, *9*, 2203–2210.
[89] P. Cnudde, K. De Wispelaere, J. Van der Mynsbrugge, M. Waroquier, V. Van Speybroeck, *J. Catal.* **2017**, *345*, 53–69.
[90] I. Yarulina, K. De Wispelaere, S. Bailleul, J. Goetze, M. Radersma, E. Abou-Hamad, I. Vollmer, M. Goesten, B. Mezari, E. J. M. Hensen, J. S. Martínez-Espín, M. Morten, S. Mitchell, J. Perez-Ramirez, U. Olsbye, B. M. Weckhuysen, V. Van Speybroeck, F. Kapteijn, J. Gascon, *Nat. Chem.* **2018**, *10*, 804–812.
[91] K. Yang, J. Zheng, Y. Zhao, D. G. Truhlar, *J. Chem. Phys.* **2010**, *132*, 164117.
[92] P. E. Blöchl, *Phys. Rev. B* **1994**, *50*, 17953–17979.
[93] G. Kresse, D. Joubert, *Phys. Rev. B* **1999**, *59*, 1758–1775.
[94] S. Grimme, J. Antony, S. Ehrlich, H. Krieg, *J. Chem. Phys.* **2010**, *132*, 154104.
[95] N. Hansen, T. Kerber, J. Sauer, A. T. Bell, F. J. Keil, *J. Am. Chem. Soc.* **2010**, *132*, 11525–11538.
[96] S. Svelle, C. Tuma, X. Rozanska, T. Kerber, J. Sauer, *J. Am. Chem. Soc.* **2009**, *131*, 816–825.
[97] V. Van Speybroeck, J. Van der Mynsbrugge, M. Vandichel, K. Hemelsoet, D. Lesthaeghe, A. Ghysels, G. B. Marin, M. Waroquier, *J. Am. Chem. Soc.* **2011**, *133*, 888–899.
[98] G. Piccini, M. Alessio, J. Sauer, *Angew. Chem. Int. Ed.* **2016**, *55*, 5235–5237.
[99] H. Eshuis, J. E. Bates, F. Furche, *Theor. Chem. Acc.* **2012**, *131*, 1084.
[100] F. Furche, *Phys. Rev. B* **2001**, *64*, 195120.
[101] J. Harl, G. Kresse, *Phys. Rev. Lett.* **2009**, *103*, 056401.
[102] Y. Zhao, D. G. Truhlar, *Acc. Chem. Res.* **2008**, *41*, 157–167.
[103] Y. Zhao, D. G. Truhlar, *J. Phys. Chem. C* **2008**, *112*, 4061–4067.
[104] Y. Zhao, D. G. Truhlar, *J. Chem. Theory Comput.* **2008**, *4*, 1849–1868.
[105] B. Boekfa, S. Choomwattana, P. Khongpracha, J. Limtrakul, *Langmuir* **2009**, *25*, 12990–12999.
[106] A. Heyden, A. T. Bell, F. J. Keil, *J. Chem. Phys.* **2005**, *123*, 224101.
[107] P. Pulay, *Chem. Phys. Lett.* **1980**, *73*, 393–398.
[108] W. H. Press, B. P. Flannery, S. A. Teukolsky, W. T. Vetterling, *Numerical Recipes: The Art of Scientific Computing*, Cambridge Univ. Press, New York, **1986**.
[109] B. A. De Moor, A. Ghysels, M.-F. Reyniers, V. Van Speybroeck, M. Waroquier, G. B. Marin, *J. Chem. Theory Comput.* **2011**, *7*, 1090–1101.
[110] K. De Wispelaere, L. Vanduyfhuys, V. Van Speybroeck, in *Model. Simul. Sci. Micro- Meso-Porous Mater.* (Eds.: C. R. A. Catlow, V. Van Speybroeck, R. A. van Santen), Elsevier, **2018**, pp. 189–228.
[111] A. Ghysels, T. Verstraelen, K. Hemelsoet, M. Waroquier, V. Van Speybroeck, *J. Chem. Inf. Model.* **2010**, *50*, 1736–1750.
[112] J. Hutter, M. Iannuzzi, F. Schiffmann, J. VandeVondele, *Wiley Interdiscip. Rev.: Comput. Mol. Sci.* **2014**, *4*, 15–25.
[113] J. VandeVondele, M. Krack, F. Mohamed, M. Parrinello, T. Chassaing, J. Hutter, *Comput. Phys. Commun.* **2005**, *167*, 103–128.
[114] G. J. Martyna, D. J. Tobias, M. L. Klein, *J. Chem. Phys.* **1994**, *101*, 4177–4189.
[115] G. Lippert, J. Hutter, M. Parrinello, *Mol. Phys.* **1997**, *92*, 477–488.
[116] G. Lippert, J. Hutter, M. Parrinello, *Theor. Chem. Acc.* **1999**, *103*, 124–140.
[117] S. Goedecker, M. Teter, J. Hutter, *Phys. Rev. B* **1996**, *54*, 1703–1710.

ChemPubSoc Europe

CHEMCATCHEM Full Papers

[118] T. Verstraelen, L. Vanduyfhuys, S. Vandenbrande, S. M. J. Rogge, "Yaff, Yet Another Force Field.," can be found under http://molmod.ugent.be/software/.
[119] S. Kumar, J. M. Rosenberg, D. Bouzida, R. H. Swendsen, P. A. Kollman, *J. Comput. Chem.* **1992**, *13*, 1011–1021.
[120] M. Souaille, B. Roux, *Comput. Phys. Commun.* **2001**, *135*, 40–57.
[121] M. Bonomi, D. Branduardi, G. Bussi, C. Camilloni, D. Provasi, P. Raiteri, D. Donadio, F. Marinelli, F. Pietrucci, R. A. Broglia, M. Parrinello, *Comput. Phys. Commun.* **2009**, *180*, 1961–1972.
[122] N. Hansen, W. F. van Gunsteren, *J. Chem. Theory Comput.* **2014**, *10*, 2632–2647.
[123] R. Demuynck, S. M. J. Rogge, L. Vanduyfhuys, J. Wieme, M. Waroquier, V. Van Speybroeck, *J. Chem. Theory Comput.* **2017**, *13*, 5861–5873.
[124] M. A. Cuendet, M. E. Tuckerman, *J. Chem. Theory Comput.* **2014**, *10*, 2975–2986.
[125] A. Barducci, M. Bonomi, M. Parrinello, *Wiley Interdiscip. Rev.: Comput. Mol. Sci.* **2011**, *1*, 826–843.
[126] D. Marx, *ChemPhysChem* **2006**, *7*, 1848–1870.
[127] A. J. Marchi, G. F. Froment, *Appl. Catal. A* **1993**, *94*, 91–106.
[128] W. Wang, A. Buchholz, M. Seiler, M. Hunger, *J. Am. Chem. Soc.* **2003**, *125*, 15260–15267.

Manuscript received: April 23, 2019
Revised manuscript received: June 5, 2019
Accepted manuscript online: June 25, 2019
Version of record online: July 9, 2019

Paper V

A supramolecular view on the cooperative role of Brønsted and Lewis acid sites in zeolites for methanol conversion

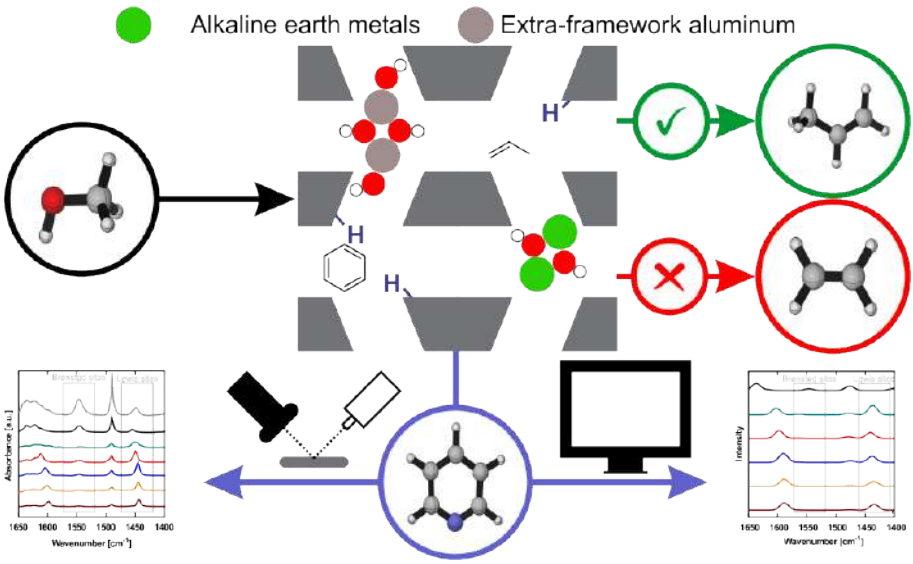

S. Bailleul, I. Yarulina, A. Hoffman, A. Dokania, E. Abou-Hamad, A. Dutta Chowdhury, G. Pieters, J. Hajek, K. De Wispelaere, M. Waroquier, J. Gascon, V. Van Speybroeck, *Journal of the American Chemical Society*, **141**, 14823–14842 (2019)

S. Bailleul performed the calculations, except the NMR calculations performed by A. Hoffman, and prepared the manuscript.

JACS JOURNAL OF THE AMERICAN CHEMICAL SOCIETY
Cite This: J. Am. Chem. Soc. XXXX, XXX, XXX−XXX
Article
pubs.acs.org/JACS

A Supramolecular View on the Cooperative Role of Brønsted and Lewis Acid Sites in Zeolites for Methanol Conversion

Simon Bailleul,[†] Irina Yarulina,[‡] Alexander E. J. Hoffman,[†] Abhay Dokania,[‡] Edy Abou-Hamad,[§] Abhishek Dutta Chowdhury,[‡] Giovanni Pieters,[†] Julianna Hajek,[†] Kristof De Wispelaere,[†] Michel Waroquier,[†] Jorge Gascon,*[,‡] and Veronique Van Speybroeck*[,†]

[†]Center for Molecular Modeling (CMM), Ghent University, Technologiepark 46, B-9052 Zwijnaarde, Belgium

[‡]King Abdullah University of Science and Technology, KAUST Catalysis Center, Advanced Catalytic Materials, Thuwal 23955-6900, Saudi Arabia

[§]King Abdullah University of Science and Technology (KAUST), Core Laboratories, Thuwal, Saudi Arabia

Supporting Information

ABSTRACT: A systematic molecular level and spectroscopic investigation is presented to show the cooperative role of Brønsted acid and Lewis acid sites in zeolites for the conversion of methanol. Extra-framework alkaline-earth metal containing species and aluminum species decrease the number of Brønsted acid sites, as protonated metal clusters are formed. A combined experimental and theoretical effort shows that postsynthetically modified ZSM-5 zeolites, by incorporation of extra-framework alkaline-earth metals or by demetalation with dealuminating agents, contain both mononuclear $[MOH]^+$ and double protonated binuclear metal clusters $[M(\mu\text{-}OH)_2M]^{2+}$ (M = Mg, Ca, Sr, Ba, and HOAl). The metal in the extra-framework clusters has a Lewis acid character, which is confirmed experimentally and theoretically by IR spectra of adsorbed pyridine. The strength of the Lewis acid sites (Mg > Ca > Sr > Ba) was characterized by a blue shift of characteristic IR peaks, thus offering a tool to sample Lewis acidity experimentally. The incorporation of extra-framework Lewis acid sites has a substantial influence on the reactivity of propene and benzene methylations. Alkaline-earth Lewis acid sites yield increased benzene methylation barriers and destabilization of typical aromatic intermediates, whereas propene methylation routes are less affected. The effect on the catalytic function is especially induced by the double protonated binuclear species. Overall, the extra-framework metal clusters have a dual effect on the catalytic function. By reducing the number of Brønsted acid sites and suppressing typical catalytic reactions in which aromatics are involved, an optimal propene selectivity and increased lifetime for methanol conversion over zeolites is obtained. The combined experimental and theoretical approach gives a unique insight into the nature of the supramolecular zeolite catalyst for methanol conversion which can be meticulously tuned by subtle interplay of Brønsted and Lewis acid sites.

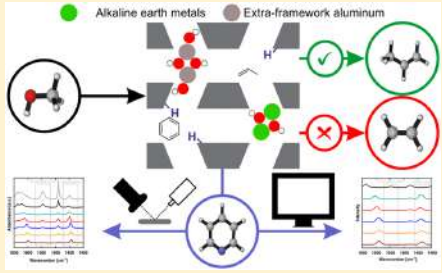

1. INTRODUCTION

To shift the global energy and chemicals economy from petroleum-based to more sustainable resources, highly efficient catalysts are needed. While innovative electro- and photocatalysis processes are being developed, there is a major window of opportunities for the optimization and design of thermal zeolite-catalyzed processes which are widely applied in the (petro)chemical industry.[1] Zeolites have been widely studied from an experimental and molecular simulations viewpoint,[2,3] and are a very stable and versatile class of materials. Many contemporary processes focus on nonconventional feedstocks containing heteroatoms, for which meticulous design of active sites in zeolites is of primary importance to ensure selective and efficient conversion.[4−7]

In this view, methanol-to-olefins (MTO) conversion over zeolite catalysts received much attention in recent decades, as it has proven to be a successful technology to bypass crude oil in the production of highly demanded light olefins, namely ethene and propene.[8−11] The reaction mechanism governing this process has been up for discussion for many years, and it is now generally accepted that instead of a direct C−C coupling between reactant molecules, a hydrocarbon pool (HP) consisting of aromatic or aliphatic molecules cocatalyzes the reactions leading to olefin production (Figure 1a).[12−14] According to the seminal work of Haw and co-workers[15] an active MTO catalyst should be regarded as a supramolecular assembly consisting of the zeolite channel system decorated with Brønsted acidic functions in which organic compounds need to be present to generate an active catalyst. Furthermore,

Received: July 14, 2019
Published: August 29, 2019

DOI: 10.1021/jacs.9b07484
J. Am. Chem. Soc. XXXX, XXX, XXX−XXX

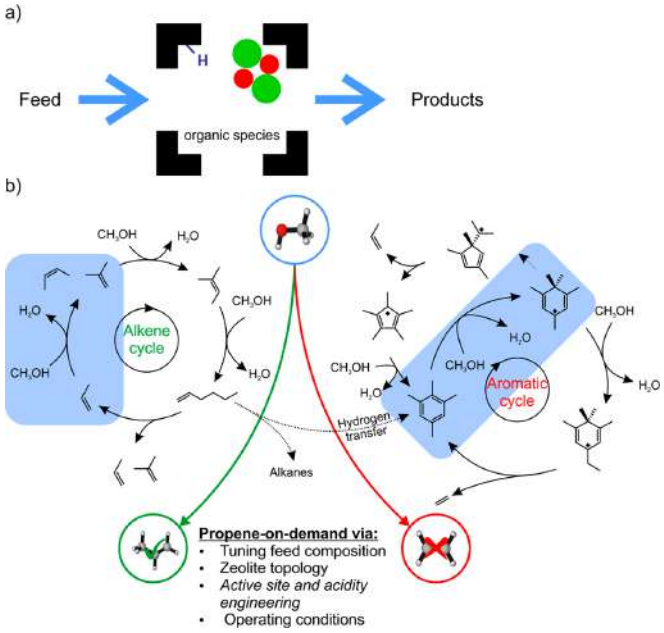

Figure 1. (a) Schematic representation of the zeolite supramolecular catalyst according to the view of Haw et al.[15] on the MTO process. (b) Schematic representation of the MTO process as solution for the disparity between propene production and demand using the dual cycle concept, which consists of the alkene and aromatic cycle. In both mechanisms, the importance of methylation reactions as initiating steps is indicated in blue. Propene selectivity can be increased by suppressing the aromatic cycle by tuning the feed composition, adapting the zeolite topology, engineering the active site, or optimizing the process. The focus of this article is on the engineering of the active site.[42]

the supramolecular system could be modified with some inorganic compound to further tune the catalytic function (Figure 1a). However, this option has to date only been explored to a more limited extent.[16−30]

A rational catalyst design to control olefin selectivity and resistance to coking requires intimate insight into the operating catalytic cycles. For the MTO process, there is current consensus that the HP mechanism (depicted in Figure 1b) consists of two interacting reaction cycles, namely the alkene and aromatic cycle, which is also referred to as the dual cycle concept.[3,8,10,31,32] In both reaction cycles, methylation reactions (indicated in blue in Figure 1) are key reactions and have been widely studied in the framework of MTO catalysis.[33−41]

According to the seminal work of Svelle and co-workers[32] on the dual cycle mechanism, the formation of ethene is mechanistically separated from the formation of propene. Ethene is supposed to be mainly formed via the aromatic cycle, whereas propene and higher olefins are formed via the alkene cycle which consists of alkene cracking reactions and methylations. This characteristic makes MTO conversion especially interesting as a propene-on-demand process as a solution for the increasing disparity between the propene production and demand.[43−46] Based on this knowledge, various strategies have been tested such as tuning the feed composition,[47] the zeolite topology,[8,10] acidity,[24,25] and operating conditions to increase the selectivity to propene by promoting the alkene cycle over the aromatic cycle. Hereafter some examples are given which illustrate the wide options that have been explored so far. Promotion of one of the reaction cycles can be obtained via cofeeding of the hydrocarbon pool species aiding in the promoted cycle. Experimental studies over SAPO-34 and ZSM-5 showed that cofeeding olefins does not have an influence on the selectivity, while cofeeding aromatics led to enhanced methane and ethene formation, suggesting aromatic cycle promotion.[12,13,47] A second possibility is to suppress a reaction cycle by conveniently selecting the catalyst topology, as was done in the study of the MTO process over H-ZSM-22 by Teketel et al.,[48,49] where they showed that the aromatic cycle was suppressed via shape selectivity due to the confined space in the 1D 10-ring channels of the TON topology. In CHA structured materials on the other hand, the aromatic cycle dominates product formation due to high concentrations of aromatics that cannot diffuse through the narrow windows of CHA cages.[36,50] In ZSM-5 (MFI) both cycles typically operate simultaneously.[32] Furthermore, the aromatic cycle can be suppressed by lowering the acid strength of the Brønsted acid sites (BASs) as shown for the AFI structured H-SAPO-5 and H-SSZ-24 materials. Even when cofeeding benzene, the alkene cycle was found to dominate under MTO conditions in the weaker acidic H-SAPO-5 material.[51−53] Also the reaction conditions may substantially impact the product selectivity as was shown by the group of Iglesia where they promoted the alkene cycle in the large pore zeolite H-BEA, characterized by the aromatic cycle,[54−57] by utilization of low temperatures (453−493 K) and high

DOI: 10.1021/jacs.9b07484
J. Am. Chem. Soc. XXXX, XXX, XXX−XXX

pressures (60−250 kPa).[58,59] Another example of adapting the process conditions to increase propene selectivity can be found in the Lurgi methanol-to-propylene (MTP) process (around atmospheric pressure and 733−753 K), where they increase propene selectivity using high siliceous H-ZSM-5 and undesired product recycles.[10,60]

Referring back to the initial supramolecular concept of the MTO catalyst, an alternative strategy to increase propene selectivity and catalyst lifetime is active site engineering by incorporation of extra-framework species in the MTO catalyst. Inorganic modification of the zeolite was explored using phosphorus,[16−18] boron,[19] transition metal,[20−23,61,62] and alkaline earth metals.[24−30] Such modifications typically reduce the Brønsted acid site density, which can also be achieved by tuning the Si/Al ratio in the zeolite synthesis stage or by postsynthetic dealumination.[25,63−65] As aromatics formation typically requires vicinal BASs,[21] many zeolite modifications reduce aromatics formation and increase the importance of the alkene cycle by creating isolated BASs.[66−70] Additionally, these modifications can exhibit catalytic activity themselves, as they are known to create Lewis acid sites (LASs).[24,25,71]

In this work, we further build on the concept of inorganic modification of the zeolite supramolecular MTO catalyst, by studying the influence of extra-framework metal containing cationic clusters on the selectivity toward the alkene or aromatic cycle. Inspired by the recent work of Yarulina et al.[24,25] where a 2-fold increase in propene selectivity and a nine times longer catalyst lifetime was obtained by Ca modification of ZSM-5, a set of alkaline-earth metal (Mg, Ca, Sr, and Ba) clusters are considered. Some earlier studies explored the beneficial effect of alkaline-earth metal incorporation in ZSM-5 on the methanol-to-olefin process, but did not receive so much attention at that time since propene was not the product of interest.[26−30,71] Yarulina et al. ascribed the enhanced performance of Ca-ZSM-5 for MTO to the reduction of the Brønsted acid site density and introduction of Lewis acid sites.[24] Such modification of the catalyst would suppress the aromatic cycle.[25] Additionally, dealumination of zeolites is known to lead to formation of both mesopores and extra-framework aluminum (EFAl) species, which exhibit a Lewis acid nature.[65,72−74] This postsynthetic modification is also known to increase propene selectivity and catalyst lifetime.[69,75,76]

For both alkaline-earth metal modifications and EFAl species, the nature and role of LASs on the zeolite supramolecular function for the methanol conversion will be investigated. Although some theoretical insights on the effect of Lewis acid sites on methanol conversion were already obtained, a systematic spectroscopic, energetic, and reactivity study at the molecular level is not available for metal containing clusters. Therefore, we aim at filling this void by performing a combined theoretical-experimental screening of several modified Lewis acid sites in zeolites to get molecular insights into their specific nature and role under MTO conditions. The series of extra-framework incorporated metal clusters are expected to have distinct differences in acidic strength, which may impact the stability and reactivity pattern of the supramolecular catalyst. In principle various multinuclear cationic complexes containing bridging O or OH ligands may be formed. The structure of these species will be assessed from an energetic and spectroscopic assessment, including solid state NMR. We aim to unravel the structure of the extra-framework species in the zeolite pores, the chemical nature of the modified active site, and how the modified active site affects the reactivity and relative importance of the alkene and aromatic cycle in the MTO process. Based on this systematic screening of Lewis acidity in zeolite pores, better design rules with complex active sites may be proposed for next generation MTO catalysts.

2. MATERIALS AND METHODS

2.1. Computational Details. To unravel the nature of the active site and its reactivity toward methylations, both static and dynamic approaches based on the Density Functional Theory (DFT) methodology are used.

Static periodic DFT calculations have been performed using the Vienna Ab Initio Simulations Package (VASP 5.4) to analyze the structure and nature of the active site, the methylation of propene, benzene, pseudocumene, and durene, and to calculate the protonation energies of the aromatics.[77−80] The unit cell of ZSM-5 used during these static simulations consists of 96 T atoms with the cell parameters being: a = 20.02 Å, b = 20.25 Å, c = 13.49 Å, α = 89.87°, β = 89.69°, and γ = 90.10°. More information on the unit cell and the performed Al substitutions for charge compensation can be found in the Supporting Information (SI), Section 1. For the DFT calculations, the PBE functional with Grimme D3 dispersion corrections are used.[81,82] This functional gives a reasonable compromise between accuracy and computational cost.[83] Other methodologies aiming at reaching chemical accuracy are far more computational expensive and beyond reach for the current study.[84,85] Nevertheless, a benchmark study on the influence of the functional and dispersion correction scheme on the methylation of propene and benzene is performed and the results are discussed in detail in Section 1.5 of the SI. These results show that the choice of functional and dispersion scheme keeps the general trend of features observed when studying differences of energies. The PBE-D3 functional turns out to follow the average behavior of the 12 various LOTs which have been considered. This methodology is further retained in the remainder of the paper to determine in a qualitative way the effects of postmodification of the catalyst. Due to the huge amount of calculations performed within this study, hierarchical cluster approaches relying on high level wave function based methods are beyond the scope for the current study.[84,86−90] Furthermore, the projector augmented wave (PAW) method, a plane-wave cutoff of 600 eV, and a self-consistent field (SCF) convergence criterion of 10^{-5} eV are used.[91,92] During the VASP calculations, the Brillouin zone is restricted to the Γ-point. Transition states are initially optimized with the improved dimer method of Heyden et al.[93] and then refined with a quasi-Newton algorithm as implemented in VASP.[94] Geometries are slightly displaced along the normal mode corresponding to the motion that leads the system over the barrier to generate starting geometries for the optimization of reactant and product states. For these calculations, a conjugate gradient algorithm is applied.[95]

Since partial Hessian vibrational analysis (PHVA) is shown to be an attractive alternative for computationally demanding full Hessian calculations (FHVA) for entropy calculations, this scheme is used for the normal-mode analysis (NMA) in this work using TAMkin.[96,97] In a PHVA calculation, not the entire system, but only a part, namely the guest molecules and part of the framework around the active site, are accounted for during the NMA. As the number of active sites per unit cell may vary depending on the performed simulation, the number of framework atoms included in the NMA will vary. Therefore, more information on the accounted atoms and performed PHVA is presented in Section 1.3 of the Supporting Information. If unwanted imaginary frequencies could not be removed due to a relatively flat potential energy surface, they are substituted with an arbitrary value of 50 cm^{-1} as is frequently done in literature; however, such substitutions were limited to an absolute minimum.[98,99]

To construct the theoretical IR spectra of pyridine adsorbed on the different active sites, the optimized configurations of adsorbed pyridine are obtained with the same VASP parameters as used for the structural analysis of the active site (*vide supra*). Afterward,

DOI: 10.1021/jacs.9b07484
J. Am. Chem. Soc. XXXX, XXX, XXX−XXX

Table 1. Textural and Acidic Properties of the Alkaline Earth Metal Modified ZSM-5 Zeolites and of the EFAl Species[a]

Catalyst	% cation	V_{pore} (cm^3/g)	V_{micro} (cm^3/g)	S_{BET} (m^2/g)	S_{meso} (m^2/g)	S_{micro} (m^2/g)	C_{BAS} ($\mu mol/g$)	C_{LAS} ($\mu mol/g$)
Mg-ZSM-5	1.4	0.22	0.14	417	95	322	76	217
Ca-ZSM-5	2.4	0.24	0.13	392	77	315	40	228
Sr-ZSM-5	5.2	0.20	0.13	379	106	273	85	108
Ba-ZSM-5	8.2	0.18	0.12	316	60	256	19	133
parent ZSM-5_80	Si/Al = 40	0.26	0.15	448	85	363	232	35
DeAl-ZSM-5	–	0.26	–	384	188	196	37	139
Parent ZSM-5_26	Si/Al = 13	0.26	–	403	148	255	631	168

[a]Note that alkaline-earth metal modified ZSM-5 zeolites have been prepared from the parent ZSM-5_80 zeolite, while the dealuminated EFAl species is extracted from the parent ZSM-5_26 zeolite.

density-functional perturbation theory (DFPT) or linear response theory (LRT) calculations are performed to be able to calculate the vibrational intensities from the Born effective charges (BEC).[100−104] Finally, the theoretical IR spectra are obtained by fitting Gaussian resolution functions with a width of 7.5 cm^{-1}. No rescaling of the obtained wavenumber was performed as IR scaling factors are mostly calculated for nonperiodic simulations and are shown to be close to 1 for PBE (see also Supporting Information Section 3), certainly for larger basis sets.[105,106] Just as for the NMA, the PHVA scheme is used (*vide supra*).

For the calculation of the protonation enthalpy,[25] the considered intermediates X are adsorbed in both protonated and neutral form in H-ZSM-5, Mg-ZSM-5, Ca-ZSM-5, Sr-ZSM-5, Ba-ZSM-5, and dealuminated ZSM-5. Thereafter, the protonation enthalpy is calculated as

$$H_{prot} = H(X^{+}_{ads}) - H(X_{ads})$$

The resulting protonation enthalpies, are depicted in Figure S31 and reported in Table S23 in the Supporting Information).

The theoretical NMR parameters in this work are also calculated with VASP. For the simulation of the chemical shielding tensors, the gauge including projector augmented wave (GIPAW) method is used,[107] Again the same VASP settings are used as for the other simulations, except for the SCF convergence criterion, which is set at 10^{-8} eV, required for an accurate estimation of the theoretical NMR parameters. The computed chemical shielding has been converted to the experimentally observed chemical shift by taking into account a linear relation between both parameters (see Supporting Information Section 1.4).

Molecular dynamics simulations have been applied to better incorporate the effects of mobility and entropy due to finite temperature in which experiments have been performed. We used the CP2K software package[108,109] and applied the PBE+D3 methodology. The time step is fixed at 0.5 fs, while an equilibration period of 5 ps is systematically respected, followed by a production run of at least 25 ps dependent on the type of application.

Two kinds of MD runs have been performed. In the first place, the dynamic behavior of the adsorbate(s) at operating conditions is studied through MD simulations at a temperature of 500 °C and a pressure of 1 atm. Second, MD simulations at 27 °C and 1 atm have been applied on ZSM-5 structures containing extra-framework complexes to generate different geometrical configurations from which average theoretical NMR parameters are determined at experimental conditions. Further details are given in Section 1.4 of the SI.

2.2. Experimental Details. *2.2.1. Catalyst Synthesis and Characterization.* The parent material for the preparation of the alkaline-earth metal modified ZSM-5 samples is based on ZSM-5_80 from Zeolist, with a Si/Al ratio of 40 (CBV8014) and a total pore volume of 0.26 mL g^{-1} (see Table 1). Prior to impregnation, the parent material was dried overnight at 120 °C. For each alkaline-earth metal modification, 3 g of parent ZSM-5 was impregnated with 0.8 mL of 2.4 M aqueous solution of $Mg(NO_3)_2{\cdot}6H_2O$, $Ca(NO_3)_2{\cdot}4H_2O$, and $Sr(NO_3)_2$. The Ba-modified sample was prepared by triple impregnation with a 0.8 M aqueous solution of $Ba(NO_3)_2$ with a drying step at 120 °C for 16 h after each impregnation. The impregnated powder was placed in a desiccator overnight to achieve complete wetting of the micropores with the precursor solution. Next, the modified zeolite was calcined for 5 h at 550 °C with a heating rate of 3 °C min^{-1}. In this way, modified samples with an alkaline-earth metal to aluminum ratio of 2 are obtained.

Structural and textural properties of the various materials used in this work resulting from the experimental characterization techniques are summarized in Table 1. They show some specific features which make them unique with respect to each other. Despite having the same parent ZSM-5, the choice of the metal in the alkaline-earth metal modified materials has a large impact on the properties. The catalyst modified with complexes of Ba, being the largest of the alkaline-earth metals considered in this work, obviously exhibits the smallest pore volume and surface area S_{BET} but also causes a 10-fold decrease in BAS concentration with respect to the parent zeolite. At the same time the concentration of LAS is sufficiently large to generate the smallest ratio C_{BAS}/C_{LAS} of all materials. Its apparently different behavior with respect to the other metal variants makes the Ba-variant extremely interesting to see its impact in the methylation reactions.

For the preparation of the EFAl species we preferred to take ZSM-5_26 as parent material since the effect of dealumination is expected to be more drastic if we start with a zeolite exhibiting a higher acidity (i.e., more BASs) (Si/Al = 13). 2 g of ZSM-5_26 zeolite was loaded onto an alumina crucible and placed in the isothermal zone of a tubular furnace. The furnace was heated at 5 °C/min to 700 °C and kept at 700 °C for 6 h under 200 mL/min flow of H_2O + N_2 mixture (20% H_2O, 80% N_2).

The dealuminated sample prepared from parent ZSM-5_26 with a high number of BASs sees a dramatic fall of these Brønsted sites but maintains its pore volume and surface area.

The impact of the acidic properties on the lifetime of the catalyst and on the MTO reaction under reaction conditions will be discussed in the dedicated sections.

2.2.2. Structural and Acidity Characterization. XRD spectra and N_2 adsorption isotherms have been measured for all samples and taken up in Section 10 of the SI. The XRD spectra confirm that the single-phase crystalline MFI structure is maintained after modification with alkaline-earth metals and dealumination. The adsorption isotherms deliver some textural properties of the various modified ZSM-5 materials compared with the pristine H-ZSM-5 zeolite (Table 1).

Acidity characterization has been accomplished with transmission FT-IR spectroscopy using pyridine as a probe molecule and using a Nicolet 6700 spectrometer equipped with an MCT/B detector. For the wafer preparation, 50 mg of catalyst were used without any dilution. The specimen was activated in vacuum at 400 °C for 16 h to remove adsorbed species. After activation, wafers were saturated with pyridine vapor and further evacuated at 160 °C for 2 h. Spectra were obtained in the 1000−4000 cm^{-1} range at 4 cm^{-1} resolution and after coaddition of 128 scans. The amount of Brønsted and Lewis acid sites was derived from the bands at 1545 and 1456 cm^{-1} as described elsewhere using extinction coefficients of 1.67 and 2.22, respectively.[110] Assuming that one molecule of pyridine is adsorbed on one

DOI: 10.1021/jacs.9b07484
J. Am. Chem. Soc. XXXX, XXX, XXX−XXX

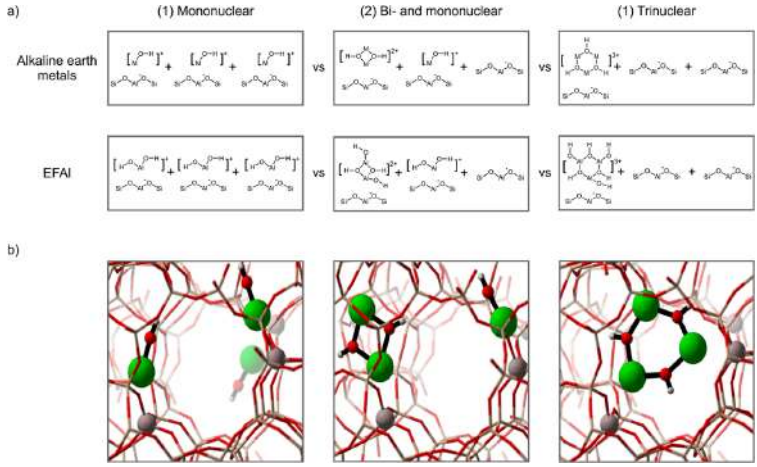

Figure 2. Schematic representation of the structures considered for the relative stability of mono- (left), bi- (center), and trinuclear (right) structures (a) and snapshots of the three considered structures for the Ca case (b).

acid site, the following expressions were used to calculate C_{BAS} and C_{LAS}:

$$C_{\mathrm{BAS}} = 1.88 \cdot IA(B) \cdot R^2/W$$

$$C_{\mathrm{LAS}} = 1.42 \cdot \mathrm{IA}(L) \cdot R^2/W$$

where IA (BAS, LAS) is the integrated absorbance of the BAS or LAS band (cm^{-1}), R is the radius of the catalyst disk (cm), and W is the mass of the catalyst sample (mg).

All magic angle spinning (MAS) solid-state NMR was performed on a 900 MHz Bruker AVANCE IV 21.1 T spectrometer equipped with 4 mm probes (for Ca) and 3.2 mm probes (for Al and H). ^{1}H, ^{27}Al, and ^{43}Ca shifts were referenced to tetramethylsilane, $Al(NO_3)_3$, and saturated $CaCl_2$ solution in D_2O, respectively. Typically recycle delays of 1 s were used in all cases. The standard Bruker quadrupolar Carr−Purcell−Meiboom−Gill (QCPMG) pulse sequence was used without modification in the case of ^{43}Ca NMR. The ^{27}Al 3QMAS spectra were obtained by utilization of a three-pulse, z-filter sequence. The rf strengths of the first two hard pulses and the third soft selective 90 deg pulse were individually optimized, and the optimized pulse lengths were typically 4.2, 1.4 (both at power level = 282 W), and 25 ms (at power level = 0.5W) for the consecutive pulses. Other relevant acquisition parameters were described in figure captions.

2.2.3. Catalytic Testing. Catalytic experiments were carried out in a Microactivity Reference unit (PID Eng&Tech) at 500 °C and ambient pressure. The catalyst (pressed, crushed, and sieved to particle sizes 250−420 μm) was placed in a fixed bed with an internal diameter of 9 mm for standard experiments. An ISCO pump was used to feed methanol to the reactor system. A w8 hly space velocity (WHSV) of 8 $g_{\mathrm{MeOH}}\ g_{\mathrm{cat}}^{-1}\ h^{-1}$, a N_2/MeOH = 1:1 molar feed composition, and atmospheric pressure were utilized. Conversion, selectivities, and yields were calculated on a molar carbon basis. Thus, conversion was defined as the carbon-based fraction of light oxygenates (methanol and dimethyl ether) consumed during the reaction:

$$X = \frac{n_{\mathrm{C,MeOH_{in}}} - n_{\mathrm{C,MeOH_{out}}} - 2 \cdot n_{\mathrm{C,DME_{out}}}}{n_{\mathrm{C,MeOH_{in}}}} \cdot 100\%$$

The selectivity toward hydrocarbon products was calculated based on the carbon number. For example, ethene and propene selectivity was calculated as follows:

$$S_{\mathrm{ethene}} = \frac{2 \cdot n_{\mathrm{C_2H_4}}}{n_{\mathrm{C,MeOH_{in}}} - n_{\mathrm{C,oxy_{out}}}} \cdot 100\%$$

$$S_{\mathrm{propene}} = \frac{3 \cdot n_{\mathrm{C_3H_6}}}{n_{\mathrm{C,MeOH_{in}}} - n_{\mathrm{C,oxy_{out}}}} \cdot 100\%$$

and the yield of a component i was defined from its selectivity and methanol conversion:

$$Y_i = \frac{S_i \cdot X}{100}\%$$

The performance results are presented in graphs as a function of the methanol mass throughput per amount of catalyst used ($g_{\mathrm{MeOH}}\ g_{\mathrm{cat}}^{-1}$), and defined as the overall amount MeOH fed through the catalytic bed before the conversion of oxygenates drops below 80%. Presented selectivities are integral values.

3. RESULTS AND DISCUSSION

3.1. Structural Analysis of the Active Site. Depending on the nature of the metal incorporation, the extra-framework species might be present in the zeolite pores as metal cations or charged metal oxide clusters.[2,111] In earlier work of some of us, these extra-framework LASs were systematically assumed to be composed of binuclear species bridged by O and OH ligands. In this sense both $[Ca(\mu\text{-}O)(\mu\text{-}OH)Ca]^+$ and $[Ca(\mu\text{-}OH)_2Ca]^{2+}$ moieties were proposed as possible modified active sites in Ca-ZSM-5.[24,25] This suggestion was based on findings in literature that, next to alkaline-earth metals, many other metals such as Fe, Ga, Zn, Cu, and Al have the tendency to self-organize into multinuclear clusters within the confined space of a zeolite.[65,111−116]

In this work we aim to achieve a deeper understanding of the structure of active sites after incorporation of alkaline-earth metals Mg, Ca, Sr, or Ba in ZSM-5 in a combined theoretical-experimental effort. Theoretically, DFT calculations were carried out to compare the stability of different types of multinuclear complexes. A similar methodology was followed by Liu et al.[65] in exploring the different nature of extra-framework aluminum in faujasite zeolite. In the present work

DOI: 10.1021/jacs.9b07484
J. Am. Chem. Soc. XXXX, XXX, XXX−XXX

the occurrence of mono-, bi-, and trinuclear alkaline-earth metal complexes and EFAls was also explored experimentally by means of a structural analysis on the samples with Ca modified ZSM-5 materials with ^{43}Ca solid-state solid state NMR. To facilitate the interpretation of the NMR spectra also theoretical calculations were performed to predict the chemical shifts and quadrupole coupling constants of various metal containing species.

3.1.1. Theoretical Study of the Relative Stability of Mono-, Bi-, and Trinuclear Structures. Extra-framework metal clusters within the zeolite could be represented by multinuclear species such as monomeric, dimeric, or trinuclear species with bridging O or OH ligands. It is realistic to assume that apart from binuclear complexes also monomeric and trinuclear species may be formed in the channels of ZSM-5. In each case, the introduction of metal containing species leads to the deprotonation of neighboring BASs, decreasing the BAS density of the material. For binuclear species, it is explicitly shown in Section 2 of the SI that doubly protonated species, i.e. $[M(\mu\text{-}OH)_2M]^{2+}$, are more stable than lower protonated species.

As a first criterion for the possible occurrence of various multinuclear species, the relative stability of monomeric, dimeric, and trimeric LAS species was investigated. To this end, we construct three structures displayed in Figure 2a with respect to full mass balance in order to enable a straightforward energetic comparison.

To keep charge neutrality, we consider three Al substitutions per unit cell. In principle, their positions are arbitrary, but it is commonly assumed that some positions are more favorable than others as discussed in ref 117. In Section 1.2 of the SI a plausible configuration is suggested and visualized in Figure S1a, and with respect to these three Al substitutions, optimized structures of mono-, bi-, and trinuclear species are constructed and visualized in Figure 2b in the case of a Ca-modified ZSM-5 material. The free energies and enthalpies resulting from periodic DFT calculations are summarized in Table 2 and indicate that the formation of mononuclear alkaline-earth metal species is energetically disfavored with respect to binuclear complexes, except for one of the EFAl species which is discussed further. The self-organization of isolated mononuclear cations into binuclear $[M(\mu\text{-}OH)_2M]^{2+}$ is a highly exothermic process. Multinuclear structures are even more stabilized as far as they can be fitted into the pores of the ZSM-5 zeolite. This result follows the general trend that larger clusters better stabilize the system, as they are submitted to a higher number of coordination interactions with the zeolite framework. However, due to confinement the size of the cluster is obviously limited and we therefore discard the possibility that larger clusters than trinuclear alkaline-earth metal complexes will be formed in the ZSM-5 channels, which may play an essential role in the methanol conversion.

Table 2. Free Energies (ΔG) and Enthalpies (ΔH) Relative to the Mononuclear Case for All Structures Indicated in Figure 2 (in kJ/mol) and Calculated at 500 °C

	(1) mononuclear		(2) bi- and mononuclear		(3) Trinuclear	
	ΔH	ΔG	ΔH	ΔG	ΔH	ΔG
EFAl/I	0	0	+55	+114	+5	+101
EFAl/II	0	0	−94	−79	+20	+66
Mg	0	0	−102	−48	−186	−104
Ca	0	0	−153	−120	−237	−194
Sr	0	0	−111	−71	−198	−158
Ba	0	0	−94	−73	−156	−112

The same procedure was applied for the EFAl complexes. However, our study shows that the position of the aluminum substitutions in the framework may have a large effect on the stability of some EFAl species. For the binuclear EFAl species, two configurations were considered, EFAl/I with respect to the same Al substitutions as used for the alkaline-earth metals, whereas EFAl/II is based on a different position of the third Al substitution as visualized in Figure S1b. In the case of EFAl/I, the binuclear complex is less stabilized relative to the monomer (see Table 2), whereas EFAl/II yields binuclear species which are more stable than the monomeric ones, as was found for the alkaline-earth metals. In the remainder of the paper, we will consider both EFAl species to illustrate their noticeable differences in acidic and catalytic properties.

At this point it is interesting to compare our findings with the work of Liu et al.[65] These authors studied the structure and stability of a wide range of mono-, bi-, tri-, and tetranuclear EFAl complexes at different locations in faujasite. They found similar results as ours and also the reaction energies in the self-organization process are of the same order. The formation of a tri- or tetranuclear cluster was found to be strongly dependent on their location in the zeolite. The preferred position of these multinuclear (cationic) EFAls was found to be localized in the smaller inaccessible sodalite cages of faujasite due to the multiple interactions with the framework. Such locations are expected to interact less with active reacting species due to restricted space available. This is also an indication that not the largest multinuclear moieties but the smaller mono- and binuclear cations will probably have the largest impact on the methylation reaction.

The structures displayed in Figure 2 with three monomers in a unit cell were only used for the computation of stabilization energies. In the following we only regard a single extra-framework complex in a unit cell. In the case of a monomer, its structure was optimized with respect to the first Al substitution Al1. Dimeric species are positioned with respect to Al1 and Al2 (Figure S1). Optimized structures of mono-, bi-, and trinuclear species are visualized in Figure 3 in the case of a Ca-modified ZSM-5 material.

3.1.2. Solid-State NMR on Ca-Modified ZSM-5 Zeolites. To further structurally characterize the nature of the metal containing clusters, a solid state NMR characterization has been performed on Ca-modified ZSM-5 zeolites from both an experimental and theoretical point of view. For the NMR simulations, the mono-, bi-, and trinuclear extra-framework Ca species, as discussed in the previous section, are considered. Note that in this case only one mono-, bi-, or trinuclear species have been considered per unit cell, which is charge compensated by one, two, or three aluminum atoms. Periodic DFT calculations of NMR parameters in large zeolite systems, such as ZSM-5, have become feasible lately, as is demonstrated by the works of Dib et al.[118] and Holzinger et al.[119] In the first instance, the NMR parameters of the geometrically optimized structures, visualized in Figure 3, will be discussed. The resulting NMR chemical shifts of the ^{43}Ca isotope are listed in Table 3.

The Ca atom in the mononuclear structure has the lowest chemical shift, which indicates that it is shielded most efficiently. This may seem initially unexpected, as it has only

DOI: 10.1021/jacs.9b07484
J. Am. Chem. Soc. XXXX, XXX, XXX−XXX

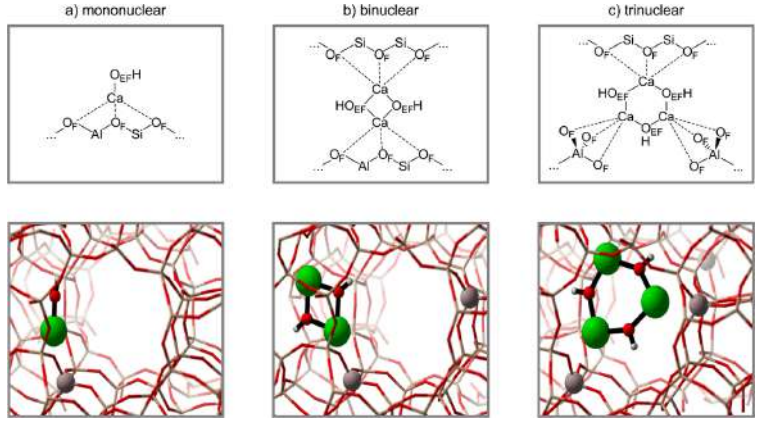

Figure 3. Schematic representation and snapshots of the optimized structures of the isolated extra-framework Ca species in ZSM-5, namely mononuclear (left), binuclear (center), and trinuclear (right).

Table 3. Computed Chemical Shifts of the ^{43}Ca Isotope in Extra-Framework Species and Geometry Optimized Distances between the Ca Atom and the O Atoms in ZSM-5 Containing Extra-Framework Species

	δ_{iso} (ppm)	$CaO_{EF,1}$ (Å)	$CaO_{EF,2}$ (Å)	$CaO_{F,1}$ (Å)	$CaO_{F,2}$ (Å)	$CaO_{F,3}$ (Å)
after geometry optimization						
mononuclear	−0.32	1.99	–	2.40	2.43	2.71
binuclear	5.06	2.17	2.18	2.52	2.59	2.86
	21.05	2.23	2.24	2.42	2.43	2.76
trinuclear	37.34	2.23	2.24	2.39	2.49	3.27
	26.86	2.19	2.21	2.45	2.59	2.88
	23.63	2.26	2.27	2.47	2.50	2.64
MD snapshots (300 K)						
mononuclear (average)	−22.86					
mononuclear (min)	−32.23					
mononuclear (max)	−6.79					
binuclear (average)	6.73					
binuclear (min)	−11.45					
binuclear (max)	23.85					
trinuclear (average)	13.63					
trinuclear (min)	−21.55					
trinuclear (max)	36.22					

one covalent bond, in contrast to multinuclear species. However, a clear correlation between the chemical shifts and the distances between Ca and the neighboring oxygens may be established. Hereby a distinction is made between framework oxygens and extra-framework oxygens, labeled as O_F and O_{EF}, respectively as schematically shown in Figure 3. The distances for each of the structures are given in Table 3. The distances from the Ca-atom of the monomer to the framework and extra-framework oxygens are shorter than in the case of binuclear or trinuclear species. Furthermore, clearly an asymmetry in the CaO_{EF} bond distances is observed for the binuclear structure, which gives a lower chemical shift for one of the two Ca atoms. The trinuclear structure has clearly the highest chemical shift indicating the lowest shielding, which is related to the longer average distance from each Ca atom to the nearest framework oxygens.

Previous analysis shows that the chemical shift is very sensitive to the geometrical configuration and in particular the CaO distances. In this sense, we opted to also calculate NMR properties at finite temperature taking snapshots from MD simulations (see Supporting Information Section 1 for more details), as the NMR experiments were performed at 300 K (vide infra). The results are presented in Table 3.

At 0 K, the monomer exhibits a chemical shift of −0.32 ppm, but taking into account the framework flexibility and mobility of this structure at finite temperature it is observed that the chemical shift becomes more negative with an average of −23 ppm. In the static case, the monomer is only 4-fold coordinated (left panel in Figure 3); however, at finite temperatures the Ca-atom centers itself between multiple framework oxygens, hence increasing the chemical shielding. Note that this structure resembles the ZO−Ca−OH site, as suggested by Zhang et al.[27] More information can be found in the SI (Section 2.2.1 and Figure S14). For the binuclear complex, two Ca-atoms contribute to the NMR spectrum, which yields an average chemical shift of 6.73 ppm. However,

DOI: 10.1021/jacs.9b07484
J. Am. Chem. Soc. XXXX, XXX, XXX−XXX

the ^{43}Ca chemical shifts can cover a broad range of 35 ppm (−11−24 ppm).

The trinuclear moiety is less mobile, the third substituted Al atom lies at the next intersection of the straight and zigzag channel (see Al3 in Figure S 1 of the SI), and its configuration is more or less anchored in the channels. Its structure during the MD simulation at 300 K does not vary too much from its 0 K structure, yielding an average chemical shift around 13 ppm compared to the static value of 30 ppm (Table 3). They are expected to mainly contribute to the positive range of the NMR spectrum.

In order to complement the theoretical investigation, several high-field solid-state NMR spectroscopic experiments on ^{43}Ca-enriched ZSM5 have been performed. ^{43}Ca solid state NMR is intrinsically challenging because ^{43}Ca is a quadrupolar nucleus (spin = 7/2) with relatively low gyromagnetic ratios as well as with a very low natural abundance (only 0.135%). Until now, the scientific community only measured simple Ca-salts (e.g., $CaCO_3$ or hydroxyapatites), which are characteristically homogeneous in nature.[120−122] However, no real efforts have been made to investigate more complex and heterogeneous materials (particularly entrapped/embedded/grafted into a porous material), and thus, our attempt constitute a challenge by itself.

The solid-state Hahn Echo NMR spectrum (Figure 4) of ^{43}Ca-enriched ZSM5 displays a relatively broader response (than usual Ca-salts), the peak with the highest intensity centered around 0.6 ppm, which inevitably advocates for the heterogeneity within the sample. Next, to derive more structural information about the residual Ca-species and enhance the sensitivity, quadrupolar Carr−Purcell−Meiboom−Gill (QCPMG) measurement has been performed (Figure 4). Interestingly, the observed nonsymmetric nature of the QCPMG spectrum reveals the existence of more than one nonidentical Ca-species. If we compare the experimental peak positions with our simulated chemical shift values at 300 K (δ_{iso} values in MD snapshots) as well as after the geometry optimizations, it is safe to conclude that binuclear species definitely exist in the Ca-ZSM5 sample. As no substantial contribution in the positive range of the Ca chemical shift spectrum is observed, it is reasonable to assume that trinuclear species will only be present to a minor extent. In addition, ^{1}H−^{1}H two-dimensional double-quantum (DQ) NMR experiments clearly reveal the existence of a new peak around 3.50 ppm (indicated in red in Figure 5) in addition to the usual 1.4−1.6 ppm peak due to the BAS of zeolite (Figure 5), which could be attributed to the hydroxy group attached to the multinuclear Ca-species.

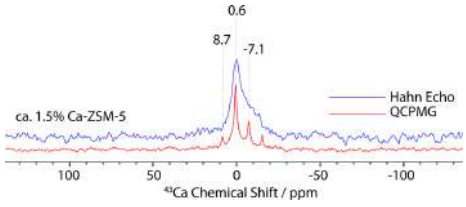

Figure 4. ^{43}Ca magic angle spinning (MAS) solid-state hahnecho (blue) and QCPMG (red) NMR spectra of ca. 1.5% Ca-ZSM-5 [900 MHz, 10 kHz MAS, recycle delays = 1 s, Number of scans = 14k].

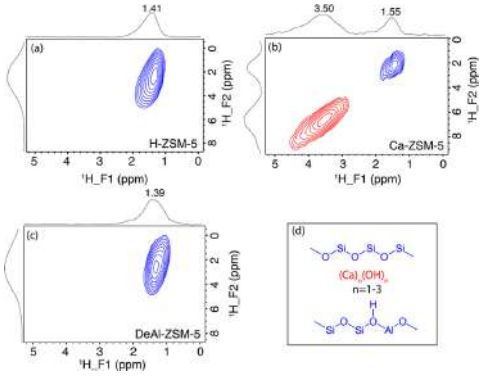

Figure 5. ^{1}H−^{1}H Two-dimensional DQ MAS NMR spectra of zeolite (a) ZSM-5, (b) 6% Ca-ZSM-5, (c) dealuminated ZSM-5, and (d) simplified pictorial representation of responsible proton containing entities.

Previous analysis gives indirect evidence that both mono- and binuclear species may be present in the alkaline-earth metal modified ZSM-5 catalysts. In the remainder of this paper, we have systematically performed the acidity characterization simulations and methylation reactions with both mono- and binuclear species. However, as will become clear (vide infra), mononuclear species impact the catalytic activity to a lesser extent, advocating our earlier assumptions on the nature of extra-framework binuclear species in postsynthetically modified samples.

3.2. Acidity Characterization: BAS/LAS Nature of the Active Site. From the previous analysis, it was shown that metal oxide clusters reduce the number of vicinal BASs, yielding new Lewis acid sites associated with the metal oxide clusters. Furthermore also EFAl species have Lewis acid properties.[24,25,72−74] The nature and strength of acid sites can be characterized experimentally by various techniques.[123−127] Herein we characterized the acidic properties using IR spectroscopy with pyridine as a probe molecule from both an experimental and theoretical point of view. Pyridine adsorption is able to discriminate between Brønsted and Lewis acid sites as distinct peaks in the region from 1700 cm^{-1} until 1400 cm^{-1} appear in the spectra. Pyridine is protonated upon adsorption on a BAS forming a pyridinium ion and only coordinatively bonds toward an LAS.[128,129] This difference leads to a characteristic peak in the IR spectrum around 1545 and 1450 cm^{-1} for a BAS and LAS, respectively.[24,45,128,130−134] Furthermore, the vibrational mode in the region of 1580−1630 cm^{-1} is indicative for the global acidic strength as was shown by Velthoen et al.[129]

To characterize the BASs and LASs theoretically, pyridine adsorption is studied on both mono- and binuclear alkaline-earth metal modified ZSM-5, on EFAls, and on pristine H-ZSM-5 with a specific number of BASs as reference. The resulting optimized structures together with the adsorption enthalpy are depicted in Figure 6 confirming the distinct adsorption on a BAS and LAS. On a BAS, pyridine is immediately protonated, whereas on the metal complexes—both mono- and binuclear—pyridine makes a coordination with the alkaline earth metal or Al in the EFAl species,

DOI: 10.1021/jacs.9b07484
J. Am. Chem. Soc. XXXX, XXX, XXX−XXX

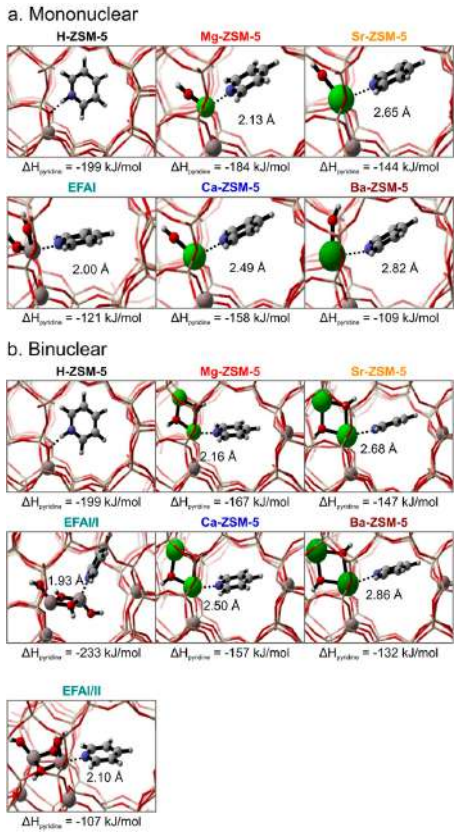

Figure 6. Pyridine adsorption to a mononuclear LAS (a) and a binuclear LAS (b). Also given are the adsorption enthalpies in kJ/mol belonging to the optimized structures at 0 K of pyridine adsorbed in pristine H-ZSM-5, extra-framework aluminum in ZSM-5 and Mg, Ca, Sr or Ba-ZSM-5. To keep the charge in balance frameworks with only one Al substitution are considered in case of monomers, and with two Al substitutions in case of the binuclear species. In the pristine H-ZSM-5 only one single BAS and thus one Al substitution is taken into account. For the snapshots, the following color code is used: white is H, light gray is C, blue is N, red is O, gray is Al, beige is Si, and green is the alkaline earth metal.

confirming the presence of Lewis acid sites. Special attention is given to the two embedded $[HOAl(\mu\text{-}OH)_2AlOH]^{2+}$ structures (EFAl/I and EFAl/II) to illustrate the impact their position in the channels of the zeolite has on acidic and catalytic properties, as shown by the adsorption distance and adsorption enthalpy in Figure 6.

A further characterization of the LAS and BAS is performed by comparing simulated and experimental IR spectra. The experimental spectra of all samples are collected in Figure 7. They are compared with the theoretical spectra obtained after adsorption of pyridine on binuclear modified ZSM-5 materials. There is a very good agreement between theory and experiment.

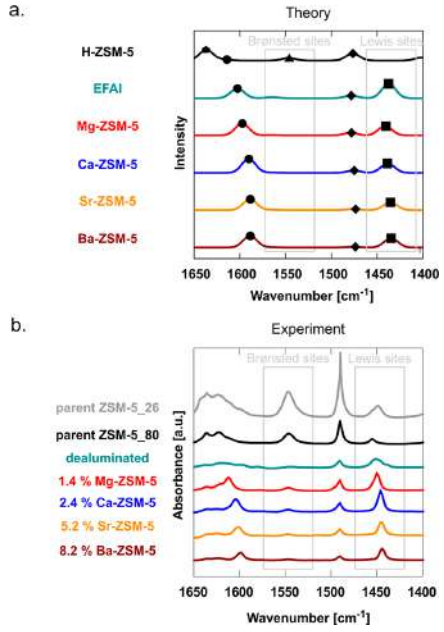

Figure 7. FTIR spectra of various zeolitic materials using pyridine as a probe molecule. (a) Theoretical spectrum of pyridine adsorbed on modified ZSM-5 materials with binuclear species, (b) experimental spectrum.

First, the peak corresponding to the BAS, around 1545 cm^{-1}, can be recognized in both the theoretical (Δ) and experimental spectrum of pristine H-ZSM-5. On the other hand, this peak is also found in the experimental spectrum for modified ZSM-5, albeit with a lower intensity, and it does not appear in the theoretical spectrum. This difference could be because a fraction of isolated BASs is still present in the actual modified catalyst, while this is not considered in the unit cell in the theoretical calculations where the number of Al substitutions is restricted to a minimum to impose charge neutrality. Second, the LAS peak, around 1450 cm^{-1}, is encountered in the theoretical (□) and experimental spectra of dealuminated, Mg-, Ca-, Sr-, and Ba-ZSM-5. This band is also found in the experimental pristine H-ZSM-5 spectrum, but not in the corresponding theoretical spectrum. This peak is experimentally assigned to extra-framework Al species,[24,135] which are again not accounted for in the unit cell used during the theoretical simulations of pristine H-ZSM-5, thus explaining the difference. Furthermore, the assignment of this peak to EFAl species is confirmed by the simulations of an isolated EFAl structure, as its IR spectrum shows this Lewis acid site peak.

Finally, a peak not ascribed to either the BAS or the LAS appears in both the theoretical (◊) and experimental spectra for all considered structures around 1475 cm^{-1}, which can be related to some specific molecular surface vibrations as described in detail in Section 3 of the Supporting Information.

Our theoretical and experimental spectra confirm that Lewis acid sites are introduced in the modified catalyst, which goes

DOI: 10.1021/jacs.9b07484
J. Am. Chem. Soc. XXXX, XXX, XXX−XXX

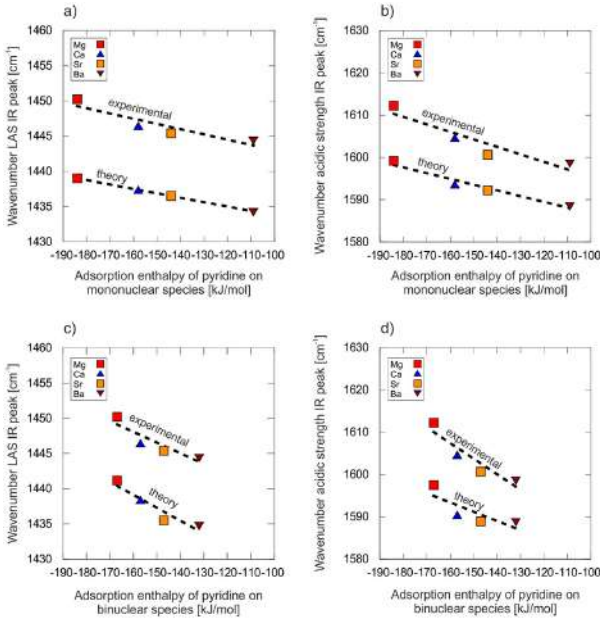

Figure 8. Shifts in the LAS (a and c) and global acidity (b and d) peaks in the IR spectrum with respect to changes in the strength of the incorporated mono- (a and b) or binuclear (c and d) LASs.

hand in hand with the elimination of Brønsted acid sites. The correspondence between theoretical and experimental spectra gives strong evidence that the $[M(\mu\text{-}OH)_2M]^{2+}$ representation of the active site on a molecular level is realistic, although the monomeric $[M(\mu\text{-}OH)]^{+}$ alkaline-earth metal complexes yield a similar behavior.

Depending on the nature of the metal incorporated cationic cluster, subtle shifts are found in the peak at 1450 cm^{-1} assigned to Lewis acidity. Furthermore blue-shifted vibrational modes in the region (1580−1630 cm^{-1}) are also characteristic for the global acidic strength of the complex as shown in the work of Velthoen et al.[129] It is now interesting to investigate whether a correlation can be found between these blue shifts and the strength of the incorporated LASs in the zeolite framework. To this end we calculated the adsorption enthalpy of pyridine on the mono- and binuclear metal oxide clusters. The results are shown in Figure 6 together with the distance between the nitrogen of pyridine and the metal of the cluster. The absolute values may be compared to some other adsorption enthalpies in zeotype materials.[136] As can be expected, the results for the alkaline earth metals show that a more negative adsorption enthalpy leads to a shortened nitrogen−metal distance and thus a stronger Lewis acidity (Mg > Ca > Sr > Ba). More interestingly, for the alkaline earth metals, the adsorption enthalpies can be correlated to the information on the IR peak that is characteristic for the LAS (around 1450 cm^{-1}) and peak characteristic for the global acidic strength (1580−1630 cm^{-1}), as a stronger adsorption enthalpy yields an increased wavenumber and thus blue-shifted peaks. This correlation is close to linear for both peaks as can be seen on the plots depicted in Figure 8. This correlation might serve as a very insightful catalyst design guideline, as it directly yields information on the strength of incorporated LASs in zeolites.

For both mono- and binuclear alkali-earth metals we observe a very good agreement between theory and experiment. Both experimental and theoretical data points clearly show a linear relationship. The slope of the linear regression is even perfectly reproduced. We need only a rescaling of the theoretical estimates for an exact reproduction.

A special note should be made to the binuclear EFAl species, as their acidic properties are very much dependent on the used Al substitutions (EFAl/I vs EFAl/II). More information is given in Section 3.2 of the SI. While the data points of the EFAl/I complexes have a tendency to lie on the linear regression, those belonging to EFAl/II do not show any relationship with the alkaline-earth metals. A further investigation on the nature of all possible EFAl species is beyond the scope of this work, but our results clearly show that the exact nature of EFAl species should be further investigated in future studies.

3.3. Reactivity Properties of the Active Site. From the previous analysis a decreased Lewis acid strength was observed in the following series Mg, Ca, Sr, and Ba. To assess the influence of these intrinsic acidic properties on the catalytic behavior, we studied methylation reactions of propene and benzene and some other methylated aromatic species, which are typically present in the hydrocarbon pool, with methanol. Both reactions are initiating steps in the aromatics and alkene cycle of the MTO process (Figure 1) and are identified as key reaction steps for carbon incorporation.[33−41] Furthermore the influence of LAS incorporation on the formation of the

DOI: 10.1021/jacs.9b07484
J. Am. Chem. Soc. XXXX, XXX, XXX−XXX

protonated, and thus activated,[25,35,137] form of some HP intermediates (depicted in Figure 1) is also investigated. In our earlier work we found evidence that incorporation of LASs selectively destabilizes crucial cyclic carbocationic HP compounds.[25]

We first assess the impact of the presence of binuclear $[M(\mu\text{-}OH)_2M]^{2+}$ moieties in the catalyst on the methylation kinetics. The reactions are studied at three distinct active sites as shown in Figure 9. We distinguish an isolated BAS, a BAS in the vicinity of a LAS, and an isolated LAS, since methylation is also known to occur over Lewis acid sites.[138,139] Furthermore the experimental IR spectra in Figure 7 suggest that both BAS and LAS are encountered in every considered catalyst. On an isolated LAS, methanol is activated by adsorption on the LAS of the $[M(\mu\text{-}OH)_2M]^{2+}$ moiety, rather than being adsorbed on the weak bridging Brønsted acidic OH site of the metal species. But in the case of a combined LAS/BAS catalyst, the reactants can freely adsorb on the two acid sites. Therefore we considered two cases, namely the BAS/$[M(\mu\text{-}OH)_2M]^{2+}$ where the methanol is first adsorbed on the BAS and the $M(\mu\text{-}OH)_2M]^{2+}$/BAS where methanol is first adsorbed on the LAS.

The corresponding free energy diagrams at 500 °C for all cases are shown in Figure 10, and the detailed free energies along the reaction profile are tabulated in Table S13 and Table S14. The corresponding results for the EFAl species are discussed in Section 7 of the SI. Furthermore, the results of the mononuclear $[CaOH]^+$ species are discussed in Section 6 of the SI and further in this section.

The empty zeolite and methanol and the hydrocarbon (propene or benzene) in the gas phase are chosen as the reference state. Methanol adsorbs first on the BAS or isolated LAS, after which the hydrocarbon coadsorbs, which is the standard procedure to construct methylation reaction profiles.[140,141] Overall our adsorption data on H-ZSM-5 agree well with literature data; only the coadsorption of benzene is slightly underestimated, as indicated by the enthalpy data in Section 5 of the Supporting Information.[140−143]

The adsorption of methanol shows two clear trends. First, adsorption of methanol on a BAS is barely influenced by a nearby $[M(\mu\text{-}OH)_2M]^{2+}$ moiety, since the reaction profiles practically coincide in the first step of Figure 10a and Figure 10b. Second, the adsorption enthalpies listed in Table S15 and Table S16 of the Supporting Information show that methanol is slightly weaker adsorbed on an isolated alkaline earth metal cluster than on a BAS. This trend is in perfect agreement with the pyridine adsorption data and the Lewis acidity scale proposed in Figure 8 with the following Lewis acidity order Mg > Ca > Sr > Ba. In any case, the adsorption is assumed to be strong enough in all cases to activate the methanol, to ensure sufficient methanol coverage on the active site and to allow us to model the methylation reaction in the same manner on both active sites. A more detailed discussion on the difference between adsorption on a LAS and BAS can be found in Section 4 of the Supporting Information.[83,143,144]

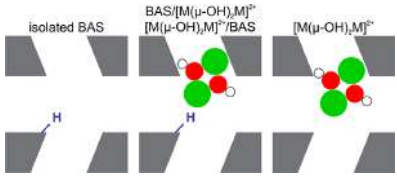

Figure 9. Schematic representation of the three active sites considered for the methylation reactions, namely an isolated BAS, a BAS near a $[M(\mu\text{-}OH)_2M]^{2+}$ moiety, and an isolated $[M(\mu\text{-}OH)_2M]^{2+}$ moiety.

For the coadsorption of benzene or propene, a higher stability for the coadsorbed methanol and benzene/propene is observed for the BAS/$[M(\mu\text{-}OH)_2M]^{2+}$ active sites. This effect can be ascribed to the availability of both a BAS and LAS, enabling the possibility for methanol to adsorb on the BAS, whereas the hydrocarbon is coordinatively bound to the LAS via orientation of the π-electrons toward the metal of the $[M(\mu\text{-}OH)_2M]^{2+}$ moieties. A snapshot is presented in Figure 11. The cooperative role of the LAS and BAS yields in this case an extra stabilization as the reactants can freely adsorb on the two acid sites. In principle we could interchange the adsorption on the BAS and the LAS. To this end, all adsorption and reaction steps of the methylation profile are recalculated but now with methanol first adsorbing on the LAS and the hydrocarbon on the BAS (notation $[M(\mu\text{-}OH)_2M]^{2+}$/BAS). The resulting profile is displayed in Figure 10e and f and compared with the previous results (BAS/$[M(\mu\text{-}OH)_2M]^{2+}$ and isolated $[M(\mu\text{-}OH)_2M]^{2+}$). The interchange of the order of the active sites has a significant influence on the coadsorption and kinetics of the methylation reaction. The state in which both methanol and benzene are coadsorbed shows a significant destabilization in the $[M(\mu\text{-}OH)_2M]^{2+}$/BAS case compared to the BAS/$[M(\mu\text{-}OH)_2M]^{2+}$ case. Furthermore, the overall free energy barriers are at least 100 kJ/mol higher in $[M(\mu\text{-}OH)_2M]^{2+}$/BAS than in BAS/$[M(\mu\text{-}OH)_2M]^{2+}$, implying that methanol will preferentially adsorb on the BAS and the hydrocarbon on the LAS. Those results are in agreement with the stronger adsorption energies of pyridine on a pristine BAS site compared to the various LAS sites (Figure 6). We also observe that the results on the transition state region of $[M(\mu\text{-}OH)_2M]^{2+}$/BAS are quite similar to the isolated LAS moiety.

A double adsorption site is not available for the isolated BAS and isolated $[M(\mu\text{-}OH)_2M]^{2+}$ systems, where benzene or propene are coadsorbed in the zeolites without any specific interactions with an active site, as indicated in the snapshots shown in Figure 11.

The presence of $[M(\mu\text{-}OH)_2M]^{2+}$ moieties also significantly affects the intrinsic free energy barriers for methylation of benzene, as can be seen in Table S13 in the Supporting Information. The resulting free energy barriers may be compared with available data in literature and are of the same order of magnitude.[25,84,85,140,141,145] For LASs there is only limited literature data available from the work of Vos et al.[146] on electrophilic aromatic substitution, which were obtained at a rather low level of theory.

Our data summarized in Table S12 show that in all cases the intrinsic free energy barrier for methylation reactions taking place on a BAS near an LAS or on an LAS are substantially higher than on a pristine BAS site. When considering the alkaline earth metals, the observed increase is higher for methylations of benzene compared to those of propene. For the methylations, a $[M(\mu\text{-}OH)_2M]^{2+}$ moiety in the neighborhood of the BAS leads to an increase of the intrinsic free energy barrier of 42 to 107 kJ/mol for benzene and an increase of 14 to 40 kJ/mol for propene, depending on the considered metal oxide cluster. On the other hand, the methylation over

DOI: 10.1021/jacs.9b07484
J. Am. Chem. Soc. XXXX, XXX, XXX−XXX

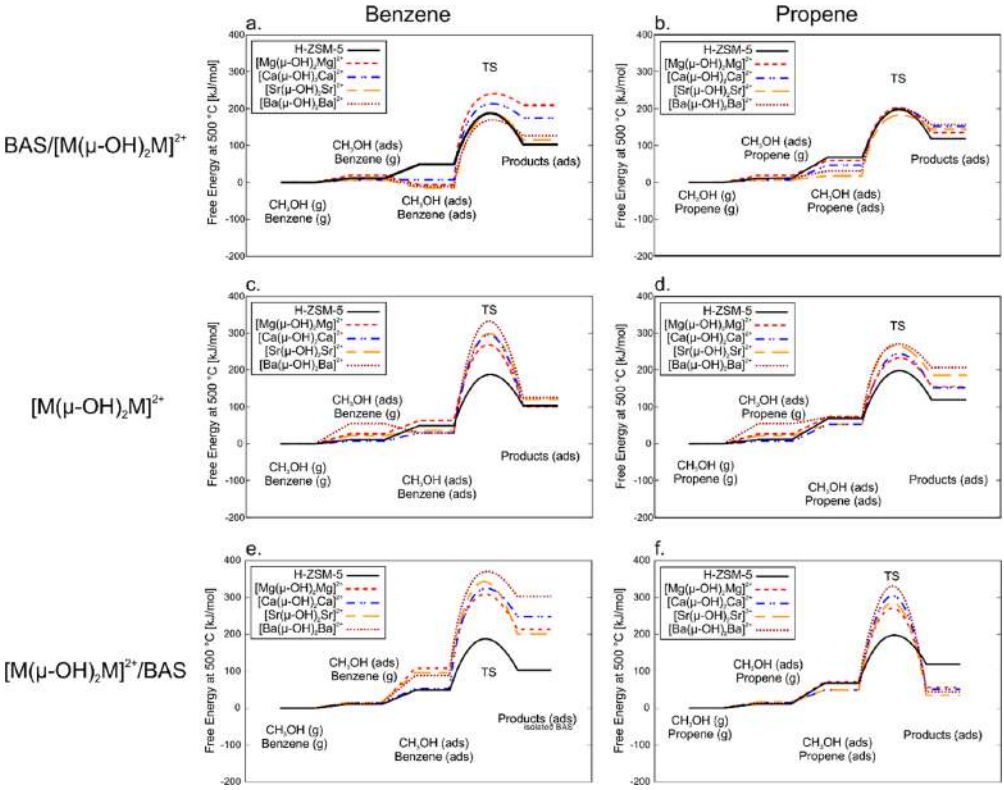

Figure 10. Free energy profiles at 500 °C for the methylation of benzene and propene over several active sites, namely an isolated BAS (full black line), a BAS near an $[M(\mu\text{-}OH)_2M]^{2+}$ where the methanol is adsorbed on the BAS (a and b), an isolated $[M(\mu\text{-}OH)_2M]^{2}$ (c and d) and a $[M(\mu\text{-}OH)_2M]^{2+}$ moiety near a BAS, indicated by $[M(\mu\text{-}OH)_2M]^{2+}$/BAS, where the methanol is adsorbed on the LAS (e and f). M is one of the considered alkaline earth metals (Mg, Ca, Sr, or Ba).

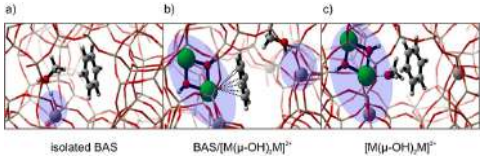

Figure 11. Snapshots of the prereactive complex for the methylation of benzene in Ca-ZSM-5 as representative for the other considered metal substituted clusters (M= AlOH, Mg, Ca, Sr, and Ba), showing the two available adsorption sites (indicated in blue) in the BAS/$[M(\mu OH)_2M]^{2+}$ case (b) in contrast to the isolated BAS (a) and isolated LAS (c).

an isolated $[M(\mu\text{-}OH)_2M]^{2+}$ moiety leads to an increase of the intrinsic free energy barrier of 70 to 165 kJ/mol and 29 to 85 kJ/mol compared to an isolated BAS for benzene and propene, respectively. The behavior of the isolated EFAl species deviates from those of the alkaline-earth metal species. We therefore opt to separate their results from the other metals and to discuss their reaction kinetics in a separate energy profile (Figure S30 in Section 7 of the SI).

The overall increase of the reaction barrier noticed in the alkaline-earth metal complexes can be linked to a deformation of the transition states over a BAS near an LAS or an isolated LAS. In the snapshots depicted in Figure 12 for benzene methylation over an isolated BAS and an isolated $[Ca(\mu\text{-}OH)_2Ca]^{2+}$, a deviation of the planarity of the transferred

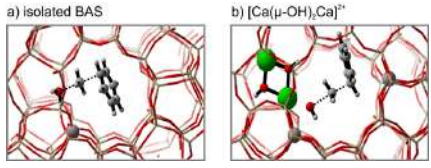

Figure 12. Snapshots of the transition state of the methylation of benzene over an isolated BAS (a) and an isolated $[Ca(\mu\text{-}OH)_2Ca]^{2+}$ cluster showing the planarity deviation of the methyl group near the LAS. More snapshots can be found in Figure S26 of the SI.

DOI: 10.1021/jacs.9b07484
J. Am. Chem. Soc. XXXX, XXX, XXX−XXX

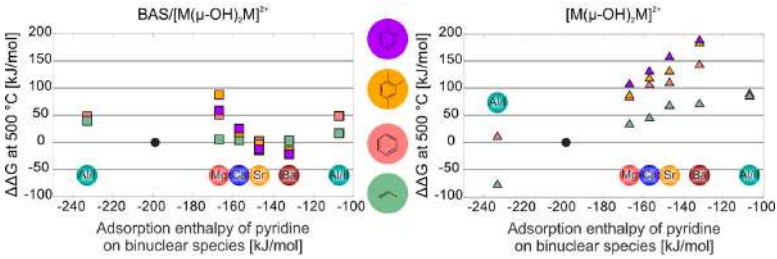

Figure 13. Change in the overall free energy barrier at 500 °C of the methylation of benzene (red), propene (green), pseudocumene (orange), and durene (purple) over an BAS near a $[M(\mu\text{-}OH)_2M]^{2+}$ moiety (left and □) and an isolated $[M(\mu\text{-}OH)_2M]^{2+}$ moiety (right and Δ) relative to the methylation rate over an isolated BAS (black circle) is plotted in function of the pyridine adsorption enthalpy. For the dealuminated species both EFAl/I and EFAl/II variants are considered.

methyl group can be distinguished compared to the transition state over an isolated BAS. Snapshots for other methylation reactions can be found in Figure S26 in the SI. The deformation is quantified by calculating the dihedral angle of the methyl group for the different transition states which is tabulated in Table S11 of the Supporting Information. The values confirm the deviation for all alkaline earth metals and show that it is more significant for benzene than for propene. Furthermore the observed effects can be corroborated with the statement of Iglesia and co-workers that transition states with more localized charges are less influenced by the Brønsted acid strength than those exhibiting more diffuse charges.[147] Since the positive charge is more diffuse on benzene due to its conjugated π-system, the increase of the intrinsic barrier is more significant than for propene. The combined effects explain the more significant effect of LAS incorporation on the intrinsic free energy barrier of benzene methylation compared to propene methylation. Additionally, free energy profiles shown in Figure 10 indicate a destabilization of the product state, for all metal oxide incorporated zeolites. The destabilization can be ascribed to the formation of a carbocation, which is unfavorable near the positively charged alkaline-earth metal cluster as depicted in the reaction schemes in Figure S25 of the SI.

As stated earlier, also mononuclear species can act as a possible LAS after alkaline-earth metal impregnation. In order to be able to compare with their binuclear analogs we investigated the kinetics of the methylation of benzene and propene over the mononuclear $[CaOH]^+$ species. Free energy profiles are shown in Figure S29 of the SI. The isolated LAS predicts a significantly higher barrier for both the benzene and propene methylation, suggesting a significantly lower reactivity of these species. Second, the BAS near LAS results for both benzene and propene indicate that the indirect effect of the LAS is less pronounced for the mononuclear case, as the global barrier is closer to the isolated BAS case. We conclude that the influence of mononuclear species on the methylation reactions is less significant than the impact of binuclear species. These conclusions allow us to mainly focus on the binuclear results in this manuscript.

The methylation profiles thus suggest a significant influence of the presence of binuclear Lewis acid sites on the reactivity. To quantify the relative rate of methylation in the neighborhood of a Lewis acid site to the methylation over an isolated BAS, the difference in overall free energy at 500 °C between the modified active site and an isolated BAS ($\Delta\Delta G$) is studied. We opt to use the overall free energy barrier rather than the apparent free energy barrier. This would assume that methanol coverage is one, as typically done in kinetic studies on methylation reactions,[40,41,141] which is not necessarily true at the high temperatures applied in this work (500 °C) as suggested by the positive free energies of adsorption for methanol on the various active sites (*vide supra*). Correlation plots between the differences in overall free energies and the Lewis acidity characterized by the adsorption enthalpy of pyridine are shown in Figure 13. Furthermore, to enable us to further generalize the conclusions, we also included the results belonging to durene and pseudocumene as an HP reactant representing the aromatic cycle over the alkaline earth metals. Lastly, to finalize all conclusions, the results for the methylation of propene and benzene over the two considered binuclear EFAl species are also included in Figure 13.

The following trends can be deduced from the correlation plots. The methylation of all hydrocarbons is found to be more activated over an isolated alkaline earth metal $[M(\mu\text{-}OH)_2M]^{2+}$ moiety, leading to relatively high reaction barriers over isolated cationic alkaline-earth metal clusters. An almost linear relation is found between the acidity strength of the LAS and the overall free energy barrier. The EFAl/I species have a much stronger Lewis acidity and may even accelerate the methylation reactions, as is the case for propene. A decrease of 76 kJ/mol is observed for the EFAl/I species compared to methylation on a pristine BAS. As discussed in Section 7 of the SI, this can mainly be attributed to the poor stabilization of the EFAl/I species by the framework. Most interesting for catalytic purposes is the distinct difference the LAS has on the methylation of benzene compared to propene, except for EFAl/II. LASs clearly slow down methylation reactions of benzene, which is manifestly confirmed by the methylation of the two other HP species: durene and pseudocumene over alkaline earth metals. Translated to the various catalytic cycles operative in the methanol to olefin process; this means that the aromatic cycle would be suppressed in the LAS incorporated zeolites.

Secondly, it is interesting to study the effect on methylation free energy barriers taking place on a BAS but with proximity of a LAS. The effects on the methylation reactions are much less pronounced for a BAS nearby an LAS. Methylation barriers over a BAS near an $[M(\mu\text{-}OH)_2M]^{2+}$ moiety (□) converge to the rate over an isolated BAS with decreased Lewis acid strength of the alkaline earth metaloxide, as the difference in free energy barrier with an isolated BAS becomes smaller

DOI: 10.1021/jacs.9b07484
J. Am. Chem. Soc. XXXX, XXX, XXX−XXX

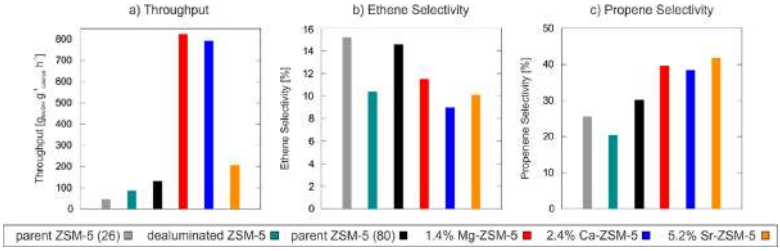

Figure 14. Experimental results obtained at 500 °C for the throughput (a), selectivity to ethene (b), and selectivity to propene (c) for the MTO reaction over dealuminated ZSM-5 (green), 1.4% Mg-ZSM-5 (red), 2.4% Ca-ZSM-5 (blue), and 5.2% Sr-ZSM-5 (orange) relative to the parent ZSM-5 as a function of the adsorption enthalpy of pyridine.[25] Results for 8.2% Ba-ZSM-5 are not reported, as this sample showed a conversion below 5%.

than 10−20 kJ/mol, which is the typical accuracy of our DFT simulations.[3,85] Therefore, these differences are assumed to be insignificant. The EFAl species do not follow this trend. Only for BAS/EFAl/I, BAS/EFAl/II, BAS/$[Mg(\mu\text{-}OH)_2Mg]^{2+}$, and BAS/$[Ca(\mu\text{-}OH)_2Ca]^{2+}$ a significant increase in the free energy methylation barriers is observed. Furthermore, the increase is more pronounced for methylation of benzene compared to propene in the case of EFAl/II, Ca, and Mg incorporated LASs. While benzene and propene methylation rates only exhibit minor differences on an isolated BAS in H-ZSM-5 (overall free energy barriers of 187 and 197 kJ/mol), the results depicted in Figure 13 suggest that LASs induce an increase in the difference between benzene and propene methylation kinetics over the neighboring BAS. Based on the calculated difference in overall barrier, Mg and Ca most selectively decrease benzene methylation rates over a BAS near a $[M(\mu\text{-}OH)_2M]^{2+}$ moiety, while propene methylation is barely affected on this active site. Methylation of the two other HP species even reinforces these differences. The introduction of Sr and Ba seems to have a limited influence on the neighboring BAS, probably due to their weaker Lewis acidity. Relative free energy differences $\Delta\Delta G$ with respect to the isolated BAS even become negative for durene and pseudocumene. When EFAl species are present, methylation on nearby BASs are substantially more activated, but based on the methylation kinetics on the EFAl/I species itself, it can be concluded that in this case the reactions will preferably occur on the EFAl/I species and also in this case methylations of aromatic species are disfavored.

Previous results suggest that incorporation of LAS sites selectively slow down benzene, durene and pseudocumene methylations, both on isolated LASs as on BASs with proximate LASs. The effect is more pronounced for LASs with stronger acidity. In the latter case the reaction might preferably take place on a pristine LAS rather than on a BAS. Previous findings suggest that incorporation of LAS sites might selectively suppress the aromatic cycle; however, when the Lewis acidity becomes too strong, the BASs might not be the most active sites and reactions might take place on LASs.

As the formation of a carbocation could explain the increased methylation barriers and thus suppression of the aromatic cycle, the stability of some carbocation typical for the aromatic and alkene cycle (see Figure 1b) is assessed using their protonation enthalpy.[25] Figure 1b shows that the aromatic cycle is characterized by cationic six and five ring species, while the alkenes make up the cocatalysts in the alkene cycle. The selection of the aromatic MTO intermediates considered in this paragraph is inspired by the work of Fang and co-workers[148] in which the most stable carbenium ions in H-ZSM-5 are theoretically predicted extended with other intermediates of both the paring and side-chain mechanism.[149] To represent the alkene cycle, propene, hexene, and isobutene are selected. For these intermediates, the protonation enthalpy is calculated as defined in our earlier work[25] and the Computational details. This protonation enthalpy is used as a measure for the stability of the protonated form of the intermediates relative to the neutral species. The more negative this enthalpic value becomes, the more stable the protonated structure becomes. The protonation enthalpy is calculated for each intermediate for both an isolated BAS and on a BAS near a $[M(\mu\text{-}OH)_2M]^{2+}$ moiety of the considered cationic clusters. As the resulting protonation enthalpies are in line with the results discussed in earlier work,[25] the interested reader is referred to Section 8 of the Supporting Information for the in-depth discussion. The results show a destabilization of the cyclic carbenium ions, while the influence on the alkenes is far less pronounced, suggesting a suppression of the aromatic cycle.[25] Dealuminated zeolites that follow the trends attributed to Lewis acid strength indicate an improved performance.[72,73]

3.4. Relation between Experimental and Theoretical Findings. Our theoretical results predict incorporation of Mg or Ca as the most efficient candidates to suppress the aromatic HP mechanism. Furthermore, our theoretical structural analysis showed that all $[M(\mu\text{-}OH)_2M]^{2+}$ with M = Mg, Ca, Sr, Ba, or HOAl are formed at the expense of reducing the number of vicinal BASs. To correlate these findings with experimental observations, catalytic tests were performed on a series of modified ZSM-5 catalysts. The results for the activity and selectivity experiments as performed in earlier work of the current authors[25] over the parent and the alkaline-earth metal modified ZSM-5 are depicted in Figure 14. New catalytic tests have been performed on the dealuminated sample extracted from the parent ZSM-5_26. The results for 8.2% Ba-ZSM-5 are not added to the graphs, as conversion over this catalyst was below 5%, which might be due to blockage of the catalyst pores by the large barium oxide clusters or due to the low Lewis acid strength of this oxide leading to increased reaction barriers (see Figure 13). Furthermore, for the different materials under study, Figure S37 in the SI visualizes the various conversion and yield plots.

The experimental results show two clear trends upon incorporation of LASs. First, Figure 14a shows an increased

DOI: 10.1021/jacs.9b07484
J. Am. Chem. Soc. XXXX, XXX, XXX−XXX

catalyst lifetime upon modification, though the influence seems to depend on the strength of the incorporated Lewis acid sites. These results thus confirm the importance of Lewis acidic characteristics for increased catalyst lifetimes. Second, LAS incorporation leads to an increased selectivity toward propene and decreased selectivity toward ethene. The dealuminated species does not have an increased propene selectivity, but instead an increase in the C_4 selectivity is found. Nevertheless, it should be noted that both propene and higher alkenes production are linked to the alkene cycle. This is not surprising since the increased selectivity toward C_3 and C_4 alkenes is supposed to be ascribed to isolation of BASs by incorporation of LASs. Indeed the incorporation of alkali-earth metal or EFAl species gives rise to a reduction of the number of vicinal BASs, as was discussed in the structural analysis of the metal oxide clusters in Section 2 of the SI.[25] The lowered BAS density was ascribed to prevent the successive reactions leading to aromatization and coking.[25]

Based on the conversion and yield plots given in Figure S37 of the SI, the role of the LAS additive on the catalyst activity, stability, and selectivity for making propene versus ethene can now easily be derived. The lifetime of the catalyst is drastically increased when the material is doped with Ca and Mg. The selectivity for propene has increased in the alkaline earth metal modified catalysts compared with their parent ZSM-5_80 zeolite. The selectivity for propene remains constant during the whole active lifecycle (~100 h) of the modified Ca-catalyst and differs substantially from the parent ZSM-5_80 zeolite which only at the end shows a propene yield of 35%. The other alkaline-earth metals (Mg and Sr) show a similar behavior to that of their parent material but shifted to higher values of the yields of ethene, propene and butene. Based on these data a clear volcano plot dependency of the catalyst lifetime versus ratio between BAS and LAS is observed (see Figure S36).

The results presented in this work give evidence that LASs suppress the reactivity of methylations of HP species, as demonstrated for benzene, durene, and pseudocumene. Furthermore, intermediates of the aromatic cycle seem to be less stabilized in the LAS modified zeolites. This follows from the protonation enthalpies shown in Figure S31 in the Supporting Information. A significant destabilization of carbocationic, cyclic HP species due to the interaction with any of the neighboring Lewis acid sites is observed, whereas alkene intermediates are less severely affected. Both the increase in methylation barriers of the HP species and decreased stabilization of cyclic carbocations of the aromatic cycle in the LAS modified zeolites give evidence that the aromatic cycle is suppressed with the presence of LASs. Svelle et al.[32] showed that ethene formation is mechanistically separated from the propene formation. The aromatic cycle is believed to be responsible for ethene formation whereas the alkene cycle yields propene (Figure 1b). Our theoretical data are thus in line with the experimental findings on increased propene selectivity.

The LAS modified zeolites also show an increased lifetime with respect to their parent material. To date the mechanisms leading to aromatic growth and coke formation are not fully unraveled yet. Various coke mechanisms might be active during methanol conversion.[150] Our findings here suggest that cyclic carbocations of the aromatic cycle are less stable. The stabilization of the protonated cyclic intermediates will also decrease their reactivity in further coke formation routes.[25,35,137] Also methylated aromatics are considered as coke precursors,[151,152] which are less easily formed on LAS modified zeolites due to the increase in methylation barriers of the aromatics. However, to obtain more mechanistic insight into the increased lifetime a comprehensive study including all possible coke aromatics formation routes would have to be conducted, which is beyond the scope of this work.

4. CONCLUSION

Understanding the influence of catalyst modification on product selectivity and catalyst lifetime in the methanol-to-olefins process is of utmost importance in the optimization of the process toward a flexible propene-on-demand production. Therefore, we investigated the effect of metal containing cations in the zeolites on the nature of the active site, adsorption, and reactivity properties. Both alkaline-earth metal containing oxides as EFAl species were considered. The latter are obtained after dealumination.

The structural analysis of the cationic metal oxide clusters in the zeolite pores showed that introduction of metal oxides enables a reduction of original BASs, since protonation of the bridging free oxygen led to a significant stabilization for all metal oxide species. These extra-framework moieties may be present as mono-, bi-, and/or trinuclear metal complexes. From a theoretical point of view, we find that binuclear $[M(\mu\text{-}OH)_2M]^{2+}$ species are more stable than mononuclear species. A structural characterization comprising solid state NMR gave indirect evidence for the presence of both monomeric and binuclear species. The acidity characterization of the zeolite modified structures was systematically performed for both mono- and binuclear species and led to consistent results for both types of metal clusters. The newly proposed active sites were shown to possess well-defined Lewis acid sites. This was shown via experimental and theoretical IR spectra for the adsorption of pyridine. An excellent agreement was obtained between theoretical and experimental IR spectra, which gives evidence that our model of the modified active site captures the most important properties and can confidently be used for further kinetic studies. Furthermore, a blue shift in the IR peak characteristic for the LAS was found to correlate linearly with the adsorption enthalpy of pyridine and thus with the Lewis acid strength of the modified active site. This agreement allows the position of the LAS IR peak to be related to the strength of the Lewis acid site, thus creating an experimental tool to check the Lewis acid strength. For the alkaline-earth metal modifications studied, the following acidity scale was found: Mg > Ca > Sr > Ba.

Subsequently, the combined experimental and theoretical analysis of the reactivity properties of modified active sites confirmed the importance of Brønsted acid site isolation and the suppression of the aromatic cycle by the LAS. Experimentally a higher propene selectivity was observed which was most pronounced for the alkaline-earth metal modified zeolites. Furthermore, all LAS modified zeolites show an increased catalyst lifetime with respect to their parent material confirming the conclusions made in earlier work.[25] All our findings point toward a suppression of the aromatic cycle, as methylation barriers of aromatic HP species are substantially higher on LAS modified zeolites and typical cyclic carbocations are less well stabilized in the presence of additional LASs. The influence on the alkene cycle was rather limited. An optimal combination of catalyst lifetime and propene selectivity was found for the Mg and Ca modified zeolites. This could be assigned to a subtle interplay between the influence of the LAS

DOI: 10.1021/jacs.9b07484
J. Am. Chem. Soc. XXXX, XXX, XXX−XXX

on the neighboring BAS and the strength of the LAS itself, as for Sr and Ba the weaker LAS is not strong enough to influence the BAS, while for the EFAl species, the strong acidity might make the LAS too reactive on its own. However, the behavior of EFAl species might be strongly dependent on the aluminum positions in the framework. Further investigations are necessary to elucidate the behavior of EFAl species on the catalysis. Our theoretical results show that the impact of mononuclear species is less pronounced on the governing catalytic reactions of the methanol conversion.

Our findings further support the supramolecular concept of the MTO catalyst, which may be tailored at the molecular level. The overall catalyst performance cannot simply be explained using the properties of the BAS but is rather the result of an interplay of the intrinsic zeolite properties, organic compounds, and its proximity to additional LASs. Two opposing effects should be considered when modifying zeolite catalysts with Lewis acid sites. Increased acidic strength of the LAS yields a more pronounced effect on the reactivity of the neighboring BAS, but the LAS itself may become active for catalysis too.

Such modifications together with all other options for tunability such as variability of hydrocarbons, the zeolite channel's dimensions, composition, and acidity support the idea of supramolecular design of the catalyst. It must be emphasized that previous options for modifications may not be regarded independently from each other but introduce an entangled effect on the overall catalyst performance. Design of such a catalyst toward the desired properties may seem extremely challenging; however, more advanced spectroscopic and analysis tools have become available to characterize to a deeper extent the properties of the catalyst. Specifically, for this study pyridine adsorption offered an experimental tool to sample the Lewis acidic strength. The principles of supramolecular catalyst design suggested here may be an inspiration for tuning zeolite catalysts within other application processes.

■ ASSOCIATED CONTENT

Supporting Information

The Supporting Information is available free of charge on the ACS Publications website at DOI: 10.1021/jacs.9b07484.

Additional computational details on the used ZSM-5 unit cell, Partial Hessian Vibrational Analysis (PHVA), NMR calculations, detailed structural analysis of the Lewis acid sites, additional theoretical vibrational analysis, analysis of the theoretical IR spectrum of adsorbed pyridine, adsorption analysis of methylation reactants on the Lewis acid site, free energy data for the methylation of benzene and propene, results of the calculations of the protonation energy, Cartesian coordinates of the optimized structures obtained from VASP (PDF)

■ AUTHOR INFORMATION

Corresponding Authors

*veronique.vanspeybroeck@ugent.be

*jorge.gascon@kaust.edu.sa

ORCID

Alexander E. J. Hoffman: 0000-0002-1529-4705

Abhishek Dutta Chowdhury: 0000-0002-4121-7375

Jorge Gascon: 0000-0001-7558-7123

Veronique Van Speybroeck: 0000-0003-2206-178X

Notes

The authors declare no competing financial interest.

■ ACKNOWLEDGMENTS

We acknowledge the Research Foundation - Flanders (FWO), the Research Board of Ghent University (BOF), and funding from the European Union's Horizon 2020 research and innovation program (consolidator ERC Grant Agreement No. 647755 – DYNPOR (2015–2020)). The computational resources and services used were provided by Ghent University (Stevin Supercomputer Infrastructure) and the VSC (Flemish Supercomputer Center), funded by the Research Foundation - Flanders (FWO).

■ REFERENCES

(1) *Zeolites for Cleaner Technologies*; Guisnet, M., Gilson, J.-P., Eds.; Catalytic science series; Imperial College Press: London, 2002.

(2) Van Speybroeck, V.; Hemelsoet, K.; Joos, L.; Waroquier, M.; Bell, R. G.; Catlow, C. R. A. Advances in Theory and Their Application within the Field of Zeolite Chemistry. *Chem. Soc. Rev.* **2015**, *44* (20), 7044–7111.

(3) Van Speybroeck, V.; De Wispelaere, K.; Van der Mynsbrugge, J.; Vandichel, M.; Hemelsoet, K.; Waroquier, M. First Principle Chemical Kinetics in Zeolites: The Methanol-to-Olefin Process as a Case Study. *Chem. Soc. Rev.* **2014**, *43* (21), 7326–7357.

(4) Čejka, J.; Centi, G.; Perez-Pariente, J.; Roth, W. J. Zeolite-Based Materials for Novel Catalytic Applications: Opportunities, Perspectives and Open Problems. *Catal. Today* **2012**, *179* (1), 2–15.

(5) Chal, R.; Gérardin, C.; Bulut, M.; van Donk, S. Overview and Industrial Assessment of Synthesis Strategies towards Zeolites with Mesopores. *ChemCatChem* **2011**, *3* (1), 67–81.

(6) Jacobs, P. A.; Dusselier, M.; Sels, B. F. Will Zeolite-Based Catalysis Be as Relevant in Future Biorefineries as in Crude Oil Refineries? *Angew. Chem., Int. Ed.* **2014**, *53* (33), 8621–8626.

(7) Roth, W. J.; Nachtigall, P.; Morris, R. E.; Čejka, J. Two-Dimensional Zeolites: Current Status and Perspectives. *Chem. Rev.* **2014**, *114* (9), 4807–4837.

(8) Hemelsoet, K.; Van der Mynsbrugge, J.; De Wispelaere, K.; Waroquier, M.; Van Speybroeck, V. Unraveling the Reaction Mechanisms Governing Methanol-to-Olefins Catalysis by Theory and Experiment. *ChemPhysChem* **2013**, *14* (8), 1526–1545.

(9) Park, Y.-K.; Lee, C. W.; Kang, N. Y.; Choi, W. C.; Choi, S.; Oh, S. H.; Park, D. S. Catalytic Cracking of Lower-Valued Hydrocarbons for Producing Light Olefins. *Catal. Surv. Asia* **2010**, *14* (2), 75–84.

(10) Olsbye, U.; Svelle, S.; Bjørgen, M.; Beato, P.; Janssens, T. V. W.; Joensen, F.; Bordiga, S.; Lillerud, K. P. Conversion of Methanol to Hydrocarbons: How Zeolite Cavity and Pore Size Controls Product Selectivity. *Angew. Chem., Int. Ed.* **2012**, *51* (24), 5810–5831.

(11) Yarulina, I.; Chowdhury, A. D.; Meirer, F.; Weckhuysen, B. M.; Gascon, J. Recent Trends and Fundamental Insights in the Methanol-to-Hydrocarbons Process. *Nat. Catal.* **2018**, *1* (6), 398–411.

(12) Dahl, I. M.; Kolboe, S. On the Reaction Mechanism for Hydrocarbon Formation from Methanol over SAPO-34: I. Isotopic Labeling Studies of the Co-Reaction of Ethene and Methanol. *J. Catal.* **1994**, *149* (2), 458–464.

(13) Dahl, I. M.; Kolboe, S. On the Reaction Mechanism for Hydrocarbon Formation from Methanol over SAPO-34:2. Isotopic Labeling Studies of the Co-Reaction of Propene and Methanol. *J. Catal.* **1996**, *161* (1), 304–309.

(14) Dahl, I.; Kolboe, S. On the Reaction-Mechanism for Propene Formation in the MTO Reaction Over SAPO-34. *Catal. Lett.* **1993**, *20* (3–4), 329–336.

(15) Haw, J. F.; Marcus, D. M. Well-Defined (Supra)Molecular Structures in Zeolite Methanol-to-Olefin Catalysis. *Top. Catal.* **2005**, *34* (1–4), 41–48.

(16) Abubakar, S. M.; Marcus, D. M.; Lee, J. C.; Ehresmann, J. O.; Chen, C.-Y.; Kletnieks, P. W.; Guenther, D. R.; Hayman, M. J.;

Pavlova, M.; Nicholas, J. B.; Haw, J. F. Structural and Mechanistic Investigation of a Phosphate-Modified HZSM-5 Catalyst for Methanol Conversion. *Langmuir* **2006**, *22* (10), 4846−4852.
(17) Derewinski, M.; Sarv, P.; Sun, X.; Müller, S.; van Veen, A. C.; Lercher, J. A. Reversibility of the Modification of HZSM-5 with Phosphate Anions. *J. Phys. Chem. C* **2014**, *118* (12), 6122−6131.
(18) van der Bij, H. E.; Weckhuysen, B. M. Phosphorus Promotion and Poisoning in Zeolite-Based Materials: Synthesis, Characterisation and Catalysis. *Chem. Soc. Rev.* **2015**, *44* (20), 7406−7428.
(19) Klyueva, N. V.; Tien, N. D.; Ione, K. G. Hydrocarbon Synthesis from Methanol on Erionite and Mordenite Catalysts Synthesized in the Presence of B3+, Ga3+ or Fe3+. *React. Kinet. Catal. Lett.* **1985**, *29* (2), 427−432.
(20) Esquivel, D.; Cruz-Cabeza, A. J.; Jiménez-Sanchidrián, C.; Romero-Salguero, F. J. Transition Metal Exchanged *β* Zeolites: Characterization of the Metal State and Catalytic Application in the Methanol Conversion to Hydrocarbons. *Microporous Mesoporous Mater.* **2013**, *179* (Supplement C), 30−39.
(21) Dusselier, M.; Deimund, M. A.; Schmidt, J. E.; Davis, M. E. Methanol-to-Olefins Catalysis with Hydrothermally Treated Zeolite SSZ-39. *ACS Catal.* **2015**, *5* (10), 6078−6085.
(22) Van der Borght, K.; Galvita, V. V.; Marin, G. B. Ethanol to Higher Hydrocarbons over Ni, Ga, Fe-Modified ZSM-5: Effect of Metal Content. *Appl. Catal., A* **2015**, *492* (Supplement C), 117−126.
(23) Deimund, M. A.; Harrison, L.; Lunn, J. D.; Liu, Y.; Malek, A.; Shayib, R.; Davis, M. E. Effect of Heteroatom Concentration in SSZ-13 on the Methanol-to-Olefins Reaction. *ACS Catal.* **2016**, *6* (2), 542−550.
(24) Yarulina, I.; Bailleul, S.; Pustovarenko, A.; Martinez, J. R.; De Wispelaere, K.; Hajek, J.; Weckhuysen, B. M.; Houben, K.; Baldus, M.; Van Speybroeck, V.; Kapteijn, F.; Gascon, J. Suppression of the Aromatic Cycle in Methanol-to-Olefins Reaction over ZSM-5 by Post-Synthetic Modification Using Calcium. *ChemCatChem* **2016**, *8* (19), 3057−3063.
(25) Yarulina, I.; De Wispelaere, K.; Bailleul, S.; Goetze, J.; Radersma, M.; Abou-Hamad, E.; Vollmer, I.; Goesten, M.; Mezari, B.; Hensen, E. J. M.; Martínez-Espín, J. S.; Morten, M.; Mitchell, S.; Perez-Ramirez, J.; Olsbye, U.; Weckhuysen, B. M.; Van Speybroeck, V.; Kapteijn, F.; Gascon, J. Structure−Performance Descriptors and the Role of Lewis Acidity in the Methanol-to-Propylene Process. *Nat. Chem.* **2018**, *10* (8), 804−812.
(26) Suzuki, K.; Kiyozumi, Y.; Matsuzaki, K.; Ikai, S.; Shin, S. Effect of Modification of ZSM-5 Type Zeolite with Calcium Phosphate on Its Physico-Chemical and Catalytic Properties. *Appl. Catal.* **1988**, *39*, 315−324.
(27) Zhang, S.; Zhang, B.; Gao, Z.; Han, Y. Methanol to Olefin over Ca-Modified HZSM-5 Zeolites. *Ind. Eng. Chem. Res.* **2010**, *49* (5), 2103−2106.
(28) Zhang, S.; Zhang, B.; Gao, Z.; Han, Y. Ca Modified ZSM-5 for High Propylene Selectivity from Methanol. *React. Kinet., Mech. Catal.* **2010**, *99* (2), 447−453.
(29) MAN, J.; ZHANG, Q.; XIE, H.; PAN, J.; TAN, Y.; HAN, Y. Effects of Reaction Atmosphere on Dimethyl Ether Conversion to Propylene Process over Ca/ZSM-5. *J. Fuel Chem. Technol.* **2011**, *39* (1), 42−46.
(30) Chen, C.; Zhang, Q.; Meng, Z.; Li, C.; Shan, H. Effect of Magnesium Modification over H-ZSM-5 in Methanol to Propylene Reaction. *Appl. Petrochem. Res.* **2015**, *5* (4), 277−284.
(31) Sun, X.; Mueller, S.; Liu, Y.; Shi, H.; Haller, G. L.; Sanchez-Sanchez, M.; van Veen, A. C.; Lercher, J. A. On Reaction Pathways in the Conversion of Methanol to Hydrocarbons on HZSM-5. *J. Catal.* **2014**, *317*, 185−197.
(32) Svelle, S.; Joensen, F.; Nerlov, J.; Olsbye, U.; Lillerud, K.-P.; Kolboe, S.; Bjørgen, M. Conversion of Methanol into Hydrocarbons over Zeolite H-ZSM-5: Ethene Formation Is Mechanistically Separated from the Formation of Higher Alkenes. *J. Am. Chem. Soc.* **2006**, *128* (46), 14770−14771.
(33) De Wispelaere, K.; Bailleul, S.; Van Speybroeck, V. Towards Molecular Control of Elementary Reactions in Zeolite Catalysis by Advanced Molecular Simulations Mimicking Operating Conditions. *Catal. Sci. Technol.* **2016**, *6* (8), 2686−2705.
(34) Van Speybroeck, V.; Hemelsoet, K.; De Wispelaere, K.; Qian, Q.; Van der Mynsbrugge, J.; De Sterck, B.; Weckhuysen, B. M.; Waroquier, M. Mechanistic Studies on Chabazite-Type Methanol-to-Olefin Catalysts: Insights from Time-Resolved UV/Vis Microspectroscopy Combined with Theoretical Simulations. *ChemCatChem* **2013**, *5* (1), 173−184.
(35) Hemelsoet, K.; Qian, Q.; De Meyer, T.; De Wispelaere, K.; De Sterck, B.; Weckhuysen, B. M.; Waroquier, M.; Van Speybroeck, V. Identification of Intermediates in Zeolite-Catalyzed Reactions by In Situ UV/Vis Microspectroscopy and a Complementary Set of Molecular Simulations. *Chem. - Eur. J.* **2013**, *19* (49), 16595−16606.
(36) De Wispelaere, K.; Hemelsoet, K.; Waroquier, M.; Van Speybroeck, V. Complete Low-Barrier Side-Chain Route for Olefin Formation during Methanol Conversion in H-SAPO-34. *J. Catal.* **2013**, *305*, 76−80.
(37) Lesthaeghe, D.; De Sterck, B.; Van Speybroeck, V.; Marin, G. B.; Waroquier, M. Zeolite Shape-Selectivity in the Gem-Methylation of Aromatic Hydrocarbons. *Angew. Chem., Int. Ed.* **2007**, *46* (8), 1311−1314.
(38) McCann, D. M.; Lesthaeghe, D.; Kletnieks, P. W.; Guenther, D. R.; Hayman, M. J.; Van Speybroeck, V.; Waroquier, M.; Haw, J. F. A Complete Catalytic Cycle for Supramolecular Methanol-to-Olefins Conversion by Linking Theory with Experiment. *Angew. Chem., Int. Ed.* **2008**, *47* (28), 5179−5182.
(39) Wang, C.-M.; Wang, Y.-D.; Xie, Z.-K.; Liu, Z.-P. Methanol to Olefin Conversion on HSAPO-34 Zeolite from Periodic Density Functional Theory Calculations: A Complete Cycle of Side Chain Hydrocarbon Pool Mechanism. *J. Phys. Chem. C* **2009**, *113* (11), 4584−4591.
(40) Svelle, S.; Rønning, P. O.; Kolboe, S. Kinetic Studies of Zeolite-Catalyzed Methylation Reactions: 1. Coreaction of [12C]Ethene and [13C]Methanol. *J. Catal.* **2004**, *224* (1), 115−123.
(41) Svelle, S.; Rønning, P. O.; Olsbye, U.; Kolboe, S. Kinetic Studies of Zeolite-Catalyzed Methylation Reactions. Part 2. Co-Reaction of [12C]Propene or [12C]n-Butene and [13C]Methanol. *J. Catal.* **2005**, *234* (2), 385−400.
(42) Lesthaeghe, D.; Van der Mynsbrugge, J.; Vandichel, M.; Waroquier, M.; Van Speybroeck, V. Full Theoretical Cycle for Both Ethene and Propene Formation during Methanol-to-Olefin Conversion in H-ZSM-5. *ChemCatChem* **2011**, *3* (1), 208−212.
(43) Lin, B.; Zhang, Q.; Wang, Y. Catalytic Conversion of Ethylene to Propylene and Butenes over H−ZSM-5. *Ind. Eng. Chem. Res.* **2009**, *48* (24), 10788−10795.
(44) Takahashi, A.; Xia, W.; Wu, Q.; Furukawa, T.; Nakamura, I.; Shimada, H.; Fujitani, T. Difference between the Mechanisms of Propylene Production from Methanol and Ethanol over ZSM-5 Catalysts. *Appl. Catal., A* **2013**, *467*, 380−385.
(45) Zhang, H.; Ning, Z.; Shang, J.; Liu, H.; Han, S.; Qu, W.; Jiang, Y.; Guo, Y. A Durable and Highly Selective PbO/HZSM-5 Catalyst for Methanol to Propylene (MTP) Conversion. *Microporous Mesoporous Mater.* **2017**, *248*, 173−178.
(46) Prakash, N.; Lee, M.-H.; Yoon, S.; Jung, K.-D. Role of Acid Solvent to Prepare Highly Active PtSn/*θ*-Al2O3 Catalysts in Dehydrogenation of Propane to Propylene. *Catal. Today* **2017**, *293*, 33−41.
(47) Sun, X.; Mueller, S.; Shi, H.; Haller, G. L.; Sanchez-Sanchez, M.; van Veen, A. C.; Lercher, J. A. On the Impact of Co-Feeding Aromatics and Olefins for the Methanol-to-Olefins Reaction on HZSM-5. *J. Catal.* **2014**, *314*, 21−31.
(48) Teketel, S.; Svelle, S.; Lillerud, K.-P.; Olsbye, U. Shape-Selective Conversion of Methanol to Hydrocarbons Over 10-Ring Unidirectional-Channel Acidic H-ZSM-22. *ChemCatChem* **2009**, *1* (1), 78−81.
(49) Teketel, S.; Olsbye, U.; Lillerud, K.-P.; Beato, P.; Svelle, S. Selectivity Control through Fundamental Mechanistic Insight in the Conversion of Methanol to Hydrocarbons over Zeolites. *Microporous Mesoporous Mater.* **2010**, *136* (1−3), 33−41.

Q

DOI: 10.1021/jacs.9b07484
J. Am. Chem. Soc. XXXX, XXX, XXX−XXX

(50) Hereijgers, B. P. C.; Bleken, F.; Nilsen, M. H.; Svelle, S.; Lillerud, K.-P.; Bjørgen, M.; Weckhuysen, B. M.; Olsbye, U. Product Shape Selectivity Dominates the Methanol-to-Olefins (MTO) Reaction over H-SAPO-34 Catalysts. *J. Catal.* **2009**, *264* (1), 77−87.
(51) Westgård Erichsen, M.; Svelle, S.; Olsbye, U. H-SAPO-5 as Methanol-to-Olefins (MTO) Model Catalyst: Towards Elucidating the Effects of Acid Strength. *J. Catal.* **2013**, *298*, 94−101.
(52) Westgård Erichsen, M.; Svelle, S.; Olsbye, U. The Influence of Catalyst Acid Strength on the Methanol to Hydrocarbons (MTH) Reaction. *Catal. Today* **2013**, *215*, 216−223.
(53) Westgård Erichsen, M.; De Wispelaere, K.; Hemelsoet, K.; Moors, S. L. C.; Deconinck, T.; Waroquier, M.; Svelle, S.; Van Speybroeck, V.; Olsbye, U. How Zeolitic Acid Strength and Composition Alter the Reactivity of Alkenes and Aromatics towards Methanol. *J. Catal.* **2015**, *328*, 186−196.
(54) Svelle, S.; Olsbye, U.; Joensen, F.; Bjørgen, M. Conversion of Methanol to Alkenes over Medium- and Large-Pore Acidic Zeolites: Steric Manipulation of the Reaction Intermediates Governs the Ethene/Propene Product Selectivity. *J. Phys. Chem. C* **2007**, *111* (49), 17981−17984.
(55) Bjørgen, M.; Joensen, F.; Lillerud, K.-P.; Olsbye, U.; Svelle, S. The Mechanisms of Ethene and Propene Formation from Methanol over High Silica H-ZSM-5 and H-Beta. *Catal. Today* **2009**, *142* (1−2), 90−97.
(56) Bjørgen, M.; Akyalcin, S.; Olsbye, U.; Benard, S.; Kolboe, S.; Svelle, S. Methanol to Hydrocarbons over Large Cavity Zeolites: Toward a Unified Description of Catalyst Deactivation and the Reaction Mechanism. *J. Catal.* **2010**, *275* (1), 170−180.
(57) Bjørgen, M.; Olsbye, U.; Petersen, D.; Kolboe, S. The Methanol-to-Hydrocarbons Reaction: Insight into the Reaction Mechanism from [12C]Benzene and [13C]Methanol Coreactions over Zeolite H-Beta. *J. Catal.* **2004**, *221* (1), 1−10.
(58) Ahn, J. H.; Temel, B.; Iglesia, E. Selective Homologation Routes to 2,2,3-Trimethylbutane on Solid Acids. *Angew. Chem., Int. Ed.* **2009**, *48* (21), 3814−3816.
(59) Simonetti, D. A.; Ahn, J. H.; Iglesia, E. Mechanistic Details of Acid-Catalyzed Reactions and Their Role in the Selective Synthesis of Triptane and Isobutane from Dimethyl Ether. *J. Catal.* **2011**, *277* (2), 173−195.
(60) Koempel, H.; Liebner, W. Lurgi's Methanol To Propylene (MTP) Report on a Successful Commercialisation. In *Studies in Surface Science and Catalysis*; Noronha, F. B., Schmal, M., Sousa-Aguiar, E. F., Eds.; Natural Gas Conversion VIII Proceedings of the 8th Natural Gas Conversion Symposium; Elsevier: 2007; Vol. *167*, pp 261−267.
(61) Kosinov, N.; Liu, C.; Hensen, E. J. M.; Pidko, E. A. Engineering of Transition Metal Catalysts Confined in Zeolites. *Chem. Mater.* **2018**, *30* (10), 3177−3198.
(62) Zheng, H.; Ma, D.; Bao, X.; Hu, J. Z.; Kwak, J. H.; Wang, Y.; Peden, C. H. F. Direct Observation of the Active Center for Methane Dehydroaromatization Using an Ultrahigh Field 95Mo NMR Spectroscopy. *J. Am. Chem. Soc.* **2008**, *130* (12), 3722−3723.
(63) Beyer, H. K. Dealumination Techniques for Zeolites. *Post-Synthesis Modification I*; Molecular Sieves; Springer: Berlin, Heidelberg, 2002; pp 203−255.
(64) Jin, L.; Hu, H.; Zhu, S.; Ma, B. An Improved Dealumination Method for Adjusting Acidity of HZSM-5. *Catal. Today* **2010**, *149* (1), 207−211.
(65) Liu, C.; Li, G.; Hensen, E. J. M.; Pidko, E. A. Nature and Catalytic Role of Extraframework Aluminum in Faujasite Zeolite: A Theoretical Perspective. *ACS Catal.* **2015**, *5* (11), 7024−7033.
(66) Dyballa, M.; Becker, P.; Trefz, D.; Klemm, E.; Fischer, A.; Jakob, H.; Hunger, M. Parameters Influencing the Selectivity to Propene in the MTO Conversion on 10-Ring Zeolites: Directly Synthesized Zeolites ZSM-5, ZSM-11, and ZSM-22. *Appl. Catal., A* **2016**, *510* (Supplement C), 233−243.
(67) Jabbari, A.; Abbasi, A.; Zargarnezhad, H.; Riazifar, M. A Study on the Effect of SiO2/Al2O3 Ratio on the Structure and Performance of Nano-Sized ZSM-5 in Methanol to Propylene Conversion. *React. Kinet., Mech. Catal.* **2017**, *121* (2), 763−772.
(68) Dai, W.; Cao, G.; Yang, L.; Wu, G.; Dyballa, M.; Hunger, M.; Guan, N.; Li, L. Insights into the Catalytic Cycle and Activity of Methanol-to-Olefin Conversion over Low-Silica AlPO-34 Zeolites with Controllable Brønsted Acid Density. *Catal. Sci. Technol.* **2017**, *7* (3), 607−618.
(69) Rostamizadeh, M.; Yaripour, F. Dealumination of High Silica H-ZSM-5 as Long-Lived Nanocatalyst for Methanol to Olefin Conversion. *J. Taiwan Inst. Chem. Eng.* **2017**, *71*, 454−463.
(70) Kong, C.; Zhu, J.; Liu, S.; Wang, Y. SAPO-34 with a Low Acidity Outer Layer by Epitaxial Growth and Its Improved MTO Performance. *RSC Adv.* **2017**, *7* (63), 39889−39898.
(71) Stöcker, M. Methanol-to-Hydrocarbons: Catalytic Materials and Their Behavior. *Microporous Mesoporous Mater.* **1999**, *29* (1−2), 3−48.
(72) Mei, C.; Wen, P.; Liu, Z.; Liu, H.; Wang, Y.; Yang, W.; Xie, Z.; Hua, W.; Gao, Z. Selective Production of Propylene from Methanol: Mesoporosity Development in High Silica HZSM-5. *J. Catal.* **2008**, *258* (1), 243−249.
(73) Milina, M.; Mitchell, S.; Michels, N.-L.; Kenvin, J.; Pérez-Ramírez, J. Interdependence between Porosity, Acidity, and Catalytic Performance in Hierarchical ZSM-5 Zeolites Prepared by Post-Synthetic Modification. *J. Catal.* **2013**, *308*, 398−407.
(74) Brus, J.; Kobera, L.; Schoefberger, W.; Urbanová, M.; Klein, P.; Sazama, P.; Tabor, E.; Sklenak, S.; Fishchuk, A. V.; Dědeček, J. Structure of Framework Aluminum Lewis Sites and Perturbed Aluminum Atoms in Zeolites as Determined by 27Al{1H} REDOR (3Q) MAS NMR Spectroscopy and DFT/Molecular Mechanics. *Angew. Chem., Int. Ed.* **2015**, *54* (2), 541−545.
(75) Zhang, L.; Wang, H.; Liu, G.; Gao, K.; Wu, J. Methanol-to-Olefin Conversion over H-MCM-22 Catalyst. *J. Mol. Catal. A: Chem.* **2016**, *411*, 311−316.
(76) Zhang, L.; Wang, H.; Liu, G.; Gao, K.; Wu, J. Conversion of Methanol to Light Olefins over H-MCM-22 Dealuminated with Different Methods. *J. Chem. Technol. Biotechnol.* **2017**, *92* (6), 1353−1361.
(77) Kresse, G.; Hafner, J. Ab Initio Molecular Dynamics for Liquid Metals. *Phys. Rev. B: Condens. Matter Mater. Phys.* **1993**, *47* (1), 558−561.
(78) Kresse, G.; Hafner, J. Ab Initio Molecular-Dynamics Simulation of the Liquid-Metal Amorphous-Semiconductor Transition in Germanium. *Phys. Rev. B: Condens. Matter Mater. Phys.* **1994**, *49* (20), 14251−14269.
(79) Kresse, G.; Furthmüller, J. Efficiency of Ab-Initio Total Energy Calculations for Metals and Semiconductors Using a Plane-Wave Basis Set. *Comput. Mater. Sci.* **1996**, *6* (1), 15−50.
(80) Kresse, G.; Furthmüller, J. Efficient Iterative Schemes for Ab Initio Total-Energy Calculations Using a Plane-Wave Basis Set. *Phys. Rev. B: Condens. Matter Mater. Phys.* **1996**, *54* (16), 11169−11186.
(81) Perdew, J. P.; Burke, K.; Ernzerhof, M. Generalized Gradient Approximation Made Simple. *Phys. Rev. Lett.* **1996**, *77* (18), 3865−3868.
(82) Grimme, S.; Antony, J.; Ehrlich, S.; Krieg, H. A Consistent and Accurate Ab Initio Parametrization of Density Functional Dispersion Correction (DFT-D) for the 94 Elements H-Pu. *J. Chem. Phys.* **2010**, *132* (15), 154104.
(83) Hajek, J.; Van der Mynsbrugge, J.; De Wispelaere, K.; Cnudde, P.; Vanduyfhuys, L.; Waroquier, M.; Van Speybroeck, V. On the Stability and Nature of Adsorbed Pentene in Brønsted Acid Zeolite H-ZSM-5 at 323 K. *J. Catal.* **2016**, *340*, 227−235.
(84) Svelle, S.; Tuma, C.; Rozanska, X.; Kerber, T.; Sauer, J. Quantum Chemical Modeling of Zeolite-Catalyzed Methylation Reactions: Toward Chemical Accuracy for Barriers. *J. Am. Chem. Soc.* **2009**, *131* (2), 816−825.
(85) Piccini, G.; Alessio, M.; Sauer, J. Ab Initio Calculation of Rate Constants for Molecule−Surface Reactions with Chemical Accuracy. *Angew. Chem., Int. Ed.* **2016**, *55* (17), 5235−5237.

DOI: 10.1021/jacs.9b07484
J. Am. Chem. Soc. XXXX, XXX, XXX−XXX

(86) Tuma, C.; Sauer, J. Treating Dispersion Effects in Extended Systems by Hybrid MP2:DFT Calculations—Protonation of Isobutene in Zeolite Ferrierite. *Phys. Chem. Chem. Phys.* **2006**, *8* (34), 3955−3965.
(87) Tuma, C.; Kerber, T.; Sauer, J. The Tert-Butyl Cation in H-Zeolites: Deprotonation to Isobutene and Conversion into Surface Alkoxides. *Angew. Chem., Int. Ed.* **2010**, *49* (27), 4678−4680.
(88) Hansen, N.; Kerber, T.; Sauer, J.; Bell, A. T.; Keil, F. J. Quantum Chemical Modeling of Benzene Ethylation over H-ZSM-5 Approaching Chemical Accuracy: A Hybrid MP2:DFT Study. *J. Am. Chem. Soc.* **2010**, *132* (33), 11525−11538.
(89) Rybicki, M.; Sauer, J. Ab Initio Prediction of Proton Exchange Barriers for Alkanes at Brønsted Sites of Zeolite H-MFI. *J. Am. Chem. Soc.* **2018**, *140* (51), 18151−18161.
(90) Goncalves, T. J.; Plessow, P. N.; Studt, F. On the Accuracy of Density Functional Theory in Zeolite Catalysis. *ChemCatChem* **2019**, *11*, 1−10.
(91) Blöchl, P. E. Projector Augmented-Wave Method. *Phys. Rev. B: Condens. Matter Mater. Phys.* **1994**, *50* (24), 17953−17979.
(92) Kresse, G.; Joubert, D. From Ultrasoft Pseudopotentials to the Projector Augmented-Wave Method. *Phys. Rev. B: Condens. Matter Mater. Phys.* **1999**, *59* (3), 1758−1775.
(93) Heyden, A.; Bell, A. T.; Keil, F. J. Efficient Methods for Finding Transition States in Chemical Reactions: Comparison of Improved Dimer Method and Partitioned Rational Function Optimization Method. *J. Chem. Phys.* **2005**, *123* (22), 224101.
(94) Pulay, P. Convergence Acceleration of Iterative Sequences. the Case of Scf Iteration. *Chem. Phys. Lett.* **1980**, *73* (2), 393−398.
(95) Press, W. H.; Flannery, B. P.; Teukolsky, S. A.; Vetterling, W. T. *Numerical Recipes: The Art of Scientific Computing*; Cambridge Univ. Press: New York, 1986.
(96) De Moor, B. A.; Ghysels, A.; Reyniers, M.-F.; Van Speybroeck, V.; Waroquier, M.; Marin, G. B. Normal Mode Analysis in Zeolites: Toward an Efficient Calculation of Adsorption Entropies. *J. Chem. Theory Comput.* **2011**, *7* (4), 1090−1101.
(97) Ghysels, A.; Verstraelen, T.; Hemelsoet, K.; Waroquier, M.; Van Speybroeck, V. TAMkin: A Versatile Package for Vibrational Analysis and Chemical Kinetics. *J. Chem. Inf. Model.* **2010**, *50* (9), 1736−1750.
(98) De Moor, B. A.; Reyniers, M.-F.; Marin, G. B. Physisorption and Chemisorption of Alkanes and Alkenes in H-FAU: A Combined Ab Initio−Statistical Thermodynamics Study. *Phys. Chem. Chem. Phys.* **2009**, *11* (16), 2939−2958.
(99) Martinez-Espin, J. S.; De Wispelaere, K.; Westgård Erichsen, M.; Svelle, S.; Janssens, T. V. W.; Van Speybroeck, V.; Beato, P.; Olsbye, U. Benzene Co-Reaction with Methanol and Dimethyl Ether over Zeolite and Zeotype Catalysts: Evidence of Parallel Reaction Paths to Toluene and Diphenylmethane. *J. Catal.* **2017**, *349*, 136−148.
(100) Baroni, S.; de Gironcoli, S.; Dal Corso, A.; Giannozzi, P. Phonons and Related Crystal Properties from Density-Functional Perturbation Theory. *Rev. Mod. Phys.* **2001**, *73* (2), 515−562.
(101) Wu, X.; Vanderbilt, D.; Hamann, D. R. Systematic Treatment of Displacements, Strains, and Electric Fields in Density-Functional Perturbation Theory. *Phys. Rev. B: Condens. Matter Mater. Phys.* **2005**, *72* (3), 035105.
(102) Gajdoš, M.; Hummer, K.; Kresse, G.; Furthmüller, J.; Bechstedt, F. Linear Optical Properties in the Projector-Augmented Wave Methodology. *Phys. Rev. B: Condens. Matter Mater. Phys.* **2006**, *73* (4), 045112.
(103) Karhánek, D.; Bučko, T.; Hafner, J. A Density-Functional Study of the Adsorption of Methane-Thiol on the (111) Surfaces of the Ni-Group Metals: II. Vibrational Spectroscopy. *J. Phys.: Condens. Matter* **2010**, *22* (26), 265006.
(104) Hoffman, A. E. J.; Vanduyfhuys, L.; Nevjestić, I.; Wieme, J.; Rogge, S. M. J.; Depauw, H.; Van Der Voort, P.; Vrielinck, H.; Van Speybroeck, V. Elucidating the Vibrational Fingerprint of the Flexible Metal−Organic Framework MIL-53(Al) Using a Combined Experimental/Computational Approach. *J. Phys. Chem. C* **2018**, *122* (5), 2734−2746.
(105) Laury, M. L.; Carlson, M. J.; Wilson, A. K. Vibrational Frequency Scale Factors for Density Functional Theory and the Polarization Consistent Basis Sets. *J. Comput. Chem.* **2012**, *33* (30), 2380−2387.
(106) Merrick, J. P.; Moran, D.; Radom, L. An Evaluation of Harmonic Vibrational Frequency Scale Factors. *J. Phys. Chem. A* **2007**, *111* (45), 11683−11700.
(107) Pickard, C. J.; Mauri, F. All-Electron Magnetic Response with Pseudopotentials: NMR Chemical Shifts. *Phys. Rev. B: Condens. Matter Mater. Phys.* **2001**, *63* (24), 245101.
(108) Hutter, J.; Iannuzzi, M.; Schiffmann, F.; VandeVondele, J. Cp2k: Atomistic Simulations of Condensed Matter Systems. *Wiley Interdiscip. Rev. Comput. Mol. Sci.* **2014**, *4* (1), 15−25.
(109) VandeVondele, J.; Krack, M.; Mohamed, F.; Parrinello, M.; Chassaing, T.; Hutter, J. Quickstep: Fast and Accurate Density Functional Calculations Using a Mixed Gaussian and Plane Waves Approach. *Comput. Phys. Commun.* **2005**, *167* (2), 103−128.
(110) Emeis, C. A. Determination of Integrated Molar Extinction Coefficients for Infrared Absorption Bands of Pyridine Adsorbed on Solid Acid Catalysts. *J. Catal.* **1993**, *141* (2), 347−354.
(111) Pidko, E. A.; Hensen, E. J. M.; van Santen, R. A. Self-Organization of Extraframework Cations in Zeolites. *Proc. R. Soc. London, Ser. A* **2012**, *468* (2143), 2070−2086.
(112) Pidko, E. A.; Hensen, E. J. M.; Zhidomirov, G. M.; van Santen, R. A. Non-Localized Charge Compensation in Zeolites: A Periodic DFT Study of Cationic Gallium-Oxide Clusters in Mordenite. *J. Catal.* **2008**, *255* (2), 139−143.
(113) Pidko, E. A.; van Santen, R. A.; Hensen, E. J. M. Multinuclear Gallium-Oxide Cations in High-Silica Zeolites. *Phys. Chem. Chem. Phys.* **2009**, *11* (16), 2893−2902.
(114) Li, G.; Pidko, E. A.; van Santen, R. A.; Feng, Z.; Li, C.; Hensen, E. J. M. Stability and Reactivity of Active Sites for Direct Benzene Oxidation to Phenol in Fe/ZSM-5: A Comprehensive Periodic DFT Study. *J. Catal.* **2011**, *284* (2), 194−206.
(115) Li, G.; Pidko, E. A.; van Santen, R. A.; Li, C.; Hensen, E. J. M. Stability of Extraframework Iron-Containing Complexes in ZSM-5 Zeolite. *J. Phys. Chem. C* **2013**, *117* (1), 413−426.
(116) Li, G.; Pidko, E. A.; Filot, I. A. W.; van Santen, R. A.; Li, C.; Hensen, E. J. M. Catalytic Properties of Extraframework Iron-Containing Species in ZSM-5 for N2O Decomposition. *J. Catal.* **2013**, *308*, 386−397.
(117) Knott, B. C.; Nimlos, C. T.; Robichaud, D. J.; Nimlos, M. R.; Kim, S.; Gounder, R. Consideration of the Aluminum Distribution in Zeolites in Theoretical and Experimental Catalysis Research. *ACS Catal.* **2018**, *8* (2), 770−784.
(118) Dib, E.; Mineva, T.; Veron, E.; Sarou-Kanian, V.; Fayon, F.; Alonso, B. ZSM-5 Zeolite: Complete Al Bond Connectivity and Implications on Structure Formation from Solid-State NMR and Quantum Chemistry Calculations. *J. Phys. Chem. Lett.* **2018**, *9* (1), 19−24.
(119) Holzinger, J.; Nielsen, M.; Beato, P.; Brogaard, R. Y.; Buono, C.; Dyballa, M.; Falsig, H.; Skibsted, J.; Svelle, S. Identification of Distinct Framework Aluminum Sites in Zeolite ZSM-23: A Combined Computational and Experimental 27Al NMR Study. *J. Phys. Chem. C* **2019**, *123* (13), 7831−7844.
(120) Bryce, D. L. Calcium Binding Environments Probed by 43Ca NMR Spectroscopy. *Dalton Trans* **2010**, *39* (37), 8593−8602.
(121) Aebi, D.; Bultz, E. B.; Bryce, D. L. Calcium-43 Chemical Shift Tensors as Probes of Calcium Binding Environments. Insight into the Structure of the Vaterite CaCO3 Polymorph by 43Ca Solid-State NMR Spectroscopy. *J. Am. Chem. Soc.* **2008**, *130* (29), 9282−9292.
(122) Lee, D.; Leroy, C.; Crevant, C.; Bonhomme-Coury, L.; Babonneau, F.; Laurencin, D.; Bonhomme, C.; De Paëpe, G. Interfacial Ca2+ Environments in Nanocrystalline Apatites Revealed by Dynamic Nuclear Polarization Enhanced 43Ca NMR Spectroscopy. *Nat. Commun.* **2017**, *8*, 14104.

DOI: 10.1021/jacs.9b07484
J. Am. Chem. Soc. XXXX, XXX, XXX−XXX

(123) Jiang, Y.; Huang, J.; Dai, W.; Hunger, M. Solid-State Nuclear Magnetic Resonance Investigations of the Nature, Property, and Activity of Acid Sites on Solid Catalysts. *Solid State Nucl. Magn. Reson.* **2011**, *39* (3), 116−141.
(124) Derouane, E. G.; Védrine, J. C.; Pinto, R. R.; Borges, P. M.; Costa, L.; Lemos, M. A. N. D. A.; Lemos, F.; Ribeiro, F. R. The Acidity of Zeolites: Concepts, Measurements and Relation to Catalysis: A Review on Experimental and Theoretical Methods for the Study of Zeolite Acidity. *Catal. Rev.: Sci. Eng.* **2013**, *55* (4), 454−515.
(125) Zheng, A.; Liu, S.-B.; Deng, F. Acidity Characterization of Heterogeneous Catalysts by Solid-State NMR Spectroscopy Using Probe Molecules. *Solid State Nucl. Magn. Reson.* **2013**, *55* (Supplement C), 12−27.
(126) Hadjiivanov, K. Chapter Two - Identification and Characterization of Surface Hydroxyl Groups by Infrared Spectroscopy. In *Advances in Catalysis*; Jentoft, F. C., Ed.; Academic Press: 2014; Vol. *57*, pp 99−318.
(127) Sandoval-Díaz, L.-E.; González-Amaya, J.-A.; Trujillo, C.-A. General Aspects of Zeolite Acidity Characterization. *Microporous Mesoporous Mater.* **2015**, *215* (Supplement C), 229−243.
(128) Parry, E. P. An Infrared Study of Pyridine Adsorbed on Acidic Solids. Characterization of Surface Acidity. *J. Catal.* **1963**, *2* (5), 371−379.
(129) Velthoen, M. E. Z.; Nab, S.; Weckhuysen, B. M. Probing Acid Sites in Solid Catalysts with Pyridine UV-Vis Spectroscopy. *Phys. Chem. Chem. Phys.* **2018**, *20* (33), 21647−21659.
(130) Cannings, F. R. Acidic Sites on Mordenite: An Infrared Study of Adsorbed Pyridine. *J. Phys. Chem.* **1968**, *72* (13), 4691−4693.
(131) Barzetti, T.; Selli, E.; Moscotti, D.; Forni, L. Pyridine and Ammonia as Probes for FTIR Analysis of Solid Acid Catalysts. *J. Chem. Soc., Faraday Trans.* **1996**, *92* (8), 1401−1407.
(132) Meloni, D.; Laforge, S.; Martin, D.; Guisnet, M.; Rombi, E.; Solinas, V. Acidic and Catalytic Properties of H-MCM-22 Zeolites. *Appl. Catal., A* **2001**, *215* (1), 55−66.
(133) Nishi, K.; Kamiya, N.; Yokomori, Y. Single-Crystal Structure of a Pyridine Sorption Complex of Zeolite HZSM-5 (H-MFI). *Microporous Mesoporous Mater.* **2007**, *101* (1−2), 83−89.
(134) Zhang, L.; Gao, J.; Hu, J.; Li, W.; Wang, J. Lanthanum Oxides-Improved Catalytic Performance of ZSM-5 in Toluene Alkylation with Methanol. *Catal. Lett.* **2009**, *130* (3−4), 355−361.
(135) Sartipi, S.; Parashar, K.; Valero-Romero, M. J.; Santos, V. P.; van der Linden, B.; Makkee, M.; Kapteijn, F.; Gascon, J. Hierarchical H-ZSM-5-Supported Cobalt for the Direct Synthesis of Gasoline-Range Hydrocarbons from Syngas: Advantages, Limitations, and Mechanistic Insight. *J. Catal.* **2013**, *305*, 179−190.
(136) Boscoboinik, J. A.; Yu, X.; Emmez, E.; Yang, B.; Shaikhutdinov, S.; Fischer, F. D.; Sauer, J.; Freund, H.-J. Interaction of Probe Molecules with Bridging Hydroxyls of Two-Dimensional Zeolites: A Surface Science Approach. *J. Phys. Chem. C* **2013**, *117* (26), 13547−13556.
(137) Nicholas, J. B.; Haw, J. F. The Prediction of Persistent Carbenium Ions in Zeolites. *J. Am. Chem. Soc.* **1998**, *120* (45), 11804−11805.
(138) Peña, L. F. G.; Sad, M. E.; Padró, C. L.; Apesteguía, C. R. Study of the Alkylation of Phenol with Methanol on Zn(H)-Exchanged NaY Zeolites. *Catal. Lett.* **2011**, *141* (7), 939−947.
(139) Li, X.; Lu, J.; Li, Y.; Yu, J. Roles of Hydroxyl Groups During Side-Chain Alkylation of Toluene with Methanol over Zeolite Na-Y: A Density Functional Theory Study. *Chin. J. Chem.* **2017**, *35* (5), 716−722.
(140) Van Speybroeck, V.; Van der Mynsbrugge, J.; Vandichel, M.; Hemelsoet, K.; Lesthaeghe, D.; Ghysels, A.; Marin, G. B.; Waroquier, M. First Principle Kinetic Studies of Zeolite-Catalyzed Methylation Reactions. *J. Am. Chem. Soc.* **2011**, *133* (4), 888−899.
(141) Van der Mynsbrugge, J.; Visur, M.; Olsbye, U.; Beato, P.; Bjørgen, M.; Van Speybroeck, V.; Svelle, S. Methylation of Benzene by Methanol: Single-Site Kinetics over H-ZSM-5 and H-Beta Zeolite Catalysts. *J. Catal.* **2012**, *292*, 201−212.
(142) Van der Mynsbrugge, J.; Moors, S. L. C.; De Wispelaere, K.; Van Speybroeck, V. Insight into the Formation and Reactivity of Framework-Bound Methoxide Species in H-ZSM-5 from Static and Dynamic Molecular Simulations. *ChemCatChem* **2014**, *6* (7), 1906−1918.
(143) Van der Mynsbrugge, J.; Hemelsoet, K.; Vandichel, M.; Waroquier, M.; Van Speybroeck, V. Efficient Approach for the Computational Study of Alcohol and Nitrile Adsorption in H-ZSM-5. *J. Phys. Chem. C* **2012**, *116* (9), 5499−5508.
(144) Cnudde, P.; De Wispelaere, K.; Van der Mynsbrugge, J.; Waroquier, M.; Van Speybroeck, V. Effect of Temperature and Branching on the Nature and Stability of Alkene Cracking Intermediates in H-ZSM-5. *J. Catal.* **2017**, *345*, 53−69.
(145) Moors, S. L. C.; De Wispelaere, K.; Van der Mynsbrugge, J.; Waroquier, M.; Van Speybroeck, V. Molecular Dynamics Kinetic Study on the Zeolite-Catalyzed Benzene Methylation in ZSM-5. *ACS Catal.* **2013**, *3* (11), 2556−2567.
(146) Vos, A. M.; Schoonheydt, R. A.; De Proft, F.; Geerlings, P. DFT Study on the Electrophilic Aromatic Substitution Catalyzed by Lewis Acids. *J. Catal.* **2003**, *220* (2), 333−346.
(147) Macht, J.; Carr, R. T.; Iglesia, E. Consequences of Acid Strength for Isomerization and Elimination Catalysis on Solid Acids. *J. Am. Chem. Soc.* **2009**, *131* (18), 6554−6565.
(148) Fang, H.; Zheng, A.; Xu, J.; Li, S.; Chu, Y.; Chen, L.; Deng, F. Theoretical Investigation of the Effects of the Zeolite Framework on the Stability of Carbenium Ions. *J. Phys. Chem. C* **2011**, *115* (15), 7429−7439.
(149) Lesthaeghe, D.; Horré, A.; Waroquier, M.; Marin, G. B.; Van Speybroeck, V. Theoretical Insights on Methylbenzene Side-Chain Growth in ZSM-5 Zeolites for Methanol-to-Olefin Conversion. *Chem. - Eur. J.* **2009**, *15* (41), 10803−10808.
(150) Olsbye, U.; Svelle, S.; Lillerud, K. P.; Wei, Z. H.; Chen, Y. Y.; Li, J. F.; Wang, J. G.; Fan, W. G. The Formation and Degradation of Active Species during Methanol Conversion over Protonated Zeotype Catalysts. *Chem. Soc. Rev.* **2015**, *44* (20), 7155−7176.
(151) Mores, D.; Kornatowski, J.; Olsbye, U.; Weckhuysen, B. M. Coke Formation during the Methanol-to-Olefin Conversion: In Situ Microspectroscopy on Individual H-ZSM-5 Crystals with Different Brønsted Acidity. *Chem. - Eur. J.* **2011**, *17* (10), 2874−2884.
(152) Janssens, T. V. W.; Svelle, S.; Olsbye, U. Kinetic Modeling of Deactivation Profiles in the Methanol-to-Hydrocarbons (MTH) Reaction: A Combined Autocatalytic−Hydrocarbon Pool Approach. *J. Catal.* **2013**, *308*, 122−130.

DOI: 10.1021/jacs.9b07484
J. Am. Chem. Soc. XXXX, XXX, XXX−XXX

Paper VI

Ab initio enhanced sampling kinetic study on MTO ethene methylation reaction

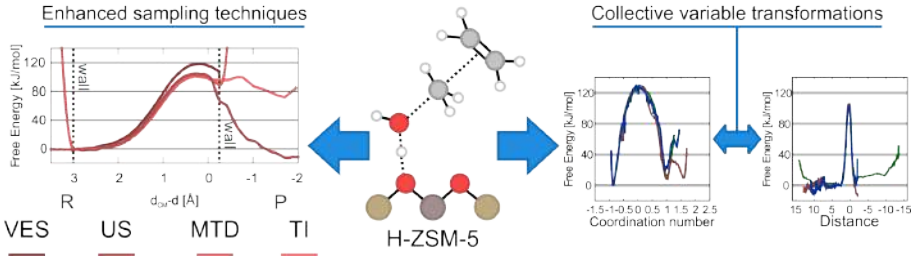

S. Bailleul, L. Vanduyfhuys M. Waroquier, V. Van Speybroeck, *Journal of Catalysis*, (2019), Submitted

S. Bailleul performed the calculations and prepared the manuscript.

Ab initio enhanced sampling kinetic study on MTO ethene methylation reaction

Simon Bailleul, Louis Vanduyfhuys, Michel Waroquier, Veronique Van Speybroeck*

Center for Molecular Modeling (CMM), Ghent University, Technologiepark 46, B-9052 Zwijnaarde, Belgium

*Corresponding author: veronique.vanspeybroeck@ugent.be

Acknowledgements

We acknowledge the Fund for Scientific Research - Flanders (FWO), the Research Board of Ghent University (BOF) and funding from the European Union's Horizon 2020 research and innovation program (consolidator ERC grant agreement No 647755 – DYNPOR (2015-2020)). The computational resources and services used were provided by Ghent University (Stevin Supercomputer Infrastructure) and the VSC (Flemish Supercomputer Center), funded by the Research Foundation - Flanders (FWO).

ABSTRACT (150-250 words)

The methylation reaction of ethene with methanol over the Brønsted acidic ZSM-5 catalyst is one of the prototype reactions within zeolite catalysis for which experimental kinetic data is available. It is one of the premier reactions within the methanol-to-olefins process and has been the subject of extensive theoretical testing to predict the reaction rates. Herein, we apply, for the first time, first principle molecular dynamics methods to determine the intrinsic reaction kinetics taking into account the full configurational entropy. As chemical reactions are rare events, enhanced sampling methods are necessary to obtain sufficient sampling of the configurational space at the activated region. A plethora of methods is available which depend on specific choices like the selection of collective variables along which the dynamics is enhanced. Herein, a thorough first principle molecular dynamics study is presented to determine the reaction kinetics via various enhanced MD techniques on an exemplary reaction within zeolite catalysis for which reference theoretical and experimental data are available.

KEY WORDS – collective variables, DFT, enhanced sampling, molecular dynamics, ethene methylation, ZSM-5

1. Introduction

In the last decades, significant progress has been made in the field of computational zeolite catalysis. [1] New methods entered the scene such as advanced molecular dynamics methods, which have the potential to model chemical reactions at operating conditions. [1–4] These techniques can help us to optimize the design of heterogeneous catalysts, for which a thorough understanding of elementary reaction steps on a molecular level is crucial. Solely based on experimental data, it has been shown to be extremely challenging to gather such information due to the large number of reactions that take place simultaneously. However, this hurdle can be overcome by complementing the experimental information with theoretical simulations. [5–13] It is generally accepted that ab initio predictions attain chemical accuracy if they reproduce energy barriers within an error less than 2 kcal/mol (8.4 kJ/mol) and that they attain kinetic accuracy when the factor $f_k = k_{theory}/k_{experiment}$ (with k_i the reaction rate constant) deviates less than one order of magnitude. [2,14,15]

A seminal contribution in this field was done by Piccini et al. [16] who proposed a divide-and-conquer strategy, which enabled to attain chemical accuracy for the methylation of ethene, propene and trans-2-butene over the zeolite catalyst H-ZSM-5. These methylation reactions, depicted schematically for ethene in Scheme 1, are of utmost importance in the methanol-to-olefins (MTO) process and are therefore frequently used as a dataset for the benchmarking of theoretical procedures. [15–17] It is one of the few reactions within zeolite catalysis for which kinetic experimental data are available by meticulously tuning the experimental conditions. [18,19] The MTO process is of industrial relevance as it is one of the most prominent technologies to bypass crude oil in the production of light olefins, like ethene and propene.[20–22] The reaction mechanism governing this process has been a point of discussion, but intensive research performed in the last decades led to the general consensus of the hydrocarbon pool (HP) mechanism. In this mechanism, organic compounds which are present in the zeolite pores, act as a co-catalyst in the conversion of methanol to olefins. [23–27] Two interacting reaction cycles

have been proposed, namely the alkene and aromatic cycle, which differ by the type of HP species considered. [20,21,28,29] Earlier studies show that the methylation reactions of the co-catalysts are key elementary reaction steps in the conversion of methanol over the zeolite catalyst, as they are responsible for the growth of the HP species via incorporation of carbon. [3,30,18,19,31–34]

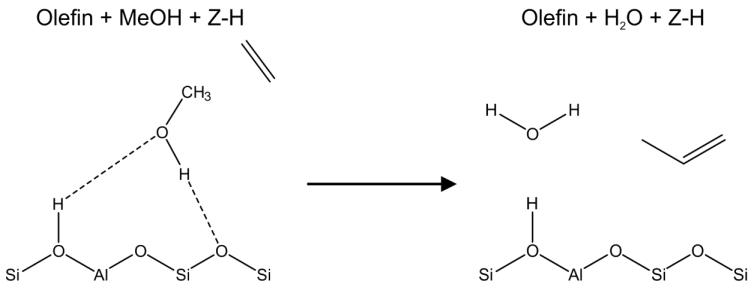

Scheme 1: Schematic representation of the methylation of ethene with methanol yielding propene.

One of the main conclusions of the work of Piccini et al.[16] is the importance of accounting for anharmonic corrections in the calculation of enthalpy barriers and rate constants. In principle, MD based techniques allow to account for anharmonic effects in a rather natural way, however the disentanglement of entropic an enthalpic contributions remains problematic. [2,35–37] MD techniques have the advantage that the sampling of the potential energy surface (PES) is not limited to the static geometry optimization at 0 K of three stationary points, namely reactant, transition state and product, but is extended to a larger part of the PES. [2,3] For methylation reactions in large pore zeolites like AFI, it was shown that not one single transition state could be found but various quasi energetic complexes were localized. In this case, it is more appropriate to introduce the concept of an activated region. [5] Besides the computational effort, the main disadvantage of regular MD is that sampling is limited to the most probable states of the system, making the sampling of states high in energy, like transition states, rare events. [38,39] Sampling of these improbable regions can be obtained by applying advanced molecular dynamics or enhanced sampling techniques. [38,39] Several enhanced sampling

techniques are reviewed in literature. [38–41] These reviews show that three components of a free energy calculation have to be taken into account when performing free energy calculations, namely: [39,40,42]

i. The choice of a suitable model for the Hamiltonian
ii. The selection of the sampling protocol to explore all relevant parts of the PES
iii. The choice of the estimator to obtain the free energy difference [43]

First of all, for the selection of the Hamiltonian, one needs to compromise between the accuracy and efficiency of the model. [39] In this case where chemical bonds are constantly broken and formed it is mandatory to use a quantum-mechanical description of the system rather than a force field based approach. Albeit force fields are computationally much more efficient, one would have to turn to reactive force fields such as ReaxFF, however there are still some limitations to this approach. [44,45] Currently, DFT based methods are commonly used as a compromise between accuracy and efficiency compared to more expensive (post-)HF wave function based methods such as RPA. [46,47] In this work, as an extremely large number of points need to be sampled on the PES, a pragmatic approach is followed by using DFT calculations with Grimme (D3) dispersion interactions. [17,15,48–51] Some caution needs to be taken into account in interpreting the absolute quantitative values as the energies might be sensitive to the dispersion correction scheme and choice of the exchange-correlation functional. [2,15–17,52] However, this is not the topic of the current study.

Secondly, several decisions must be made concerning the sampling protocol to visit the relevant parts of the PES and to obtain the ensemble of configurations. This protocol can be based on molecular dynamics and/or Monte Carlo simulations [39,42] but in this work, MD based methods are chosen. As stated earlier, insufficient sampling will be obtained via regular MD if free energy differences of more than a few times *RT* (attaining 5.2 kJ/mol at 623 K) have to be sampled. As the reported reaction barriers are significantly higher [15–19], enhanced sampling methods are necessary. A plethora of enhanced sampling methods has been proposed in

literature. [38–41] The selection of the sampling protocol depends on the possible existence of a collective variable (CV), a function of the microscopic coordinates, that differentiates between the interesting metastable and transition states, thus representing the reaction coordinate. In this work, we apply the definition of a collective variable and a reaction coordinate as introduced in the work of Peters. [42,53,54] If this variable is unknown, all degrees of freedom can be enhanced, for example by increasing the temperature as applied in replica exchange. [55–57] On the other hand, if this function is known, enhancement of the sampling can be limited to this collective variable. [39,42] Examples are umbrella sampling (US) [58–60], thermodynamic integration (TI) [61–67], metadynamics (MTD) [68–70] and variationally enhanced sampling (VES). [71–73] As not all collective variables are a good reaction coordinate, a good selection of the tested collective variable is tedious, but of utmost importance [53,54,74] and should fulfill three requirements of the reaction coordinate, namely: [53]

a. It should only depend on the instantaneous point in configuration space
b. It should vary monotonically while moving from the reactant over the transition state to the product
c. Projection of the free energy on the CV should result in a one-dimensional free energy profile with reduced dynamics which are consistent with the full phase space

Due to the importance of the used collective variable and enhanced sampling method [37], several collective variables, discussed in Section 2.4, and methods, discussed in Section 2.5, will be compared in this work. We will specifically investigate in how far the final reaction kinetics depends on the particular choice of CV.

As prescribed by step iii, the estimator to obtain the free energy from the sampling simulations needs to be chosen. Most sampling methods are correlated with a particular estimator. [43] Umbrella sampling uses several bias potentials from which the free energy surface (FES) is estimated with for instance the weighted histogram method (WHAM). [75,76] In the Blue Moon method, the FES can be reconstructed from the constrained simulations using

thermodynamic integration. [61] Furthermore, as metadynamics is based on adapting the bias potential by adding Gaussian hills, and variationally enhanced sampling on adapting the bias potential based on the variational principle, the inverted final bias can be used as an estimate of the FES. [68,70,72]

In this work, several enhanced sampling methods will be tested and benchmarked to the data available on the methylation of ethene. This reaction is taken as a case study as many experimental and theoretical reference data exist. [15–19] Since several collective variables can be distinguished to simulate this reaction, as discussed in Section 2.4, different CVs will subsequently be tested using umbrella sampling and compared by transforming the free energy profiles from one CV to another. This will allow us to study in how far the kinetic data depend on the specific choice of CV. Subsequently, the obtained barriers are validated by comparison with available static and experimental data. To compare with existing literature data, [15–19] the relation needs to be made between intrinsic and apparent reaction rates. Our MD results yield intrinsic free energy barriers and extra static calculations [9,47,77–79] are applied to overcome this hurdle and discussed in the last part of this work. The performed study presents a fundamental methodological benchmark for various enhanced MD techniques on an exemplary reaction within zeolite catalysis.

2. Computational details and theoretical background

2.1. Catalyst model

In this work, we investigate H-ZSM-5 (at 623 K), which is the same catalyst as in the data set obtained from literature which reports enthalpic reaction barriers of the methylation of ethene. [15–19] It exhibits the MFI topology which is characterized by a 3D network of sinusoidal and straight 10-ring channels leading to medium sized pores. [80] All simulations are performed using periodic DFT simulations with a unit cell of H-ZSM-5 consisting of 96 T atoms. In this unit cell, one silicon atom is replaced by an aluminum atom to create the Brønsted acid site (BAS). There is no simple rule for the occupation of Al atoms on the 24 distinguishable framework T sites, because it depends on the conditions of the zeolite synthesis. [81] Hence, the substitution is based on earlier work and performed at the T12 position at the intersection of the straight and sinusoidal channels. [50,82] The unit cell parameters used during the simulations depend on the used methods, as the unit cell used in the static calculations is optimized at 0 K, while the unit cell parameters for the dynamic simulations are equilibrated at 623 K. The equilibration procedures are described in Section 1 of the ESI. The resulting parameters are summarized in Table S 1 of the ESI.

2.2. Reference static calculations

Apart from the MD based simulations also reference static periodic Density Functional Theory simulations are performed [9,77–79] with the Vienna Ab Initio Simulations Package (VASP 5.3). [83–86] Furthermore, the revPBE functional [87] is chosen because of its improved performance for solid-state calculations compared to the commonly used PBE functional. [88] Additionally, Grimme D3 dispersion corrections are used to account for attractive London dispersion interactions. [89] Other interesting specifications are the use of the projector augmented wave (PAW) method, a plane-wave cutoff of 600 eV and a self-consistent field (SCF) convergence criterion of 10^{-5} eV. [90,91] During the VASP calculations, the Brillouin zone

is restricted to the Γ-point. Transition states are initially optimized with the improved dimer method of Heyden et al. [92] and then refined with a quasi-Newton algorithm as implemented in VASP. [93] Geometries are slightly displaced along the normal mode corresponding to the motion that leads the system over the barrier to generate starting geometries for the optimization of reactant and product states. For these calculations, a conjugate gradient algorithm is applied. [94]

Since partial Hessian vibrational analysis (PHVA) is shown to be an attractive alternative for computationally demanding full Hessian calculations (FHVA) for entropy calculations, this scheme is used for the normal mode analysis (NMA) in this work using TAMkin. [95,96] In a PHVA calculation, only a part of the system is taken into account during the NMA, namely the guest molecules and the 8T cluster of the framework around the active site indicated in Figure S 1 of the ESI.

2.3. Molecular dynamics

To equilibrate the volume and unit cell parameters at operating conditions, i.e. 623 K and 1 atm, regular ab initio molecular dynamics simulations in the NPT ensemble are performed using the CP2K software package. [97,98] During the ab initio MD simulations, the temperature is controlled by a chain of five Nosé-Hoover thermostats [35] and the pressure by an MTK barostat. [99] Again, the revPBE functional [87] is chosen because of its improved performance for solid-state calculations compared to the commonly used PBE functional. [88] Furthermore, the combined Gaussian and Plane Wave (GPW) basis sets approach is used. [100,101] The DZVP-GTH basis set and pseudopotentials [102] were used, and Grimme D3 dispersion corrections [89] are added. The time step for integration of the equations of motion is set to 0.5 fs. All systems are first equilibrated for 5 ps, followed by a production run of 50 ps used to average the unit cell parameters and volume. In all following regular and enhanced sampling MD simulations, the unit cell parameters and thus the volume is kept constant, leading to simulations in the

NVT ensemble, as explained in Section 1.2 of the ESI. Further details on the enhanced sampling MD simulations are given in Section 2.5.

2.4. Collective variables

2.4.1. Possible collective variables

Several collective variables can be proposed which may be used as suitable reaction coordinates to enhance sampling along the methylation reaction of ethene in HZSM-5. They are visually displayed in Figure 1, and may be classified in two types. One type (type CN) consists of coordination numbers (CNs) between two atoms describing the breaking and formation of the C-O and the C-C bond. [2,51,103] CN_{ij} represents the coordination number between the atoms i and j defined as:

$$CN_{ij} = \sum_{i,j} \frac{1 - \left(\frac{r_{ij}}{r_0}\right)^{nn}}{1 - \left(\frac{r_{ij}}{r_0}\right)^{nd}}$$

with r_{ij} the interatomic distance and r_0 the reference distance, set to 2 Å, which approximately represents the C-C distance in the transition state. Furthermore, the parameters nn and nd where chosen to be 6 and 12, respectively. As such, two collective variables are needed to describe the methylation reaction: CV1 being the coordination number CN_{OC} between the oxygen and carbon of the methanol (green and red in Figure 1) and CV2 being the coordination number CN_{CC} between the carbon of methanol and the two carbons of ethene (red and blue in Figure 1).

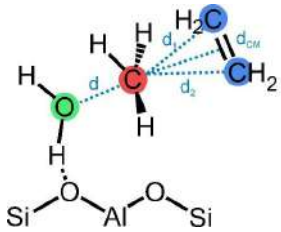

			CV1	CV2
Coordination numbers	Type CN		CN_{CC}	CN_{CC}
Distances	Type DI	DI	d	d_{CM}
		1D-DI	d_{CM}-d	-

Figure 1: Schematic representation of the collective variables used to describe the methylation reaction of ethene. There expected values at the reactant, transition and product state are summarized in Table S 1.

The second type (type DI) of collective variables is based on distances of the breaking and forming bonds. The first collective variable CV1 is simply the bond distance d between carbon and oxygen of the methanol. For the second collective variable CV2 the two carbon atoms of ethene (blue) need to be taken into account. We account for both by choosing the distance d_{CM} between the C of methanol and the center-of-mass of the ethene molecule.

Finally, we also introduce a one-dimensional collective variable (type 1D-DI), namely the difference d_{CM}-d between the two collective variables in variant DI. The option to choose a 1D-CV has the advantage that it seriously speeds up the sampling. [70] This 1D-CV is used in the first part of this work to compare the different enhanced sampling methods.

2.4.2. Transformations between various collective variables

When using different collective variables, one cannot straightforwardly compare free energies obtained in various CVs, as explained hereafter. Suppose one defines two sets of collective variables, q_1 and q_2, which have both the goal of describing the same process or reaction. If one would perform enhanced simulations using both collective variables, it would give rise two free energy profiles $F_{q_1}(q_1)$ and $F_{q_2}(q_2)$, which can in general not be compared directly since different collective variables give rise to different integrations over microstates. However, if both collective variables indeed describe the same process, they are expected to be correlated and the free energy profiles should be related to each other. By means of

statistical mechanics, as shown in Section 6 of the ESI, one can show that a free energy profile in terms of one collective variable can be transformed to a free energy profile in terms of another collective variable as:

$$F_{q2}(q_2) = -k_B T \ln\left(\frac{q_{20}}{q_{10}} \int_{-\infty}^{+\infty} p_{2|1}(q_2|q_1) e^{-\beta F_{q_1}(q_1)} dq_1\right)$$

Here, the factors q_{10} and q_{20} were introduced to keep the factor $\frac{q_{20}}{q_{10}} \int_{-\infty}^{+\infty} p_{2|1}(q_2|q_1) e^{-\beta F_{q_1}(q_1)} dq_1$ dimensionless. The derivation of the corresponding relation for 1D profiles is given in the work of Demuynck et al. [54] and its extension towards 2D profiles is summarized in Section 6 of the ESI. Furthermore, the corresponding expression for transforming a 1D profile to a 2D profile is also provided in the ESI.

Here, $p_{2|1}(q_2|q_1)$ is the conditional probability of the collective variable q_2 in terms of the collective variable q_1. The precision of this transformed free energy profile largely depends on the quality of the sampling of the phase space spanned by the variables q_1 and q_2. A sufficient sampling of q_2 coordinate for each relevant value of q_1 yields a proper conditional probability. In the frame of this work, it is useful to observe that the conditional probability can also be computed for simulations in which a bias along q_1 was applied (Section 6.2 of the ESI). The transformation is further illustrated in Figure 2 for the case of 1D profiles, in which the integral is represented as an average of the Boltzmann probability weighted by the conditional probability (indicated by the shaded area on the figure).

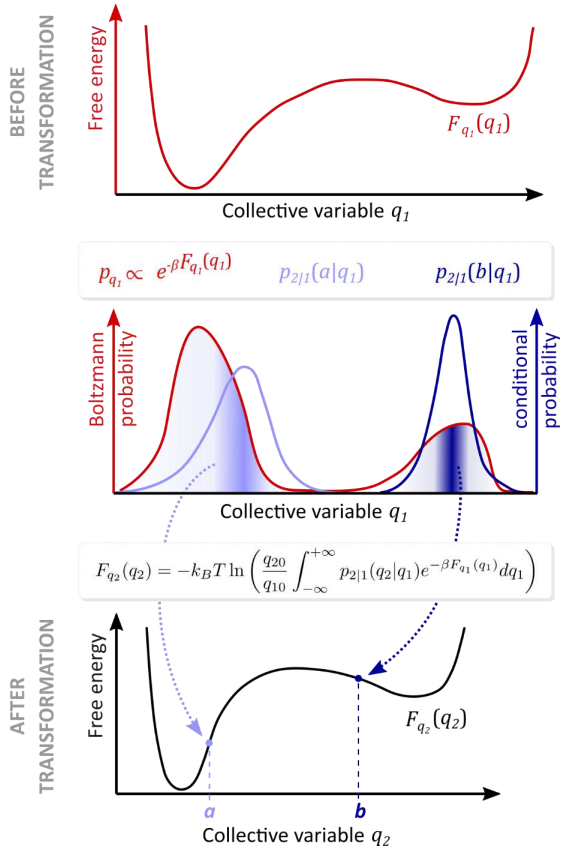

Figure 2 Graphical representation of a free energy profile $F_{q_1}(q_1)$, which was computed by sampling along q_1 and expressed as a function of q_1, and its transformation to the corresponding free energy profile $F_{q_2}(q_2)$ as a function of q_2. The integral can be interpreted as a weighted average of the Boltzmann probability, with weights given by the conditional probability and indicated through the shading in the middle pane.

Finally, a one-dimensional projection of the obtained 2D free energy profile $F_{12}(q_1, q_2)$ is performed, as a 1D-profile is more convenient to interpret. This can be done by fixing a new collective variable q as a function of q_1 and q_2 ($q = q(q_1, q_2)$), and to perform an integration of

the 2D probability distribution (also described in Section 6.4 of the ESI). Another alternative is the elaborated search for the lowest free energy path [104]. In this work, the 2D profile is projected on the difference between the two collective variables ($q = q_2 - q_1$) as:

$$F_q(q) = -k_B T \ln\left(\frac{q_0}{q_{10}q_{20}} \iint_{-\infty}^{+\infty} e^{-\beta F_{12}(q_1,q_2)} \delta(q_2 - q_1 - q) dq_1 dq_2\right)$$

$$= -k_B T \ln\left(\frac{q_0}{q_{10}q_{20}} \int_{-\infty}^{+\infty} e^{-\beta F_{12}(q_1,q_1+q)} dq_1\right)$$

2.5. Enhanced sampling methods

In rare events – such as the methylation reaction on ethene in H-ZSM-5- regular MD simulations fail in sufficiently sampling the entire configuration space as metastable states are separated by free-energy barriers which lie on the basis that highly activated regions are not visited. A variety of enhanced sampling techniques are available in literature. [38–41] In this work only a selection is made of all these methodologies and these are summarized in Figure 3. We only retain those methods which enhance the sampling along certain degrees of freedom, the so-called collective variables. The concept in all selected methods is based on the introduction of a bias potential allowing a decent sampling of all important and relevant regions of the configuration space. The way such a bias potential is introduced can vary per method.

The enhanced sampling simulations are performed using the CP2K software package [97,98] interfaced with the advanced simulations library PLUMED. [105] The simulations are performed in the NVT ensemble at 623 K. The temperature is again controlled by a chain of five Nosé-Hoover thermostats. [35] Time-averaged cell parameters obtained from the NPT runs are used as constant values as summarized in Table S 1 of the ESI. The remainder of the settings are kept the same as for the MD simulations described in Section 2.3.

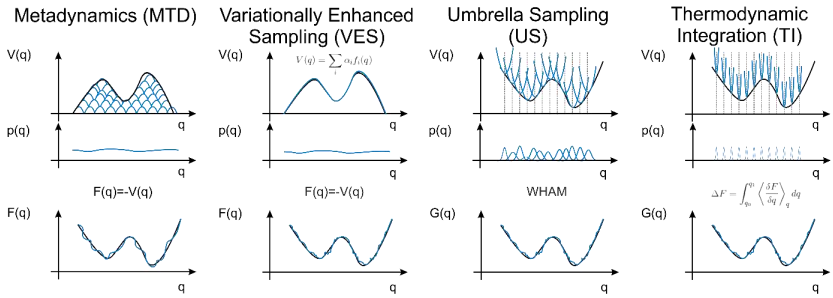

Figure 3: Schematic representation of the enhanced sampling methodologies considered in this work, namely metadynamics (MTD), variationally enhanced sampling (VES), umbrella sampling (US) and thermodynamic integration (TI). [42]

2.5.1. Metadynamics

In this method the bias potential is constructed on the fly by gradually adding Gaussian shaped hills. The bias potential $V_G(q,t)$, after the simulation becomes then the sum of all Gaussians: [106]

$$V_G(q,t) = h \sum_{\substack{t'=\tau_G,2\tau_G,\dots \\ t'<t}} \exp\left(-\frac{(q-q(t'))^2}{2\,w^2}\right)$$

The amplitude h and width w of the Gaussian contributions, which are added to the system after each time interval τ_G, are systematically updated during the simulation, to allow for an accurate and fast convergence. This sampling technique has been first proposed by Laio et al. [68,69] After a sufficiently long simulation time, the bias potential is related to the free energy $F(q)$ via:

$$\lim_{t\to\infty} V_G(q,t) \sim -F(q)$$

The FES of the system can be reconstructed based on an inversion of the time dependent bias potential as displayed in Figure 3.

Computational details of this metadynamics (MTD) technique as applied in this work are the following. We directly constructed a one-dimensional free energy surface, by selecting a 1D reaction coordinate (1D-DI in Figure 1). The initial height of the Gaussian potentials is set to 5 kJ/mol and after each recrossing of the transition point, the height of the added Gaussian hills is adequately halved to enhance the FES convergence, until a value of 0.3125 kJ/mol was obtained. A new hill was spawned every 100 time steps. The width of all Gaussians is set to 0.04. The integration time step is set to 0.5 fs for all MTD simulations. Furthermore, quadratic walls were used to restrict the simulations to an area of interest on the FES, by limiting the diffusion of ethene and the formed water. Therefore, a quadratic upper wall is added at a value of 3.0 Å and a quadratic lower wall at -0.25 Å both with a force constant equal to 2000 kJ/(mol*Å²).

2.5.2. Variationally enhanced sampling

Variationally enhanced sampling (VES) is a relatively new enhanced sampling technique introduved by Valsson and Parrinello [72] and recently applied in the construction of free energy profiles in structural transformations taking place in flexible MOFs. [42] The variational principle embedded in VES allows to introduce an arbitrary target distribution $p(q)$ that specifically target the region we are interested in. The bias potential $V(q)$ is constructed variationally by minimizing a functional of the bias potential:

$$\Omega[V] = \frac{1}{\beta}\ln\left(\frac{\int \exp(-\beta[F(q)+V(q)])\,dq}{\int \exp\big(-\beta F(q)\big)\,dq}\right) + \int p(q)V(q)dq$$

It can be shown that this functional is convex with a minimum at:

$$V(q) = -F(q) - \frac{1}{\beta}\ln(p(q))$$

The free energy $F(q)$ can thus be calculated from the target distribution and the bias. An additional aspect of VES is that the minimization of the functional $\Omega[V]$ is equivalent to

minimizing the Kullback-Leibler divergence between the sampled distribution p_b and the target distribution p:

$$KL\langle p|p_b\rangle = \int p(q) \ln\left(\frac{p(q)}{p_b(q)}\right) dq$$

Subsequently, the variational principle can be introduced by expanding the bias potential $V(q)$ in some basis functions $f_i(q)$, which in our work are Legendre polynomials:

$$V(q) = \sum_i \alpha_i f_i(q)$$

with expansion coefficients α_i. The expansion coefficients which minimize the functional $\Omega[V]$ can then be obtained via an efficient stochastic gradient descent algorithm. [107] Once convergence is reached, the bias potential is in a quasi-stationary state. The advantage of this method is its flexibility. There is a large flexibility in choosing the target distribution, which allows us to tailor the sampling.

In the simulations performed in this work, a uniform target distribution was chosen. Furthermore, Legendre polynomials of the 25th order are chosen as basis set. For the optimization algorithm, two parameters need to be chosen, namely the stride and step size. The stride is set to 100 steps as was done for the metadynamics simulations. The stepsize is first set to 5.0 kJ/mol and after some recrosses lowered to 1.0 kJ/mol, to have a similar procedure as in the metadynamics simulations. The same walls as in the metadynamics simulations are introduced to limit the sampling to the region of interest.

2.5.3. Umbrella sampling

In umbrella sampling (US) an external potential is added to the true Hamiltonian to enhance the sampling in low probability regions. The external potential depends on the collective variable q. The free energy $F(q)$ of the unbiased system can be obtained from the free energy of the biased system $F_b(q)$:

$$F_b(q) = F(q) + V_b(q)$$

In order to perform a decent sampling of all important regions of the configuration space, the reaction path is divided into distinct windows, as shown in Figure 3. In each window, the reaction coordinate is restrained to a target value q_i by applying a bias potential on each window. Often, a harmonic bias potential with force constant K is used to keep the system close to the target value:

$$V_i(q) = \frac{K}{2}(q - q_i)^2$$

In each window, the system mainly samples perpendicular to the collective variable. After the simulations have run, the probability distribution of all windows is combined to a total distribution function using the weighted histogram analysis (WHAM) method. [75,108]

To create the snapshots used as a starting point for each window, a moving restrained MD simulation is used in which a bias potential is moved from one minimum to the other. Along this trajectory, 34-46 umbrellas are selected as summarized in Table S 2 (ESI) giving the location for each window. Subsequently, a restrained ab initio MD simulation of 50 ps is run for each umbrella to ensure sufficient sampling and overlap between the different windows. During umbrella sampling simulations, the force constants, K, are set to 1500 kJ/mol for the coordination numbers or 1500 kJ/(mol*Å²) for most windows in case distances are used. Windows with lower force constants are added to the reactant region when using distances as collective variables to sample the broadness of the reactant region. In those cases, the force constants are added between brackets in Table S 2 (ESI).

2.5.4. Thermodynamic integration

It is a general approach that can be regarded as a method to calculate free energy differences in constrained molecular dynamics. The constraint is imposed on the reaction coordinate q and on each point along the path $[q_0, q_1]$ the mean force is calculated being the

ensemble average of the constrained MD. It contains two contributions: a force due to the potential energy and a force due to the constraint.

The free energy difference between two configurations belonging to reaction coordinates q_0 and q_1 is then given by

$$\Delta F(q_0, q_1) = \int_{q_0}^{q_1} \langle \frac{\delta F}{\delta q} \rangle_q \, dq$$

in which $-\frac{\delta F}{\delta q}$ is the force needed to maintain the reaction coordinate constraint during the simulation. The constraint is imposed during the MD by placing strong quadratic potentials.

In this work we keep the 40 windows (not including the broad reactant state windows) along the reaction coordinate which have been introduced during the umbrella sampling simulations of type 1D-DI, but the force constant K is set an order of magnitude higher. Again, 50 ps restrained MD simulations for each window are performed over which the mean force is calculated. The use of a distance as a constraint allows to omit terms that unbias the measured force to that of the unconstrained ensemble, thus simplifying these simulations. [65,109]

3. Results and Discussion

Before selecting the most appropriate sampling method and reaction coordinate, we first make an assessment of the performance of the various enhanced sampling techniques which have been proposed in the previous sections. [38–40,42] Subsequently, the different types of collective variables to describe the methylation of ethene, are also applied in the advanced MD runs.

3.1. The influence of the enhanced sampling method on the intrinsic barrier

Four enhanced sampling methods are considered here, namely metadynamics (MTD), variationally enhanced sampling (VES), umbrella sampling (US) and thermodynamic integration (TI). For the selection of the most appropriate method, the sampling is performed using the one-dimensional collective variable, denoted type 1D-DI in Figure 1. This CV has two advantages. First of all, the use of a distance as a constraint allows to omit terms that unbias the measured force to that of the unconstrained ensemble in the thermodynamic integration simulations, thus simplifying these simulations. [65,109] Secondly, as the efficiency of methods like metadynamics scale exponentially with the number of collective variables, the 1D CV will speed up these simulations substantially. [70] The resulting free energy profiles are depicted in Figure 4 together with an estimation of the corresponding errors. The procedures for error estimation are discussed in Section 4 of the SI.

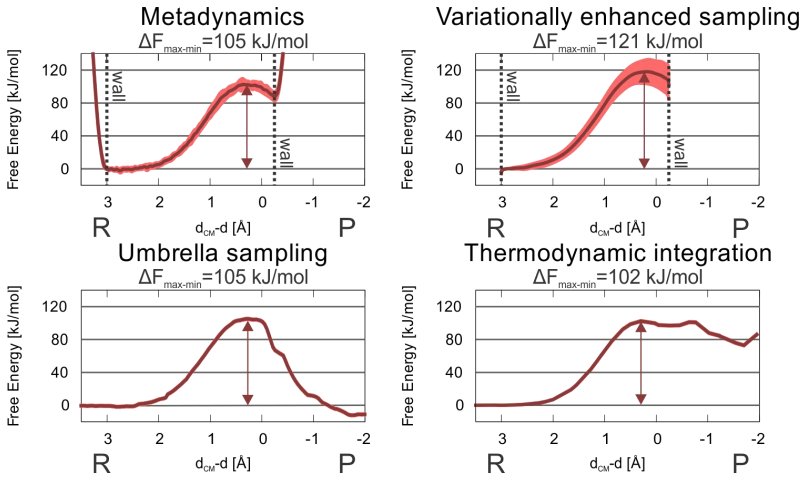

Figure 4: Free energy profiles and error bars at 623 K in function of the one-dimensional collective variable 1D-DI obtained with different enhanced sampling methods. Furthermore, the minimum-maximum barrier is shown on the graphs for each method. The reactant (R) and product (P) side of the reaction are also indicated. The error estimation is discussed in Section 4 of the ESI.

Several interesting conclusions can be drawn from Figure 4. First, the VES result is distinct from the other sampling techniques by a higher forward barrier, as indicated in the subtitles of Figure 4 (120 kJ/mol instead of 100 kJ/mol) and higher error bars. This is not conform the standard performance of VES in other benchmark studies, where free-energy profiles are constructed for structural transformations in MOFs with the volume of the unit cell as a perfect one-dimensional collective variable. [42,72] Thus, insufficient sampling could be on the basis of this discrepancy. In addition, the VES protocol requires several barrier recrossings to obtain converged free energy estimates, similar as in metadynamics. For this specific reason, two walls are placed at some specific values of the one-dimensional collective variable (d_{CM}-d) , as indicated in Figure 4, to oppose the diffusion of ethene on the one hand, and to avoid sampling of the product state on the other hand, as several products can be formed, e.g. propene, cyclopropane, propoxide, propanol… These auxiliary tools are not needed in US and TI in this specific application, and therefore US and TI are preferred over MTD and VES. This conclusion

is in contrast to earlier work of the current authors, [110] where MTD was preferred over US, as for the system under study there, the disadvantage of using walls was outweighed by the fact that less prior knowledge on the reaction path is needed within MTD. [111] As the walls necessary for the system used here are more stringent, the methods which do not use walls are preferential.

When concentrating on the reactant side of the reaction the free-energy profiles for US and TI, these show large similarities with a forward barrier of about 100 kJ/mol. We don't focus on the product side of the reaction, as several product states are sampled in the US and TI simulations due to the instability of the primary product, protonated propene, as discussed in Section 5 of the SI, giving rise to the discrepancies observed for the two techniques. The lower force constants used in US allow to converge to a more stable product, while the TI runs are stuck in a less stable product.

As we are only interested in the forward barrier, no preference is given to one of both techniques. However, in the execution of the TI method correction factors need to be incorporated in the computation of the sampled mean force when coordination numbers are considered as collective variables. [65,109] US is free of this cumbersome task and therefore selected as the most appropriate method. A similar conclusion was made by an earlier benchmark study where force fields were used to compare the efficiency of enhanced sampling techniques in the construction of free energy profiles for breathing metal-organic frameworks. [42] Nevertheless, it should be noted that this choice largely depends on the system under study. We will systematically make use of this methodology to assess the influence of collective variables discussed in the next paragraph.

3.2. The influence of the collective variable on the intrinsic barrier

Several suggestions of suitable collective variables to describe the methylation of ethene in H-ZSM-5 are proposed in Figure 1. We distinguish between two types of collective variables.

The first type consists of coordination numbers (CNs) used as a reaction coordinate describing the breaking and formation of the C-O and C-C bond. [2,51,103] The second type of CVs consists of distances between the atoms of the breaking and forming bonds.

We will analyze the influence of the collective variable on the free energy profile using US, as this technique is selected as the most appropriate method for the envisaged application in this work. Umbrella sampling simulations are performed along the various classes of CVs introduced in Figure 1. The collective variables of type CN and DI are two-dimensional, and the free-energy surface should be projected into a 1D-profile which can be done by integration of the 2D probability distribution also defined in Section 2.4.2. This results into the 1D free-energy profiles displayed in Figure 5. The plots clearly show that the free energy profiles in terms of the various collective variables have not only different shapes but also different barriers if they are determined by the energy gap between the maximum and the minimum of the profile as done in earlier work. [79] For Type CN a barrier of ± 127 kJ/mol is observed, while in the type DI collective variables the barrier is systematically lower (± 100 kJ/mol).

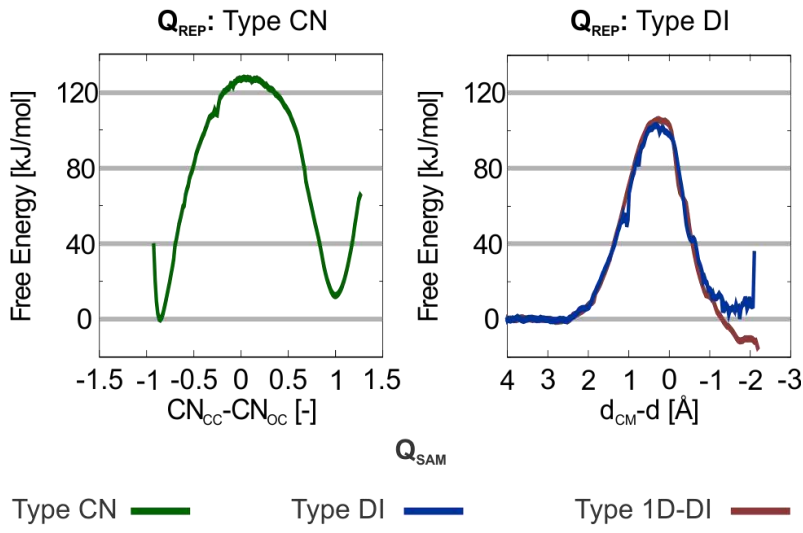

Figure 5: Free energy profiles at 623 K obtained by sampling in the different collective variable spaces (Q_{SAM}), namely Type CN (green), Type DI (blue) and Type 1D-DI (red) and represented (Q_{REP}) in Type CN (left panel) and Type DI (right panel). As discussed in Section 2.4, the profiles for Type CN and Type DI are obtained by sampling in a 2D collective variable space followed by a projection of the free energy surface on a 1D-profile.

To enable direct comparison of the free energy profiles obtained by sampling in different collective variable spaces, the transformations defined in Section 2.4.2 need to be applied. From here on, we will distinguish between the collective variable in which the sampling is performed during the simulation, labeled Q_{SAM}, and the collective variable Q_{REP} in which the free energy profile is plotted. Q_{REP} does not necessarily coincide with Q_{SAM}, as a transformation of the free energy profile can be performed. In Figure 6, both the free energy profile in function of the original collective variable (Q_{SAM}), also shown in Figure 5, and the transformed profiles are shown. The procedure is illustrated for the free energy profile in function of the reaction coordinate CN_{CC}-CN_{OC} shown in the left panel of Figure 6. A direct way is an US simulation in a two-dimensional grid of collective variables CN_{CC} and CN_{OC} and a reduction to the 1D-profile yielding the green profile in the left panel of Figure 5 and Figure 6. In this case, the sampled

collective variable (Q_{SAM}) is thus of type CN and the collective variable used to represent the free energy profile (Q_{REP}) is the difference between CN_{CC} and CN_{OC}. It yields the reference profile in this category. On the left panel of Figure 6, also the transformed profiles are shown, where first an US simulation is done on a one- or two-dimensional grid of collective variables of type 1D-DI or DI (Q_{SAM}), which are afterwards transformed to a 2D-profile with CN_{OC} and CN_{CC} as 2D reaction coordinates. Finally, the 2D-profile is reduced to the 1D-profile with CN_{CC}-CN_{OC} as Q_{REP}. This yields the blue and red profile in the left panel of Figure 6. Their accuracy depends on the conditional probability $p_{2|1}(CN_{OC}, CN_{CC}|d_{CM} - d)$ or $p_{2|1}(CN_{OC}, CN_{CC}|d, d_{CM})$, which should be extracted from the 1D or 2D simulations. A similar protocol is applied for the free energy profiles in the right panel of Figure 6.

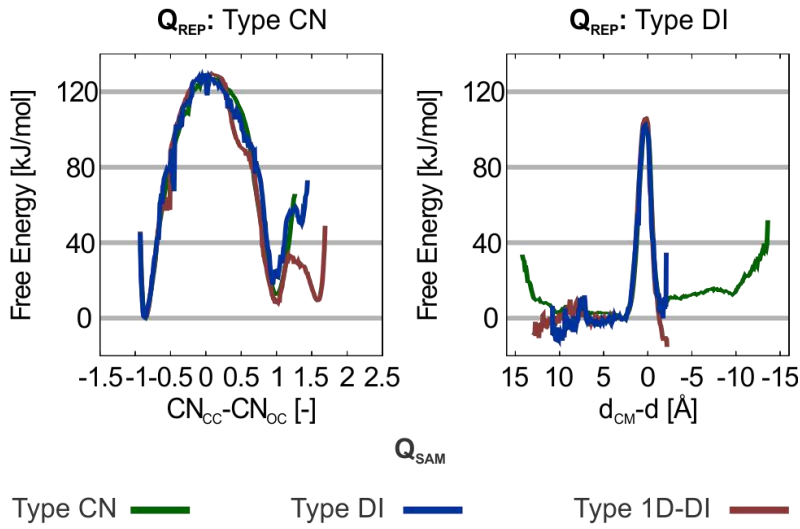

Figure 6: Free energy profiles at 623 K in function of 1D-CVs (Q_{REP}) defined as the difference in coordination numbers (CN_{CC}-CN_{OC}, left panel) or in distance (d_{CM}-d, right). Left panel: plots belonging to CVs Type 1D-DI and Type DI are obtained after transformation as explained in the text. Right panel: plots belonging to Type CN are obtained after transformation as explained in the text.

It is important to note that the energy profiles between the reactant valley and the transition state region all coincide quite nicely, after applying the transformations. The most accurate plot should correspond with the profile expressed in the same CV space, wherein the sampling has been accomplished. The product region does not coincide. However, if the sampling is sufficient, the profiles should nearly coincide after applying the transformation. The discrepancy is inherently related to the rather unstable carbocations formed after the methylation, which transform into various intermediates, such as propene, cyclopropane, propoxide, propanol… As a result, the product region is not equally well sampled in the various simulations. We will no longer focus on this issue since this is not the scope of this work.

There are some interesting features regarding the shape of the profiles which require some attention. The $F(CN_{CC} - CN_{OC})$ profile shows a thin well for the reactants, predicted by all the types of CVs, while in the $F(d_{CM} - d)$ profiles a broad range of configurations is observed. This can partly be ascribed to the way a coordination number is determined by the bond distance, as given in Eq. (1). In the reactant valley the distance d in the methanol is of the order of 1 Å, giving a coordination number of $CN_{OC} \sim 1$, while the distance between methanol and ethene (reflected by d_{CM}) can amount to several Ångström, without affecting the coordination number CN_{CC} (see Figure S 8). This last number remains zero, and this is further illustrated by the mobility pots of methanol and ethene in the reactant state (Figure S 9). In the enhanced sampling simulations using coordination numbers as collective variables (Type CN) we observe a large mobility of the ethene molecule. This is reflected into a broad valley of distances d_{CM}-d after transformation from coordination number space to distance space, as the free energy relates to the probability to sample a state.

Summarizing, different collective variables may be used, in principle, which all lead to specific free energy profiles. However, if sampling is sufficiently done, they are all exactly reproduced by application of proper transformations. In the subsequent section, we further use this knowledge to describe the reaction kinetics properly.

3.3. Reaction kinetics

Previous analysis suggests that the configurational freedom in the reactant and transition state should be accounted for in order to obtain proper reaction rates. This can be done by defining transition rates instead of free energy barriers to get a collective variable independent measure to compare the speed of different reactions as explained hereafter and derived in detail in Section 10 of the SI.

Transition state theory allows to derive an expression for the rate of a reaction $R \rightarrow P$ based on the definition of the transition state as a dividing surface separating the reactants (*R*) from the products (*P*). [112–116] The theory is based on some key assumptions among which: (1) thermodynamic equilibrium must prevail throughout the entire system for all degrees of freedom and (2) any trajectory crossing the dividing surface will not turn back to the reactant valley or recross the dividing surface. The expression for the reaction rate can be written as: [117]

$$k = \sqrt{\frac{1}{2\pi\beta}} \cdot \frac{\int \delta(q(\vec{x}^N) - q^*) \left|\vec{\nabla}_x q\right| e^{-\beta U(\vec{x}^N)} d\vec{x}^N}{\int_R e^{-\beta U(\vec{x}^N)} d\vec{x}^N}$$

Herein, q is a function of the molecular configuration, represented by the mass-weighted coordinates $\vec{x}^N$, and describes the progress along the reaction, q^* represents its value in the transition state, δ represents the Dirac delta function and the integral in the denominator runs over all reactant states, i.e. for $q(\vec{x}^N) < q^*$. If the system under consideration would only have a single degree of freedom, this formula reduces to the well-known expression from classical transition state theory. Starting from previous expression, it is further rewritten in terms of the free energy profile $F(q)$ computed by means of the enhanced sampling molecular simulations:

$$k = A\frac{e^{-\beta F(q^*)}}{\bar{Z}_R} = \frac{1}{\sqrt{2\pi\beta}} \langle \left|\vec{\nabla}_x q\right| \rangle_{q^*} \cdot \frac{e^{-\beta F(q^*)}}{\int_{-\infty}^{q^*} e^{-\beta F(q)} dq}$$

with $\beta = \frac{1}{k_B T}$. Herein, A represents a prefactor which can be computed from molecular simulations and is expressed in terms of the gradient of the collective variable, which in turn is related to the rate of change of the collective variable, evaluated at the transition state. Therefore, it mainly depends on the width of the transition state region. The factor $e^{-\beta F(q^*)}$ is expressed in terms of the maximum of the free energy profile in terms of the collective variable in the transition state region. Together with A, it contains information on the stability of the transition state. Finally, $\bar{Z}_R$, which has a dimension identical to that of the collective variable, is proportional to the partition function of the reactant and yields information on the width and depth of the free energy profile in terms of the collective variable in the reactant region. More details can be found in Section 10 of the ESI. We computed the rate constants according to this equation for the methylation reaction and investigate the influence of the choice of the collective variable. As stated earlier, the enhanced sampling simulations were performed using the various collective variable(s). The collective variable(s) employed to act as reaction coordinate(s) during the enhanced sampling simulations is denoted as Q_{SAM}. Second, the resulting free energy profile can be expressed in terms of this same collective variable – in this case $Q_{REP} = Q_{SAM}$ –, but it can also be transformed to a profile in terms of one of the other CVs. The table below tabulates the rate constant for various combinations of Q_{SAM} and Q_{REP}. Each row reports the rate constants derived from MD simulations based on the same type of collective variables.

Table 1: Reaction rate k (in 1/s) at 623 K.

Q_{SAM} \ Q_{REP}	**CN_{cc}-CN_{OC}**	**d_{CM}-d**
Type CN	1.58 10^3	2.83 10^3
Type DI	1.14 10^3	8.82 10^2
Type 1D-DI	9.74 10^2	5.95 10^2

Inspection of all values reported in Table 1 learns that all reaction rate constant are differing only less than one order of magnitude, [16] even though the free energy barrier by subtracting the minimum from the maximum itself was dependent on the choice of the collective variable as illustrated previously and summarized in Table S 5 of the ESI. Since the rate constant represents a macroscopically measurable quantity, it should indeed be independent of the way we describe it microscopically. Therefore, one cannot simply rely on the free energy barrier to make statements on how fast a reaction will occur. Instead, one needs to compute all contributions to the reaction rate consistently. By calculating the rate expression, we are also accounting for the width and the depth of various parts of the $F(q)$ profile. Finally, the impact of Q_{SAM} , the CV used to perform the enhanced sampling, can also readily be extracted from Table 1, by examining the reaction rates belonging to a single column. The influence is also rather limited, indicating that each CV succeeds in a correct description of the reaction and associated reaction rate.

By comparing the formula for the reaction rate with the Eyring-Polanyi equation [118], a phenomenological free energy barrier ΔF can be introduced, as was done earlier by Bučko et al. [119] and the current authors:[110]

$$\Delta F = F(q^*) + k_B T \ln\left(\frac{k_B T \bar{Z}_R}{hA}\right)$$

The resulting values are summarized in Table 2, and surprisingly they are very similar within a range of 7%. We may conclude that the phenomenological free energy barrier associated to a chemical process, which in this example stands for the methylation of ethene in H-ZSM-5, represents a quantity which is independent of the choice of the collective variable used during sampling (Q_{SAM}) of the configuration space. It is a more correct and physical representation of a barrier than the difference between maximum and minimum on a free energy profile along a certain collective variable, which largely depends on the choice of this last coordinate, as demonstrated in this paper.

Table 2: Phenomenological free energy difference obtained via $\Delta F = F(q^*) + k_B T \ln\left(\frac{k_B T \bar{Z}_R}{hA}\right)$ (in kJ/mol) at 623 K.

Q_{SAM} \ Q_{REP}	CN_{CC}-CN_{OC}	d_{CM}-d
Type CN	118.3	115.2
Type Da	120.0	121.3
Type Da-1D	120.8	123.3

To test the reliability of the results, they are submitted to a committor analysis in Section 11 of the ESI. A molecular dynamics simulation is performed using the obtained free energy profile as a bias, as discussed in Section 12 of the ESI. Furthermore, the results are compared to available data of literature. The latter is discussed in the following Section.

3.4. Comparison to theoretical and experimental literature data

Reliable intrinsic rates and free energy barriers could be obtained irrespective of the collective variable provided proper transformations between the collective variables are applied and provided we account for the width and the depth of various parts of the $F(q)$ profile. At this moment, it is instructive to compare the here obtained rates and free energies with earlier literature data. The methylation of ethene in H-ZSM-5 has been the topic of various comparative studies [15–17] with experimental kinetic data. [18,19] Experimentally, one obtains apparent rates, which are in this case referred to the state where methanol is adsorbed on the Brønsted acid site while ethene is still in the gas phase. Indeed, the reaction was determined to be zeroth order with respect to methanol and first order with respect to ethene [18,19] and could be described by the following rate equation:

$$r = k p_{methanol}^{0} p_{ethene}^{1}$$

with $p_{methanol}$ and p_{ethene} the partial pressures of methanol and ethene. The reaction rate constants obtained here with the MD approach correspond to intrinsic kinetics where all reactants, thus methanol and ethene, are adsorbed on the zeolite. These values cannot directly be compared with experiment. However, in ref [15] also intrinsic rates were reported using at that time a rigid rotor harmonic oscillator model and a finite cluster model consisting of 46 T atoms. At the ONIOM(B3LYP/6-31+g(d):HF/6-31+g(d))-D//ONIOM(B3LYP/6-31+g(d):MNDO) level of theory a value of 5.5 10^3 s^{-1} at 623 K for k_{int} was obtained, which is in very good agreement with the values obtained here (Table 1).

It is however interesting to also compare with the values of Svelle et al. [17] and Piccini et al. [16] Svelle et al. who used a composite scheme to obtain apparent enthalpy barriers with chemical accuracy, whereas Piccini et al. used anharmonic corrections to get better estimates of the pre-exponential factor. In previous methods, no molecular dynamics simulations were done to sample the configurational space. A direct comparison with the values of Svelle and Piccini is hampered as they did not report intrinsic free energy barriers or intrinsic reaction rates. This makes a direct comparison very difficult, as there are no generally accepted methodologies to extract enthalpic barriers and adsorption enthalpies from ab initio molecular dynamics methods. To allow a comparison with experimental data and earlier theoretical data, we calculated the co-adsorption free energy for ethene $\Delta G_{ads,ethene}$ from static periodic DFT calculations and determined the apparent rate constant k_{app} based on the equilibrium constant K_1 as: [120]

$$k_{app} = K_1 k_{int}$$

This formula is derived in Section 13 of the ESI. The two adsorbed complexes [Z-H,CH_3OH(ads),ethene(g)] and [Z-H,CH_3OH(ads), ethene(ads)] are in equilibrium determined by the equilibrium constant:

$$K_1 = V_0 \exp(-\frac{\Delta G_{ads,ethene}}{RT})$$

with V_0 the molar volume of an ideal gas which equals 0.0518 m³/mol at 623 K and 1 atm, R the gas constant and introducing the co-adsorption free energy $\Delta G_{ads,ethene}$ of ethene as illustrated in Figure 7 and further discussed in Section 13 of the ESI.

The computation of a co-adsorption energy is always very sensitive to the used level of theory and in particular to the selected dispersion scheme. Large variations are common practice in this field, and to get a reliable estimate about the spreading of the adsorption energies we performed single point energy calculations with a whole set of functionals and dispersion schemes frequently used in literature [47,77] starting from optimized structures obtained using revPBE-D3. These calculations are discussed in detail in Section 13 of the ESI. Co-adsorption electronic energies are found in the range of -11 to -37 kJ/mol , thus corresponding quite well with the experimental co-adsorption enthalpies -24 – -31 kJ/mol. [17,121] The two extreme values are taken up in Table 3, as well those results corresponding to revPBE-D3 and the hybrid method B3LYP-D3.

Table 3: Apparent reaction rate constants in 1/(s.mbar) at 623 K for the methylation reaction of ethene derived from the expression $k_{app} = K_1 k_{int}$. For the intrinsic rate constants only the smallest and the highest values of the predictions in Table 1 are considered. A selection of four co-adsorption energies of ethene is retained from the list obtained with various levels of theory (Table S 11 of the ESI): the smallest adsorption energy (lower limit) is predicted by revPBE-dDsC, [122,123] while the upper limit is delivered by vdW-DF. [124,125]

	Lower limit	B3LYP-D3	revPBE-D3	Upper limit	Lower limit	B3LYP-D3	revPBE-D3	Upper limit	exp
k_{int}	$5.95\ 10^{2}$				$2.83\ 10^{3}$				
$\Delta E_{ads,ethene}$ [kJ/mol]	-11.0	-20.3	-22.7	-36.8	-11.0	-20.3	-22.7	-36.8	-24 – -31 [17,121]
$\Delta G_{ads,ethene}$ [kJ/mol]	41.7	32.5	30.1	16.0	41.7	32.5	30.1	16.0	
K_1 [m³/mol]	$1.64\ 10^{-5}$	$9.75\ 10^{-5}$	$1.57\ 10^{-4}$	$2.35\ 10^{-3}$	$1.64\ 10^{-5}$	$9.75\ 10^{-5}$	$1.57\ 10^{-4}$	$2.35\ 10^{-3}$	
k_{app} [m³/(mol.s)]	$9.76\ 10^{-3}$	$5.8\ 10^{-2}$	$9.31\ 10^{-2}$	1.40	$4.64\ 10^{-2}$	$2.76\ 10^{-1}$	$4.43\ 10^{-1}$	6.64	
k_{app} [1/mbar.s)]	$1.88\ 10^{-4}$	$1.12\ 10^{-3}$	$1.80\ 10^{-3}$	$2.69\ 10^{-2}$	$8.96\ 10^{-4}$	$5.33\ 10^{-3}$	$8.55\ 10^{-3}$	$1.28\ 10^{-1}$	$1.95\ 10^{-4}$ [18]

The difference running up to 25 kJ/mol leads to two orders of magnitude variation in the equilibrium constant, indicating that prudence is required in making conclusions when

assessing apparent kinetics extracted from intrinsic rate constants. Nevertheless we take note that the experimental value of 1.95 10^{-4} (mbar s)$^{-1}$ [18] is within the theoretically proposed range of values (see Table 3). Looking more closely to the revPBE-D3 results, which are used in both the static as the dynamic simulations, values ranging from 1.8 10^{-3} to 8.55 10^{-3} (mbar s)$^{-1}$ are attained, on the verge of kinetic accuracy.

The results discussed here thus show that by combining static and enhanced sampling methodologies, one can almost attain kinetic accuracy, although the selection of DFT functional and dispersion scheme remains a crucial factor in the finally attained accuracy. As such, further testing and benchmarking of both static and enhanced sampling methodologies for zeolite catalysis remain essential for the development of a generally applicable quantum mechanical methodology.

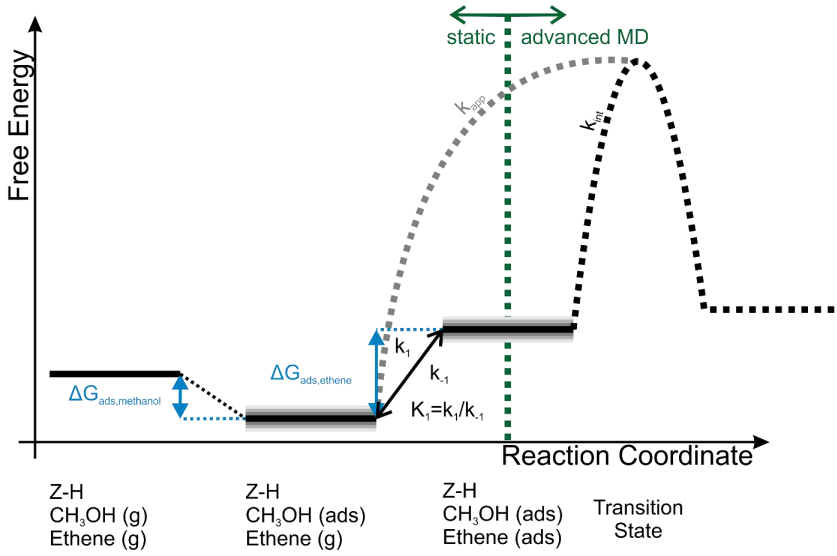

Figure 7: Schematic representation of the relation between apparent and intrinsic kinetics. For the calculation of $\Delta G_{ads,ethene}$ various schemes are used, shown by the grey uncertainty in the co-adsorption step of ethene. The value of k_{int} is obtained dynamically in this work.

4. Conclusion

In this work, we thoroughly studied the methylation of ethene in H-ZSM-5 in the framework of the MTO process with enhanced sampling MD techniques. The reaction at hand is one of the best characterized reactions both from theoretical and experimental viewpoint within zeolite science. In this work we presented a protocol in which the kinetics of the reaction can be described independent of the choice of the collective variable representing the reaction coordinate and the enhanced sampling technique.

This work consists of different parts, each with a specific task in the determination of the final optimal protocol to describe the kinetics of a reaction. In the first part, the forward intrinsic methylation free energy barrier was calculated using four enhanced sampling techniques, namely metadynamics, variationally enhanced sampling, umbrella sampling and thermodynamic integration. The four different methodologies give similar results, though some had disadvantages compared to others. The most favorite technique cannot uniquely be propagated. Advantages/Disadvantages are strongly dependent on the specific type of the reaction. In the study of the methylation reaction of ethene, MTD and VES techniques require the introduction of walls to limit sampling in the region of interest, which is not trivial without prior knowledge of the position of the transition state and interesting reactants. TI had the disadvantage that correction factors are needed to go from the sampled mean force to the unbiased ensemble when not using distances as CV. [65,109] Therefore, umbrella sampling was selected as the most appropriate technique to further study the methylation of ethene.

In the second part, several collective variables were proposed which could differentiate between the reactant, transition and product state of the studied methylation reaction, and their influence on the free energy barrier was subsequently examined. Therefore, three types of collective variables were defined, and the resulting free energy profiles were compared. We have proven the importance of transformation from one collective variable space to another. Nevertheless, the free energy profile still depends on the collective variable used to represent

it and a collective variable invariant measure is necessary for enhanced sampling to be competitive with static methodologies. Therefore, reaction rates were introduced which demonstrated the importance of accounting for the configurational freedom in the reactant state when calculating free energy barriers from enhanced sampling simulations. This procedure led to reaction rates and phenomenological free energy barriers which are nearly independent on the particular choice of the collective variable.

Finally, we validated our resulting intrinsic reaction rate constants by comparison with theoretical and experimental data available in literature. Our data correspond very well with the intrinsic reaction rate constant of 5.5 10^3 1/s at 623 K reported by Van Speybroeck et al. [15]. Direct comparison with other theoretical work and experimental work was impeded, as only apparent rates were reported in literature. These apparent kinetics were related with Intrinsic kinetics extracted from the advanced MD simulations by the equilibrium constant for the co-adsorption of ethene which can be calculated using static DFT approaches. By taking into account a whole set of functionals and dispersion schemes a range of apparent rate constants is extracted, including the experimental value of 1.95 1/(mbar.s). When consequently using revPBE-D3 in both the static and enhanced sampling simulations, results within the range of kinetic accuracy is obtained.

The results presented in this work show that ab initio enhanced sampling techniques have the potential to upgrade the insights obtained in computational chemistry when describing chemical reactions in complex environments. This observation combined with the expensiveness of ab initio molecular dynamics simulations make it difficult to use these methods as stand-alone. Therefore, combined static and dynamic studies and further exploration of the ab initio enhanced sampling techniques are of utmost importance for their general application.

References

(1) Van Speybroeck, V.; Hemelsoet, K.; Joos, L.; Waroquier, M.; Bell, R. G.; Catlow, C. R. A. Advances in Theory and their Application within the Field of Zeolite Chemistry. *Chem. Soc. Rev.* **2015**, *44* (20), 7044–7111.

(2) Van Speybroeck, V.; De Wispelaere, K.; Van der Mynsbrugge, J.; Vandichel, M.; Hemelsoet, K.; Waroquier, M. First Principle Chemical Kinetics in Zeolites: The Methanol-to-Olefin Process as a Case Study. *Chem. Soc. Rev.* **2014**, *43* (21), 7326–7357.

(3) De Wispelaere, K.; Bailleul, S.; Van Speybroeck, V. Towards Molecular Control of Elementary Reactions in Zeolite Catalysis by Advanced Molecular Simulations Mimicking Operating Conditions. *Catal. Sci. Technol.* **2016**, *6* (8), 2686–2705.

(4) Grajciar, L.; Heard, C. J.; Bondarenko, A. A.; Polynski, M. V.; Meeprasert, J.; Pidko, E. A.; Nachtigall, P. Towards Operando Computational Modeling in Heterogeneous Catalysis. *Chem. Soc. Rev.* **2018**, *47* (22), 8307–8348.

(5) Westgård Erichsen, M.; De Wispelaere, K.; Hemelsoet, K.; Moors, S. L. C.; Deconinck, T.; Waroquier, M.; Svelle, S.; Van Speybroeck, V.; Olsbye, U. How Zeolitic Acid Strength and Composition Alter the Reactivity of Alkenes and Aromatics towards Methanol. *J. Catal.* **2015**, *328*, 186–196.

(6) Dai, W.; Wang, C.; Dyballa, M.; Wu, G.; Guan, N.; Li, L.; Xie, Z.; Hunger, M. Understanding the Early Stages of the Methanol-to-Olefin Conversion on H-SAPO-34. *ACS Catal.* **2015**, *5* (1), 317–326.

(7) De Wispelaere, K.; Wondergem, C. S.; Ensing, B.; Hemelsoet, K.; Meijer, E. J.; Weckhuysen, B. M.; Van Speybroeck, V.; Ruiz-Martínez, J. Insight into the Effect of Water on the Methanol-to-Olefins Conversion in H-SAPO-34 from Molecular Simulations and in Situ Microspectroscopy. *ACS Catal.* **2016**, 1991–2002.

(8) Yarulina, I.; Bailleul, S.; Pustovarenko, A.; Martinez, J. R.; De Wispelaere, K.; Hajek, J.; Weckhuysen, B. M.; Houben, K.; Baldus, M.; Van Speybroeck, V.; Kapteijn, F.; Gascon, J. Suppression of the Aromatic Cycle in Methanol-to-Olefins Reaction over ZSM-5 by Post-Synthetic Modification Using Calcium. *ChemCatChem* **2016**, *8* (19), 3057–3063.

(9) Yarulina, I.; De Wispelaere, K.; Bailleul, S.; Goetze, J.; Radersma, M.; Abou-Hamad, E.; Vollmer, I.; Goesten, M.; Mezari, B.; Hensen, E. J. M.; Martínez-Espín, J. S.; Morten, M.; Mitchell, S.; Perez-Ramirez, J.; Olsbye, U.; Weckhuysen, B. M.; Van Speybroeck, V.; Kapteijn, F.; Gascon, J. Structure–Performance Descriptors and the Role of Lewis Acidity in the Methanol-to-Propylene Process. *Nat. Chem.* **2018**, *10* (8), 804–812.

(10) Rohling, R. Y.; Uslamin, E.; Zijlstra, B.; Tranca, I. C.; Filot, I. A. W.; Hensen, E. J. M.; Pidko, E. A. An Active Alkali-Exchanged Faujasite Catalyst for p-Xylene Production via the One-Pot Diels–Alder Cycloaddition/Dehydration Reaction of 2,5-Dimethylfuran with Ethylene. *ACS Catal.* **2018**, *8* (2), 760–769.

(11) Wang, C.; Chu, Y.; Xu, J.; Wang, Q.; Qi, G.; Gao, P.; Zhou, X.; Deng, F. Extra-Framework Aluminum-Assisted Initial C–C Bond Formation in Methanol-to-Olefins Conversion on Zeolite H-ZSM-5. *Angew. Chem. Int. Ed.* **2018**, *57* (32), 10197–10201.

(12) Velthoen, M. E. Z.; Nab, S.; Weckhuysen, B. M. Probing Acid Sites in Solid Catalysts with Pyridine UV-Vis Spectroscopy. *Phys. Chem. Chem. Phys.* **2018**, *20* (33), 21647–21659.

(13) Bailleul, S.; Yarulina, I.; Hoffman, A. E. J.; Dokania, A.; Abou-Hamad, E.; Chowdhury, A. D.; Pieters, G.; Hajek, J.; De Wispelaere, K.; Waroquier, M.; Gascon, J.; Van Speybroeck, V. A Supramolecular View on the Cooperative Role of Brønsted and Lewis Acid Sites in Zeolites for Methanol Conversion. *J. Am. Chem. Soc.* **2019**, *141* (37), 14823–14842.

(14) Van Speybroeck, V.; Van Cauter, K.; Coussens, B.; Waroquier, M. Ab Initio Study of Free-Radical Polymerizations: Cost-Effective Methods to Determine the Reaction Rates. *ChemPhysChem* **2005**, *6* (1), 180–189.

(15) Van Speybroeck, V.; Van der Mynsbrugge, J.; Vandichel, M.; Hemelsoet, K.; Lesthaeghe, D.; Ghysels, A.; Marin, G. B.; Waroquier, M. First Principle Kinetic Studies of Zeolite-Catalyzed Methylation Reactions. *J. Am. Chem. Soc.* **2011**, *133* (4), 888–899.
(16) Piccini, G.; Alessio, M.; Sauer, J. Ab Initio Calculation of Rate Constants for Molecule–Surface Reactions with Chemical Accuracy. *Angew. Chem. Int. Ed.* **2016**, *55* (17), 5235–5237.
(17) Svelle, S.; Tuma, C.; Rozanska, X.; Kerber, T.; Sauer, J. Quantum Chemical Modeling of Zeolite-Catalyzed Methylation Reactions: Toward Chemical Accuracy for Barriers. *J. Am. Chem. Soc.* **2009**, *131* (2), 816–825.
(18) Svelle, S.; Rønning, P. O.; Kolboe, S. Kinetic Studies of Zeolite-Catalyzed Methylation Reactions: 1. Coreaction of [12C]Ethene and [13C]Methanol. *J. Catal.* **2004**, *224* (1), 115–123.
(19) Svelle, S.; Rønning, P. O.; Olsbye, U.; Kolboe, S. Kinetic Studies of Zeolite-Catalyzed Methylation Reactions. Part 2. Co-Reaction of [12C]Propene or [12C]n-Butene and [13C]Methanol. *J. Catal.* **2005**, *234* (2), 385–400.
(20) Olsbye, U.; Svelle, S.; Bjørgen, M.; Beato, P.; Janssens, T. V. W.; Joensen, F.; Bordiga, S.; Lillerud, K. P. Conversion of Methanol to Hydrocarbons: How Zeolite Cavity and Pore Size Controls Product Selectivity. *Angew. Chem. Int. Ed.* **2012**, *51* (24), 5810–5831.
(21) Hemelsoet, K.; Van der Mynsbrugge, J.; De Wispelaere, K.; Waroquier, M.; Van Speybroeck, V. Unraveling the Reaction Mechanisms Governing Methanol-to-Olefins Catalysis by Theory and Experiment. *ChemPhysChem* **2013**, *14* (8), 1526–1545.
(22) Yarulina, I.; Chowdhury, A. D.; Meirer, F.; Weckhuysen, B. M.; Gascon, J. Recent Trends and Fundamental Insights in the Methanol-to-Hydrocarbons Process. *Nat. Catal.* **2018**, *1* (6), 398–411.
(23) Haw, J. F.; Marcus, D. M. Well-Defined (Supra)Molecular Structures in Zeolite Methanol-to-Olefin Catalysis. *Top. Catal.* **2005**, *34* (1–4), 41–48.
(24) Haw, J. F.; Song, W.; Marcus, D. M.; Nicholas, J. B. The Mechanism of Methanol to Hydrocarbon Catalysis. *Acc. Chem. Res.* **2003**, *36* (5), 317–326.
(25) Dahl, I.; Kolboe, S. On the Reaction-Mechanism for Propene Formation in the MTO Reaction Over SAPO-34. *Catal. Lett.* **1993**, *20* (3–4), 329–336.
(26) Dahl, I. M.; Kolboe, S. On the Reaction Mechanism for Hydrocarbon Formation from Methanol over SAPO-34: I. Isotopic Labeling Studies of the Co-Reaction of Ethene and Methanol. *J. Catal.* **1994**, *149* (2), 458–464.
(27) Dahl, I. M.; Kolboe, S. On the Reaction Mechanism for Hydrocarbon Formation from Methanol over SAPO-34: 2. Isotopic Labeling Studies of the Co-Reaction of Propene and Methanol. *J. Catal.* **1996**, *161* (1), 304–309.
(28) Svelle, S.; Joensen, F.; Nerlov, J.; Olsbye, U.; Lillerud, K.-P.; Kolboe, S.; Bjørgen, M. Conversion of Methanol into Hydrocarbons over Zeolite H-ZSM-5: Ethene Formation Is Mechanistically Separated from the Formation of Higher Alkenes. *J. Am. Chem. Soc.* **2006**, *128* (46), 14770–14771.
(29) Sun, X.; Mueller, S.; Liu, Y.; Shi, H.; Haller, G. L.; Sanchez-Sanchez, M.; van Veen, A. C.; Lercher, J. A. On Reaction Pathways in the Conversion of Methanol to Hydrocarbons on HZSM-5. *J. Catal.* **2014**, *317*, 185–197.
(30) Van Speybroeck, V.; Hemelsoet, K.; De Wispelaere, K.; Qian, Q.; Van der Mynsbrugge, J.; De Sterck, B.; Weckhuysen, B. M.; Waroquier, M. Mechanistic Studies on Chabazite-Type Methanol-to-Olefin Catalysts: Insights from Time-Resolved UV/Vis Microspectroscopy Combined with Theoretical Simulations. *ChemCatChem* **2013**, *5* (1), 173–184.
(31) Lesthaeghe, D.; De Sterck, B.; Van Speybroeck, V.; Marin, G. B.; Waroquier, M. Zeolite Shape-Selectivity in the Gem-Methylation of Aromatic Hydrocarbons. *Angew. Chem. Int. Ed.* **2007**, *46* (8), 1311–1314.
(32) McCann, D. M.; Lesthaeghe, D.; Kletnieks, P. W.; Guenther, D. R.; Hayman, M. J.; Van Speybroeck, V.; Waroquier, M.; Haw, J. F. A Complete Catalytic Cycle for Supramolecular Methanol-to-Olefins Conversion by Linking Theory with Experiment. *Angew. Chem. Int. Ed.* **2008**, *47* (28), 5179–5182.

(33) Wang, C.-M.; Wang, Y.-D.; Xie, Z.-K.; Liu, Z.-P. Methanol to Olefin Conversion on HSAPO-34 Zeolite from Periodic Density Functional Theory Calculations: A Complete Cycle of Side Chain Hydrocarbon Pool Mechanism. *J. Phys. Chem. C* **2009**, *113* (11), 4584–4591.
(34) De Wispelaere, K.; Hemelsoet, K.; Waroquier, M.; Van Speybroeck, V. Complete Low-Barrier Side-Chain Route for Olefin Formation during Methanol Conversion in H-SAPO-34. *J. Catal.* **2013**, *305*, 76–80.
(35) Frenkel, D.; Smit, B. *Understanding Molecular Simulation: From Algorithms to Applications*; Academic Press, 2001.
(36) De Wispelaere, K.; Vanduyfhuys, L.; Van Speybroeck, V. Chapter 6 - Entropy Contributions to Transition State Modeling. In *Modelling and Simulation in the Science of Micro- and Meso-Porous Materials*; Catlow, C. R. A., Van Speybroeck, V., van Santen, R. A., Eds.; Elsevier, 2018; pp 189–228.
(37) Rey, J.; Gomez, A.; Raybaud, P.; Chizallet, C.; Bučko, T. On the Origin of the Difference between Type A and Type B Skeletal Isomerization of Alkenes Catalyzed by Zeolites: The Crucial Input of Ab Initio Molecular Dynamics. *J. Catal.* **2019**, *373*, 361–373.
(38) Abrams, C.; Bussi, G. Enhanced Sampling in Molecular Dynamics Using Metadynamics, Replica-Exchange, and Temperature-Acceleration. *Entropy* **2013**, *16* (1), 163–199.
(39) Christ, C. D.; Mark, A. E.; van Gunsteren, W. F. Basic Ingredients of Free Energy Calculations: A Review. *J. Comput. Chem.* **2010**, *31* (8), 1569–1582.
(40) Hansen, N.; van Gunsteren, W. F. Practical Aspects of Free-Energy Calculations: A Review. *J. Chem. Theory Comput.* **2014**, *10* (7), 2632–2647.
(41) Pietrucci, F. Strategies for the Exploration of Free Energy Landscapes: Unity in Diversity and Challenges Ahead. *Rev. Phys.* **2017**, *2*, 32–45.
(42) Demuynck, R.; Rogge, S. M. J.; Vanduyfhuys, L.; Wieme, J.; Waroquier, M.; Van Speybroeck, V. Efficient Construction of Free Energy Profiles of Breathing Metal–Organic Frameworks Using Advanced Molecular Dynamics Simulations. *J. Chem. Theory Comput.* **2017**, *13* (12), 5861–5873.
(43) Cuendet, M. A.; Tuckerman, M. E. Free Energy Reconstruction from Metadynamics or Adiabatic Free Energy Dynamics Simulations. *J. Chem. Theory Comput.* **2014**, *10* (8), 2975–2986.
(44) van Duin, A. C. T.; Dasgupta, S.; Lorant, F.; Goddard, W. A. ReaxFF: A Reactive Force Field for Hydrocarbons. *J. Phys. Chem. A* **2001**, *105* (41), 9396–9409.
(45) Han, Y.; Jiang, D.; Zhang, J.; Li, W.; Gan, Z.; Gu, J. Development, Applications and Challenges of ReaxFF Reactive Force Field in Molecular Simulations. *Front. Chem. Sci. Eng.* **2016**, *10* (1), 16–38.
(46) Eichinger, M.; Tavan, P.; Hutter, J.; Parrinello, M. A Hybrid Method for Solutes in Complex Solvents: Density Functional Theory Combined with Empirical Force Fields. *J. Chem. Phys.* **1999**, *110* (21), 10452–10467.
(47) Wieme, J.; Lejaeghere, K.; Kresse, G.; Speybroeck, V. V. Tuning the Balance between Dispersion and Entropy to Design Temperature-Responsive Flexible Metal-Organic Frameworks. *Nat. Commun.* **2018**, *9* (1), 1–10.
(48) De Moor, B. A.; Reyniers, M.-F.; Marin, G. B. Physisorption and Chemisorption of Alkanes and Alkenes in H-FAU: A Combined Ab Initio–Statistical Thermodynamics Study. *Phys. Chem. Chem. Phys.* **2009**, *11* (16), 2939–2958.
(49) De Moor, B. A.; Reyniers, M.-F.; Gobin, O. C.; Lercher, J. A.; Marin, G. B. Adsorption of C2−C8 N-Alkanes in Zeolites. *J. Phys. Chem. C* **2011**, *115* (4), 1204–1219.
(50) Van der Mynsbrugge, J.; Hemelsoet, K.; Vandichel, M.; Waroquier, M.; Van Speybroeck, V. Efficient Approach for the Computational Study of Alcohol and Nitrile Adsorption in H-ZSM-5. *J. Phys. Chem. C* **2012**, *116* (9), 5499–5508.
(51) Moors, S. L. C.; De Wispelaere, K.; Van der Mynsbrugge, J.; Waroquier, M.; Van Speybroeck, V. Molecular Dynamics Kinetic Study on the Zeolite-Catalyzed Benzene Methylation in ZSM-5. *ACS Catal.* **2013**, *3* (11), 2556–2567.

(52) Hansen, N.; Kerber, T.; Sauer, J.; Bell, A. T.; Keil, F. J. Quantum Chemical Modeling of Benzene Ethylation over H-ZSM-5 Approaching Chemical Accuracy: A Hybrid MP2:DFT Study. *J. Am. Chem. Soc.* **2010**, *132* (33), 11525–11538.
(53) Peters, B. Reaction Coordinates and Mechanistic Hypothesis Tests. *Annu. Rev. Phys. Chem.* **2016**, *67* (1), 669–690.
(54) Demuynck, R.; Wieme, J.; Rogge, S. M. J.; Dedecker, K. D.; Vanduyfhuys, L.; Waroquier, M.; Van Speybroeck, V. Protocol for Identifying Accurate Collective Variables in Enhanced Molecular Dynamics Simulations for the Description of Structural Transformations in Flexible Metal–Organic Frameworks. *J. Chem. Theory Comput.* **2018**, *14* (11), 5511–5526.
(55) Swendsen, R. H.; Wang, J.-S. Replica Monte Carlo Simulation of Spin-Glasses. *Phys. Rev. Lett.* **1986**, *57* (21), 2607–2609.
(56) Sugita, Y.; Okamoto, Y. Replica-Exchange Molecular Dynamics Method for Protein Folding. *Chem. Phys. Lett.* **1999**, *314* (1), 141–151.
(57) Jing, Z.; Xin, L.; Sun, H. Replica Exchange Reactive Molecular Dynamics Simulations of Initial Reactions in Zeolite Synthesis. *Phys. Chem. Chem. Phys.* **2015**, *17* (38), 25421–25428.
(58) Torrie, G. M.; Valleau, J. P. Monte Carlo Free Energy Estimates Using Non-Boltzmann Sampling: Application to the Sub-Critical Lennard-Jones Fluid. *Chem. Phys. Lett.* **1974**, *28* (4), 578–581.
(59) Torrie, G. M.; Valleau, J. P. Nonphysical Sampling Distributions in Monte Carlo Free-Energy Estimation: Umbrella Sampling. *J. Comput. Phys.* **1977**, *23* (2), 187–199.
(60) Kästner, J. Umbrella Sampling. *Wiley Interdiscip. Rev. Comput. Mol. Sci.* **2011**, *1* (6), 932–942.
(61) Kirkwood, J. G. Statistical Mechanics of Fluid Mixtures. *J. Chem. Phys.* **1935**, *3* (5), 300–313.
(62) Carter, E. A.; Ciccotti, G.; Hynes, J. T.; Kapral, R. Constrained Reaction Coordinate Dynamics for the Simulation of Rare Events. *Chem. Phys. Lett.* **1989**, *156* (5), 472–477.
(63) Paci, E.; Ciccotti, G.; Ferrario, M.; Kapral, R. Activation Energies by Molecular Dynamics with Constraints. *Chem. Phys. Lett.* **1991**, *176* (6), 581–587.
(64) Straatsma, T. P.; McCammon, J. A. Multiconfiguration Thermodynamic Integration. *J. Chem. Phys.* **1991**, *95* (2), 1175–1188.
(65) den Otter, W. K.; Briels, W. J. The Calculation of Free-Energy Differences by Constrained Molecular-Dynamics Simulations. *J. Chem. Phys.* **1998**, *109* (11), 4139–4146.
(66) Kelly, E.; Seth, M.; Ziegler, T. Calculation of Free Energy Profiles for Elementary Bimolecular Reactions by Ab Initio Molecular Dynamics: Sampling Methods and Thermostat Considerations. *J. Phys. Chem. A* **2004**, *108* (12), 2167–2180.
(67) De Meyer, T.; Ensing, B.; Rogge, S. M. J.; De Clerck, K.; Meijer, E. J.; Van Speybroeck, V. Acidity Constant (PKa) Calculation of Large Solvated Dye Molecules: Evaluation of Two Advanced Molecular Dynamics Methods. *ChemPhysChem* **2016**, *17* (21), 3447–3459.
(68) Laio, A.; Parrinello, M. Escaping Free-Energy Minima. *Proc. Natl. Acad. Sci.* **2002**, *99* (20), 12562–12566.
(69) Iannuzzi, M.; Laio, A.; Parrinello, M. Efficient Exploration of Reactive Potential Energy Surfaces Using Car-Parrinello Molecular Dynamics. *Phys. Rev. Lett.* **2003**, *90* (23), 238302.
(70) Laio, A.; Gervasio, F. L. Metadynamics: A Method to Simulate Rare Events and Reconstruct the Free Energy in Biophysics, Chemistry and Material Science. *Rep. Prog. Phys.* **2008**, *71* (12), 126601.
(71) Bilionis, I.; Koutsourelakis, P. S. Free Energy Computations by Minimization of Kullback–Leibler Divergence: An Efficient Adaptive Biasing Potential Method for Sparse Representations. *J. Comput. Phys.* **2012**, *231* (9), 3849–3870.
(72) Valsson, O.; Parrinello, M. Variational Approach to Enhanced Sampling and Free Energy Calculations. *Phys. Rev. Lett.* **2014**, *113* (9), 090601.
(73) Valsson, O.; Tiwary, P.; Parrinello, M. Enhancing Important Fluctuations: Rare Events and Metadynamics from a Conceptual Viewpoint. *Annu. Rev. Phys. Chem.* **2016**, *67* (1), 159–184.

(74) Rohrdanz, M. A.; Zheng, W.; Clementi, C. Discovering Mountain Passes via Torchlight: Methods for the Definition of Reaction Coordinates and Pathways in Complex Macromolecular Reactions. *Annu. Rev. Phys. Chem.* **2013**, *64* (1), 295–316.
(75) Kumar, S.; Rosenberg, J. M.; Bouzida, D.; Swendsen, R. H.; Kollman, P. A. The Weighted Histogram Analysis Method for Free-Energy Calculations on Biomolecules. I. The Method. *J. Comput. Chem.* **1992**, *13* (8), 1011–1021.
(76) Kumar, S.; Rosenberg, J. M.; Bouzida, D.; Swendsen, R. H.; Kollman, P. A. Multidimensional Free-Energy Calculations Using the Weighted Histogram Analysis Method. *J. Comput. Chem.* **1995**, *16* (11), 1339–1350.
(77) Hajek, J.; Van der Mynsbrugge, J.; De Wispelaere, K.; Cnudde, P.; Vanduyfhuys, L.; Waroquier, M.; Van Speybroeck, V. On the Stability and Nature of Adsorbed Pentene in Brønsted Acid Zeolite H-ZSM-5 at 323 K. *J. Catal.* **2016**, *340*, 227–235.
(78) Hajek, J.; Bueken, B.; Waroquier, M.; De Vos, D.; Van Speybroeck, V. The Remarkable Amphoteric Nature of Defective UiO-66 in Catalytic Reactions. *ChemCatChem* **2017**, *9* (12), 2203–2210.
(79) Cnudde, P.; De Wispelaere, K.; Van der Mynsbrugge, J.; Waroquier, M.; Van Speybroeck, V. Effect of Temperature and Branching on the Nature and Stability of Alkene Cracking Intermediates in H-ZSM-5. *J. Catal.* **2017**, *345*, 53–69.
(80) Database of Zeolite Structures http://www.iza-structure.org/databases/ (accessed Dec 29, 2014).
(81) Dědeček, J.; Sklenak, S.; Li, C.; Wichterlová, B.; Gábová, V.; Brus, J.; Sierka, M.; Sauer, J. Aluminum Siting in the Framework of Silicon Rich Zeolites. A ZSM-5 Study. In *Zeolites and related materials: Trends, targets and challenges*; Gédéon, A., Massiani, P., Babonneau, F., Eds.; Studies in Surface Science and Catalysis; Elsevier, 2008; Vol. 174, pp 781–786.
(82) Bhan, A.; Joshi, Y. V.; Delgass, W. N.; Thomson, K. T. DFT Investigation of Alkoxide Formation from Olefins in H-ZSM-5. *J. Phys. Chem. B* **2003**, *107* (38), 10476–10487.
(83) Kresse, G.; Hafner, J. Ab Initio Molecular Dynamics for Liquid Metals. *Phys. Rev. B* **1993**, *47* (1), 558–561.
(84) Kresse, G.; Hafner, J. Ab Initio Molecular-Dynamics Simulation of the Liquid-Metal Amorphous-Semiconductor Transition in Germanium. *Phys. Rev. B* **1994**, *49* (20), 14251–14269.
(85) Kresse, G.; Furthmüller, J. Efficiency of Ab-Initio Total Energy Calculations for Metals and Semiconductors Using a Plane-Wave Basis Set. *Comput. Mater. Sci.* **1996**, *6* (1), 15–50.
(86) Kresse, G.; Furthmüller, J. Efficient Iterative Schemes for Ab Initio Total-Energy Calculations Using a Plane-Wave Basis Set. *Phys. Rev. B* **1996**, *54* (16), 11169–11186.
(87) Zhang, Y.; Yang, W. Comment on ``Generalized Gradient Approximation Made Simple''. *Phys. Rev. Lett.* **1998**, *80* (4), 890–890.
(88) Yang, K.; Zheng, J.; Zhao, Y.; Truhlar, D. G. Tests of the RPBE, RevPBE, τ-HCTHhyb, ωB97X-D, and MOHLYP Density Functional Approximations and 29 Others against Representative Databases for Diverse Bond Energies and Barrier Heights in Catalysis. *J. Chem. Phys.* **2010**, *132* (16), 164117.
(89) Grimme, S.; Antony, J.; Ehrlich, S.; Krieg, H. A Consistent and Accurate Ab Initio Parametrization of Density Functional Dispersion Correction (DFT-D) for the 94 Elements H-Pu. *J. Chem. Phys.* **2010**, *132* (15), 154104.
(90) Blöchl, P. E. Projector Augmented-Wave Method. *Phys. Rev. B* **1994**, *50* (24), 17953–17979.
(91) Kresse, G.; Joubert, D. From Ultrasoft Pseudopotentials to the Projector Augmented-Wave Method. *Phys. Rev. B* **1999**, *59* (3), 1758–1775.
(92) Heyden, A.; Bell, A. T.; Keil, F. J. Efficient Methods for Finding Transition States in Chemical Reactions: Comparison of Improved Dimer Method and Partitioned Rational Function Optimization Method. *J. Chem. Phys.* **2005**, *123* (22), 224101.
(93) Pulay, P. Convergence Acceleration of Iterative Sequences. the Case of Scf Iteration. *Chem. Phys. Lett.* **1980**, *73* (2), 393–398.

(94) Press, W. H.; Flannery, B. P.; Teukolsky, S. A.; Vetterling, W. T. *Numerical Recipes: The Art of Scientific Computing*; Cambridge Univ. Press, New York, 1986.
(95) De Moor, B. A.; Ghysels, A.; Reyniers, M.-F.; Van Speybroeck, V.; Waroquier, M.; Marin, G. B. Normal Mode Analysis in Zeolites: Toward an Efficient Calculation of Adsorption Entropies. *J. Chem. Theory Comput.* **2011**, *7* (4), 1090–1101.
(96) Ghysels, A.; Verstraelen, T.; Hemelsoet, K.; Waroquier, M.; Van Speybroeck, V. TAMkin: A Versatile Package for Vibrational Analysis and Chemical Kinetics. *J. Chem. Inf. Model.* **2010**, *50* (9), 1736–1750.
(97) Hutter, J.; Iannuzzi, M.; Schiffmann, F.; VandeVondele, J. Cp2k: Atomistic Simulations of Condensed Matter Systems. *Wiley Interdiscip. Rev. Comput. Mol. Sci.* **2014**, *4* (1), 15–25.
(98) VandeVondele, J.; Krack, M.; Mohamed, F.; Parrinello, M.; Chassaing, T.; Hutter, J. Quickstep: Fast and Accurate Density Functional Calculations Using a Mixed Gaussian and Plane Waves Approach. *Comput. Phys. Commun.* **2005**, *167* (2), 103–128.
(99) Martyna, G. J.; Tobias, D. J.; Klein, M. L. Constant Pressure Molecular Dynamics Algorithms. *J. Chem. Phys.* **1994**, *101* (5), 4177–4189.
(100) Lippert, G.; Hutter, J.; Parrinello, M. A Hybrid Gaussian and Plane Wave Density Functional Scheme. *Mol. Phys.* **1997**, *92* (3), 477–488.
(101) Lippert, G.; Hutter, J.; Parrinello, M. The Gaussian and Augmented-Plane-Wave Density Functional Method for Ab Initio Molecular Dynamics Simulations. *Theor. Chem. Acc.* **1999**, *103* (2), 124–140.
(102) Goedecker, S.; Teter, M.; Hutter, J. Separable Dual-Space Gaussian Pseudopotentials. *Phys. Rev. B* **1996**, *54* (3), 1703–1710.
(103) Van der Mynsbrugge, J.; Moors, S. L. C.; De Wispelaere, K.; Van Speybroeck, V. Insight into the Formation and Reactivity of Framework-Bound Methoxide Species in H-ZSM-5 from Static and Dynamic Molecular Simulations. *ChemCatChem* **2014**, *6* (7), 1906–1918.
(104) Ensing, B.; Laio, A.; Parrinello, M.; Klein, M. L. A Recipe for the Computation of the Free Energy Barrier and the Lowest Free Energy Path of Concerted Reactions. *J. Phys. Chem. B* **2005**, *109* (14), 6676–6687.
(105) Bonomi, M.; Branduardi, D.; Bussi, G.; Camilloni, C.; Provasi, D.; Raiteri, P.; Donadio, D.; Marinelli, F.; Pietrucci, F.; Broglia, R. A.; Parrinello, M. PLUMED: A Portable Plugin for Free-Energy Calculations with Molecular Dynamics. *Comput. Phys. Commun.* **2009**, *180* (10), 1961–1972.
(106) Bučko, T. Ab Initio Calculations of Free-Energy Reaction Barriers. *J. Phys. Condens. Matter* **2008**, *20* (6), 064211.
(107) Bach, F.; Moulines, E. Non-Strongly-Convex Smooth Stochastic Approximation with Convergence Rate O(1/n). In *Advances in Neural Information Processing Systems 26*; Burges, C. J. C., Bottou, L., Welling, M., Ghahramani, Z., Weinberger, K. Q., Eds.; Curran Associates, Inc., 2013; pp 773–781.
(108) Souaille, M.; Roux, B. Extension to the Weighted Histogram Analysis Method: Combining Umbrella Sampling with Free Energy Calculations. *Comput. Phys. Commun.* **2001**, *135* (1), 40–57.
(109) Kılıç, M.; Ensing, B. Acidity Constants of Lumiflavin from First Principles Molecular Dynamics Simulations. *Phys. Chem. Chem. Phys.* **2014**, *16* (35), 18993–19000.
(110) Bailleul, S.; Rogge, S. M. J.; Vanduyfhuys, L.; Van Speybroeck, V. Insight into the Role of Water on the Methylation of Hexamethylbenzene in H-SAPO-34 from First Principle Molecular Dynamics Simulations. *ChemCatChem* **2019**, *11* (16), 3993–4010.
(111) Barducci, A.; Bonomi, M.; Parrinello, M. Metadynamics. *Wiley Interdiscip. Rev. Comput. Mol. Sci.* **2011**, *1* (5), 826–843.
(112) Pelzer, H.; Wigner, E. Über Die Geschwindigkeitskonstante von Austauschreaktionen. *Z. Für Phys. Chem.* **1932**, *15B* (1), 445–471.
(113) Eyring, H. The Activated Complex in Chemical Reactions. *J. Chem. Phys.* **1935**, *3* (2), 107–115.

(114) Wynne-Jones, W. F. K.; Eyring, H. The Absolute Rate of Reactions in Condensed Phases. *J. Chem. Phys.* **1935**, *3* (8), 492–502.
(115) Evans, M. G.; Polanyi, M. Some Applications of the Transition State Method to the Calculation of Reaction Velocities, Especially in Solution. *Trans. Faraday Soc.* **1935**, *31* (0), 875–894.
(116) Truhlar, D. G.; Garrett, B. C.; Klippenstein, S. J. Current Status of Transition-State Theory. *J. Phys. Chem.* **1996**, *100* (31), 12771–12800.
(117) Hänggi, P.; Talkner, P.; Borkovec, M. Reaction-Rate Theory: Fifty Years after Kramers. *Rev. Mod. Phys.* **1990**, *62* (2), 251–341.
(118) Atkins, P.; Paula, J. de; Keeler, J. *Atkins' Physical Chemistry*, Eleventh Edition.; Oxford University Press: Oxford, New York, 2017.
(119) Bučko, T.; Chibani, S.; Paul, J.-F.; Cantrel, L.; Badawi, M. Dissociative Iodomethane Adsorption on Ag-MOR and the Formation of AgI Clusters: An Ab Initio Molecular Dynamics Study. *Phys. Chem. Chem. Phys.* **2017**, *19* (40), 27530–27543.
(120) De Sterck, B.; Vaneerdeweg, R.; Du Prez, F.; Waroquier, M.; Van Speybroeck, V. Solvent Effects on Free Radical Polymerization Reactions: The Influence of Water on the Propagation Rate of Acrylamide and Methacrylamide. *Macromolecules* **2010**, *43* (2), 827–836.
(121) Jakobtorweihen, S.; Hansen, N.; Keil, F. J. Molecular Simulation of Alkene Adsorption in Zeolites. *Mol. Phys.* **2005**, *103* (4), 471–489.
(122) Steinmann, S. N.; Corminboeuf, C. A Generalized-Gradient Approximation Exchange Hole Model for Dispersion Coefficients. *J. Chem. Phys.* **2011**, *134* (4), 044117.
(123) Steinmann, S. N.; Corminboeuf, C. Comprehensive Benchmarking of a Density-Dependent Dispersion Correction. *J. Chem. Theory Comput.* **2011**, *7* (11), 3567–3577.
(124) Dion, M.; Rydberg, H.; Schröder, E.; Langreth, D. C.; Lundqvist, B. I. Van Der Waals Density Functional for General Geometries. *Phys. Rev. Lett.* **2004**, *92* (24), 246401.
(125) Klimeš, J.; Bowler, D. R.; Michaelides, A. Van Der Waals Density Functionals Applied to Solids. *Phys. Rev. B* **2011**, *83* (19), 195131.

SUPPORTING INFORMATION: AB INITIO ENHANCED SAMPLING KINETIC STUDY ON MTO ETHENE METHYLATION REACTION

Simon Bailleul, Louis Vanduyfhuys, Michel Waroquier, Veronique Van Speybroeck*

Center for Molecular Modeling (CMM), Ghent University, Technologiepark 46, B-9052 Zwijnaarde, Belgium

*Corresponding author: veronique.vanspeybroeck@ugent.be

TABLE OF CONTENT

1. Unit cell ZSM-5 1

1.1. Static method 1

1.2. Dynamic method 2

2. Characteristic values for the collective variables 5

3. Windows used in US and TI simulations 6

4. Enhanced sampling error estimation 9

4.1. Metadynamics 9

4.2. Variationally enhanced sampling 10

4.3. Umbrella sampling 11

4.4. Thermodynamic integration 12

5. Product state analysis US and TI using collective variable 1D-DI 13

6. Derivation transformation formula 16

6.1. Introduction – statistical physics 16

6.2. Transformation of 1D free energy profiles 17

6.3. Transformation of 2D free energy profiles 18

6.4. Projecting 2D free energy surface to 1D profile 19

7. Free energy barriers by subtracting minimum from maximum 21

8. Definition of a coordination number 23

9. Analysis of the mobility of the reactants 24

10. Reaction rate calculations 26

11. Committor analysis 30

12. Biased molecular dynamics 32

13. Static results 34

References..... 1

1. UNIT CELL ZSM-5

As discussed in the manuscript, a unit cell of H-ZSM-5 consisting of 96 T atoms is used, as shown in Figure S 1. In this unit cell, one silicon atom is replaced by an aluminum atom to create the Brønsted acid site (BAS). As there is no simple rule for the occupation of Al atoms on the 24 distinguishable framework T sites because it depends on the conditions of the zeolite synthesis [1], the substitutions are made based on earlier work. For this, a substitution is performed at the T12 position. [2,3] The unit cell parameters used during the simulations depends on the used methods, as the unit cell used in the static calculations is equilibrated at 0 K, while the unit cell parameters for the dynamic simulations are obtained at 623 K. Both methods are discussed in the subsequent sections.

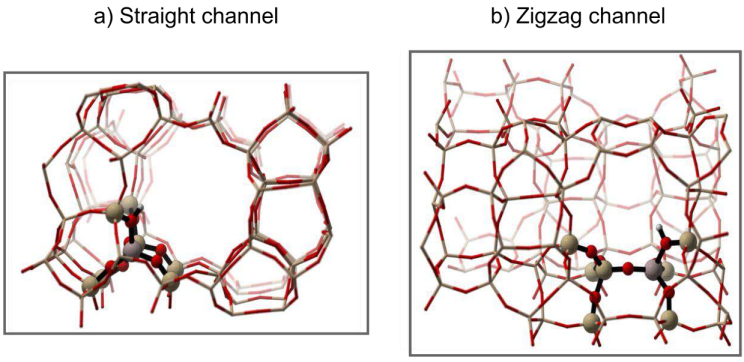

Figure S 1: H-ZSM-5 unit cell used during this study, indicating the 8T cell used during the partial Hessian vibrational analysis (PHVA).

1.1. STATIC METHOD

During all static VASP simulations, the unit cell parameters are kept constant as was done in earlier work. [4,5] Therefore, the optimal volume of the empty unit cell of H-ZSM-5 is calculated by a least square fit to the Birch Murnaghan equation of state curve of the data points

depicted in Figure S 2. This led to an optimal unit cell volume of 5467.56 Å³. The used unit cell parameters are summarized in Table S 1.

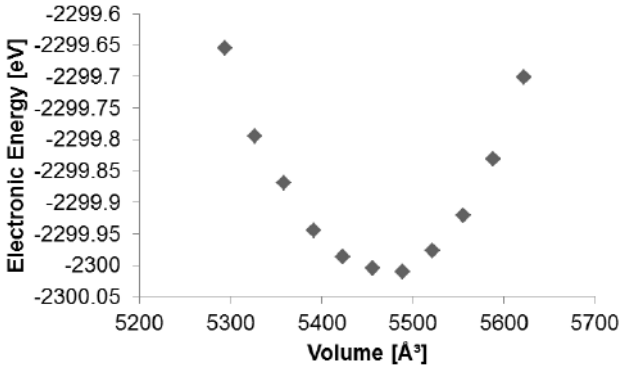

Figure S 2: Data points used for the least square fit to the Birch Murnaghan equation of state curve. [4,5]

1.2. DYNAMIC METHOD

During dynamics simulations, the system is sampled at more realistic conditions than during the 0 K static calculations. Therefore, the unit cell parameters are averaged over a 50 ps ab initio molecular dynamics simulations in the NPT ensemble at 1 atm and 623 K, as was already done elsewhere. [6] In this simulation, ethene and methanol are already adsorbed. This procedure allows us to account for the framework flexibility and the interaction with the guest molecules. The enhanced sampling simulations are performed in the NVT ensemble as there are several arguments to not perform NPT simulations in the system here:

(i) To computationally model systems in which not only the cell volume but also the cell shape may fluctuate experimentally, such as for flexible zeolites and metal-organic frameworks, we demonstrated earlier that the most ideal ensemble is the constant-temperature constant-stress ensemble, or $(N, P, \boldsymbol{\sigma}_a = \mathbf{0}, T)$ ensemble. [7] In this ensemble, not only the pressure is controlled, as in the NPT ensemble, but also the deviatoric stress $\boldsymbol{\sigma}_a$ is

controlled by the barostat piston. However, this improved description of the dynamics of the simulation cell comes with an important drawback. To evaluate the effect of the piston on the cell, one needs to determine the instantaneous virial stress and therefore perform a computationally expensive extra force evaluation. As a result, application of such a barostat would increase the simulation time at least twofold (the exact increase in computational time depends on the implementation of the Trotter expansion of the Liouville operator). This is not the case when applying a thermostat, as the equivalent property to be calculated here is the instantaneous kinetic energy, which only depends on the velocities of the different atoms and not the interatomic forces.

(ii) Modelling techniques such as thermostats and barostats for molecular dynamics simulations are often introduced as perturbations to the basic (velocity) Verlet algorithm, which integrates the equations of motion in the microcanonical or NVE ensemble. While the effect of these perturbations can be tuned to a large extent through, for instance, the thermostat and barostat relaxation times, it has been demonstrated that application of most conventionally used thermostats and barostats artificially alters the dynamics of the system. [7,8] This does not come as a surprise, as barostats introduce an artificial inertia into the system, which should mimic the inertia from the surrounding cells in the real material.

The resulting unit cell parameters, which are used during the enhanced sampling simulations, are summarized in Table S 1.

Table S 1: Unit cell parameters used during the static and dynamic simulations.

	a [Å]	b [Å]	c [Å]	α [°]	β [°]	γ [°]
Static	20.02	20.25	13.49	89.87	89.69	90.10
Dynamic (623 K)	20.38	20.19	13.58	90	90	90

2. CHARACTERISTIC VALUES FOR THE COLLECTIVE VARIABLES

To be a good reaction coordinate, a collective variable needs to be at least able to distinguish between the reactant, transition and product state. Therefore, the characteristic value at these three states for the proposed collective variables are summarized in Table S 2. [9,10]

Table S 2: Characteristic values of the proposed collective variables at the reactant, transition and product state.

	Reactant		Transition		Product	
	CV1	CV2	CV1	CV2	CV1	CV2
Type CN	1.0	0.0	0.5	0.5	0.0	1.0 - 2.0
Type DI	1.4 Å	5.0 Å	2.0 Å	2.4 Å	3.7 Å	1.7 Å
Type 1D-DI	3.6 Å	-	0.3 Å	-	-1.9 Å	-

3. WINDOWS USED IN US AND TI SIMULATIONS

As discussed in the manuscript, 34-43 windows are used during the sampling used to obtain free energy profiles with umbrella sampling (US) and thermodynamic integration (TI). The positions of the restraints are summarized in Table S 3.

Table S 3: Positions of the restraints used during the US and TI simulation using different collective variables.

	Type CN		Type DI		Type 1D-DI
	CN_{OC}	CN_{CC}	d	d_{CM}	d_{CM}-d
window1	0.903	0.009	1.433	5.080	3.648
window2	0.902	0.018	1.442	5.051	3.610
window3	0.894	0.014	1.381	4.947	3.565
window4	0.889	0.010	1.446	4.924	3.478
window5	0.884	0.008	1.408	4.839	3.431
window6	0.890	0.013	1.536	4.881	3.346
window7	0.892	0.017	1.413	4.610	3.197
window8	0.877	0.008	1.401	4.531	3.131
window9	0.873	0.009	1.414	4.412	2.997
window10	0.830	0.009	1.390	4.360	2.971
window11	0.809	0.034	1.400	4.150	2.750
window12	0.825	0.111	1.400	4.000	2.600
window13	0.807	0.151	1.572	3.859	2.287
window14	0.807	0.205	1.500	3.650	2.150
window15	0.884	0.353	1.500	3.500	2.000
window16	0.814	0.409	1.554	3.207	1.652
window17	0.700	0.430	1.573	3.120	1.547
window18	0.653	0.453	1.564	2.836	1.272

window19	0.580	0.400	1.600	2.750	1.150
window20	0.459	0.511	1.429	2.494	1.065
window21	0.427	0.674	1.566	2.428	0.862
window22	0.389	0.733	1.765	2.413	0.648
window23	0.303	0.673	1.821	2.460	0.639
window24	0.294	0.747	1.914	2.414	0.500
window25	0.267	0.866	2.056	2.354	0.298
window26	0.176	0.903	2.109	2.137	0.029
window27	0.145	0.938	2.302	2.310	0.008
window28	0.104	1.025	2.147	2.103	-0.045
window29	0.099	1.020	2.322	2.060	-0.262
window30	0.071	1.069	2.500	2.047	-0.453
window31	0.072	1.072	2.592	1.957	-0.636
window32	0.086	1.193	2.687	1.921	-0.766
window33	0.036	1.164	2.868	1.852	-1.015
window34	0.026	1.205	2.887	1.850	-1.037
window35	n.a.	n.a.	3.064	1.832	-1.232
window36	n.a.	n.a.	3.071	1.830	-1.241
window37	n.a.	n.a.	2.971	1.727	-1.244
window38	n.a.	n.a.	3.300	1.750	-1.550
window39	n.a.	n.a.	3.471	1.770	-1.701
window40	n.a.	n.a.	3.664	1.715	-1.949
window41	n.a.	n.a.	1.433 (500.0)	5.080 (500.0)	3.648 (500.0)
window42	n.a.	n.a.	1.433 (50.0)	5.080 (50.0)	3.648 (50.0)
window43	n.a.	n.a.	1.433	5.080	3.648 (5.0)

			(5.0)	(5.0)	
window44	n.a.	n.a.	1.433 (5.0)	6.080 (5.0)	4.648 (5.0)
window45	n.a.	n.a.	1.433 (1.0)	7.080 (1.0)	5.648 (1.0)
window46	n.a.	n.a.	n.a.	n.a.	6.648 (1.0)

4. ENHANCED SAMPLING ERROR ESTIMATION

For all enhanced sampling methods considered in Section 3.1 of the main manuscript, an estimate of the error on the profile is made in the following sections. An overview of the maximum error is given in Table S 4. These errors are comparable for metadynamics and lower for umbrella sampling compared to similar work performed by the current authors. [11] The decreased error for US can be explained by the fact that parallel simulations were performed to estimate the error in earlier work, while bootstrapping is used here, thus offering and underestimate of the error.

Table S 4: Error estimations for the considered enhanced sampling methods (in kJ/mol).

Method	**Maximum error**
MTD	7.48
VES	18.52
US	1.5
TI	0.85

4.1. METADYNAMICS

To estimate an error on the metadynamics simulations, 10 parallel metadynamics simulations are performed. The resulting profiles are first translated so the free energy equals 0 kJ/mol at d_{CM}-d equal to 3 Å, leading to the profiles depicted in Figure S 3. Subsequently, an average profile and standard deviation are calculated based on these 10 profiles, resulting in the data depicted in Figure 5 of the manuscript.

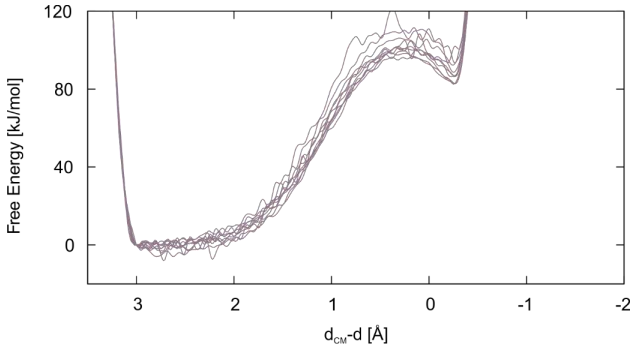

Figure S 3: Free energy profiles obtained for 10 parallel metadynamics simulations using collective variable Type 1D-DI.

4.2. VARIATIONALLY ENHANCED SAMPLING

The same methodology as for metadynamics is used to estimate the error on the variationally enhanced sampling simulations, but only 5 parallel simulations are performed. The resulting profiles are first translated so the free energy equals 0 kJ/mol at d_{CM}-d equal to 3 Å, leading to the profiles depicted in Figure S 4. Subsequently, an average profile and standard deviation are calculated based on these 5 profiles, resulting in the data depicted in Figure 5 of the manuscript. There is still a lot of variation between the profiles, suggesting insufficient sampling, but as this technique has the disadvantage that it needs wall to enhance recrossing, further sampling is omitted.

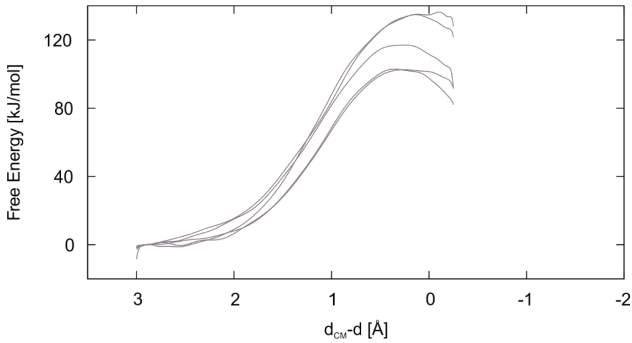

Figure S 4: Free energy profiles obtained for 5 parallel VES simulations using collective variable Type 1D-DI.

4.3. UMBRELLA SAMPLING

Since it requires around 40 windows, each corresponding with a 50 ps constrained MD simulation to obtain a free energy profile from umbrella sampling simulations, it is computationally too expensive to perform several parallel calculations for the error estimation. Therefore, bootstrapping is performed to assure decent sampling. For each window, random snapshots are selected in the trajectory to obtain new 50 ps trajectories that are used to recalculate the free energy profile and corresponding error. The resulting profiles are depicted in Figure S 5 and the profile with error bars in Figure 5 of the manuscript.

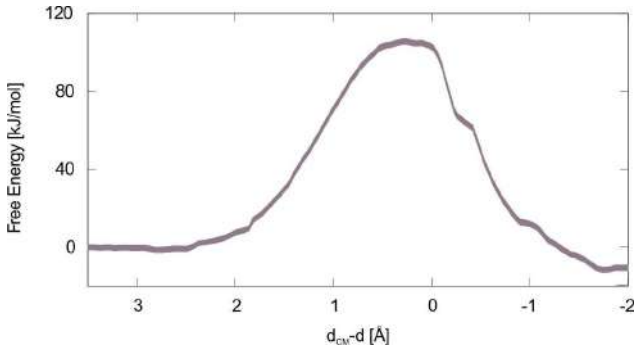

Figure S 5: Free energy profiles obtained by performing bootstrapping 100 times on the umbrella sampling simulations obtained using collective variable Type 1D-DI.

4.4. THERMODYNAMIC INTEGRATION

Similar as for the US simulations, around 40 windows with each a 50 ps constrained MD simulation are necessary to obtain a free energy profile from thermodynamic integration simulations. Therefore, it is computationally too expensive to perform several parallel calculations for the error estimation. Instead, bootstrapping is performed to assure decent sampling. For each window, random snapshots are selected in the trajectory to obtain new 50 ps trajectories that are used to recalculate the free energy profile and corresponding error. The resulting profiles are depicted in Figure S 6 and the profile with error bars in Figure 5 of the manuscript.

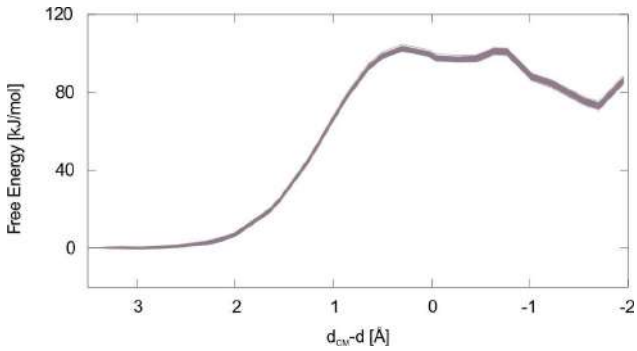

Figure S 6: Free energy profiles obtained by performing bootstrapping 100 times on the thermodynamic integration simulations obtained using collective variable Type 1D-DI.

5. PRODUCT STATE ANALYSIS US AND TI USING COLLECTIVE VARIABLE 1D-DI

As the product state of the umbrella sampling and thermodynamic integration seem to be quite different, it seems interesting to have a look at the visited product states. These are summarized in Table S 5. The results show that this is indeed a zoo of states visited as the primary product, protonated propene seems very unstable. A more detailed analysis of these product states is out of the scope of this project, as we are mainly interested in comparing the forward barrier.

Table S 5: Product state analysis of the umbrella sampling and thermodynamic integration.

	US	TI
window25	TS	TS
window26	TS	TS
window27	TS/Propoxide	TS
window28	TS/Propoxide	TS
window29	TS	TS/Primary propanol
window30	Propene	Secondary propanol
window31	Primary propanol	Secondary propanol
window32	Propoxide	Primary propanol
window33	Propoxide	Propoxide
window34	Protonated cyclopropane	Propene
window35	Cyclopropane	Propoxide
window36	Propoxide	Cyclopropane
window37	Propoxide	Propoxide
window38	Cyclopropane	Cyclopropane
window39	Cyclopropane	Propoxide

window40	Propoxide	Primary propanol

The fact that more stable products are sampled during US simulations could be ascribed to the lower force constants used in these restrained simulations. These allow US to converge to a more stable product, while the TI runs are stuck in a less stable product. This wider sampling of the CV space in US is illustrated in the histograms obtained over all windows for both methods, depicted Figure S 7.

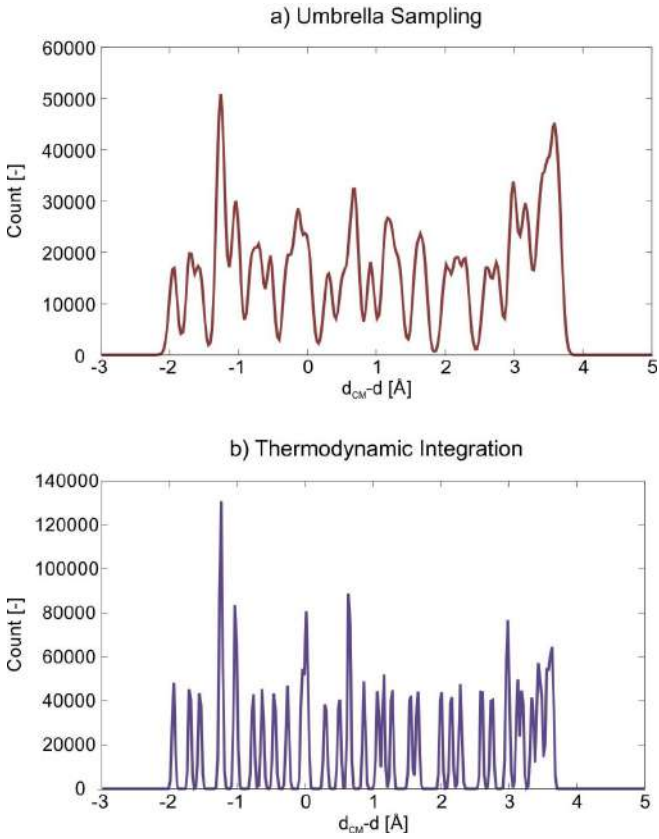

Figure S 7: Histograms showing the collective variables sampled by combining all windows of the umbrella sampling (a) and thermodynamic integrations (b) simulations. Remark: the broader reactant state windows used in umbrella sampling are not account for yet, as they are not sampled during thermodynamic integration.

6. DERIVATION TRANSFORMATION FORMULA

6.1. INTRODUCTION – STATISTICAL PHYSICS

According to classical statistical mechanics, the partition function Z and free energy F in the canonical ensemble of a system described by the Hamiltonian $\mathcal{H}(\vec{r}^N, \vec{p}^N) = T(\vec{p}^N) + V(\vec{r}^N)$ is given by:

$$Z = \frac{1}{h^{3N} N!} \int e^{-\beta \mathcal{H}(\vec{r}^N, \vec{p}^N)} d\vec{r}^N d\vec{p}^N$$

$$F = -k_B T \ln Z$$

Herein, the factor $N!$ only applies if the N particles are indistinguishable. We can now introduce a collective variable, i.e. a function of the coordinates describing a collective motion of the particles of the system $Q(\vec{r}^N)$, and further partition the partition function into contributions Z_q for fixed value of $Q(\vec{r}^N) = q$:

$$Z_q(q) = \frac{q_0}{h^{3N} N!} \int \delta(Q(\vec{r}^N) - q) e^{-\beta \mathcal{H}(\vec{r}^N, \vec{p}^N)} d\vec{r}^N d\vec{p}^N$$

The factor q_0 was introduced to make $Z_q(q)$ dimensionless. Furthermore, the new partition function satisfies:

$$\frac{1}{q_0} \int_{-\infty}^{+\infty} Z_q(q) dq = Z$$

This also allows us to define a probability distribution p_q such that $p_q(q)dq$ represents the probability for the system to be in a state for which $Q(\vec{r}^N) \in [q, q + dq]$:

$$p_q(q) = \frac{Z_q(q)}{Z q_0}$$

Through the relation between the partition function Z and the free energy F, we can relate Z_q to the free energy profile F_q:

$$F_q(q) = -k_B T \ln\left(Z_q(q)\right)$$

6.2. TRANSFORMATION OF 1D FREE ENERGY PROFILES

Suppose one defines two collective variables $Q_1(\vec{r}^N)$ and $Q_2(\vec{r}^N)$, which both describe the same process. This would give rise to two partition functions Z_{q1} and Z_{q2}, two probability densities p_{q1} and p_{q2} and two free energy profiles F_{q1} and F_{q2} If both collective variables indeed describe the same process, they are expected to be correlated and the free energy profiles belonging to each of the collective variables should be related to each other. Indeed, given the free energy profile $F_{q1}(q_1)$, one can derive the free energy profile $F_{q2}(q_2)$ as follows:

$$p_{q2}(q_2) = \int_{-\infty}^{+\infty} p_{12}(q_1, q_2) dq_1 = \int_{-\infty}^{+\infty} p_{2|1}(q_2|q_1) p_1(q_1) dq_1$$

$$\frac{Z_{q2}(q_2)}{Zq_{20}} = \int_{-\infty}^{+\infty} p_{2|1}(q_2|q_1) \frac{Z_{q1}(q_1)}{Zq_{10}} dq_1$$

$$e^{-\beta F_{q2}(q_2)} = \frac{q_{20}}{q_{10}} \int_{-\infty}^{+\infty} p_{2|1}(q_2|q_1) e^{-\beta F_{q1}(q_1)} dq_1$$

$$F_{q2}(q_2) = -k_B T \ln\left(\frac{q_{20}}{q_{10}} \int_{-\infty}^{+\infty} p_{2|1}(q_2|q_1) e^{-\beta F_{q1}(q_1)} dq_1\right)$$

Herein, $p_{12}(q_1, q_2)$ and $p_{2|1}(q_2|q_1)$ represent the joint and conditional probability respectively. The conditional probability encodes the correlation between the two collective variables, i.e. can we predict the value of Q_2 if we know Q_1? It can be estimated from a molecular simulation by constructing histograms of the occurrence of $Q_2 = q_2$ in the subset of the simulation data for which $Q_1 = q_1$. Furthermore, it is important for this work, that the conditional probability $p_{2|1}(q_2|q_1)$ can also be computed for simulations in which a bias along Q_1 was applied:

$$p_{2|1}(q_2|q_1) = \frac{p_{12}(q_1,q_2)}{p_{q1}(q_1)} = \frac{\frac{Z_{12}(q_1,q_2)}{Zq_{10}q_{20}}}{\frac{Z_{q1}(q_1)}{Zq_{10}}}$$

$$= \frac{\int \delta(Q_1(\vec{r}^N)-q_1)\delta(Q_2(\vec{r}^N)-q_2)e^{-\beta\mathcal{H}(\vec{r}^N,\vec{p}^N)}d\vec{r}^N d\vec{p}^N}{\int \delta(Q_1(\vec{r}^N)-q_1)e^{-\beta\mathcal{H}(\vec{r}^N,\vec{p}^N)}d\vec{r}^N d\vec{p}^N}$$

$$= \frac{\int \delta(Q_1(\vec{r}^N)-q_1)\delta(Q_2(\vec{r}^N)-q_2)e^{-\beta\mathcal{H}(\vec{r}^N,\vec{p}^N)}d\vec{r}^N d\vec{p}^N}{\int \delta(Q_1(\vec{r}^N)-q_1)e^{-\beta\mathcal{H}(\vec{r}^N,\vec{p}^N)}d\vec{r}^N d\vec{p}^N} \cdot \frac{e^{-\beta U_b(q_1)}}{e^{-\beta U_b(q_1)}}$$

$$= \frac{\int \delta(Q_1(\vec{r}^N)-q_1)\delta(Q_2(\vec{r}^N)-q_2)e^{-\beta[\mathcal{H}(\vec{r}^N,\vec{p}^N)+U_b(q_1)]}d\vec{r}^N d\vec{p}^N}{\int \delta(Q_1(\vec{r}^N)-q_1)e^{-\beta[\mathcal{H}(\vec{r}^N,\vec{p}^N)+U_b(q_1)]}d\vec{r}^N d\vec{p}^N}$$

$$= \frac{\int \delta(Q_1(\vec{r}^N)-q_1)\delta(Q_2(\vec{r}^N)-q_2)e^{-\beta\left[\mathcal{H}(\vec{r}^N,\vec{p}^N)+U_b\left(Q_1(\vec{r}^N)\right)\right]}d\vec{r}^N d\vec{p}^N}{\int \delta(Q_1(\vec{r}^N)-q_1)e^{-\beta\left[\mathcal{H}(\vec{r}^N,\vec{p}^N)+U_b\left(Q_1(\vec{r}^N)\right)\right]}d\vec{r}^N d\vec{p}^N}$$

$$= \frac{Z^b_{12}(q_1,q_2)}{q_{20}Z^b_{q1}(q_1)} = \frac{p^b_{12}(q_1,q_2)}{p^b_{q1}(q_1)}$$

$$= p^b_{2|1}(q_2|q_1)$$

If Q_1 and Q_2 are perfectly correlated, i.e. Q_2 can be expressed as a deterministic function of Q_1, through the relation $Q_2 = f(Q_1)$, the conditional probability is given by $p_{2|1}(q_2|q_1) = \delta\big(q_2 - f(q_1)\big)$ and the expression for $F_{q2}(q_2)$ reduces to:

$$F_{q2}(q_2) = F_{q1}\big(f^{-1}(q_2)\big) + k_B T \ln\left(\frac{q_{10}}{q_{20}}\left|f'\big(f^{-1}(q_2)\big)\right|\right)$$

6.3. TRANSFORMATION OF 2D FREE ENERGY PROFILES

The above transformation formula for one-dimensional profiles can be extended to transform a two-dimensional profile $F_q(q_1,q_2)$ in terms of collective variables q_1 and q_2 into a two-dimensional profile $F_u(u_1,u_2)$ in terms of u_1 and u_2:

$$p_u(u_1,u_2) = \iint_{-\infty}^{+\infty} p_{qu}(q_1,q_2,u_1,u_2)dq_1dq_2 = \iint_{-\infty}^{+\infty} p_{u|q}(u_1,u_2|q_1,q_2)p_q(q_1,q_2)dq_1dq_2$$

$$\frac{Z_u(u_1,u_2)}{Zu_{10}u_{20}} = \iint_{-\infty}^{+\infty} p_{u|q}(u_1,u_2|q_1,q_2)\frac{Z_q(q_1,q_2)}{Zq_{10}q_{20}}dq_1dq_2$$

$$e^{-\beta F_u(u_1,u_2)} = \frac{u_{10}u_{20}}{q_{10}q_{20}} \iint_{-\infty}^{+\infty} p_{u|q}(u_1,u_2|q_1,q_2) e^{-\beta F_q(q_1,q_2)} dq_1 dq_2$$

$$F_u(u_1,u_2) = -k_B T \ln\left(\frac{u_{10}u_{20}}{q_{10}q_{20}} \iint_{-\infty}^{+\infty} p_{u|q}(u_1,u_2|q_1,q_2) e^{-\beta F_q(q_1,q_2)} dq_1 dq_2 \right)$$

Finally, one can also extend the formula to transform a one-dimensional profile $F_q(q)$ in terms of the collective variable q into a two-dimensional profile $F_u(u_1,u_2)$ in terms of u_1 and u_2:

$$p_u(u_1,u_2) = \int_{-\infty}^{+\infty} p_{qu}(q,u_1,u_2) dq = \int_{-\infty}^{+\infty} p_{u|q}(u_1,u_2|q) p_q(q) dq$$

$$\frac{Z_u(u_1,u_2)}{Zu_{10}u_{20}} = \int_{-\infty}^{+\infty} p_{u|q}(u_1,u_2|q) \frac{Z_q(q)}{Zq_0} dq$$

$$e^{-\beta F_u(u_1,u_2)} = \frac{u_{10}u_{20}}{q_0} \int_{-\infty}^{+\infty} p_{u|q}(u_1,u_2|q) e^{-\beta F_q(q)} dq$$

$$F_u(u_1,u_2) = -k_B T \ln\left(\frac{u_{10}u_{20}}{q_0} \int_{-\infty}^{+\infty} p_{u|q}(u_1,u_2|q) e^{-\beta F_q(q)} dq \right)$$

6.4. PROJECTING 2D FREE ENERGY SURFACE TO 1D PROFILE

Assume a molecular simulation was performed that resulted in a 2D free energy surface $F_{12}(q_1,q_2)$ in terms of the collective variables $Q_1(\vec{r}^N)$ and $Q_2(\vec{r}^N)$. We now outline how to project the 2D FES onto a 1D profile in terms of a collective variable $Q = f(Q_1,Q_2)$. Similar as in the previous section, the 1D profile can be obtained through integration of the 2D probability distribution:

$$p_q(q) = \iint_{-\infty}^{+\infty} p_{12}(q_1,q_2) \delta(f(q_1,q_2) - q) dq_1 dq_2$$

$$F_q(q) = -k_B T \ln\left(\frac{q_0}{q_{10}q_{20}} \iint_{-\infty}^{+\infty} e^{-\beta F_{12}(q_1,q_2)} \delta(f(q_1,q_2) - q) dq_1 dq_2 \right)$$

We illustrate this further for the case of the projection on the difference between the two collective variables $Q = Q_2 - Q_1$:

$$F_q(q) = -k_B T \ln\left(\frac{q_0}{q_{10}q_{20}} \iint_{-\infty}^{+\infty} e^{-\beta F_{12}(q_1,q_2)} \delta(q_2 - q_1 - q) dq_1 dq_2\right)$$

$$= -k_B T \ln\left(\frac{q_0}{q_{10}q_{20}} \int_{-\infty}^{+\infty} e^{-\beta F_{12}(q_1,q_1+q)} dq_1\right)$$

7. FREE ENERGY BARRIERS BY SUBTRACTING MINIMUM FROM MAXIMUM

As stated in the manuscript, the obtained free energy profiles can only be compared to one another after the transformation described in Section 6 is applied. All the profiles obtained in this manner, depicted in Figure 7 of the main manuscript, show quite good agreement in the forward barriers after sampling in different collective variable (Q_{SAM}) spaces but transforming to the same (Q_{REP}) space. On the other hand, profiles transformed to other Q_{REP} do differ significantly.

This becomes even more clear when calculating the barrier, just considering the minimum and maximum in the profile, [12] resulting in Table S 6, as this shows a big discrepancy, mainly between Type CN on the one hand and Type DI on the other hand. The reason behind this difference can be understood by looking at the green profile in all graphs. These show that while there is a well-defined, thin well for the reactants in the Type CN space, this actually corresponds with a broad range of configurations in the Type DI space. This is also represented by the mobility plots depicted in Figure S 9 discussed in Section 9 of this ESI. The broader sampling is due to the relation between a coordination number and a distance, as can be seen in Figure S 8. It shows that for short and large distances, the states are projected on the values one and zero, respectively, due to the shape of the function. As the free energy relates to the probability to sample a state, the increased probability to sample the states zero and one, will lower their free energy. After the transformation to a Type DI space, we see that this corresponds to several states with similar free energy. How one can account for this configuration freedom is discussed in the main manuscript and Section 10 of this ESI.

Table S 6: Free energy barriers (kJ/mol) for the profiles depicted in Figure 8 of the main manuscript by subtracting the minimum from the maximum.

Q_{SAM} \ Q_{REP}	CN_{CC}-CN_{OC}	d_{CM}-d
Type CN	127.3	102.4
Type DI	129.1	114.6
Type 1D-DI	129.7	116.6

8. DEFINITION OF A COORDINATION NUMBER

As discussed in the main manuscript, a coordination number can be used to describe the methylation of ethene. In Section 2.4.1. of the main manuscript, a coordination number is defined as:

$$CN_{ij} = \sum_{i,j} \frac{1 - \left(\frac{r_{ij}}{r_0}\right)^{nn}}{1 - \left(\frac{r_{ij}}{r_0}\right)^{nd}}$$

This is furthermore plotted for a reference distance of 2.0 Å in Figure S 8.

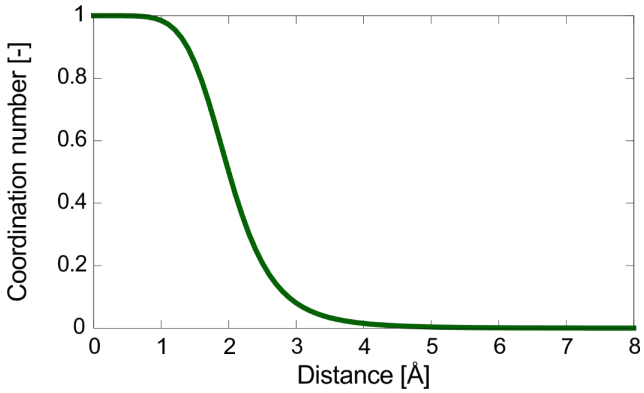

Figure S 8: Graph showing the evolution of a coordination number with reference distance 2.0 Å in function of the distance between two atoms

9. ANALYSIS OF THE MOBILITY OF THE REACTANTS

Figure 8 of the main manuscript shows that the sampling of the reactant state in the Type CN space differs, so for CN_{CC} ~ 0 (window 1), lead to a broad sampling in distance space. Therefore, the mobility of the reactants is analyzed by plotting the center-of-mass trajectory for an unbiased molecular dynamics simulation and a reactant window (window 1) using Type CN or Type 1D-DI as a collective variable, as depicted in Figure S 9. These plots show that the mobility of methanol (red) is barely influenced by applying the bias, as it stays adsorbed on the Brønsted acid site. On the other hand, the diffusional freedom of ethene (green) is significantly altered using collective variable 1D-DI, but not in the Type CN case. This can be understood by looking at the variation of the 'Coordination numbers' in function of a distance in Figure S 8. At increased distances, the coordination number quickly drops to 0, making all states at higher distances equivalently biased. When applying the bias on the distance on the other hand, increased distances will be subjected to an increased bias, thus limiting their sampling. Therefore, the reactant state is more broadly sampling considering Type CN as a collective variable, leading to a slightly more stabilized reactant state in the CN_{CC}-CN_{OC} free energy profile in Figure 8 of the main manuscript and a broader reactant state in the Type DI free energy profiles in Figure 8 of the main manuscript. To obtain similarly broad sampling in the profiles for DI and 1D-DI several more windows in the reactant space were added with a lower force constant for the bias to broaden the sampling as indicated in Table S 3.

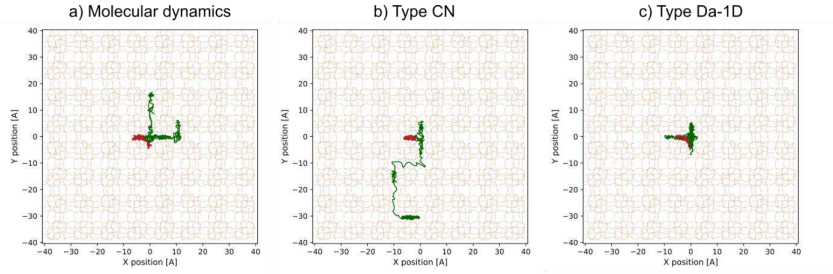

Figure S 9: Mobility plots, showing the mobility of methanol (red) and ethene (green) in the reactant state for 50 ps of molecular dynamics simulation (a), 50 ps of sampling in window 1 of the umbrella sampling simulations using Type CN (b) and 50 ps of sampling in window 1 of the umbrella sampling simulations using Type 1D-DI.

10. REACTION RATE CALCULATIONS

To compute the rate constant k for the reaction $R \rightarrow P$, we start from the transition state theory expression, which can be expressed as: [13,14]

$$k = \frac{\langle \dot{q}\theta(\dot{q})\delta(q - q^*)\rangle}{\langle \theta(q^* - q)\rangle}$$

Herein, q is a function of the molecular configuration and represents the reaction coordinate describing the progress along the reaction, while q^* represents its value in the transition state. θ and δ represent the Heaviside and Dirac delta functions respectively. Next, we apply a canonical transformation towards mass-weighted coordinates $\vec{x}_i = \sqrt{m_i} \cdot \vec{r}_i$ and momenta $\vec{P}_i = {m_i}^{-1/2} \cdot \vec{p}_i$, and perform the integrals over the momenta explicitly. As a result, the expression can be rewritten as: [13]

$$k = \sqrt{\frac{1}{2\pi\beta}} \cdot \frac{\int \delta(q(\vec{x}^N) - q^*)\left|\vec{\nabla}_x q\right| e^{-\beta U(\vec{x}^N)} d\vec{x}^N}{\int_R e^{-\beta U(\vec{x}^N)} d\vec{x}^N}$$

Herein, the integral in the denominator runs over all reactant states, i.e. for $q(\vec{x}^N) < q^*$. Finally, through the introduction of the free energy profile *F* in terms of the collective variable *q*, which was computed by means of an enhanced sampling method, we rewrite the expression further as:

$$k = A \frac{e^{-\beta F(q^*)}}{\bar{Z}_R} \qquad \text{(1a)}$$

In which $F(q^*)$ represents the free energy at the transition, A represents a prefactor, and $\bar{Z}_R$ is proportional to the partition function of the reactant. These quantities can be computed as follows:

$$A = \sqrt{\frac{1}{2\pi\beta}} \cdot \langle \left|\vec{\nabla}_x q\right| \rangle_{q^*} \qquad \text{(1b)}$$

$$\bar{Z}_R = \int_{-\infty}^{q^*} e^{-\beta F(q)} dq \qquad (1c)$$

Although the expression for the prefactor A indicates that a molecular simulation needs to be performed in which the system is constrained to be in the exact transition state ($q = q^*$), this is not necessarily required. The prefactor can also be estimated from a molecular simulation which is instead biased by a certain bias potential $U_b(q)$ (for example during Umbrella Sampling):

$$\langle|\vec{\nabla}_x q|\rangle_{q^*} = \frac{\langle\delta(q-q^*)|\vec{\nabla}_x q|\rangle_{U_b}}{\langle\delta(q-q^*)\rangle_{U_b}}$$

In the simplest case of a one-dimensional system, i.e. a particle with mass m moving in a one-dimensional potential $U(r)$ as function of the position r (with $x = \sqrt{m}\cdot r$ the mass weighted position), the rate becomes:

$$\langle|\vec{\nabla}_x q|\rangle_{q^*} = \langle|\vec{\nabla}_x r|\rangle_{r^*} = \langle\frac{dr}{dx}\rangle = \langle\frac{1}{\sqrt{m}}\rangle_{r^*} = \frac{1}{\sqrt{m}}$$

$$k_{1D} = \sqrt{\frac{1}{2\pi\beta m}} \cdot \frac{e^{-\beta U(r^*)}}{\int_{-\infty}^{r^*} e^{-\beta U(r)} dr}$$

This rate constant can also be cast into the more familiar format:

$$k_{1D} = \frac{kT}{h} \cdot \frac{1}{Z_R} \cdot e^{-\beta U(r^*)}$$

$$Z_R = \frac{1}{h}\int e^{-\beta\left[\frac{p^2}{2m}+U(r)\right]} dr dp = \frac{1}{\Lambda}\int e^{-\beta U(r)} dr$$

$$\Lambda = \sqrt{\frac{h^2\beta}{2\pi m}}$$

This simple case can serve as inspiration for an approximation for the more complex case of a N-particle molecular system in 3 dimensions. This approximation assumes the system is described by a single degree of freedom given by the collective variable q, to which a mass m is associated and which moves in the potential $F(q)$. As a result, the rate constant becomes:

$$\tilde{k} = \underbrace{\sqrt{\frac{1}{2\pi\beta m}}}_{\triangleq B} \cdot \frac{e^{-\beta F(q^*)}}{\int_{-\infty}^{q^*} e^{-\beta F(q)} dq}$$

Hence, *B* represents the approximated value of *A*. Unfortunately, it is not trivial to associate a mass to a certain collective variable. Therefore, we estimate the rate constant using Eq (1) in this work. We computed the rate constants according to Eq. (1), as well as the various contributions to it, for the methylation reaction. Furthermore, to investigate the influence of the choice of the collective variable, we computed the rate constant through various approaches. First, the enhanced sampling simulations were performed using the various collective variables defined in this work. This collective variable is denoted as Q_{SAM}. Second, the resulting free energy profile can be expressed in terms of this same collective variable, but it can also be transformed to a profile in terms of one of the other CVs. The collective variable used to express the free energy profile is denoted as Q_{REP}. The reference of the free energy profiles is always chosen such that the minimum in the reactant valley is set to zero, leading to the free energy differences summarized in Table S 6. Furthermore, Table S 7 and Table S 8 below indicate the other contributions from Eq. (1) for various combinations of Q_{SAM} and Q_{REP}.

Table S 7: Prefactor A (in units [au]/s, with [au] atomic units of the CV) figuring in the expression of the rate constant (Eq. 1).

Q_{SAM} \ Q_{REP}	CN_{CC}-CN_{OC}	d_{CM}-d
Type CN	$4.82\ 10^{12}$	$1.09\ 10^{13}$
Type DI	$4.77\ 10^{12}$	$1.13\ 10^{13}$
Type 1D-DI	$4.98\ 10^{12}$	$1.17\ 10^{13}$

Table S 8: Factor proportional to the partition function of the reactant $\bar{Z}_R$ (in atomic units of the CV). This factor expresses the stability of the reactant.

Q_{SAM} \ Q_{REP}	CN_{CC}-CN_{OC}	d_{CM}-d
Type CN	$6.50\ 10^{-2}$	$1.00\ 10^{1}$
Type DI	$6.30\ 10^{-2}$	$3.15\ 10^{0}$
Type 1D-DI	$6.83\ 10^{-2}$	$3.28\ 10^{0}$

As can be concluded from these tables, the free energy barrier is clearly dependent on the choice of the collective variable (see Table S 6). However, when computing the rate constants (Table 2 of the main manuscript), this dependence is to a very large extent compensated with the factors $\bar{Z}_R$ and A. The remaining differences can be assumed to be due to numerical errors. These results imply, that one cannot simply rely on the free energy barrier to make statements on how fast a reaction will occur. Instead, one needs to compute all contributions to the reaction rate consistently.

11. COMMITTOR ANALYSIS

A first test to estimate the reliability of the obtained free energy profiles consists of calculating the committor at the transition state suggested by the resulting free energy profiles, as a consideration of the entire transition path becomes too expensive using ab initio calculations. [10] A committor is the fraction, $p_P(q)$, of trajectories which are launched from a configuration with the collective variable equal to q that end up in the product state, P, before visiting the reactant state, R. [10] At the transition state, this should equal 0.5. The committor is calculated for the energy profiles resulting from the enhanced MD simulations with the collective variables of type CN and 1D-DI. From the selected snapshots – obtained in the window that samples the transition region – MD simuations are started. For Type 1D-DI snapshots with d_{CM}-d near 0.2795 Å are selected and for Type CN snapshots with CN_{CC}-CN_{OC} near 0.028, leading to 291 and 102 snapshots, respectively. The committor is calculated to get values of 0.76 and 0.70, respectively. Furthermore, the histograms shown in Figure S 10 and Figure S 11 show a rather broad range of values sampled for the committor in both cases. This could either be due to insufficient simulations in the committor analysis or it suggests that these collective variables are not perfectly describing this methylation reaction and extra orthogonal directions should be accounted for. Systematic protocols exist to identify better collective variables by obtaining the slowest order parameters describing the transformation from reactant to product via time-structure based independent component analysis (tICA). [15–17] As MD data containing transitions are required to perform this analysis, this becomes computationally to expensive and out of scope of this work.

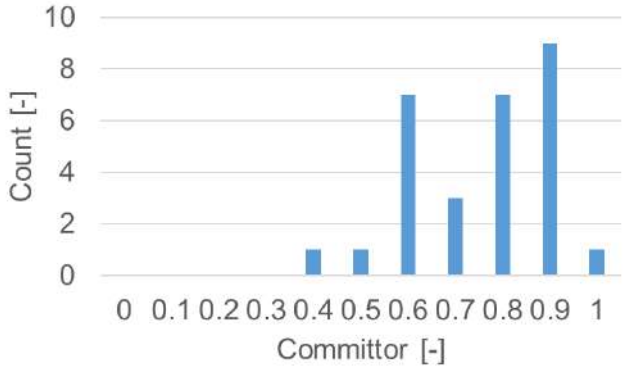

Figure S 10: Committor histogram obtained for the transition state of CV Type 1D-DI.

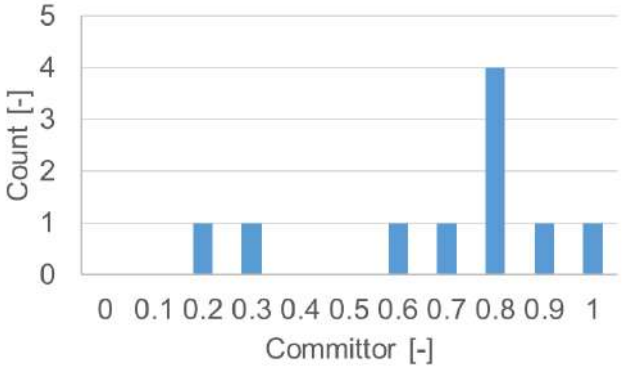

Figure S 11: Committor histogram obtained for the transition state of CV Type CN.

12. BIASED MOLECULAR DYNAMICS

In this section, we investigate whether our free energy barrier is underestimated because important degrees of freedom were ignored during the simulations or whether it is too high as the system gets trapped in local minima. [10,18–21] . In this way, a too low barrier will not let us sample the transition state in this simulation, while a to high barrier will only let us sample the transition state. This is tested by performing a biased MD simulation, in which the inverse of the free energy profile obtained by collective variable 1D-DI is used as bias

To use the free energy profile obtained using Type 1D-DI as a bias in PLUMED [22], a 14th order polynomial is first fitted to the profile. The fitting is shown in Figure S 12 and leads to following bias used in PLUMED:

$$w(\xi) = -0.0000329\,\xi^{14} - 0.00146\,\xi^{13} + 0.0246\,\xi^{12} - 0.118\,\xi^{11} + 0.0468\,\xi^{10} + 1.271\,\xi^{9} - 3.185\,\xi^{8} - 2.805\,\xi^{7} + 20.041\,\xi^{6} - 9.635\,\xi^{5} - 56.623\,\xi^{4} + 49.717\,\xi^{3} + 96.910\,\xi^{2} - 70.297\,\xi^{1} - 118.642$$

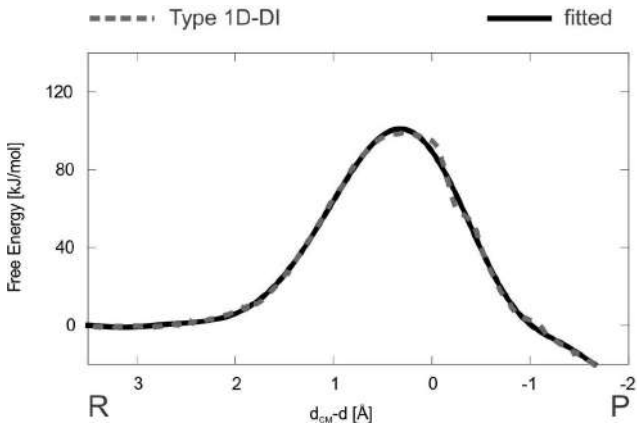

Figure S 12: 14th order polynomial fit to the free energy profile obtained via collective variable 1D-DI.

As we again are only interested in the forward barrier, the walls used during metadynamics and variationally enhanced sampling are again applied to avoid sampling uninteresting

configurations and to increase our efficiency. The time evolution of this CV is shown in Figure S 13.

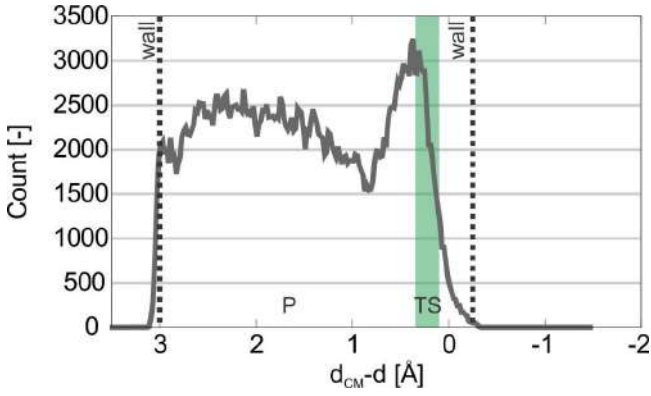

Figure S 13: Histogram of the collective variable 1D-DI for the biased MD simulation.

This plot shows that the collective variable indeed samples all the reactant and transition state region during the biased MD simulation, thus confirming our obtained free energy profile. Nevertheless, the histogram drops significantly after the transition region (0.1 - 0.35 Å), again confirming the problems we encounter with the product region in the current work. However, the histogram shows that the forward barrier is trustworthy.

13. STATIC RESULTS

As stated in the main manuscript, a direct comparison of our dynamic results with theoretical and experimental data found in literature [23–27] is hampered as they did not report intrinsic free energy barriers or intrinsic reaction rates. There are no generally accepted methodologies to extract enthalpic barriers and adsorption enthalpies directly from ab initio molecular dynamics methods. Two methodologies are proposed to overcome this hurdle.

In a first instance, we also simulated the reactions using periodic DFT calculations in the rigid rotor harmonic oscillator model, to allow a comparison with experimental data and earlier theoretical data. The resulting enthalpy, entropy and free energy data relative to the gas phase for the different steps of the methylation of ethene are summarized in Table S 9. Furthermore, the static results are compared with available literature data in Table S 10.

Inspection of the results learns that the obtained adsorption enthalpy for methanol, -99.8 kJ/mol, is very close to the value obtained by Van Speybroeck et al. [27] using cluster calculations, and revealing a slight underestimation of the experimental value of -115 ± 5 kJ/mol. [26,28] The subsequent co-adsorption enthalpy for ethene attains -13.2 kJ/mol, which is again similar to the -10.35 kJ/mol obtained by Van Speybroeck et al. [27] and underestimating the experimental value varying from -24 and -31 kJ/mol. [26,29] Finally, the apparent enthalpy barrier amounts to 86.8 kJ/mol, close to the value of Van Speybroeck et al. but 17 kJ/mol lower than the experimental value of 104 kJ/mol. [23–27]

Subsequently, free energy data can be generated from our static results via a post-analysis methodology making use of the in-house developed TAMkin software [30,31] as applied in recent papers by some of the current authors [5,12,32,33]. This value can be compared with the free energy barrier predicted by the MD simulations. The static intrinsic free energy barrier attains a value of 139.5 kJ/mol, thus overestimating the values obtained via the enhanced sampling methods in this work, as tabulated in Table 2 of the main manuscript. As no

experimental data is available for this free energy barrier, it is difficult to put forward which of the two values is correct.

Secondly, apparent reaction rate constants k_{app} can be obtained from intrinsic reaction rate constants k_{int} by calculating the equilibrium constant for the co-adsorption of ethene, K_1 as follows: [34]

$$CH_3OH\ (ads) + ethene\ (gas) \underset{k_{-1}}{\overset{k_1}{\rightleftharpoons}} CH_3OH\ (ads) + ethene\ (ads) = PRC$$

$$PRC \xrightarrow{k_{int}} Products$$

$$r = k_{int}[PRC]$$

$$\frac{d[PRC]}{dt} = 0 = -k_{int}[PRC] + k_1[ethene(gas)][methanol(ads)] - k_{-1}[PRC]$$

$$r = k_{app}[ethene(gas)][methanol(ads)] = \frac{k_1 \times k_{int}}{k_{-1} + k_{int}}[ethene(gas)][methanol(ads)]$$

$$= K_1\, k_{int}[ethene(gas)][methanol(ads)]$$

$$k_{app} = K_1\, k_{int}$$

where the co-adsorbed methanol and ethene are treated as a pre-reactive complex, PRC. Furthermore, a pseudo-stationary state hypothesis is applied on the PRC and the factor k_{int} in the denominator is assumed to be smaller than k_{-1}, as the reaction is assumed to be kinetically controlled. The equilibrium constant can be calculated from the co-adsorption free energy for ethene $\Delta G_{ads,ethene}$ as:

$$K_1 = V_0 \exp\left(\frac{-\Delta G_{ads,ethene}}{RT}\right)$$

with V_0 the molar volume of an ideal gas at 623 K and 1 atm, equal to 0.0518 m³/mol.

The relation between intrinsic and apparent rate constants can also easily be derived based on statistical mechanics with the introduction of Gibbs free energies in the determination of reaction rate constants (see Scheme S 1).

(i) The apparent rate constant of the bimolecular reaction:

$$CH_3OH\ (ads) + ethene\ (gas) \rightarrow TS$$

is given by:

$$k_{app} = \frac{k_B T}{h} V_0 \exp(-\frac{\Delta G_{app}}{RT})$$

(ii) The intrinsic rate constant of the monomolecular reaction:

$$PRC \rightarrow TS$$

is given by

$$k_{int} = \frac{k_B T}{h} \exp(-\frac{\Delta G_{int}}{RT})$$

(iii) The equilibrium reaction:

$$CH_3OH\ (ads) + ethene\ (gas) \rightleftharpoons PRC$$

is characterized by its equilibrium constant

$$K_1 = V_0\ exp(-\frac{\Delta G_{ads,ethene}}{RT}) = \frac{k_{+1}}{k_{-1}}$$

Based on the free energy relation $\Delta G_{app} = \Delta G_{ads,ethene} + \Delta G_{int}$, one readily derives $k_{app} = K_1 k_{int}$.

As the co-adsorption free energy $\Delta G_{ads,alkene}$ of alkenes in the MTO process are very functional and dispersion scheme dependent, single point energy calculations are performed with a set of functionals frequently used in literature [32,35] starting from optimized structures obtained using revPBE-D3. In this work the following set is considered. The revPBE functional can be combined with diverse dispersion schemes. To study their influence, we take several schemes into consideration: D2 corrections, [36] D3 corrections with Becke Johnson damping (BJ), [37] the many body dispersion (MBD) scheme of Tkatchenko-Scheffler, [38] both conventional and with iterative Hirshfeld partitioning (MBD-HI), [39–41] the many body dispersion energy method of Tkatechenko based on the random phase expression for the

correlation energy (MBD-rsSCS) [42,43] and the dDsC dispersion correction. [44,45] In addition, we also consider multiple functionals of different type: revPBE used as basis for the calculations with vdW-DF of Dion et al. [46,47] , BEEF-vdW, [48] B3LYP-D3 [49] as hybrid functional and SCAN-rVV10. [50] The obtained $\Delta G_{ads,ethene}$ are summarized in Table S 11. The corresponding equilibrium constants can be found in Table S 12. The results are discussed in detail in Section 3.4 of the main manuscript.

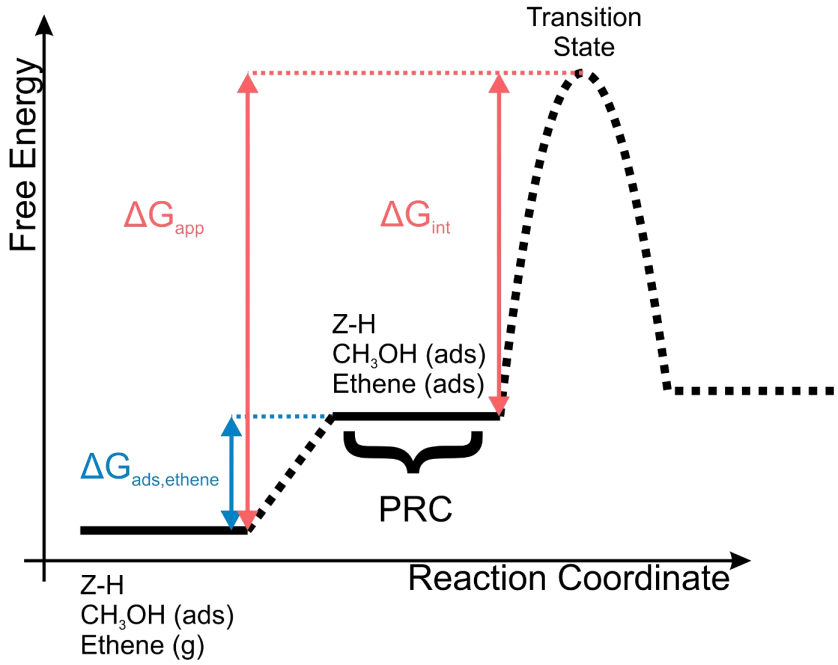

Scheme S 1: Schematic representation of the free energy profile

Table S 9: Enthalpy, entropy and free energy data at 623 K relative to the gas phase for the different steps of the methylation profile of ethene (in kJ/mol).

	CH_3OH (g) Ethene (g) Z-H	CH_3OH (ads) Ethene (g) Z-H	CH_3OH (ads) Ethene (ads) Z-H	Transition State	Product
ΔH	0.0	-99.8	-113.0	-13.0	-129.2
$-T\Delta S$	0.0	93.9	137.2	176.6	160.3
ΔG	0.0	-5.9	24.2	163.6	31.0

Table S 10: Enthalpy values (kJ/mol) from literature and obtained in the current paper of the various steps for the methylation of ethene at 623 K (unless stated otherwise).

	Experimental	Svelle et al. [26]	Van Speybroeck et al. [27]	Piccini et al. [23]	Current paper
$\Delta H_{ads,methanol}$	-115±5[a] [26,28]	-115[c]	-97.3[e]	n.a.	-99.8
$\Delta H_{co-ads,ethene}$	-24 - -31[b] [26,29]	-37[c]	1.6 (-10.4[e])	n.a.	-13.2
$\Delta H^{\neq}_{app}$	104 [24,25]	104	83.2	105.4	86.8
$\Delta H^{\neq}_{int}$	n.a.	119[d]	84.03[e]	n.a.	100.0

[a] Only available at 400 K. [b] Only available in the range 298 – 353 K [c] Only electronic energies (0 K) with PBE-D available for these values in ref [26]. [d] Only electronic energies (0 K) with PBE available for these values in SI of ref [26]. [e] Only electronic energies with ONIOM(B3LYP/6-31+g(d):HF/6-31+g(d)) level of theory with inclusion of van der Waals corrections for these values in ref [27].

Table S 11: Adsorption energy and free energy for the co-adsorption of ethene using various functionals and dispersion corrections schemes (kJ/mol).

	revPBE-D3	revPBE-D2	revPBE-D3(BJ)	revPBE-MBD	revPBE-MBD_HI	revPBE-MBD_rSC	revPBE-DdSc	BEEF_vdW	vdW-DF of Dion	B3LYP-D3	SCAN-rVV10
$\Delta E_{ads,ethene}$	-22.7	-12.0	-22.0	-21.3	-18.7	-12.0	-11.0	-23.6	-36.8	-20.3	-11.9
$\Delta G_{ads,ethene}$	30.1	40.8	30.8	31.5	34.1	40.8	41.7	29.1	16.0	32.5	40.9

Table S 12: Equilibrium constants for the co-adsorption of ethene using various functionals and dispersion correction schemes (m³/mol).

	revPBE-D3	revPBE-D2	revPBE-D3(BJ)	revPBE-MBD	revPBE-MBD_HI	revPBE-MBD_rSC	revPBE-DdSc	BEEF_vdW	vdW-DF of Dion	B3LYP-D3	SCAN-rVV10
K_1	$1.57\ 10^{-4}$	$1.96\ 10^{-5}$	$1.36\ 10^{-4}$	$1.18\ 10^{-4}$	$7.19\ 10^{-5}$	$1.96\ 10^{-5}$	$1.64\ 10^{-5}$	$1.87\ 10^{-4}$	$2.35\ 10^{-3}$	$9.75\ 10^{-5}$	$1.94\ 10^{-5}$

REFERENCES

(1) Dědeček, J.; Sklenak, S.; Li, C.; Wichterlová, B.; Gábová, V.; Brus, J.; Sierka, M.; Sauer, J. Aluminum Siting in the Framework of Silicon Rich Zeolites. A ZSM-5 Study. In *Zeolites and related materials: Trends, targets and challenges*; Gédéon, A., Massiani, P., Babonneau, F., Eds.; Studies in Surface Science and Catalysis; Elsevier, 2008; Vol. 174, pp 781–786.

(2) Van der Mynsbrugge, J.; Hemelsoet, K.; Vandichel, M.; Waroquier, M.; Van Speybroeck, V. Efficient Approach for the Computational Study of Alcohol and Nitrile Adsorption in H-ZSM-5. *J. Phys. Chem. C* **2012**, *116* (9), 5499–5508.

(3) Bhan, A.; Joshi, Y. V.; Delgass, W. N.; Thomson, K. T. DFT Investigation of Alkoxide Formation from Olefins in H-ZSM-5. *J. Phys. Chem. B* **2003**, *107* (38), 10476–10487.

(4) Yarulina, I.; Bailleul, S.; Pustovarenko, A.; Martinez, J. R.; De Wispelaere, K.; Hajek, J.; Weckhuysen, B. M.; Houben, K.; Baldus, M.; Van Speybroeck, V.; Kapteijn, F.; Gascon, J. Suppression of the Aromatic Cycle in Methanol-to-Olefins Reaction over ZSM-5 by Post-Synthetic Modification Using Calcium. *ChemCatChem* **2016**, *8* (19), 3057–3063.

(5) Yarulina, I.; De Wispelaere, K.; Bailleul, S.; Goetze, J.; Radersma, M.; Abou-Hamad, E.; Vollmer, I.; Goesten, M.; Mezari, B.; Hensen, E. J. M.; Martínez-Espín, J. S.; Morten, M.; Mitchell, S.; Perez-Ramirez, J.; Olsbye, U.; Weckhuysen, B. M.; Van Speybroeck, V.; Kapteijn, F.; Gascon, J. Structure–Performance Descriptors and the Role of Lewis Acidity in the Methanol-to-Propylene Process. *Nat. Chem.* **2018**, *10* (8), 804–812.

(6) De Wispelaere, K.; Bailleul, S.; Van Speybroeck, V. Towards Molecular Control of Elementary Reactions in Zeolite Catalysis by Advanced Molecular Simulations Mimicking Operating Conditions. *Catal. Sci. Technol.* **2016**, *6* (8), 2686–2705.

(7) Rogge, S. M. J.; Vanduyfhuys, L.; Ghysels, A.; Waroquier, M.; Verstraelen, T.; Maurin, G.; Van Speybroeck, V. A Comparison of Barostats for the Mechanical Characterization of Metal–Organic Frameworks. *J. Chem. Theory Comput.* **2015**, *11* (12), 5583–5597.

(8) Basconi, J. E.; Shirts, M. R. Effects of Temperature Control Algorithms on Transport Properties and Kinetics in Molecular Dynamics Simulations. *J. Chem. Theory Comput.* **2013**, *9* (7), 2887–2899.

(9) Demuynck, R.; Rogge, S. M. J.; Vanduyfhuys, L.; Wieme, J.; Waroquier, M.; Van Speybroeck, V. Efficient Construction of Free Energy Profiles of Breathing Metal–Organic Frameworks Using Advanced Molecular Dynamics Simulations. *J. Chem. Theory Comput.* **2017**, *13* (12), 5861–5873.

(10) Peters, B. Reaction Coordinates and Mechanistic Hypothesis Tests. *Annu. Rev. Phys. Chem.* **2016**, *67* (1), 669–690.

(11) Bailleul, S.; Rogge, S. M. J.; Vanduyfhuys, L.; Van Speybroeck, V. Insight into the Role of Water on the Methylation of Hexamethylbenzene in H-SAPO-34 from First Principle Molecular Dynamics Simulations. *ChemCatChem* **2019**, *11* (16), 3993–4010.

(12) Cnudde, P.; De Wispelaere, K.; Van der Mynsbrugge, J.; Waroquier, M.; Van Speybroeck, V. Effect of Temperature and Branching on the Nature and Stability of Alkene Cracking Intermediates in H-ZSM-5. *J. Catal.* **2017**, *345*, 53–69.

(13) Hänggi, P.; Talkner, P.; Borkovec, M. Reaction-Rate Theory: Fifty Years after Kramers. *Rev. Mod. Phys.* **1990**, *62* (2), 251–341.

(14) Frenkel, D.; Smit, B. *Understanding Molecular Simulation: From Algorithms to Applications*; Academic Press, 2001.

(15) Demuynck, R.; Wieme, J.; Rogge, S. M. J.; Dedecker, K. D.; Vanduyfhuys, L.; Waroquier, M.; Van Speybroeck, V. Protocol for Identifying Accurate Collective Variables in Enhanced Molecular Dynamics Simulations for the Description of

Structural Transformations in Flexible Metal–Organic Frameworks. *J. Chem. Theory Comput.* **2018**, *14* (11), 5511–5526.
(16) Schwantes, C. R.; Pande, V. S. Improvements in Markov State Model Construction Reveal Many Non-Native Interactions in the Folding of NTL9. *J. Chem. Theory Comput.* **2013**, *9* (4), 2000–2009.
(17) Pérez-Hernández, G.; Paul, F.; Giorgino, T.; De Fabritiis, G.; Noé, F. Identification of Slow Molecular Order Parameters for Markov Model Construction. *J. Chem. Phys.* **2013**, *139* (1), 015102.
(18) Rohrdanz, M. A.; Zheng, W.; Clementi, C. Discovering Mountain Passes via Torchlight: Methods for the Definition of Reaction Coordinates and Pathways in Complex Macromolecular Reactions. *Annu. Rev. Phys. Chem.* **2013**, *64* (1), 295–316.
(19) Krivov, S. V.; Karplus, M. Hidden Complexity of Free Energy Surfaces for Peptide (Protein) Folding. *Proc. Natl. Acad. Sci.* **2004**, *101* (41), 14766–14770.
(20) Rosta, E.; Woodcock, H. L.; Brooks, B. R.; Hummer, G. Artificial Reaction Coordinate "Tunneling" in Free-Energy Calculations: The Catalytic Reaction of RNase H. *J. Comput. Chem.* **2009**, *30* (11), 1634–1641.
(21) Li, W.; Ma, A. Recent Developments in Methods for Identifying Reaction Coordinates. *Mol. Simul.* **2014**, *40* (10–11), 784–793.
(22) Bonomi, M.; Branduardi, D.; Bussi, G.; Camilloni, C.; Provasi, D.; Raiteri, P.; Donadio, D.; Marinelli, F.; Pietrucci, F.; Broglia, R. A.; Parrinello, M. PLUMED: A Portable Plugin for Free-Energy Calculations with Molecular Dynamics. *Comput. Phys. Commun.* **2009**, *180* (10), 1961–1972.
(23) Piccini, G.; Alessio, M.; Sauer, J. Ab Initio Calculation of Rate Constants for Molecule–Surface Reactions with Chemical Accuracy. *Angew. Chem. Int. Ed.* **2016**, *55* (17), 5235–5237.
(24) Svelle, S.; Rønning, P. O.; Kolboe, S. Kinetic Studies of Zeolite-Catalyzed Methylation Reactions: 1. Coreaction of [12C]Ethene and [13C]Methanol. *J. Catal.* **2004**, *224* (1), 115–123.
(25) Svelle, S.; Rønning, P. O.; Olsbye, U.; Kolboe, S. Kinetic Studies of Zeolite-Catalyzed Methylation Reactions. Part 2. Co-Reaction of [12C]Propene or [12C]n-Butene and [13C]Methanol. *J. Catal.* **2005**, *234* (2), 385–400.
(26) Svelle, S.; Tuma, C.; Rozanska, X.; Kerber, T.; Sauer, J. Quantum Chemical Modeling of Zeolite-Catalyzed Methylation Reactions: Toward Chemical Accuracy for Barriers. *J. Am. Chem. Soc.* **2009**, *131* (2), 816–825.
(27) Van Speybroeck, V.; Van der Mynsbrugge, J.; Vandichel, M.; Hemelsoet, K.; Lesthaeghe, D.; Ghysels, A.; Marin, G. B.; Waroquier, M. First Principle Kinetic Studies of Zeolite-Catalyzed Methylation Reactions. *J. Am. Chem. Soc.* **2011**, *133* (4), 888–899.
(28) Lee, C.-C.; Gorte, R. J.; Farneth, W. E. Calorimetric Study of Alcohol and Nitrile Adsorption Complexes in H-ZSM-5. *J. Phys. Chem. B* **1997**, *101* (19), 3811–3817.
(29) Jakobtorweihen, S.; Hansen, N.; Keil, F. J. Molecular Simulation of Alkene Adsorption in Zeolites. *Mol. Phys.* **2005**, *103* (4), 471–489.
(30) De Moor, B. A.; Ghysels, A.; Reyniers, M.-F.; Van Speybroeck, V.; Waroquier, M.; Marin, G. B. Normal Mode Analysis in Zeolites: Toward an Efficient Calculation of Adsorption Entropies. *J. Chem. Theory Comput.* **2011**, *7* (4), 1090–1101.
(31) Ghysels, A.; Verstraelen, T.; Hemelsoet, K.; Waroquier, M.; Van Speybroeck, V. TAMkin: A Versatile Package for Vibrational Analysis and Chemical Kinetics. *J. Chem. Inf. Model.* **2010**, *50* (9), 1736–1750.
(32) Hajek, J.; Van der Mynsbrugge, J.; De Wispelaere, K.; Cnudde, P.; Vanduyfhuys, L.; Waroquier, M.; Van Speybroeck, V. On the Stability and Nature of Adsorbed Pentene in Brønsted Acid Zeolite H-ZSM-5 at 323 K. *J. Catal.* **2016**, *340*, 227–235.
(33) Hajek, J.; Bueken, B.; Waroquier, M.; De Vos, D.; Van Speybroeck, V. The Remarkable Amphoteric Nature of Defective UiO-66 in Catalytic Reactions. *ChemCatChem* **2017**, *9* (12), 2203–2210.

(34) De Sterck, B.; Vaneerdeweg, R.; Du Prez, F.; Waroquier, M.; Van Speybroeck, V. Solvent Effects on Free Radical Polymerization Reactions: The Influence of Water on the Propagation Rate of Acrylamide and Methacrylamide. *Macromolecules* **2010**, *43* (2), 827–836.
(35) Wieme, J.; Lejaeghere, K.; Kresse, G.; Speybroeck, V. V. Tuning the Balance between Dispersion and Entropy to Design Temperature-Responsive Flexible Metal-Organic Frameworks. *Nat. Commun.* **2018**, *9* (1), 1–10.
(36) Grimme, S. Semiempirical GGA-type density functional constructed with a long-range dispersion correction. *J. Comput. Chem.* **2006**, *27* (15), 1787–1799.
(37) Grimme, S.; Ehrlich, S.; Goerigk, L. Effect of the Damping Function in Dispersion Corrected Density Functional Theory. *J. Comput. Chem.* **2011**, *32* (7), 1456–1465.
(38) Tkatchenko, A.; Scheffler, M. Accurate Molecular Van Der Waals Interactions from Ground-State Electron Density and Free-Atom Reference Data. *Phys. Rev. Lett.* **2009**, *102* (7), 073005.
(39) Bultinck, P.; Van Alsenoy, C.; Ayers, P. W.; Carbó-Dorca, R. Critical Analysis and Extension of the Hirshfeld Atoms in Molecules. *J. Chem. Phys.* **2007**, *126* (14), 144111.
(40) Bučko, T.; Lebègue, S.; Hafner, J.; Ángyán, J. G. Improved Density Dependent Correction for the Description of London Dispersion Forces. *J. Chem. Theory Comput.* **2013**, *9* (10), 4293–4299.
(41) Bučko, T.; Lebègue, S.; Ángyán, J. G.; Hafner, J. Extending the Applicability of the Tkatchenko-Scheffler Dispersion Correction via Iterative Hirshfeld Partitioning. *J. Chem. Phys.* **2014**, *141* (3), 034114.
(42) Tkatchenko, A.; DiStasio, R. A.; Car, R.; Scheffler, M. Accurate and Efficient Method for Many-Body van Der Waals Interactions. *Phys. Rev. Lett.* **2012**, *108* (23), 236402.
(43) Ambrosetti, A.; Reilly, A. M.; DiStasio, R. A.; Tkatchenko, A. Long-Range Correlation Energy Calculated from Coupled Atomic Response Functions. *J. Chem. Phys.* **2014**, *140* (18), 18A508.
(44) Steinmann, S. N.; Corminboeuf, C. A Generalized-Gradient Approximation Exchange Hole Model for Dispersion Coefficients. *J. Chem. Phys.* **2011**, *134* (4), 044117.
(45) Steinmann, S. N.; Corminboeuf, C. Comprehensive Benchmarking of a Density-Dependent Dispersion Correction. *J. Chem. Theory Comput.* **2011**, *7* (11), 3567–3577.
(46) Dion, M.; Rydberg, H.; Schröder, E.; Langreth, D. C.; Lundqvist, B. I. Van Der Waals Density Functional for General Geometries. *Phys. Rev. Lett.* **2004**, *92* (24), 246401.
(47) Klimeš, J.; Bowler, D. R.; Michaelides, A. Van Der Waals Density Functionals Applied to Solids. *Phys. Rev. B* **2011**, *83* (19), 195131.
(48) Wellendorff, J.; Lundgaard, K. T.; Møgelhøj, A.; Petzold, V.; Landis, D. D.; Nørskov, J. K.; Bligaard, T.; Jacobsen, K. W. Density Functionals for Surface Science: Exchange-Correlation Model Development with Bayesian Error Estimation. *Phys. Rev. B* **2012**, *85* (23), 235149.
(49) Becke, A. D. Density-functional Thermochemistry. III. The Role of Exact Exchange. *J. Chem. Phys.* **1993**, *98* (7), 5648–5652.
(50) Peng, H.; Yang, Z.-H.; Perdew, J. P.; Sun, J. Versatile van Der Waals Density Functional Based on a Meta-Generalized Gradient Approximation. *Phys. Rev. X* **2016**, *6* (4), 041005.

A

Publication List

Updated December 2019

Publications in international peer-reviewed journals

1. S. Bailleul, L. Vanduyfhuys, M. Waroquier, V. Van Speybroeck, *Ab initio enhanced sampling kinetic study on MTO ethene methylation reaction*, Journal of Catalysis, Submitted
   IF: 7.723

2. S. Bailleul, I. Yarulina, A. Hoffman, A. Dokania, E. Abou-Hamad, A. Dutta Chowdhury, G. Pieters, J. Hajek, K. De Wispelaere, M. Waroquier, J. Gascon, V. Van Speybroeck, *A supramolecular view on the cooperative role of Brønsted and Lewis acid sites in zeolites for methanol conversion*, Journal of the American Chemical Society, **141**, 14823–14842 (2019)
   IF: 14.695

3. S. Bailleul, S.M.J. Rogge, L. Vanduyfhuys, V. Van Speybroeck, *Insight into the role of water on the methylation of hexamethylbenzene in H-SAPO-34 from first principle molecular dynamics simulations*, ChemCatChem, **11**, 3993–4010 (2019)
   IF: 4.495

4. I. Yarulina, K. De Wispelaere, S. Bailleul, J. Goetze, M. Radersma, E. Abou-Hamad, I. Vollmer, M. Goesten, B. Mezari, E.J.M. Hensen, J. S. Martínez-Espín, M. Morten, S. Mitchell, J. Perez-Ramirez, U. Olsbye, B.M. Weckhuysen, V. Van Speybroeck, F. Kapteijn, J. Gascon, *Structure–performance descriptors and the role of Lewis acidity in the methanol-to-propylene process*, Nature Chemistry, **10**, 804–812 (2018)
   IF: 25.870

5. I. Yarulina, S. Bailleul, A. Pustovarenko, J. Ruiz-Martinez, K. De Wispelaere, J. Hajek, B.M. Weckhuysen, K. Houben, M. Baldus, V. Van Speybroeck, F. Kapteijn, J. Gascon, *Suppression of Aromatic Cycle in Methanol-to-Olefins Reaction over ZSM-5 by post-synthetic modification using Calcium*, ChemCatChem, **8**, 3057–3063 (2016)
   IF: 4.724

6. K. De Wispelaere, S. Bailleul, V. Van Speybroeck, *Towards molecular control of elementary reactions in zeolite catalysis by advanced molecular simulations mimicking operating conditions*, Catalysis Science & Technology, **6**, 2686–2705 (2016)
   IF: 5.287

Conference contributions

Oral presentations

1. Modeling zeolite catalysis at operating conditions: an advanced molecular dynamics benchmark study
   S. Bailleul, K. De Wispelaere, R. Demuynck, V. Van Speybroeck
   13th European Congress on Catalysis (EUROPACAT 2017), Florence, Italy, 27–31 August 2017

2. Advanced molecular simulations of elementary steps in zeolite catalysis under reaction conditions
   K. De Wispelaere, S. Bailleul, V. Van Speybroeck
   251st American Chemical Society (ACS) National Meeting, San Diego, CA, USA , 13–17 March 2016

3. Ab initio molecular dynamics study on the role of water in the side-chain mechanism during methanol conversion in H-SAPO-34
   S. Bailleul, K. De Wispelaere, V. Van Speybroeck
   XVIIth Netherlands' Catalysis and Chemistry Conference (NCCC XVII), Noordwijkerhout, The Netherlands, 7–9 March 2016

4. Advanced molecular simulations of elementary steps in zeolite catalysis
   K. De Wispelaere, S. Bailleul, V. Van Speybroeck

XVIIth Netherlands' Catalysis and Chemistry Conference (NCCC XVII), Noordwijkerhout, The Netherlands, 7–9 March 2016

5. Towards molecular control of zeolite-catalyzed reactions by advanced molecular simulations mimicking operating conditions
K. De Wispelaere, S. Bailleul, V. Van Speybroeck
IAP 7 - PL3 meeting, Ghent, Belgium, 1 March 2016

Poster presentations

1. Molecular level-based study on the formation of aromatics in zeolites starting from polyenes
D. De Saegher, S. Bailleul, J. Hajek, V. Van Speybroeck
XXth Netherlands' Catalysis and Chemistry Conference (NCCC XX), Noordwijkerhout, The Netherlands, 4 – 6 March 2019

2. Ab initio benchmark study of enhanced sampling methods for methylation of MTO intermediates
S. Bailleul, K. De Wispelaere, R. Demuynck, V. Van Speybroeck
XIXth Netherlands' Catalysis and Chemistry Conference (NCCC XIX), Noordwijkerhout, The Netherlands, 5 – 7 March 2018

3. Mechanistic study on the early stages of the MTO process using advanced molecular simulations in H-SAPO-34
V. Kotov, S. Bailleul, K. De Wispelaere, V. Van Speybroeck
XIXth Netherlands' Catalysis and Chemistry Conference (NCCC XIX), Noordwijkerhout, The Netherlands, 5 – 7 March 2018

4. Mechanistic study the zeolite-catalyzed formation of aromatics with advanced molecular simulations C. Naessens, S. Bailleul, K. De Wispelaere, V. Van Speybroeck
XIXth Netherlands' Catalysis and Chemistry Conference (NCCC XIX), Noordwijkerhout, The Netherlands, 5 – 7 March 2018

5. Modeling zeolite catalysis at operating conditions: an advanced molecular dynamics benchmark study
S. Bailleul, K. De Wispelaere, J. Hajek, R. Demuynck, V. Van Speybroeck
XVIIIth Netherlands' Catalysis and Chemistry Conference (NCCC XVIII), Noordwijkerhout, The Netherlands, 6 – 8 March 2017

6. Molecular engineering of active sites to increase propene selectivity and catalyst lifetime under MTH conditions
G. Pieters, S. Bailleul, P. Cnudde, K. De Wispelaere, V. Van Speybroeck
XVIIIth Netherlands' Catalysis and Chemistry Conference (NCCC XVIII), Noordwijkerhout, The Netherlands, 6 – 8 March 2017

7. Ab initio study on the impact of a mixed water-methanol feed on olefin formation during the MTO process
   S. Bailleul, K. De Wispelaere, R. Demuynck, V. Van Speybroeck
   MARVEL School on Variationally Enhanced Sampling 2017, Lugano, Switzerland, 14–17 February 2017

8. Ab initio study on the impact of a mixed water methanol feed on olefin formation during the MTO process
   S. Bailleul, Y. Pauwels, K. De Wispelaere, V. Van Speybroeck
   Chemical Research in Flanders Symposium (CRF-1), Blankenberge, Belgium, 24–26 October 2016

9. Ab initio study on the impact of a mixed water-methanol feed on olefin formation during the MTO process, S. Bailleul, K. De Wispelaere, V. Van Speybroeck
   IAP Day 2016 - final meeting, Liège, Belgium, 12 September 2016

10. Impact of a mixed water methanol feed on olefin formation during the MTO process
    Y. Pauwels, K. De Wispelaere, S. Bailleul, V. Van Speybroeck
    XVIIth Netherlands' Catalysis and Chemistry Conference (NCCC XVII), Noordwijkerhout, The Netherlands, 7–9 March 2016

11. Ab initio molecular dynamics study on the influence of water on methanol conversion in H-SAPO-34
    S. Bailleul, K. De Wispelaere, J. Van der Mynsbrugge, K. Hemelsoet, V. Van Speybroeck
    MolSim 2016: Understanding Molecular Simulation, Amsterdam, The Netherlands , 4–15 January 2016

12. Ab initio molecular dynamics study on the influence of water on methanol conversion in H-SAPO-34
    S. Bailleul, K. De Wispelaere, J. Van der Mynsbrugge, K. Hemelsoet, V. Van Speybroeck
    IAP Annual Meeting, Hasselt, Belgium, 11 September 2015

13. Ab initio study on the influence of water on methanol conversion in H-SAPO-34
    S. Bailleul, K. De Wispelaere, J. Van der Mynsbrugge, K. Hemelsoet, V. Van Speybroeck, XVIth Netherlands' Catalysis and Chemistry Conference (NCCC XVI), Noordwijkerhout, The Netherlands, Mon, 2–4 March 2015

B

Weighted histogram analysis method

As stated in Section 2.4.3, several schemes are proposed to obtain the unbiased probability from the biased histograms in umbrella sampling, [292, 293] but in this work we will focus on the weighted histogram analysis method (WHAM). [205, 294–296] This method starts from the idea that the unbiased probability can be written as function of the biased probabilities as:

$$p(q) = p_b^i(q) \exp(\beta U_b^i(q)) \frac{Z_b^i}{Z} \tag{B.1}$$

Nevertheless, the partition function Z_b^i cannot be computed due to the unfeasible integration. Therefore, a weight w_i is assigned to each histogram H_i (and thus probability p_b^i) to calculate the global distribution as a weighted average of the distributions of the individual windows: [292]

$$p(q) = \sum_i w_i p_b^i(q) \exp(\beta U_b^i(q)) \frac{Z_b^i}{Z} \tag{B.2}$$

In WHAM, the weights are chose as to minimize the statistical error of the unbiased probability:

$$\frac{\partial \sigma^2(p(q))}{\partial w_i} = 0 \tag{B.3}$$

under the condition that the weights add up to 1, $\sum_i w_i = 1$. This minimization leads to: [294, 296]

$$w_i = \frac{\exp(-\beta U_b^i(q)) M_i Z / Z_b^i}{\sum_i \exp(-\beta U_b^i(q)) M_i Z / Z_b^i} \tag{B.4}$$

Combining this with Eq. B.2 leads to the following expression for the global probability, with only the ratio Z_b^i/Z as unknown:

$$p(q) = \frac{\sum_i H_i(q)}{\sum_i \exp(-\beta U_b^i(q)) M_i Z / Z_b^i} \tag{B.5}$$

with $H_i(q)$ the counts within $[q, q+dq]$ when applying the external bias $U_b^i(q)$. Finally, an estimate of the last unknown (Z_b^i/Z) can be obtained via an iterative scheme based on the definition of a partition function and the previous expression of the global distribution:

$$Z_b^i = \int \exp(-\beta(\hat{H}(\mathbf{r},\mathbf{p}) + U_b^i(Q(\mathbf{r},\mathbf{p})))) d\mathbf{r} d\mathbf{p} \tag{B.6}$$

$$Z_b^i = \int Z p(q) \exp(-\beta(U_b^i(Q(\mathbf{r},\mathbf{p})))) dq \tag{B.7}$$

$$Z_b^i = \int \exp(-\beta(U_b^i(Q(\mathbf{r},\mathbf{p})))) \frac{\sum_i H_i(q)}{\sum_i \exp(-\beta U_b^i(q)) M_i / Z_b^i} dq \tag{B.8}$$

By solving this self-consistent cycle, the free energy profile can be obtained (within a constant value).

C

Acknowledgement

This project has received funding from the European Union's Horizon 2020 research and innovation programme [consolidator ERC grant agreement no. 647755–DYNPOR (2015–2020)].

Computational resources and services used in this work were provided by the Stevin Supercomputer Infrastructure of Ghent University and by the VSC (Flemish Supercomputer Center), funded by the Hercules Foundation and the Flemish Government – department EWI.

Bibliography

[1] R. W. Bentley, "Global oil & gas depletion: an overview," *Energy Policy*, vol. 30, pp. 189–205, Feb. 2002.

[2] A. Corma, S. Iborra, and A. Velty, "Chemical Routes for the Transformation of Biomass into Chemicals," *Chem. Rev.*, vol. 107, pp. 2411–2502, June 2007.

[3] C. Briens, J. Piskorz, and F. Berruti, "Biomass valorization for fuel and chemicals production - A review," *Int. J. Chem. React. Eng.*, vol. 6, no. 1, p. R2, 2008. WOS:000256301700006.

[4] P. Sudarsanam, R. Zhong, S. V. d. Bosch, S. M. Coman, V. I. Parvulescu, and B. F. Sels, "Functionalised heterogeneous catalysts for sustainable biomass valorisation," *Chem. Soc. Rev.*, vol. 47, pp. 8349–8402, Nov. 2018.

[5] P. L. Spath and D. C. Dayton, "Preliminary Screening – Technical and Economic Assessment of Synthesis Gas to Fuels and Chemicals with Emphasis on the Potential for Biomass-Derived Syngas," Tech. Rep. NREL/TP-510-34929, National Renewable Energy Lab., Golden, CO. (US), Dec. 2003.

[6] F. L. Bleken, S. Chavan, U. Olsbye, M. Boltz, F. Ocampo, and B. Louis, "Conversion of methanol into light olefins over ZSM-5 zeolite: Strategy to enhance propene selectivity," *Applied Catalysis A: General*, vol. 447-448, pp. 178–185, Dec. 2012.

[7] S. Abrol and C. M. Hilton, "Modeling, simulation and advanced control of methanol production from variable synthesis gas feed," *Computers & Chemical Engineering*, vol. 40, pp. 117–131, May 2012.

[8] U. Olsbye, S. Svelle, M. Bjørgen, P. Beato, T. V. W. Janssens, F. Joensen, S. Bordiga, and K. P. Lillerud, "Conversion of Methanol to Hydrocarbons: How Zeolite Cavity and Pore Size Controls Product Selectivity," *Angew. Chem. Int. Ed.*, vol. 51, pp. 5810–5831, June 2012.

[9] K. Hemelsoet, J. Van der Mynsbrugge, K. De Wispelaere, M. Waroquier, and V. Van Speybroeck, "Unraveling the Reaction Mechanisms Governing Methanol-to-Olefins Catalysis by Theory and Experiment," *ChemPhysChem*, vol. 14, pp. 1526–1545, June 2013.

[10] I. Yarulina, A. D. Chowdhury, F. Meirer, B. M. Weckhuysen, and J. Gascon, "Recent trends and fundamental insights in the methanol-to-hydrocarbons process," *Nature Catalysis*, vol. 1, pp. 398–411, June 2018.

[11] G. A. Olah, "Beyond Oil and Gas: The Methanol Economy," *Angewandte Chemie International Edition*, vol. 44, no. 18, pp. 2636–2639, 2005.

[12] G. A. Olah, "Towards Oil Independence Through Renewable Methanol Chemistry," *Angewandte Chemie International Edition*, vol. 52, no. 1, pp. 104–107, 2013.

[13] G. A. Olah, A. Goeppert, and G. K. S. Prakash, *Beyond Oil and Gas: The Methanol Economy*. John Wiley & Sons, June 2018. Google-Books-ID: 65xiDwAAQBAJ.

[14] W.-C. Liu, J. Baek, and G. A. Somorjai, "The Methanol Economy: Methane and Carbon Dioxide Conversion," *Top Catal*, vol. 61, pp. 530–541, June 2018.

[15] S. L. Meisel, J. P. McCullough, C. H. Lechtaler, and P. B. Weisz, "Gasoline from methanol in one step," *Chemtech*, vol. 6, p. 86, Feb. 1976.

[16] C. D. Chang and A. J. Silvestri, "The conversion of methanol and other O-compounds to hydrocarbons over zeolite catalysts," *Journal of Catalysis*, vol. 47, pp. 249–259, May 1977.

[17] C. D. Chang, "Hydrocarbons from Methanol," *Catalysis Reviews*, vol. 25, pp. 1–118, Jan. 1983.

[18] C. D. Chang, "Methanol Conversion to Light Olefins," *Catalysis Reviews*, vol. 26, pp. 323–345, Aug. 1984.

[19] F. J. Keil, "Methanol-to-hydrocarbons: process technology," *Microporous and Mesoporous Materials*, vol. 29, pp. 49–66, June 1999.

[20] M. R. Gogate, "Methanol-to-olefins process technology: current status and future prospects," *Petroleum Science and Technology*, vol. 37, pp. 559–565, Mar. 2019.

[21] S. Ilias and A. Bhan, "Mechanism of the Catalytic Conversion of Methanol to Hydrocarbons," *ACS Catal.*, vol. 3, pp. 18–31, Jan. 2013.

[22] V. Van Speybroeck, K. De Wispelaere, J. Van der Mynsbrugge, M. Vandichel, K. Hemelsoet, and M. Waroquier, "First principle chemical kinetics in zeolites: the methanol-to-olefin process as a case study," *Chem. Soc. Rev.*, vol. 43, pp. 7326–7357, Oct. 2014.

[23] U. Olsbye, S. Svelle, K. P. Lillerud, Z. H. Wei, Y. Y. Chen, J. F. Li, J. G. Wang, and W. B. Fan, "The formation and degradation of active species during methanol conversion over protonated zeotype catalysts," *Chemical Society Reviews*, vol. 44, no. 20, pp. 7155–7176, 2015.

[24] H. Koempel and W. Liebner, "Lurgi's Methanol To Propylene (MTP®) Report on a successful commercialisation," in *Studies in Surface Science and Catalysis* (M. S. a. E. F. S.-A. Fábio Bellot Noronha, ed.), vol. 167 of *Natural Gas Conversion VIII Proceedings of the 8th Natural Gas Conversion Symposium*, pp. 261–267, Elsevier, 2007.

[25] J. Q. Chen, A. Bozzano, B. Glover, T. Fuglerud, and S. Kvisle, "Recent advancements in ethylene and propylene production using the UOP/Hydro MTO process," *Catalysis Today*, vol. 106, pp. 103–107, Oct. 2005.

[26] J. Liang, H. Li, S. Zhao, W. Guo, R. Wang, and M. Ying, "Characteristics and performance of SAPO-34 catalyst for methanol-to-olefin conversion," *Applied Catalysis*, vol. 64, pp. 31–40, Sept. 1990.

[27] J. Cejka, A. Corma, and S. Zones, *Zeolites and Catalysis: Synthesis, Reactions and Applications*. John Wiley & Sons, May 2010. Google-Books-ID: zMOghsHzg1YC.

[28] J. Cejka, B. Wichterlova, and S. Bednarova, "Alkylation of toluene with ethene over H-ZSM-5 zeolites," *Applied Catalysis A: General*, vol. 79, pp. 215–226, Dec. 1991.

[29] G. Centi and S. Perathoner, "Environmental Catalysis over Zeolites," in *Zeolites and Catalysis*, pp. 745–774, John Wiley & Sons, Ltd, 2010.

[30] G. Centi, B. Wichterlová, and A. T. Bell, *Catalysis by Unique Metal Ion Structures in Solid Matrices: From Science to Application*. Springer Science & Business Media, Dec. 2012. Google-Books-ID: EaUjCQAAQBAJ.

[31] J. Čejka, J. Peréz-Pariente, and W. J. Roth, *Zeolites: From Model Materials to Industrial Catalysts*. Transworld Research Network, Jan. 2008. Google-Books-ID: JJiEPwAACAAJ.

[32] J. Liang, Z. Liang, R. Zou, and Y. Zhao, "Heterogeneous Catalysis in Zeolites, Mesoporous Silica, and Metal–Organic Frameworks," *Advanced Materials*, vol. 29, no. 30, p. 1701139, 2017.

[33] Z. Liu, N. Fujita, K. Miyasaka, L. Han, S. M. Stevens, M. Suga, S. Asahina, B. Slater, C. Xiao, Y. Sakamoto, M. W. Anderson, R. Ryoo, and O. Terasaki, "A review of fine structures of nanoporous materials as evidenced by microscopic methods," *Microscopy (Oxf)*, vol. 62, pp. 109–146, Feb. 2013.

[34] J. B. Nagy, P. Bodart, I. Hannus, and I. Kiricsi, *Synthesis, characterization and use of zeolitic microporous materials*. DecaGen Ltd., 1998.

[35] C. S. Cundy and P. A. Cox, "The Hydrothermal Synthesis of Zeolites: History and Development from the Earliest Days to the Present Time," *Chem. Rev.*, vol. 103, pp. 663–702, Mar. 2003.

[36] "Database of Zeolite Structures."

[37] B. Smit and T. L. M. Maesen, "Towards a molecular understanding of shape selectivity," *Nature*, vol. 451, pp. 671–678, Feb. 2008.

[38] B. P. C. Hereijgers, F. Bleken, M. H. Nilsen, S. Svelle, K.-P. Lillerud, M. Bjørgen, B. M. Weckhuysen, and U. Olsbye, "Product shape selectivity dominates the Methanol-to-Olefins (MTO) reaction over H-SAPO-34 catalysts," *Journal of Catalysis*, vol. 264, pp. 77–87, May 2009.

[39] E. M. Gallego, M. T. Portilla, C. Paris, A. León-Escamilla, M. Boronat, M. Moliner, and A. Corma, ""Ab initio" synthesis of zeolites for preestablished catalytic reactions," *Science*, vol. 355, pp. 1051–1054, Mar. 2017.

[40] S. Bailleul, S. M. J. Rogge, L. Vanduyfhuys, and V. Van Speybroeck, "Insight into the Role of Water on the Methylation of Hexamethylbenzene in H-SAPO-34 from First Principle Molecular Dynamics Simulations," *ChemCatChem*, vol. 11, no. 16, pp. 3993–4010, 2019.

[41] S. L. C. Moors, K. De Wispelaere, J. Van der Mynsbrugge, M. Waroquier, and V. Van Speybroeck, "Molecular Dynamics Kinetic Study on the Zeolite-Catalyzed Benzene Methylation in ZSM-5," *ACS Catal.*, vol. 3, pp. 2556–2567, Nov. 2013.

[42] J. Van der Mynsbrugge, K. Hemelsoet, M. Vandichel, M. Waroquier, and V. Van Speybroeck, "Efficient Approach for the Computational Study of Alcohol and Nitrile Adsorption in H-ZSM-5," *J. Phys. Chem. C*, vol. 116, pp. 5499–5508, Mar. 2012.

[43] J. Van der Mynsbrugge, M. Visur, U. Olsbye, P. Beato, M. Bjørgen, V. Van Speybroeck, and S. Svelle, "Methylation of benzene by methanol: Single-site kinetics over H-ZSM-5 and H-beta zeolite catalysts," *Journal of Catalysis*, vol. 292, pp. 201–212, Aug. 2012.

[44] J. Van der Mynsbrugge, S. L. C. Moors, K. De Wispelaere, and V. Van Speybroeck, "Insight into the Formation and Reactivity of Framework-Bound Methoxide Species in H-ZSM-5 from Static and Dynamic Molecular Simulations," *ChemCatChem*, vol. 6, pp. 1906–1918, July 2014.

[45] L.-T. Yuen, S. I. Zones, T. V. Harris, E. J. Gallegos, and A. Auroux, "Product selectivity in methanol to hydrocarbon conversion for isostructural compositions of AFI and CHA molecular sieves," *Microporous Materials*, vol. 2, pp. 105–117, Feb. 1994.

[46] M. Westgård Erichsen, S. Svelle, and U. Olsbye, "The influence of catalyst acid strength on the methanol to hydrocarbons (MTH) reaction," *Catalysis Today*, vol. 215, pp. 216–223, Oct. 2013.

[47] M. Westgård Erichsen, S. Svelle, and U. Olsbye, "H-SAPO-5 as methanol-to-olefins (MTO) model catalyst: Towards elucidating the effects of acid strength," *Journal of Catalysis*, vol. 298, pp. 94–101, Feb. 2013.

[48] M. Westgård Erichsen, K. De Wispelaere, K. Hemelsoet, S. L. C. Moors, T. Deconinck, M. Waroquier, S. Svelle, V. Van Speybroeck, and U. Olsbye, "How zeolitic acid strength and composition alter the reactivity of alkenes and aromatics towards methanol," *Journal of Catalysis*, vol. 328, pp. 186–196, Aug. 2015.

[49] J. F. Haw, W. Song, D. M. Marcus, and J. B. Nicholas, "The Mechanism of Methanol to Hydrocarbon Catalysis," *Acc. Chem. Res.*, vol. 36, no. 5, pp. 317–326, 2003.

[50] M. Stöcker, "Methanol-to-hydrocarbons: catalytic materials and their behavior," *Microporous and Mesoporous Materials*, vol. 29, pp. 3–48, June 1999.

[51] D. Lesthaeghe, V. Van Speybroeck, G. B. Marin, and M. Waroquier, "Understanding the Failure of Direct C–C Coupling in the Zeolite-Catalyzed Methanol-to-Olefin Process," *Angewandte Chemie International Edition*, vol. 45, pp. 1714–1719, Mar. 2006.

[52] D. Lesthaeghe, V. Van Speybroeck, G. B. Marin, and M. Waroquier, "The Rise and Fall of Direct Mechanisms in Methanol-to-Olefin Catalysis: An Overview of Theoretical Contributions," *Ind. Eng. Chem. Res.*, vol. 46, pp. 8832–8838, Dec. 2007.

[53] N. Y. Chen and W. J. Reagan, "Evidence of autocatalysis in methanol to hydrocarbon reactions over zeolite catalysts," *Journal of Catalysis*, vol. 59, pp. 123–129, Aug. 1979.

[54] A. D. Chowdhury, K. Houben, G. T. Whiting, M. Mokhtar, A. M. Asiri, S. A. Al-Thabaiti, S. N. Basahel, M. Baldus, and B. M. Weckhuysen, "Initial Carbon–Carbon Bond Formation during the Early Stages of the Methanol-to-Olefin Process Proven by Zeolite-Trapped Acetate and Methyl Acetate," *Angew. Chem. Int. Ed.*, vol. 55, pp. 15840–15845, Dec. 2016.

[55] A. D. Chowdhury, A. L. Paioni, K. Houben, G. T. Whiting, M. Baldus, and B. M. Weckhuysen, "Bridging the Gap between the Direct and Hydrocarbon Pool Mechanisms of the Methanol-to-Hydrocarbons Process," *Angewandte Chemie International Edition*, vol. 57, no. 27, pp. 8095–8099, 2018.

[56] H. Yamazaki, H. Shima, H. Imai, T. Yokoi, T. Tatsumi, and J. N. Kondo, "Evidence for a "Carbene-like" Intermediate during the Reaction of Methoxy Species with Light Alkenes on H-ZSM-5," *Angewandte Chemie International Edition*, vol. 50, no. 8, pp. 1853–1856, 2011.

[57] A. Comas-Vives, M. Valla, C. Copéret, and P. Sautet, "Cooperativity between Al Sites Promotes Hydrogen Transfer and Carbon–Carbon Bond Formation upon Dimethyl Ether Activation on Alumina," *ACS Cent. Sci.*, vol. 1, pp. 313–319, Sept. 2015.

[58] Y. Liu, S. Müller, D. Berger, J. Jelic, K. Reuter, M. Tonigold, M. Sanchez-Sanchez, and J. A. Lercher, "Formation Mechanism of the First Carbon–Carbon Bond and the First Olefin in the Methanol Conversion into Hydrocarbons," *Angew. Chem. Int. Ed.*, vol. 55, pp. 5723–5726, May 2016.

[59] X. Wu, S. Xu, W. Zhang, J. Huang, J. Li, B. Yu, Y. Wei, and Z. Liu, "Direct Mechanism of the First Carbon–Carbon Bond Formation in the Methanol-to-Hydrocarbons Process," *Angewandte Chemie International Edition*, vol. 56, no. 31, pp. 9039–9043, 2017.

[60] W. Wang and M. Hunger, "Reactivity of Surface Alkoxy Species on Acidic Zeolite Catalysts," *Acc. Chem. Res.*, vol. 41, pp. 895–904, Aug. 2008.

[61] Y. Jiang, W. Wang, V. R. Reddy Marthala, J. Huang, B. Sulikowski, and M. Hunger, "Effect of organic impurities on the hydrocarbon formation via the decomposition of surface methoxy groups on acidic zeolite catalysts," *Journal of Catalysis*, vol. 238, pp. 21–27, Feb. 2006.

[62] W. Dai, C. Wang, M. Dyballa, G. Wu, N. Guan, L. Li, Z. Xie, and M. Hunger, "Understanding the Early Stages of the Methanol-to-Olefin Conversion on H-SAPO-34," *ACS Catal.*, vol. 5, pp. 317–326, Jan. 2015.

[63] W. Li and A. Ma, "Recent developments in methods for identifying reaction coordinates," *Molecular Simulation*, vol. 40, pp. 784–793, Aug. 2014.

[64] Z. Wei, Y.-Y. Chen, J. Li, P. Wang, B. Jing, Y. He, M. Dong, H. Jiao, Z. Qin, J. Wang, and W. Fan, "Methane formation mechanism in the initial methanol-to-olefins process catalyzed by SAPO-34," *Catal. Sci. Technol.*, vol. 6, pp. 5526–5533, July 2016.

[65] P. N. Plessow and F. Studt, "Unraveling the Mechanism of the Initiation Reaction of the Methanol to Olefins Process Using ab Initio and DFT Calculations," *ACS Catal.*, vol. 7, pp. 7987–7994, Nov. 2017.

[66] P. N. Plessow and F. Studt, "Theoretical Insights into the Effect of the Framework on the Initiation Mechanism of the MTO Process," *Catal Lett*, vol. 148, pp. 1246–1253, Apr. 2018.

[67] Bollini Praveen and Bhan Aditya, "Improving HSAPO-34 Methanol-to-Olefin Turnover Capacity by Seeding the Hydrocarbon Pool," *ChemPhysChem*, vol. 19, pp. 479–483, Jan. 2018.

[68] B. T. W. Lo, L. Ye, G. G. Z. Chang, K. Purchase, S. Day, C. C. Tang, D. Mei, and S. C. E. Tsang, "Dynamic modification of pore opening of SAPO-34 by adsorbed surface methoxy species during induction of catalytic methanol-to-olefins reactions," *Applied Catalysis B: Environmental*, vol. 237, pp. 245–250, Dec. 2018.

[69] X. Wu, S. Xu, Y. Wei, W. Zhang, J. Huang, S. Xu, Y. He, S. Lin, T. Sun, and Z. Liu, "Evolution of C–C Bond Formation in the Methanol-to-Olefins Process: From Direct Coupling to Autocatalysis," *ACS Catal.*, vol. 8, pp. 7356–7361, Aug. 2018.

[70] T. Omojola, D. B. Lukyanov, N. Cherkasov, V. L. Zholobenko, and A. C. van Veen, "Influence of Precursors on the Induction Period and Transition Regime of Dimethyl Ether Conversion to Hydrocarbons over ZSM-5 Catalysts," *Ind. Eng. Chem. Res.*, vol. 58, pp. 16479–16488, Sept. 2019.

[71] T. Omojola, D. B. Lukyanov, and A. C. v. Veen, "Transient kinetic studies and microkinetic modeling of primary olefin formation from dimethyl ether over ZSM-5 catalysts," *International Journal of Chemical Kinetics*, vol. 51, no. 7, pp. 528–537, 2019.

[72] R. M. Dessau and R. B. LaPierre, "On the mechanism of methanol conversion to hydrocarbons over HZSM-5," *Journal of Catalysis*, vol. 78, pp. 136–141, Nov. 1982.

[73] R. M. Dessau, "On the H-ZSM-5 catalyzed formation of ethylene from methanol or higher olefins," *Journal of Catalysis*, vol. 99, pp. 111–116, May 1986.

[74] T. Mole, J. A. Whiteside, and D. Seddon, "Aromatic co-catalysis of methanol conversion over zeolite catalysts," *Journal of Catalysis*, vol. 82, pp. 261–266, Aug. 1983.

[75] T. Mole, G. Bett, and D. Seddon, "Conversion of methanol to hydrocarbons over ZSM-5 zeolite: An examination of the role of aromatic hydrocarbons using 13carbon- and deuterium-labeled feeds," *Journal of Catalysis*, vol. 84, pp. 435–445, Dec. 1983.

[76] B. E. Langner, "Reactions of methanol on zeolites with different pore structures," *Applied Catalysis*, vol. 2, pp. 289–302, Apr. 1982.

[77] I. Dahl and S. Kolboe, "On the Reaction-Mechanism for Propene Formation in the MTO Reaction Over SAPO-34," *Catal. Lett.*, vol. 20, no. 3-4, pp. 329–336, 1993. WOS:A1993LU35400017.

[78] I. M. Dahl and S. Kolboe, "On the Reaction Mechanism for Hydrocarbon Formation from Methanol over SAPO-34: I. Isotopic Labeling Studies of the Co-Reaction of Ethene and Methanol," *Journal of Catalysis*, vol. 149, pp. 458–464, Oct. 1994.

[79] I. M. Dahl and S. Kolboe, "On the Reaction Mechanism for Hydrocarbon Formation from Methanol over SAPO-34: 2. Isotopic Labeling Studies of the Co-reaction of Propene and Methanol," *Journal of Catalysis*, vol. 161, pp. 304–309, June 1996.

[80] W. Song, J. F. Haw, J. B. Nicholas, and C. S. Heneghan, "Methylbenzenes Are the Organic Reaction Centers for Methanol-to-Olefin Catalysis on HSAPO-34," *J. Am. Chem. Soc.*, vol. 122, pp. 10726–10727, Nov. 2000.

[81] W. Song, H. Fu, and J. F. Haw, "Selective Synthesis of Methylnaphthalenes in HSAPO-34 Cages and Their Function as Reaction Centers in Methanol-to-Olefin Catalysis," *J. Phys. Chem. B*, vol. 105, no. 51, pp. 12839–12843, 2001.

[82] B. Arstad and S. Kolboe, "Methanol-to-hydrocarbons reaction over SAPO-34. Molecules confined in the catalyst cavities at short time on stream," *Catalysis Letters*, vol. 71, pp. 209–212, Feb. 2001.

[83] B. Arstad and S. Kolboe, "The Reactivity of Molecules Trapped within the SAPO-34 Cavities in the Methanol-to-Hydrocarbons Reaction," *J. Am. Chem. Soc.*, vol. 123, pp. 8137–8138, Aug. 2001.

[84] S. Svelle, P. O. Rønning, and S. Kolboe, "Kinetic studies of zeolite-catalyzed methylation reactions: 1. Coreaction of [12c]ethene and [13c]methanol," *Journal of Catalysis*, vol. 224, pp. 115–123, May 2004.

[85] S. Svelle, P. O. Rønning, U. Olsbye, and S. Kolboe, "Kinetic studies of zeolite-catalyzed methylation reactions. Part 2. Co-reaction of [12c]propene or [12c]n-butene and [13c]methanol," *Journal of Catalysis*, vol. 234, pp. 385–400, Sept. 2005.

[86] S. Svelle, F. Joensen, J. Nerlov, U. Olsbye, K.-P. Lillerud, S. Kolboe, and M. Bjørgen, "Conversion of Methanol into Hydrocarbons over Zeolite H-ZSM-5: Ethene Formation Is Mechanistically Separated from the Formation of Higher Alkenes," *J. Am. Chem. Soc.*, vol. 128, no. 46, pp. 14770–14771, 2006.

[87] X. Sun, S. Mueller, Y. Liu, H. Shi, G. L. Haller, M. Sanchez-Sanchez, A. C. van Veen, and J. A. Lercher, "On reaction pathways in the conversion of methanol to hydrocarbons on HZSM-5," *Journal of Catalysis*, vol. 317, pp. 185–197, Aug. 2014.

[88] X. Sun, S. Mueller, H. Shi, G. L. Haller, M. Sanchez-Sanchez, A. C. van Veen, and J. A. Lercher, "On the impact of co-feeding aromatics and olefins for the methanol-to-olefins reaction on HZSM-5," *Journal of Catalysis*, vol. 314, pp. 21–31, May 2014.

[89] S. Wang, Y. Chen, Z. Wei, Z. Qin, H. Ma, M. Dong, J. Li, W. Fan, and J. Wang, "Polymethylbenzene or Alkene Cycle? Theoretical Study on Their Contribution to the Process of Methanol to Olefins over H-ZSM-5 Zeolite," *J. Phys. Chem. C*, vol. 119, pp. 28482–28498, Dec. 2015.

[90] J. F. Haw and D. M. Marcus, "Well-defined (supra)molecular structures in zeolite methanol-to-olefin catalysis," *Top Catal*, vol. 34, pp. 41–48, May 2005.

[91] S. Bailleul, I. Yarulina, A. E. J. Hoffman, A. Dokania, E. Abou-Hamad, A. D. Chowdhury, G. Pieters, J. Hajek, K. De Wispelaere, M. Waroquier, J. Gascon, and V. Van Speybroeck, "A Supramolecular View on the Cooperative Role of Brønsted and Lewis Acid Sites in Zeolites for Methanol Conversion," *J. Am. Chem. Soc.*, vol. 141, pp. 14823–14842, Sept. 2019.

[92] Q. Qian, J. Ruiz-Martínez, M. Mokhtar, A. M. Asiri, S. A. Al-Thabaiti, S. N. Basahel, and B. M. Weckhuysen, "Single-Particle Spectroscopy of Alcohol-to-Olefins over SAPO-34 at Different Reaction Stages: Crystal Accessibility and Hydrocarbons Reactivity," *ChemCatChem*, vol. 6, pp. 772–783, Mar. 2014. WOS:000332072300018.

[93] Q. Qian, J. Ruiz-Martínez, M. Mokhtar, A. M. Asiri, S. A. Al-Thabaiti, S. N. Basahel, and B. M. Weckhuysen, "Single-catalyst particle spectroscopy of alcohol-to-olefins conversions: Comparison between SAPO-34 and SSZ-13," *Catalysis Today*, vol. 226, pp. 14–24, May 2014.

[94] Q. Qian, C. Vogt, M. Mokhtar, A. M. Asiri, S. A. Al-Thabaiti, S. N. Basahel, J. Ruiz-Martínez, and B. M. Weckhuysen, "Combined Operando UV/Vis/IR Spectroscopy Reveals the Role of Methoxy and Aromatic Species during the Methanol-to-Olefins Reaction over H-SAPO-34," *ChemCatChem*, vol. 6, no. 12, pp. 3396–3408, 2014.

[95] K. Hemelsoet, A. Nollet, M. Vandichel, D. Lesthaeghe, V. Van Speybroeck, and M. Waroquier, "The Effect of Confined Space on the Growth of Naphthalenic Species in a Chabazite-Type Catalyst: A Molecular Modeling Study," *ChemCatChem*, vol. 1, pp. 373–378, Nov. 2009.

[96] K. Hemelsoet, A. Nollet, V. Van Speybroeck, and M. Waroquier, "Theoretical Simulations Elucidate the Role of Naphthalenic Species during Methanol Conversion within H-SAPO-34," *Chem. Eur. J.*, vol. 17, pp. 9083–9093, Aug. 2011.

[97] K. Hemelsoet, Q. Qian, T. De Meyer, K. De Wispelaere, B. De Sterck, B. M. Weckhuysen, M. Waroquier, and V. Van Speybroeck, "Identification of Intermediates in Zeolite-Catalyzed Reactions by In Situ UV/Vis Microspectroscopy and a Complementary Set of Molecular Simulations," *Chem. Eur. J.*, vol. 19, pp. 16595–16606, Dec. 2013.

[98] H. Fu, W. Song, and J. F. Haw, "Polycyclic Aromatics Formation in HSAPO-34 During Methanol-to-Olefin Catalysis: Ex Situ Characterization After Cryogenic Grinding," *Catalysis Letters*, vol. 76, pp. 89–94, Sept. 2001.

[99] F. Bleken, M. Bjørgen, L. Palumbo, S. Bordiga, S. Svelle, K.-P. Lillerud, and U. Olsbye, "The Effect of Acid Strength on the Conversion of Methanol to Olefins Over Acidic Microporous Catalysts with the CHA Topology," *Top Catal*, vol. 52, pp. 218–228, Apr. 2009.

[100] M. Bjørgen, F. Joensen, K.-P. Lillerud, U. Olsbye, and S. Svelle, "The mechanisms of ethene and propene formation from methanol over high silica H-ZSM-5 and H-beta," *Catalysis Today*, vol. 142, pp. 90–97, Apr. 2009.

[101] D. M. Bibby, R. F. Howe, and G. D. McLellan, "Coke formation in high-silica zeolites," *Applied Catalysis A: General*, vol. 93, pp. 1–34, Dec. 1992.

[102] D. Lesthaeghe, B. De Sterck, V. Van Speybroeck, G. Marin, and M. Waroquier, "Zeolite Shape-Selectivity in the gem-Methylation of Aromatic Hydrocarbons," *Angewandte Chemie International Edition*, vol. 46, no. 8, pp. 1311–1314, 2007.

[103] D. McCann, D. Lesthaeghe, P. Kletnieks, D. Guenther, M. Hayman, V. Van Speybroeck, M. Waroquier, and J. Haw, "A Complete Catalytic Cycle for Supramolecular Methanol-to-Olefins Conversion by Linking Theory with Experiment," *Angewandte Chemie International Edition*, vol. 47, pp. 5179–5182, June 2008.

[104] C.-M. Wang, Y.-D. Wang, Z.-K. Xie, and Z.-P. Liu, "Methanol to Olefin Conversion on HSAPO-34 Zeolite from Periodic Density Functional Theory Calculations: A Complete Cycle of Side Chain Hydrocarbon Pool Mechanism," *J. Phys. Chem. C*, vol. 113, pp. 4584–4591, Mar. 2009.

[105] K. De Wispelaere, K. Hemelsoet, M. Waroquier, and V. Van Speybroeck, "Complete low-barrier side-chain route for olefin formation during methanol conversion in H-SAPO-34," *Journal of Catalysis*, vol. 305, pp. 76–80, Sept. 2013.

[106] V. Van Speybroeck, K. Hemelsoet, K. De Wispelaere, Q. Qian, J. Van der Mynsbrugge, B. De Sterck, B. M. Weckhuysen, and M. Waroquier, "Mechanistic Studies on Chabazite-Type Methanol-to-Olefin Catalysts: Insights from Time-Resolved UV/Vis Microspectroscopy Combined with Theoretical Simulations," *ChemCatChem*, vol. 5, pp. 173–184, Jan. 2013.

[107] K. De Wispelaere, S. Bailleul, and V. Van Speybroeck, "Towards molecular control of elementary reactions in zeolite catalysis by advanced molecular simulations mimicking operating conditions," *Catal. Sci. Technol.*, vol. 6, pp. 2686–2705, Apr. 2016.

[108] M. Bjørgen, S. Svelle, F. Joensen, J. Nerlov, S. Kolboe, F. Bonino, L. Palumbo, S. Bordiga, and U. Olsbye, "Conversion of methanol to hydrocarbons over zeolite H-ZSM-5: On the origin of the olefinic species," *Journal of Catalysis*, vol. 249, pp. 195–207, July 2007.

[109] S. Teketel, U. Olsbye, K.-P. Lillerud, P. Beato, and S. Svelle, "Selectivity control through fundamental mechanistic insight in the conversion of methanol to hydrocarbons over zeolites," *Microporous and Mesoporous Materials*, vol. 136, pp. 33–41, Dec. 2010.

[110] S. Svelle, M. Visur, U. Olsbye, Saepurahman, and M. Bjørgen, "Mechanistic Aspects of the Zeolite Catalyzed Methylation of Alkenes and Aromatics with Methanol: A Review," *Top Catal*, vol. 54, pp. 897–906, Sept. 2011.

[111] Q. Qian, J. Ruiz-Martínez, M. Mokhtar, A. M. Asiri, S. A. Al-Thabaiti, S. N. Basahel, H. E. van der Bij, J. Kornatowski, and B. M. Weckhuysen, "Single-Particle Spectroscopy on Large SAPO-34 Crystals at Work: Methanol-to-Olefin versus Ethanol-to-Olefin Processes," *Chem. Eur. J.*, vol. 19, pp. 11204–11215, Aug. 2013.

[112] I. I. Ivanova and A. Corma, "Surface Species Formed and Their Reactivity during the Alkylation of Toluene by Methanol and Dimethyl Ether on Zeolites As Determined by in Situ 13c MAS NMR," *J. Phys. Chem. B*, vol. 101, pp. 547–551, Jan. 1997.

[113] A. M. Vos, K. H. L. Nulens, F. De Proft, R. A. Schoonheydt, and P. Geerlings, "Reactivity Descriptors and Rate Constants for Electrophilic Aromatic Substitution: Acid Zeolite Catalyzed Methylation of Benzene and Toluene," *J. Phys. Chem. B*, vol. 106, pp. 2026–2034, Feb. 2002.

[114] S. Svelle, S. Kolboe, U. Olsbye, and O. Swang, "A Theoretical Investigation of the Methylation of Methylbenzenes and Alkenes by Halomethanes over Acidic Zeolites," *J. Phys. Chem. B*, vol. 107, pp. 5251–5260, June 2003.

[115] R. Y. Brogaard, R. Henry, Y. Schuurman, A. J. Medford, P. G. Moses, P. Beato, S. Svelle, J. K. Nørskov, and U. Olsbye, "Methanol-to-hydrocarbons conversion: The alkene methylation pathway," *Journal of Catalysis*, vol. 314, pp. 159–169, May 2014.

[116] T. Maihom, B. Boekfa, J. Sirijaraensre, T. Nanok, M. Probst, and J. Limtrakul, "Reaction Mechanisms of the Methylation of Ethene with Methanol and Dimethyl Ether over H-ZSM-5: An ONIOM Study," *J. Phys. Chem. C*, vol. 113, pp. 6654–6662, Apr. 2009.

[117] M. N. Mazar, S. Al-Hashimi, A. Bhan, and M. Cococcioni, "Methylation of Ethene by Surface Methoxides: A Periodic PBE+D Study across Zeolites," *J. Phys. Chem. C*, vol. 116, pp. 19385–19395, Sept. 2012.

[118] A. J. Jones and E. Iglesia, "Kinetic, Spectroscopic, and Theoretical Assessment of Associative and Dissociative Methanol Dehydration Routes in Zeolites," *Angew. Chem. Int. Ed.*, vol. 53, pp. 12177–12181, Nov. 2014.

[119] K. De Wispelaere, J. S. Martínez-Espín, M. J. Hoffmann, S. Svelle, U. Olsbye, and T. Bligaard, "Understanding zeolite-catalyzed benzene methylation reactions by methanol and dimethyl ether at operating conditions from first principle microkinetic modeling and experiments," *Catalysis Today*, vol. 312, pp. 35–43, Aug. 2018.

[120] I. Yarulina, S. Bailleul, A. Pustovarenko, J. R. Martínez, K. De Wispelaere, J. Hajek, B. M. Weckhuysen, K. Houben, M. Baldus, V. Van Speybroeck, F. Kapteijn, and J. Gascon, "Suppression of the Aromatic Cycle in Methanol-to-Olefins Reaction over ZSM-5 by Post-Synthetic Modification Using Calcium," *ChemCatChem*, vol. 8, pp. 3057–3063, Oct. 2016.

[121] I. Yarulina, K. De Wispelaere, S. Bailleul, J. Goetze, M. Radersma, E. Abou-Hamad, I. Vollmer, M. Goesten, B. Mezari, E. J. M. Hensen, J. S. Martínez-Espín, M. Morten, S. Mitchell, J. Perez-Ramirez, U. Olsbye, B. M. Weckhuysen, V. Van Speybroeck, F. Kapteijn, and J. Gascon, "Structure–performance descriptors and the role of Lewis acidity in the methanol-to-propylene process," *Nature Chemistry*, vol. 10, pp. 804–812, Aug. 2018.

[122] S. Teketel, S. Svelle, K.-P. Lillerud, and U. Olsbye, "Shape-Selective Conversion of Methanol to Hydrocarbons Over 10-Ring Unidirectional-Channel Acidic H-ZSM-22," *ChemCatChem*, vol. 1, pp. 78–81, Aug. 2009.

[123] S. Teketel, W. Skistad, S. Benard, U. Olsbye, K. P. Lillerud, P. Beato, and S. Svelle, "Shape Selectivity in the Conversion of Methanol to Hydrocarbons: The Catalytic Performance of One-Dimensional 10-Ring Zeolites: ZSM-22, ZSM-23, ZSM-48, and EU-1," *ACS Catal.*, vol. 2, no. 1, pp. 26–37, 2011.

[124] S. Teketel, U. Olsbye, K. P. Lillerud, P. Beato, and S. Svelle, "Co-conversion of methanol and light alkenes over acidic zeolite catalyst H-ZSM-22: Simulated recycle of non-gasoline range products," *Applied Catalysis A: General*, vol. 494, pp. 68–76, Mar. 2015.

[125] J. Li, Y. Wei, J. Chen, P. Tian, X. Su, S. Xu, Y. Qi, Q. Wang, Y. Zhou, Y. He, and Z. Liu, "Observation of Heptamethylbenzenium Cation over SAPO-Type Molecular Sieve DNL-6 under Real MTO Conversion Conditions," *J. Am. Chem. Soc.*, vol. 134, pp. 836–839, Jan. 2012.

[126] M. Westgård Erichsen, M. Mortén, S. Svelle, O. Sekiguchi, E. Uggerud, and U. Olsbye, "Conclusive Evidence for Two Unimolecular Pathways

to Zeolite-Catalyzed De-alkylation of the Heptamethylbenzenium Cation," *ChemCatChem*, vol. 7, no. 24, pp. 4143–4147, 2015.

[127] A. Hwang, T. T. Le, Z. Shi, H. Dai, J. D. Rimer, and A. Bhan, "Effects of diffusional constraints on lifetime and selectivity in methanol-to-olefins catalysis on HSAPO-34," *Journal of Catalysis*, vol. 369, pp. 122–132, Jan. 2019.

[128] I. M. Dahl, R. Wendelbo, A. Andersen, D. Akporiaye, H. Mostad, and T. Fuglerud, "The effect of crystallite size on the activity and selectivity of the reaction of ethanol and 2-propanol over SAPO-34," *Microporous and Mesoporous Materials*, vol. 29, pp. 159–171, June 1999.

[129] D. Mores, E. Stavitski, M. H. F. Kox, J. Kornatowski, U. Olsbye, and B. M. Weckhuysen, "Space- and Time-Resolved In-situ Spectroscopy on the Coke Formation in Molecular Sieves: Methanol-to-Olefin Conversion over H-ZSM-5 and H-SAPO-34," *Chemistry – A European Journal*, vol. 14, no. 36, pp. 11320–11327, 2008.

[130] M. Dusselier, M. A. Deimund, J. E. Schmidt, and M. E. Davis, "Methanol-to-Olefins Catalysis with Hydrothermally Treated Zeolite SSZ-39," *ACS Catal.*, vol. 5, pp. 6078–6085, Oct. 2015.

[131] H. K. Beyer, "Dealumination Techniques for Zeolites," in *Post-Synthesis Modification I*, Molecular Sieves, pp. 203–255, Springer, Berlin, Heidelberg, 2002.

[132] L. Jin, H. Hu, S. Zhu, and B. Ma, "An improved dealumination method for adjusting acidity of HZSM-5," *Catalysis Today*, vol. 149, pp. 207–211, Jan. 2010.

[133] C. Liu, G. Li, E. J. M. Hensen, and E. A. Pidko, "Nature and Catalytic Role of Extraframework Aluminum in Faujasite Zeolite: A Theoretical Perspective," *ACS Catal.*, vol. 5, pp. 7024–7033, Nov. 2015.

[134] M. Dyballa, P. Becker, D. Trefz, E. Klemm, A. Fischer, H. Jakob, and M. Hunger, "Parameters influencing the selectivity to propene in the MTO conversion on 10-ring zeolites: directly synthesized zeolites ZSM-5, ZSM-11, and ZSM-22," *Applied Catalysis A: General*, vol. 510, pp. 233–243, Jan. 2016.

[135] A. Jabbari, A. Abbasi, H. Zargarnezhad, and M. Riazifar, "A study on the effect of SiO2/Al2o3 ratio on the structure and performance of nano-sized ZSM-5 in methanol to propylene conversion," *Reac Kinet Mech Cat*, vol. 121, pp. 763–772, Aug. 2017.

[136] W. Dai, G. Cao, L. Yang, G. Wu, M. Dyballa, M. Hunger, N. Guan, and L. Li, "Insights into the catalytic cycle and activity of methanol-to-olefin

conversion over low-silica AlPO-34 zeolites with controllable Brønsted acid density," *Catal. Sci. Technol.*, vol. 7, pp. 607–618, Feb. 2017.

[137] M. Rostamizadeh and F. Yaripour, "Dealumination of high silica H-ZSM-5 as long-lived nanocatalyst for methanol to olefin conversion," *Journal of the Taiwan Institute of Chemical Engineers*, vol. 71, pp. 454–463, Feb. 2017.

[138] C. Kong, J. Zhu, S. Liu, and Y. Wang, "SAPO-34 with a low acidity outer layer by epitaxial growth and its improved MTO performance," *RSC Advances*, vol. 7, no. 63, pp. 39889–39898, 2017.

[139] B. Lin, Q. Zhang, and Y. Wang, "Catalytic Conversion of Ethylene to Propylene and Butenes over H–ZSM-5," *Ind. Eng. Chem. Res.*, vol. 48, pp. 10788–10795, Dec. 2009.

[140] A. Takahashi, W. Xia, Q. Wu, T. Furukawa, I. Nakamura, H. Shimada, and T. Fujitani, "Difference between the mechanisms of propylene production from methanol and ethanol over ZSM-5 catalysts," *Applied Catalysis A: General*, vol. 467, pp. 380–385, Oct. 2013.

[141] H. Zhang, Z. Ning, J. Shang, H. Liu, S. Han, W. Qu, Y. Jiang, and Y. Guo, "A durable and highly selective PbO/HZSM-5 catalyst for methanol to propylene (MTP) conversion," *Microporous and Mesoporous Materials*, vol. 248, pp. 173–178, Aug. 2017.

[142] N. Prakash, M.-H. Lee, S. Yoon, and K.-D. Jung, "Role of acid solvent to prepare highly active PtSn/θ-Al2O3 catalysts in dehydrogenation of propane to propylene," *Catalysis Today*, vol. 293, pp. 33–41, Sept. 2017.

[143] S. M. Abubakar, D. M. Marcus, J. C. Lee, J. O. Ehresmann, C.-Y. Chen, P. W. Kletnieks, D. R. Guenther, M. J. Hayman, M. Pavlova, J. B. Nicholas, and J. F. Haw, "Structural and Mechanistic Investigation of a Phosphate-Modified HZSM-5 Catalyst for Methanol Conversion," *Langmuir*, vol. 22, pp. 4846–4852, May 2006.

[144] M. Derewinski, P. Sarv, X. Sun, S. Müller, A. C. van Veen, and J. A. Lercher, "Reversibility of the Modification of HZSM-5 with Phosphate Anions," *J. Phys. Chem. C*, vol. 118, pp. 6122–6131, Mar. 2014.

[145] H. E. van der Bij and B. M. Weckhuysen, "Phosphorus promotion and poisoning in zeolite-based materials: synthesis, characterisation and catalysis," *Chem. Soc. Rev.*, vol. 44, pp. 7406–7428, Oct. 2015.

[146] N. V. Klyueva, N. D. Tien, and K. G. Ione, "Hydrocarbon synthesis from methanol on erionite and mordenite catalysts synthesized in the presence of B3+, Ga3+ or Fe3+," *React Kinet Catal Lett*, vol. 29, pp. 427–432, Sept. 1985.

[147] H. Zheng, D. Ma, X. Bao, J. Z. Hu, J. H. Kwak, Y. Wang, and C. H. F. Peden, "Direct Observation of the Active Center for Methane Dehydroaromatization Using an Ultrahigh Field 95mo NMR Spectroscopy," *J. Am. Chem. Soc.*, vol. 130, pp. 3722–3723, Mar. 2008.

[148] D. Esquivel, A. J. Cruz-Cabeza, C. Jiménez-Sanchidrián, and F. J. Romero-Salguero, "Transition metal exchanged β zeolites: Characterization of the metal state and catalytic application in the methanol conversion to hydrocarbons," *Microporous and Mesoporous Materials*, vol. 179, pp. 30–39, Sept. 2013.

[149] K. Van der Borght, V. V. Galvita, and G. B. Marin, "Ethanol to higher hydrocarbons over Ni, Ga, Fe-modified ZSM-5: Effect of metal content," *Applied Catalysis A: General*, vol. 492, pp. 117–126, Feb. 2015.

[150] M. A. Deimund, L. Harrison, J. D. Lunn, Y. Liu, A. Malek, R. Shayib, and M. E. Davis, "Effect of Heteroatom Concentration in SSZ-13 on the Methanol-to-Olefins Reaction," *ACS Catal.*, vol. 6, pp. 542–550, Feb. 2016.

[151] N. Kosinov, C. Liu, E. J. M. Hensen, and E. A. Pidko, "Engineering of Transition Metal Catalysts Confined in Zeolites," *Chem. Mater.*, vol. 30, pp. 3177–3198, May 2018.

[152] K. Suzuki, Y. Kiyozumi, K. Matsuzaki, S. Ikai, and S. Shin, "Effect of modification of ZSM-5 type zeolite with calcium phosphate on its physicochemical and catalytic Properties," *Applied Catalysis*, vol. 39, pp. 315–324, May 1988.

[153] S. Zhang, B. Zhang, Z. Gao, and Y. Han, "Methanol to Olefin over Ca-Modified HZSM-5 Zeolites," *Ind. Eng. Chem. Res.*, vol. 49, pp. 2103–2106, Mar. 2010.

[154] S. Zhang, B. Zhang, Z. Gao, and Y. Han, "Ca modified ZSM-5 for high propylene selectivity from methanol," *Reac Kinet Mech Cat*, vol. 99, pp. 447–453, Jan. 2010.

[155] J.-m. MAN, Q.-d. ZHANG, H.-j. XIE, J.-x. PAN, Y.-s. TAN, and Y.-z. HAN, "Effects of reaction atmosphere on dimethyl ether conversion to propylene process over Ca/ZSM-5," *Journal of Fuel Chemistry and Technology*, vol. 39, pp. 42–46, Jan. 2011.

[156] C. Chen, Q. Zhang, Z. Meng, C. Li, and H. Shan, "Effect of magnesium modification over H-ZSM-5 in methanol to propylene reaction," *Appl Petrochem Res*, vol. 5, pp. 277–284, Aug. 2015.

[157] V. Van Speybroeck, K. Hemelsoet, L. Joos, M. Waroquier, R. G. Bell, and C. R. A. Catlow, "Advances in theory and their application within the field of zeolite chemistry," *Chem. Soc. Rev.*, vol. 44, pp. 7044–7111, Oct. 2015.

[158] E. A. Pidko, E. J. M. Hensen, and R. A. van Santen, "Self-organization of extraframework cations in zeolites," *Proc. R. Soc. A*, vol. 468, pp. 2070–2086, July 2012.

[159] P. Kumar, J. W. Thybaut, S. Svelle, U. Olsbye, and G. B. Marin, "Single-Event Microkinetics for Methanol to Olefins on H-ZSM-5," *Ind. Eng. Chem. Res.*, vol. 52, pp. 1491–1507, Jan. 2013.

[160] E. Borodina, F. Meirer, I. Lezcano-González, M. Mokhtar, A. M. Asiri, S. A. Al-Thabaiti, S. N. Basahel, J. Ruiz-Martínez, and B. M. Weckhuysen, "Influence of the Reaction Temperature on the Nature of the Active and Deactivating Species during Methanol to Olefins Conversion over H-SSZ-13," *ACS Catal.*, vol. 5, pp. 992–1003, Feb. 2015.

[161] E. Borodina, H. Sharbini Harun Kamaluddin, F. Meirer, M. Mokhtar, A. M. Asiri, S. A. Al-Thabaiti, S. N. Basahel, J. Ruiz-Martínez, and B. M. Weckhuysen, "Influence of the Reaction Temperature on the Nature of the Active and Deactivating Species During Methanol-to-Olefins Conversion over H-SAPO-34," *ACS Catal.*, vol. 7, pp. 5268–5281, Aug. 2017.

[162] D. Chen, H. P. Rebo, A. Grønvold, K. Moljord, and A. Holmen, "Methanol conversion to light olefins over SAPO-34: kinetic modeling of coke formation," *Microporous and Mesoporous Materials*, vol. 35-36, pp. 121–135, Apr. 2000.

[163] D. Chen, K. Moljord, and A. Holmen, "A methanol to olefins review: Diffusion, coke formation and deactivation on SAPO type catalysts," *Microporous and Mesoporous Materials*, vol. 164, pp. 239–250, Dec. 2012.

[164] P. L. Benito, A. G. Gayubo, A. T. Aguayo, M. Olazar, and J. Bilbao, "Deposition and Characteristics of Coke over a H-ZSM5 Zeolite-Based Catalyst in the MTG Process," *Ind. Eng. Chem. Res.*, vol. 35, pp. 3991–3998, Jan. 1996.

[165] S. Svelle, U. Olsbye, F. Joensen, and M. Bjørgen, "Conversion of Methanol to Alkenes over Medium– and Large–Pore Acidic Zeolites: Steric Manipulation of the Reaction Intermediates Governs the Ethene/Propene Product Selectivity," *J. Phys. Chem. C*, vol. 111, no. 49, pp. 17981–17984, 2007.

[166] M. Bjørgen, U. Olsbye, D. Petersen, and S. Kolboe, "The methanol-to-hydrocarbons reaction: insight into the reaction mechanism from [12c]benzene and [13c]methanol coreactions over zeolite H-beta," *Journal of Catalysis*, vol. 221, pp. 1–10, Jan. 2004.

[167] M. Bjørgen, S. Akyalcin, U. Olsbye, S. Benard, S. Kolboe, and S. Svelle, "Methanol to hydrocarbons over large cavity zeolites: Toward a unified description of catalyst deactivation and the reaction mechanism," *Journal of Catalysis*, vol. 275, pp. 170–180, Sept. 2010.

[168] J. Ahn, B. Temel, and E. Iglesia, "Selective Homologation Routes to 2,2,3-Trimethylbutane on Solid Acids," *Angewandte Chemie International Edition*, vol. 48, pp. 3814–3816, May 2009.

[169] D. A. Simonetti, J. H. Ahn, and E. Iglesia, "Mechanistic details of acid-catalyzed reactions and their role in the selective synthesis of triptane and isobutane from dimethyl ether," *Journal of Catalysis*, vol. 277, pp. 173–195, Jan. 2011.

[170] S. Tjandra, R. G. Anthony, and A. Akgerman, "Low hydrogen/carbon monoxide ratio synthesis gas conversion to methanol in a trickle bed reactor," *Ind. Eng. Chem. Res.*, vol. 32, pp. 2602–2607, Nov. 1993.

[171] X. Yin, D. Y. C. Leung, J. Chang, J. Wang, Y. Fu, and C. Wu, "Characteristics of the Synthesis of Methanol Using Biomass-Derived Syngas," *Energy Fuels*, vol. 19, pp. 305–310, Jan. 2005.

[172] A. Demirbas, "Progress and recent trends in biofuels," *Progress in Energy and Combustion Science*, vol. 33, pp. 1–18, Feb. 2007.

[173] A. J. Marchi and G. F. Froment, "Catalytic conversion of methanol to light alkenes on SAPO molecular sieves," *Applied Catalysis*, vol. 71, pp. 139–152, Apr. 1991.

[174] X. Wu and R. G. Anthony, "Effect of feed composition on methanol conversion to light olefins over SAPO-34," *Applied Catalysis A: General*, vol. 218, pp. 241–250, Sept. 2001.

[175] K. De Wispelaere, C. S. Wondergem, B. Ensing, K. Hemelsoet, E. J. Meijer, B. M. Weckhuysen, V. Van Speybroeck, and J. Ruiz-Martínez, "Insight into the Effect of Water on the Methanol-to-Olefins Conversion in H-SAPO-34 from Molecular Simulations and in Situ Microspectroscopy," *ACS Catal.*, pp. 1991–2002, Feb. 2016.

[176] R. Y. Rohling, E. Uslamin, B. Zijlstra, I. C. Tranca, I. A. W. Filot, E. J. M. Hensen, and E. A. Pidko, "An Active Alkali-Exchanged Faujasite Catalyst for p-Xylene Production via the One-Pot Diels–Alder Cycloaddition/Dehydration Reaction of 2,5-Dimethylfuran with Ethylene," *ACS Catal.*, vol. 8, pp. 760–769, Feb. 2018.

[177] C. Wang, Y. Chu, J. Xu, Q. Wang, G. Qi, P. Gao, X. Zhou, and F. Deng, "Extra-Framework Aluminum-Assisted Initial C–C Bond Formation in Methanol-to-Olefins Conversion on Zeolite H-ZSM-5," *Angewandte Chemie International Edition*, vol. 57, pp. 10197–10201, Aug. 2018.

[178] M. E. Z. Velthoen, S. Nab, and B. M. Weckhuysen, "Probing acid sites in solid catalysts with pyridine UV-Vis spectroscopy," *Phys. Chem. Chem. Phys.*, vol. 20, pp. 21647–21659, Aug. 2018.

[179] S. Raimondeau and D. G. Vlachos, "Recent developments on multiscale, hierarchical modeling of chemical reactors," *Chemical Engineering Journal*, vol. 90, pp. 3–23, Nov. 2002.

[180] M. Salciccioli, M. Stamatakis, S. Caratzoulas, and D. G. Vlachos, "A review of multiscale modeling of metal-catalyzed reactions: Mechanism development for complexity and emergent behavior," *Chemical Engineering Science*, vol. 66, pp. 4319–4355, Oct. 2011.

[181] F. J. Keil, "Multiscale Modelling in Computational Heterogeneous Catalysis," in *Multiscale Molecular Methods in Applied Chemistry* (B. Kirchner and J. Vrabec, eds.), Topics in Current Chemistry, pp. 69–107, Berlin, Heidelberg: Springer Berlin Heidelberg, 2012.

[182] N. López, N. Almora-Barrios, G. Carchini, P. Błoński, L. Bellarosa, R. García-Muelas, G. Novell-Leruth, and M. García-Mota, "State-of-the-art and challenges in theoretical simulations of heterogeneous catalysis at the microscopic level," *Catal. Sci. Technol.*, vol. 2, pp. 2405–2417, Nov. 2012.

[183] A. C. T. van Duin, S. Dasgupta, F. Lorant, and W. A. Goddard, "ReaxFF: A Reactive Force Field for Hydrocarbons," *J. Phys. Chem. A*, vol. 105, pp. 9396–9409, Oct. 2001.

[184] Y. Han, D. Jiang, J. Zhang, W. Li, Z. Gan, and J. Gu, "Development, applications and challenges of ReaxFF reactive force field in molecular simulations," *Front. Chem. Sci. Eng.*, vol. 10, pp. 16–38, Mar. 2016.

[185] H. Eyring, "The Activated Complex in Chemical Reactions," *J. Chem. Phys.*, vol. 3, pp. 107–115, Feb. 1935.

[186] K. De Wispelaere, L. Vanduyfhuys, and V. Van Speybroeck, "Chapter 6 - Entropy Contributions to Transition State Modeling," in *Modelling and Simulation in the Science of Micro- and Meso-Porous Materials* (C. R. A. Catlow, V. Van Speybroeck, and R. A. van Santen, eds.), pp. 189–228, Elsevier, Jan. 2018.

[187] L. Grajciar, C. J. Heard, A. A. Bondarenko, M. V. Polynski, J. Meeprasert, E. A. Pidko, and P. Nachtigall, "Towards operando computational modeling in heterogeneous catalysis," *Chem. Soc. Rev.*, vol. 47, pp. 8307–8348, Nov. 2018.

[188] E. A. Pidko, "Toward the Balance between the Reductionist and Systems Approaches in Computational Catalysis: Model versus Method Accuracy for the Description of Catalytic Systems," *ACS Catal.*, vol. 7, pp. 4230–4234, July 2017.

[189] K. De Wispelaere, B. Ensing, A. Ghysels, E. J. Meijer, and V. Van Speybroeck, "Complex Reaction Environments and Competing Reaction Mechanisms in Zeolite Catalysis: Insights from Advanced Molecular Dynamics," *Chem. Eur. J.*, vol. 21, pp. 9385–9396, June 2015.

[190] L. Benco, T. Bučko, and J. Hafner, "Dehydrogenation of propane over ZnMOR. Static and dynamic reaction energy diagram," *Journal of Catalysis*, vol. 277, pp. 104–116, Jan. 2011.

[191] T. Bučko, L. Benco, J. Hafner, and J. G. Ángyán, "Monomolecular cracking of propane over acidic chabazite: An ab initio molecular dynamics and transition path sampling study," *Journal of Catalysis*, vol. 279, pp. 220–228, Apr. 2011.

[192] T. Bučko and J. Hafner, "The role of spatial constraints and entropy in the adsorption and transformation of hydrocarbons catalyzed by zeolites," *Journal of Catalysis*, vol. 329, pp. 32–48, Sept. 2015.

[193] T. Bučko, S. Chibani, J.-F. Paul, L. Cantrel, and M. Badawi, "Dissociative iodomethane adsorption on Ag-MOR and the formation of AgI clusters: an ab initio molecular dynamics study," *Phys. Chem. Chem. Phys.*, vol. 19, pp. 27530–27543, Oct. 2017.

[194] J. Rey, A. Gomez, P. Raybaud, C. Chizallet, and T. Bučko, "On the origin of the difference between type A and type B skeletal isomerization of alkenes catalyzed by zeolites: The crucial input of ab initio molecular dynamics," *Journal of Catalysis*, vol. 373, pp. 361–373, May 2019.

[195] C. Abrams and G. Bussi, "Enhanced Sampling in Molecular Dynamics Using Metadynamics, Replica-Exchange, and Temperature-Acceleration," *Entropy*, vol. 16, pp. 163–199, Dec. 2013.

[196] C. D. Christ, A. E. Mark, and W. F. van Gunsteren, "Basic ingredients of free energy calculations: A review," *J. Comput. Chem.*, vol. 31, pp. 1569–1582, June 2010.

[197] A. Laio and M. Parrinello, "Escaping free-energy minima," *PNAS*, vol. 99, pp. 12562–12566, Jan. 2002.

[198] M. Iannuzzi, A. Laio, and M. Parrinello, "Efficient Exploration of Reactive Potential Energy Surfaces Using Car-Parrinello Molecular Dynamics," *Phys. Rev. Lett.*, vol. 90, p. 238302, June 2003.

[199] A. Laio and F. L. Gervasio, "Metadynamics: a method to simulate rare events and reconstruct the free energy in biophysics, chemistry and material science," *Rep. Prog. Phys.*, vol. 71, p. 126601, Dec. 2008.

[200] I. Bilionis and P. S. Koutsourelakis, "Free energy computations by minimization of Kullback–Leibler divergence: An efficient adaptive biasing potential method for sparse representations," *Journal of Computational Physics*, vol. 231, pp. 3849–3870, May 2012.

[201] O. Valsson and M. Parrinello, "Variational Approach to Enhanced Sampling and Free Energy Calculations," *Phys. Rev. Lett.*, vol. 113, p. 090601, Aug. 2014.

[202] O. Valsson, P. Tiwary, and M. Parrinello, "Enhancing Important Fluctuations: Rare Events and Metadynamics from a Conceptual Viewpoint," *Annu. Rev. Phys. Chem.*, vol. 67, pp. 159–184, May 2016.

[203] G. M. Torrie and J. P. Valleau, "Monte Carlo free energy estimates using non-Boltzmann sampling: Application to the sub-critical Lennard-Jones fluid," *Chemical Physics Letters*, vol. 28, pp. 578–581, Oct. 1974.

[204] G. M. Torrie and J. P. Valleau, "Nonphysical sampling distributions in Monte Carlo free-energy estimation: Umbrella sampling," *Journal of Computational Physics*, vol. 23, pp. 187–199, Feb. 1977.

[205] J. Kästner, "Umbrella sampling," *WIREs Comput Mol Sci*, vol. 1, pp. 932–942, Nov. 2011.

[206] J. G. Kirkwood, "Statistical Mechanics of Fluid Mixtures," *J. Chem. Phys.*, vol. 3, pp. 300–313, May 1935.

[207] E. A. Carter, G. Ciccotti, J. T. Hynes, and R. Kapral, "Constrained reaction coordinate dynamics for the simulation of rare events," *Chemical Physics Letters*, vol. 156, pp. 472–477, Apr. 1989.

[208] T. P. Straatsma and J. A. McCammon, "Multiconfiguration thermodynamic integration," *The Journal of Chemical Physics*, vol. 95, pp. 1175–1188, July 1991.

[209] E. Paci, G. Ciccotti, M. Ferrario, and R. Kapral, "Activation energies by molecular dynamics with constraints," *Chemical Physics Letters*, vol. 176, pp. 581–587, Feb. 1991.

[210] W. K. den Otter and W. J. Briels, "The calculation of free-energy differences by constrained molecular-dynamics simulations," *J. Chem. Phys.*, vol. 109, pp. 4139–4146, Sept. 1998.

[211] E. Kelly, M. Seth, and T. Ziegler, "Calculation of Free Energy Profiles for Elementary Bimolecular Reactions by ab Initio Molecular Dynamics: Sampling Methods and Thermostat Considerations," *J. Phys. Chem. A*, vol. 108, pp. 2167–2180, Mar. 2004.

[212] T. De Meyer, B. Ensing, S. M. J. Rogge, K. De Clerck, E. J. Meijer, and V. Van Speybroeck, "Acidity Constant (pKa) Calculation of Large Solvated Dye Molecules: Evaluation of Two Advanced Molecular Dynamics Methods," *ChemPhysChem*, vol. 17, pp. 3447–3459, Nov. 2016.

[213] S. Svelle, C. Tuma, X. Rozanska, T. Kerber, and J. Sauer, "Quantum Chemical Modeling of Zeolite-Catalyzed Methylation Reactions: Toward Chemical Accuracy for Barriers," *J. Am. Chem. Soc.*, vol. 131, pp. 816–825, Jan. 2009.

[214] V. Van Speybroeck, J. Van der Mynsbrugge, M. Vandichel, K. Hemelsoet, D. Lesthaeghe, A. Ghysels, G. B. Marin, and M. Waroquier, "First Principle Kinetic Studies of Zeolite-Catalyzed Methylation Reactions," *J. Am. Chem. Soc.*, vol. 133, pp. 888–899, Feb. 2011.

[215] G. Piccini, M. Alessio, and J. Sauer, "Ab Initio Calculation of Rate Constants for Molecule–Surface Reactions with Chemical Accuracy," *Angew. Chem. Int. Ed.*, vol. 55, pp. 5235–5237, Apr. 2016.

[216] E. Schrödinger, "An Undulatory Theory of the Mechanics of Atoms and Molecules," *Phys. Rev.*, vol. 28, pp. 1049–1070, Dec. 1926.

[217] M. Born and R. Oppenheimer, "Zur Quantentheorie der Molekeln," *Annalen der Physik*, vol. 389, no. 20, pp. 457–484, 1927.

[218] V. Fock, "Näherungsmethode zur Lösung des quantenmechanischen Mehrkörperproblems," *Z. Physik*, vol. 61, pp. 126–148, Jan. 1930.

[219] Hartree Douglas Rayner and Hartree W., "Self-consistent field, with exchange, for beryllium," *Proceedings of the Royal Society of London. Series A - Mathematical and Physical Sciences*, vol. 150, pp. 9–33, May 1935.

[220] C. Møller and M. S. Plesset, "Note on an Approximation Treatment for Many-Electron Systems," *Phys. Rev.*, vol. 46, pp. 618–622, Oct. 1934.

[221] L. H. Thomas, "The calculation of atomic fields," *Mathematical Proceedings of the Cambridge Philosophical Society*, vol. 23, pp. 542–548, Jan. 1927.

[222] E. Fermi, "Un Metodo Statistico per la Determinazione di alcune Prioprietà dell'Atomo," *Rend. Accad. Naz. Lincei.*, vol. 6, pp. 602–607, 1927.

[223] P. Hohenberg and W. Kohn, "Inhomogeneous Electron Gas," *Phys. Rev.*, vol. 136, pp. B864–B871, Nov. 1964.

[224] W. Kohn and L. J. Sham, "Self-Consistent Equations Including Exchange and Correlation Effects," *Phys. Rev.*, vol. 140, pp. A1133–A1138, Nov. 1965.

[225] W. Kohn, "Nobel Lecture: Electronic structure of matter—wave functions and density functionals," *Rev. Mod. Phys.*, vol. 71, pp. 1253–1266, Oct. 1999.

[226] J. P. Perdew and K. Schmidt, "Jacob's ladder of density functional approximations for the exchange-correlation energy," *AIP Conference Proceedings*, vol. 577, pp. 1–20, July 2001.

[227] J. P. Perdew, A. Ruzsinszky, J. Tao, V. N. Staroverov, G. E. Scuseria, and G. I. Csonka, "Prescription for the design and selection of density functional approximations: More constraint satisfaction with fewer fits," *J. Chem. Phys.*, vol. 123, p. 062201, Aug. 2005.

[228] R. G. Parr and Y. Weitao, *Density-Functional Theory of Atoms and Molecules*. Oxford University Press, May 1994. Google-Books-ID: mGOpScSIwU4C.

[229] W. Koch and M. C. Holthausen, *A chemist's guide to density functional theory*. Wiley-VCH, Apr. 2000. Google-Books-ID: rCApAAAAYAAJ.

[230] R. Jones, "Density functional theory: Its origins, rise to prominence, and future," *Rev. Mod. Phys.*, vol. 87, pp. 897–923, Aug. 2015.

[231] N. Mardirossian and M. Head-Gordon, "Thirty years of density functional theory in computational chemistry: an overview and extensive assessment of 200 density functionals," *Molecular Physics*, vol. 115, pp. 2315–2372, Oct. 2017.

[232] G. R. Schleder, A. C. M. Padilha, C. M. Acosta, M. Costa, and A. Fazzio, "From DFT to machine learning: recent approaches to materials science–a review," *J. Phys. Mater.*, vol. 2, p. 032001, May 2019.

[233] S. Grimme, "Semiempirical GGA-type density functional constructed with a long-range dispersion correction," *Journal of Computational Chemistry*, vol. 27, no. 15, pp. 1787–1799, 2006.

[234] S. Grimme, J. Antony, T. Schwabe, and C. Mück-Lichtenfeld, "Density functional theory with dispersion corrections for supramolecular structures, aggregates, and complexes of (bio)organic molecules," *Org. Biomol. Chem.*, vol. 5, pp. 741–758, Feb. 2007.

[235] S. Grimme, J. Antony, S. Ehrlich, and H. Krieg, "A consistent and accurate ab initio parametrization of density functional dispersion correction (DFT-D) for the 94 elements H-Pu," *The Journal of Chemical Physics*, vol. 132, p. 154104, Apr. 2010.

[236] S. Grimme, S. Ehrlich, and L. Goerigk, "Effect of the damping function in dispersion corrected density functional theory," *Journal of Computational Chemistry*, vol. 32, no. 7, pp. 1456–1465, 2011.

[237] A. Tkatchenko and M. Scheffler, "Accurate Molecular Van Der Waals Interactions from Ground-State Electron Density and Free-Atom Reference Data," *Phys. Rev. Lett.*, vol. 102, p. 073005, Feb. 2009.

[238] M. Dion, H. Rydberg, E. Schröder, D. C. Langreth, and B. I. Lundqvist, "Van der Waals Density Functional for General Geometries," *Phys. Rev. Lett.*, vol. 92, p. 246401, June 2004.

[239] T. Thonhauser, V. R. Cooper, S. Li, A. Puzder, P. Hyldgaard, and D. C. Langreth, "Van der Waals density functional: Self-consistent potential and the nature of the van der Waals bond," *Phys. Rev. B*, vol. 76, p. 125112, Sept. 2007.

[240] A. Gulans, M. J. Puska, and R. M. Nieminen, "Linear-scaling self-consistent implementation of the van der Waals density functional," *Phys. Rev. B*, vol. 79, p. 201105, May 2009.

[241] Y. Zhao, N. E. Schultz, and D. G. Truhlar, "Design of Density Functionals by Combining the Method of Constraint Satisfaction with Parametrization for Thermochemistry, Thermochemical Kinetics, and Noncovalent Interactions," *J. Chem. Theory Comput.*, vol. 2, pp. 364–382, Mar. 2006.

[242] Y. Zhao and D. G. Truhlar, "Density Functionals with Broad Applicability in Chemistry," *Acc. Chem. Res.*, vol. 41, pp. 157–167, Feb. 2008.

[243] Y. Zhao and D. G. Truhlar, "Benchmark Data for Interactions in Zeolite Model Complexes and Their Use for Assessment and Validation of Electronic Structure Methods," *J. Phys. Chem. C*, vol. 112, pp. 6860–6868, May 2008.

[244] Y. Zhao and D. G. Truhlar, "The M06 suite of density functionals for main group thermochemistry, thermochemical kinetics, noncovalent interactions, excited states, and transition elements: two new functionals and systematic testing of four M06-class functionals and 12 other functionals," *Theor Chem Account*, vol. 120, pp. 215–241, May 2008.

[245] Y. Zhao and D. G. Truhlar, "Exploring the Limit of Accuracy of the Global Hybrid Meta Density Functional for Main-Group Thermochemistry, Kinetics, and Noncovalent Interactions," *J. Chem. Theory Comput.*, vol. 4, pp. 1849–1868, Nov. 2008.

[246] K. Yang, J. Zheng, Y. Zhao, and D. G. Truhlar, "Tests of the RPBE, revPBE, τ-HCTHhyb, ωB97x-D, and MOHLYP density functional approximations and 29 others against representative databases for diverse bond energies and barrier heights in catalysis," *The Journal of Chemical Physics*, vol. 132, p. 164117, Apr. 2010.

[247] N. Hansen, T. Kerber, J. Sauer, A. T. Bell, and F. J. Keil, "Quantum Chemical Modeling of Benzene Ethylation over H-ZSM-5 Approaching Chemical Accuracy: A Hybrid MP2:DFT Study," *J. Am. Chem. Soc.*, vol. 132, pp. 11525–11538, Aug. 2010.

[248] P. Bultinck, C. Van Alsenoy, P. W. Ayers, and R. Carbó-Dorca, "Critical analysis and extension of the Hirshfeld atoms in molecules," *J. Chem. Phys.*, vol. 126, p. 144111, Apr. 2007.

[249] T. Bučko, S. Lebègue, J. Hafner, and J. G. Ángyán, "Improved Density Dependent Correction for the Description of London Dispersion Forces," *J. Chem. Theory Comput.*, vol. 9, pp. 4293–4299, Oct. 2013.

[250] T. Bučko, S. Lebègue, J. G. Ángyán, and J. Hafner, "Extending the applicability of the Tkatchenko-Scheffler dispersion correction via iterative Hirshfeld partitioning," *J. Chem. Phys.*, vol. 141, p. 034114, July 2014.

[251] A. Tkatchenko, R. A. DiStasio, R. Car, and M. Scheffler, "Accurate and Efficient Method for Many-Body van der Waals Interactions," *Phys. Rev. Lett.*, vol. 108, p. 236402, June 2012.

[252] A. Ambrosetti, A. M. Reilly, R. A. DiStasio, and A. Tkatchenko, "Long-range correlation energy calculated from coupled atomic response functions," *J. Chem. Phys.*, vol. 140, p. 18A508, Feb. 2014.

[253] S. N. Steinmann and C. Corminboeuf, "A generalized-gradient approximation exchange hole model for dispersion coefficients," *J. Chem. Phys.*, vol. 134, p. 044117, Jan. 2011.

[254] S. N. Steinmann and C. Corminboeuf, "Comprehensive Benchmarking of a Density-Dependent Dispersion Correction," *J. Chem. Theory Comput.*, vol. 7, pp. 3567–3577, Nov. 2011.

[255] J. Klimeš, D. R. Bowler, and A. Michaelides, "Van der Waals density functionals applied to solids," *Phys. Rev. B*, vol. 83, p. 195131, May 2011.

[256] J. Wellendorff, K. T. Lundgaard, A. Møgelhøj, V. Petzold, D. D. Landis, J. K. Nørskov, T. Bligaard, and K. W. Jacobsen, "Density functionals for surface science: Exchange-correlation model development with Bayesian error estimation," *Phys. Rev. B*, vol. 85, p. 235149, June 2012.

[257] A. D. Becke, "Density-functional thermochemistry. III. The role of exact exchange," *J. Chem. Phys.*, vol. 98, pp. 5648–5652, Apr. 1993.

[258] H. Peng, Z.-H. Yang, J. P. Perdew, and J. Sun, "Versatile van der Waals Density Functional Based on a Meta-Generalized Gradient Approximation," *Phys. Rev. X*, vol. 6, p. 041005, Oct. 2016.

[259] B. Arstad, J. B. Nicholas, and J. F. Haw, "Theoretical Study of the Methylbenzene Side-Chain Hydrocarbon Pool Mechanism in Methanol to Olefin Catalysis," *J. Am. Chem. Soc.*, vol. 126, pp. 2991–3001, Mar. 2004.

[260] B. Arstad, S. Kolboe, and O. Swang, "Theoretical study of protonated xylenes: ethene elimination and H,C-scrambling reactions," *Journal of Physical Organic Chemistry*, vol. 17, no. 11, pp. 1023–1032, 2004.

[261] B. Arstad, S. Kolboe, and O. Swang, "Theoretical Study of the Heptamethylbenzenium Ion. Intramolecular Isomerizations and C2, C3, C4 Alkene Elimination," *J. Phys. Chem. A*, vol. 109, pp. 8914–8922, Oct. 2005.

[262] B. Arstad, S. Kolboe, and O. Swang, "Theoretical study of carbon atom scrambling in benzenium ions with ethyl or isopropyl groups," *Journal of Physical Organic Chemistry*, vol. 19, pp. 81–92, Feb. 2006.

[263] S. R. Blaszkowski and R. A. van Santen, "Density Functional Theory Calculations of the Activation of Methanol by a Broensted Zeolitic Proton," *J. Phys. Chem.*, vol. 99, pp. 11728–11738, July 1995.

[264] S. R. Blaszkowski, M. A. C. Nascimento, and R. A. van Santen, "Activation of C–H and C–C Bonds by an Acidic Zeolite: A Density Functional Study," *J. Phys. Chem.*, vol. 100, pp. 3463–3472, Jan. 1996.

[265] S. R. Blaszkowski and R. A. van Santen, "Theoretical Study of C–C Bond Formation in the Methanol-to-Gasoline Process," *J. Am. Chem. Soc.*, vol. 119, pp. 5020–5027, May 1997.

[266] S. R. Blaszkowski and R. A. van Santen, "Theoretical Study of the Mechanism of Surface Methoxy and Dimethyl Ether Formation from Methanol Catalyzed by Zeolitic Protons," *J. Phys. Chem. B*, vol. 101, pp. 2292–2305, Mar. 1997.

[267] J. Van der Mynsbrugge, J. De Ridder, K. Hemelsoet, M. Waroquier, and V. Van Speybroeck, "Enthalpy and Entropy Barriers Explain the Effects of Topology on the Kinetics of Zeolite-Catalyzed Reactions," *Chem. Eur. J.*, vol. 19, no. 35, pp. 11568–11576, 2013.

[268] D. Frenkel and B. Smit, *Understanding Molecular Simulation: From Algorithms to Applications*. Academic Press, Oct. 2001.

[269] J. D. Head, "Computation of vibrational frequencies for adsorbates on surfaces," *International Journal of Quantum Chemistry*, vol. 65, no. 5, pp. 827–838, 1997.

[270] H. Li and J. H. Jensen, "Partial Hessian vibrational analysis: the localization of the molecular vibrational energy and entropy," *Theor Chem Acc*, vol. 107, pp. 211–219, Apr. 2002.

[271] A. Ghysels, D. V. Neck, V. V. Speybroeck, T. Verstraelen, and M. Waroquier, "Vibrational modes in partially optimized molecular systems," *The Journal of Chemical Physics*, vol. 126, p. 224102, June 2007.

[272] B. A. De Moor, A. Ghysels, M.-F. Reyniers, V. Van Speybroeck, M. Waroquier, and G. B. Marin, "Normal Mode Analysis in Zeolites: Toward an Efficient Calculation of Adsorption Entropies," *J. Chem. Theory Comput.*, vol. 7, pp. 1090–1101, Apr. 2011.

[273] A. Ghysels, T. Verstraelen, K. Hemelsoet, M. Waroquier, and V. Van Speybroeck, "TAMkin: A Versatile Package for Vibrational Analysis and Chemical Kinetics," *J. Chem. Inf. Model.*, vol. 50, pp. 1736–1750, Sept. 2010.

[274] R. Car and M. Parrinello, "Unified Approach for Molecular Dynamics and Density-Functional Theory," *Phys. Rev. Lett.*, vol. 55, pp. 2471–2474, Nov. 1985.

[275] V. Van Speybroeck and R. J. Meier, "A recent development in computational chemistry: chemical reactions from first principles molecular dynamics simulations," *Chem. Soc. Rev.*, vol. 32, pp. 151–157, Apr. 2003.

[276] J. Hutter, "Car–Parrinello molecular dynamics," *Wiley Interdisciplinary Reviews: Computational Molecular Science*, vol. 2, no. 4, pp. 604–612, 2012.

[277] J. Hutter, M. Iannuzzi, F. Schiffmann, and J. VandeVondele, "cp2k: atomistic simulations of condensed matter systems," *WIREs Comput Mol Sci*, vol. 4, pp. 15–25, Jan. 2014.

[278] J. VandeVondele, M. Krack, F. Mohamed, M. Parrinello, T. Chassaing, and J. Hutter, "Quickstep: Fast and accurate density functional calculations using a mixed Gaussian and plane waves approach," *Computer Physics Communications*, vol. 167, pp. 103–128, Apr. 2005.

[279] S. Nosé, "A unified formulation of the constant temperature molecular dynamics methods," *The Journal of Chemical Physics*, vol. 81, pp. 511–519, July 1984.

[280] G. J. Martyna, D. J. Tobias, and M. L. Klein, "Constant pressure molecular dynamics algorithms," *The Journal of Chemical Physics*, vol. 101, pp. 4177–4189, Sept. 1994.

[281] N. Hansen and W. F. van Gunsteren, "Practical Aspects of Free-Energy Calculations: A Review," *J. Chem. Theory Comput.*, vol. 10, pp. 2632–2647, July 2014.

[282] F. Pietrucci, "Strategies for the exploration of free energy landscapes: Unity in diversity and challenges ahead," *Reviews in Physics*, vol. 2, pp. 32–45, Nov. 2017.

[283] M. A. Cuendet and M. E. Tuckerman, "Free Energy Reconstruction from Metadynamics or Adiabatic Free Energy Dynamics Simulations," *J. Chem. Theory Comput.*, vol. 10, pp. 2975–2986, Aug. 2014.

[284] B. A. De Moor, M.-F. Reyniers, and G. B. Marin, "Physisorption and chemisorption of alkanes and alkenes in H-FAU: a combined ab initio–statistical thermodynamics study," *Phys. Chem. Chem. Phys.*, vol. 11, pp. 2939–2958, Apr. 2009.

[285] B. A. De Moor, M.-F. Reyniers, O. C. Gobin, J. A. Lercher, and G. B. Marin, "Adsorption of C2–C8 n-Alkanes in Zeolites," *J. Phys. Chem. C*, vol. 115, pp. 1204–1219, Feb. 2011.

[286] M. Eichinger, P. Tavan, J. Hutter, and M. Parrinello, "A hybrid method for solutes in complex solvents: Density functional theory combined with empirical force fields," *J. Chem. Phys.*, vol. 110, pp. 10452–10467, May 1999.

[287] R. H. Swendsen and J.-S. Wang, "Replica Monte Carlo Simulation of Spin-Glasses," *Phys. Rev. Lett.*, vol. 57, pp. 2607–2609, Nov. 1986.

[288] Y. Sugita and Y. Okamoto, "Replica-exchange molecular dynamics method for protein folding," *Chemical Physics Letters*, vol. 314, pp. 141–151, Nov. 1999.

[289] Z. Jing, L. Xin, and H. Sun, "Replica exchange reactive molecular dynamics simulations of initial reactions in zeolite synthesis," *Phys. Chem. Chem. Phys.*, vol. 17, pp. 25421–25428, Sept. 2015.

[290] R. Demuynck, S. M. J. Rogge, L. Vanduyfhuys, J. Wieme, M. Waroquier, and V. Van Speybroeck, "Efficient Construction of Free Energy Profiles of Breathing Metal–Organic Frameworks Using Advanced Molecular Dynamics Simulations," *J. Chem. Theory Comput.*, vol. 13, pp. 5861–5873, Dec. 2017.

[291] F. Bach and E. Moulines, "Non-strongly-convex smooth stochastic approximation with convergence rate O(1/n)," in *Advances in Neural Information Processing Systems 26* (C. J. C. Burges, L. Bottou, M. Welling, Z. Ghahramani, and K. Q. Weinberger, eds.), pp. 773–781, Curran Associates, Inc., 2013.

[292] A. M. Ferrenberg and R. H. Swendsen, "New Monte Carlo technique for studying phase transitions," *Phys. Rev. Lett.*, vol. 61, pp. 2635–2638, Dec. 1988.

[293] A. M. Ferrenberg and R. H. Swendsen, "Optimized Monte Carlo data analysis," *Phys. Rev. Lett.*, vol. 63, pp. 1195–1198, Sept. 1989.

[294] S. Kumar, J. M. Rosenberg, D. Bouzida, R. H. Swendsen, and P. A. Kollman, "The weighted histogram analysis method for free-energy calculations on biomolecules. I. The method," *J. Comput. Chem.*, vol. 13, pp. 1011–1021, Oct. 1992.

[295] S. Kumar, J. M. Rosenberg, D. Bouzida, R. H. Swendsen, and P. A. Kollman, "Multidimensional free-energy calculations using the weighted histogram analysis method," *Journal of Computational Chemistry*, vol. 16, pp. 1339–1350, Nov. 1995.

[296] M. Souaille and B. Roux, "Extension to the weighted histogram analysis method: combining umbrella sampling with free energy calculations," *Computer Physics Communications*, vol. 135, pp. 40–57, Mar. 2001.

[297] M. Sprik and G. Ciccotti, "Free energy from constrained molecular dynamics," *J. Chem. Phys.*, vol. 109, pp. 7737–7744, Nov. 1998.

[298] G. Ciccotti and M. Ferrario, "Blue Moon Approach to Rare Events," *Molecular Simulation*, vol. 30, pp. 787–793, Sept. 2004.

[299] G. Ciccotti, R. Kapral, and E. Vanden-Eijnden, "Blue Moon Sampling, Vectorial Reaction Coordinates, and Unbiased Constrained Dynamics," *ChemPhysChem*, vol. 6, no. 9, pp. 1809–1814, 2005.

[300] A. Barducci, M. Bonomi, and M. Parrinello, "Metadynamics," *Wiley Interdisciplinary Reviews: Computational Molecular Science*, vol. 1, no. 5, pp. 826–843, 2011.

[301] M. Kılıç and B. Ensing, "Acidity constants of lumiflavin from first principles molecular dynamics simulations," *Phys. Chem. Chem. Phys.*, vol. 16, pp. 18993–19000, Aug. 2014.

[302] B. Peters, *Reaction Rate Theory and Rare Events*. Elsevier, Mar. 2017. Google-Books-ID: WeKoBAAAQBAJ.

[303] P. L. Geissler, C. Dellago, and D. Chandler, "Kinetic Pathways of Ion Pair Dissociation in Water," *J. Phys. Chem. B*, vol. 103, pp. 3706–3710, May 1999.

[304] P. G. Bolhuis, C. Dellago, and D. Chandler, "Reaction coordinates of biomolecular isomerization," *PNAS*, vol. 97, pp. 5877–5882, May 2000.

[305] R. Demuynck, J. Wieme, S. M. J. Rogge, K. D. Dedecker, L. Vanduyfhuys, M. Waroquier, and V. Van Speybroeck, "Protocol for Identifying Accurate Collective Variables in Enhanced Molecular Dynamics Simulations for the Description of Structural Transformations in Flexible Metal–Organic Frameworks," *J. Chem. Theory Comput.*, vol. 14, pp. 5511–5526, Nov. 2018.

[306] B. Peters, "Reaction Coordinates and Mechanistic Hypothesis Tests," *Annu. Rev. Phys. Chem.*, vol. 67, pp. 669–690, May 2016.

[307] M. A. Rohrdanz, W. Zheng, and C. Clementi, "Discovering Mountain Passes via Torchlight: Methods for the Definition of Reaction Coordinates and Pathways in Complex Macromolecular Reactions," *Annu. Rev. Phys. Chem.*, vol. 64, pp. 295–316, Apr. 2013.

[308] S. V. Krivov and M. Karplus, "Hidden complexity of free energy surfaces for peptide (protein) folding," *PNAS*, vol. 101, pp. 14766–14770, Oct. 2004.

[309] E. Rosta, H. L. Woodcock, B. R. Brooks, and G. Hummer, "Artificial reaction coordinate "tunneling" in free-energy calculations: The catalytic reaction of RNase H," *J. Comput. Chem.*, vol. 30, pp. 1634–1641, Aug. 2009.

[310] P. Cnudde, K. De Wispelaere, J. Van der Mynsbrugge, M. Waroquier, and V. Van Speybroeck, "Effect of temperature and branching on the nature and stability of alkene cracking intermediates in H-ZSM-5," *Journal of Catalysis*, vol. 345, pp. 53–69, Jan. 2017.

[311] H. Pelzer and E. Wigner, "Über die Geschwindigkeitskonstante von Austauschreaktionen," *Zeitschrift für Physikalische Chemie*, vol. 15B, no. 1, pp. 445–471, 1932.

[312] W. F. K. Wynne-Jones and H. Eyring, "The Absolute Rate of Reactions in Condensed Phases," *J. Chem. Phys.*, vol. 3, pp. 492–502, Aug. 1935.

[313] M. G. Evans and M. Polanyi, "Some applications of the transition state method to the calculation of reaction velocities, especially in solution," *Trans. Faraday Soc.*, vol. 31, pp. 875–894, Jan. 1935.

[314] D. G. Truhlar, B. C. Garrett, and S. J. Klippenstein, "Current Status of Transition-State Theory," *J. Phys. Chem.*, vol. 100, pp. 12771–12800, Aug. 1996.

[315] P. Hänggi, P. Talkner, and M. Borkovec, "Reaction-rate theory: fifty years after Kramers," *Rev. Mod. Phys.*, vol. 62, pp. 251–341, Apr. 1990.

[316] P. Atkins, J. d. Paula, and J. Keeler, *Atkins' Physical Chemistry*. Oxford, New York: Oxford University Press, eleventh edition ed., Dec. 2017.

[317] B. De Sterck, R. Vaneerdeweg, F. Du Prez, M. Waroquier, and V. Van Speybroeck, "Solvent Effects on Free Radical Polymerization Reactions: The Influence of Water on the Propagation Rate of Acrylamide and Methacrylamide," *Macromolecules*, vol. 43, pp. 827–836, Jan. 2010.

[318] J. Wieme, K. Lejaeghere, G. Kresse, and V. V. Speybroeck, "Tuning the balance between dispersion and entropy to design temperature-responsive flexible metal-organic frameworks," *Nat Commun*, vol. 9, pp. 1–10, Nov. 2018.

[319] J. Hajek, J. Van der Mynsbrugge, K. De Wispelaere, P. Cnudde, L. Vanduyfhuys, M. Waroquier, and V. Van Speybroeck, "On the stability and nature of adsorbed pentene in Brønsted acid zeolite H-ZSM-5 at 323 K," *Journal of Catalysis*, vol. 340, pp. 227–235, Aug. 2016.

[320] Y. Zhang and W. Yang, "Comment on "Generalized Gradient Approximation Made Simple"," *Phys. Rev. Lett.*, vol. 80, pp. 890–890, Jan. 1998.

[321] S. Jakobtorweihen, N. Hansen, and F. J. Keil, "Molecular simulation of alkene adsorption in zeolites," *Molecular Physics*, vol. 103, pp. 471–489, Feb. 2005.

[322] A. M. Al-Jarallah, U. A. El-Nafaty, and M. M. Abdillahi, "Effects of metal impregnation on the activity, selectivity and deactivation of a high silica MFI zeolite when converting methanol to light alkenes," *Applied Catalysis A: General*, vol. 154, pp. 117–127, June 1997.

[323] J. Liu, C. Zhang, Z. Shen, W. Hua, Y. Tang, W. Shen, Y. Yue, and H. Xu, "Methanol to propylene: Effect of phosphorus on a high silica HZSM-5 catalyst," *Catalysis Communications*, vol. 10, pp. 1506–1509, June 2009.

[324] J. C. Védrine, A. Auroux, P. Dejaifve, V. Ducarme, H. Hoser, and S. Zhou, "Catalytic and physical properties of phosphorus-modified ZSM-5 zeolite," *Journal of Catalysis*, vol. 73, pp. 147–160, Jan. 1982.

[325] E. A. Pidko, E. J. M. Hensen, G. M. Zhidomirov, and R. A. van Santen, "Non-localized charge compensation in zeolites: A periodic DFT study of cationic gallium-oxide clusters in mordenite," *Journal of Catalysis*, vol. 255, pp. 139–143, Apr. 2008.

[326] E. A. Pidko, R. A. van Santen, and E. J. M. Hensen, "Multinuclear gallium-oxide cations in high-silica zeolites," *Phys. Chem. Chem. Phys.*, vol. 11, pp. 2893–2902, Apr. 2009.

[327] G. Li, E. A. Pidko, R. A. van Santen, Z. Feng, C. Li, and E. J. M. Hensen, "Stability and reactivity of active sites for direct benzene oxidation to phenol in Fe/ZSM-5: A comprehensive periodic DFT study," *Journal of Catalysis*, vol. 284, pp. 194–206, Dec. 2011.

[328] G. Li, E. A. Pidko, R. A. van Santen, C. Li, and E. J. M. Hensen, "Stability of Extraframework Iron-Containing Complexes in ZSM-5 Zeolite," *J. Phys. Chem. C*, vol. 117, pp. 413–426, Jan. 2013.

[329] G. Li, E. A. Pidko, I. A. W. Filot, R. A. van Santen, C. Li, and E. J. M. Hensen, "Catalytic properties of extraframework iron-containing species in ZSM-5 for N2o decomposition," *Journal of Catalysis*, vol. 308, pp. 386–397, Dec. 2013.

[330] C. Mei, P. Wen, Z. Liu, H. Liu, Y. Wang, W. Yang, Z. Xie, W. Hua, and Z. Gao, "Selective production of propylene from methanol: Mesoporosity development in high silica HZSM-5," *Journal of Catalysis*, vol. 258, pp. 243–249, Aug. 2008.

[331] M. Milina, S. Mitchell, N.-L. Michels, J. Kenvin, and J. Pérez-Ramírez, "Interdependence between porosity, acidity, and catalytic performance in hierarchical ZSM-5 zeolites prepared by post-synthetic modification," *Journal of Catalysis*, vol. 308, pp. 398–407, Dec. 2013.

[332] J. Brus, L. Kobera, W. Schoefberger, M. Urbanová, P. Klein, P. Sazama, E. Tabor, S. Sklenak, A. V. Fishchuk, and J. Dědeček, "Structure of framework aluminum Lewis sites and perturbed aluminum atoms in zeolites as determined by 27al{1H} REDOR (3q) MAS NMR spectroscopy and DFT/molecular mechanics," *Angew. Chem. Int. Ed.*, vol. 54, pp. 541–545, Jan. 2015.

[333] E. P. Parry, "An infrared study of pyridine adsorbed on acidic solids. Characterization of surface acidity," *Journal of Catalysis*, vol. 2, pp. 371–379, Oct. 1963.

[334] F. R. Cannings, "Acidic sites on mordenite: an infrared study of adsorbed pyridine," *J. Phys. Chem.*, vol. 72, pp. 4691–4693, Dec. 1968.

[335] T. Barzetti, E. Selli, D. Moscotti, and L. Forni, "Pyridine and ammonia as probes for FTIR analysis of solid acid catalysts," *J. Chem. Soc., Faraday Trans.*, vol. 92, pp. 1401–1407, Jan. 1996.

[336] D. Meloni, S. Laforge, D. Martin, M. Guisnet, E. Rombi, and V. Solinas, "Acidic and catalytic properties of H-MCM-22 zeolites," *Applied Catalysis A: General*, vol. 215, pp. 55–66, July 2001.

[337] K. Nishi, N. Kamiya, and Y. Yokomori, "Single-crystal structure of a pyridine sorption complex of zeolite HZSM-5 (H-MFI)," *Microporous and Mesoporous Materials*, vol. 101, pp. 83–89, Apr. 2007.

[338] L. Zhang, J. Gao, J. Hu, W. Li, and J. Wang, "Lanthanum Oxides-Improved Catalytic Performance of ZSM-5 in Toluene Alkylation with Methanol," *Catal Lett*, vol. 130, pp. 355–361, July 2009.

[339] S. Baroni, S. de Gironcoli, A. Dal Corso, and P. Giannozzi, "Phonons and related crystal properties from density-functional perturbation theory," *Rev. Mod. Phys.*, vol. 73, pp. 515–562, July 2001.

[340] X. Wu, D. Vanderbilt, and D. R. Hamann, "Systematic treatment of displacements, strains, and electric fields in density-functional perturbation theory," *Phys. Rev. B*, vol. 72, p. 035105, July 2005.

[341] M. Gajdoš, K. Hummer, G. Kresse, J. Furthmüller, and F. Bechstedt, "Linear optical properties in the projector-augmented wave methodology," *Phys. Rev. B*, vol. 73, p. 045112, Jan. 2006.

[342] D. Karhánek, T. Bučko, and J. Hafner, "A density-functional study of the adsorption of methane-thiol on the (111) surfaces of the Ni-group metals: II. Vibrational spectroscopy," *J. Phys.: Condens. Matter*, vol. 22, no. 26, p. 265006, 2010.

[343] A. E. J. Hoffman, L. Vanduyfhuys, I. Nevjestić, J. Wieme, S. M. J. Rogge, H. Depauw, P. Van Der Voort, H. Vrielinck, and V. Van Speybroeck, "Elucidating the Vibrational Fingerprint of the Flexible Metal–Organic Framework MIL-53(Al) Using a Combined Experimental/Computational Approach," *J. Phys. Chem. C*, vol. 122, pp. 2734–2746, Feb. 2018.

[344] H. Fang, A. Zheng, J. Xu, S. Li, Y. Chu, L. Chen, and F. Deng, "Theoretical Investigation of the Effects of the Zeolite Framework on the Stability of Carbenium Ions," *J. Phys. Chem. C*, vol. 115, pp. 7429–7439, Apr. 2011.

[345] D. Lesthaeghe, V. V. Speybroeck, and M. Waroquier, "Theoretical evaluation of zeolite confinement effects on the reactivity of bulky intermediates," *Phys. Chem. Chem. Phys.*, vol. 11, pp. 5222–5226, June 2009.

[346] J. B. Nicholas and J. F. Haw, "The Prediction of Persistent Carbenium Ions in Zeolites," *J. Am. Chem. Soc.*, vol. 120, pp. 11804–11805, Nov. 1998.

[347] D. Mores, J. Kornatowski, U. Olsbye, and B. M. Weckhuysen, "Coke Formation during the Methanol-to-Olefin Conversion: In Situ Microspectroscopy on Individual H-ZSM-5 Crystals with Different Brønsted Acidity," *Chem. Eur. J.*, vol. 17, pp. 2874–2884, Mar. 2011.

[348] T. V. W. Janssens, S. Svelle, and U. Olsbye, "Kinetic modeling of deactivation profiles in the methanol-to-hydrocarbons (MTH) reaction: A combined autocatalytic–hydrocarbon pool approach," *Journal of Catalysis*, vol. 308, pp. 122–130, Dec. 2013.

[349] L. Vanduyfhuys, A. Ghysels, S. M. J. Rogge, R. Demuynck, and V. V. Speybroeck, "Semi-analytical mean-field model for predicting breathing in metal–organic frameworks," *Molecular Simulation*, vol. 41, pp. 1311–1328, Nov. 2015.

[350] V. Termath, F. Haase, J. Sauer, J. Hutter, and M. Parrinello, "Understanding the Nature of Water Bound to Solid Acid Surfaces. Ab Initio Simulation on HSAPO-34," *J. Am. Chem. Soc.*, vol. 120, pp. 8512–8516, Aug. 1998.

[351] G. Sastre, D. W. Lewis, and C. R. A. Catlow, "Structure and Stability of Silica Species in SAPO Molecular Sieves," *J. Phys. Chem.*, vol. 100, pp. 6722–6730, Jan. 1996.

[352] D. Marx, "Proton Transfer 200 Years after von Grotthuss: Insights from Ab Initio Simulations," *ChemPhysChem*, vol. 7, no. 9, pp. 1848–1870, 2006.

[353] J. Macht, R. T. Carr, and E. Iglesia, "Consequences of Acid Strength for Isomerization and Elimination Catalysis on Solid Acids," *J. Am. Chem. Soc.*, vol. 131, pp. 6554–6565, May 2009.

[354] N. Nikbin, P. T. Do, S. Caratzoulas, R. F. Lobo, P. J. Dauenhauer, and D. G. Vlachos, "A DFT study of the acid-catalyzed conversion of 2,5-dimethylfuran and ethylene to p-xylene," *Journal of Catalysis*, vol. 297, pp. 35–43, Jan. 2013.

[355] N. Nikbin, S. Feng, S. Caratzoulas, and D. G. Vlachos, "p-Xylene Formation by Dehydrative Aromatization of a Diels–Alder Product in Lewis and Brønsted Acidic Zeolites," *J. Phys. Chem. C*, vol. 118, pp. 24415–24424, Oct. 2014.

[356] E. A. Pidko and R. A. v. Santen, "Molecular recognition in cation-exchanged zeolites," *International Journal of Quantum Chemistry*, vol. 110, no. 1, pp. 210–220, 2010.

[357] T. E. Markland and M. Ceriotti, "Nuclear quantum effects enter the mainstream," *Nature Reviews Chemistry*, vol. 2, p. 0109, Mar. 2018.

[358] S. Habershon, T. E. Markland, and D. E. Manolopoulos, "Competing quantum effects in the dynamics of a flexible water model," *J. Chem. Phys.*, vol. 131, p. 024501, July 2009.

[359] C. Vega, M. M. Conde, C. McBride, J. L. F. Abascal, E. G. Noya, R. Ramirez, and L. M. Sesé, "Heat capacity of water: A signature of nuclear quantum effects," *J. Chem. Phys.*, vol. 132, p. 046101, Jan. 2010.

[360] M. Ceriotti, J. Cuny, M. Parrinello, and D. E. Manolopoulos, "Nuclear quantum effects and hydrogen bond fluctuations in water," *PNAS*, vol. 110, pp. 15591–15596, Sept. 2013.

[361] M. Ceriotti, W. Fang, P. G. Kusalik, R. H. McKenzie, A. Michaelides, M. A. Morales, and T. E. Markland, "Nuclear Quantum Effects in Water and Aqueous Systems: Experiment, Theory, and Current Challenges," *Chem. Rev.*, vol. 116, pp. 7529–7550, July 2016.

[362] A. Lamaire, J. Wieme, S. M. J. Rogge, M. Waroquier, and V. Van Speybroeck, "On the importance of anharmonicities and nuclear quantum effects in modelling the structural properties and thermal expansion of MOF-5," *J. Chem. Phys.*, vol. 150, p. 094503, Mar. 2019.

[363] C. R. Schwantes and V. S. Pande, "Improvements in Markov State Model Construction Reveal Many Non-Native Interactions in the Folding of NTL9," *J. Chem. Theory Comput.*, vol. 9, pp. 2000–2009, Apr. 2013.

[364] G. Pérez-Hernández, F. Paul, T. Giorgino, G. De Fabritiis, and F. Noé, "Identification of slow molecular order parameters for Markov model construction," *J. Chem. Phys.*, vol. 139, p. 015102, July 2013.

[365] C. R. Schwantes and V. S. Pande, "Modeling Molecular Kinetics with tICA and the Kernel Trick," *J. Chem. Theory Comput.*, vol. 11, pp. 600–608, Feb. 2015.

[366] W. Chen and A. L. Ferguson, "Molecular enhanced sampling with autoencoders: On-the-fly collective variable discovery and accelerated free energy landscape exploration," *Journal of Computational Chemistry*, vol. 39, no. 25, pp. 2079–2102, 2018.

[367] W. Chen, A. R. Tan, and A. L. Ferguson, "Collective variable discovery and enhanced sampling using autoencoders: Innovations in network architecture and error function design," *J. Chem. Phys.*, vol. 149, p. 072312, May 2018.

[368] C. Wehmeyer and F. Noé, "Time-lagged autoencoders: Deep learning of slow collective variables for molecular kinetics," *J. Chem. Phys.*, vol. 148, p. 241703, Mar. 2018.

[369] D. Branduardi, F. L. Gervasio, and M. Parrinello, "From A to B in free energy space," *The Journal of Chemical Physics*, vol. 126, p. 054103, Feb. 2007.

[370] P. G. Bolhuis, D. Chandler, C. Dellago, and P. L. Geissler, "TRANSITION PATH SAMPLING: Throwing Ropes Over Rough Mountain Passes, in the Dark," *Annu. Rev. Phys. Chem.*, vol. 53, pp. 291–318, Oct. 2002.

[371] T. S. van Erp, D. Moroni, and P. G. Bolhuis, "A novel path sampling method for the calculation of rate constants," *J. Chem. Phys.*, vol. 118, pp. 7762–7774, Apr. 2003.

[372] D. Moroni, T. S. van Erp, and P. G. Bolhuis, "Investigating rare events by transition interface sampling," *Physica A: Statistical Mechanics and its Applications*, vol. 340, pp. 395–401, Sept. 2004.

[373] A. J. Medford, C. Shi, M. J. Hoffmann, A. C. Lausche, S. R. Fitzgibbon, T. Bligaard, and J. K. Nørskov, "CatMAP: A Software Package for Descriptor-Based Microkinetic Mapping of Catalytic Trends," *Catal Lett*, vol. 145, pp. 794–807, Mar. 2015.

[374] A. J. Medford, A. Vojvodic, J. S. Hummelshøj, J. Voss, F. Abild-Pedersen, F. Studt, T. Bligaard, A. Nilsson, and J. K. Nørskov, "From the Sabatier principle to a predictive theory of transition-metal heterogeneous catalysis," *Journal of Catalysis*, vol. 328, pp. 36–42, Aug. 2015.

[375] L. C. Grabow, F. Studt, F. Abild-Pedersen, V. Petzold, J. Kleis, T. Bligaard, and J. K. Nørskov, "Descriptor-Based Analysis Applied to HCN Synthesis

from NH3 and CH4," *Angewandte Chemie International Edition*, vol. 50, no. 20, pp. 4601–4605, 2011.

[376] A. A. Latimer, A. R. Kulkarni, H. Aljama, J. H. Montoya, J. S. Yoo, C. Tsai, F. Abild-Pedersen, F. Studt, and J. K. Nørskov, "Understanding trends in C-H bond activation in heterogeneous catalysis," *Nat Mater*, vol. 16, pp. 225–229, Feb. 2017.

[377] M. K. Sabbe, M.-F. Reyniers, and K. Reuter, "First-principles kinetic modeling in heterogeneous catalysis: an industrial perspective on best-practice, gaps and needs," *Catal. Sci. Technol.*, vol. 2, pp. 2010–2024, Sept. 2012.

[378] A. Banerjee, A. P. van Bavel, H. P. C. E. Kuipers, and M. Saeys, "CO Activation on Realistic Cobalt Surfaces: Kinetic Role of Hydrogen," *ACS Catal.*, vol. 7, pp. 5289–5293, Aug. 2017.

[379] I. A. W. Filot, R. J. P. Broos, J. P. M. van Rijn, G. J. H. A. van Heugten, R. A. van Santen, and E. J. M. Hensen, "First-Principles-Based Microkinetics Simulations of Synthesis Gas Conversion on a Stepped Rhodium Surface," *ACS Catal.*, vol. 5, pp. 5453–5467, Sept. 2015.

[380] C.-M. Wang, R. Y. Brogaard, B. M. Weckhuysen, J. K. Nørskov, and F. Studt, "Reactivity Descriptor in Solid Acid Catalysis: Predicting Turnover Frequencies for Propene Methylation in Zeotypes," *J. Phys. Chem. Lett.*, vol. 5, pp. 1516–1521, May 2014.

[381] C.-M. Wang, R. Y. Brogaard, Z.-K. Xie, and F. Studt, "Transition-state scaling relations in zeolite catalysis: influence of framework topology and acid-site reactivity," *Catal. Sci. Technol.*, vol. 5, pp. 2814–2820, Apr. 2015.

[382] R. Y. Brogaard, C.-M. Wang, and F. Studt, "Methanol–Alkene Reactions in Zeotype Acid Catalysts: Insights from a Descriptor-Based Approach and Microkinetic Modeling," *ACS Catal.*, vol. 4, pp. 4504–4509, Dec. 2014.

[383] M. Vandichel, D. Lesthaeghe, J. V. d. Mynsbrugge, M. Waroquier, and V. Van Speybroeck, "Assembly of cyclic hydrocarbons from ethene and propene in acid zeolite catalysis to produce active catalytic sites for MTO conversion," *Journal of Catalysis*, vol. 271, pp. 67–78, Apr. 2010.

[384] R. Khare, S. S. Arora, and A. Bhan, "Implications of Cofeeding Acetaldehyde on Ethene Selectivity in Methanol-to-Hydrocarbons Conversion on MFI and Its Mechanistic Interpretation," *ACS Catal.*, vol. 6, pp. 2314–2331, Apr. 2016.

[385] S. Seghers, L. Protasova, S. Mullens, J. W. Thybaut, and C. V. Stevens, "Improving the efficiency of the Diels–Alder process by using flow chemistry and zeolite catalysis," *Green Chemistry*, vol. 19, no. 1, pp. 237–248, 2017.

[386] C. Bernardon, B. Louis, V. Bénéteau, and P. Pale, "Diels–Alder Reaction between Isoprene and Methyl Acrylate over Different Zeolites: Influence of Pore Topology and Acidity," *ChemPlusChem*, vol. 78, no. 9, pp. 1134–1141, 2013.

[387] T. R. Carlson, T. P. Vispute, and G. W. Huber, "Green Gasoline by Catalytic Fast Pyrolysis of Solid Biomass Derived Compounds," *ChemSusChem*, vol. 1, no. 5, pp. 397–400, 2008.

[388] R. E. Patet, M. Koehle, R. F. Lobo, S. Caratzoulas, and D. G. Vlachos, "General Acid-Type Catalysis in the Dehydrative Aromatization of Furans to Aromatics in H-[Al]-BEA, H-[Fe]-BEA, H-[Ga]-BEA, and H-[B]-BEA Zeolites," *J. Phys. Chem. C*, vol. 121, pp. 13666–13679, June 2017.

[389] S. Müller, Y. Liu, M. Vishnuvarthan, X. Sun, A. C. van Veen, G. L. Haller, M. Sanchez-Sanchez, and J. A. Lercher, "Coke formation and deactivation pathways on H-ZSM-5 in the conversion of methanol to olefins," *Journal of Catalysis*, vol. 325, pp. 48–59, May 2015.